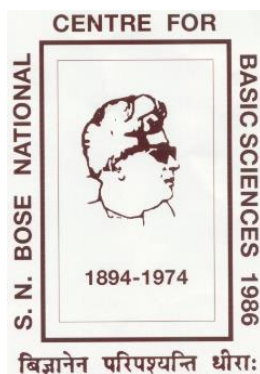# Understanding the Structural and Dynamical Complexities of Neat and Multi-component Media

Thesis Submitted for the degree of

Doctor of Philosophy (Science)

of

Jadavpur University

By

Narayan Chandra Maity

Department of Chemical, Biological and Macromolecular Sciences

S. N. Bose National Centre for Basic Sciences

Block - JD, Sector - III, Salt Lake

Kolkata - 700106, India

August 2024

S.N. Bose National Centre for Basic Sciences
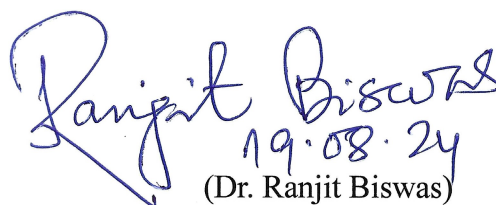### Sector - III, Block - JD, Salt Lake, Kolkata - 700098

Dr. Ranjit Biswas
Senior Professor
Chemical and Biological Sciences

Phone: 033 2335 5706-08 (O)
email: ranjit@bose.res.in
Fax: 033 2335 3477

CERTIFICATE FROM THE SUPERVISOR

This is to certify that the thesis entitled "**Understanding the Structural and Dynamical Complexities of Neat and Multi-component Media**" submitted by Sri Narayan Chandra Maity (Index No. – 31/19/Chem./26 and Registration No.: SCHEM1103119) who got his name registered on 21/08/2019 for the award of Ph.D. (Science) degree of Jadavpur University, is absolutely based upon his own work under the supervision of Prof. Ranjit Biswas and that neither this thesis nor any part of it has been submitted for either any degree/diploma or any other academic award anywhere before.

Ranjit Biswas
19·08·24
(Dr. Ranjit Biswas)

DR. RANJIT BISWAS
Senior Professor
Dept. of Chemical, Biological & Macromolecular Sciences
S. N. Bose National Centre for Basic Sciences
Block - JD, Sector-III, Salt Lake, Kolkata - 700 106, India

Dedicated to

my Parents Badal Chandra Maity and Bani Maity

my wife Santana Maity

my sister's Sulekha Patra and Radharani Maity

my brother-in-law's Ashok Patra and Soumen Maity

Acknowledgement

Abstract

The thesis entitled "**Understanding the Structural and Dynamical Complexities of Neat and Multi-component Media**" investigates the structure and relaxation dynamics of various neat solvents and multi-component complex media. By delving into the fundamental aspects of these systems, this research aims to enhance our understanding of their behaviour and properties, contributing to the advancements in fields such as pharmaceuticals, cryopreservation, energy storage, and biomedical applications. The goal is to provide a foundation for further research and practical applications where fundamental scientific understanding is lacking.

The first begins with the investigating water-octanol mixtures across various water mole fractions, which are pivotal in structural biology, drug delivery, and pharmaceutical chemistry. The second focus is to explore the interaction, dynamics, and solution heterogeneity in multi-component cryoprotectant mixtures with glucose/ethylene glycol and disaccharides dehydrates/glycerol based cryoprotectant mixtures (where disaccharides used as trehalose and sucrose) which are biodegradable, non-toxic and cheap cost, and play a crucial role in preserving organ, live cell, tissues, DNA, proteins and other substances at very low temperatures. The third area of interest is to explore the interaction and dynamics of electrolyte media used in lithium-ion batteries, capacitors, and energy storage devices for electrical vehicles. The fourth area of interest is the investigation of the sol→gel transition of biopolymer in aqueous media, which undergo structural transitions in response to external stimuli such as agitation or temperature. Understanding the structure, interaction, and relaxation dynamics of this biopolymer is essential for the development of tissue engineering, cell culture, and bioscaffold, particularly in the biomedical field of fibrosis leading to organ dysfunction.

In this thesis, dielectric relaxation (DR) spectroscopy is employed in the Hz-GHz frequency range (20 HZ to 50 GHZ) to investigate the reorientation dynamics of dipolar species in specific media. To elucidate system interactions and spatial-temporal heterogeneity, the research employs steady-state fluorescence, and time-resolved fluorescence (TRF) techniques, including time-correlated single photon counting (TCSPC) and two-dimensional streak camera (2DSC) measurements. Additionally, a variety of experimental techniques and computer simulations are employed to thoroughly investigate these complex media. Such experiments are dynamic light scattering (DLS), differential scanning calorimetry (DSC), and cryo-transmission electron microscopy (cryo-TEM).

Chapter 1 of this Thesis provides an introductory overview of the research work and reviews pertinent literature. In Chapter 2, a succinct explanation of the experimental techniques and data analysis procedures employed in this Thesis is presented. Moving on to Chapter 3, a thorough investigation is undertaken on octanol-water mixtures within the octanol-rich region. This exploration unveils water concentration-dependent alterations in structure, reorientation dynamics, intra and inter-species hydrogen bonding, and dielectric properties of these mixtures, along with variations in angle distribution and tetrahedral order parameters of water. This comprehensive analysis is conducted through experimental techniques such as DRS and DSC, coupled with computer simulations. Chapter 4 provides an exploration of the interactions, dynamics, and solution heterogeneity of pure octanol and water/octanol mixtures. This investigation employs steady state fluorescence and TRF measurements within the temperature range of 283≤T/K≤323, considering various mole fractions of water in the octanol-rich aqueous solution. In Chapter 5 and Chapter 6, an extensive investigation is conducted on glucose concentrations dependent glucose/ethylene glycol cryoprotectant mixtures, exploring various aspects such as thermo-physical properties, particle size, reorientation relaxation dynamics, ultrafast Stokes dynamics, viscosity coupling, and solution heterogeneity. This comprehensive exploration utilizes diverse experimental techniques, including DSC, DLS, DRS, steady state fluorescence, TRF-2DSC, and TRF-TCSPC measurements. In Chapter 7, a systematic investigation unfolds, delving into the interaction, dynamics, and solution structure of disaccharides dihydrate/glycerol cryoprotectant mixtures. This exploration employs a combination of experimental techniques and molecular dynamics simulation methods. Chapter 8, a detailed exploration of the co-solvent concentration-dependent melting temperature, conductivity, dielectric properties, reorientation relaxation dynamics, and viscosity coupling of LIB electrolytes are explored through experiments. Additionally, molecular-level insights into solvation structure, component-wise diffusion, transport number, and ionic conductivity are revealed through molecular dynamics simulations. Chapter 9 focuses on the investigation of sol→gel transition with hyaluronic acid (HA) concentration (wt% of HA= 0, 0.15, 0.3, 0.5, 0.65, 0.75, 1, 1.5, 2). This exploration is carried out through refractive index measurement and steady-state fluorescence intensity measurement of Triflavin-T (ThT). The chapter also explores the hydrogel structure, reversibility, and the interactions of different organic fluorophore solutes to gain insights into the characteristics of hydrogels that could find applications in various fields and address pathology and dysfunction health issues in humans. Finally, Chapter 10 wraps up the thesis by providing concluding remarks and highlighting important areas for future exploration

সারমর্ম

এই থিসিসে বিভিন্ন রকমের পরীক্ষামূলক পদ্ধতি এবং কম্পিউটার সিমুলেশন ব্যবহার করে ভিন্ন প্রকার শুদ্ধ এবং সংমিশ্রিত তরল মাধ্যমের কাঠামোগত এবং গতিবিদ্যা সংক্রান্ত ধর্মগুলি আলোচনা করা হয়েছে। এই গবেষণার লক্ষ্য হলো এই মাধ্যমগুলির মৌলিক দিকগুলির অনুসন্ধান করে তাদের আচরণ এবং বৈশিষ্ট্যগুলি সম্পর্কে জ্ঞান অর্জন করা যা ফার্মাসিউটিক্যালস, ক্রায়োপ্রিজারভেশন, শক্তি সঞ্চয়স্থান এবং বায়োমেডিকাল শিল্পগুলির অগ্রগতিতে সহায়ক হবে। এই গবেষণার আরও একটি দিক হলো গবেষণা এবং ব্যবহারিক প্রয়োগের জন্য একটি ভিত্তি প্রদান করা যেখানে মৌলিক বৈজ্ঞানিকদের বোঝার অভাব রয়েছে।

এই থিসিসে, প্রথমত বিভিন্ন অনুপাতে অক্টানলের মধ্যে জল মিশিয়ে অক্টানল-জল মিশ্রণের তদন্ত করা হয়েছে, যা কাঠামোগত জীববিজ্ঞান, ওষুধ সরবরাহ এবং ফার্মাসিউটিক্যাল রসায়নে গুরুত্বপূর্ণ। দ্বিতীয়ত গ্লুকোজ/ইথিলিন গ্লাইকোল এবং দুই অনু জল যুক্ত দ্বি-স্যাকারাইডস/গ্লিসারল ক্রায়োপ্রোটেক্ট্যান্ট মিশ্রণের মিথস্ক্রিয়া, গতিশীলতা এবং দ্রাবনের বৈচিত্র্য অন্বেষণ করা, যেখানে দ্বি-স্যাকারাইড হিসাবে ট্রিহ্যালোজ এবং সুক্রোজ ব্যাবহার করা হয়েছে। এই ক্রায়োপ্রোটেক্ট্যান্ট মিশ্রণগুলি বেছে নেওয়ার কারণ হলো: দামে কম, অণুজীব দ্বারা পচনশীল, কোন রকম ক্ষতিকারক দিক নেই, এবং খুব কম তাপমাত্রায় অঙ্গ, জীবন্ত কোষ, ডিএনএ, প্রোটিন এবং অন্যান্য পদার্থ সংরক্ষণে একটি গুরুত্বপূর্ণ ভূমিকা পালন করে। তৃতীয়ত লিথিয়াম-আয়ন ব্যাটারি, ক্যাপাসিটর এবং বৈদ্যুতিক যানবাহনের জন্য শক্তি সঞ্চয়কারী যন্ত্রপাতিতে ব্যবহৃত ইলেক্ট্রোলাইট দ্রাবনের মিথস্ক্রিয়া এবং গতিশীলতা অন্বেষণ করা। চতুর্থ ক্ষেত্রে জলীয় মাধ্যমে হায়ালুরনিক অ্যাসিডের সল—➤জেল রূপান্তর তদন্ত করা হয়েছে, যা উদ্দীপনা প্রতিক্রিয়ায় কাঠামোগত পরিবর্তনের মধ্য দিয়ে যায়। এই হায়ালুরনিক অ্যাসিডের গঠন, মিথস্ক্রিয়া এবং গতিবিদ্যা বোঝা টিস্যু ইঞ্জিনিয়ারিং, কোষ সংস্কৃতি এবং বায়োস্ক্যাফোল্ডের নির্মাণ বিকাশের জন্য অপরিহার্য, বিশেষ করে ফাইব্রোসিসের রোগ যা মানবদেহে অঙ্গ বিকল করে দেয়।

এই থিসিসে, ডাইলেকট্রিক রিলাক্সেশন স্পেকট্রোস্কোপি (২০ হার্জ থেকে ৫০ গিগাহার্জ ফ্রিকোয়েন্সি পরিসীমাতে) দ্বারা নির্দিষ্ট দ্বিপোলার মাধ্যমের পুনর্বিন্যাস গতিবিদ্যা তদন্ত করা হয়। তরল মাধ্যমের মিথস্ক্রিয়া এবং স্থানিক-সময়গত বৈচিত্র্যকে ব্যাখ্যা করার জন্য, গবেষণায় স্থির-অবস্থা ফ্লুরোসেন্স এবং টাইম-অধীন ফ্লুরোসেন্স (যার জন্য টাইম কোরিরেলেটেড সিংগল ফটোন কউন্টিং এবং দ্বি-মাত্রিক স্ট্রিক ক্যামেরা ব্যবহার করা হয়েছে) কৌশলগুলি নিয়োগ করা হয়েছে। উপরন্তু, এই জটিল মাধ্যমগুলি পুঙ্খানুপুঙ্খভাবে তদন্ত করার জন্য বিভিন্ন পরীক্ষামূলক কৌশল এবং কম্পিউটার সিমুলেশন নিযুক্ত করা হয়। এই ধরনের পরীক্ষাগুলি হল ডাইনামিক লাইট স্ক্যাটারিং, ডিফারেনশিয়াল স্ক্যানিং ক্যালোরিমেট্রি, এবং ক্রায়ো-ট্রান্সমিশন ইলেক্ট্রন মাইক্রোস্কোপি।

এই থিসিসের প্রথম অধ্যায়ে গবেষণার কাজের সঙ্গে সম্পর্কিত কাজগুলির পর্যালোচনা করা হয়েছে। দ্বিতীয় অধ্যায়ে এই থিসিসে নিযুক্ত পরীক্ষামূলক কৌশল এবং তথ্য বিশ্লেষণ পদ্ধতির একটি সংক্ষিপ্ত ব্যাখ্যা উপস্থাপন করা হয়েছে। তৃতীয় অধ্যায়ে অক্টানল-সমৃদ্ধ অঞ্চলের অক্টানল-জলের মিশ্রণের উপর একটি পুঙ্খানুপুঙ্খ তদন্ত করা হয়। এই অন্বেষণটি জলের ঘনত্ব-নির্ভর পরিবর্তনগুলিকে উন্মোচন করে যা গঠন, পুনর্বিন্যাস গতিবিদ্যা, অন্তঃ এবং আন্তঃ-হাইড্রোজেন বন্ধন, এবং জলের অনুগুলির মধ্যে কোনের বন্টন এবং জলের টেট্রাহেড্রাল অর্ডার পারামিটার তারতম্য বোঝাযায়। এই তদন্তটি ডিআরএস এবং ডিএসসির মতো পরীক্ষামূলক কৌশল এবং কম্পিউটার সিমুলেশনের বিশ্লেষণ মাধ্যমে সম্পন্ন হয়েছে। চতুর্থ অধ্যায় বিশুদ্ধ অক্টানল এবং জল/অক্টানল মিশ্রণের মিথস্ক্রিয়া, গতিশীলতা এবং দ্রাবনের বৈচিত্র্যের একটি

অনুসন্ধান প্রদান করে। এই তদন্তটি ২৮৩ থেকে ৩২৩ তাপমাত্রার সীমার মধ্যে গবেষণায় স্থির-অবস্থা ফ্লুরোসেন্স এবং টাইম-অধীন ফ্লুরোসেন্স পরিমাপ করা হয় যা অক্টানল-সমৃদ্ধ জলীয় দ্রবণে জলের বিভিন্ন মোল ভগ্নাংশ পরিবর্তন করে। পঞ্চম এবং ষষ্ঠ অধ্যায়ে, গ্লুকোজ ঘনত্বের উপর নির্ভরশীল গ্লুকোজ/ইথিলিন গ্লাইকোল ক্রায়োপ্রোটেক্ট্যান্ট মিশ্রণের উপর একটি বিস্তৃত তদন্ত পরিচালিত হয়েছে, যেখানে ভৌততাপ পরিবতনের বৈশিষ্ট্য, যৌগিক কণাগুলির আকার, পুনর্বিন্যাস গতিবিদ্যা, অতিদ্রুত সময়ের স্টোকস স্থানতর গতিবিদ্যা, সান্দ্রতার সহিত গতিবিদ্যার মিথস্ক্রিয়া এবং দ্রবনের বৈচিত্র উন্মোচন হয়েছে। এই বিস্তৃত অন্বেষণটি বিভিন্ন পরীক্ষামূলক কৌশল ব্যবহার করাহয়, যার মধ্যে রয়েছে ডাইনামিক লাইট স্ক্যাটারিং, ডিফারেনশিয়াল স্ক্যানিং ক্যালোরিমেট্রি, ডাইলেকট্রিক রিলাক্সেশন স্পেকট্রোস্কোপি, স্থির-অবস্থা ফ্লুরোসেন্স এবং সময়ের-অধীন ফ্লুরোসেন্স (যার জন্য টাইম কোরিরেলেটেড সিংগল ফোটোন কউন্টিং এবং দ্বি-মাত্রিক স্ট্রিক ক্যামেরা ব্যবহার করা হয়েছে)। সপ্তম অধ্যায়ে, দ্বি-স্যাকারাইডস দ্বি-হাইড্রেট/গ্লিসারল ক্রায়োপ্রোটেক্ট্যান্ট মিশ্রণের মিথস্ক্রিয়া, গতিশীলতা এবং দ্রবনের কাঠামোর মধ্যে একটি পদ্ধতিগত তদন্ত কার হয়েছে। এই অন্বেষণ পরীক্ষামূলক কৌশল এবং কম্পিউটার সিমুলেশন পদ্ধতির সংমিশ্রণ নিযুক্ত করে। অষ্টম অধ্যায়, সহ-দ্রাবক ঘনত্ব-নির্ভর লিথিয়াম আয়ন ইলেক্ট্রোলাইটগুলির গলনের তাপমাত্রা, পরিবাহিতা, ডাইইলেকট্রিক বৈশিষ্ট্য, পুনর্বিন্যাস গতিবিদ্যা, এবং সান্দ্রতার সহিত গতিবিদ্যার মিথস্ক্রিয়া পরীক্ষামূলক অন্বেষণ করা হয়েছে। উপরন্তু, গঠন বৈচিত্র, উপাদান ভিত্তিক চলন, ট্রান্সপোর্ট নম্বর এবং আয়নিক পরিবাহিতা সম্পর্কে আণবিক-স্তরের কম্পিউটার সিমুলেশনের মাধ্যমে প্রকাশিত হয়েছে। নবম অধ্যায়ে হায়ালুরোনিক অ্যাসিড ঘনত্বের (০, ০.১৫, ০.৩, ০.৫, ০.৬৫, ০.৭৫, ১, ১.৫, ২) সাথে সল →জেল পরিবর্তনের তদন্তের উপর দৃষ্টি নিবদ্ধ করে। এই অন্বেষণটি প্রতিসরাঙ্ক সূচক পরিমাপ এবং থাওফ্লাভিন-টি এর ফ্লুরোসেন্স তীব্রতা পরিমাপের মাধ্যমে বাহিত হয়। অধ্যায়টি হাইড্রোজেলের গঠন, তাপমাত্রার সহিত প্রত্যাবর্তনযোগ্যতা, এবং বিভিন্ন জৈব ফ্লুরোফোর অনুর মিথস্ক্রিয়া অন্বেষণ করে, যা বিভিন্ন ক্ষেত্রে প্রয়োগ এবং মানুষের মধ্যে অঙ্গ বিকালের সমস্যাগুলির সমাধান করা যেতে পারে। পরিশেষে, দশম অধ্যায় সংক্ষিপ্ত উপসংহার প্রদান করে এবং ভবিষ্যতের অন্বেষণের জন্য গুরুত্বপূর্ণ ক্ষেত্রগুলিকে দৃষ্টিগোচর করে থিসিসটি সমাপ্ত করে।

List of publications

1. "Impact and structure of water in aqueous octanol mixtures: Hz-GHz dielectric relaxation measurements and computer simulations" by **Narayan Chandra Maity**, Atanu Baksi, Kajal Kumbhakar and Ranjit Biswas, *J. Photochem. Photobiol. A: Chem, 2023, **439**, 114600**.

2. "Insight water mediated spatio-temporal heterogeneity in octanol-water mixture in octanol rich region: Revealing via time-resolved fluorescence measurements and molecular dynamic simulation" by **Narayan Chandra Maity**, Atanu Baksi, Kajal Kumbhakar and Ranjit Biswas, ***J. Mol. Liq.** (Submitted)*.

3. "Exploring glucose-dependent solution structure, dynamics and thermo-physical properties of glucose/ethylene glycol cryoprotectant mixtures: A comprehensive investigation" by **Narayan Chandra Maity**, Jayanta Mondal and Ranjit Biswas, *(To be Submitted)*.

4. "Ultrafast Solvation Dynamics and Viscosity Decoupling in Glucose/Ethylene glycol Cryoprotectant Mixture: A Steady State and Time-Resolve Fluorescence Measurement Using Streak Camera and TCSPC Techniques" by **Narayan Chandra Maity**, and Ranjit Biswas, *(To be Submitted)*.

5. "Unravelling the Molecular-Level Insight into the Structure and Dynamics of Glycerol-Disaccharides Dihydrate Binary Mixtures: Integrating Experimental Observations and Molecular Dynamics Simulation" by **Narayan Chandra Maity** and Ranjit Biswas, (*To be Submitted*)

6. "Co-solvent dependent modulation of solutions structure and dynamics of Li-based battery electrolytes" by **Narayan Chandra Maity**, Sudipta Mitra and Ranjit Biswas, (*To be Submitted*).

7. "Sol-Gel transition of Hyaluronic Acid Leading to Organ Dysfunction: Exploring the Critical Concentration for Sol-Gel Transition, Sol-Gel Structure and Dynamics of Organic Solutes in Aqueous Solutions of Hyaluronic Acid: A Comprehensive Exploration Using Various Spectroscopic Techniques" by **Narayan Chandra Maity**[†], Jayanta Mondal[†] and Ranjit Biswas, (*To be Submitted*) [[†] equal contribution].

8. *"Mechanistic insight into functionally different human islet polypeptide (hIAPP) amyloid: the intrinsic role of the C-terminal structural motifs" by Dibakar Sarkar, **Narayan Chandra Maity**, Gourav Shome, Kyriakos Gabriel Varnava, Vijayalekshmi Sarojini, Subramanian

Vivekanandan, Nirakar Sahoo, Sourav Kumar, Atin Kumar Mandal, Ranjit Biswas, Anirban Bhunia, *Phys. Chem. Chem. Phys.*, 2022, **24**, 22250–22262.

9. *"Detection of ultrafast solvent dynamics employing a streak camera" by Jayanta Mondal[†], **Narayan Chandra Maity**[†], Ranjit Biswas, *J. Chem. Sci.*, 2023, **135**, 1–12. [[†] equal contribution].

10. *"Modulatory role of copper on hIAPP aggregation and toxicity in presence of insulin" by Dipanwita Roy, **Narayan Chandra Maity**, Sourav Kumar, Anupam Maity, Bhisma N. Ratha, Ranjit Biswas, Nakul Chandra Maiti, Atin Kumar Mandal, Anirban Bhunia, *Int. J. Biol. Macromol.*, 2023, 124470.

11. *"Structure and dynamics of a glucose-based cryoprotectant mixture: A computer simulation study" by Dhrubajyoti Maji, **Narayan Chandra Maity**, Ranjit Biswas, *Theor. Chem. Acc.*, 2023, **142**, 1–15.

12. *"Identical Diffusion Distributions and Co-Cluster Formation Dictate Azeotrope Formation: Microscopic Evidences and Experimental Signatures" by Shrestha Chowdhury, **Narayan Chandra Maity**, Kajal Kumbhakar, Pradip Ghorai, Ranjit Biswas, *J. Phys. Chem. B*, 2023, **127**, 8417–8431.

13. *"Anomalous Concentration Fluctuation in Amphiphilic-Water Binary Mixtures: Independent Confirmation via Label-Free SPR Measurements" by Jayeta Banerjee, **Narayan Chandra Maity**, Manik Pradhan and Ranjit Biswas (*To be Submitted*).

*not included in this thesis.

Contents

Chapter 6: Ultrafast Solvation Dynamics and Viscosity Decoupling in Glucose/Ethylene glycol Cryoprotectant Mixture: Time-Resolve Fluorescence Measurements Using Streak Camera and TCSPC Techniques

Chapter 9: Sol-Gel Transition of Hyaluronic Acid Leading to Organ Dysfunction: Exploring the Critical Concentration for Sol-Gel Transition, Structure and Dynamics of Organic Solutes in Aqueous Solutions of Hyaluronic Acid……………………………297

Chapter 1

Introduction

In contemporary research and technological advancement, there is a remarkable shift towards the synthesis of tailored media. The properties of constituent components in the liquid state play a vital role in shaping diverse reactions within these media.[1–7] Understanding the structural, dynamical and thermophysical properties of neat and multicomponent complex media is crucial, given their widespread applications in fields such as biomedical applications[8–14], cryopreservation technology[15–22], and battery electrolytes[23–29] etc. Such an understanding can help designing new media with desired properties. Altering the components or their ratio in binary and multicomponent media allows for the fine-tuning of structural, dynamical, and other properties.[30–33] Moreover, the interplay between viscosity and polarity within a medium can alter the reaction barrier along the reaction coordinate.[24,27,34–37] In parallel, considerations of non-toxicity, good glass-forming ability, and hydrogen bond formation are integral to the solvent design for preservation technology.[20,38–41] This area of interest holds significant importance in tailoring reactions through a meticulous design of reaction media.[42,43] Simultaneously, the chemical components employed in neat and multicomponent media must align with criteria such as cost-effectiveness, biodegradability, eco-friendliness, recyclability, and a natural-source origin.[32–34,42,44,45] The collective effort of extensive experimental and computer simulation now offers accessible insights into the microscopic structures, dynamics, and other parameters of both neat and multicomponent complex media.[46–61] This confluence of scientific investigation paves the way for advancements in the designing and engineering of new media that are not only effective but also environmentally less hazardous and economically viable.

This Thesis examines a range of complex systems that hold significance in both basic science aspects and technology sector. The selection process involves a scrupulous consideration of potential systems, ensuring a comprehensive and systematic investigation. For this Thesis, the investigation focuses on membrane-mimicking systems like octanol-water system, which holds

great importance in the fields of structural biology and the pharmaceutical industry.[14,62–70] Understanding the impact of water on structure, dynamics, interaction with foreign solutes, and solute dynamics in aqueous-octanol systems is necessary for the development of structural biology and the pharmaceutical industry. Furthermore, research interest has been directed towards cryopreservation systems, which have significant importance in the field of preservation technology for proteins, DNA, tissues, cells, and organs.[71–75] A wide variety of osmolytes (termed as cryoprotectants) like ethylene glycol (EG), glycerol (Gl), glucose, trehalose, sucrose, etc., are used in designing neat and multicomponent cryoprotectant systems.[19,20,76–79] The efficiency of these cryopreservation systems depends on the properties of cryoprotectant components that are desirable to be non-toxic, have a suitable glass transition temperature, and have a good propensity for hydrogen bond formation. Hence, exploration of properties like glass transition temperature, structure, dynamics, and solution heterogeneity of cryopreservation systems will be helpful in the development of the cryopreservation industry.

Next, the investigation extends to liquid electrolyte systems with several applications in electrochemical devices such as Li-ion primary and secondary batteries, supercapacitors, solar cells, sensors, etc.[23,27,28,47,56,80–92] In electrolyte solutions, changes in electrolyte salt concentration, solvent polarity, and transport properties like viscosity, or the addition of cosolvent, brings in improvements in the efficiency and durability of electrochemical devices.[56,93,94] Polar solvents like ethylene carbonate (EC), adiponitrile (ADN), and glutaronitrile (GLN) with high to moderate static dielectric constant (ε_s) and low viscosity provide a good solvent for designing electrolyte solutions.[83,84,92,94] Lithium bis-(trifluoromethane sulfonyl) imide (LiTFSI) has been used as a lithium salt in electrolyte solutions for its good electrochemical efficacy, stability to anodic reactions, high thermal stability, and high solubility in different organic solvents.[83,95,96] Finally, there is an interest in external stimuli-dependent (like mechanical shaking) sol-gel transition of aqueous bio-polymer like hyaluronic acid (HA).[10,97–99] This HA is a major component of the skin and various parts of the body such as the lung, kidneys, brain, muscle, and liver.[98–100] Organ dysfunction due to HA aggregation (called fibrosis) is an issue in the medical field.[101,102] This complex system has potential applications in drug delivery, tissue engineering, and biomedical applications.[10,97,103–105] Exploring sol-gel transformation, characterizing the structure, and interaction dynamics of

different organic solutes will be helpful in curing fibrosis disease for medical complications of organ dysfunction.

Dielectric relaxation spectroscopy (DRS), steady-state UV-Vis absorption, steady-state fluorescence emission, time-resolved fluorescence (TRF) emission spectroscopy (time-correlated single-photon counting (TCSPC) and two-dimensional streak camera (2DSC)), and computer simulation have been employed to investigate the structure, dynamics of these neat and multicomponent complex chemical systems.[45,56,106–112] DRS measurement is a technique that measures dipole moment reorientation of dipolar species present in a complex polar system.[106,108–110] An electromagnetic wave (generally MHz to GHz) generated from alternative current (AC) is applied, and simultaneously, the total polarization relaxation (mainly from dipole orientation and ion diffusion) is collected from the investigated system, providing knowledge on dipolar relaxation dynamics. This experimental technique is extensively employed in neat and multi-component complex systems to explore relaxation dynamics associated with simple or cooperative dipole reorientation of dipolar species present in these media.[111,113–116] This experimental method in electrolyte solution mixture gives indirect but useful information about ion-pair formation, ion-solvent interactions. Note that special attention is needed for the analysis of DRS data collected from conducting solutions due to the divergence of conductivity at $\nu \rightarrow 0$.[111,115] Understanding the different types of water dynamics (like bulk, bound, confinement, and hydration water) in aqueous systems of polymers, micelles, biological systems, and water as an ultra-low component, DRS has been used as a standard measurement technique.

Next, steady-state UV-visible absorption, steady-state fluorescence emission, and time-resolved fluorescence (TRF) emission spectroscopy have been employed to explore external solute-centric probe-medium interactions, dynamics, and solution heterogeneity in investigated systems.[117–119] Two non-reactive well-known probes, Coumarin 153 (C153) and Coumarin 343 (C343), are employed to detect different microenvironments in these complex systems because of their different chemical nature.[45,120,121] Another two reactive probes, reactive trans-2-[4'-(dimethylamino)styryl]benzothiazole (DMASBT) and Thioflavin-T (ThT), have been used for different purposes.[122–126] Widely different average fluorescence lifetimes ($\langle \tau_{fl} \rangle$) of two different types of probes (non-reactive: 2-5 ns, reactive: 50-500 ps)[117,121–123,125,126] have been

employed for the detection of slower and faster density fluctuations, and probing heterogeneous solvation environments in the investigated complex media.[55,56,127]

According to Kasha's rule[128,129], fluorescence emission of the excited solute occurs from the lowest vibrational energy level in the first excited electronic state, known as the singlet state (S1). Earlier studies of photo-selective excitation wavelength-dependent fluorescence emission or red-edge excitation spectroscopy (REES) measurements in complex systems have revealed a considerable shift in the emission wavelength towards the red end with red-edge excitation energy.[127,129,130] This phenomenon is explained by the fact that emissions after exciting photo-selected populations come from fluorophores that are solvated in different microdomains in the complex system. The interconversion time scale of these micro-domains is longer than $\langle \tau_{fl} \rangle$ of the solute. This spectroscopic technique provides information about persistence spatial heterogeneity in various types of complex systems.

In this thesis, the TRF technique has been employed for exploring solvent and solute dynamics by dynamic Stokes shift and rotational anisotropy measurements. Immediately after the photo-excitation of the dissolved dipolar fluorescence probe from the ground electronic energy state (S0) to the first excited electronic energy state (S1), the equilibrium charge distribution of the solute molecule changes. A non-equilibrium solvent configuration arises due to this charge redistribution of the solute which induces a dipole moment change. For this reason, the solvent dipole configuration around the excited fluorescence solute changes with time to get an equilibrated minimum energy solvent configuration. Time-resolved emission spectra (TRES) of the solute after immediate excitation are captured via time-resolved experimental techniques (TCSPC and 2DSC). Hence, external solute-centric medium dynamics in neat and multicomponent media are obtained from TRES.[55,117,119,131] On the other hand, rotational diffusion of the fluorescence solute extracted from time-resolved fluorescence anisotropy measurements gives a clear picture of the medium friction experienced during solute rotation. The anisotropy decay $(r(t))$ is calculated from parallel and perpendicular fluorescence emissions with respect to the polarization of the excitation pulse. The average rotation time $(\langle \tau_r \rangle)$ of the fluorophore is estimated from the time-integration of the measured $r(t)$.[129]

Other than the above experimental techniques, some other experiments have been performed such as the measurement of density, refractive index, viscosity, dynamic light scattering (DLS), differential scanning calorimetry (DSC), and cryogenic transmission electron microscopy (cryo-SEM) to extract valuable information on these complex media.

This thesis deals with 10 chapters where the first chapter introduces the overall thesis. Chapter 2 gives a brief discussion of experimental techniques, data collection, and the method of data analysis used in the investigation of these complex media.

In Chapter 3, investigations were conducted on water-octanol binary mixtures within the temperature range of 283 K to 323 K, at water mole fractions X_{H_2O} = 0.05, 0.10, 0.20, and moisture saturated aqueous octanol at 298 K[132]. DRS measurements were performed within the frequency window, $0.00002 \leq \nu/MHz \leq 10$ and $0.2 \leq \nu/GHz \leq 50$. The outcomes revealed reduction in the static dielectric constant (ε_s) upon addition of water to octanol across all experimental temperatures. Bimodal DR processes were observed, characterized by two distinct time constants, approximately ~3.1 - 0.3 ns and ~110 - 40 ps, signifying the absence of bulk-like water (DR time ~10 ps) in these binary mixtures. This observation was further supported by differential scanning calorimetry (DSC) measurements of octanol + water mixtures, emphasizing the exclusive influence of water-dependent colligative properties on these solutions. Molecular dynamics (MD) simulations of these systems (X_{H_2O} = 0.05, 0.10, 0.20) provided insights into the experimental results concerning structure, hydrogen bond network, tetrahedrality (for water), and dielectric properties. H-bonding analysis among water molecules in aqueous octanol mixtures indicated a decrease in average water-water H-bonding ($<NHB_{W-W}>$) per water molecule in these systems. The distribution of O-O-O angles in a range of $0° \leq \theta \leq 60°$ and a negative average tetrahedral order parameter ($\langle Q \rangle$) suggested a substantial breakdown in the tetrahedral network structure of water in these mixtures. Component-wise ε_s illustrated the minimal effects of water (ε_s water ~2) on ε_s in this octanol-rich region.

In Chapter 4, temperature-dependent ($283 \leq T/K \leq 323$) and water concentration-dependent (X_{H_2O} = 0.05, 0.10, 0.20) steady-state and time-resolved fluorescence (TRF) emission spectroscopic investigations were performed for water-octanol mixtures, particularly in the

octanol-rich region. Three external dipolar solutes, C153, C343, and DMASBT, served as local reporters to elucidate 'solute'-centric interactions, dynamics, and solution heterogeneity via fluorescence measurements. Steady-state absorption and fluorescence emission studies of these probes suggested no significant changes in solution structure. Photo-selective excitation frequency (ν_{exc})-dependent fluorescence measurements of DMASBT reported a maximum emission shift ($\sim$ 600 cm^{-1}) between blue and red edge excitation, indicating spatial heterogeneity within the systems.[127] This phenomenon suggested that the average lifetime of DMASBT ($\langle \tau_{fl} \rangle \sim$ 30-80 ps) is sensitive to the heterogeneous domain relaxation timescale, which is faster than the other two probes, C153 and C343 (3.4-3.7 ns and 2.5-3 ns, respectively). Temperature and water concentration-dependent Stokes's shift measurements of C153 and C343 in these systems revealed solute-centric solvent relaxation. The missing percentage, calculated from estimated dynamic Stoke shift ($\Delta \nu_{est}^{t}$) and observed Stokes shift $\Delta \nu_{obs}^{t}$), depended not only on temperature and water concentration but also on the chemical nature of the probes. Although the impact of temperature and water on Stokes shift measurements were similar, the solvent response function ($S(t)$), described by two-time constants characterized hydrogen bond relaxation followed by solvent molecules' diffusion in these systems. TRF anisotropy measurements of C153/C343 displayed bimodal friction exerted by the medium with two significantly different timescales, 200 ps and a nanosecond time component. The Stokes-Einstein-Debye (SED) relation for solute rotation and the coupling comparison between dynamics (solvent and solute) and medium viscosity $\langle \tau_r \rangle = A(\eta/T)^p$, $\langle \tau_s \rangle = A(\eta/T)^p$) suggested that aqueous octanol, including neat octanol, is dynamically heterogeneous. The activation energy estimated from the Arrhenius equation for both probes (in probe rotation and solvation) was widely different. Furthermore, correlations between rotation and solvation processes of two probes, C153 and C343, strongly reflected that the microenvironment around the two probe molecules is different in these media.

In Chapter 5, the exploration focuses on the glucose concentration (wt%) dependent different characteristics such as glass transition temperature, cluster size, dynamics, and spatio-temporal heterogeneity within glucose/ethylene glycol (EG) cryoprotectant mixtures, utilizing measurements such as DSC, DLS, steady-state fluorescence, and DRS. Glucose wt% varies from 0 to 40 in EG within the temperature window of 298 $\leq$ T/K $\leq$ 328 K for all investigated systems. Results from DSC measurements reveal that the inclusion of glucose (minimum 10

wt%) not only suppresses melting/freezing of ethylene glycol during heating and cooling but also modifies (increases) the glass transition temperature (T_g). Spatial heterogeneity, assessed through photo-selective excitation-dependent steady-state fluorescence emission measurements of three fluorescence probes (C153, C343, and DMASBT), suggests an increase with rising glucose wt% in glucose/EG cryoprotectant mixtures. The fluorescent probes with different fluorescence lifetimes report separately on faster and slower heterogeneous domain relaxations, with C343 indicating a strong presence of spatial heterogeneity. Additionally, all three probes demonstrate both faster and slower density fluctuations in the 40 wt% glucose-containing mixture, indicating strong spatial heterogeneity compared to other mixtures.

In Chapter 6, steady state UV-visible absorption, steady state fluorescence, and TRF study of C153 in glucose/EG cryoprotectant mixtures including neat EG are described at temperature 293 K. We focussed in this work on exploring the interaction, ultrafast solvation dynamics through Stokes shift measurement and solution heterogeneity through viscosity decoupling of solute or solvent dynamics in glucose/EG mixtures at varying glucose concentrations (wt % = 0, 10, 20, 30, 40). TRF measurements were conducted with two measurement setups as TCSPC and 2DSC. Earlier 2DSC based solvation dynamics measurement of C153 in normal solvent captured considerable sub-picosecond solvent response.[133] Here, C153 was utilized to explore solvation dynamics and decoupling phenomena of solute or solvent dynamics from medium viscosity in glucose/EG cryoprotectant mixtures. Dynamic Stokes shift measurements were carried out via 2DSC experiments with a 2 ps instrumental resolution. The observed solvent response times in these systems lengthen with increasing glucose concentrations. Measured time-resolved fluorescence (TRF) anisotropy of C153 in these cryoprotectant systems indicated bimodal decay. The correlation between solvent/solute dynamics and medium viscosity revealed an increase in the extent of viscosity decoupling with higher glucose concentrations.

Chapter 7 describes a systematic investigation of the interaction, dynamics, and solution structure of disaccharides dihydrate/glycerol cryoprotectant mixtures, including neat glycerol and glycerol-water systems. Four systems are investigated in this Chapter, namely, glycerol (GL), glycerol/water (GL-W), trehalose dihydrate/glycerol (TRE_GL_W), and sucrose dihydrate/glycerol. DSC, DLS, DRS measurements, and molecular dynamics simulations have been carried out to access microscopic information on structure and dynamics of the studied

systems. DSC is performed to determine the glass transition temperature of complex systems. Results reveal that the ultra-trace amount of water can change T_g of the cryoprotectant system and compensates for the T_g increment observed in the disaccharides dihydrate systems. The order of T_g, TRE_GL_W > SUC_GL_W > GL > GL_W, indicating the potential for tuning T_g and system fragility, that may help enhancing the cryopreservation capabilities of those systems. DLS measurements of these disaccharide systems reveal that the particle size in TRE_GL_W and SUC_GL_W systems depends on experimental temperature, although the trehalose system has a larger particle size than the sucrose system. DRS experiments of pure GL, GL_W, TRE_GL_W, and SUC_GL_W systems are described by multi-Debye DR relaxation. Again, the average dielectric relaxation time $\langle \tau_{DR} \rangle$ abruptly changes in disaccharide systems due to solute-induced increasing viscosity. The p values (varying from 0.75 to 0.80) of these investigating systems suggest that those systems are mild dynamic heterogeneity. From MD-simulations, radial distribution functions (RDFs) and spatial distribution function (SDF) are calculated to explore the microscopic structure of these complex cryoprotectant systems near room temperature. These analyses reveal that solute-solute interaction in the trehalose system is more prominent than the sucrose system, and this result agrees well with earlier DLS measurements. Hydrogen bonding (H-bonding) analysis shows water-water H-bonding is largely damaged in these complex systems. The network structure of water molecules is verified by the distribution of angle $P(\theta)$ and tetrahedral order parameter $P(Q)$ between three central oxygen atoms of the three nearest neighbor water molecules. Simulations suggest that water molecules in these complex systems are far from bulk-like. Water-water H-bond lifetime (continuous ($\langle \tau_{S_{HB}} \rangle$) and structural ($\langle \tau_{C_{HB}} \rangle$)) lengthen in these systems.

In Chapter 8, dynamical and thermophysical properties of 1M LiTFSI in ADN and EC binary solvent (xEC + (1−x) ADN) are investigated via conductivity measurements, DSC, DRS (0.2 ≤ GHz ≤ 50), and MD-simulations, where x (0, 0.2, 0.4, 0.6, 0.8, 1) denotes the mole fraction of EC. Conductivities of electrolyte solutions increase with increasing EC. This can be explained by the fact that EC-dependent improvement of salt dissolution and reduction in medium viscosity. DSC measurements reveal that EC mole fraction of 0.6 results in the lowest melting temperature, indicating an extended working temperature range for this battery electrolyte. Despite an increase in the static dielectric constant (ε_s) of electrolyte solutions with EC concentrations, a dielectric decrement from those neat or binary solvents to electrolyte

solutions is observed. This phenomenon is attributed to ion-induced dipole randomization, as later explained by the Kirkwood G_k factor. Multiple DR times suggest distinct reorientational processes in the solvation shell of ions and in TFSI$^-$ anion side group. The relation $\langle \tau_{DR} \rangle = A(\eta/T)^p$ and $\langle \sigma_{dc} \rangle = A(T/\eta)^p$, and activation energies E_η, E_{DR}, and E_σ associated with viscosity, DR, and conductivity in these electrolyte solutions suggest that solution heterogeneity decreases with increasing EC concentrations and rotation-diffusion coupling becomes prominent at high EC mole fractions ($X_{EC} \geq 0.6$). The radial distribution function (RDF) and coordination number (CN) analysis confirm solvent replacement and improved salt dissolution with EC concentrations in these electrolyte solutions. The activation energy of the self-diffusion coefficient of all the species reveals an anomalous dependence of diffusion activation for TFSI$^-$ ion with EC concentrations. The total conductivity of electrolyte solutions has been explored in terms of Nernst-Einstein conductivity ($\sigma_{NE} = \sigma_{self}^+ + \sigma_{self}^-$ from the self-diffusion part), and intra and inter-species distinct ionic conductivity like cation-cation ($\sigma_{distinct}^{++}$), anion-anion ($\sigma_{distinct}^{--}$), and cation-anion (σ^{+-}) (due to correlated motion of ions). EC concentration-dependent deviation of net conductivity from σ_{NE} due to anion anti-correlation, and transport number values suggest that low to moderate EC-containing electrolyte systems are efficient choices for LIBs.

Chapter 9 undertakes a systematic exploration of concentration dependent sol→gel transition of aqueous hyaluronic acid (HA), that is associated with the pathology organ dysfunction or fibrosis (like lung, kidneys, brain, muscle, and liver).[101,102] This investigation is crucial for elucidating the critical concentration threshold for HA aggregation (specifically in the wt% range 0, 0.15, 0.3, 0.5, 0.65, 0.75, 1, 1.5, 2), exploring concentration-dependent structural alterations, and interactions with external solutes. Multiple measurement techniques, including refractive index (RI), steady-state fluorescence, TRF, and cryo-SEM measurements, are employed to comprehensively characterize these aspects. Combination of RI and steady-state fluorescence intensity measurements, particularly focusing on Thioflavin-T (ThT), reveals the occurrence of the sol→gel transition within aqueous solutions containing 0.5 to 0.65 wt% HA. Time-resolved fluorescence (TRF) lifetime measurements of ThT indicate the impact of the sol→gel transition on the excitation state relaxation of probes. The TRF anisotropy of both solutes C343 and C153, dependent on HA concentration, exhibits contrasting trends post-gel formation. This suggests that the location of the two solutes within these systems is not uniform

and is predominantly influenced by the functional groups present in their ring frameworks. The cryo-SEM images of these systems validate the hypothesis that the transformation from sol to gel state takes place within the range of 0.5 to 0.65 wt% HA concentration. The morphology of the hydrogel systems undergoes a transition from spider-like polymer formation to a honeycomb-like structure with increasing HA concentration.

The concluding Chapter 10 offers a concise summary of the findings from Chapter 3 to Chapter 9, and briefly discuss a few potential problems for future research.

Reference

1   B. Bagchi, *Annu. Rev. Phys. Chem.*, 1989, **40**, 115–141.

2   A. G. Zawadzki and J. T. Hynes, *J. Mol. Liq.*, 1991, **48**, 183–196.

3   P. M. Kiefer and J. T. Hynes, *Proton Transfer Reactions and Hydrogen Bonding in Solution, eds. T Elsaesser. H. J. Bakker, Ultrafast Hydrogen Bonding Dynamics and Proton Transfer Prosesses in the Condensed Phase. Understanding Chemical Reactivity*, Springer, Dordrecht, 2002.

4   W. H. Thompson and J. T. Hynes, *J. Phys. Chem. A*, 2001, **105**, 2582–2590.

5   E. Pines, B. Z. Magnes, M. J. Lang and G. R. Fleming, *Chem. Phys. Lett.*, 1997, **281**, 413–420.

6   K. Dahl, R. Biswas, N. Ito and M. Maroncelli, *J. Phys. Chem. B*, 2005, **109**, 1563–1585.

7   A. Baksi and R. Biswas, *J. Chem. Sci.*, 2022, **134**, 1–8.

8   M. A. Bag and L. M. Valenzuela, *Int. J. Mol. Sci.*, 2017, **18**, 1422.

9   H. Tian, Z. Tang, X. Zhuang, X. Chen and X. Jing, *Prog. Polym. Sci.*, 2012, **37**, 237–280.

10   C. B. Highley, G. D. Prestwich and J. A. Burdick, *Curr. Opin. Biotechnol.*, 2016, **40**, 35–40.

11   E. Caló and V. V. Khutoryanskiy, *Eur. Polym. J.*, 2015, **65**, 252–267.

12   C. Peetla, A. Stine and V. Labhasetwar, *Mol. Pharm.*, 2009, **6**, 1264–1276.

13   R. Mannhold, H. Kubinyi and G. Folkers, *Drug bioavailability: estimation of solubility, permeability, absorption and bioavailability*, 2009.

14   G. Klopman and H. Zhu, *Mini-Rev. Med. Chem.*, 2012, **5**, 127–133.

15   S. Barun and S. Barun, *The Beats Nat. Sci.*, 2015, 2, 1-6.

16   A. S. Rudolph and J. H. Crowe, *Cryobiology*, 1985, **22**, 367–377.

17   L. M. Crowe, J. H. Crowe, A. Rudolph, C. Womersley and L. Appel, *Arch. Biochem. Biophys.*, 1985, **242**, 240–247.

18   F. Franks, *J. Solution Chem.*, 1995, **24**, 1093–1097.

19   M. De, L. Reyes, L. Saenz, L. Lapierre, J. Crosby, C. Barros and M. De Los Reyes, *Vet. Rec.*, 2002, **151**, 477–480.

20   M. T. Cicerone and C. L. Soles, *Biophys. J.*, 2004, **86**, 3836–3845.

21   G. D. Elliott, S. Wang and B. J. Fuller, *Cryobiology*, 2017, **76**, 74–91.

22   C. A. Angell, R. D. Bressel, J. L. Green, H. Kanno, M. Oguni and E. J. Sare, *Water in Foods*, 1994, 115–142.

23   C. Zhong, Y. Deng, W. Hu, J. Qiao, L. Zhang and J. Zhang, *Chem. Soc. Rev.*, 2015, **44**, 7484–7539.

24   F. Croce, G. B. Appetecchi, L. Persi and B. Scrosati, *Nature*, 1998, **394**, 456–458.

25   J. M. Tarascon and M. Armand, *Nature*, 2001, **414**, 359–367.

26   M. Armand and J.-M. Tarascon, *Nature*, 2008, **451**, 652–657.

27   K. Xu, *Chem. Rev.*, 2004, **104**, 4303–4417.

28   P. Simon and Y. Gogotsi, *Nat. Materials*, 2008, **7**, 845–854.

29   Y. C. Lu, Z. Xu, H. A. Gasteiger, S. Chen, K. Hamad-Schifferli and Y. Shao-Horn, *J. Am. Chem. Soc.*, 2010, **132**, 12170–12171.

30   D. V. Wagle, H. Zhao and G. A. Baker, *Acc. Chem. Res.*, 2014, **47**, 2299–2308.

31   M. Francisco, A. Van Den Bruinhorst and M. C. Kroon, *Angew. Chem. Int. Ed.*, 2013, **52**, 3074–3085.

32   A. Paiva, R. Craveiro, I. Aroso, M. Martins, R. L. Reis and A. R. C. Duarte, *ACS Sustainable Chem. Eng.*, 2014, **2**, 1063–1071.

33   E. L. Smith, A. P. Abbott and K. S. Ryder, *Chem. Rev.*, 2014, **114**, 11060–11082.

34   Y. Dai, J. van Spronsen, G. J. Witkamp, R. Verpoorte and Y. H. Choi, *Anal. Chim. Acta*, 2013, **766**, 61–68.

35   M. Espino, M. de los Ángeles Fernández, F. J. V. Gomez and M. F. Silva, *TrAC, Trends Anal. Chem.*, 2016, **76**, 126–136.

36   T. Asano, *Pure Appl. Chem.*, 1999, **71**, 1691–1704.

37   R. Li, A. J. D'souza, B. B. Laird, R. L. Schowen, R. T. Borchardt, E. M. Topp, A. J. D'Souza, E. M. Topp, D. Souza, A. J. Laird and B. B. Schowen, *J. Pept. Res.*, 2000, **56**, 326–334.

38   D. Averett, M. T. Cicerone, J. F. Douglas and J. J. De Pablo, *Soft Matter*, 2012, **8**, 4936–4945.

39   L. M. Crowe, D. S. Reid and J. H. Crowe, *Biophys. J*, 1996, **71**, 2087-2093.

40   J. H. Crowe, J. F. Carpenter and L. M. Crowe, *Annu. Rev. Physiol.*, 2003, **60**, 73–103.

41   W. Wang, *Int. J. Pharm.*, 2000, **203**, 1–60.

42   S. Khandelwal, Y. K. Tailor and M. Kumar, *J. Mol. Liq.*, 2016, **215**, 345–386.

43   B. Nagy, I. Bakos, E. Geissler and K. László, *Materials*, 2019, **12**, 4208.

44   A. Baksi, J. Rajbangshi and R. Biswas, *Phys. Chem. Chem. Phys.*, 2021, **23**, 12191–12203.

45   E. Tarif, J. Mondal and R. Biswas, *J. Phys. Chem. B*, 2019, **123**, 9378–9387.

46 B. Klassen, R. Aroca, M. Nazri and G. A. Nazri, *J. Phys. Chem. B*, 1998, **102**, 4795–4801.

47 L. Yang, A. Xiao and B. L. Lucht, *J. Mol. Liq.*, 2010, **154**, 131–133.

48 L. Aguilera, S. Xiong, J. Scheers and A. Matic, *J. Mol. Liq.*, 2015, **210**, 238–242.

49 T. Yamaguchi, T. Yamaguchi, T. Yonezawa, K. Yoshida, M. Nagao, A. Faraone and S. Seki, *J. Phys. Chem. B*, 2015, **119**, 15675–15682.

50 R. Kosaki, K. Watande and Y. Yamaguchi, *Cancer. Res.*, 1999, **59**, 1141–1145.

51 M. Flämig, L. Gabrielyan, R. Minikejew, S. Markarian and E. A. Rössler, *Phys. Chem. Chem. Phys.*, 2020, **22**, 9014–9028.

52 S. Indra and R. Biswas, *J. Phys. Chem. B*, 2016, **120**, 11214–11228.

53 K. Mukherjee, A. Barman and R. Biswas, *J. Mol. Liq.*, 2016, **222**, 495–502.

54 K. Mukherjee, S. Das, E. Tarif, A. Barman and R. Biswas, *J. Chem. Phys.*, 2018, **149**, 124501.

55 B. Guchhait, S. Daschakraborty and R. Biswas, *J. Chem. Phys.*, 2012, **136**, 174503.

56 K. Kumbhakar, E. Tarif, K. Mukherjee and R. Biswas, *J. Mol. Liq.*, 2019, **290**, 111225.

57 N. C. Maity, A. Baksi, K. Kumbhakar and R. Biswas, *J. Photochem. Photobiol. A: Chem.*, 2023, **439**, 114600.

58 S. Daschakraborty, T. Pal and R. Biswas, *J. Chem. Phys.*, 2013, **139**, 164503.

59 S. Kaur, A. Gupta, H. K. Kashyap and H. K. Kashyap, *J. Phys. Chem. B*, 2020, **124**, 2230–2237.

60 H. K. Kashyap and R. Biswas, *J. Chem. Phys.*, 2007, **127**, 184502.

61 K. Shimizu, A. A. Freitas, R. Atkin, G. G. Warr, P. A. FitzGerald, H. Doi, S. Saito, K. Ueno, Y. Umebayashi, M. Watanabe and J. N. Canongia Lopes, *Phys. Chem. Chem. Phys.*, 2015, **17**, 22321–22335.

62 C. Giaginis and A. Tsantili-Kakoulidou, *J. Pharm. Sci.*, 2008, **97**, 2984–3004.

63 A. Leo, C. Hansch and D. Elkins, *Chem. Rev.*, 1971, **71**, 525–616.

64 C. Hansch, J. P. Björkroth and A. Leo, *J. Pharm. Sci.*, 1987, **76**, 663–687.

65 R. N. Smith, C. Hansch and M. M. Ames, *J. Pharm. Sci.*, 1975, **64**, 599–606.

66 W. C. Wimley and S. H. White, *Nat. Struct. Mol. Biol.*, 1996, **3**, 842–848.

67 W. C. Wimley, T. P. Creamer and S. H. White, *Biochemistry*, 1996, **35**, 5109–5124.

68 P. C. Stein, M. Di Cagno and A. Bauer-Brandl, *Pharm. Res.*, 2011, **28**, 2140–2146.

69 G. Klopman and H. Zhu, *Mini-Rev. Med. Chem.*, 2005, **5**, 127–133.

70 Z. Liu and A. E. Clark, *Chem. Sci.*, 2021, **12**, 2294–2303.

71   S. D. Rowley, W. I. Bensinger, T. A. Gooley and C. Dean Buckner, *Blood*, 1994, **83**, 2731–2736.

72   J. K. Lewis, J. C. Bischof, I. Braslavsky, K. G. M. Brockbank, G. M. Fahy, B. J. Fuller, Y. Rabin, A. Tocchio, E. J. Woods, B. G. Wowk, J. P. Acker and S. Giwa, *Cryobiology*, 2016, **72**, 169–182.

73   J. Donnez, B. Martinez-Madrid, P. Jadoul, A. Van Langendonckt, D. Demylle and M. M. Dolmans, *Hum. Reprod. Update*, 2006, **12**, 519–535.

74   C. Olsson, H. Jansson and J. Swenson, *J. Phys. Chem. B*, 2016, **120**, 4723–4731.

75   Y. Xin, C. Kielar, S. Zhu, C. Sikeler, X. Xu, C. Möser, G. Grundmeier, T. Liedl, A. Heuer-Jungemann, D. M. Smith and A. Keller, *Small*, 2020, **16**, 1905959.

76   L. L. Kuleshova, D. R. Macfarlane, A. O. Trounson and J. M. Shaw, *Cryobiology*, 1999, **38**, 119–130.

77   D. C. C. Brito, S. F. S. Domingues, A. P. R. Rodrigues, J. R. Figueiredo, R. R. Santos and J. C. Pieczarka, *Cryobiology*, 2018, **83**, 97–99.

78   R. R. Santos, T. Tharasanit, J. R. Figueiredo, T. Van Haeften and R. Van Den Hurk, *Cell Tissue Res.*, 2006, **325**, 523–531.

79   A. M. da Silva, L. G. P. Bezerra, E. C. G. Praxedes, S. S. J. Moreira, C. M. P. de Souza, M. F. de Oliveira, A. F. Pereira, P. Comizzoli and A. R. Silva, *Cryobiology*, 2019, **91**, 53–60.

80   N. von Aspern, G. V. Röschenthaler, M. Winter and I. Cekic-Laskovic, *Angew. Chem., Int. Ed.*, 2019, **58**, 15978–16000.

81   L. Lu, X. Han, J. Li, J. Hua and M. Ouyang, *J. Power Sources*, 2013, **226**, 272–288.

82   S. Li, D. Zhao, P. Wang, X. Cui and F. Tang, *Electrochim. Acta*, 2016, **222**, 668–677.

83   M. Dahbi, F. Ghamouss, M. Anouti, D. Lemordant and F. Tran-Van, *J. Appl. Electrochem.*, 2013, **43**, 375–385.

84   M. Dahbi, F. Ghamouss, M. Anouti, D. Lemordant and F. Tran-Van, *J. Appl. Electrochem.*, 2013, **43**, 375–385.

85   Y. Abu-Lebdeh and I. Davidson, *J. Electrochem. Soc.*, 2009, **156**, A60.

86   D. Farhat, F. Ghamouss, J. Maibach, K. Edström and D. Lemordant, *ChemPhysChem*, 2017, **18**, 1333–1344.

87   A. Narayanan Kirshnamoorthy, K. Oldiges, M. Winter, A. Heuer, I. Cekic-Laskovic, C. Holm and J. Smiatek, *Phys. Chem. Chem. Phys.*, 2018, **20**, 25701–25715.

88   T. R. Kartha and B. S. Mallik, *J. Physi. Chem. B*, 2021, **125**, 7231–7240.

89   J. Wu, Z. Lan, J. Lin, M. Huang, Y. Huang, L. Fan and G. Luo, *Chem*, 2015, **115**, 2136–2173.

90 F. Ghamouss, A. Brugere and J. Jacquemin, *J. Phys. Chem. C*, 2014, **118**, 14107–14123.

91 Y. Ugata, M. L. Thomas, T. Mandai, K. Ueno, K. Dokko and M. Watanabe, *Phys. Chem. Chem. Phys.*, 2019, **21**, 9759–9768.

92 K. M. Kim and S. Kim, *Bull. Korean. Chem. Soc.*, 2015, **36**, 99–103.

93 K. Xu, *Chem. Rev.*, 2014, **114**, 11503–11618.

94 S. Tobishima, M. Arakawa, T. Hirai and J. Yamaki, *J. Power Sources*, 1989, **26**, 449–454.

95 C. J. Franko, C.-H. Yim, F. Årén, G. Åvall, P. S. Whitfield, P. Johansson, Y. A. Abu-Lebdeh and G. R. Goward, *J Electrochem Soc*, 2020, **167**, 160532.

96 V. Nilsson, D. Bernin, D. Brandell, K. Edström and P. Johansson, *ChemPhysChem*, 2020, **21**, 1166–1176.

97 M. Hemshekhar, R. M. Thushara, S. Chandranayaka, L. S. Sherman, K. Kemparaju and K. S. Girish, *Int. J. Biol. Macromol.*, 2016, **86**, 917–928.

98 M. N. Collins and C. Birkinshaw, *Carbohydr. Polym.*, 2013, **92**, 1262–1279.

99 A. Mero and M. Campisi, *Polymers,* 2014, **6**, 346–369.

100 J. R. E. Fraser, T. C. Laurent and U. B. G. Laurent, *J. Intern. Med.*, 1997, **242**, 27–33.

101 A. Stecco, M. Cowman, N. Pirri, P. Raghavan and C. Pirri, *Bioengineering*, 2022, **9**, 159.

102 P. G. Pavan, A. Stecco, R. Stern and C. Stecco, *Curr. Pain Headache Rep.*, 2014, **18**, 1–8.

103 R. James, G. Kesturu, G. Balian and A. B. Chhabra, *J. Hand Surg.*, 2008, **33**, 102–112.

104 K. S. Girish and K. Kemparaju, *Life Sci.*, 2007, **80**, 1921–1943.

105 B. P. Toole, *Nat. Rev. Cancer*, 2004, **4**, 528–539.

106 C. J. F. Böttcher and P. Bordewijk, *Theory of Electric Polarization: Dielectrics in Time-dependent*, Elsevier, Amsterdam, 1978.

107 A. Schönhals and F. Kremer, *Theory of Dielectric Relaxation*, Springer Berlin Heidelberg, 2003.

108 R. Buchner, *Pure Appl. Chem.*, 2008, **80**, 1239–1252.

109 U. Kaatze and K. Giese, *J. Phys. E. Sci. Instrum.*, 1980, **13**, 133–141.

110 D. W. Davidson and R. H. Cole, *J. Chem. Phys.*, 1951, **19**, 1484–1490.

111 J. Barthel and R. Buchner, *Pure Appl. Chem.*, 1986, **58**, 1077–1090.

112 T. Pradhan, P. Ghoshal and R. Biswas, *J. Phys. Chem. A*, 2008, **112**, 915–924.

113 N. Nandi, K. Bhattacharyya and B. Bagchi, *Chem. Rev.*, 2000, **100**, 2013–2045.

114   R. Buchner, J. Barthel and J. Stauber, *Chem.Phys. Lett.*, 1999, **306**, 57–63.

115   R. Buchner and G. Hefter, *Phys. Chem. Chem. Phys.*, 2009, **11**, 8984–8999.

116   T. Sato and R. Buchner, *J. Chem. Phys.*, 2003, **118**, 4606.

117   M. L. Horng, J. A. Gardecki, A. Papazyan and M. Maroncelli, *J. Phys. Chem.*, 1995, **99**, 17311–17337.

118   M. L. Horng, J. A. Gardecki and M. Maroncelli, *J. Phys. Chem. A*, 1997, **101**, 1030–1047.

119   M. Maroncelli and G. R. Fleming, *J. Chem. Phys.*, 1987, **86**, 6221–6239.

120   E. Tarif, K. Mukherjee, K. Kumbhakar, A. Barman and R. Biswas, *J. Chem. Phys.*, 2019, **151**, 154902.

121   K. Kumbhakar, B. Saha, P. De and R. Biswas, *J. Phys. Chem. B*, 2019, **123**, 11042–11054.

122   M. Kondo, X. Li and M. Maroncelli, *J. Phys. Chem. B*, 2013, **117**, 12224–12233.

123   P. K. Singh, M. Kumbhakar, H. Pal and S. Nath, *Phys. Chem. Chem. Phys.*, 2011, **13**, 8008–8014.

124   P. K. Singh, M. Kumbhakar, H. Pal and S. Nath, *J. Phys. Chem. B*, 2010, **114**, 2541–2546.

125   V. I. Stsiapura, A. A. Maskevich, V. A. Kuzmitsky, V. N. Uversky, I. M. Kuznetsova and K. K. Turoverov, *J. Phys. Chem. B*, 2008, **112**, 15893–15902.

126   A. I. Sulatskaya, A. A. Maskevich, I. M. Kuznetsova, V. N. Uversky and K. K. Turoverov, *PLoS One*, 2010, **5**, e15385.

127   A. Das and R. Biswas, *J. Phys. Chem. B*, 2015, **119**, 10102–10113.

128   M. Kasha, *Discuss. Faraday Soc.*, 1950, **9**, 14–19.

129   J. R. Lakowicz, *Principles of Fluorescence Spectroscopy*, Springer, New York, 3rd eds., 2006.

130   P. K. Mandal, M. Sarkar and A. Samanta, *J. Phys. Chem. A*, 2004, **108**, 9048–9053.

131   B. Guchhait, R. Biswas and P. K. Ghorai, *J. Phys. Chem. B*, 2013, **117**, 3345–3361.

132   B. E. Lang, *J. Chem. Eng. Data*, 2012, **57**, 2221–2226.

133   J. Mondal, N. C. Maity and R. Biswas, *J. Chem. Sci.*, 2023, **135**, 1–12.

Chapter 2

Experimental Details, Data Collection and Analysis Method

In this Thesis, different types of experimental techniques are used in order to investigate neat and multi-component mixtures. The most used of these experimental techniques are dielectric relaxation spectroscopy, steady state absorption and emission spectroscopy, time-resolved fluorescence spectroscopy using time-correlated single photon Counting (TCSPC) technique and two-dimensional streak camera (2DSC) detection. These experimental techniques are briefly described in this chapter.

2.1 Dielectric Relaxation Spectroscopy

2.1.1 Introduction

The motion of microscopic species such as molecules, atoms and ions in room liquid has a characteristic time (≤ 1 μs) to build up a polarisation. When the time dependent variation of an external electric filed ($\vec{E}(t)$) is comparable to the characteristic time, the motion of species will be insufficient for instantaneously reaching the equilibrium polarisation. For this reason, dielectric displacement ($\vec{D}(t)$) is observed with variable electric field. The relation between $\vec{D}(t)$ and $\vec{E}(t)$ written as[1]

$$\vec{D}(t) = \varepsilon^* \varepsilon_0 \vec{E}(t) \tag{2.1}$$

Where ε^* and ε_0 are complex permittivity and free space permittivity (8.854×10^{-12} Fm^{-1}) respectively. For oscillating electric filed, $\vec{E}(t)$ is expressed as $\vec{E}(t) = \vec{E_0}\exp(i\omega t)$ where ω is angular frequency and $i = \sqrt{-1}$. The frequency dependent complex permittivity (ε^*) of the system is given as[1]

$$\varepsilon^*(\omega) = \varepsilon'(\omega) - i\varepsilon''(\omega) \tag{2.2}$$

ε' and ε'' are relative permittivity and dielectric loss of the complex dielectric spectrum respectively. Dielectric relaxation spectroscopy (DRS) enables measurement of external perturbation field ($\vec{E}(t)$) induced microscopic electric polarization in the liquid phase. The

response frequency (ω) provides valuable massage about molecular level phenomena (like molecular reorientation, cooperative interaction, libration, etc) in the liquid system.[2,3]

2.1.2 DRS Instrumental Set-ups

Three dielectric set-ups[4] are used for measuring DR of liquid samples. The E4990A impedance analyser with 16452A liquid test fixture has been used for low frequency measurement from 20 Hz to 10 MHz. A schematic presentation of this DR instrumental set-up is shown in the Figure 2.1. The E4990A with 16452A fixture has been employed to measure relative complex permittivity by monitoring the capacitance of experimental sample that was incorporated into two parallel electrodes. The instrument impedance analyser was calibrated by short compensation (between 100 ohms resistance and parallel plate fixture) and air capacitance measurements. Complex permittivity was performed via capacitance measurement of liquid sample after correctly calibrating DRS instrument.
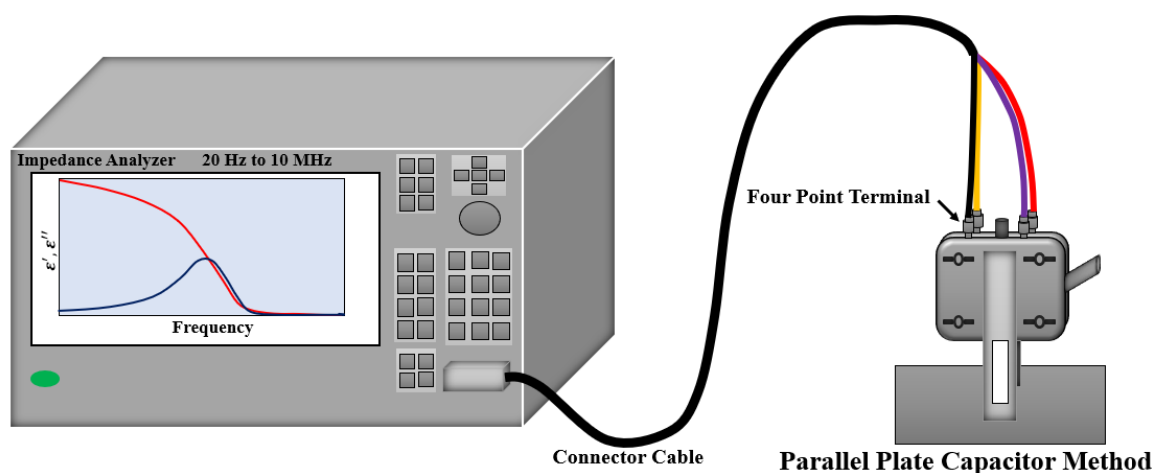
Figure 2.1: Schematic diagram of DR instrumental of impedance analyser set-up with parallel plate probe method in the frequency range 20 Hz to 10 MHz.

The E4991B impedance analyser (10 MHz to 500 MHz) and the N5235B PNA-L network analyser (500 MHz to 50 GHz) with open ended coaxial probe kit (N1501A, high temperatures probe for E4991B and performance probe for N5235B) were used for DR measurements of liquid. A schematic presentations of these DR instrumental set-up are shown in the Figure 2.2

and Figure 2.3. An instrumental calibration was done using humidity-controlled air, shorting block, and water at 298K following open, short and load respectively. A schematic diagram of calibration for coaxial probe method with performance probe is shown in Figure 2.4. More details about DRS measurements are available elsewhere. [1,4–7]
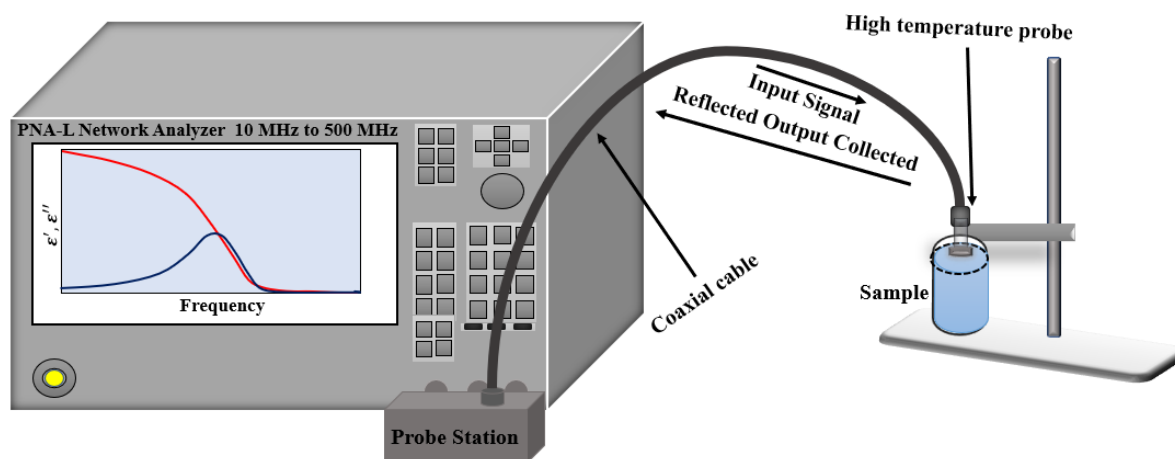
Figure 2.2: Schematic diagram of DR instrumental of impedance analyzer set-up with coaxial probe (high temperature probe) method; frequency range 10 MHz to 500 MHz.
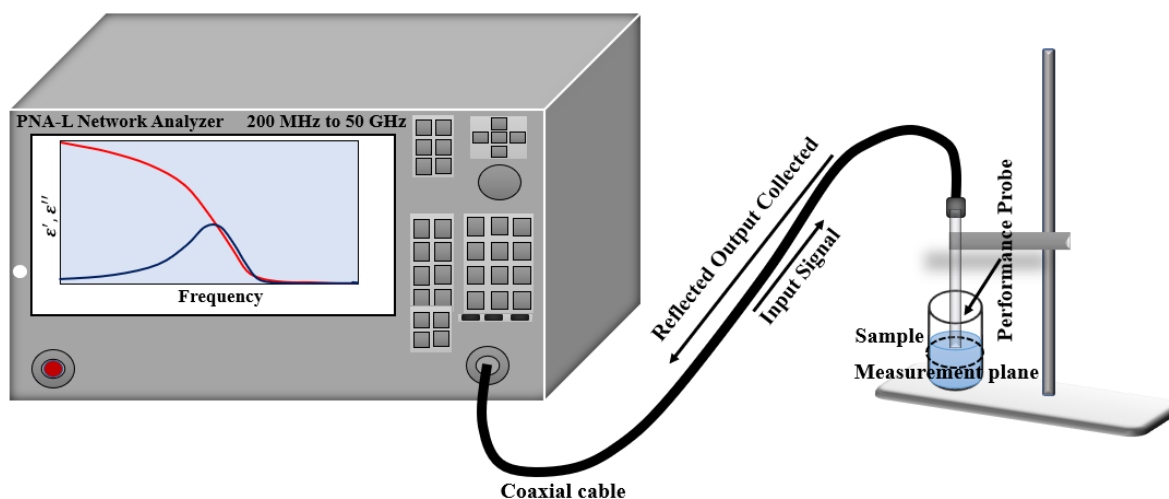
Figure 2.3: Schematic diagram of DR instrumental PNA-L network analyser set-up with coaxial probe (performance probe) method; frequency range 500 MHz to 50 GHz.
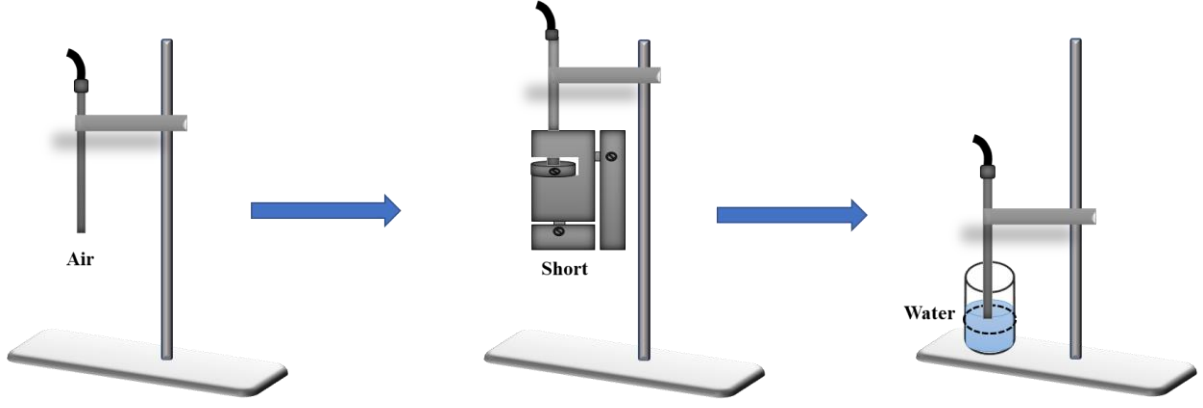
Figure 2.4: Schematic diagram of coaxial prob method calibration.

2.1.3 Mathematical Models and Data Analysis

In order to explore the characteristics of orientational polarisation, number of mathematical models are described in this section. These are given below.

2.1.3.1 Debye Model

Frequency dependent complex dielectric response ($\varepsilon^*(\omega)$) is expressed by the simplest Debye model as[8]

$$\varepsilon^* = \varepsilon_\infty + \Delta\varepsilon/(1 + i\omega\tau_D) \tag{2.3}$$

with the total dielectric dispersion ($\Delta\varepsilon = \varepsilon_s - \varepsilon_\infty$) is equal to the difference between static dielectric constant (ε_s) at low frequency (where the real part of the complex dielectric spectra develops a plateau) and the infinite frequency dielectric constant ($\varepsilon_\infty, \omega \to \infty$) where $\varepsilon_\infty = n_D^2$, n_D denoted refractive index of medium. ω is angular frequency and it is related to linear frequency (ν) through relation $\omega = 2\pi\nu$. τ_D denotes Debye relaxation time.

2.1.3.2 Non-Debye Model

Depending on the broadening of dielectric function, two other model are also used to fit measured dielectric spectra. First, symmetric broadening of dielectric function is described by Cole-Cole model (CC)[9] model and express as

$$\varepsilon^* = \varepsilon_\infty + \Delta\varepsilon/[1 + (i\omega\tau_{CC})^{1-\alpha}], \tag{2.4}$$

where τ_{CC} and α are the relaxation time and symmetric broadening parameter with $0 \leq \alpha < 1$.
Second, asymmetric broadening of dielectric function is described by Cole-Davidson (CD)[10,11] model and presented as

$$\varepsilon^* = \varepsilon_\infty + \Delta\varepsilon/[1 - i\omega\tau_{CD}]^\beta \,, \tag{2.5}$$

where τ_{CD} and β are the relaxation time and asymmetric broadening parameter with $0 < \beta \leq 1$. Besides these two types of broadening, another dielectric function is described as superposition of above two dielectric relaxations and it is known as Havriliak-Negami (HN) model for experimental data analysis which is as follows

$$\varepsilon^* = \varepsilon_\infty + \sum_j \frac{\Delta\varepsilon_j}{\left(1+(i2\pi v\tau_j)^{1-\alpha_j}\right)^{\beta_j}}, \tag{2.6}$$

with $0 \leq \alpha_j < 1$ and $0 < \beta_j \leq 1$.

τ_j is time necessary for the jth DR corresponding to the dielectric dispersion magnitude $\Delta\varepsilon_j$.

2.1.3.3 Data Analysis

To explore the physical significance from complex dielectric spectra, appropriate fit model is needed to fit experimental data. So, simultaneous fitting of $\varepsilon'(\omega)$ and $\varepsilon''(\omega)$ by non-linear least square method generated relaxation parameters. The quality of fitting was examined by both residual and the "goodness-of-fit" parameter χ^2. The evaluation of χ^2 is defined as[6]

$$\chi^2 = \frac{1}{2m-l}\sum_{i=1}^{m}\left[\left(\frac{\delta\varepsilon_i'}{\sigma\varepsilon_i'}\right)^2 + \left(\frac{\delta\varepsilon_i''}{\sigma\varepsilon_i''}\right)^2\right], \tag{2.7}$$

where m is the number of data triplet $(v, \varepsilon', \varepsilon'')$, and l, $\delta\varepsilon_i$, and $\sigma\varepsilon_i$ are express as number of adjustable parameters, residual and standard deviation for corresponding ith datapoint, respectively.

2.1.3.4 Conductivity Correction

Analysis of the imaginary part in complex dielectric relaxation spectra is very difficult for conducting system because dc conductivity vitiates the imaginary part. Frequency dependent conductivity included in imaginary part of dielectric spectrum is eliminated from imaginary part of dielectric spectra using the following equation[1,12]

$$\varepsilon^*(v) = \varepsilon'(v) - \left[i\varepsilon''(v) + \frac{i\sigma}{2\pi\varepsilon_0 v}\right]. \tag{2.8}$$

where $v = \omega/2\pi$ denoted linear frequency, σ is dc conductivity of ionic system. ε_0 is the free space permittivity. Conductivity correction of dielectric data analysis was carried out for all of these systems present in this Thesis.

2.2 Steady State Ultra Violet and Visible (UV-Vis) Absorption Spectroscopy

The UV-Vis absorption spectra were acquired using a UV-2600 spectrophotometer manufactured by SHIMADZU. Figure 2.5 illustrates the essential components of a UV-Vis absorption spectrophotometer. To cover the visible and ultraviolet wavelength ranges, two light sources are employed: a tungsten lamp for the visible region and a deuterium lamp for the ultraviolet region. The emitted light from these lamps is directed by a mirror towards a filter and subsequently onto a monochromator. The monochromator serves the purpose of splitting the incoming polychromatic light into various monochromatic rays. The light of a specific wavelength is then divided into two separate paths: one directed towards the reference and the other passing through the sample. Both the transmitted light from the reference and the sample eventually reaches photodiode detectors. Following a series of sequential data processing steps, including signal enhancement and analog-to-digital conversion, the final absorption spectra are recorded.

The fundamental principle underlying UV-Vis absorption spectroscopy is the well-established Beer-Lambert Law. According to this law, the absorbance (A) of a sample is directly proportional to the product of the path length (*l*) and the concentration (*c*) of the sample, represented as $A = log_{10}\frac{I_0}{I} = \varepsilon cl$. Where I_0 and I are defined as the intensity of the incident light and intensity of the transmitted light, respectively. The proportionality constant in the Beer-Lambert law is denoted as ε, and it is commonly referred to as the molar extinction coefficient or molar absorptivity. Note, throughout this thesis, all absorption measurements were conducted with a fixed path length (*l*) of 1 centimetre, and the concentration of the sample (*c*) was restricted to values less than or equal to 10^{-5} M.
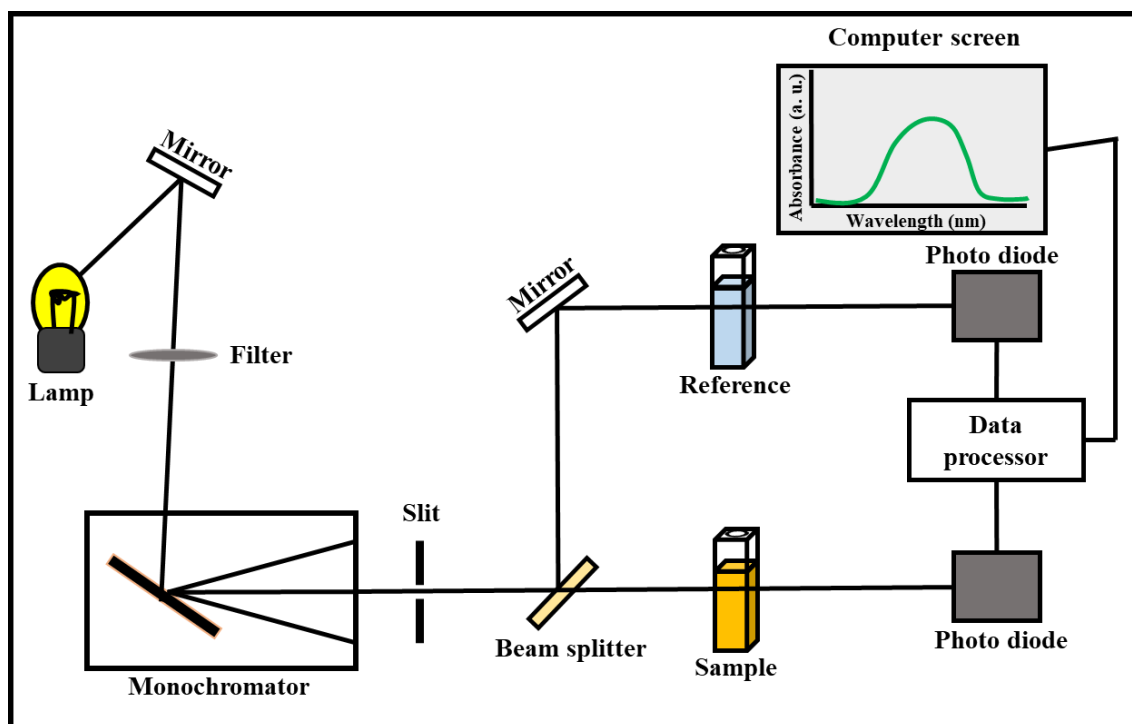
Figure 2.5: Schematic representation of an UV-Vis absorption spectrophotometer.

2.3 Steady State Fluorescence Spectroscopy

The fluorescence emission measurements described in the thesis were conducted using a fluorimeter, specifically the Fluorolog model from Jobin-Yvon, Horiba. Figure 2.6 provides an illustrative representation of the fluorescence spectrophotometer's key components and working principle. For excitation, a continuous xenon (Xe) lamp serves as the light source. The emitted light from the xenon lamp is directed through an excitation monochromator, which not only splits the light into monochromatic components but also filters out any undesired wavelengths, effectively eliminating stray light. The monochromator is equipped with a motor that enables automatic selection and scanning of wavelengths. The monochromatic light of the desired wavelength is used to excite the sample under investigation. The emitted fluorescence light is then directed to an emission monochromator, which is positioned at a right angle with respect to the path of the excitation light. Following this, the fluorescence emission is detected by a photomultiplier tube (PMT). The collected signal is subsequently amplified and subjected to appropriate electronic conversion. Finally, the fluorescence emission data is displayed on a computer screen for further analysis and interpretation.
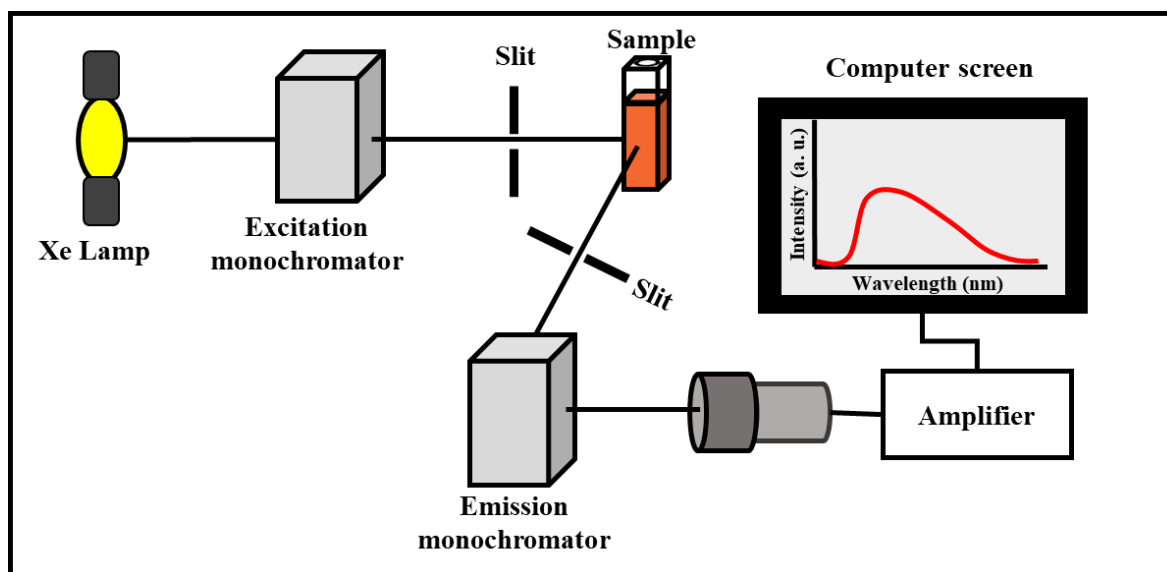
Figure 2.6: Schematic diagram of a fluorescence spectrophotometer.

2.4 Time-Resolved Fluorescence Measurements from TCSPC measurement: Technique, Data Collection and Analysis

The time-resolved fluorescence investigations presented in this thesis primarily relied on the time-correlated single photon counting (TCSPC) technique[13–15]. We employed pulsed diode lasers with wavelengths of 409 nm and 375 nm in our time-resolved fluorescence measurements.

2.4.1 TCSPC Measurement Technique

For time-resolved fluorescence measurements, we utilized the LifeSpec-ps system from Edinburgh Instruments (Livingston, U.K). In our TCSPC setup, we operated in reverse mode. Figure 2.7 provides an illustrative overview of a typical TCSPC setup in reverse mode. In this setup, a pulsed diode laser was employed to excite the sample. The first excitation pulse, which was vertically polarized, excited the fluorophore molecules present in the sample within a quartz cuvette. Simultaneously, a signal was generated and passed through a constant fraction discriminator (CFD). The signal corresponding to the first photon emitted by the excited fluorophores traversed through the CFD to record its arrival time. Subsequently, this signal was directed to a time-to-amplitude converter (TAC), where a voltage ramp was triggered. The voltage within the TAC increased with time until the stop signal was detected.

In the reverse mode of TCSPC, a simultaneous signal was generated when the second excitation pulse from the laser excited the sample. This signal was also directed through the CFD and subsequently to the TAC to halt the voltage ramp. The output pulse from the TAC, which is proportionate to the delay time (Δt) between the start and stop signals, was processed through an analog-to-digital converter (ADC) and forwarded to a multichannel analyzer (MCA) to generate numerical values. Repeating this process multiple times yielded a decay histogram containing photon counts and time channel information in the MCA.
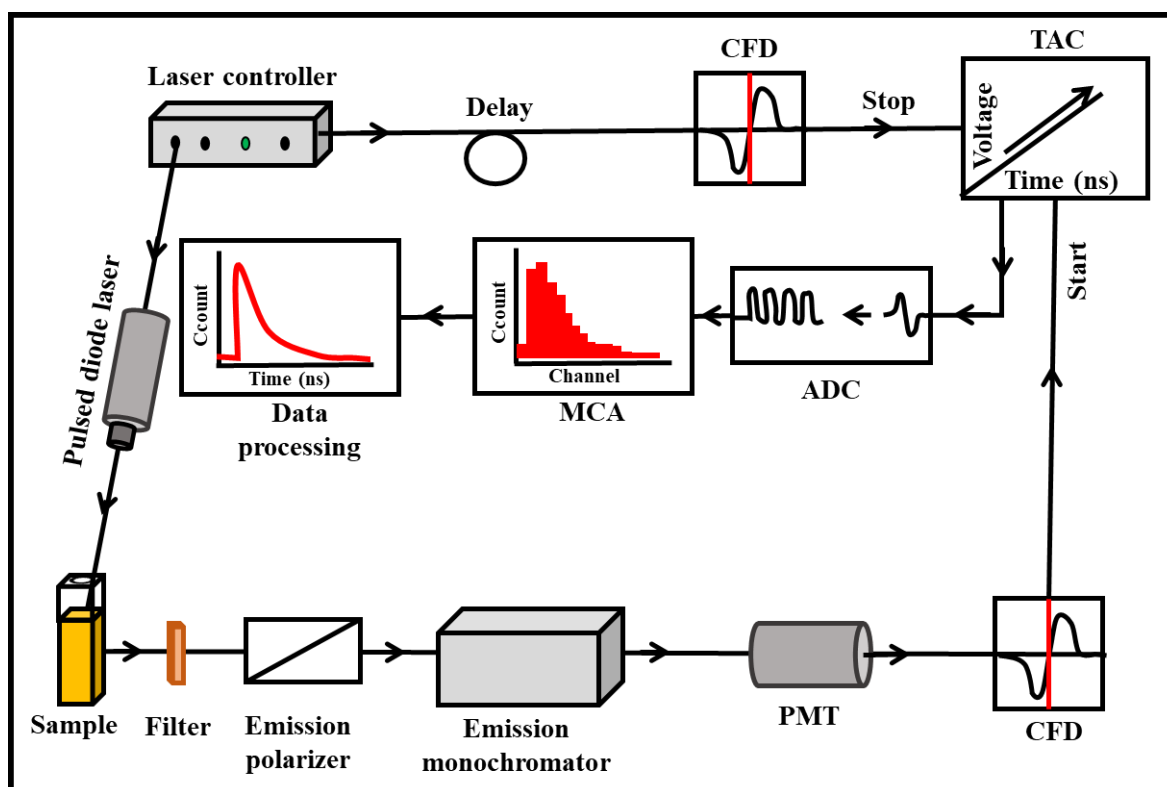
Figure 2.7: Schematic presentation of a TCSPC set-up.

2.4.2 Data Analysis

Prior to collecting the emission decay data from the fluorophore dissolved in the systems, we verified the instrument's response function using a scattering medium. Specifically, we employed a scattering medium, such as dust in water, and measured the intensity decay at 409 nm after excitation by the 409 nm laser. This measurement yielded a full width at half maximum (FWHM) of the instrument response function (IRF) of approximately 85-90 picoseconds (ps).

2.4.2.1 Fluorescence Lifetime and Solvation Dynamics

The fluorescence decay ($N(t)$) obtained through TCSPC represents a convolution of the instrument response function (IRF) ($R(t)$) and the sample's response ($I(t)$). To extract $I(t)$ from $N(t)$ and $R(t)$ data, we employed an iterative reconvolution method[16] using nonlinear least-square analysis.

We fitted the experimental I(t) with a sum of multi-exponential functions as follows:

$$I(t) = \sum_{i=1}^{N} \alpha_i \exp\left(-t/\tau_i\right) \tag{2.9}$$

Here, α_i and τ_i represent the pre-exponential factors and characteristic lifetimes, respectively.

Average fluorescence lifetime, $\langle \tau_{fl} \rangle$ of fluorophore in sample was determined by time integrating the multi-exponential fits of the collected magic angle (54.7°) fluorescence emission decays with the emission polarizer set to the emission peak wavelength of fluorophore in the samples. The formula used to calculate $\langle \tau_{fl} \rangle$ is:

$$\langle \tau_{fl} \rangle = \int_0^\infty dt \sum_i \alpha_i exp[-t/\tau_i] = \sum_i \alpha_i \tau_i \tag{2.10}$$

with $\sum_i \alpha_i = 1$.

In solvation dynamics, often referred to as Stokes shift dynamics, a series of 14-16 magic angle (54.7°) decays at equally spaced wavelengths across the steady-state emission spectrum of the fluorophore dissolved in the sample are typically recorded. The hallmark of dynamic Stokes shift is when one observes fluorescence decay at the blue end and rise followed by decay at the red end fluorescence emission spectrum.

Time-resolved emission spectra (TRES) were reconstructed for each of the systems based on the collected intensity decays, following standard protocols.[13,16,17] As discussed earlier, the fluorescence decays recorded at various wavelengths (λ_i) were fitted with a multi-exponential function:

$$I(\lambda_j, t) = \sum_{i=1}^{N} \alpha_i(\lambda_j) \exp\left(-t/\tau_i(\lambda_j)\right), \tag{2.11}$$

where $\alpha_i(\lambda_j)$ represents the pre-exponential factor for a specific wavelength, with $\sum_i \alpha_i(\lambda_j) = 1$. Subsequently, a new set of normalized intensity decays were generated to ensure that the time-integrated intensity at each wavelength was equal to the steady-state

intensity at that wavelength, denoted as $F(\lambda_j)$. The normalization factor is adjusted accordingly to achieve this.

$$H(\lambda_j, t) = \frac{F(\lambda_j)}{\int_0^\infty I(\lambda_j,t)dt} = \frac{F(\lambda_j)}{\sum_i \alpha_i(\lambda_j)\tau_i(\lambda_j)} \tag{2.12}$$

To obtain the appropriate normalized function, the normalization factor $(H(\lambda_i))$ was multiplied with $I(\lambda_j, t)$.

The normalized function is expressed as:

$$I'(\lambda_j, t) = H(\lambda_j)I(\lambda_j, t) = \sum_{i=1}^N \alpha_i'(\lambda_j)\exp(-t/\tau_i(\lambda_j)) , \tag{2.13}$$

where $\alpha_i'(\lambda_j) = H(\lambda_j)\alpha_i(\lambda_j)$. TRES at any wavelength and time can be calculated from $\Gamma(\lambda_i, t)$. For further analysis, the TRES were converted into frequency representation by appropriately weighting the intensity with λ^2. Each of the TRES was fitted with a log-normal shape function to obtain a continuous representation of the spectrum. The peak frequencies derived from the fitted spectra were then used to construct the solvation response function $S(t)$[17],

$$S(t) = \frac{\nu(t)-\nu(\infty)}{\nu(0)-\nu(\infty)} \tag{2.14}$$

The terms $\nu(0)$, $\nu(t)$, and $\nu(\infty)$ represent the frequencies, usually corresponding to the peak, for the reconstructed time-resolved emission spectrum at different times: immediately after excitation (t = 0), at any given instant (t), and at a sufficiently long time (t = ∞) when the solvent has fully relaxed. The solvation response function $S(t)$ is a normalized function that starts at unity at t = 0 and gradually decreases to zero as the solvent relaxes in response to the rapid change in charge distribution of the solute (the fluorophore) caused by photo-excitation. For a specific system, it is expected that $\nu(\infty)$ will be equal to the steady-state emission peak frequency. However, in some cases, the steady-state emission spectrum exhibits a slight blue shift when compared to the time-resolved emission spectrum at t = ∞, indicating that the excited fluorophore is surrounded by an incompletely relaxed solvent environment. This observed blue shift is a consequence of the steady-state emission originating from an excited solute within an environment that hasn't fully relaxed yet.

Subsequently, the average solvation time, denoted as $\langle\tau_s\rangle$, is determined by time-integrating the measured $S(t)$ decays using the following expression:

$$\langle \tau_s \rangle = \int_0^\infty dt\, S(t) = \int_0^\infty dt \sum_{i=1}^n a_i exp[-t/\tau_i] = \sum_{i=1}^n a_i \tau_i \tag{2.15}$$

Where $\sum_{i=1}^n a_i = 1$, a_i and τ_i represent the amplitude and time constants associated with the ith component of the S(t) decay, respectively. The summation is taken over all components contributing to the solvation response function.

2.4.2.2 Rotational Dynamics

The TCSPC technique was also employed to investigate the reorientational relaxation dynamics of a fluorophore dissolved in the medium and to assess the time-dependent frictional profile of the medium.[13,16,18] The principle of reorientational dynamics measurements involves selectively exciting those fluorophores whose absorption transition dipole aligns with the electric vector of the polarized excitation light. The intensity decays of emissions collected in parallel ($I_{para}(t)$) and perpendicular ($I_{perp}(t)$) polarizations depend on the reorientation of the excited fluorophore and change over time. The difference between $I_{para}(t)$ and $I_{perp}(t)$ gradually decreases with time. This reduction in anisotropy is leveraged to extract information about the reorientational dynamics, with the condition that the lifetime of the fluorophore, when dissolved in a given medium, should be comparable to or greater than its reorientational time. Fluorescence anisotropy measurements are conducted at the peak wavelength of the steady-state emission spectrum by collecting emissions with vertical polarization ($I_{para}(t)$) and horizontal polarization ($I_{perp}(t)$) concerning the vertically polarized excitation. The dynamic fluorescence anisotropy, denoted as $r(t)$, is generated as follows[13]:

$$r(t) = \frac{I_{para}(t) - I_{perp}(t)}{I_{para}(t) + 2I_{perp}(t)} \tag{2.16}$$

The polarization characteristics of the optical setup play a crucial role in influencing the measured anisotropy, and it is essential to correct for instrumental biases towards specific polarizations. This correction factor, denoted as the geometric factor (G), is defined as the ratio between the transmission efficiency for vertically polarized ($I_{para}(t)$) and horizontally polarized ($I_{perp}(t)$) light: $G = I_{para}(t)/I_{perp}(t)$. The geometric factor ($G$) is determined through the tail matching of vertically (parallel) and horizontally (perpendicular) polarized fluorescence emission intensity decays. Once the geometric factor is known, the corrected time-resolved fluorescence anisotropy, $r(t)$, is represented as:

$$r(t) = \frac{I_{\text{para}}(t) - GI_{\text{perp}}(t)}{I_{\text{para}}(t) + 2GI_{\text{perp}}(t)} \tag{2.17}$$

The obtained $r(t)$ values can then be fitted with single or multi-exponential functions for further analysis.

$$r(t) = r(0) \sum_i \alpha_i \exp(-t/\tau_i), \tag{2.18}$$

with $\sum_i \alpha_i = 1$.

The value for the initial anisotropy, r_0, was taken as 0.376 for C153[18] and 0.35 for C343[19].

The average rotational correlation time of solute can be estimated as follows:

$$\langle \tau_{rot} \rangle = \int_0^\infty dt [r(t)/r(0)] = \sum_{i=1}^n \alpha_i \tau_i \text{ with } \sum_{i=1}^n \alpha_i = 1. \tag{2.19}$$

2.5 Time-Resolved Fluorescence Measurements from Two-Dimensional Streak Camera Measurement: Technique, Data Collection and Analysis

In this thesis experimental setup, for ultrafast solvent response detection, we collected time-resolved fluorescence spectra using a two-dimensional streak camera (2DSC, Optoscope SC-10).[20] Figure 2.8 provides an illustrative overview of a typical 2DSC setup. To achieve this, we employed a spectrograph (HRS-300SS, Princeton Instruments) with a 300 mm path length and a grating constant of 300 grooves/mm. Excitation light was generated using a Ti:Sapphire laser (Mai Tai, Spectra Physics, Newport Corporation, Irvine, CA), featuring a pulse duration of 150 fs and a repetition rate of 80 MHz. The frequency-doubled light at 440 nm was produced using a BBO crystal from an 880 nm laser pulse.

In this setup, this 440 nm pulsed laser was employed to excite the sample. The first excitation pulse, which was vertically polarized, excited the fluorophore molecules present in the sample within a 1 cm path length quartz cuvette, and the excitation was focused onto the sample after passing through a 440 nm interference filter. Simultaneously, emitted fluorescence was collected at a right angle concerning the excitation and focused by two lenses onto the entrance slit of the monochromator, which had a slit width of 10 μm and a height of 4 mm. A bandpass filter at 475 nm was used to eliminate scattering, and the fluorescence data were collected at the magic angle (54.7°) polarization. During this event, the central wavelength of the spectrograph was fixed at the peak wavelength of steady state fluorescence emission spectrum of the fluorophore dissolved in the solvent under investigation. The entire fluorescence emission was diffracted in the spectrograph, with the central wavelength fixed at the emission

peak maximum of each system, offering a spectral resolution of 0.09 nm. The wavelength-dispersed fluorescence was then focused onto the entrance of the streak camera. The streak camera system was operated in the photon counting mode, featuring a 1392 (time) × 1040 (wavelength) pixel 2D image. One pixel in the time axis corresponded to 206.7 fs, and one pixel in the wavelength axis corresponded to 1.4 Å. The instrument response function (IRF) of the streak camera using scattering medium was recorded at the peak maxima 440 nm after excitation by the 440 nm laser ray. This measurement yielded a full width at half maximum (FWHM) of the instrument response function (IRF) of approximately 2 ps. All images were collected in 1000 acquisitions, with the MCP gain set at 800 V and a delay at 32.5% with a sweep speed of 15 ps/mm.
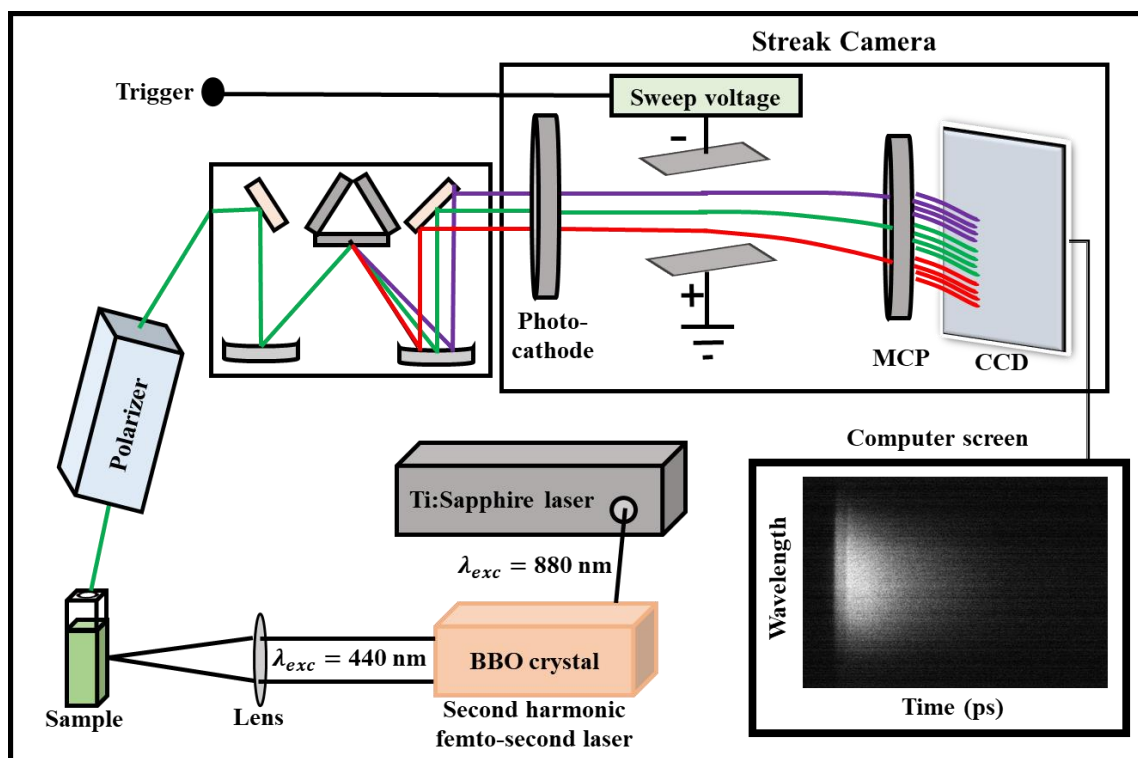
Figure 2.8: Schematic presentation of a 2DSC set-up.

To obtain the TRES at specific delay times from the streak image, the wavelength-time 2D fluorescence profile was divided into the required time intervals. Zero time was chosen from the streak image where the fluorescence decay began. The TRES were obtained at intervals of 207 fs (1 pixel) from 0 to 2 ps, followed by 1034 fs (5 pixels) intervals up to 20–30 ps, and then 4.961 ps (24 pixels) intervals up to 60–70 ps, with the rest in 10 ps intervals (48 pixels). This time division scheme was adjusted as needed for different systems under investigation.

Following the acquisition of TRES spectra, they were fitted with a log-normal line shape function, and all analyses were performed in the wavenumber domain. The peak frequency was determined from each TRES and used to derive the spectral response function ($S(t)$) as described in Section 2.4.2.1.

Reference

1   C. J. F. Böttcher and P. Bordewijk, *Theory of Electric Polarization: Dielectrics in Time-dependent*, Elsevier, Amsterdam, 1978.

2   R. Buchner, *Pure Appl. Chem.*, 2008, **80**, 1239–1252.

3   U. Kaatze and K. Giese, *J. Phys. E. Sci. Instrum.*, 1980, **13**, 133–141.

4   N. C. Maity, A. Baksi, K. Kumbhakar and R. Biswas, *J. Photochem. Photobiol. A: Chem.*, 2023, **439**, 114600.

5   A. Schönhals and F. Kremer, *Theory of Dielectric Relaxation*, Springer Berlin Heidelberg, 2003.

6   P. R. Bevington and. D. K. Robinson, *Data reduction and error analysis for the physical sciences*, McGraw-Hill Education, New York, 3rdEdition, 2003.

7   K. Mukherjee, A. Barman and R. Biswas, *J. Mol. Liq.*, 2016, **222**, 495–502.

8   P. J. W. Debye, *Polar Molecules*, Chemical Catalog Company, Incorporated, 1929.

9   K. S. Cole and R. H. Cole, *J Chem Phys*, 1941, **9**, 341–351.

10   D. W. Davidson and R. H. Cole, *J. Chem. Phys.*, 1950, 18, 1417.

11   D. W. Davidson and R. H. Cole, *J. Chem. Phys.*, 1951, **19**, 1484–1490.

12   R. Buchner and J. Barthel, *Annu. Rep. Sect. C Phys. Chem.*, 1994, **91**, 71–106.

13   J. R. Lakowicz, *Principles of Fluorescence Spectroscopy*, Springer, New York, 3rd edn., 2006.

14   D. V. O'Connor and D. Phillips, *Time-correlated single photon counting*, Academic Press London, 1984.

15   M. C. Chang, S. H. Courtney, A. J. Cross, R. J. Gulotty, J. W. Petrich and G. R. Fleming, *Instrum. Sci. Technol.*, 1985, **14**, 433–464.

16   D. J. S. Birch and R. E. Imhof, *Topics in Fluorescence Spectroscopy*, 2002, 1–95.

17   M. L. Horng, J. A. Gardecki, A. Papazyan and M. Maroncelli, *J. Phys. Chem.*, 1995, **99**, 17311–17337.

18   M. L. Horng, J. A. Gardecki and M. Maroncelli, *J. Phys. Chem. A*, 1997, **101**, 1030–1047.

19   S. Koley, H. Kaur and S. Ghosh, *Phys. Chem. Chem. Phys.*, 2014, **16**, 22352–22363.

20   J. Mondal, N. C. Maity and R. Biswas, *J. Chem. Sci.*, 2023, **135**, 1–12.

Chapter 3

Impact and Structure of Water in Aqueous Octanol Mixtures: Hz-GHz Dielectric Relaxation Measurements and Computer Simulations

3.1 Introduction

Neat 1-octanol (henceforth octanol) and aqueous octanol have been extensively used in pharmaceutical industry for exploring and understanding kinetic properties of drugs in aqueous-membrane systems.[1–4] Hydrophobic or hydrophilic characteristics in a series of drug molecules have been predicted by their partition coefficients in water-octanol system.[1,3,5] On the other hand, partitioning of drugs in water-membrane is well predicted by their water-octanol partition coefficient than that in water-hydrocarbon systems.[1,2] Permeability of active pharmaceutical ingredients (APIs) in the biological membrane is well understood by dynamic exchange of APIs in water-octanol interface.[6] In structural biology, the helix structure of peptides in transmembrane can be predicted by partitioning of peptides in water-phospholipid bilayer[7] and water+octanol mixture[8]. Structural organization of neat octanol has been explored at ambient condition by a number of studies using X-ray diffraction [9,10], infrared spectroscopy [11–13], thermodynamic measurements [14], Raman spectroscopy[11,15], and Rayleigh- Brilliouin spectroscopy[15,16]. Presence of pre-peak (~0.4 Å) in X-ray diffraction experiments has signaled self-aggregation and long-range order in liquid neat octanol.[9,10] Water saturated octanol (also termed as 'wet-octanol') has also been investigated for water-mediated structural organization in water saturated octanol through X-ray scattering[9] measurements, Raman scattering[15] experiments and computer simulation studies.[17–20] Molecular dynamics (MD) simulations of water in 1-octanol have revealed reverse micellar like structure with polar regions enriched with hydroxyl groups, and non-polar regions populated by hydrocarbon units.[19] With increasing water concentration, hydrogen-bonded clusters formed by the alcohol head (hydroxyl) groups and water molecules results nearly spherical regions in the resultant aqueous solutions, although the original aggregated structure of neat octanol does not undergo any qualitative or drastic changes.[9] However, these studies did not closely examine the separate structure and dynamics of water molecules that were present in the aqueous octanol solutions

considered. The present study focuses on this aspect and carries out a combined experimental and simulation investigation.

Dielectric relaxation spectroscopic (DRS) measurements of primary alcohols have been extensively performed in order to explore the inherent polarization dynamics and interactions in these H-bonded systems.[21–23] These measurements have supplied important and useful information on the impact of H-bonding on relaxation dynamics and also on the role of amphiphilic interactions in governing the liquid structure. DR of primary alcohols indicate three-step DR process. The slowest among them has been attributed to the cooperative process involving the H-bond network of the alcohols, while the intermediate timescale is ascribed to rotation of alcohol molecules. The fastest one with DR timescales ~ 1 ps has been interpreted as arising from the collective high frequency dynamics made of intermolecular vibrations and librations[24–28]. DR measurements of water have been carried out extensively and the relaxation signatures strongly indicate the impact of the intermolecular H-bond network.[29–31]

The DR properties of binary aqueous mixtures of alcohol have also been investigated by several authors.[32–37] Interestingly, the DR features of aqueous solutions of alcohols in water-rich region are different from those in alcohol-rich solutions. At very low alcohol concentrations in water, aggregates of alcohol molecules are formed due to polarity induced hydrophobic stacking of alkanols.[38,39] Alcohol rich region of aqueous mixtures exhibits moderate-to-strong heterogeneous solution features because of reverse micelles like micro-clusters formation.[32–34,40] Water solubility in primary alcohol depends on alkyl chain length, and primary alcohols with C1 to C3 carbon and tertiary butanol are fully soluble in water. Addition of water in alcohols perturbs the liquid phase H-bonded structure of both neat water and neat alcohol and undergoes a substantial change after addition of water at a certain concentration.[41–44] This concentration, if termed as 'transition concentration', depends on the identity of the alcohols because of their amphiphilic character. Structural and dynamical aspects of aqueous solutions of alcohols have been followed via steady-state UV-VIS absorption and fluorescence, and time dependent fluorescence measurements. [38,39,45–47] These measurements have indicated both water-induced structural and dynamical transitions, and the latter has been connected recently to the solution H-bond fluctuations[47]. A miscibility gap in water+alcohol binary systems always exists because of the presence of hydrophobic alkyl group and hydrophilic -OH moiety in alcohols.[48] As a result, the miscibility gap depends on temperature and alkyl chain length. Static dielectric (ε_s) measurements of water+alcohol binary mixtures have shown anomalous

composition dependence except for methanol, ethanol and propanol.[32–34,36] For primary alcohols containing alkyl chain with C > 4, ε_s goes through a minimum when followed as a function of water mole fraction.[34,35] In addition, the minimum value of ε_s depends on temperature and alkyl chain length.[34] This peculiarity in dielectric behavior of aqueous solutions of primary alcohols with C > 4 is not understood and the specific role of water not investigated yet.

This brings our present work into focus: a systematic study of temperature and composition dependent measurements of DR in octanol+water binary mixtures, suitably complemented with computer simulations, has been carried out to unravel the impact of water and possible changes, if any, of its own bulk H-bond network structure. This is highly warranted considering that DR measurements of neat octanol[21], isomeric octanol[49–57] and non-aqueous binary mixtures of octanol[58–65] are already available in the literature but with no microscopic explanations. In the present work we have performed temperature (283 K to 323 K) and water concentration (X_{H_2O} = 0, 0.05, 0.10, 0.20, saturated aqueous octanol at 298 K[66]) dependent DR measurements of aqueous octanol solutions. This has been complemented by performing simulations at a few representative water concentrations. These simulations assist to interpret experimental findings in terms of the modified solution structure, H-bond network, tetrahedrality and dielectric properties of water. Considering the aqueous octanol solutions being studied here are in the alcohol rich region, water-water interactions are expected to significantly different from those in the bulk phase. Our study suggests significant changes in water-water interactions and considerable modifications of water-water, water-octanol, and octanol-octanol H-bonding in these mixtures, and a severe compromise on the tetrahedrality of bulk water. The latter has led to weak or negligible impact of water on the solution static dielectric constant, ε_s.

3.2 Experimental and Computational Details

3.2.1 Materials and Sample Preparation

Octanol (anhydrous, ≥99%) was used as received from Sigma-Aldrich. Millipore water was used for sample preparation. Aqueous-octanol binary mixtures were prepared with water mole fractions $0 \leq X_{H_2O} \leq 0.20$ via sonication after mixing the required amounts of water and octanol in glass containers for 15 minutes. Subsequently, the binary aqueous mixtures were shaken (200 rpm, shaker incubator) for 2 hours, producing colourless transparent solution at each of the mole fractions chosen. Water saturated octanol ($X_{H_2O} \sim 0.27$)[66] was prepared employing the

same procedure, followed by separating the water-saturated octanol layer from the remaining water layer by using a separating funnel. Proper care was taken to avoid presence of excess water in water-saturated octanol. Samples thus prepared at 298 ± 1 K were then used for DRS and other relevant measurements. Temperature dependent measurements were performed after ensuring proper thermal equilibration for all samples at each of the desired temperatures.

3.2.2 Density, Viscosity and Refractive Index Measurements

Density (ρ) and viscosity coefficient (η) measurements were performed by using an automated temperature-controlled density-cum-sound analyser (Anton Paar, model DSA 5000) and microviscometer (AMVn, Anton Paar), respectively.[67,68] Refractive index (n_D) was recorded using an automated temperature-controlled refractometer (RUDOLPH, J357).[69] Temperature dependent η, ρ and n_D values are summarized in Table A3.1 (Appendix)

3.2.3 DRS Data Collection and Analysis

Two dielectric set-ups[70] were used for measuring DR of liquid samples. The E4990A impedance analyser with 16452A liquid test fixture has been used for low frequency measurement from 20 Hz to 10 MHz. The N5235B PNA-L network analyser (500 MHz to 50 GHz) with open ended coaxial probe kit (performance probe for N5235B) were used for DR measurement of liquid. Details of the measurements protocols and data analyses are the same as those discussed in chapter 2. More details about DRS measurements are available ref [70–74] Temperature dependent DRS experiments were performed at 283 K to 323 K.

3.2.4 Differential Scanning Calorimetry (DSC) Measurement

To explore water mole fraction dependence melting temperature (T_m) in octanol + water mixtures, the differential scanning calorimetry (DSC) (DSC, TA Instruments Q200) measurements were carried out.[70] The temperature window (113 K to 323 K) with constant heat flow 5 K/min was held on to for all DSC measurements. The samples were contained in an airtight aluminum pan with an aluminum cap (40 μl, Tzero, TA Instruments).

3.2.5 Simulation Details

The standard equilibrium molecular dynamics simulation technique was employed to study octanol+ water binary mixtures. Three binary mixture compositions with water mole-fractions 0.05, 01 and 0.2 were considered for our simulations. The non-polarizable three-point SPC/E model[75] of water was employed to represent water in these binary mixtures as well as for neat bulk water. The OPLS-AA[76] parameters for octanol were generated with CM1A (Atomic Charge Model-I) charge (scaled with a factor of 1.14 for neutral molecules) using the LigParGen web server[77–80].

Besides binary mixtures, neat components (octanol and water) were simulated for understanding the impact of water through a comparison between the neat and the mixture results. The number of constituent water and octanol molecules for these three binary mixtures and two neat systems are provided in Table A3.2 (Appendix).

Initial configurations of molecules within a cubic box were built using the Packmol software[81]. The initial configurations were subjected to energy minimization via the steepest-decent algorithm. Then a short NVT equilibration was carried out for 500 ps at 303 K. This temperature was chosen for proper comparison with experimental data. Subsequently, a final NPT equilibration for 10 ns was carried out. The well converged density values thus obtained were in good agreement with the experimental densities. These are provided in Table A3.3 (Appendix). During the NPT equilibration, the Noose-Hoover thermostat[82,83] with 0.5 ps time-constant was employed to maintain the temperature at 303 K. The pressure was maintained at 1 bar via employing Parrinello-Rahman barostat[84] with a time-constant of 2 ps. The cut-off distance for bonded and non-bonded interactions were considered to be 1.4 nm. The Particle Mesh Ewald (PME)[85,86] method was employed to deal with electrostatic interactions.

Then a 10 ns long production run was carried out employing the NVT ensemble using the pre-equilibrated structures. In this final NVT production run the trajectories were saved with a time-gap of 0.1 ps.

For simulations of dielectric properties, a production run of 100 ns long in the NPT ensemble was carried out and the trajectories were saved with a time-gap of 0.1 ps. Pressure and temperature of the simulated binary mixtures were controlled via the Parrinello-Rahman barostat[84] with 2 ps time-constant and the Noose-Hoover thermostat[82,83] with 0.5 ps time-constant. These simulations were run at a single temperature and the temperature was fixed at 303 K. Note here that a 100 ns production run was necessary for convergence of the collective

dipole moment fluctuations and the minimization of errors associated with calculated dielectric properties. A leap-frog algorithm for integrating Newton's equations of motion was used with a timestep of 1 fs. Periodic boundary conditions in all three directions and minimum image convention were implemented throughout the simulation. All simulations carried out here were performed using the GROMACS 4.6.5 MD simulation package.[87–91]

Dielectric constants for the systems studied were ensemble-averaged from the longtime portions (approximately the last 20 ns) of the 100 ns NPT production run when dipole fluctuations were found to be sufficiently softened. The solution static dielectric constant (ε_s) was calculated from the following formula[92,93],

$$\varepsilon_s = 1 + \frac{<M^2> - <M>^2}{3\varepsilon_0 k_B T <V>} \; , \tag{3.1}$$

where M is the total dipole moment of the simulation box. T being the temperature and $< V >$ the ensemble averaged volume of the simulation box over the time considered for the calculation. ε_0 denotes the free space permittivity. While calculating ε_s for the individual constituents in these aqueous solutions (octanol and water in the binary mixtures), M would be the total dipole moment of that constituent within the box.

Although the OPLS-AA force field employed for neat octanol underestimates ε_s in comparison to that reported in experiments, the existing simulation studies[17,94] (see Table A3.4 (Appendix) support our simulation results for neat octanol. The simulated ε_s value for neat SPC/E water also corroborates well with those from earlier reports.[95] We would like to mention here that there exist no simulation studies as yet on dielectric relaxations of octanol+water binary mixtures.

3.3 Results and Discussion

In this section we would first present our experimental results on composition dependent dielectric relaxations of octanol+water binary mixtures in the temperature range, 283 K to 323 K and discuss the impact of water on solution dielectric properties in light of the findings from our DSC measurements. Subsequently, we present our representative simulation results in order to provide microscopic explanations for the solution dielectric behaviour in terms of water H-bond structure, tetrahedrality and dynamics.
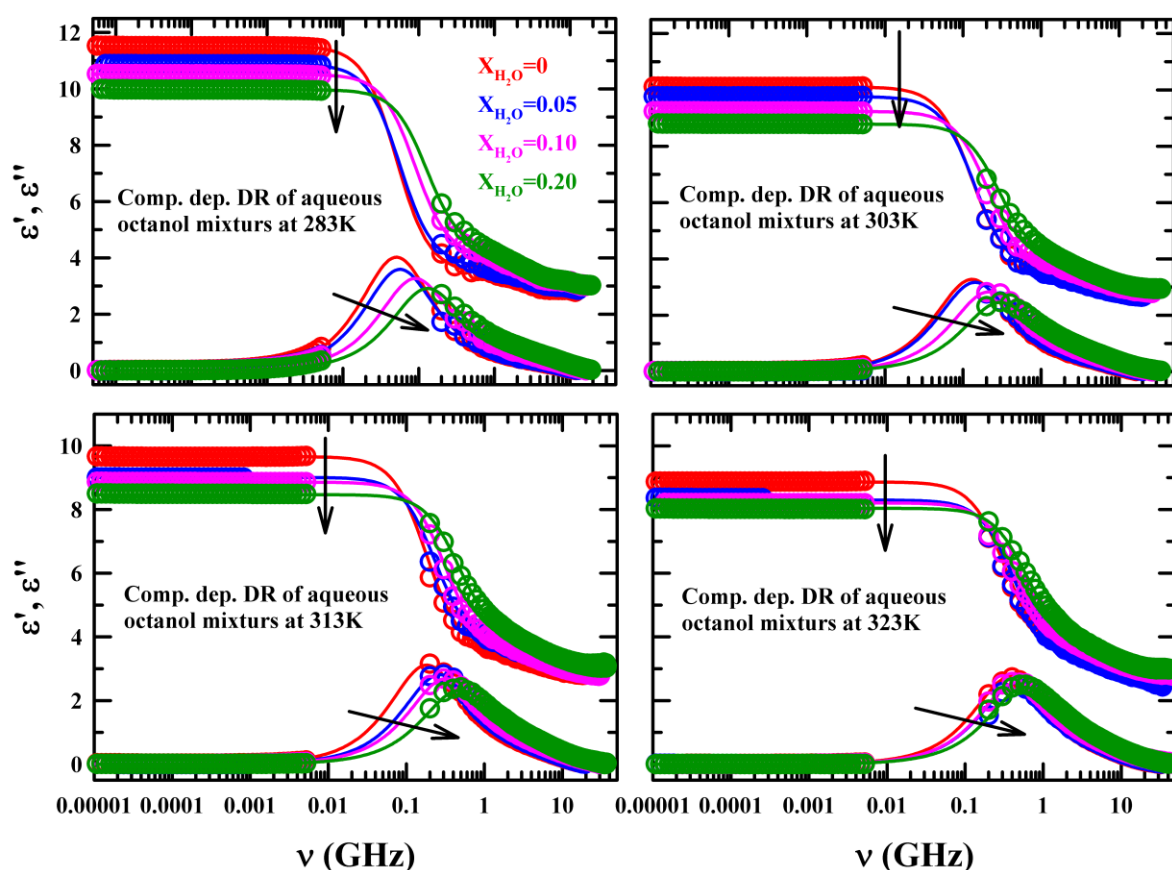
Figure 3.1: Composition dependent real (ε') and imaginary (ε'') components of the complex dielectric spectra recorded for aqueous octanol mixtures at different temperatures (283 K, 293 K, 313 K and 323 K). Experimental data are shown by symbols while lines passing through the data represent double-Debye fits. All representations are colour-coded.

3.3.1 Composition and Temperature Dependent DR Measurements: Impact of Water

Figure 3.1 presents the composition dependent dielectric relaxation spectra of aqueous octanol solutions at four different temperatures, (283 K, 293 K, 313 K and 323 K), along with the 2D fits. The fit parameters are provided in Table 3.1. Data presented in Figure 3.1 and the fit parameters in Table 3.1 clearly indicate that the value of $\varepsilon(\nu \rightarrow 0) \equiv \varepsilon_s$ decreases gradually upon successive addition of water with a concomitant shortening of the relaxation times. The water-induced decrease of ε_s for octanol has been observed before and explained[9] in terms of rearrangement of octanol in aqueous solutions 'into a structure of reduced polarizability.' The specific role of water in inducing such solution phase rearrangement and modifications of its own dielectric and structural properties, however, was not explained in microscopic terms in those studies. Temperature dependent DR spectra of these liquid media (X_{H_2O} = 0, 0.05, 0.1

and 0.2) shown in Figure A3.5 (appendix) and the corresponding 2D fit parameters summarized in Table A3.6 (appendix) also indicate decrease of ε_s with faster relaxation upon increasing solution temperature. This is summarized in Figure 3.2 which highlights the qualitatively similar effects of both water and temperature on ε_s of octanol. The 'temperature-like' impact of water on ε_s is counter-intuitive and thus striking, although such an impact of water on ε_s was found earlier in DR measurements of aqueous solutions of pentanol.[35.] We will come back to this aspect when we present our simulation results in the next section.

Table 3.1: Composition dependent double-Debye fit parameters of experimentally measured DR spectra (frequency regime: 20 Hz to 5 MHz, and 200 MHz to 50 GHz) in aqueous octanol mixtures at 293K.[a]

X_{H_2O}	ε_s	$\Delta\varepsilon_1$	τ_1/ps	$\Delta\varepsilon_2$	τ_2/ps	ε_∞	$\langle\tau_{DR}\rangle$/ps
			283 K				
0	11.51	8 (93)[b]	3138	0.64 (07)	107	2.87	2926
0.05	10.86	7.12 (90)	2823	0.78 (10)	114	2.96	2552
0.10	10.51	6.43 (87)	1794	0.97 (13)	98	3.11	1573
0.20	9.97	5.65 (82)	1250	1.22 (18)	89	3.10	1041
			293 K				
0	10.47	7.09 (91)[b]	1729	0.66 (09)	76	2.72	1580
0.05	10.10	6.56 (89)	1404	0.78 (11)	75	2.76	1258
0.10	9.66	6.15 (88)	1134	0.80 (12)	55	2.72	1004
0.20	9.34	5.23 (83)	786	1.09 (17)	64	3.02	663
Water	80.7			74.7	10	6.0	10
			303 K				
0	10.10	6.17 (87)	1233	0.96 (13)	68	2.97	1082
0.05	9.75	6.31 (90)	1018	0.68 (10)	66	2.76	922
0.10	9.23	5.58 (88)	760	0.76 (12)	50	2.89	675
0.20	8.78	4.67 (81)	559	1.11 (19)	58	3.00	463
			313 K				
0	9.66	6.14 (90)	883	0.64 (10)	61	2.88	801

0.05	8.99	5.52 (91)	604	0.52 (09)	60	2.95	555
0.10	8.68	5.20 (87)	510	0.78 (13)	46	2.88	450
0.20	8.46	4.37 (82)	347	0.94 (18)	51	3.15	294
323 K							
0	8.82	5.38 (90)	420	0.59 (10)	51	2.85	383
0.05	8.27	4.93 (89)	380	0.6 (11)	40	2.74	342
0.10	821	4.5 (85)	354	0.82 (15)	38	2.77	307
0.20	8.04	4.04 (81)	268	0.94 (19)	43	3.05	225

[a]Individual time constants and corresponding amplitudes can be reproduced within ±5 % of the reported values.

[b]Number in parenthesis shows percentage of dispersion amplitude of a given DR dispersion step to total dispersion.
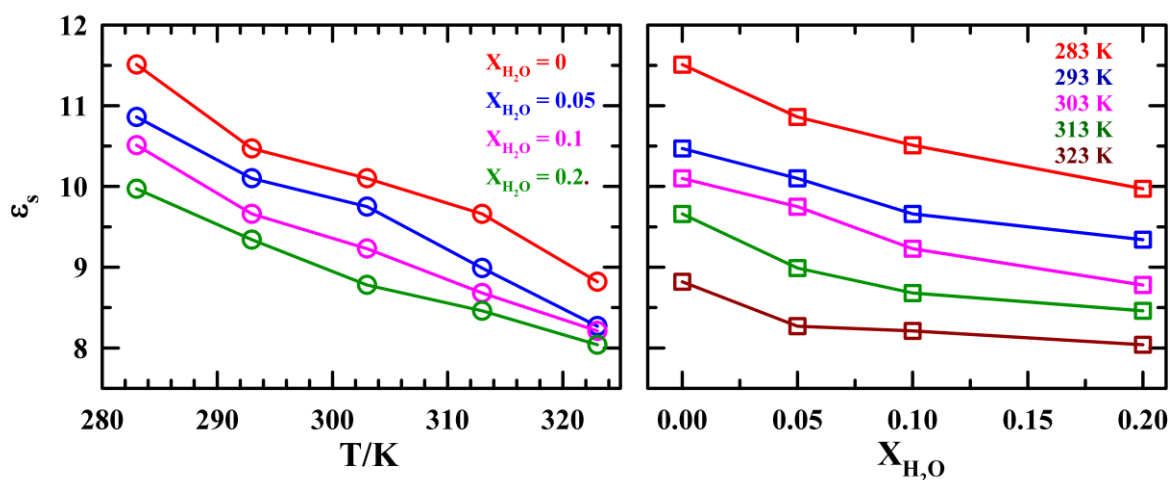
Figure 3.2: Temperature and water mole fraction (X_{H_2O}) dependent static dielectric constant (ε_s) of octanol+water binary mixtures. All representations are colour-coded.

The mixture composition dependence of the individual and average relaxation times is quite interesting as the decrease of them upon increasing water mole fraction is more pronounced than the concomitant reduction of solution viscosity. This is shown in Figure 3.3 Results in this figure suggest that a change of the liquid system from neat octanol to the binary mixture at X_{H_2O} = 0.2 reduces the average DR time by ~40-70% at these temperatures, whereas the

solution viscosity decreases by only ~4-6%. This difference of nearly an order of magnitude between the impacts of water on η and $\langle \tau_{DR} \rangle$ clearly indicates that the measured DR is not governed by the bulk solution viscosity but by the local friction environment. It is already known that water in these binary mixtures occupies the interstices of spherical polar region formed via the self-aggregation of alcohol hydroxyl groups leading to swelling and deformation.[9] The measured DR therefore reflects the water-altered polarization relaxation of this polar environment created jointly by the hydration water and octanol -OH groups. Consequently, the time-dependent friction of this polar environment regulates the DR, allowing the detected orientational relaxation [96,97] to partially decouple from the bulk solution viscosity.
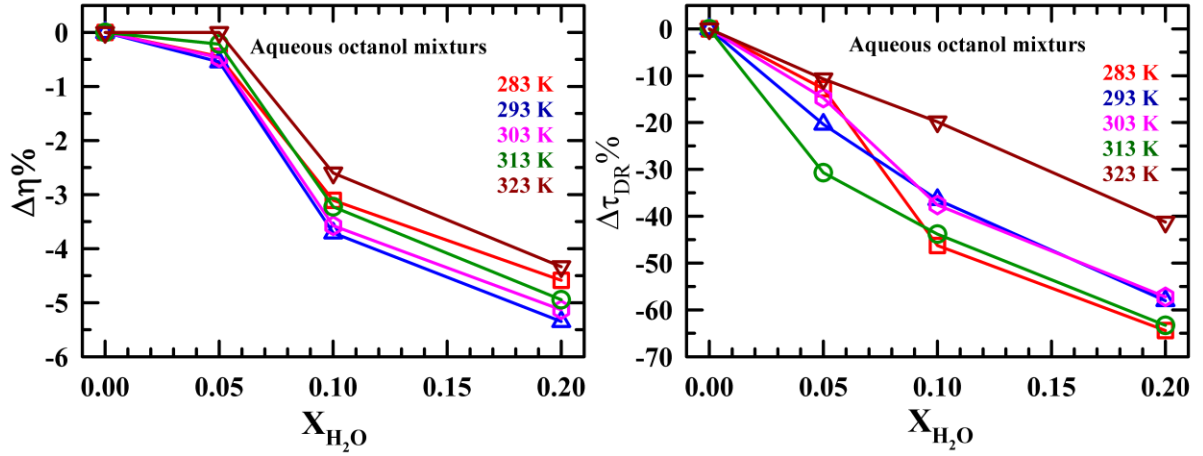
Figure 3.3: Representative plot of water mole fraction (X_{H_2O}) dependent $\Delta\eta\%$ (left panel) and $\Delta\tau_{DR}\%$ (right panel) for octanol + water mixture at different temperatures (283 K to 323 K,). and $\Delta\eta\% = \left[\eta_{X_{H_2O}} - \eta_{octanol}\right] \times 100/\eta_{octanol}$ $\Delta\tau_{DR}\% = \left[\langle\tau_{DR}\rangle_{X_{H_2O}} - \langle\tau_{DR}\rangle_{octanol}\right] \times 100/\langle\tau_{DR}\rangle_{octanol}$ where η and $\langle\tau_{DR}\rangle$ are average viscosities and DR times of these systems.

Next, we examine the DR time constants and the associated amplitudes (summarized in Table 3.1) in order to understand the role of water in DR of these aqueous solutions. Notice in Table 3.1 that the slower of the two relaxation components accounts for ~80-90% of the total dielectric dispersion measured. This is qualitatively similar to what was found in earlier DR measurements of aqueous solutions of shorter chain primary alcohols[35,37,98–100]. However, there is a difference: the amplitudes and time constants associated with DR of octanol+water binary mixtures do not show, unlike those for aqueous solutions of shorter chain alcohols, any abrupt composition dependencies; rather, a regular X_{H_2O} dependence for them is observed. Interestingly, water-doping of octanol does not produce, in addition to the two-step relaxation

processes detected already for neat octanol, a third water-like relaxation component (with a DR time constant ~10 ps)[98,101]. This suggests that bulk-like 'free' water is probably absent even at
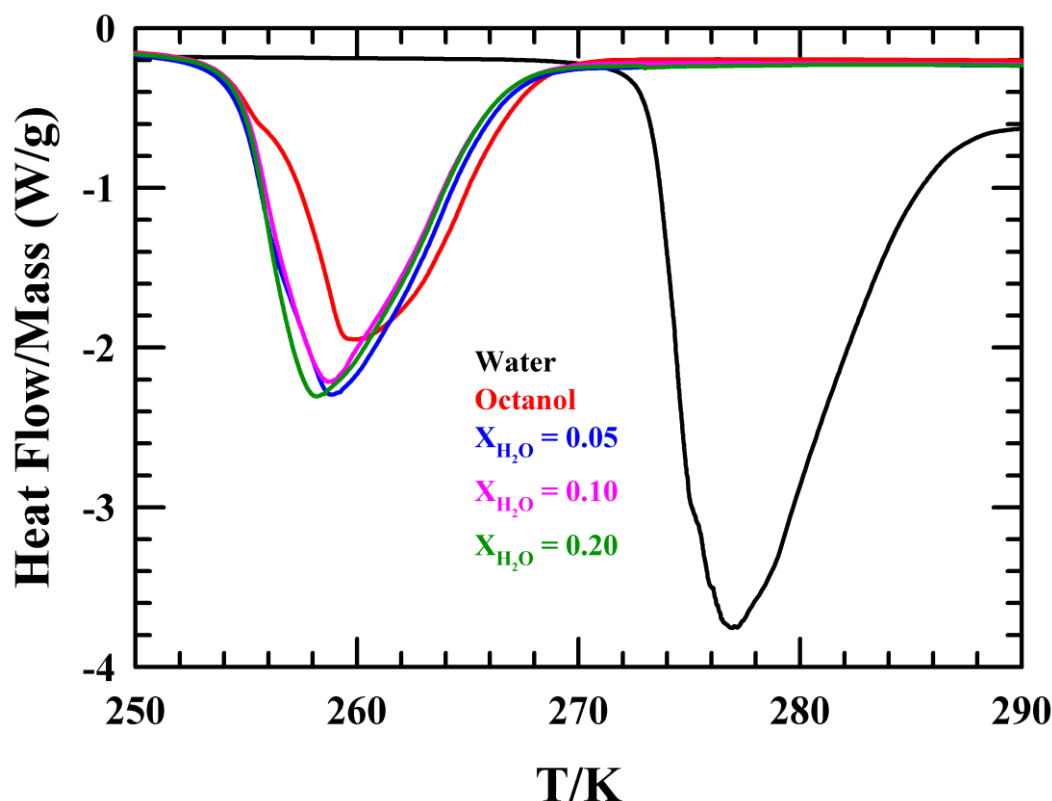
Figure 3.4: Water mole fraction dependent ($X_{H_2O} = 0$, 0.05, 0.1, 0.2, 1) DSC thermogram of octanol + water mixtures. During DSC experiment 5 K/min heating rate was maintained.

the highest water mole fraction studied, $X_{H_2O} = 0.2$. This can only happen when these added water molecules are engaged primarily in hydrating the octanol hydroxyl groups.[102–104] The presence of the ~30-120 ps DR timescale requires further investigation as this timescale may arise from the reorientational relaxation of the freezable 'bound' water molecules.[105–108] The presence of freezable bound water has been investigated via differential scanning calorimetric (DSC) measurements. The composition dependent DSC thermograms for octanol+water mixtures are shown in Figure 3.4 along with that for neat water. Clearly, there is no signature of free bulk water as the endothermic peaks are in the close proximity to that of neat octanol and are much away from the corresponding position for neat water. Notice also that these composition peak shapes are featureless indicating only composition dependent melting points of these binary mixtures. The weak shift of the endothermic peak toward lower temperature with X_{H_2O} reflects solute-induced depression of freezing point and represents colligative behaviour of these binary systems. The absence of any additional sub-zero feature[101] in these DSC data, therefore, indicate that the added water molecules are totally engaged in hydrating

the octanol hydroxyl groups, leaving no free water molecules to form the second solvation shell and establish a dynamic equilibrium with those in the primary layer.
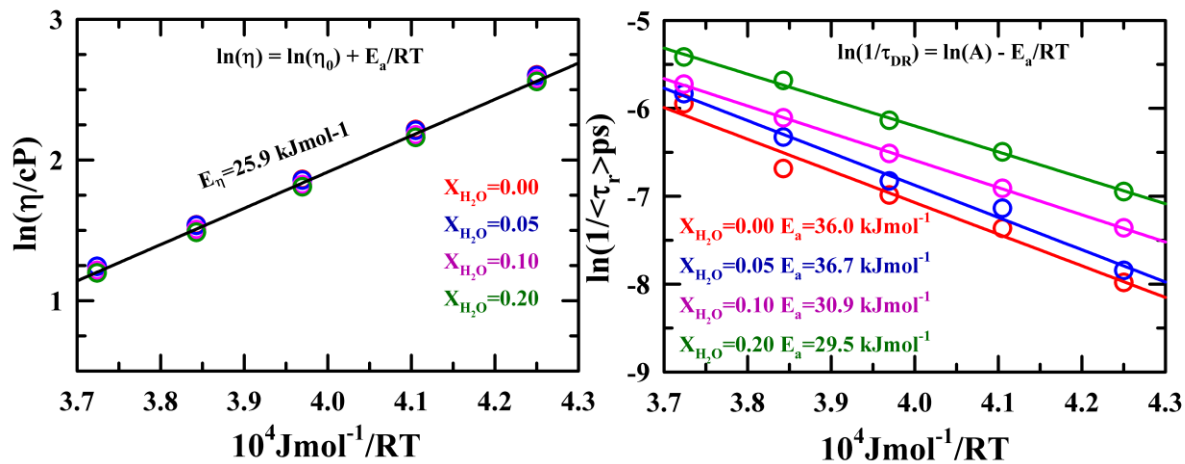
Figure 3.5: Arrhenius-type temperature dependence of medium viscosity (left panel) and average DR time ($\langle \tau_{DR} \rangle$) (right panel) for Octanol + water mixtures. Estimated activation energies at different water mole fraction (X_{H_2O}) in aqueous octanol mixtures are shown. Solid lines passing through the data points represent linear fits. All representations are colour-coded.

The DSC thermograms presented above then opens up the following questions: (i) how 'watery' are these water molecules with respect to structure, H-bond network, tetrahedrality and dielectric behaviour, and (ii) what are the likely origins of the two-step DR processes detected in the present measurements and how is the double Debye relaxation detected for neat octanol impacted by the added water? We address the second concern first. The hydrodynamic rotations of the 'spherical' polar regions formed by neat octanol[9] and by its hydrated counterpart cannot account for the slower of these two DR time constants as indicated in a comparison between measurements and theoretical predictions in Table A3.7 (Appendix). This observation in conjunction with the DSC results suggests that these two DR time constants have probably originated from the underlying biphasic temporal frictional profile that characterizes the orientational relaxation of the local polar environment. Experimentally observed multi-exponential dynamic fluorescence anisotropy decays of polar solutes in neat polar solvents[109] provides a qualitative support to the above argument. Available computer simulation studies[25,96,97,110] have repeatedly suggested that these multi-phasic orientational frictional profiles derive contributions from both polar rotations and collective H-bond relaxations in associated solvents. These two mechanisms would be involved in the measured

DR response for the systems studied here, although this proposition requires separate simulations of composition dependent reorientational and structural H-bond relaxations of the composite polar moiety formed via the H-bond interaction of octanol hydroxyl groups with the hydration water.

The above discussion essentially points towards a break-down of the hydrodynamic relations in predicting the measured average DR times by using the medium bulk viscosity. This is further highlighted in Figure 3.5 where X_{H_2O} dependent DR activation energies ($E_a^{\langle \tau_{DR} \rangle}$) are compared with viscosity activation energies (E_a^η) for these systems. The difference between the estimated $E_a^{\langle \tau_{DR} \rangle}$ and E_a^η clearly indicates bulk viscosity not being the governing factor. This is further highlighted in the analyses of viscosity coupling of the measured average DR times provided in Figure A3.8 (Appendix) which fortuitously predicts a close proximity between the measured DR times and the stick hydrodynamic predictions for octanol rotation times, signalling homogeneous solution dynamics. This is erroneous because X-ray measurements[9] and previous simulations[17,19] have confirmed heterogeneous solution features.

3.3.2 Water in Octanol + Water Mixtures: Structure, H-bonding, Tetrahedrality and Dielectric Property

3.3.2.1 Structure

Figure 3.6 (a) depicts the radial distribution function (RDF) between oxygen pairs of two water molecules (Ow-Ow RDF) in octanol-water solution at three compositions and in neat water. Difference in the interaction between water molecules in octanol solution and in neat water can be clearly understood from this figure. The very high intensity of the first peak of the RDF compared to neat bulk water suggests increased water-water interactions in these binary aqueous mixtures. Note that as the water concentration is increased, the height of this peak first increases and then decreases (see inset for a clearer description). This is qualitatively similar to earlier observation for alcohol-alcohol RDF in water rich aqueous solutions of alcohols other than octanol.[111–117] This has been explained in terms of alcohol aggregation at very low concentration of alcohol. However, water aggregation in the alcohol-rich region of aqueous alcohol solutions is a new finding and has not been reported before. Similar results have also been obtained for aqueous solutions of tertiary butyl alcohol (TBA) at these water concentrations (X_{H_2O}= 0, 0.05, 0.1, and 0.2, see Figure A3.9 (appendix). These results therefore

indicate stronger interaction among water molecules when present at low concentrations in aqueous solutions of alcohols, leading to aggregation of water molecules.

Figure 3.6 (b) depicts the RDF between the pair of oxygen sites of two octanol molecules. For better comparison RDF corresponding to neat octanol system is also provided. Note here that the RDF peak height is increased over that for the neat octanol at the lowest X_{H_2O} studied here, followed by a decrease below the neat value at higher X_{H_2O}. The latter is a reflection of the dilution effect on oxygen-oxygen interactions among octanol molecules of water at higher concentrations. The interaction between the oxygen atoms of octanol and oxygen of water and that between the central carbon atoms (C4) of octanol are presented in the Figure A3.10 (Appendix). These figures indicate increased interaction between the intermolecular oxygen sites at the lowest X_{H_2O} studied, followed by a reduction of the same upon further addition of water in the mixture, while the intermolecular interactions between the alkyl groups show some changes initially and then remain unaltered upon further increase of X_{H_2O} in the mixture.
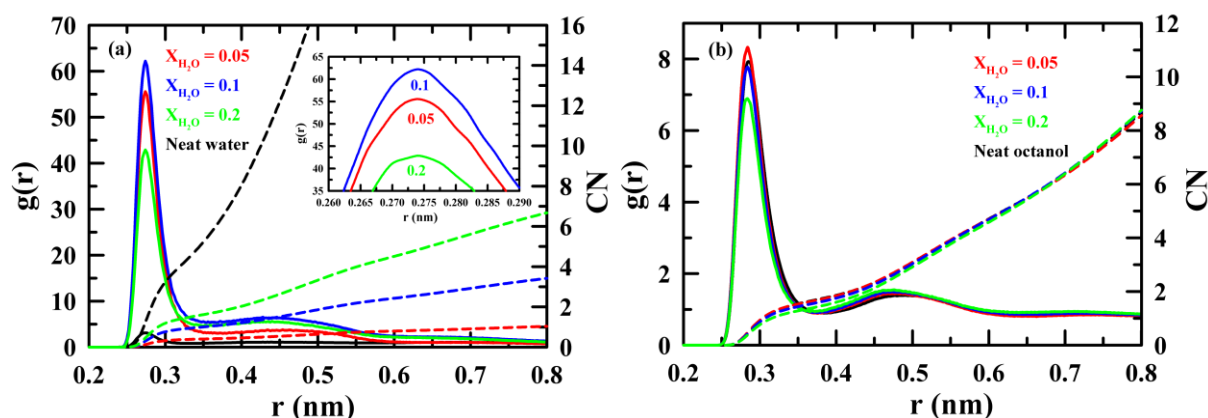
Figure 3.6: Representative plot of water mole fraction (X_{H_2O}) dependent radial distribution function (RDF, solid lines) and cumulative RDF (short dashed lines) of two intra-species oxygen sites (a) water-water (left panel) (b) octanol-octanol for three octanol-water systems (right panel). Corresponding RDF and cumulative RDF for neat systems are also shown in the same plot. Inset of panel 6(a) represents water-water RDF peak in 0.05, 0.1, and 0.2 mole fraction of water in octanol+water mixture.

3.3.2.2 Intra- and Inter-species H-bonding: Water-water H-bond Distributions

The following condition has been followed to detect H-bonds between water molecules[118,119]:
a) the distance between the donor oxygen atom and the acceptor oxygen atom is less than 0.35
nm, b) the O-H (donor) -O (acceptor) angle is less than 30°, and c) the distance between the
oxygen (O) and hydrogen (H) atoms must be less than 0.245 nm.

For monitoring the octanol-octanol H-bonding, the geometrical criteria[120] that have been
considered are as follows: a) the distance between the donor and acceptor oxygen atoms is less
than 0.35 nm, b) the O-H (acceptor)-O (donor) angle is less than 30°, and c) the distance
between O (donor) and H (acceptor) is less than 0.28 nm. These criteria for detecting H-
bonding between Octanol molecules have also been followed for monitoring the H-bonding
between octanol and water molecules in these binary mixtures.

The fractions of octanol and water molecules participated to intra- and inter-species H-bonding
have been calculated in order to find non-participation of any of the species at any mixture
composition. Results obtained in this analysis is expected to compliment the results on X_{H_2O}
dependence of average number of H-bonds per octanol or water molecule. While calculating
average number of H-bonds per molecule we have considered only the participant molecules,
not all the molecules of a given species that are present in a solution at a particular X_{H_2O}.

Table 3.2 summarizes the average number of H-bonds in between water-water, octanol-octanol
and water-octanol species. Notice here that the average values reported here are averaged over
the participating molecules and not over the whole system. We find that at $X_{H_2O} = 0.05$, only
$\sim 33\%$ of the total number of water molecules in this mixture are H-bonded within themselves
(water-water intermolecular) with an average number of H-bonds 1.13 per water molecule,
whereas ~13% water molecules are H-bonded with octanol with average number of water-
octanol H-bonds ~1.06 per water molecule. This implies that *not* all water molecules are inter-
or intra-molecularly H-bonded. On the other hand, ~84% of octanols are intramolecularly H-
bonded with an average number of intramolecular H-bonds ~1.52 per octanol molecule.
Interestingly, for neat octanol similar population (~81%) of octanol molecules is involved in
intramolecular (octanol-octanol) H-bonding with average H-bonds 1.52 per octanol molecule.
This suggests that the existence of non-hydrogen bonded *'free'* water molecules because of the
lack of H-bonding sites. As the water mole fraction increases from $X_{H_2O} = 0.05$ to 0.20, the
populations of water molecules participating in water-water and octanol-water H-bonding
increase by a large margin but the average number of H-bonds between water molecules (1.67)

are far from its neat value (3.58). Also, nearly all water molecules become H-bonded with water, octanol or with both.

Table 3.2: Average number of water-water, octanol-octanol and water-octanol H-bonds

X_{H_2O}	<NHB$_{W-W}$>	<NHB$_{O-O}$>	<NHB$_{O-W}$>
0.0	------	1.54 (81.8%)	------
0.05	1.13 (32.25%)	1.52 (83.9%)	1.06 (12.7%)
0.1	1.46 (58.77%)	1.49 (80.5%)	1.18 (20%)
0.2	1.67 (78.30%)	1.42 (72.9%)	1.16 (37%)
Neat water	3.58 (100%)	------	-----

Figure 3.7 depicts the distribution of water-water H-bonds per water molecule, $P(N_{HB}/water)$, in these mixtures at three different water mole fractions. For a proper comparison, we have also presented the same distribution for neat ambient water. Clearly, $P(N_{HB}/water)$ in these mixtures are quite different from that for the neat system. The population of water molecules with *zero* water-water H-bonds is the largest at $X_{H_2O} = 0.05$ among the three mole fractions investigated and it decreases rapidly upon increasing the water concentration. Interestingly, water molecules with four H-bonds are nearly non-existent at these X_{H_2O}. There exists a very small population of water which have three water-water H-bonds. With respect to water-water H-bonds, therefore, water in octanol+water binary mixtures in the alcohol-rich region at these water mole-fractions are very different from bulk water. Moreover, clustering of water molecules is also predicted in these solutions.

3.3.2.3 Angle Distributions and Tetrahedrality: Evolution of Extremely 'Constrained' H-bond Network

The tetrahedral order parameter (Q) defined as follows[121]:

$$Q_i = 1 - \frac{3}{8}\sum_{j=1}^{3}\sum_{k=j+1}^{4}(cos\theta_{ijk} + {}^1/_3)^2 \text{ and } \langle Q \rangle = \frac{1}{n_{water}}\sum_i Q_i, \tag{4.2}$$

where Q_i is the tetrahedral order parameter of the ith water, θ_{ijk}- the angle subtended by each pair (designated by j and k) of the nearest four water molecules on the central ith water molecule. For a random and uniform distribution of these angles, $Q = 0$; for a perfect tetrahedral structure, on the other hand, $Q = 1$.
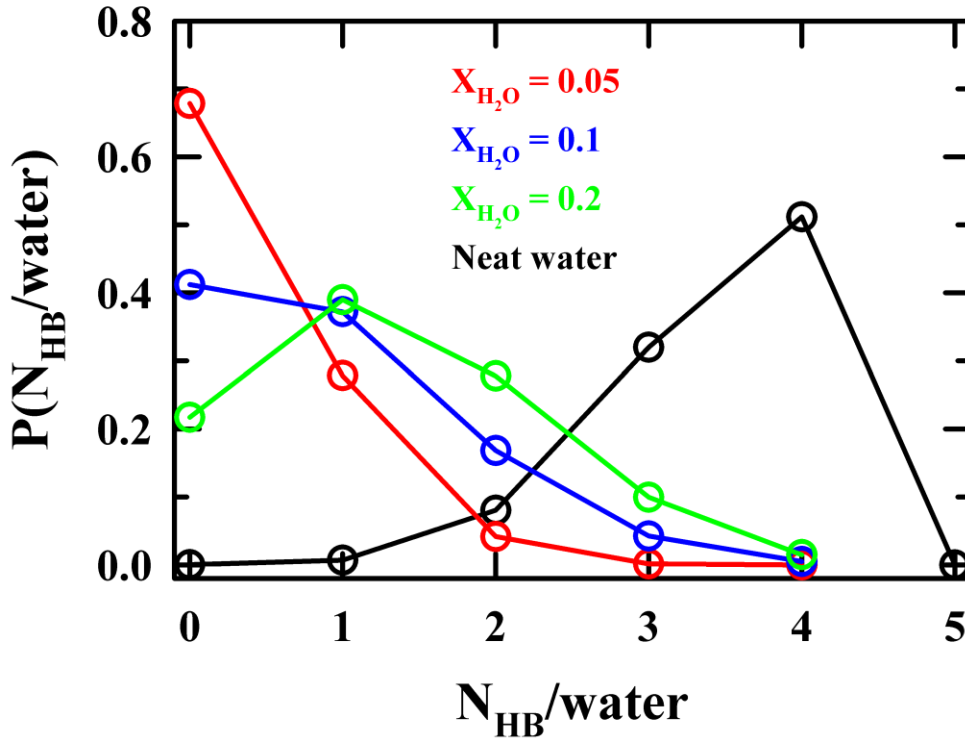
Figure 3.7: Distribution of number of water-water hydrogen bonds per water molecule $P(N_{HB}/water)$ for three octanol-water systems and neat ambient water.

Figure 3.8 depicts the distribution of angle $P(\theta)$ between three oxygen atoms of the three nearest neighbour H-bonded water molecules (see Figure A3.11(appendix) for a schematic representation). Fig. 9 shows the distribution of tetrahedral order parameter $P(Q)$ of water molecules in these binary mixtures. $P(\theta)$ and $P(Q)$ obtained for neat water are also presented in the same plot for a comparison. Notice in Figure 3.8 that angle distributions for water in these binary mixtures are broader than that for neat ambient water. Also, the population with $\theta \sim 104^o$ in bulk water is largely transferred to water populations in these binary mixtures that are compelled to assume angles $0^o \leq \theta \leq 60^o$. It is quite interesting that in these binary mixtures water can sustain appreciable populations assuming angles $\theta < 50^o$ with peaks at $\theta \sim 10^o$ and $\theta \sim 40^o$ for $X_{H_2O} = 0.1$ and 0.2, whereas bulk water has none in this regime. This arrangement with $\theta \sim 50 - 60^o$ is the triangular arrangement of water molecules which can be found in neat water also. Angular structures of water molecules with $\theta \sim 10^o$, 40° and 100° are schematically presented in Figure A3.12 (appendix). Water molecules with angles $0^o \leq \theta \leq 60^o$ are therefore orientationally highly constrained and, as a result, appreciable number of water molecules in these binary mixtures are far from 'water-like'.
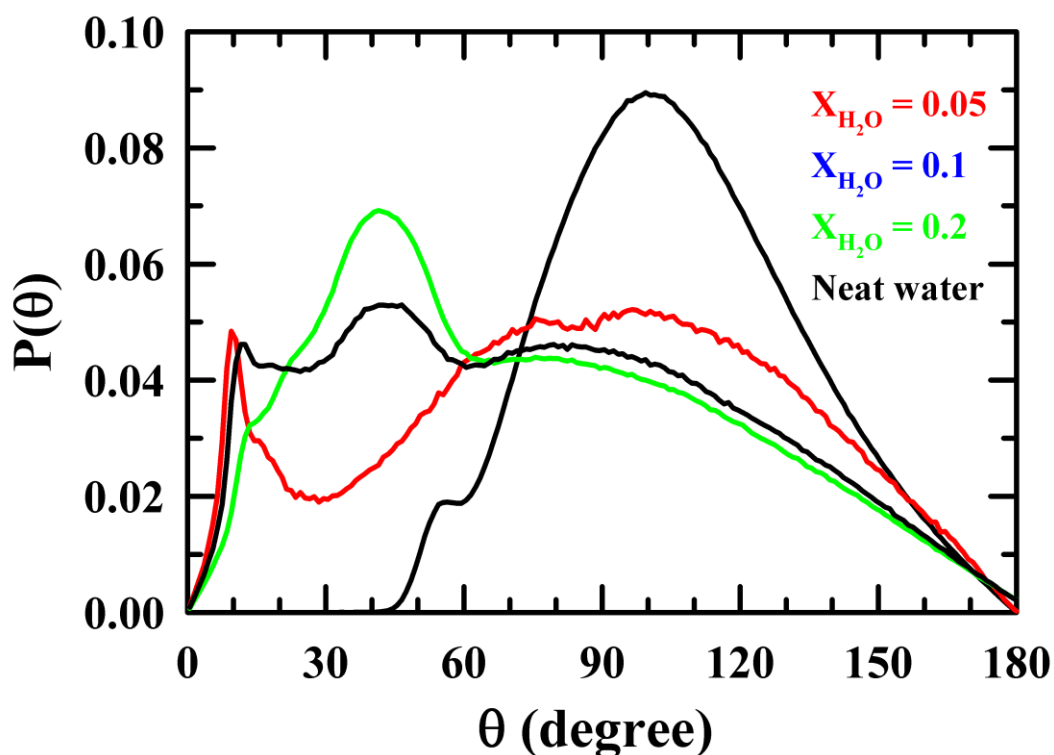
Figure 3.8: Distribution of tetrahedral angle between three nearest neighbour hydrogen bonded water molecules $P(\theta)$ for three octanol-water systems. Corresponding distribution for neat water system also given here.

Similar deviation from neat water can also be observed in Figure 3.9 where the composition dependent order parameter distribution, $P(Q)$, is shown as function of the order parameter, Q. Table A3.13 (appendix) summarizes the ensemble averaged tetrahedral order parameter values ($< Q >$). Notice in this table that $< Q >$ ranges from zero to large negative values for water in these octanol+water binary mixtures, whereas $< Q > \sim 0.62$ for neat ambient water. This implies that the overall tetrahedrality of water in these binary mixtures has been severely compromised, although there exists a certain population which possess tetrahedral order parameter as found for bulk water.
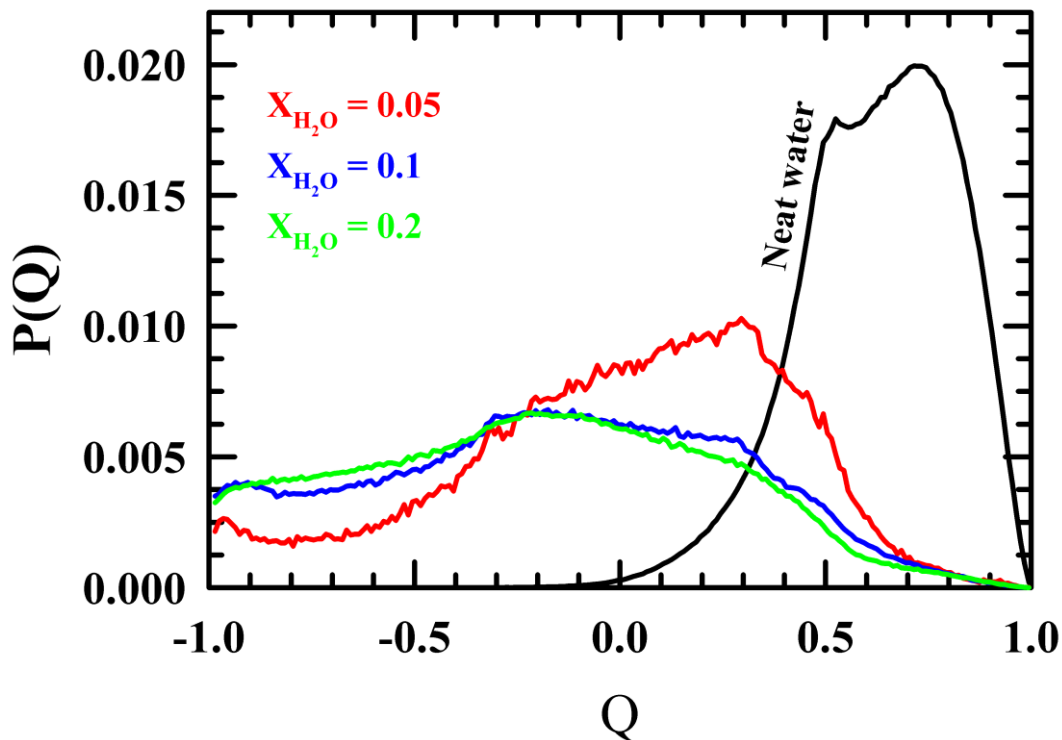
Figure 3.9: Distribution of tetrahedral order parameter $P(Q)$ for three octanol-water systems. Corresponding distribution for neat water system also given here.

Although the common perception regarding negative tetrahedral order parameter cannot provide any new information, we presented the full probability distribution of Q that covers both the positive and the negative values. Note here that a few existing studies[122] presents only positive Q values with a slowly decaying tail extending to the negative Q region. In addition, there are also several previous studies [123–125] that have reported negative Q region for water trapped in confined environments. Interestingly, equation 5 itself suggests that there could be a set of nearest neighbour angles for which Q could assume negative values for a group of water molecules. We have separated out these two types of angles responsible for positive and negative Q values for water molecules in these aqueous binary mixtures and the corresponding probability distributions are in Figure 3.10. Angle distribution related to positive Q values are shown in the left panel, while the right panel describes the same for negative Q. These two panels depicts clearly the orientation pattern of the nearest neighbours giving rise to 'completely' broken tetrahedral structure leading to negative tetrahedral parameter values ($Q<0$). Fig. 10 also explains how this 'random' orientation of water molecules which are responsible for broken tetrahedral network depends on the composition of the octanol-water mixture.
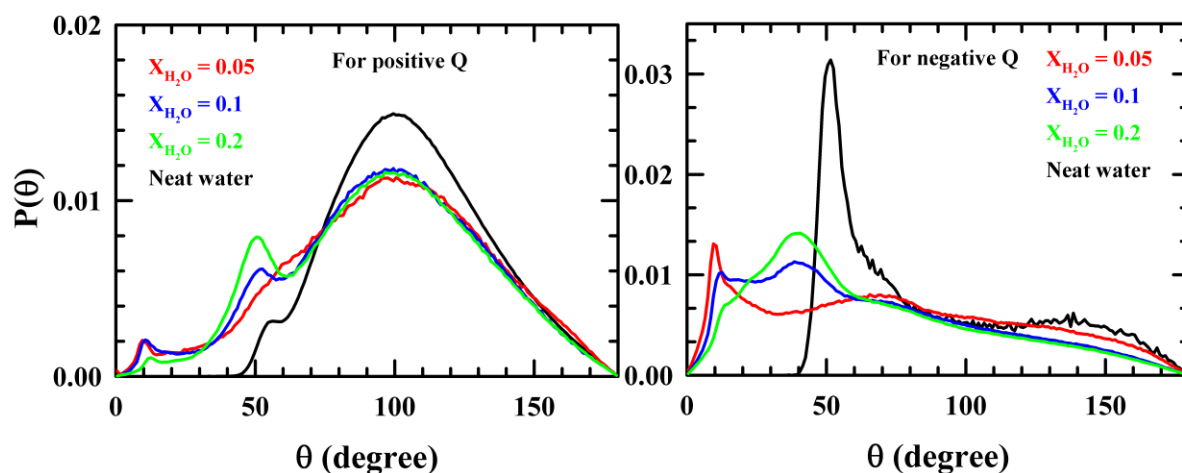
Figure 3.10: Distribution of tetrahedral angle between three nearest neighbour hydrogen bonded water molecules $P(\theta)$ for positive and negative Q values in the three octanol-water systems studied. Corresponding distributions for neat water are also shown (black lines).

3.3.2.4. Dielectric Property: Solution Static Dielectric Constant

Figure 3.11 presents the time evolution of ε_S for octanol+water binary mixtures at three water mole fractions along with those for the neat systems. Clearly, ε_S values are converging at long time during the production runs in these simulations and thus these ε_S can be regarded as the static dielectric constant values for the respective neat and binary mixtures. Table 3 summarizes the composition dependent ε_S values obtained in simulations for these mixtures and their decompositions into component-wise contributions. Errors obtained via block averaging are mentioned in accompanying parentheses. Notice first in this table that the static dielectric constant changes by a very small amount upon addition of water. The change is, however, opposite to the direction reflected in the experiments where ε_S was found to decrease upon addition of water. This may partly arise from the limitations of the model potential employed for octanol and partly from the reaction field (RF) method employed here to simulate the dielectric behaviour. Considering that neat octanol and octanol + water mixtures are microheterogeneous in nature and RF method is applicable for homogeneous systems only, the non-agreement between simulations and experiments is expected. Even with this caveat, the present simulations predict the correct size (absolute value) of the changes on octanol ε_S (~4) value effected by addition of a solvent of high dielectric constant (ε_S~73). Figure 3.11 is also demonstrating the reason for this water-induced small change; that is, the ε_S values of SPC/E water in these mixtures are dramatically reduced from that of neat water (~73) and become <2 (see Table 3.3). This is probably connected to the significantly modified H-bond network and

average number of H-bonds for water in these binary mixtures presented already in Figure 3.7, Figure 3.8 and Figure 3.9.
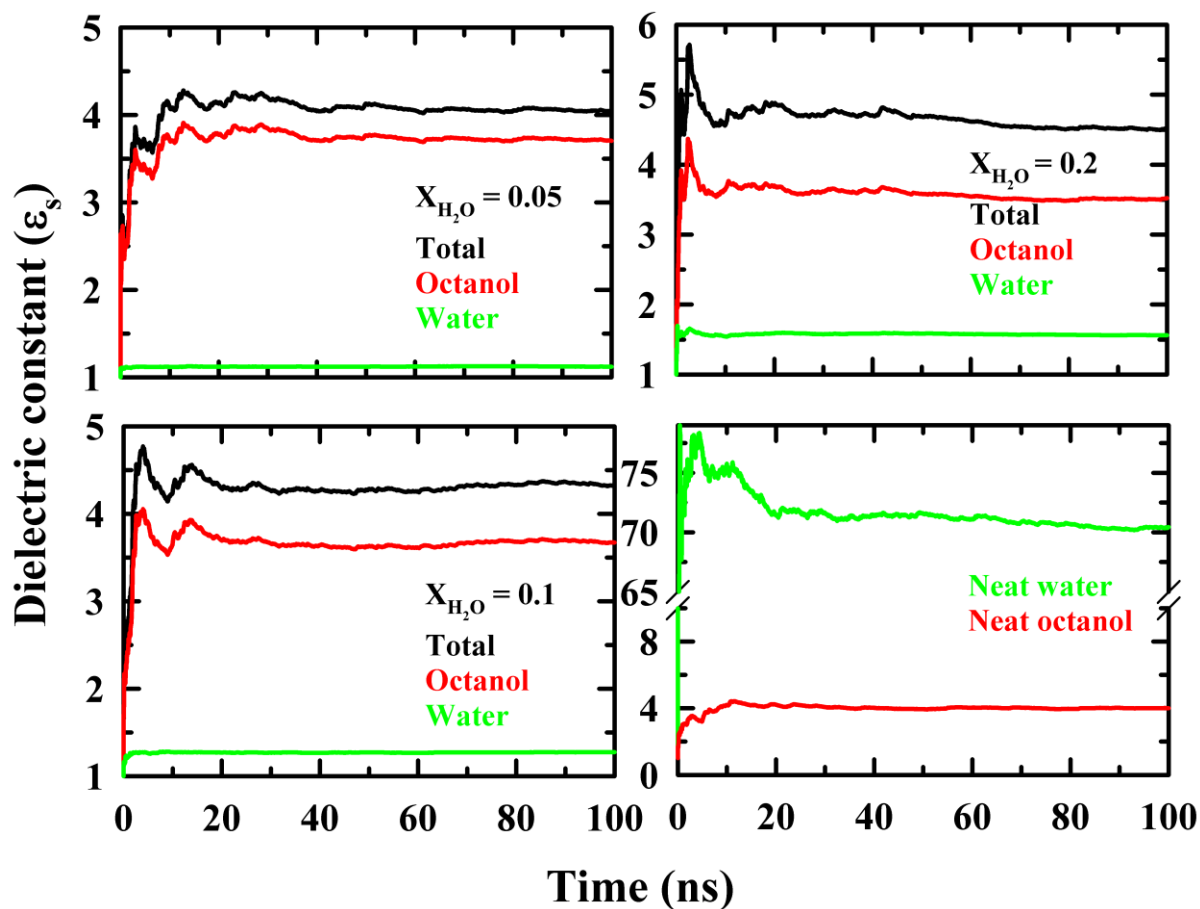
Figure 3.11: Time evolution of static dielectric constant (ε_s) of the octanol+water binary mixtures. For each binary mixtures along with the whole system contribution from octanol and water are also shown in the figure. (a) X_{H_2O}=0.05 (b) 0.10 (c) 0.20 (d) neat systems.

Table 3.3: Dielectric constant (ε_s) for neat systems and binary mixtures and their constituent molecular types reported in the present study. Maximum error associated with these calculations (block averaging) are provided in the parenthesis.

ε_s	0.05	0.10	0.20	Neat octanol	Neat water
Total system	4.01 (1.14%)	4.27 (0.71%)	4.74 (0.49%)	------	------
Octanol	3.54 (1.55%)	3.65 (1.34%)	3.67 (0.70%)	3.87 (2.1%)	------
Water	1.12 (0.06%)	1.27 (0.15%)	1.57 (0.23%)	------	72.5 (1.12%)

3.4 Conclusion

In this work, we have studied ocatnol+water binary mixtures at a few different compositions to investigate the impact and structure of water via DRS and computer simulations. Our mixture composition and temperature dependent DR measurements indicated two-step relaxations throughout the compositions together with nominal changes in the solution static dielectric constant, ε_s. In addition, no bulk water-like DR relaxation component was observed. DSC measurements supported this observation by reflecting only the water mole-fraction dependent depression of freezing point of octanol. Simulations revealed drastic compromise of the three-dimensional H-bond network of bulk water. The number of water-water H-bonds per water molecules was estimated to be ~1.13 (3.54 for bulk SPC/E bulk water). At the lowest mole fraction studied, our simulations predicted presence of a significant number of water molecules with no water-water H-bond. Water populations in these mixtures possessing near tetrahedral angles were also found to be greatly diminished with strong indications for the presence of highly constrained near-linear water. The average value for the tetrahedral order parameter ($\langle Q \rangle$) was predicted to be even negative, suggesting a severe damage to the global tetrahedrality of water in these mixtures at the alcohol-rich region. The angle distributions corresponding to negative and positive values of the tetrahedral order parameter have been obtained and explicitly shown. Large-scale compromise in the H-bond network and global tetrahedral order parameter has been found to be related the negligible impact of water on the solution static dielectric constant, rendering itself to act as a weakly polar solvent with ε_s even as low as ~2.

We would like to mention here that the experimentally measured composition dependent static dielectric constants for aqueous solutions of butanol, pentanol and hexanol show a shallow minimum within a certain region of water concentrations before increasing again upon further addition of water.[34] This indicates water mole fraction dependent modifications of water H-bond network structure and average tetrahedrality. However, solubility of alcohol in water dictates the highest water mole fraction that can be studied for such a turnaround of solution ε_s. Unfortunately for octanol, we cannot go beyond $X_{H2O} = 0.2$ because of the solubility gap associated with this binary mixture. Consequently, aqueous solutions of octanol water mole fractions higher than $X_{H2O} = 0.2$ could not be explored. Such a study for aqueous mixtures of lower alcohols is definitely possible via simulations and should be performed to track how tetrahedrality is regained at higher water mole fractions.

Appendix A3

Table A3.1: Temperature dependent and water concentration dependent densities (ρ)[a], viscosity coefficients (η)[b], & refractive indices (RI, n_D)[c] of water/octanol binary mixtures.

Temperature (T/K)	Density (ρ/gcm^{-3})	Viscosity coefficient (η/cP)	RI (n_D)
$X_{H_2O} = 0$			
283	0.8321	13.52	…..
293	0.8251	9.16	1.4269
303	0.8181	6.43	1.4259
313	0.8112	4.65	1.4244
323	0.8041	3.46	1.4232
$X_{H_2O} = 0.05$			
283	0.8333	13.46	…..
293	0.8262	9.11	1.4277
303	0.8193	6.40	1.4259
313	0.8122	4.64	1.4239
323	0.8051	3.46	1.4228
$X_{H_2O} = 0.1$			
283	0.8346	13.10	…..
293	0.8275	8.82	1.4274
303	0.8204	6.20	1.4261
313	0.8133	4.50	1.4240
323	0.8061	3.37	1.4230
$X_{H_2O} = 0.2$			
283	0.8374	12.90	…..
293	0.8302	8.67	1.4263
303	0.8232	6.10	1.4243
313	0.8160	4.42	1.4228
323	0.8086	3.31	1.4214

[a]Standard uncertainty in densities (ρ) is 0.0004.

[b]Viscosity coefficient (η) values can be reproduced within ± 5% of the reported values.

[c]Standard uncertainty in RI (n_D) is 0.00002.

Table A3.2: Number of species molecules used in the present simulation study for different compositions of water/octanol mixtures.

X_{H_2O}	$N_{Octanol}$	N_{Water}
0.0	512	---
0.05	486	26
0.1	460	52
0.2	409	103
1	---	250

Table A3.3: Comparison between simulated and experimental density for different compositions of water/octanol mixtures.at 303K

X_{H_2O}	Simulated Density (gcm^{-3})	Experimental Density (gcm^{-3})	% relative error
0.0	0.8102	0.8181	0.9%
0.05	0.8123	0.8193	0.8%
0.1	0.8133	0.8204	0.8%
0.2	0.8145	0.8232	1.05%
1.0	1.012	0.998	1.4%

Table A3.4: Static dielectric constant (ε_s) from experimental and simulation with different force fields for neat Octanol.

	Dielectric constant (Previous studies)	Dielectric constant This study
Exp	10.10	
OPLS-AA[94]	3.7	3.87
OPLS modified charge[94]	2.9	
OPLS-UA[17]	5.1	
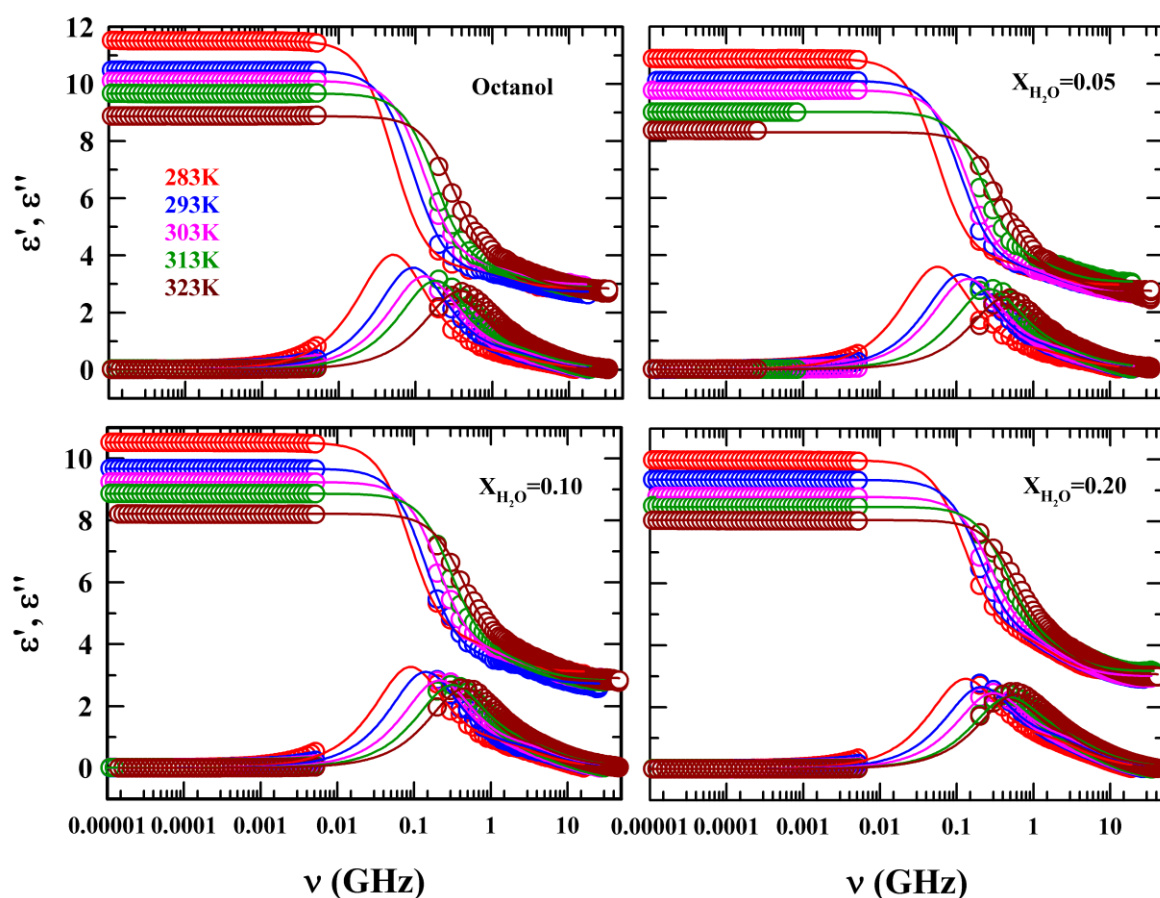
Figure A3.5: Temperature dependent real (ε') and imaginary (ε'') components of the complex dielectric spectra recorded for aqueous octanol mixtures at different water mole fraction (X_{H_2O} = 0, 0.05, 0.1 and 0.2). Experimental data points are shown as symbols while lines passing through the data point shows double-Debye fits. All representations are colour-coded.

Table A3.6: Double-Debye fit parameters of temperature dependent experimentally measured DR spectra (frequency regime: 20 Hz to 5 MHz and 200 MHz to 50 GHz) for various mole fraction of water (X_{H_2O}= 0, 0.05, 0.10, 0.20 and water saturated octanol) in octanol.[d]

T/K	ε_s	$\Delta\varepsilon_1$	τ_1/ps	$\Delta\varepsilon_2$	τ_2/ps	ε_∞	$\langle\tau_{DR}\rangle$/ps	χ^2
				X_{H_2O}= 0				
283	11.51	8 (93)[e]	3138	0.64 (07)	107	2.87	2926	0.0021
293	10.47	7.09 (91)	1729	0.66 (09)	76	2.72	1580	0.003
303	10.10	6.17 (87)	1233	0.96 (13)	68	2.97	1082	0.0041
313	9.66	6.14 (90)	883	0.64 (10)	61	2.88	801	0.0047

323	8.82	5.38 (90)	420	0.59 (10)	51	2.85	383	0.0091
$X_{H_2O}= 0.05$								
283	10.86	7.12 (90)	2823	0.78 (10)	114	2.96	2552	0.0032
293	10.10	6.56 (89)	1404	0.78 (11)	75	2.76	1258	0.0035
303	9.75	6.31 (90)	1018	0.68 (10)	66	2.76	922	0.0041
313	8.99	5.52 (91)	604	0.52 (09)	60	2.95	555	0.0064
323	8.27	4.93 (89)	380	0.6 (11)	40	2.74	342	0.0098
$X_{H_2O}= 0.10$								
283	10.51	6.43 (87)	1794	0.97 (13)	98	3.11	1573	0.0043
293	9.66	6.15 (88)	1134	0.80 (12)	55	2.72	1004	0.0042
303	9.23	5.58 (88)	760	0.76 (12)	50	2.89	675	0.0050
313	8.68	5.20 (87)	510	0.78 (13)	46	2.88	450	0.0064
323	821	4.5 (85)	354	0.82 (15)	38	2.77	307	0.068
$X_{H_2O}= 0.20$								
283	9.97	5.65 (82)	1250	1.22 (18)	89	3.10	1041	0.0044
293	9.34	5.23 (83)	786	1.09 (17)	64	3.02	663	0.0067
303	8.78	4.67 (81)	559	1.11 (19)	58	3.00	463	0.0061
313	8.46	4.37 (82)	347	0.94 (18)	51	3.15	294	0.0077
323	8.04	4.04 (81)	268	0.94 (19)	43	3.05	225	0.0086
Water saturated octanol								
293	9.02	4.82 (81)	580	1.1 (19)	44	3.1	478	0.0053
303	8.72	4.53 (78)	495	1.26 (22)	45	2.93	396	0.0056
313	8.31	4.61 (85)	320	0.80 (15)	39	2.92	277	0.0069

[d]Individual time constants and corresponding amplitudes can be reproduced within ±5 % of the reported values.

[e]Number in parenthesis shows percentage of dispersion amplitude of a given DR dispersion step to total dispersion.

Table A3.7: Hydrodynamic molecular rotation times for octanol and water at 293 K calculated using the SED relation with stick boundary condition, $\tau_r = \frac{3Vfc\eta}{K_BT}$ where for stick condition $c=1$ and also considering spherical shape i.e. $f=1$, r is radius of spherical polar region in octanol (4.39 Å) and hydrated octanol (4.99 Å) system taken from ref[9]. Calculation of τ_{rot} for hydrated octanol, only approximation we assumed that viscosity of hydrated octanol is equals to high water containing octanol + water (X_{H_2O}=0.2) system.

T/K	Pure octanol		Hydrated octanol	
	τ_{rot} (ps) stick	τ_1 (ps) in DR (Exp)	τ_{rot} (ps) stick hydrated octanol	τ_1 in DR (Exp) at X_{H_2O}=0.2
283	3678	3138	5152	1250
293	2407	1729	3345	786
303	1634	1233	2275	559
313	1143	883	1596	347
323	824	420	1158	268
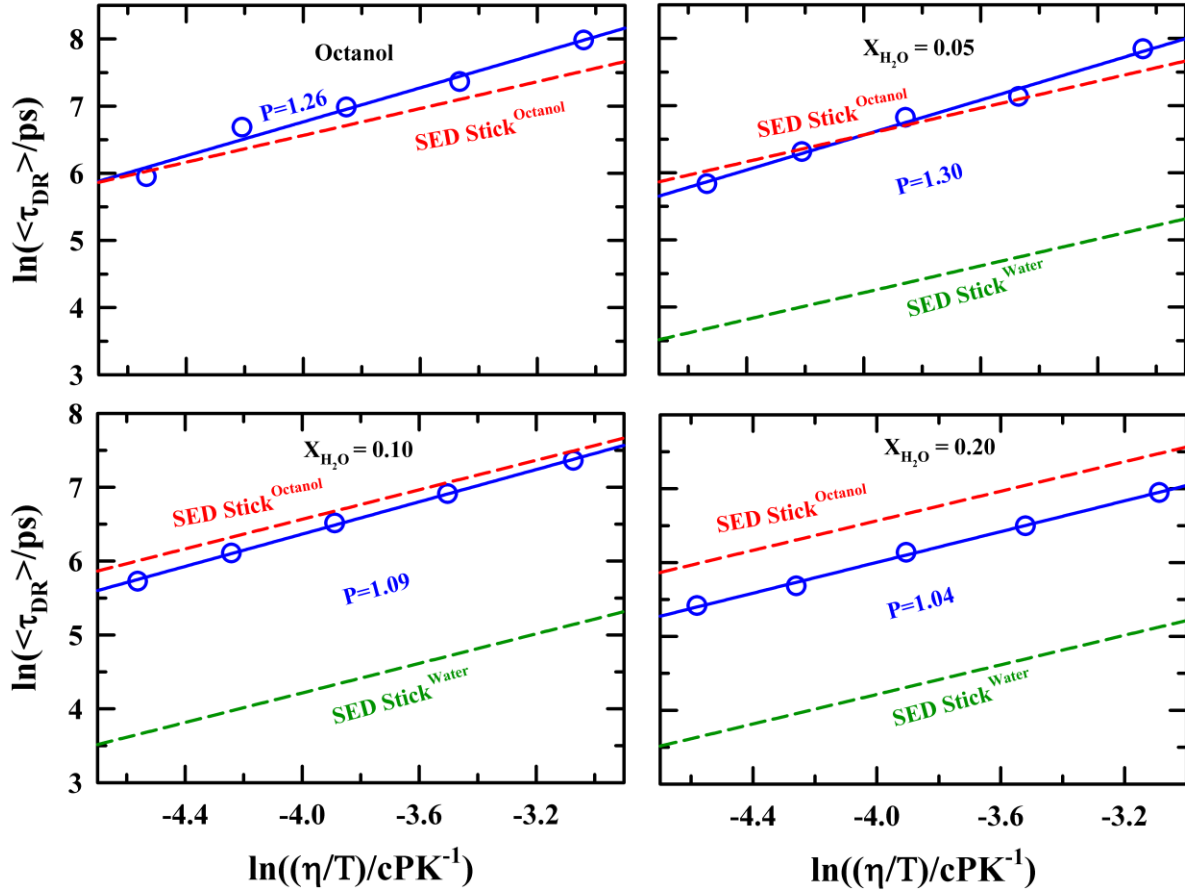
Figure A3.8: $(\frac{\eta}{T})$ dependence of the average DR relaxation times ($\langle\tau_{DR}\rangle$) for aqueous octanol mixtures at different mole fraction of water (X_{H_2O}). SED predictions with stick boundary condition for octanol and water molecules using the experimental temperature dependent solution viscosity coefficients (η) are also shown in these panels for comparison.
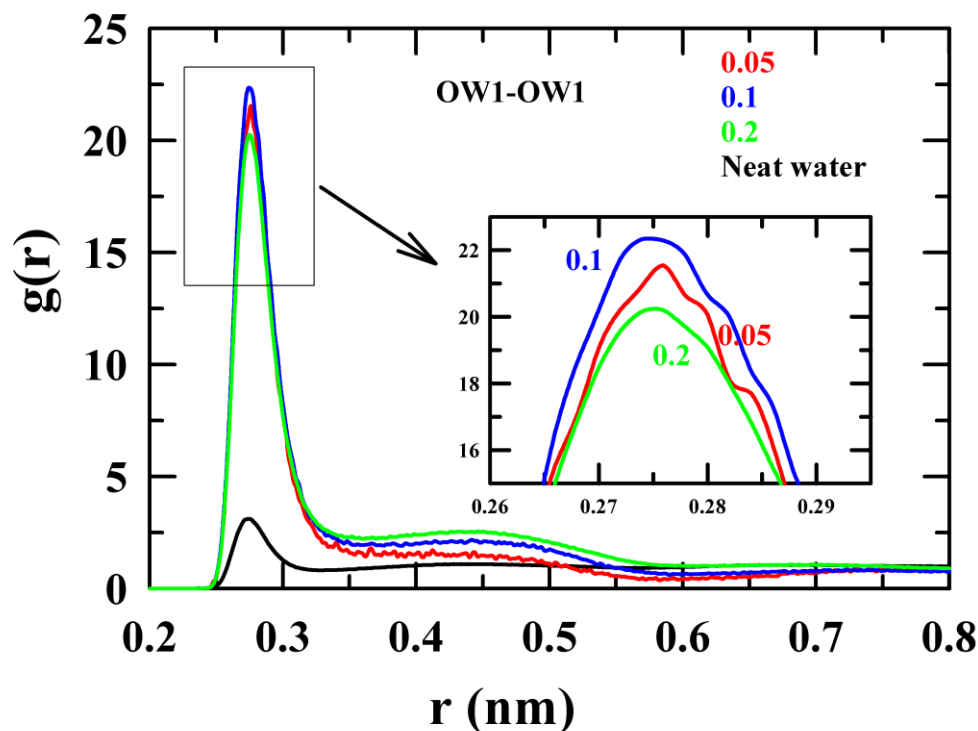
Figure A3.9: Radial distribution function (RDF) of two intra-species oxygen sites of water-water for three TBA-water systems. Corresponding RDFs for neat systems also provided in the same plot.
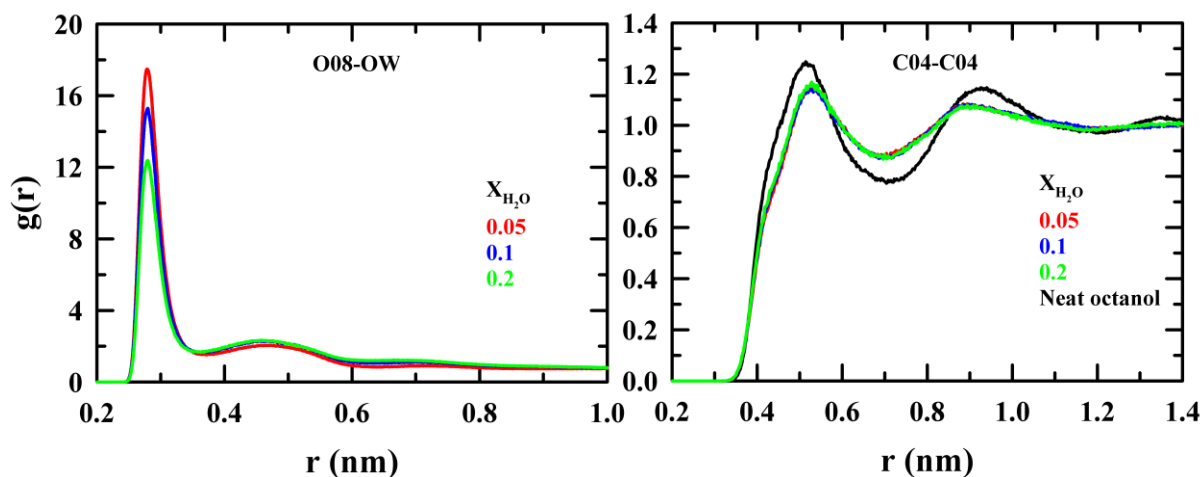
Figure A3.10: Radial distribution function (RDF) of two inter-species oxygen sites (water-octanol) for three octanol-water systems (left panel). Radial distribution function (RDF) of two central carbon sites (C04-C04) of octanol molecules for three octanol-water systems. (right panel) Corresponding RDFs for neat octanol system also provided in the same plot.
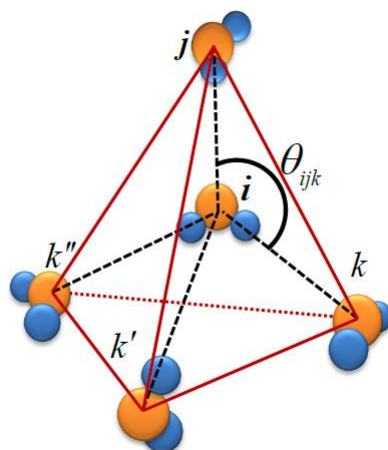
Figure A3.11: Schematic diagram of tetrahedral H-bond network for water.
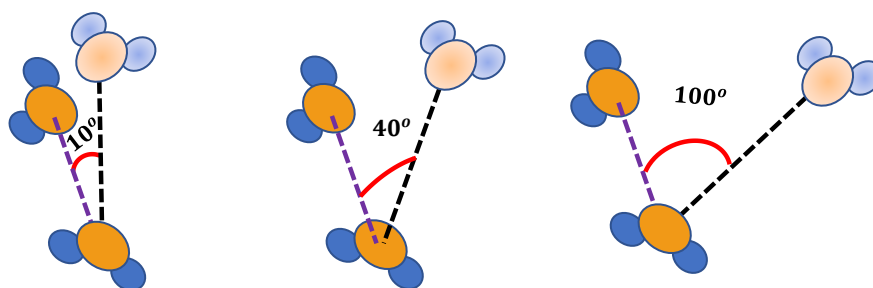
Figure A3.12: Schematic diagram of possible arrangements of water molecules in different water-octanol systems. Water orientational arrangement around the angle $\theta \sim 40^o$ can be found in both neat water and in Octanol-Water solution. The orientational arrangement around the angle $\theta \sim 10^o$ is found to be evolved in octanol-Water system only. And the orientational arrangement around the angle $\theta \sim 100^o$ has been found in both bulk and octanol-Water mixture although the population of water molecules with this orientational arrangement is much higher in neat water system compared to octanol-water mixture.

Table A3.13: Ensemble averaged tetrahedral order parameter values, $< Q >$, of water molecules in water-octanol system.

X_{H_2O}	$< Q >$ value
0.05	0.01
0.1	-0.45
0.2	-0.51
Neat water	0.62

Chapter 3

References

1   A. Leo, C. Hansch and D. Elkins, *Chem. Rev.*, 1971, **71**, 525–616.

2   R. N. Smith, C. Hansch and M. M. Ames, *J. Pharm. Sci.*, 1975, **64**, 599–606.

3   C. Hansch, J. P. Björkroth and A. Leo, *J. Pharm. Sci.*, 1987, **76**, 663–687.

4   M. N. Martinez and G. L. Amidon, *J. Clin. Pharmacol.*, 2002, **42**, 620–643.

5   A. R. Katritzky, M. Kuanar, S. Slavov, C. D. Hall, M. Karelson, I. Kahn and D. A. Dobchev, *Chem. Rev.*, 2010, **110**, 5714–5789.

6   P. C. Stein, M. Di Cagno and A. Bauer-Brandl, *Pharm. Res.*, 2011, **28**, 2140–2146.

7   W. C. Wimley and S. H. White, *Nat. Struct. Mol. Biol.*, 1996, **3**, 842–848.

8   W. C. Wimley, T. P. Creamer and S. H. White, *Biochemistry*, 1996, **35**, 5109–5124.

9   N. P. Franks, M. H. Abraham and W. R. Lieb, *J. Pharm. Sci.*, 1993, **82**, 466–470.

10   K. S. Vahvaselkä, R. Serimaa and M. Torkkeli, *J. Appl. Crystallogr.*, 1995, **28**, 189–195.

11   P. Sassi, A. Morresi, M. Paolantoni and R. S. Cataliotti, in *J. Mol. Liq.*, 2002, **96–97**, 363–377.

12   M. Paolantoni, P. Sassi, A. Morresi and R. S. Cataliotti, *Chem. Phys.*, 2005, **310**, 169–178.

13   F. Palombo, T. Tassaing, Y. Danten and M. Besnard, *J. Chem. Phys.*, 2006, **125**, 094503-undefined.

14   Y. Marcus, *J. Solution Chem.*, 1990, **19**, 507–517.

15   P. Sassi, M. Paolantoni, R. S. Cataliotti, F. Palombo and A. Morresi, *J. Phys. Chem. B*, 2004, **108**, 19557–19565.

16   P. Sassi, A. Marcelli, M. Paolantoni, A. Morresi and R. S. Cataliotti, *J. Phys. Chem. A*, 2003, **107**, 6243–6248.

17   S. E. DeBolt and P. A. Kollman, *J. Am. Chem. Soc.*, 1995, **117**, 5316–5340.

18   S. A. Best, K. M. Merz and C. H. Reynolds, *J. Phys. Chem. B*, 1999, **103**, 714–726.

19   J. L. MacCallum and D. P. Tieleman, *J. Am. Chem. Soc.*, 2002, **124**, 15085–15093.

20   C. D. Wick and T. M. Chang, *J. Phys. Chem. B*, 2014, **118**, 7785–7791.

21   S. K. Garg and C. P. Smyth, *J. Phys. Chem.*, 1965, **69**, 1294–1301.

22   J. Barthel and R. Buchner, *Pure & Appl. Chem.*, 1991, **63**, 1473–1482.

23   T. Sato, A. Chiba and R. Nozaki, *J. Chem. Phys.*, 1999, **110**, 2508–2521.

24   J. T. Kindt and C. A. Schmuttenmaer, *J. Phys. Chem.*, 1996, **100**, 10373–10379.

25   S. Das, R. Biswas and B. Mukherjee, *J. Phys. Chem. B*, 2015, **119**, 274–283.

26   R. Biswas, N. Nandi and B. Bagchi, *J. Phys. Chem. B*, 1997, **101**, 2968–2979.

27   M. L. Horng, J. A. Gardecki, A. Papazyan and M. Maroncelli, *J. Phys. Chem.*, 1995, **99**, 17311–17337.

28   B. Bagchi and R. Biswas, *Adv. Chem. Phys.*, 1999, **109**, 207–433.

29   F. Yang, X. Wang, M. Yang, A. Krishtal, C. van Alsenoy, P. Delarue and P. Senet, *Phys. Chem. Chem. Phys.*, 2010, **12**, 9239–9248.

30   X. Ge and D. Lu, *Phys Rev B*, 2017, **96**, 075114.

31   A. Catenaccio, Y. Daruich and C. Magallanes, *Chem. Phys. Lett.*, 2003, **367**, 669–671.

32   A. S. C. Lawrence, M. P. McDonald and J. v. Stevens, *Trans. Faraday Soc.*, 1969, **65**, 3231–3244.

33   B. C. Lippold and M. S. Adel, *Arch. Pharm.*, 1972, **305**, 417–426.

34   A. D'Aprano, D. I. Donato and E. Caponetti, *J. Solution Chem.*, 1979, **8**, 135–146.

35   S. Mashimo, S. Kuwabara, S. Yagihara and K. Higasi, *J. Chem. Phys.*, 1989, **90**, 3292–3294.

36   U. Kaatze, A. Schumacher and R. Pottel, *Ber. Bunsenges. Phys. Chem. 95 (1991) No. 5*, 1991, **95**, 585–592.

37   A. C. Kumbharkhane, S. M. Puranik and S. C. Mehrotra, *J. Chem. Soc. Faraday Trans.*, 1991, **87**, 1569–1573.

38   T. Pradhan, P. Ghoshal and R. Biswas, *J. Chem. Sci.*, 2008, **120**, 275–287.

39   T. Pradhan, P. Ghoshal and R. Biswas, *Journal of Physical Chemistry A*, 2008, **112**, 915–924.

40   S. M. Mejía, J. F. Orrego, J. F. Espinal, P. Fuentealba and F. Mondragón, *Int. J. Quantum Chem.*, 2011, **111**, 3080–3096.

41   S. Y. Noskov, G. Lamoureux and B. Roux, *J. Phys. Chem. B*, 2005, **109**, 6705–6713.

42   S. Dixit, J. Crain, W. C. K. Poon, J. L. Finney and A. K. Soper, *Nature*, 2002, **416**, 829–832.

43   S. Lenton, N. H. Rhys, J. J. Towey, A. K. Soper and L. Dougan, *J. Phys. Chem. B*, 2018, **122**, 7884–7894.

44   T. Lopian, S. Schöttl, S. Prévost, S. Pellet-Rostaing, D. Horinek, W. Kunz and T. Zemb, *ACS Cent. Sci.*, 2016, **2**, 467–475.

45   H. A. R. Gazi and R. Biswas, *J. Phys. Chem. A*, 2011, **115**, 2447–2455.

46   S. Indra and R. Biswas, *Journal of Chemical Physics*, 2015, **142**, 204501.

47   A. Baksi and R. Biswas, *ACS Omega*, 2022, **7**, 10970–10984.

48   Barton A. F. M., *Solubility Data Series: Alcohols with Water*, Elsevier, 1st eds., 1994, vol. 15.

49   W. Dannhauser, *J. Chem. Phys.*, 1968, **48**, 1918–1923.

50   C. P. Johari and W. Dannhauser, *J. Chem. Phys.*, 1969, **50**, 1862–1876.

51   M. Shablakh, L. A. Dissado and R. M. Hill, *J. Chem. Soc. Faraday Trans. 2*, 1983, **79**, 369–417.

52   U. Poser and A. Wiirflinger, *Ber. Bunsenges. Phys. Chem.*, 1988, **92**, 765–770.

53   S. Toshiomi, *Bull. Chem. Soc. Jpn.*, 1989, **62**, 3636–3642.

54   R. Brand, P. Lunkenheimer and A. Loidl, *Phys. Rev. B*, 1997, **56**, R5713–R5716.

55   M. Tyagi and S. S. N. Murthy, *J. Chem. Phys.*, 2001, **114**, 3640–3652.

56   L. M. Wang and R. Richert, *J. Chem. Phys.*, 2004, **121**, 11170–11176.

57   E. Thoms, S. Kołodziej, M. Wikarek, S. Klotz, S. Pawlus and M. Paluch, *J. Chem. Phys.*, 2018, **149**, 214502.

58   Komooka. Hitoshi, *Bull. Chem. Soc. Jpn.*, 1972, **45**, 1696–1700.

59   C. Campbell, J. Crossley and L. Glasser, *Adv. mol. relax. processes*, 1976, **9**, 63–77.

60   K. Ramachandran, K. Dharmalingam, P. Sivagurunathan, B. Prabhakar Undre, P. W. Khirade and S. C. Mehrotra, *Main Group Chem.*, 2005, **4**, 303–308.

61   K. Dharmalingam, K. Ramachandran, P. Sivagurunathan, B. Prabhakar Undre, P. W. Khirade and S. C. Mehrotra, *Bull. Korean Chem. Soc*, 2006, **27**, 2040–2044.

62   K. Ramachandran, P. Sivagurunathan, K. Dharmalingam and S. C. Mehrotra, *Acta Phys. -Chim. Sin.*, 2007, **23**, 1508–1514.

63   P. Sivagurunathan, K. Dharmalingam, K. Ramachandran, B. Prabhakar Undre, P. W. Khirade and S. C. Mehrotra, *J. Mol. Liq.*, 2007, **133**, 139–145.

64   F. Liakath, A. Khan, P. Sivagurunathan, S. Muhammad and S. C. Mehrotra, *Indian J. Phys.*, 2007, **81**, 665–672.

65   G. Ravi, P. B. Undre, K. Ramachandran and K. Samuvel, *S. Afr. J. Chem. Eng.*, 2017, **24**, 71–81.

66   B. E. Lang, *J. Chem. Eng. Data*, 2012, **57**, 2221–2226.

67   H. A. L. Rasidgazi, H. K. Kashyap and R. Biswas, *J. Chem. Sci.*, 2015, **127**, 61–70.

68   A. Das and R. Biswas, *Journal of Physical Chemistry B*, 2015, **119**, 10102–10113.

69   K. Mukherjee, A. Das, S. Choudhury, A. Barman and R. Biswas, *Journal of Physical Chemistry B*, 2015, **119**, 8063–8071.

70   N. C. Maity, A. Baksi, K. Kumbhakar and R. Biswas, *J. Photochem. Photobiol. A: Chem.*, 2023, **439**, 114600.

71   C. J. F. Böttcher and P. Bordewijk, *Theory of Electric Polarization: Dielectrics in Time-dependent*, Elsevier, Amsterdam, 1978.

72   A. Schönhals and F. Kremer, *Theory of Dielectric Relaxation*, Springer Berlin Heidelberg, 2003.

73   P. R. Bevington and D. K. Robinson, *Data reduction and error analysis for the physical sciences*, McGraw-Hill Education, New York, 3rdEdition, 2003.

74   K. Mukherjee, A. Barman and R. Biswas, *J. Mol. Liq.*, 2016, **222**, 495–502.

75   M. Iannuzzi, A. Laio and M. Parrinello, *Phys. Rev. Lett.*, 2003, **90**, 4.

76   T. Kulschewski and J. Pleiss, *Mol Simul*, 2013, **39**, 754–767.

77   L. S. Dodda, I. C. De Vaca, J. Tirado-Rives and W. L. Jorgensen, *Nucleic Acids Res.*, 2017, **45**, W331–W336.

78   W. L. Jorgensen and J. Tirado-Rives, *PNAS*, 2005, **102**, 6665-6670.

79   L. S. Dodda, J. Z. Vilseck, J. Tirado-Rives and W. L. Jorgensen, *J. Phys. Chem. B*, 2017, **121**, 3864–3870.

80   http://zarbi.chem.yale.edu/ligpargen/.

81   L. Martinez, R. Andrade, E. G. Birgin and J. M. Martínez, *J. Comput. Chem.*, 2009, **30**, 2157–2164.

82   S. Nosé, *Mol. Phys.*, 2006, **52**, 255–268.

83   W. G. Hoover, *Phys. Rev. A*, 1985, **31**, 1695.

84   M. Parrinello and A. Rahman, *J. Appl. Phys.*, 1998, **52**, 7182.

85   T. Darden, D. York and L. Pedersen, *J. Chem. Phys.*, 1998, **98**, 10089.

86   A. Aguado and P. A. Madden, *J. Chem. Phys.*, 2003, **119**, 7471.

87   H. Bekker, H. Berendsen, E. Dijkstra, S. Achterop, R. Van Drunen, D. Van der Spoel, A. Sijbers, H. Keegstra, B. Reitsma and M. G. Renardus, *World Scientific Singapore*, 1993, **92**, 252–256.

88   H. J. C. Berendsen, D. van der Spoel and R. van Drunen, *Comput. Phys. Commun.*, 1995, **91**, 43–56.

89   E. Lindahl, B. Hess and D. van der Spoel, *Mol. Model. Annu.*, 2001, **7**, 306–317.

90   D. Van Der Spoel, E. Lindahl, B. Hess, G. Groenhof, A. E. Mark and H. J. C. Berendsen, *J. Comput. Chem.*, 2005, **26**, 1701–1718.

91   D. Hess and E. Lindahl, *Univ. Gron.*, 2001, **2010**, 1991–2000.

92   J.-P. Hansen and I. R. McDonald, *Theory of Simple Liquids With Applications to Soft Matter*, Elsevier, Fourth Edition., 2013.

93   C. J. F. Böttcher and P. Bordewijk, *Theory of Electric Polarization: Dielectrics in Time-dependent*, Elsevier, Amsterdam, 1978.

94   T. Kulschewski and J. Pleiss, *Mol Simul*, 2013, **39**, 754–767.

95   M. Rami Reddy and M. Berkowitz, *Chem. Phys. Lett.*, 1989, **155**, 173–176.

96   J. Rajbangshi, K. Mukherjee and R. Biswas, *J. Phys. Chem. B*, 2021, **125**, 5920–5936.

97   D. Maji, S. Indra and R. Biswas, *J. Chem. Sci.*, 2021, **133**, 104.

98   T. Sato and R. Buchner, *J. Phys. Chem. A*, 2004, **108**, 5007–5015.

99   R. L. Smith, S. B. Lee, H. Komori and K. Arai, *Fluid Phase Equilib*, 1998, **144**, 315–322.

100   T. Sato and R. Buchner, *J. Chem. Phys.*, 2003, **118**, 4606.

101   K. Mukherjee, A. Barman and R. Biswas, *J. Chem.Phys.*, 2019, **151**, 184901.

102   Y. Sakai, S. Kuroki and M. Satoh, *Langmuir*, 2008, **24**, 6981–6987.

103   M. A. Bag and L. M. Valenzuela, *Int. J. Mol. Sci.*, 2017, **18**, 1422.

104   K. Mukherjee, A. Barman and R. Biswas, *J. Mol. Liq.*, 2016, **222**, 495–502.

105   B. Gestblom, *J. Phys. Chem.*, 1991, **95**, 6064–6066.

106   S. Mashimo, S. Kuwabara, S. Yagihara and K. Higasi, *J. Phys. Chem.*, 1987, **91**, 6337–6338.

107   N. Nandi and B. Bagchi, *J. Phys. Chem. B*, 1997, **101**, 10954–10961.

108   N. Nandi, K. Bhattacharyya and B. Bagchi, *Chem. Rev.*, 2000, **100**, 2013–2045.

109   M. L. Horng, J. A. Gardecki and M. Maroncelli, *J. Phys. Chem. A*, 1997, **101**, 1030–1047.

110   S. Das, R. Biswas and B. Mukherjee, *J. Chem. Phys.*, 2016, **145**, 084504.

111   S. Banerjee, J. Furtado and B. Bagchi, *J. Chem. Phys.*, 2014, **140**, 194502.

112   R. Gupta and G. N. Patey, *J. Chem. Phys.*, 2012, **137**, 034509.

113   P. G. Kusalik, A. P. Lyubartsev, D. L. Bergman and A. Laaksonen, *J. Phys. Chem. B*, 2000, **104**, 9526–9532.

114   P. G. Kusalik, A. P. Lyubartsev, D. L. Bergman and A. Laaksonen, *J. Phys. Chem. B*, 2000, **104**, 9533–9539.

115   S. Paul and G. N. Patey, *J. Phys. Chem. B*, 2006, **110**, 10514–10518.

116   S. D. Overduin and G. N. Patey, *J. Chem. Phys.*, 2017, **147**, 024503.

117   S. D. Overduin, A. Perera and G. N. Patey, *J. Chem. Phys.*, 2019, **150**, 184504.

118   A. Luzar, *Faraday Discuss*, 1996, **103**, 29–40.

119   A. Luzar and D. Chandler, *J. Chem. Phys.*, 1993, **98**, 8160–8173.

120   M. Ferrario, M. Haughney, I. R. McDonald and M. L. Klein, *J. Chem. Phys.*, 1998, **93**, 5156.

121   J. R. Errington and P. G. Debenedetti, *Nature* , 2001, **409**, 318–321.

122   S. Yadav and A. Chandra, *J. Chem. Phys.*, 2017, **147**, 244503.

123   B. Das, B. Sharma and A. Chandra, *J. Phys. Chem. C*, 2018, **122**, 9374–9388.

124   A. Baksi and R. Biswas, *J. Phys. Chem. B*, 2020, **124**, 11718–11729.

125   A. A. Sandilya, U. Natarajan and M. H. Priya, *ACS Omega*, 2020, **5**, 25655–25667.

Chapter 4

Spatio-Temporal Heterogeneity in Octanol-Water Mixture in Octanol Rich Region: Steady State and Time-Resolved Fluorescence Measurements

4.1 Introduction

A deep understanding of interactions of drugs, peptides, and different molecular moieties with the membrane and the subsequent dynamics is very important in molecular drug engineering. [1–6] Because of the high cost and difficulty associated with experimentally resolving the interaction between drug and biological membrane, bio-membrane mimic models are often used.[2,4] Aqueous mixtures of 1-octanol (henceforth, octanol) in the octanol-rich phase has been treated extensively as a model membrane mimicking system.[4,7–11] Such membrane-mimic characteristics of octanol and octanol+water are exploited to understand the pharmacokinetic properties of drug molecules in membrane+water system.[12–15] Lipophilicity of drug molecules was determined by partition co-efficient measurements in octanol+water mixtures.[1,12,16] Drug partitioning between water and pure hydrocarbon shows a poor correlation with the membrane+water systems, while octanol is considered a viable substitute for hydrocarbon in these studies.[12–15,17] The partitioning of host-guest peptides in octanol+water[18] and phospholipid+water bilayer[19] is frequently used to predict the helix structure of the peptides within the transmembrane in structural biology. Because of these versatile applications, pure octanol has been a promising subject for a number of studies using X-ray diffraction[20,21], thermodynamic measurements[22], infrared[23–25], Rayleigh- Brilliouin[26,27], Raman[23,27], and dielectric relaxation (DR)[28] experiments. These experimental studies focused on developing understanding of the structure and dynamics under ambient condition. X-ray diffraction experiments showed that the overall structural organization of octanol is supramolecular-like with a pre-peak observed at less than 0.35 Å^{-1} and remained intact after the addition of water.[20,21] Self-aggregated structure formation by pure octanol and octanol+water mixture (also termed as 'hydrated-octanol', 'wet-octanol') has been known for a long time and it was proved by small angle X-ray scattering and other different experiments, and computer simulation studies.[20,29–32] Molecular dynamics (MD) simulations[31] of water in octanol revealed that pure-

octanol forms a reverse micelle-like structure having polar regions and non-polar regions.[31] With an increase in water population in the solution, hydrogen-bonded clusters formed by polar head groups and water give rise to a reverse micelle-like structure where water molecules are found to be encapsulated in nearly spherical pockets.[31]

A gradual decrease of the static dielectric constant (ε_s) upon addition of water ($\varepsilon_s = 78$) is a general observation in n-alkanols+water mixtures (carbon number greater than 4 and ε_s is less than that of water) in n-alkanols rich region.[33–35] A good number of DRS measurements on alcohol+water mixtures already exist and these studies revealed a rich yet complex structural and dynamical information.[33–38] Interestingly, several of the previous measurements on mixtures at water-rich compositions reported water polarity induced inhomogeneous distribution of alcohol molecules,[39,40] whereas alcohol-rich compositions were found to be strongly heterogeneous due to formation of alcohol+water micro-clusters.[33–35,41,42] Several electronic spectroscopic and MD simulation studies of alcohols+water (short chain) mixtures[39,40,43,44] near water-rich regions reported solvent polarity-induced structural transition and the consequential spatial heterogeneity. These works also suggested that up to a certain alcohol concentration, alcohol from aggregated structure through alkyl group aggregation in aqueous media. Although the structure and dynamics of pure octanol as well as octanol+water binary mixtures at alcohol-rich composition were explored using diffraction experiments, DR spectroscopy and MD simulations, a systematic study of interactions and dynamics of an externally added solute as well as solvent dynamics 'seen' by that added solute has not yet been reported. The importance of monitoring fluorescent solute-based dynamics originates from the fact that fluorescence, by virtue of its high sensitivity to local environment, is capable of reflecting the friction profile at the microscopic level, which DRS completely misses out because of its extensively collective nature. MD simulations of course help in accessing the molecular picture of interaction and dynamics but the outcomes are critically dependent on choice of interaction potentials and their composition and temperature dependencies. Another interesting aspect of this work is to explore the spatiotemporal heterogeneity of these octanol+water mixtures by employing external fluorophores that differ in chemical nature.

As already mentioned, these fluorescent solutes used here as local reporters[45–56] and they are grouped as non-reactive and reactive solutes. Non-reactive solutes are those which do not undergo any reaction after photo-excitation, and coumarin 153 (C153, dipolar) and coumarin 343 (C343, ionic) are two such solutes used here. The reactive fluorophore used is trans-2-[4'-

(dimethylamino)styryl]benzothiazole (DMASBT) as it undergoes isomerization reaction upon photo-excitation and this entails sensitivity to local viscosity. These fluorophores also possess widely different average fluorescence lifetimes ($< \tau_{fl} >$) are thus capable of reporting specifically faster and slower medium density fluctuations.

Here we have taken neat-octanol and octanol+water binary mixtures with water mole fraction $0 \leq X_{H_2O} \leq 0.20$ and considered the temperature range, T = 283 - 323 K. DMASBT reports significant spatial heterogeneity at all temperatures. Dynamic Stokes shift measurements of neat octanol and octanol+water revealed different Stokes's shift characteristics for both probes C153 and C343 and reported a dependence on mixture composition and temperature. TRF studies involving fluorescence anisotropy and Stokes's shift dynamics with the two nonreactive probes, C153 and C343 in both neat and hydrated octanol revealed that both pure octanol and octanol+water mixtures are dynamically heterogenous. Analysis of coupling between relaxation dynamics (solute and solvent) and medium viscosity, as well as, estimated activation energies indicated a differential sensing of microenvironments by C153 and C343.

4.2 Methods and Materials

4.2.1 Chemicals and Preparation of Samples

Octanol (99%), laser grade C153, C343, and DMASBT were purchased from Sigma-Aldrich. Millipore water was used for octanol+water sample preparation. The chemical structures of 1-octanol, water, C153, C343, and DMASBT are shown in Scheme 4.1. Required amount of water and octanol, taken in a glass vial to prepare octanol+water binary mixtures with water mole fractions, $0 \leq X_{H_2O} \leq 0.20$, and sonicated for 15 minutes. Subsequently, the binary mixtures were shaken with a shaker incubator at 200 rpm for 2 hrs that resulted transparent colourless solutions. For optical measurements, the following methodology was followed: 2–3 μL of freshly prepared solutions of C153 in hexane (carrier solvent) was transferred in a quartz cuvette of 1 cm optical path length followed by evaporation of the carrier solvent through gently blowing hot air around the outer surface of the cuvette. Then, ~2.5–3 mL of sample was poured into that C153 loaded cuvette. In different measurements, a few crystals of C343 or DMASBT were directly added to the sample taken in a quartz cuvette. Proper care was taken to ensure the complete dissolution of fluorophores in the samples. Concentration of the fluorophores (C153/C343/DMASBT) in each of these samples studied were maintained at

$\leq 10^{-5}$ M. Although the maximum mole fractions of water miscible in octanol is $X_{H_2O} = 0.27^{57}$, we restricted our fluorescence spectroscopic measurement up to $X_{H_2O} = 0.20$ in order to avoid phase separation of the mixture in presence of added fluorophores.

4.2.2 Density, Viscosity and Refractive Index Measurements

Detailed descriptions of refractive index (n_D), densities (ρ), and viscosities (η) measurements are provided in Chapter 3. Temperature dependent n_D ρ, and η values in neat-octanol and these octanol+water binary mixtures are illustrated in Chapter 3 [Table A3.1 (Appendix)].
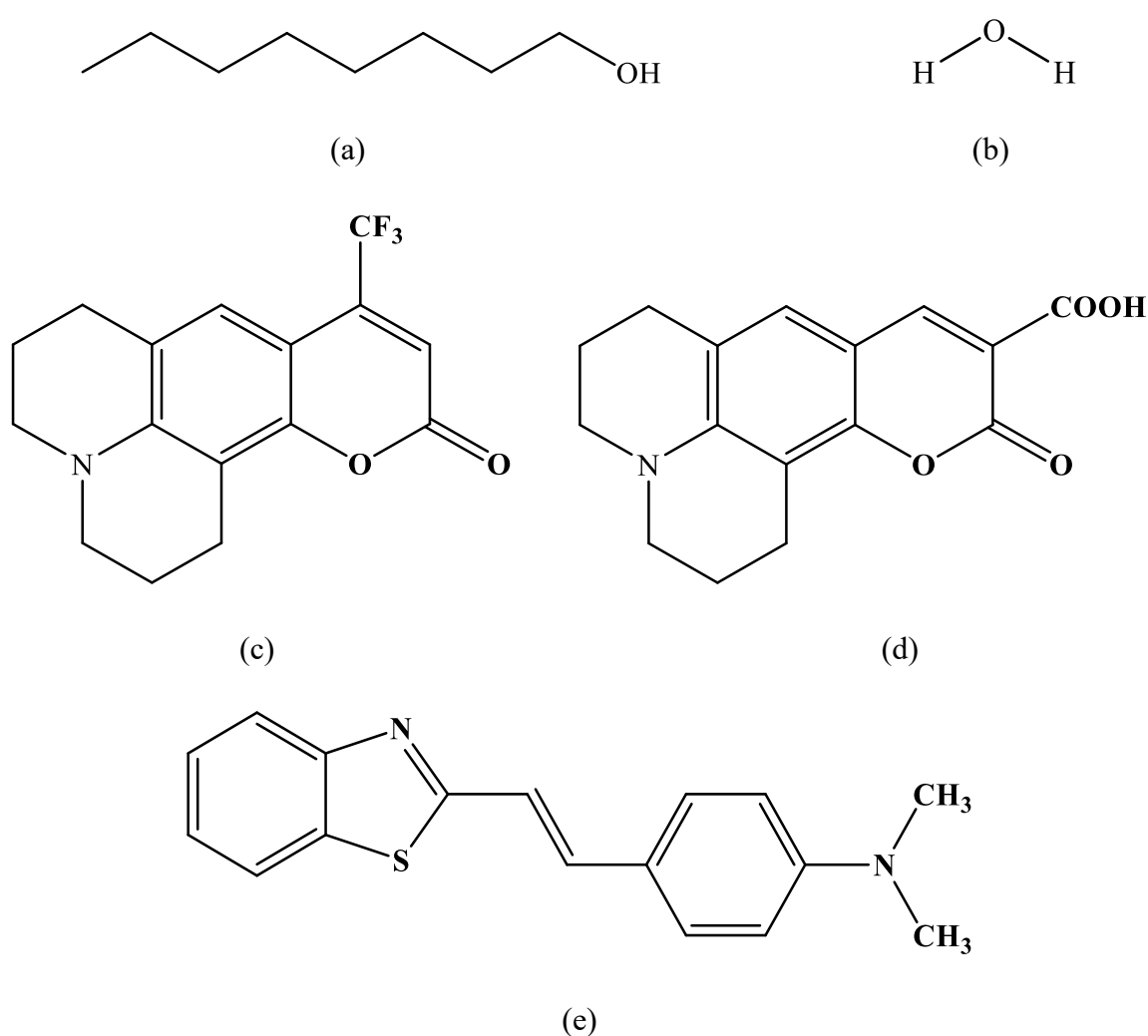
Scheme 4.1: Chemical structures of (a) 1-Octanol, (b) Water, (c) Coumarin 153, (d) Coumarin 343, (e) Trans-2-[4'-(dimethylamino)styryl]- benzothiazole.

4.2.3 Data Collection and Analysis for Steady State UV-visible Absorption and Steady State Fluorescence Emission Measurements

Steady-state UV-visible absorption and fluorescence emission spectra were recorded by using a UV-visible spectrophotometer (UV-2600, Shimadzu) and a fluorimeter (Fluorolog, Jobin-Yvon, Horiba), respectively. Temperature was controlled by a Peltier temperature controller (accuracy ±0.5K). The typical error bar for the determined spectral frequencies was ±200 cm^{-1}. The solvent-blank subtracted spectra were processed accordingly before further analyses and frequency determination.[58,59] The detailed procedures for steady-state UV-visible absorption and fluorescence techniques are described in Chapter 2.

4.2.4 Data Collection and Analysis for Time-Resolved Fluorescence Measurements

Time-resolved fluorescence measurements were performed with a time-correlated single-photon counting (TCSPC) system (LifeSpec-ps) from Edinburgh Instruments (Livingston, U.K.).[46,60] We used a 409 nm diode laser and the full width at half-maximum (FWHM) of the instrument response function (IRF) was ~85 ps. Temperature dependent measurements were performed by using a Julabo temperature controller (accuracy ±1 K). Lifetime measurements were conducted by recording magic angle decays at peak wavelengths the corresponding steady-state emission spectra of C153 and C343 dissolved in these systems. The data collection and analysis for Stokes shift dynamics and fluorescence anisotropy measurements followed the procedures outlined in Chapter 2 and references.[46,47,51,61,62]

4.3 Results and Discussions

4.3.1 Steady State UV-visible Absorption and Fluorescence Emission Spectroscopic Studies

4.3.1.1 Impact of Water and Temperature

UV-visible absorption and fluorescence emission spectra of C153, C343, and DMASBT dissolved in neat octanol and octanol+water binary mixtures with water mole fractions $0 \leq X_{H_2O} \leq 0.20$ are shown in Figure 4.1. A mild red shift in absorption and emission spectral features of either of the fluorophores upon gradual increase of X_{H_2O} indicates that the added water can not alter significantly the pre-existing solute-solvent interactions as well as medium polarity. Corresponding absorption and emission spectral average frequencies[63,64] and widths (FWHM) are summarized in Table A4.1 (Appendix). Impact of temperature on solute-medium

interactions in the octanol+water mixtures, explored via temperature dependent steady state spectral change of the dissolved solutes, is presented in Figure 4.2. Corresponding temperature dependent steady-state spectral features of octanol+water binary mixtures are presented in Table A4.2 (Appendix). With increasing temperature, the spectra are mildly blue shifted, and this is due to the temperature induced slight decrease of medium average polarity. The mild change of steady state spectral features with respect to X_{H_2O} or T variation is supported by the DRS studies in the same media.[42] Note the DRS studies in octanol+water binary mixtures reported that X_{H_2O} $(0 \leq X_{H_2O} \leq 0.20)$ have minimal impact on medium static dielectric constant (ε_s).[42]
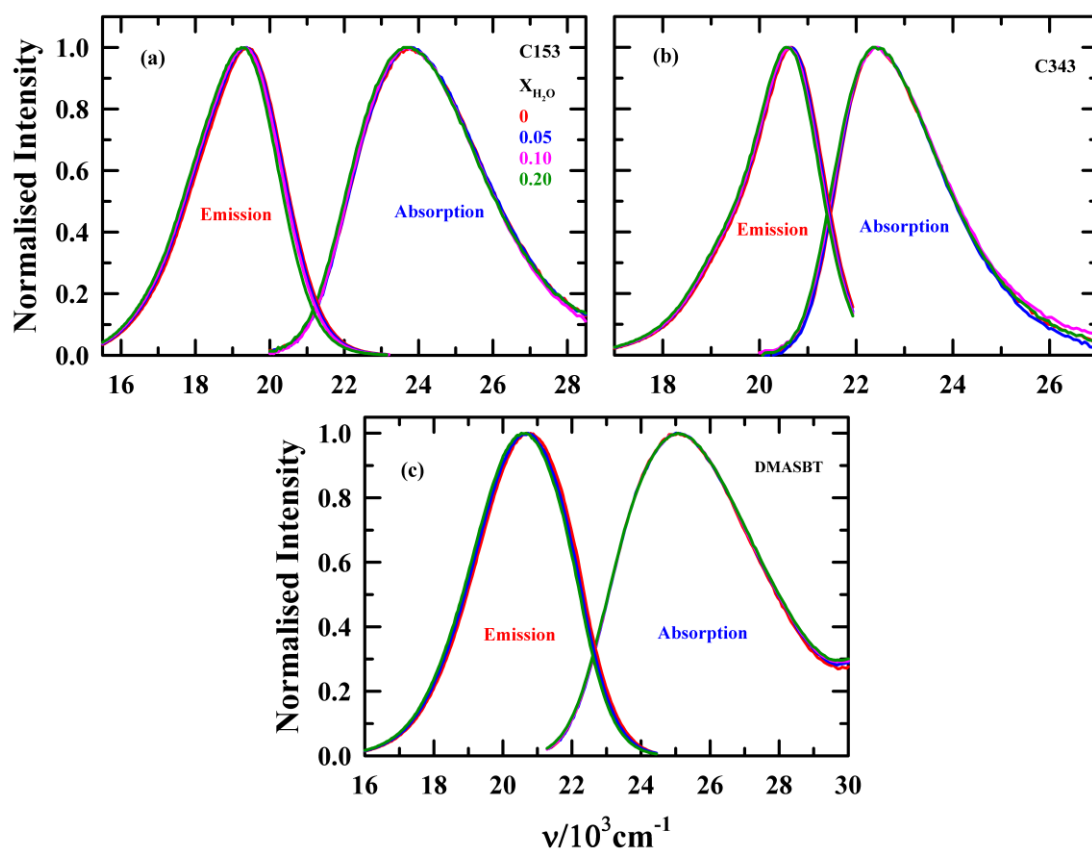
Figure 4.1: Steady-state UV-Visible absorption and emission spectra of (a) C153, (b) C343 and (c) DMASBT in octanol+water binary mixtures at three X_{H_2O} at 293 K. Corresponding spectra in neat octanol at 293K are also shown in each panel. All representations are colour-coded.
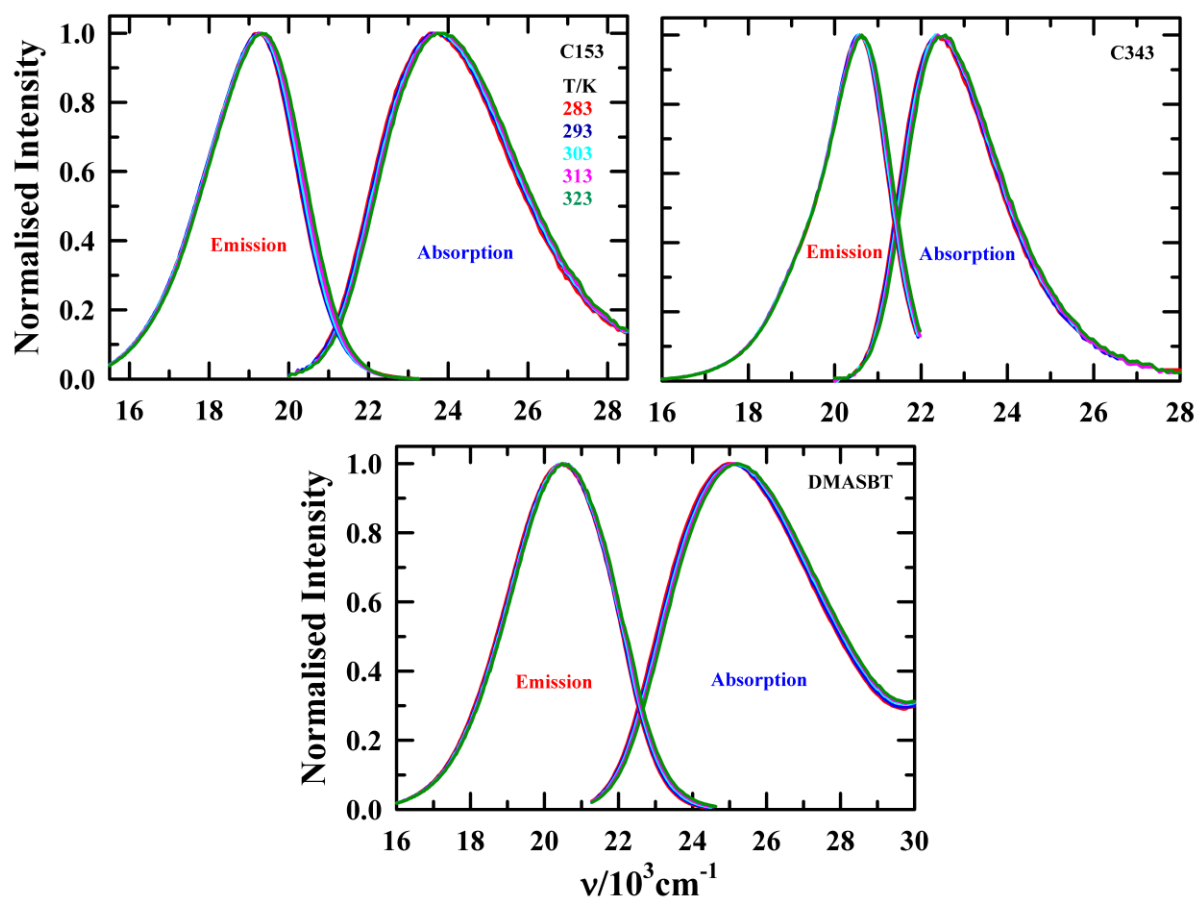
Figure 4.2: Steady state absorption and emission spectra (in same panel) of C153, C343 and DMASBT at five different temperatures at X_{H_2O} = 0.20 in octanol+water binary mixtures. All representations are colour-coded.

4.3.1.2: Excitation Wavelength Dependent Fluorescence Measurements: Signature of Spatial Heterogeneity

Next, we have explored the microheterogeneity aspect in these systems via excitation frequency (ν_{exc}) dependent shift of fluorescence emission spectra[65,66] of these three fluorescent solutes in octanol+water mixtures. A representative plot of excitation wavelength dependent fluorescence emission and its photo selection in absorption spectra of DMASBT in pure octanol at 283 K are presented in Figure A4.3 (Appendix). Figure 4.3 represents ν_{exc} dependent shifts of average emission peak frequencies ($\Delta\langle\nu_{em}\rangle$) and spectral widths ($\Gamma_{em}$) of these three solutes dissolved in octanol+water binary mixtures. Note that C343 and DMASBT report considerable ν_{exc} dependent emission spectral shift while C153 does not show any such dependence. Emission spectrum of a fluorophore depends on ν_{exc} when the local medium configurations
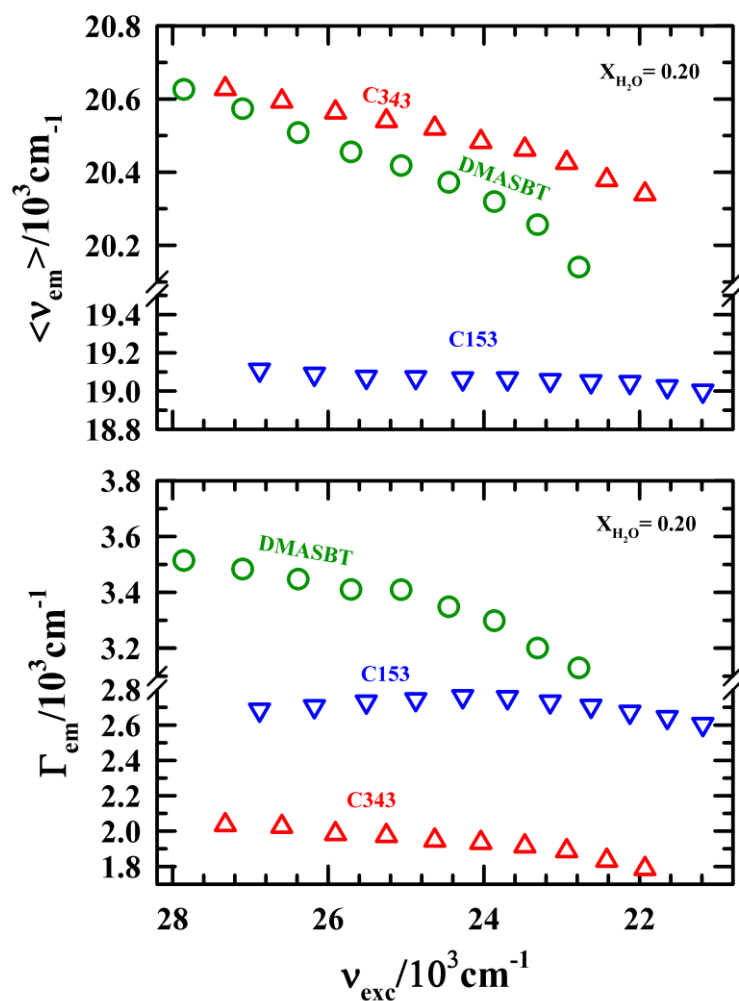
Figure 4.3: Excitation frequencies (ν_{exc}) dependent steady state emission frequency $\langle \nu_{em} \rangle$ (upper panel) and spectral width (FWHM), Γ_{em} (lower panel) of C153, C343 and DMASBT, at $X_{H_2O} = 0.20$ of water in octanol+water mixture at 293K. All representations are colour-coded.

surrounding the dissolved fluorophore solutes are different and the individual medium configuration persists for a time comparable to the excited state lifetime of the fluorophores. Therefore, results shown in Figure 4.3 suggest that the binary mixtures, within the lifetime of DMASBT and C343, are spatially heterogeneous.[67–69] A larger ν_{exc} induced red shift in $\langle \nu_{em} \rangle$ for DMASBT ($\sim$ 600-800 cm^{-1}) than C343 ($\sim$ 350 cm^{-1}) suggests that the interconversion timescales among heterogeneous medium configurations are better sensed by the relatively shorter lifetime probe DMASBT.[70] Water mole fraction dependent ν_{exc} induced total red shift in $\langle \nu_{em} \rangle$ and Γ_{em} are shown in Figure 4.4 at two representative temperatures. Interestingly, ν_{exc} dependent total magnitudes of red shift in $\langle \nu_{em} \rangle$ and the corresponding total changes in width (Γ_{em}) remain nearly invariant with water mole fraction for both the solute probes. These

results indicate that the overall solution structure of both neat and the present octanol+water mixtures are probably very similar.
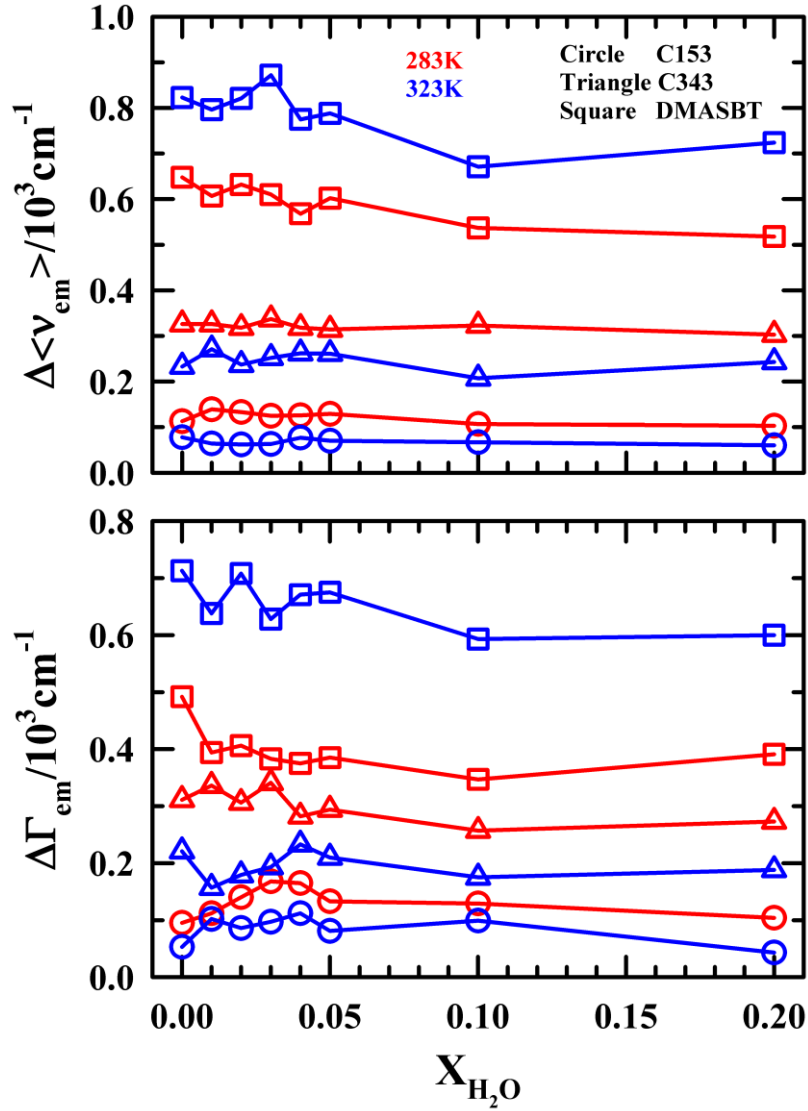
Figure 4.4: Water concentrations dependent excitation frequency (ν_{exc}) induced total emission red shift ($\Delta\langle\nu_{em}\rangle$) (upper panel) and total shift in width ($\Delta\Gamma_{em}$) (lower panel) of C153 (circle), C343 (triangle), and DMASBT (square) in neat octanol and octanol+water mixtures at 283 K (red) and 323 K (blue). All representations are colour-coded.

4.3.2 Time-Resolved Fluorescence Measurements in Octanol+Water Mixtures

4.3.2.1 Lifetime Measurements

The average fluorescence lifetimes ($\langle\tau_{fl}\rangle$) of C153, C343, and DMASBT were determined from the recorded magic angle fluorescence intensity decays, collected at the steady state emission peak wavelength of the solutes dissolved in neat octanol and octanol+water binary mixtures. The lifetime decays of both C153 and C343 exhibited tri-exponential decays. On the other hand, the lifetime decays of DMASBT are bi-exponential in nature. $\langle\tau_{fl}\rangle$ values for these fluorophores are summarized in Table 4.1. Note that upon increasing X_{H_2O}, $\langle\tau_{fl}\rangle$ of C153 and C343 slightly decreases ($\sim$ 10 %). $\langle\tau_{fl}\rangle$ of DMASBT shows strong temperature dependence (60 -70% decrease against 40 K increase in temperature). With increasing solution temperature, medium viscosity as well as polarity (dielectric constant) [28,35,71] decreases. It was reported that solvent polarity and viscosity can affect the excited state lifetime of DMASBT. The $\langle\tau_{fl}\rangle$ of DMASBT shows fractional medium viscosity dependence, $\langle\tau_{fl}\rangle \propto \eta^p$, where p deviates from unity and such deviation are dependent on medium polarity.[54,56] Note temperatures and water mole fraction dependent viscosities in octanol+water mixtures are taken from Chapter 4.[42] In nonpolar solvents, a p value $\sim$ 0.5 was reported,[56] while it was $\sim$ 0.8 in strongly polar ionic media.[54] In the present study of neat and binary mixtures of octanol+water, $\langle\tau_{fl}\rangle$ of DMASBT shows a fractional viscosity dependence, $\langle\tau_{fl}\rangle \propto (\eta/T)^p$, shown in the left panel of Figure 4.5 (p =0.66). Note this p = 0.66 obtained here is slightly larger than that reported value ($p \sim$ 0.50) in non-polar solvents[56] but less than that reported in lithium-ion containing electrolyte solutions (p = 0.80).[54] $\langle\tau_{fl}\rangle$ values of DMASBT in various polar and non-polar solvents were approximated as inverse of nonradiative rate, k_{nr} (trans-cis isomerization process in S$_1$ sate),that is, $\langle\tau_{fl}\rangle \sim \frac{1}{k_{nr}}$.[56] The activation energy was found to be ($E_a^{iso} \sim$ 19 kJmol^{-1}) and shown in the right panel of Figure 4.5.

Table 4.1: Temperature dependent $< \tau_{fl} >$ of C153, C343 and DMASBT in neat octanol and octanol+water mixtures.

$< \tau_{fl} >$ /ps of C153[a]				
T/K	$X_{H_2O}=0$	$X_{H_2O}=0.05$	$X_{H_2O}=0.10$	$X_{H_2O}=0.20$
283	3656	3605	3587	3532
293	3633	3573	3542	3526
303	3610	3553	3508	3506
313	3561	3524	3446	3443
323	3472	3483	3428	3391
$< \tau_{fl} >$ /ps of C343[a]				
283	2995	2986	2762	2760
293	2976	2917	2754	2743
303	2852	2882	2707	2635
313	2773	2864	2670	2608
323	2609	2856	2642	2598
$< \tau_{fl} >$ /ps of DMASBT[b]				
283	73	68	79	68
293	55	44	59	51
303	44	38	45	39
313	34	33	36	32
323	27	27	28	26

Average lifetime ($\langle \tau_{fl} \rangle$) can be reproduced within (a) ± 5% and (b) ± 10% of the reported values.
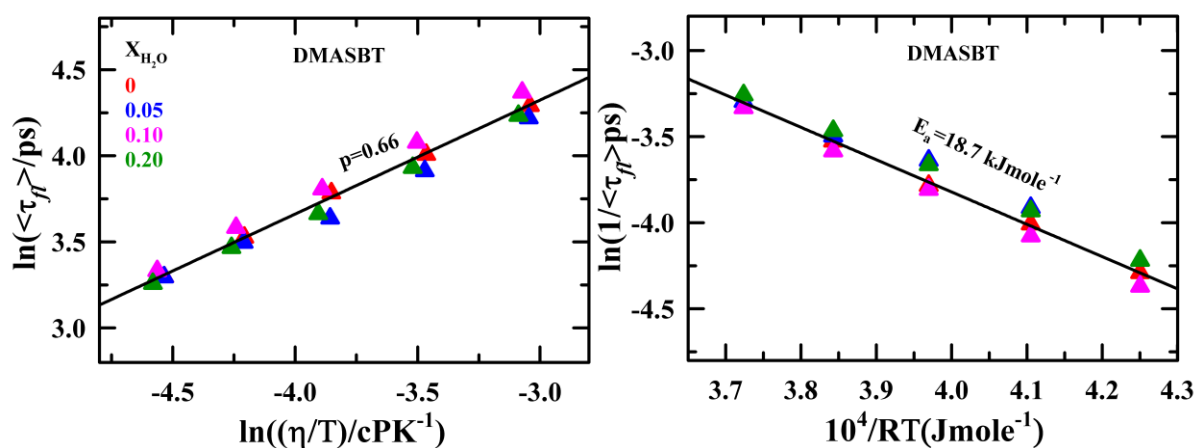
Figure 4.5: Temperature reduced viscosity (η/T) dependent average lifetime of DMASBT (in left panel) and estimation of activation energy from inverse temperature dependent natural logarithm of inverse average lifetime of DMASBT (in right panel) in four water mole fractions (X_{H_2O}) in octanol+water mixtures. All representations are colour-coded.

4.3.2.2 Dynamic Stokes Shift Measurements

Next, we have investigated temperature and water mole fractions dependent Stokes's shift dynamics in these systems. Figure A4.4 (Appendix) represents fluorescence emission decay collected at blue and red end wavelengths with respect to steady-state peak emission wavelength for C153 and C343. All these fluorescence emission decays are described by tri-exponential function. Note the observed sharp decay at the blue end emission while growth followed by decay at the red end, shown in Figure A4.4, is a characteristic signature of dynamic Stokes's shift.[59,72]
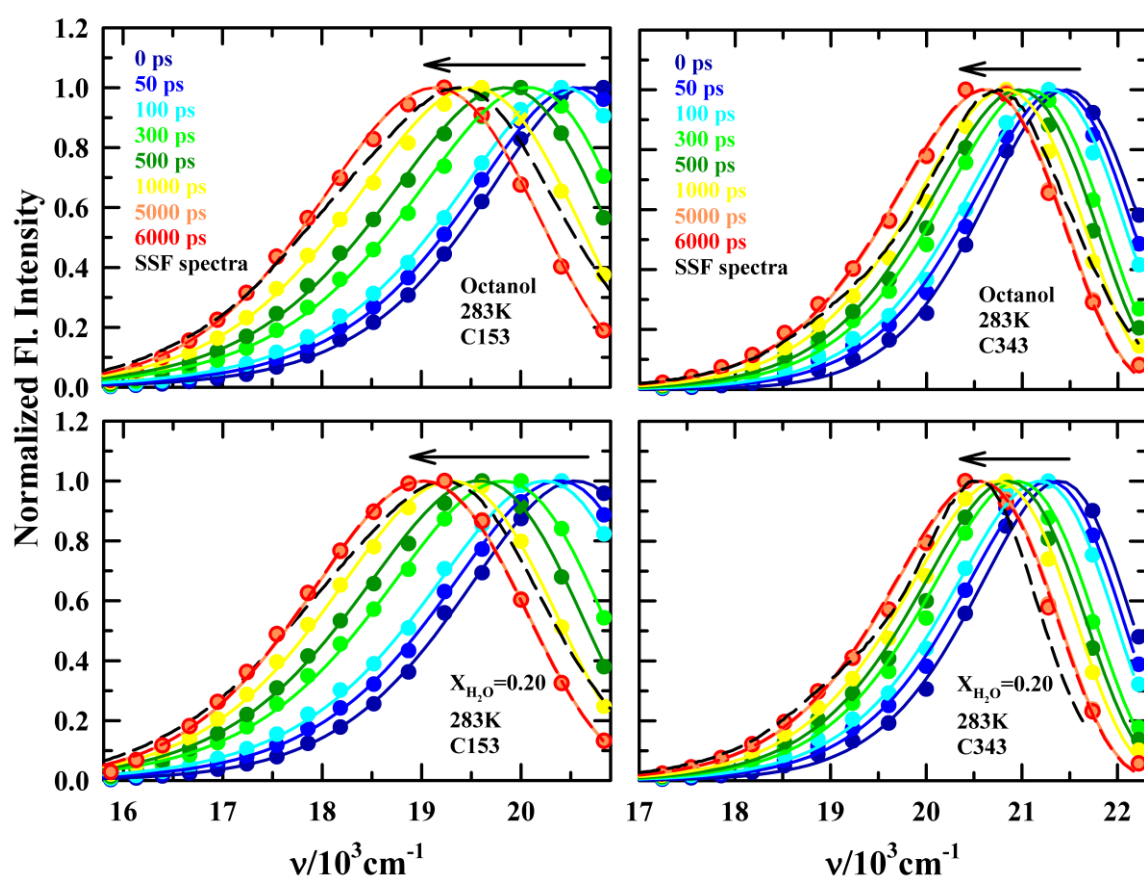
Figure 4.6: Representative reconstructed time-resolved emission spectra (TRES) of C153 (left panel), and C343 (right panel) in octanol (upper panel) and X_{H_2O} = 0.20 (lower panel) for different time intervals at 283 K. The steady state fluorescence emission spectra of both probes in each system are shown by the dashed lines. All representations are colour-coded.

Figure 4.6 represents the reconstructed time-resolved emission spectra (TRES) of C153 and C343 at different time intervals after excitation and corresponding fitting (shown as solid lines) with the lognormal line-shape function of TRES data.[45] In the same figure, we have presented

the steady-state fluorescence emission spectra of these fluorophores. Note the steady state fluorescence emission spectra are blue shifted for both probes compared to the TRES at $t = \infty$. This indicates that the steady-state emission spectra of C153 or C343 do not represent the emission from complete solvent relaxed excited state. The observed total dynamic Stokes shift for each of the probe dissolved in neat and octanol+water binary mixtures are summarized in Table 4.2. The estimated dynamic Stokes shift magnitudes (Δv_{est}^t)[73] and missing percentages are summarized in the same Table. Due to broad instrumental time resolution (FWHM of IRF is 85 ps), we have missed ~10-30% of total Stokes shift dynamics for C153 and ~ 40-50% for C343. Note the missed portion of the dynamic Stokes shift is larger for C343 than C153. This is because the hydrophilic C343 is more likely surrounded by the polar domain (-OH rich region) in octanol and in octanol+water binary mixtures. A faster collective hydrogen bond relaxation involving these alcoholic -OH groups and those of water molecules is likely to contribute significantly to the dynamic fluorescence Stokes shift of C343 in these hydroxylic systems.[74] On the other hand, the polar hydrophobic C153 resides at the interface of -OH rich region and alkyl chain dominated region. The missing percentage for both probe molecules in these systems increases with temperature and the addition of water. Temperature and water mole fraction dependent solvation response function was calculated using time-dependent peak frequency (v_{pk}) for both C153 and C343. All these $S(t)$ decays were well described by bi-exponential function. Temperature dependent $S(t)$ decays of C153 and C343 in octanol and octanol+water mixtures are shown in Figure 4.7 and Figure A4.5 (Appendix). The corresponding fit parameters of $S(t)$ decays are provided in Table 4.3. For C153, decays are described by relaxation components with time constants, τ_1 ~ 200-400 ps and τ_2 ~ 1 ns. In the case of C343, relaxation time components are τ_1 ~ 200-400 ps and τ_2 ~ 1-2 ns. The average solvation time $(\langle \tau_s \rangle)$ of both fluorescent solutes decreases with an increase of medium temperature. The faster solvation time constant (τ_1) for each of these two probes parallels the measured fastest dielectric relaxation time in octanol+water mixtures.[42] This faster ~200-400 ps solvation time for both probes probably originated from the structural H-bonding relaxation time of octanol molecules present in the solvation shell of probes.[75] Note faster component, (τ_1) for C153 in octanol is qualitatively comparable with the faster solvation timescale measured for C153 in decanol at normal temperature.[46] Next, we investigated what is the possible origin of the longer solvation timescale (τ_2). The translation and rotation diffusion time of octanol and water estimated from the Stokes-Einstein (SE) and the Stokes-Einstein-Debye (SED) relation[76], respectively, are given in Table 4.4. The rotational diffusion time of

octanol molecules calculated from the SED stick boundary condition is similar to the longer solvation response time, (τ_2) for C343 but slightly larger than C153 in pure octanol at 293K. This indicates that a relatively slow nanosecond time scale is arising from the rotational diffusion of octanol molecules.[42]

Table 4.2: Magnitudes of estimated (Δv_{est}^t), observed (Δv_{obs}^t) and missing percentages of the total dynamic Stokes shift of C153 and C343 in neat octanol and octanol+water binary mixtures at different temperatures.

X_{H_2O}	T/K	C153			C343		
		$\Delta v_{obs}^t/$ cm^{-1}	$\Delta v_{est}^t/$ cm^{-1}	% missed	$\Delta v_{obs}^t/$ cm^{-1}	$\Delta v_{est}^t/$ cm^{-1}	% missed
0	283	1639	1965	17	834	1439	42
	293	1659	1900	13	823	1449	43
	303	1623	1925	15	769	1446	47
	313	1522	1930	21	739	1471	50
	323	1500	1904	21	695	1467	53
0.05	283	1715	1928	11	803	1462	45
	293	1660	1974	16	757	1474	49
	303	1626	1967	17	729	1495	51
	313	1527	1973	23	678	1488	54
	323	1491	1965	24	633	1497	58
0.1	283	1669	1937	14	833	1459	43
	293	1630	1963	17	804	1484	46
	303	1561	1965	21	766	1495	49
	313	1508	1985	24	718	1508	52
	323	1406	1986	29	673	1516	56
0.2	283	1541	1971	22	837	1514	45
	293	1539	1990	23	771	1535	50
	303	1485	2011	27	732	1530	52
	313	1445	2017	28	688	1523	55
	323	1323	2003	34	648	1560	58
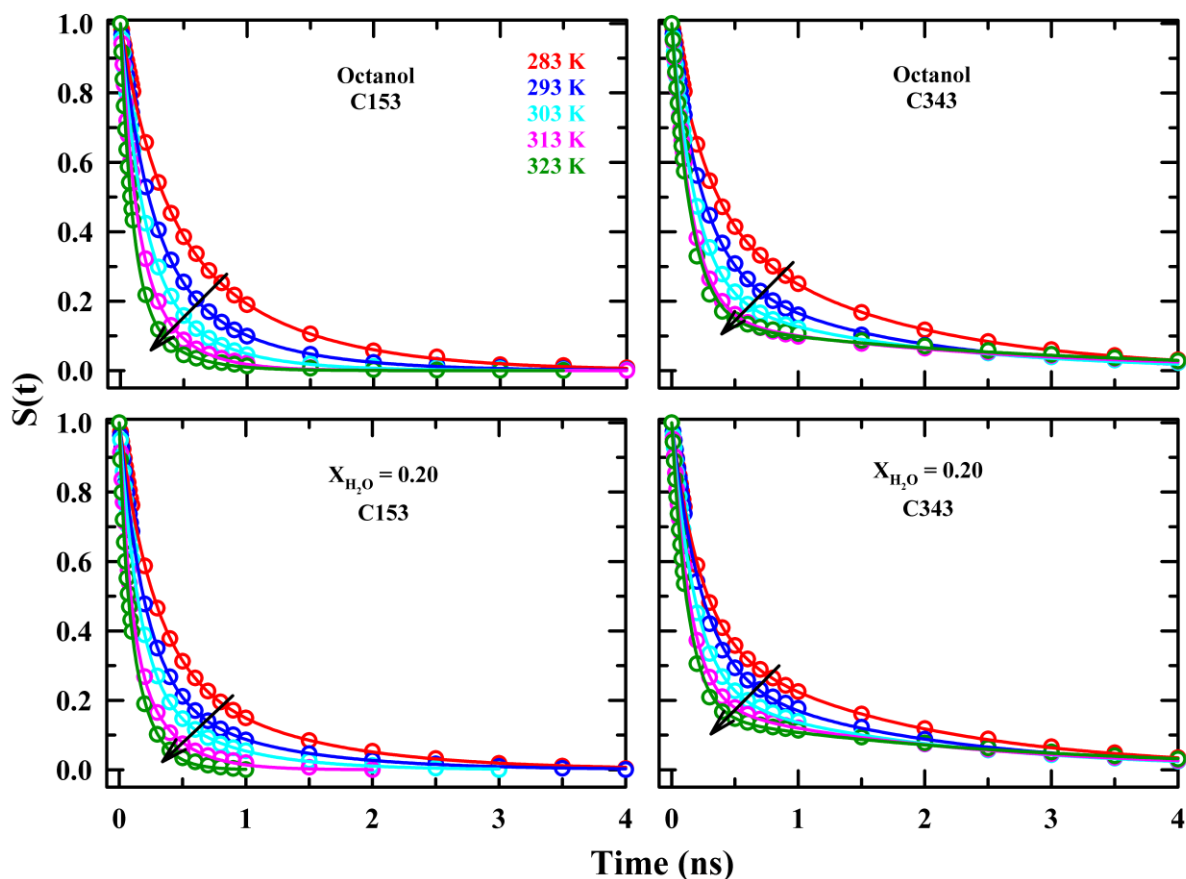
Figure 4.7: Solvation response functions (S(t)) for C153 (left panel) and C343 (right panel) in octanol (upper panel) and $X_{H_2O} = 0.20$ (lower panel) at five different temperatures. Experimental data are shown by circles; solid lines through the data represent fits. All representations are colour-coded.

Note τ_2 is always larger for C343 than C153. This is because charged C343 molecules in these systems are probably more strongly interacting with the -OH groups of octanol molecules in the solvation shell. However, hydrophobic C153 seeks more nonpolar regions where the extent of hydrogen bonding is lesser than in the former case. Note that τ_2 of C343 solvation in these media increases with temperature. We assumed that at high temperatures, octanol molecules are tightly bound to the charge C343 and form small but stable clusters. The formation of a smaller cluster is also confirmed via an increase in the extent of excitation wavelength dependent steady state fluorescence emission of DMASBT with temperature.

Table 4.3: Temperature dependent $S(t)$ fit parameters for C153 and C343 in neat-octanol and octanol+water mixtures.[c]

X_{H_2O}	T/K	a_1	τ_1/ps	a_2	τ_2/ps	$\langle\tau_s\rangle$/ps
			C153			
	283	0.45	274	0.55	903	620
	293	0.62	217	0.38	720	408
0	303	0.68	170	0.32	522	283
	313	0.59	110	0.41	320	196
	323	0.75	90	0.25	309	145
	283	0.50	219	0.50	871	544
	293	0.58	196	0.42	678	398
0.05	303	0.58	141	0.42	427	261
	313	0.54	96	0.45	296	185
	323	0.84	90	0.16	298	123
	283	0.51	222	0.49	840	524
	293	0.70	224	0.29	776	381
0.1	303	0.61	131	0.38	448	250
	313	0.59	91	0.41	320	185
	323	0.33	50	0.67	162	125
	283	0.64	258	0.36	1021	532
	293	0.75	207	0.25	906	382
0.2	303	0.73	133	0.27	624	266
	313	0.58	82	0.42	296	172
	323	0.30	42	0.70	157	122
			C343			
X_{H_2O}	T/K	a_1	τ_1/ps	a_2	τ_2/ps	$\langle\tau_s\rangle$/ps
	283	0.53	271	0.47	1453	827
	293	0.68	234	0.32	1412	610
0	303	0.77	190	0.23	1615	518
	313	0.84	160	0.16	2201	486
	323	0.86	150	0.14	2537	484
	283	0.59	274	0.41	1498	776

	293	0.74	251	0.26	1667	619
0.05	303	0.81	195	0.19	1845	509
	313	0.85	163	0.15	2065	448
	323	0.87	141	0.13	2447	441
	283	0.56	227	0.44	1417	751
	293	0.70	213	0.30	1583	624
0.1	303	0.78	179	0.22	1566	484
	313	0.83	153	0.17	1822	436
	323	0.86	134	0.14	2198	432
	283	0.60	220	0.40	1625	782
	293	0.71	232	0.29	1672	649
0.2	303	0.77	184	0.23	1756	546
	313	0.80	144	0.20	1997	514
	323	0.84	129	0.16	2483	506

[c]Individual amplitudes and time constants can be reproduced within ± 10-15% of the reported values.

Table 4.4: Using translational $D_{trans} = Kk_BT/C\pi\eta\sigma$ (where σ = diameter of molecule) translational diffusion time of molecular species presents in neat octanol as well as water octanol mixtures determined by flowing equation[76] $\tau_{trans} = \sigma^2/D_{trans} = \sigma^3 C\pi\eta/Kk_BT$ where C = 2 for slip and 3 for stick boundary condition. Hydrodynamic molecular rotation times for octanol and water at 293 K calculated using the SED relation with stick boundary condition, $\tau_r = \frac{3Vfc\eta}{k_BT}$ where for stick condition c=1. The van der Waals volume (V) of octanol and water, estimated from ref[77] are 155 Å^3 and 17 Å^3 and corresponding molecular diameter $\sigma_{Octanol} = 6.66$ Å and $\sigma_{Water} = 3.19$ Å,, Shape factor of octanol and water molecule are prolate (f=1.15)[78] and spherical (f=1) respectively.

X_{H_2O}	η/cP	Species	τ_{rot}/ns stick	τ_{trans}/ns stick	τ_{trans}/ns slip
0	9.16	Octanol	1.211	6.309	4.206
0.05	9.11	Water	0.115	0.689	0.459
		Octanol	1.205	6.275	4.183

0.10	8.82	Water	0.111	0.676	0.445
		Octanol	1.166	6.076	4.050
0.20	8.67	Water	0.109	0.656	0.437
		Octanol	1.147	5.972	3.981

4.3.2.3. Time-Resolved Fluorescence Anisotropy Study

Time-resolved fluorescence anisotropy measurements of the two non-reactive probe solutes (C153, C343) were performed in these media. This study explored how much solute rotation was influenced by the local environment.[62] A representative parallel and perpendicular fluorescence intensity decays of C153 and C343 in octanol at 293 K are shown in Figure A4.6 (Appendix). Composition and temperature dependent $r(t)$ decays for C153 and C343 are shown in Figure 4.8 and corresponding fit residuals are shown in Figure A4.7 (Appendix). The bi-exponential $r(t)$ decay fit parameters are summarized in Table 4.5. Bimodal nature of $r(t)$ decay of both solutes (C153, C343) in these systems suggests that solute molecules experience non-Markovian time-dependent friction in these media. Bi-exponential $r(t)$ decays of these solutes are expressed by a fast time component, τ_1^r ~150 - 280 ps and τ_2^r ~1-3 ns. The faster τ_1^r is in good agreement with the fastest DR relaxation time.[42] Note that the observed rotation correlation time constants of C153 in the present systems are comparable with the reported rotation time constant of C153 in decanol.[47]

Next, we focus on the longtime constant, τ_2^r, of both probes (C153, C343). Stokes-Einstein-Debye (SED) relation with stick boundary condition for estimating single molecular rotation time is given by

$$\tau_r = 6V\eta Cf_S/l(l+1)k_BT \qquad (4.1)$$

with l is rank associated with experimental method ($l = 2$ for fluorescence measurements), V and f_s are the volume and shape factor of the solute respectively, C is the coupling parameter of the rotating solute with the surrounding environment. k_B and T are Boltzmann constant and temperature in Kelvin respectively. Modified SED equation for fluorescence measurements with $l = 2$, $\tau_r^{(2)} = V\eta Cf_S/K_BT$. We have used V = 246 Å^3, f_s = 1.71, C = 0.24 (slip) and 1 (stick) for C153[79] and V = 243 Å^3, f_s= 1.99 and C = 0.18 (slip)and 1 (stick) for C343[80].
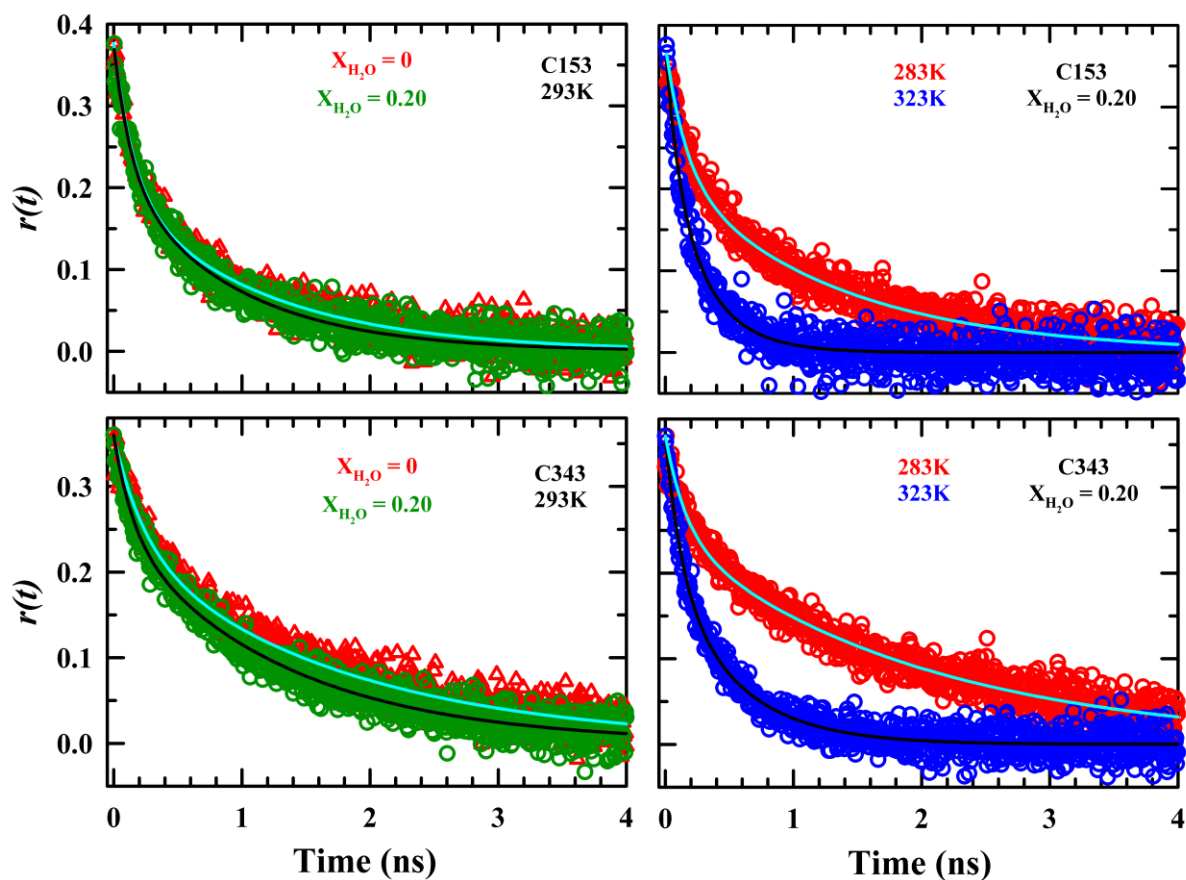
Figure 4.8: Representative fluorescence anisotropy $r(t)$ decay of C153 (upper panels) and C343 (lower panels) in neat octanol (red) and $X_{H_2O} = 0.20$ mole of water (green) in octanol (left panel) and both probes at two different temperatures (283K: red, 323K: blue) in 0.20 mole fraction water in octanol (right panels). Experimental data are shown by circle. The solid lines passing through the data points depict the bi-exponential fits. All representations are colour-coded.

Table 4.5: Temperature dependent $r(t)$ decay fit parameters for C153 and C343 in neat-octanol and octanol+water mixtures.[d]

C153						
X_{H_2O}	T/K	a_1	τ_1^r /ps	a_2	τ_2^r /ps	$\langle \tau_r \rangle$/ps
	283	0.40	183	0.60	1338	876
	293	0.47	151	0.53	1125	667
0	303	0.46	140	0.54	816	505

	313	0.49	151	0.51	630	395
	323	0.62	129	0.38	574	298
	283	0.34	175	0.66	1174	834
	293	0.39	145	0.61	923	619
0.05	303	0.44	129	0.56	769	487
	313	0.43	121	0.57	528	353
	323	0.51	106	0.49	447	273
	283	0.31	153	0.69	1142	835
	293	0.39	120	0.61	914	604
0.1	303	0.40	119	0.60	653	439
	313	0.48	115	0.52	554	343
	323	0.44	118	0.56	378	264
	283	0.41	156	0.59	1290	825
	293	0.42	131	0.58	910	585
0.2	303	0.41	124	0.59	649	434
	313	0.38	98	0.62	478	333
	323	0.37	99	0.63	310	231
C343						
X_{H_2O}	T/K	a_1	τ_1^r/ps	a_2	τ_2^r/ps	$\langle\tau_r\rangle$/ps
	283	0.36	357	0.64	2867	1963
	293	0.41	294	0.59	1971	1283
0	303	0.42	290	0.58	1361	911
	313	0.54	230	0.46	1108	633
	323	0.67	236	0.33	950	471
	283	0.39	221	0.61	2845	1822
	293	0.36	280	0.64	1753	1223
0.05	303	0.44	258	0.56	1233	804
	313	0.46	195	0.54	909	580
	323	0.42	164	0.58	589	410
	283	0.32	266	0.68	2417	1729
	293	0.33	302	0.67	1611	1179
0.1	303	0.46	265	0.54	1298	822

	313	0.52	203	0.48	957	565
	323	0.50	152	0.50	651	401
0.2	283	0.31	298	0.69	2239	1697
	293	0.35	229	0.65	1523	1070
	303	0.39	186	0.61	1115	753
	313	0.36	197	0.66	691	527
	323	0.41	154	0.59	534	378

[d]Individual amplitudes and time constants can be reproduced within ± 10-15% of the reported values.

The estimated single molecular rotation times $(\tau_r^{(2)})$ of two fluorescence probes in these systems at 293K are given in Table A4.8 (Appendix). The stick limit single molecule rotation time for C153 (953 ps) well corroborates with τ_2^r (1125 ps) at 293K. The τ_2^r of C153 is slightly longer than single molecular rotation time due to the presence of some other specific interaction.[47] On the other hand, $\tau_r^{(2)}$ of C343 (1095 ps) is comparatively lesser than the longer rotation anisotropy time ($\tau_2^r \sim$ 1971 ps). In $r(t)$ decay, both the rotational time components (τ_1^r, τ_2^r) for C343 are longer than those found for C153. This is a manifestation of strong specific interaction between the –COOH group of C343 and –OH group of octanols, which is presumed to be responsible for slowing down the rotational diffusion of C343 relative to that of C153.

Next, we explore the impact of water on solute rotation in neat octanol. Average rotation $\langle \tau_r \rangle$ time and all individual time constants become faster with the addition of water in octanol (up to X_{H_2O} = 0.20). In aqueous octanol mixtures, water is expected to accumulate in the polar domain.[31] Note, $\langle \tau_r \rangle$ of C343 (Table 4.6) is more affected by the addition of water than C153. That indicates that C343 resides in more polar hydroxyl group dominated region and C153 molecules reside near interface of polar and non-polar regions.
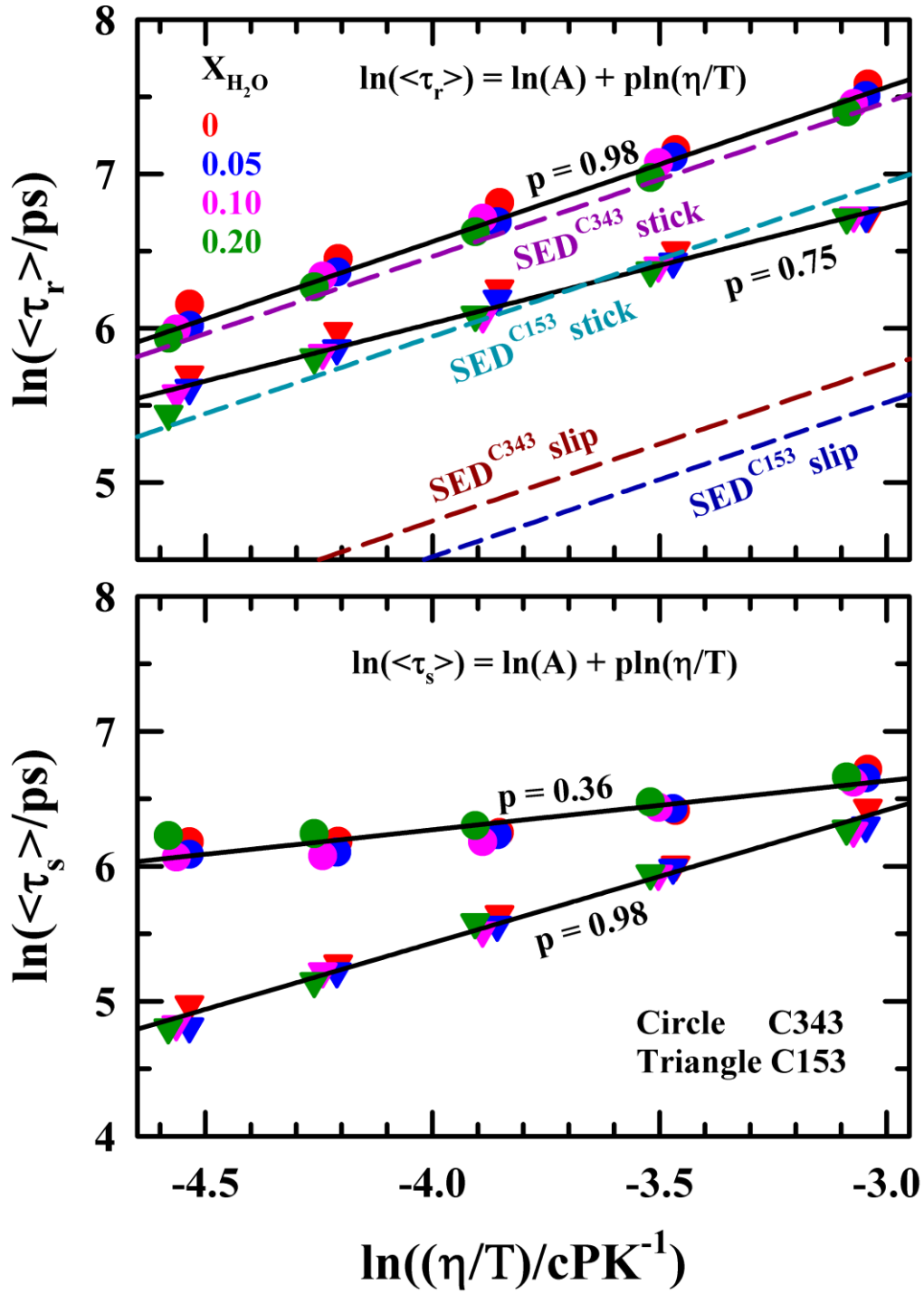
Figure 4.9: Representative plot of average rotational time, $\langle \tau_r \rangle$ vs. temperature-reduced viscosity (η/T) (upper panel) and average solvation time, $\langle \tau_s \rangle$ vs η/T (lower panel) of C153 and C343 in pure octanol and octanol+water mixtures with various X_{H_2O} in double logarithmic fashion. Calculated stick and slip lines from SED relation are presented by dashed lines. Solid lines passing through the data points represent linear fits. All representations are colour-coded.

4.3.2.4 Partial Decoupling Between Dynamics and Viscosity of Medium: Signature of Temporal Heterogeneity

Furthermore, the experimental $\langle \tau_r \rangle$ of both fluorophores have compared with estimated rotation time considering stick and slip boundary conditions of modified Stokes-Einstein-Debye (SED) according to Eq. 4.1 shown in Figure 4.9 (upper panel). Note the $\langle \tau_r \rangle$ of C153 in pure octanol and water octanol binary mixture are well correlated[47] to rotation in polar solvents shown in Figure A4.9 (Appendix). Experimental $\langle \tau_r \rangle$ of C153 moves from the stick to the sub-slip limit of the SED upon lowering the solution temperature. This can be explained by the fact that with increasing temperature reverse micelle-like structures are disassembled into smaller fragments. Therefore, the friction experienced by C153 at higher temperatures is greater than at lower temperatures. Rotation of C153 goes stick to the super-stick region of SED due to increased friction of the medium. In the other measurements, $\langle \tau_r \rangle$ value of C343 in these systems lies in the super-stick region at all experimental temperatures. This result reveals that strong specific interaction between octanol hydroxyl group and C343 carboxyl group restricts the rotation of C343.

Next, we have explored the coupling between the $\langle \tau_s \rangle$ (for C153 and C343) and medium viscosity. Figure 4.9 (lower panel) shows the strong decoupling of the measured $\langle \tau_s \rangle$ of C343 with medium viscosity whereas $\langle \tau_s \rangle$ of C153 is coupled with medium viscosity in octanol+water mixture. Solution structure and relaxation time probed in solvation measurements of two different probes may explain this type of observation.[68,81,82] Although solution viscosity is nearly the same but solution structure around two different probes is not. The chemical nature of the solutes employed is responsible for seeing different solution structures around them resulting in collective solution dynamics sensed by them in a system are different. p value was estimated ~0.36 for C343 which deviates from unity indicating presence of temporal heterogeneity. Fractional viscosity dependency of molecular motion suggests presence of temporal heterogeneity.[68,69,83–85]

4.3.2.5 Activation Energies from Solute Rotation and Solvent Dynamics, and Correlation Between Them: Confirmation of Heterogeneous Environments and Solute Location

Since the plot of viscosity with temperature in these systems is nearly linear, the activation energy of various processes was estimated using the general Arrhenius-type formula $\ln(1/\langle \tau_m \rangle) = A - E_a^m / RT$ where E_a^m denotes activation energy associated with medium relaxation during solute solvation or solute rotation. m denotes rotation (r) or solvation (s). The

average relaxation time $\langle \tau_m \rangle$ is related to medium viscosity by the relation $\tau_m = A_m \eta^p$ and $\eta = \eta_0\, exp(E_a/RT)$. Placing the temperature dependent η into the equation $\tau_m = A_m \eta^p$ results $ln(1/\langle \tau_m \rangle) = A - E_a^m/RT$ Where $E_a^m = pE_a$. The activation energies are calculated from their respective slope in $ln(\eta)$ versus $1/T$ and $ln(1/\langle \tau_m \rangle)$ versus $1/T$ plot in Figure A4.10 (Appendix) and Figure 4.10 respectively. The activation energies are correlated $E_a^r = 0.75E_a^s$ for C153 and $E_a^r = 2.82E_a^s$ for C343 in these systems. The above ratio value can be understood by the coupling phenomenon between medium viscosity and solute rotation or solvation in these media. The coupling of C343 rotation with medium viscosity is 2.8 times larger than solvation. On the other hand, C153 solvation is 1.3 times more coupled with medium viscosity than rotation. Anomalous correlation of activation energies of two probes C153 and C343 confirmed that microenvironments around two probe molecules are different and heterogenous in these media.
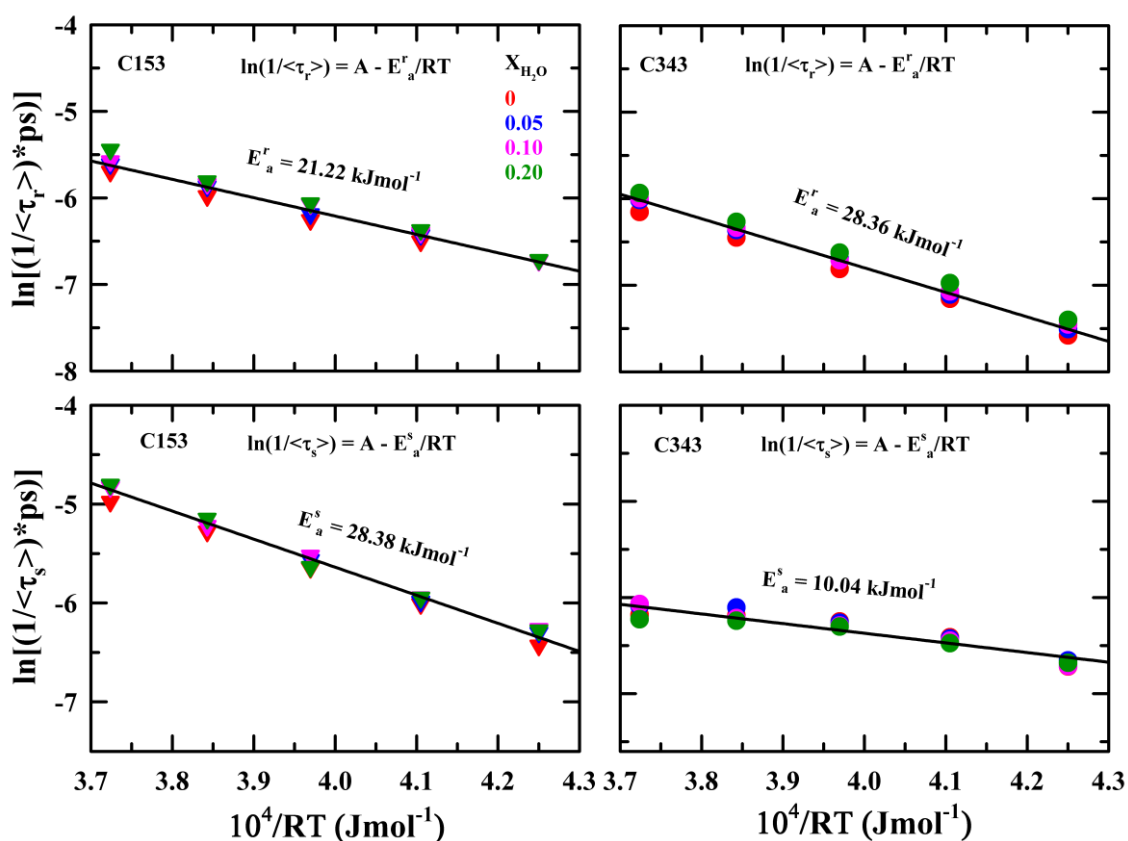
Figure 4.10: Arrhenius plot of $ln(1/\langle \tau_m \rangle)$ versus $1/T$ for C153 (left panels) and C343 (right panels), where m denotes rotation (r) (upper panels) or solvation (s) (lower panels) times in octanol+water mixtures. Solid lines represent linear fit through the respective data sets. All representations are colour-coded.
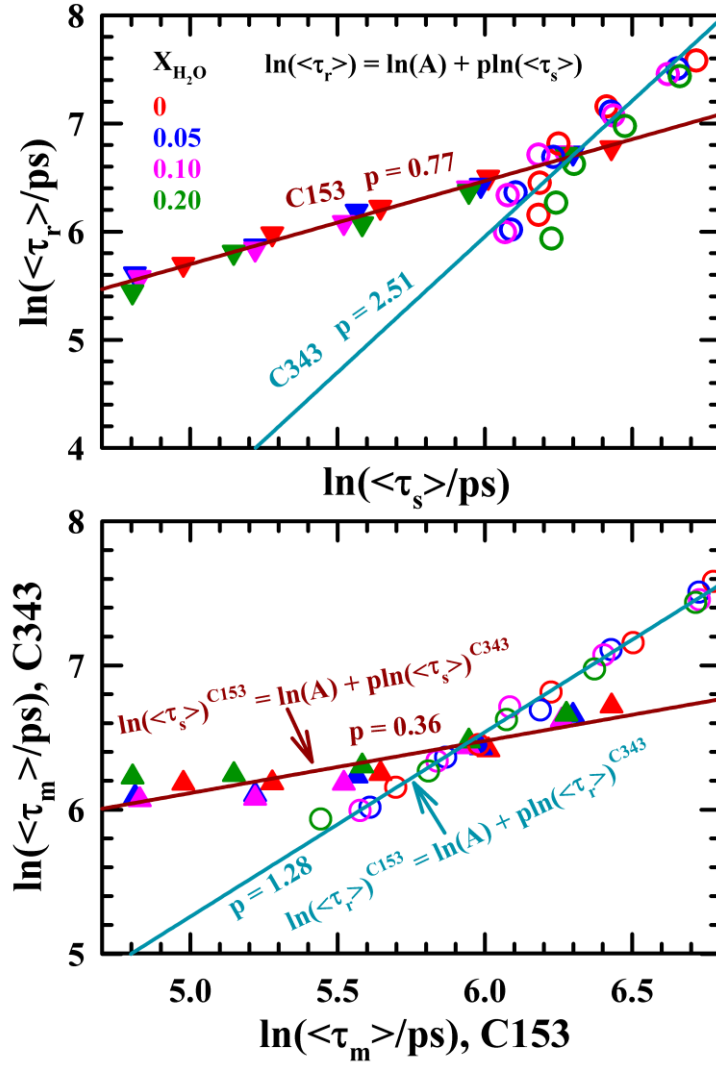
Figure 4.11: Representative logarithmic plot of average solvation time $\langle \tau_s \rangle$ vs rotational time, $\langle \tau_r \rangle$ of C153 and C343 in pure octanol and octanol+water mixtures (in same panel). And $\langle \tau_s \rangle$ vs $\langle \tau_s \rangle$ or $\langle \tau_r \rangle$ vs $\langle \tau_r \rangle$ for different probe in same medium (in lower panel) m denoted rotation (r) or solvation (s) process. Respective solid or dashed line passing through the data points represent fit by the relation $\langle \tau_m \rangle \propto (\langle \tau_{m'} \rangle)^p$ where $m \neq m'$ for upper panel and $m = m'$ for lower panel. All representations are colour-coded.

We further support our argument through the direct relation between solvation and rotation of two probes in these mixtures using the relation $\langle \tau_s \rangle \propto (\langle \tau_r \rangle)^p$ and p value is estimated from the double logarithmic plot which is shown in Figure 4.11. Estimated p values are well corroborated with early evaluated p values calculated from activation energies correlation associated with this process in these media. Again, the correlation of the same process (like solvation to solvation and rotation to rotation) between two solutes provides important

information about their local environments. The lower panel of Figure 4.11 shows two solutes deviating from their correlation with the same process. Although two probes (C153 and C343) have the same size and shape, due to their different chemical nature, they participate in the same process differently. Liquid structure of pure octanol, as well as octanol+water mixtures, are spatially heterogeneous. The heterogeneous distribution of octanol molecules resembles a lipid bilayer. Liquid neat octanol has a hydrophobic region which is made by bilayer of hydrocarbon chain molecules and a hydrophilic region made by hydroxyl groups among the octanol molecules. Also, the addition of water can not alter the overall liquid structure of octanols and water more preferably accumulates in the hydrophilic regions.[20,31,42] So hydrophobic fluorophores like C153 preferably resides interface of the hydrophobic and hydrophilic region (due to the dipolar character of C153) whereas hydrophilic C343 resides preferably in the polar region. Participation of solvent molecules in solvation and medium friction in these two solutes is completely different. The mental construction of two probe environments is shown in Scheme 4.2. This picture indicates that the chemical nature of molecular drugs, peptides, or supramolecular proteins is responsible for their region-specific solvation and their structural conformation.
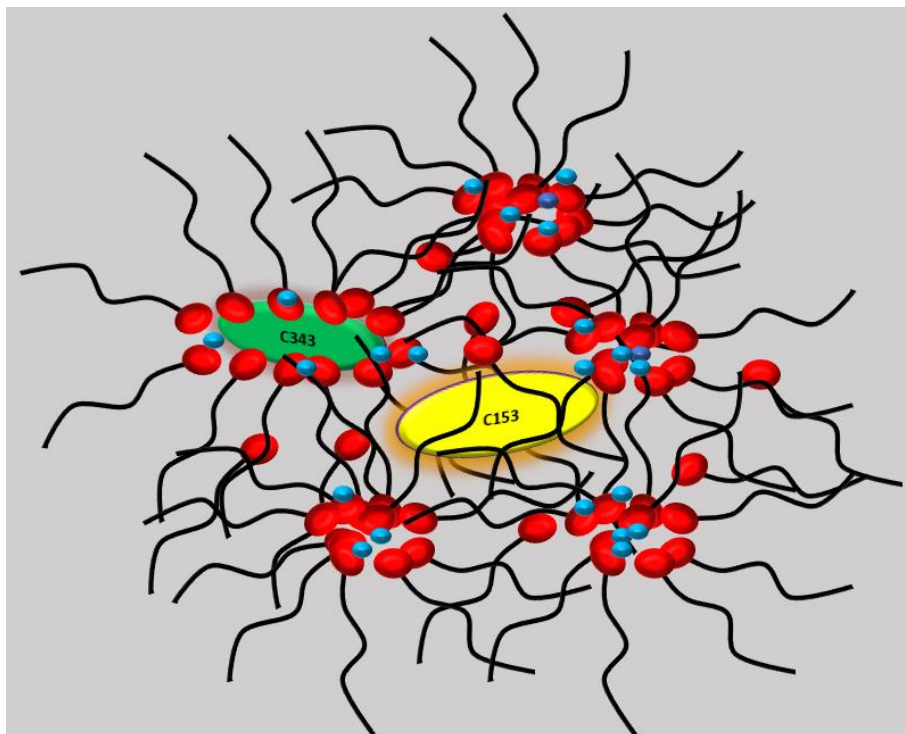
Scheme 4.2: A diagram presenting the probable location of coumarin probes in octanol+water binary mixtures.

4.4. Conclusion

The excitation wavelength dependent emission studies of probes C343 and DMASBT reveal that octanol+water system is spatially heterogeneous.[67–69] TRF measurements reveal distinct dynamic Stokes's shift detection limits for C153 and C343 and that depend on the temperature and water mole fractions. Both probes, C153 and C343, exhibit bimodal solvent relaxation times in pure octanol and octanol+water mixtures. The viscosity decoupling of C153 rotation (p = 0.75) suggests temporal heterogeneity in neat-octanol and octanol+water mixtures, while C343 (p = 0.98) reveals complete coupling with medium viscosity. The rotational time of C343 is two times slower than C153 and its rotational dynamics is strongly deviated from the SED stick prediction, supporting the result of solute (C343) caging in a cavity formed by the H-bond network organization in octanol and octanol+water mixtures. Although two probes (C153 and C343) have nearly the same size, C343 experienced relatively more averaged-out medium friction than C153 and registered less temporal heterogeneity.[81] Deviation from correlations (p < 1 or p > 1) between rotation and solvation processes of two probes C153 and C343 strongly reflect that microenvironments around two probe molecules are different in these media. These findings contribute to the broader understanding of solvation process and have implications in various fields, such as chemistry, material science, and biochemistry.

Appendix A4

Table A4.1: Absorption and emission frequencies and spectral widths (FWHM) of C153, C343 & DMASBT at four different mole fractions of octanol+water binary mixtures and neat octanol at 293K.[a]

X_{H_2O}	Absorption		Emission	
	Spectral width (FWHM) (10^3 cm^{-1})	Average frequency (10^3 cm^{-1})	Spectral width (FWHM) (10^3 cm^{-1})	Average frequency (10^3 cm^{-1})
C153				
0	4.058	24.052	2.774	19.209
0.02	3.979	24.025	2.762	19.192
0.05	4.068	24.074	2.803	19.162
0.1	4.053	24.285	2.796	19.123
0.2	4.096	23.999	2.757	19.066
C343				
0	2.517	22.890	1.840	20.458
0.02	2.543	22.772	1.850	20.453
0.05	2.532	22.755	1.846	20.431
0.1	2.602	22.803	1.832	20.413
0.2	2.600	22.763	1.834	20.379
DMASBT				
0	4.840	25.418	3.402	20.652
0.02	4.916	25.466	3.398	20.630
0.05	4.900	25.459	3.398	20.585
0.1	4.929	25.459	3.404	20.520
0.2	4.946	25.463	3.409	20.418

a) Uncertainty in spectral width and average frequency is ± 100 cm^{-1}

Table A4.2: Steady state spectral features of C153, C343 & DMASBT in octanol+water mixtures with $X_{H_2O} = 0.2$ at five different temperatures.[b]

T/K	Absorption		Emission	
	Spectral width (FWHM) (10^3 cm^{-1})	Average frequency (10^3 cm^{-1})	Spectral width (FWHM) (10^3 cm^{-1})	Average frequency (10^3 cm^{-1})
C153				
283	4.084	23.958	2.732	19.044
293	4.096	23.999	2.757	19.066
303	4.094	24.040	2.780	19.086
313	4.089	24.080	2.815	19.120
323	4.099	24.108	2.856	19.162
C343				
283	2.594	22.747	1.810	20.372
293	2.600	22.763	1.834	20.379
303	2.596	22.787	1.869	20.388
313	2.597	22.811	1.897	20.414
323	2.620	22.853	1.922	20.431
DMASBT				
283	4.949	25.423	3.428	20.392
293	4.946	25.463	3.409	20.418
303	4.974	25.514	3.417	20.420
313	4.974	25.546	3.422	20.448
323	4.976	25.590	3.434	20.483

b) Uncertainty in spectral width and average frequency is ± 100 cm^{-1}
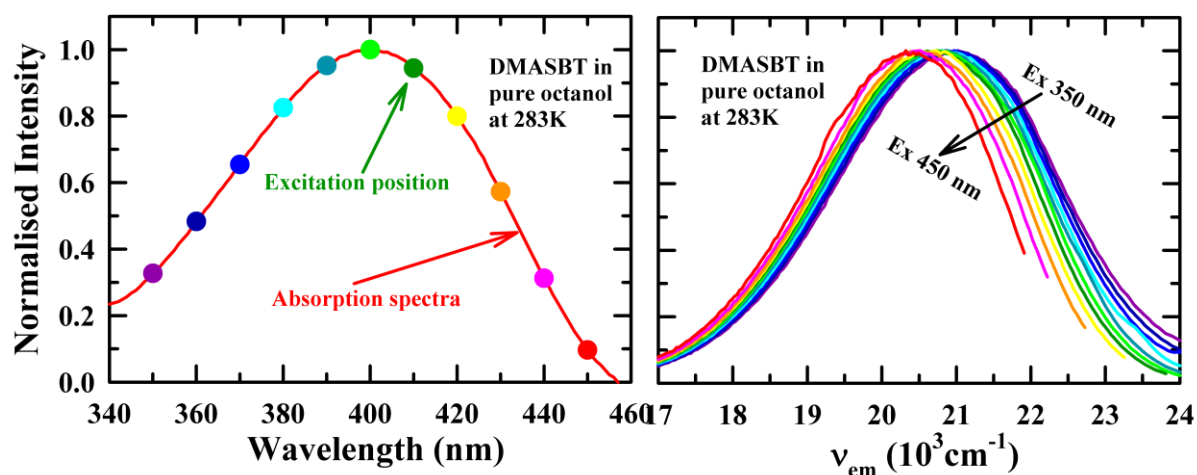
Figure A4.3: Representative photoreactive excitation position in absorption spectra (left panel) and excitation wavelength dependence (λ_{exc}) steady state fluorescence emission spectra of DMASBT (right panel) in pure octanol at 283. All vignettes are colour-coded.
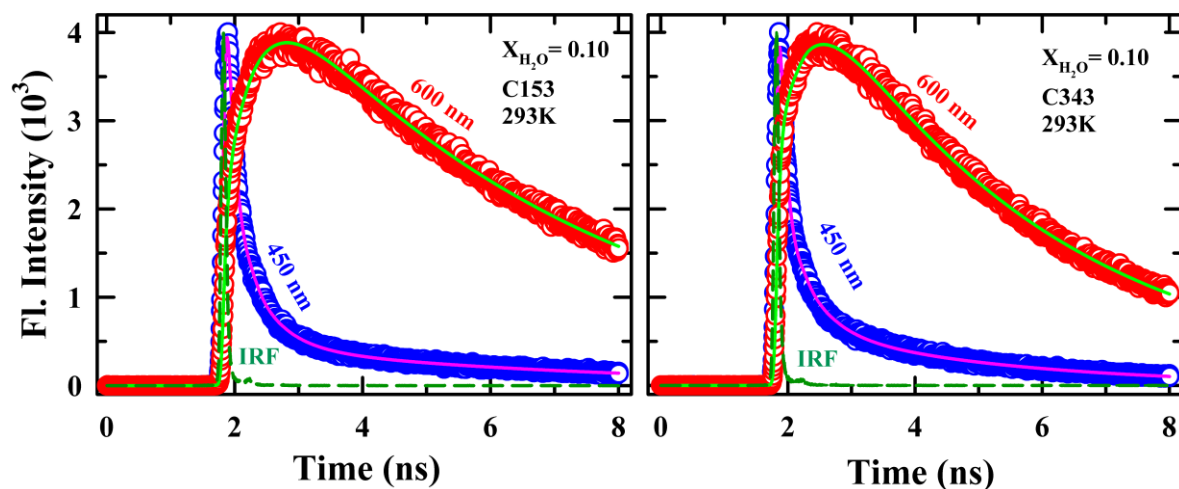
Figure A4.4: Representative fluorescence emission decay at blue end ($\lambda_{em} = 480$ nm) and red end ($\lambda_{em} = 640$ nm) with respect to peak maximum wavelength of steady state emission spectra for C153 (left panel) and at blue end ($\lambda_{em} = 450$ nm) and red end ($\lambda_{em} = 600$ nm) for C343 (right panel) in $X_{H_2O} = 0.10$ at 293K. All representations are colour-coded.
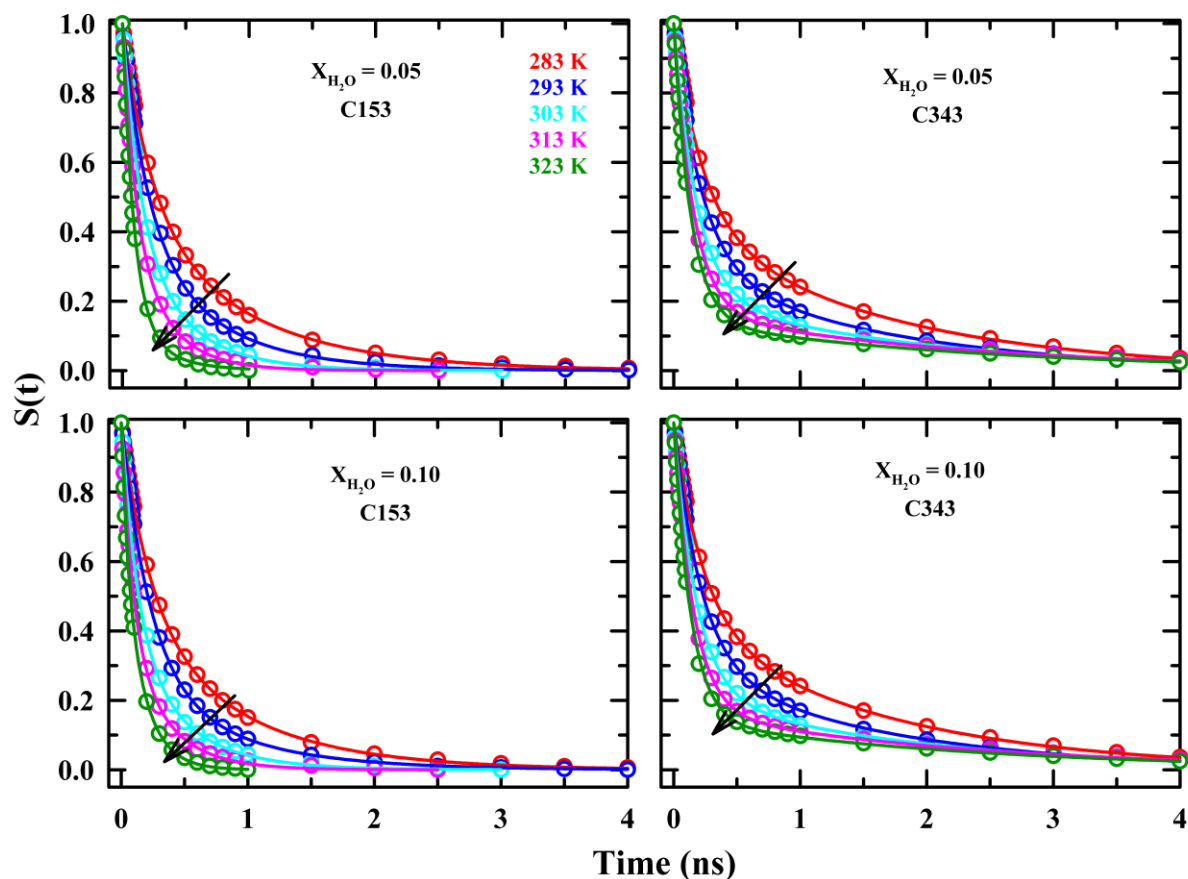
Figure A4.5: Solvation response functions ($S(t)$) for C153 (left panel) and C343 (right panel) in X_{H_2O} = 0.05 (upper panel) and X_{H_2O} = 0.10 (lower panel) at various temperatures. Experimental data are shown by circles; solid lines through the data represent fits. All representations are colour-coded.
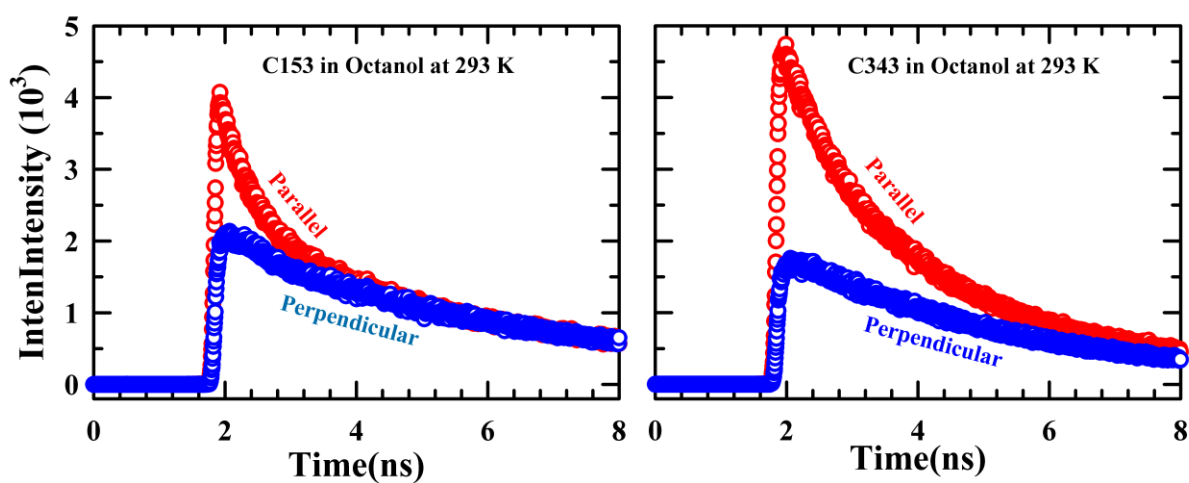
Figure A4.6: Representative Parallel and perpendicular fluorescence intensity decay of C153 (in left panel) and C343 (in right panel) in octanol at 293K. All representations are color-coded.
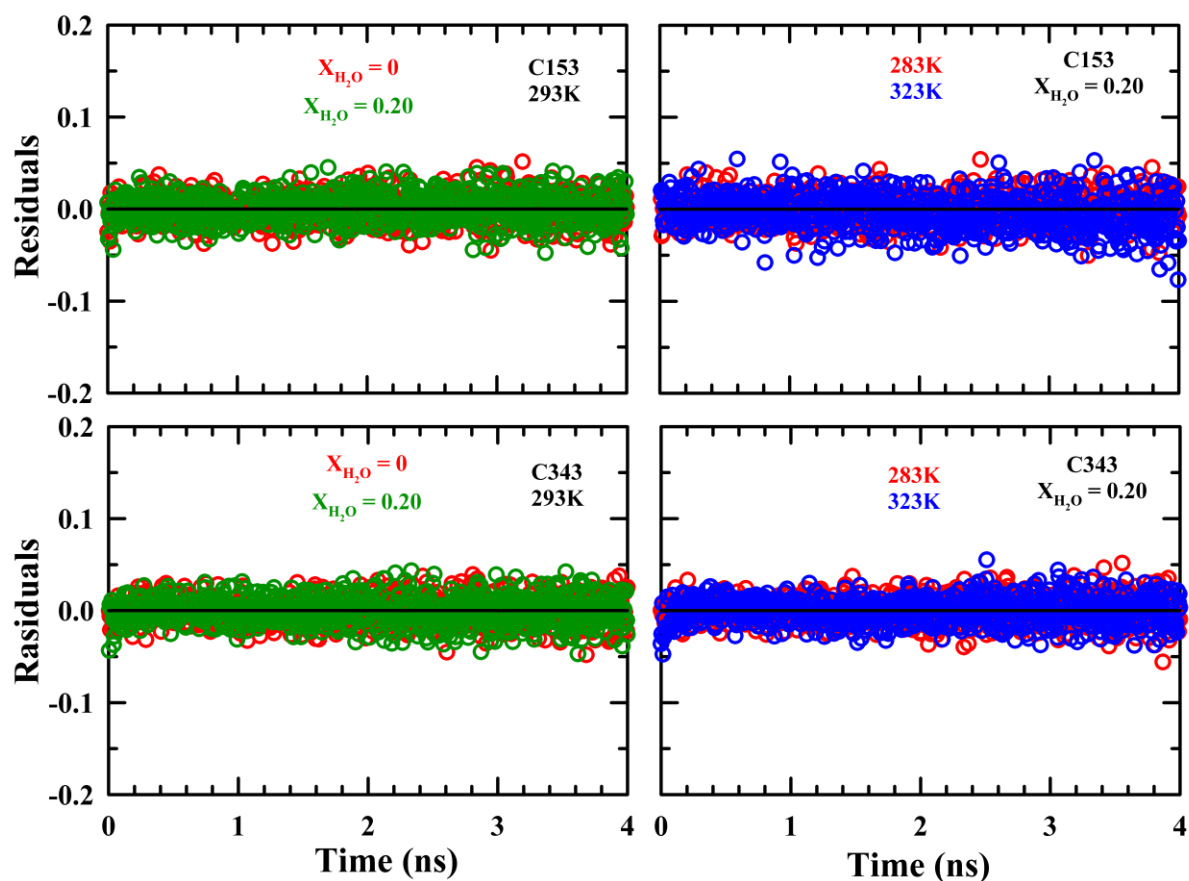
Figure A4.7: Residuals of fluorescence anisotropy $r(t)$ decay of C153 (upper panel) and C343 (lower panel) in neat octanol (red) and $X_{H_2O} = 0.20$ (green) of water with octanol (left panel) and both probes at two different temperatures (283K: red, 323K: blue) in 0.20 mole fraction water with octanol (right panels). Residuals from fit are shown by circle. All representations are colour-coded.

Table A4.8: Stokes-Einstein-Debye (SED) for stick rotational diffusion, theoretical rotational time of pure single molecular rotation, is $\tau_r = 6V\eta C f_S/l(l+1)K_B T$ with l is rank of experimental method ($l = 2$ for fluorescence measurement), V and f_s are the volume and shape factor of solute respectively, C is the coupling parameter of the solute with the surrounding environment. k_B and T are Boltzmann constant and temperature in Kelvin respectively. Modified SED equation for fluorescence measurement with $l = 2$, $\tau_r^{(2)} = V\eta C f_S/K_B T$. We have used V = 246 Å³, f_s = 1.71, C = 0.24 (slip) and 1 (stick) for C153[79] and V = 243 Å³, f_s= 1.99 and C = 0.18 (slip)and 1 (stick) for C343[80]. Estimated single molecular rotation time of both fluorescence probes in pure octanol and octanol+water mixture is given below at 293K. Longer time scale τ_2^r (ps) of $r(t)$ decays from experiments for both probes are given in same table.

X_{H_2O}	η/cP	C153			C343		
		$\tau_r^{(2)}$/ps stick	$\tau_r^{(2)}$/ps slip	τ_2^r/ps in Exp	$\tau_r^{(2)}$/ps stick	$\tau_r^{(2)}$/ps slip	τ_2^r/ps in Exp
0	9.16	953	228	1125	1095	197	1971
0.05	9.11	948	227	923	1089	196	1753
0.10	8.82	917	220	914	1055	189	1611
0.20	8.67	902	216	910	1037	186	1523
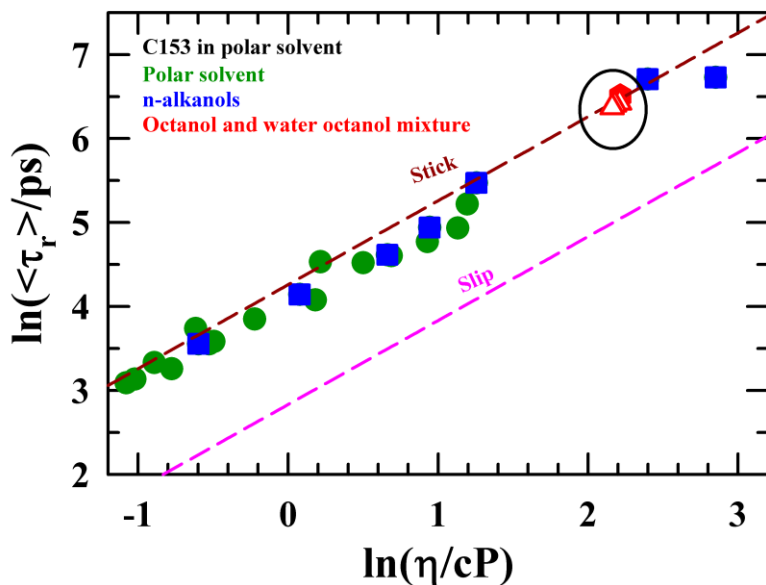
Figure A4.9: Representative double logarithmic plot of average rotational time, $\langle \tau_r \rangle$ vs. η of C153 in pure octanol (red hexagon) and various mole fractions of water in octanol (red triangle) at 293K. Average rotation time C153 and viscosity in polar solvent (dark green circle) and n-alkanols (blue square) data have been taken from Horng et al[47]. Stick and slips lines are presented by dashed lines which are calculated from Stokes-Einstein-Debye relation. All representations are colour-coded.
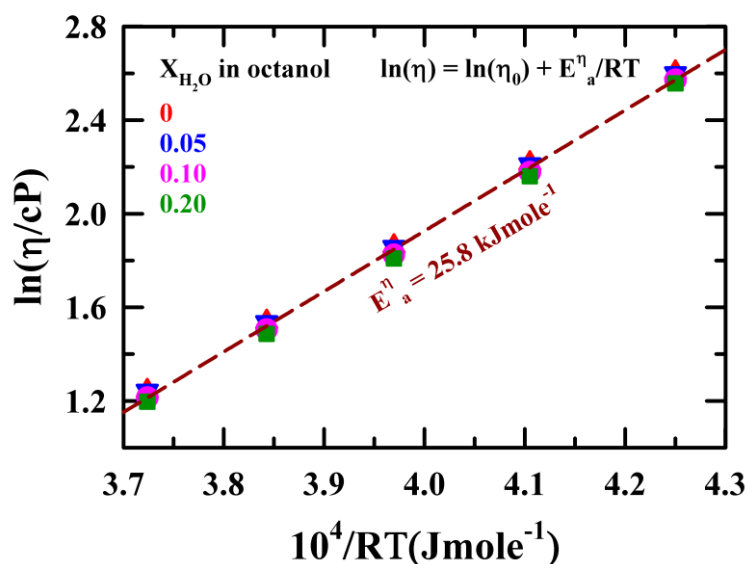
Figure A4.10: Arrhenius-type temperature dependence of medium viscosity of octanol+water mixtures. Average activation energies are estimated in different water mole fraction (X_{H_2O}) in octanol+water mixtures. Solid lines passing through the data points represent linear fits. All representations are colour-coded.

Reference

1   G. Klopman and H. Zhu, *Mini-Rev. Med. Chem.*, 2005, **5**, 127–133.

2   C. Peetla, A. Stine and V. Labhasetwar, *Mol. Pharm.*, 2009, **6**, 1264–1276.

3   A. C. L. Lee, J. L. Harris, K. K. Khanna and J. H. Hong, *Int. J. Mol. Sci.*, 2019, **20**, 2383.

4   Z. Liu and A. E. Clark, *Chem. Sci.*, 2021, **12**, 2294–2303.

5   D. B. Goldstein, *Ann. Rev. Pharmacol. Toxicol*, 1984, **24**, 43–64.

6   S. F. Malan, D. J. Chetty and J. du Plessis, *S. Afr. J. Sci.*, 2002, **98**, 385–391.

7   R. B. Gennis, *Biomembranes*, Springer New York, New York, NY, 1989.

8   A. P. Lyubartsev, S. P. Jacobsson, G. Sundholm and A. Laaksonen, *J. Phys. Chem. B*, 2001, **105**, 7775–7782.

9   G. Klopman and H. Zhu, *Mini-Rev. Med. Chem.*, 2012, **5**, 127–133.

10 T. D. Bergazin, N. Tielker, Y. Zhang, J. Mao, M. R. Gunner, K. Francisco, C. Ballatore, S. M. Kast and D. L. Mobley, *J. Comput. Aided Mol. Des.*, 2021, **35**, 771–802.

11 C. Giaginis and A. Tsantili-Kakoulidou, *J. Pharm. Sci.*, 2008, **97**, 2984–3004.

12 A. Leo, C. Hansch and D. Elkins, *Chem. Rev.*, 1971, **71**, 525–616.

13 R. N. Smith, C. Hansch and M. M. Ames, *J. Pharm. Sci.*, 1975, **64**, 599–606.

14 C. Hansch, J. P. Björkroth and A. Leo, *J. Pharm. Sci.*, 1987, **76**, 663–687.

15 M. N. Martinez and G. L. Amidon, *J. Clin. Pharmacol.*, 2002, **42**, 620–643.

16 A. R. Katritzky, M. Kuanar, S. Slavov, C. D. Hall, M. Karelson, I. Kahn and D. A. Dobchev, *Chem. Rev.*, 2010, **110**, 5714–5789.

17 G. L. Flynn, *J. Pharm. Sci.*, 1971, **60**, 345–353.

18 W. C. Wimley, T. P. Creamer and S. H. White, *Biochemistry*, 1996, **35**, 5109–5124.

19 W. C. Wimley and S. H. White, *Nat. Struct. Mol. Biol.*, 1996, **3**, 842–848.

20 N. P. Franks, M. H. Abraham and W. R. Lieb, *J. Pharm. Sci.*, 1993, **82**, 466–470.

21 K. S. Vahvaselkä, R. Serimaa and M. Torkkeli, *J. Appl. Crystallogr.*, 1995, **28**, 189–195.

22 Y. Marcus, *J. Solution Chem.*, 1990, **19**, 507–517.

23 P. Sassi, A. Morresi, M. Paolantoni and R. S. Cataliotti, in *J. Mol. Liq.*, 2002, **96–97**, 363–377.

24 M. Paolantoni, P. Sassi, A. Morresi and R. S. Cataliotti, *Chem. Phys.*, 2005, **310**, 169–178.

25 F. Palombo, T. Tassaing, Y. Danten and M. Besnard, *J. Chem. Phys.*, 2006, **125**, 094503-undefined.

26　P. Sassi, A. Marcelli, M. Paolantoni, A. Morresi and R. S. Cataliotti, *J. Phys. Chem. A*, 2003, **107**, 6243–6248.

27　P. Sassi, M. Paolantoni, R. S. Cataliotti, F. Palombo and A. Morresi, *J. Phys. Chem. B*, 2004, **108**, 19557–19565.

28　S. K. Garg and C. P. Smyth, *J. Phys. Chem.*, 1965, **69**, 1294–1301.

29　S. E. DeBolt and P. A. Kollman, *J. Am. Chem. Soc.*, 1995, **117**, 5316–5340.

30　S. A. Best, K. M. Merz and C. H. Reynolds, *J. Phys. Chem. B*, 1999, **103**, 714–726.

31　J. L. MacCallum and D. P. Tieleman, *J. Am. Chem. Soc.*, 2002, **124**, 15085–15093.

32　C. D. Wick and T. M. Chang, *J. Phys. Chem. B*, 2014, **118**, 7785–7791.

33　A. S. C. Lawrence, M. P. McDonald and J. v. Stevens, *Trans. Faraday Soc.*, 1969, **65**, 3231–3244.

34　B. C. Lippold and M. S. Adel, *Arch. Pharm.*, 1972, **305**, 417–426.

35　A. D'Aprano, D. I. Donato and E. Caponetti, *J. Solution Chem.*, 1979, **8**, 135–146.

36　S. Mashimo, S. Kuwabara, S. Yagihara and K. Higasi, *J. Chem. Phys.*, 1989, **90**, 3292–3294.

37　U. Kaatze, A. Schumacher and R. Pottel, *Ber. Bunsenges. Phys. Chem.*, 1991, **95**, 585–592.

38　A. C. Kumbharkhane, S. M. Puranik and S. C. Mehrotra, *J. Chem. Soc. Faraday Trans.*, 1991, **87**, 1569–1573.

39　T. Pradhan, P. Ghoshal and R. Biswas, *J. Chem. Sci.*, 2008, **120**, 275–287.

40　T. Pradhan, P. Ghoshal and R. Biswas, *Journal of Physical Chemistry A*, 2008, **112**, 915–924.

41　S. M. Mejía, J. F. Orrego, J. F. Espinal, P. Fuentealba and F. Mondragón, *Int. J. Quantum Chem.*, 2011, **111**, 3080–3096.

42　N. C. Maity, A. Baksi, K. Kumbhakar and R. Biswas, *J. Photochem. Photobiol. A: Chem.*, 2023, **439**, 114600.

43　H. A. R. Gazi and R. Biswas, *J. Phys. Chem. A*, 2011, **115**, 2447–2455.

44　S. Indra and R. Biswas, *Journal of Chemical Physics*, 2015, **142**, 204501.

45　M. Maroncelli and G. R. Fleming, *J. Chem. Phys.*, 1987, **86**, 6221–6239.

46　M. L. Horng, J. A. Gardecki, A. Papazyan and M. Maroncelli, *J. Phys. Chem.*, 1995, **99**, 17311–17337.

47　M. L. Horng, J. A. Gardecki and M. Maroncelli, *J. Phys. Chem. A*, 1997, **101**, 1030–1047.

48　H. Shirota and E. W. Castner, *J. Chem. Phys.*, 2000, **112**, 2367–2376.

49   R. Karmakar and A. Samanta, *J. Phys. Chem. A*, 2002, **106**, 4447–4452.

50   R. Baumann, C. Ferrante, E. Kneuper, F. W. Deeg and C. Bräuchle, *J. Phys. Chem. A*, 2003, **107**, 2422–2430.

51   S. Koley, H. Kaur and S. Ghosh, *Phys. Chem. Chem. Phys.*, 2014, **16**, 22352–22363.

52   B. Guchhait, S. Daschakraborty and R. Biswas, *J. Chem. Phys.*, 2012, **136**, 174503.

53   K. Mukherjee, A. Barman and R. Biswas, *J. Mol. Liq.*, 2016, **222**, 495–502.

54   K. Kumbhakar, E. Tarif, K. Mukherjee and R. Biswas, *J. Mol. Liq.*, 2019, **290**, 111225.

55   E. Tarif, K. Mukherjee, K. Kumbhakar, A. Barman and R. Biswas, *J. Chem. Phys.*, 2019, **151**, 154902.

56   M. Kondo, X. Li and M. Maroncelli, *J. Phys. Chem. B*, 2013, **117**, 12224–12233.

57   B. E. Lang, *J. Chem. Eng. Data*, 2012, **57**, 2221–2226.

58   T. Pradhan and R. Biswas, *J. Phys. Chem. A*, 2007, **111**, 11514–11523.

59   B. Guchhait and R. Biswas, *J. Chem. Phys.*, 2013, **138**, 114909.

60   T. Pradhan, H. Al, R. Gazi, B. Guchhait and R. Biswas, *J. Chem. Sci*, 2012, **124**, 355–373.

61   N. Sarma, J. M. Borah, S. Mahiuddin, H. A. R. Gazi, B. Guchhait and R. Biswas, *J. Phys. Chem. B*, 2011, **115**, 9040–9049.

62   J. R. Lakowicz, *Principles of Fluorescence Spectroscopy*, Springer, New York, 3rd eds., 2006.

63   R. Biswas, J. E. Lewis and M. Maroncelli, *Chem. Phys. Lett.*, 1999, **310**, 485–494.

64   J. E. Lewis, R. Biswas, A. G. Robinson and M. Maroncelli, *J. Phys. Chem. B*, 2001, **105**, 3306–3318.

65   Z. Hu and C. J. Margulis, *Proc. Natl Acad. Sci. U. S. A.*, 2006, **103**, 831–836.

66   P. K. Mandal, M. Sarkar and A. Samanta, *J. Phys. Chem. A*, 2004, **108**, 9048–9053.

67   M. D. Ediger, C. A. Angell and S. R. Nagel, *J. Phys. Chem.*, 1996, **100**, 13200–13212.

68   M. D. Ediger, *Annu. Rev. Phys. Chem.*, 2000, **51**, 99–128.

69   H. Sillescu, *J. Non-Cryst. Solids*, 1999, **243**, 81–108.

70   A. Das and R. Biswas, *Journal of Physical Chemistry B*, 2015, **119**, 10102–10113.

71   R. Buchner, J. Barthel and J. Stauber, *Chem.Phys. Lett.*, 1999, **306**, 57–63.

72   B. Guchhait, H. al Rasid Gazi, H. K. Kashyap and R. Biswas, *J. Phys. Chem. B*, 2010, **114**, 5066–5081.

73   R. S. Fee and M. Maroncelli, *Chem. Phys.*, 1994, **183**, 235–247.

74   J. A. Padró, L. Saiz and E. Guàrdia, *J. Mol. Struct.*, 1997, **416**, 243–248.

75   J. Barthel and R. Buchner, *Pure & Appl. Chem.*, 1991, **63**, 1473–1482.

76   Biman Bagchi, *Molecular relaxation in liquids*, Oxford University Press, New York, 2012.

77   Y. H. Zhao, M. H. Abraham and A. M. Zissimos, *J. Orga. Chem.*, 2003, **68**, 7368–7373.

78   J. T. Edward, *J. Chem. Educ.*, 1970, **47**, 261–270.

79   H. Jin, G. A. Baker, S. Arzhantsev, J. Dong and M. Maroncelli, *J. Phys. Chem. B*, 2007, **111**, 7291–7302.

80   G. B. Dutt and T. K. Ghanty, *J. Phys. Chem. B*, 2003, **107**, 3257–3264.

81   W. Huang and R. Richert, *Phil. Mag.*, 2007, **87**, 371–382.

82   K. Mukherjee, S. Das, E. Tarif, A. Barman and R. Biswas, *J. Chem. Phys.*, 2018, **149**, 124501.

83   M. D. Ediger, C. A. Angell and S. R. Nagel, *J. Phys. Chem.*, 1996, **100**, 13200–13212.

84   C. A. Angell, *J. Chem. Phys.*, 1967, **46**, 4673–4679.

85   I. Chang, F. Fujara, B. Geil, G. Heuberger, T. Mangel and H. Sillescu, *J. Non-Cryst. Solids*, 1994, **172**, 248–255.

Chapter 5

Exploring Glucose-Dependent Solution Structure, Dynamics and Thermo-Physical Properties of Glucose/Ethylene Glycol Cryoprotectant Mixtures: A Comprehensive Investigation

5.1 Introduction

Living organisms, such as bacteria, algae, fungi, protozoa, plant, fish, vertebrates have developed fascinating strategies to tolerate sub-zero temperatures.[1–4] These organisms synthesize various anti freezing chemicals like sugars (glucose, trehalose, sucrose, etc.)[5–7] and polyol (ethylene glycol, glycerol, etc.)[8,9] in high concentration to prevent ice nucleation in intra and inter-cellular fluid in extreme cold condition. The mechanism behind these natural defence strategies have been exploited for cryopreservation of cells, organs, tissues, proteins, and DNA in the field of biotechnology and food preservation technology.[10–14] Chemicals utilized in cryopreservation are termed as cryoprotective agents (CPA) or cryoprotectants.[15] A viable CPA should be eco-friendly, biocompatible, biodegradable, biosource origin and easily available. Glucose , a most abundant bio-precursor in plant photosynthesis, is biodegradable, biocompatible, and a readily available CPA.[16–18] Ethylene glycol (EG), a dihydroxy alcohol with 1,2-positioned -OH group, is efficiently used as glass forming material and CPA.[19–22] Biomolecules dissolved in EG can maintain their native structure.[23] Additionally, EG is employed as a solvent in organic chemistry due to its low toxicity, cheap cost and ability to dissolve a wide range of organic solutes.[24] It has been observed that cryopreservation efficiency enhanced when using mixture of two or more CPA compared to single cryoprotectant. Some of the most effective cryoprotectant mixtures include glucose/glycerol[25], glucose/ethylene glycol[26], trehalose/ethylene glycol[27], sucrose/ethylene glycol[28], trehalose/glycerol[29], ethylene glycol/dimethyl sulfoxide[30] etc.[31]

During cryopreservation, inter and intracellular ice formation is detrimental to cells, organs, tissues, and other organ less biomolecules. The CPAs can inhibit such ice formation and minimise damage from cold injury.[5,8] Vitrification, an alternative approach to cryopreservation,

is a rapid cooling process that transforms liquid to glass without crystallisation.[32–34] Vitrification in presence of CPAs leads to higher glass transition temperature ($\sim T_g$).[35,36] It has been observed that the efficiency of vitrification process is greater in presence of CPAs compared to the traditional solvents.[36] CPAs having plenty of hydrogen bond (H-bond) donor and acceptor groups, exhibit a strong propensity for H-bonding.[37–41] CPA are known to disrupt the extensive intermolecular H-bonded network of water via extensive interspecies (CPA-water) H-bonding in the extracellular fluid, results depletion of bulk water content.[39] Moreover, such H-bond disruption decreases the probability of forming ice crystal at freezing temperature in extra-cellular fluid.[39] Relative preference between three possible intra/inter species H-boding interactions: CPA-water, water-water and CPA-CPA dictate the efficiency of any CPA as cryopreserving media.[40–42] The chemical structure as well as relative concentration of CPAs play important role to tune such demand based preferential inter/intra H-bonding interaction. The CPAs present in the intracellular fluid, known as intra-cellular CPAs[43–45], facilitate the preferential exclusion of bulk water from organ-less biomolecule, preventing hydrophobic hydration and minimising the damage from ice formation. Moreover, T_g of cryopreservation system also depends on the propensity of inter and intra-molecular H-bonding of CPAs. Therefore, understanding interspecies interaction of CPA media itself is crucial prior to apply them in cryopreservation.

In the present study, we have selected two cryoprotectants: glucose as extra-cellular CPA[5,6] and EG as intra-cellular CPA[28]. Glucose, being a natural CPA along with high T_g (295K)[46] is effectively used in cryopreservation process. EG, a glass forming material ($T_g \sim 153$K), has been widely used in various field of biotechnology, pharmaceutical technology for cryogenic stabilization[47,48]. By varying relative composition of glucose and EG in the mixture, we can tune T_g and medium interactions and dynamics in order to develop varying levels of cryopreservation efficiency.

There are several reported studies on interaction and dynamics of neat EG[49,50], EG/water[51–54] or binary mixtures of EG with other solvents[55–57], and glucose/water[58–62] via dielectric relaxation spectroscopy (DRS). However, no such studies on interaction and dynamics in glucose-EG mixture are reported yet.[26,31,63,64] In our previous MD simulation studies on glucose/EG cryoprotectant mixture[65], we reported that the glucose-glucose interaction prevails over glucose-EG interaction. In this work, we are interested to explore the phase transition temperatures, cluster size, dynamics, and aspect of spatio-temporal heterogeneity of

glucose/EG mixture at varying glucose content (from 0 to 40 wt %) in EG using differential scanning calorimetry (DSC), dynamic light scattering (DLS), steady-state fluorescence spectroscopy and dielectric relaxation spectroscopy (DRS) measurements. DSC was performed to determine glass transition temperature as well as to observe if any melting appears in these glucose/EG binary cryoprotectant mixture. Excitation wavelength dependent fluorescence emission of two well-known non-reacting fluorescent probes coumarin 153 (C153, $< \tau_{life} >$ 3-5 ns),[66–74] and coumarin 343 (C343, $< \tau_{life} >$ 3-4 ns)[72] and reactive probe trans-2-[4'-(dimethylamino)styryl]benzothiazole (DMASBT, $< \tau_{life} >$ 0.5 ns)[74,75] was carried out to explore spatial heterogeneity of these media. The fluorescent probs with wide different $< \tau_{life} >$ will report separately heterogeneous domain relaxing in different time window. relaxations. Fluorescence experiments of C343 indicate a presence of strong spatial heterogeneity. Interestingly in 40 wt% glucose containing mixture, all of the three probes (C343, C153 and DMASBT) report both faster and slower relaxing microdomains, a manifestation of highly spatially heterogeneous solution structure. Dipolar relaxation was probed using DRS which revealed multi-step DR processes in these complex systems. DR has been found to be decoupled from medium viscosity revealing the presence of dynamic heterogeneity in these cryoprotectant mixtures.

5.2. Experimental Details

5.2.1 Materials and Sample Preparation

D (+) Glucose (≥99.5), EG (≥99%), C153, C343 and DMASBT were purchased from Sigma Aldrich and used for preparation of sample without purification. The chemical structures of these molecules are shown in Scheme 5.1. The binary cryoprotectant mixtures (10, 20, 30 and 40 wt% of glucose in EG) were prepared as follows: for 10 wt% glucose, requisite amounts of glucose and EG was weighed in airtight glass container followed by heating at 343 K inside an oil bath for 2-3 hrs under continuous stirring condition at 600 rpm. Finaly, we get a colourless transparent solution without any solute crystal appearance. Similarly, 20, 30 and 40 wt% glucose solution were prepared by heating at 348 K, 353 K and 365 K, respectively for 3 hrs. Photograpic image of glucose wt% dependent glucose/EG binary cryoprotectant composite before and after sample preparation are shown in Scheme A5.1 (Appendix). The prepared mixtures were cooled to room temperature before performing DSC, DLS, and DRS experiments. Steady state fluorescence measurements were done using approximately 2-3 ml

of the glucose/EG mixture, preloaded with fluorescent probes, was poured into a quartz cuvette maintaining dye concentration $\leq 10^{-5}$ M.

(a)

(b)

(c)

(d)

(e)
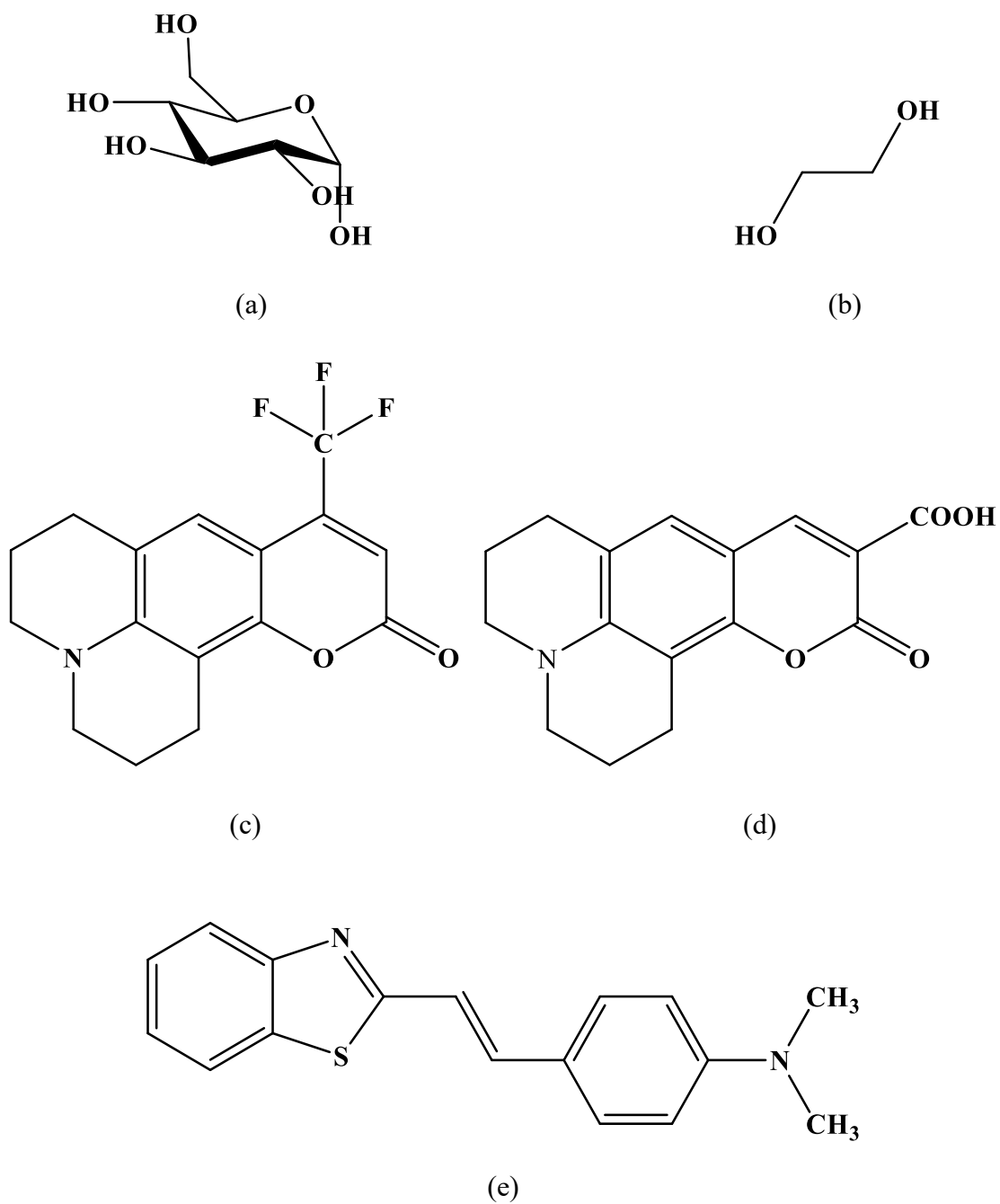
Scheme 5.1: Chemical structures of (a) Glucose, (b) EG, (c) C153 (D) C343, (e) DMASBT

5.2.2 Refractive Index, Density and Viscosity Measurements

Refractive index (n_D) was collected from an automated temperature-controlled refractometer (RUDOLPH, J357).[76] Density (ρ) of experimental solution was measured by using an automated temperature-controlled density cum sound analyser (Anton Parr, model DSA 5000).[77] Temperature and glucose concentration dependent solution viscosity coefficients (η) were measure for cryoprotectant mixtures using a Lovis 2000 M (0.5 % accuracy and 0.1 % repeatability). Temperature dependent and glucose wt% dependent n_D ρ, and η values in these glucose/EG binary cryoprotectant mixtures are illustrated in Table A5.2 (Appendix).

5.2.3 Differential Scanning Calorimetry (DSC) Measurement

Glass transition temperatures (T_g) and melting temperatures (T_m) in glucose/EG cryoprotectant binary mixtures as well as in pure EG were determined from differential scanning calorimetry (DSC) (DSC, TA Instruments Q200) measurements[78]. The heat flow and temperature for each measurement was calibrated using a standard indium sample. The temperature window from 113 K to 363 K with constant heat flow (10 K/min or 5 K/min) were maintained for all DSC measurements. The samples were completely airtight sealed in an aluminium pan by sealing with aluminium cap (40 µl, Tzero, TA Instruments).

5.2.4 Data Collection and Analyses for Steady-State Fluorescence Emission Measurement

Steady-state fluorescence emission spectra were recorded by using fluorimeter (Fluorolog, Jobin-Yvon, Horiba) respectively. Temperature was controlled by a Peltier temperature controller (accuracy ±0.5 K). The typical error bar for the determined spectral frequencies was ±200 cm^{-1}.The solvent-blank subtracted spectra were processed accordingly before further analyses and frequency determination.[79,80] Detailed description of the steady state UV-VIS absorption and steady sate fluorescence techniques are the same as those discussed in Chapter 2.

5.2.5 Dynamic Light Scattering (DLS) Measurement

Dynamic light scattering (DLS) measurements were performed by Malvern Zetasizer nano series (Malvern Instrument Ltd. Malvern, UK) DLS instrument with a He-Ne laser with 633 nm wavelength at a scattering angle of 173°. All samples were kept inside quartz cuvette with 1cm path length.

5.2.6 DRS Data Collection and Analyses

Three dielectric set-ups[78] were used for measuring DRS of liquid samples. The E4990A impedance analyser with 16452A liquid test fixture has been used for low frequency measurement from 20 Hz to 10 MHz. The E4991B impedance analyzer (10 MHz to 500 MHz) and the N5235B PNA-L network analyser (200 MHz to 50 GHz) with open ended coaxial probe kit (N1501A, high temperatures probe for E4991B and performance probe for N5235B) were used. Details of the measurements protocols and data analyses are the same as those discussed in Chapter 2. More details about DRS measurements are available in ref [78,81–84] Temperature dependent DRS experiments were performed from 298 K to 328 K.

5.3 Result and Discussion

5.3.1 DSC Measurements: Glass Transition Temperature Modification of Cryoprotectant Mixtures

The DSC thermogram in Figure A5.3 (Appendix) illustrates the heating process of pure EG within the temperature window 130 K to 350 K. Glucose concentration dependent glass-transition temperature (T_g) are measured from DSC measurement and corresponding DSC graphs are shown in Figure 5.1. T_g, T_m (melting temperature) and heating rate for all of these samples are given in Table 5.1. In this DSC analysis, a prominent endothermic peak was observed at 262 K during heating, its corresponding to melting of pure EG. These observations are in good agreement with previous DSC experiments.[47,48] However, the DSC data have not shown the glass transition characteristics of EG. The DSC results of pure EG shown in our experiments and other reported results[47,48,85] suggest that pure EG does not fully transform from liquid to glass at the accessible colling rate in DSC but it forms partially amorphous glass along with crystalline state. Upon adding 10% glucose in glucose/EG binary cryo-mixture, the DSC thermogram (see Figure 5.1) revealed the appearance of T_g at 163 K during heating. The presence of glucose significantly suppressed the crystallization processes of EG. This suppression of crystallization process can be explained by inter-molecular H-bonding between glucose and EG. α-D-glucopyranose (glucose) molecule possess six H-bond accepting and five H-bond donating sites. High intermolecular H-bonding propensity of glucose enhances the number of hydrogen bond between glucose and EG, while simultaneously reducing the probability of EG-EG intermolecular H-bonding probability. This extensive inter-species H-

bonding inhibits the process of crystal nucleation among EG during cooling and thereby facilitating the formation of a glassy state within our experimental limits.

Further addition of glucose from 20 to 40 wt% in EG, the phenomenon of crystallization is completely eliminated. Additionally, T_g gradually increases with glucose concentrations. These findings demonstrate that the addition of glucose allows for modulation of both T_g and cryopreservation ability of cryoprotectant mixtures in cryopreservation technology.
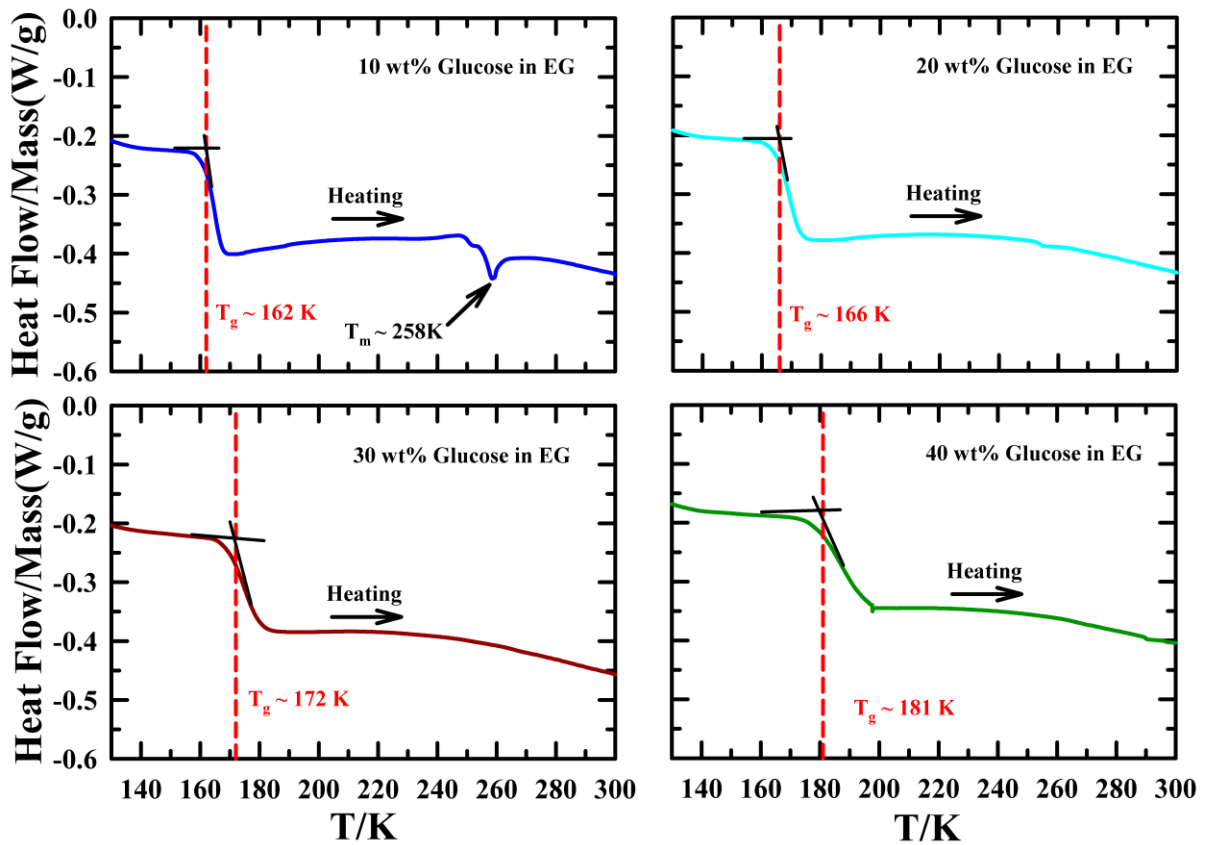
Figure 5.1: Glucose concentration dependent ($10 \leq wt\% \leq 40$) DSC thermogram of glucose/EG binary cryoprotectant mixtures with the temperature window $130 \leq T/K \leq 300$. During DSC experiment 10K/min cooling or heating rate was maintained.

Table 5.1: Glucose concentration dependent glass transition temperature (T_g) and melting temperature (T_m) determined from DSC measurement in Glucose/EG cryoprotectant mixture.

Sample	T_g (K)	T_m (K)	C/H Rate (min/K)	remark
Literature				
Glucose	295			Ref 46
EG	153	262	10	Ref 47
EG	153	260	20	Ref 48
EG		262	10	
10 wt% glucose	162	258	10	
20 wt% glucose	166		10	
30 wt% glucose	172		10	
40 wt% glucose	181		10	
40 wt% glucose	180		5	

5.3.2 Glucose wt % Dependent Cluster Size Determination: Signature of Micro-cluster

Hydrodynamic diameter (D_h) of microscopic particles or clusters in solvent was determined by DLS measurements. This is shown in Figure 5.2. Below 40 wt% glucose concentrations in EG, the D_h ranges from 1 to 2 nm. However, there is a sudden increase in D_h for 40 wt% glucose/EG cryoprotectant mixture, where D_h reaches around 8-10 nm. Previous molecular dynamics studies on glucose oligomers have demonstrated the presence of larger sugar-sugar H-bonding cluster in intermediate concentration (33-66 wt%) of aqueous sugar solutions.[41] Similarly, earlier light scattering study of aqueous glucose solutions have revealed an existence of glucose-glucose larger cluster above 30 mol% glucose solutions.[86] Our previous MD simulations of glucose/EG mixtures [65] have also shown an increase in glucose-glucose coordination number with increasing glucose concentration. Approximate diameter of glucose-EG cluster, considering first solvation shell, can be estimated as $d_{glucose} + 2d_{EG} \sim 1.632$ nm where $d_{glucose}$ and d_{EG} are denoted diameter of glucose (0.656 nm) and EG (0.488 nm).[87] Based on the above discussion, it is clear that monomers or dimers of glucose solvated in EG up to 30 wt% ($\sim$ 13 mol %) glucose containing cryoprotectant mixtures. However, beyond this threshold concentration (40 wt% glucose), glucose-glucose interactions favour the formation

of macromolecule like clusters. To explore the effects of temperature on cluster size, we performed temperature dependent DLS measurements for 30 and 40 wt % glucose mixtures, as shown in Figure A5.4 (Appendix). This suggest that the cluster size decreases with temperatures for both 30 and 40 wt% glucose mixtures, but that effect is prominent for 40 wt% glucose mixture. This indicates that temperature induced kinetic energy disrupts the larger clusters into smaller sizes, which is further examined via ν_{exc} dependence fluorescence emission in next section.
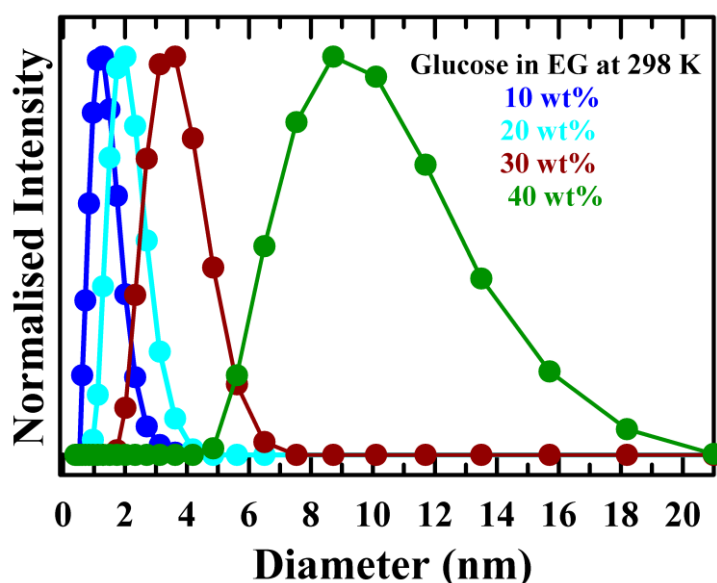
Figure 5.2: Glucose concentration dependent particle size in glucose/EG from dynamic light scattering (DLS) measurement at 298K. All representations are colour-coded.

5.3.3 Excitation Wavelength Dependent Steady State Fluorescence Emission: Spatial Heterogeneity

Steady state excitation and fluorescence emission spectra of C153, C343, DMASBT in pure EG and glucose/EG binary mixtures with different glucose concentrations are shown in Figure A5.5 (Appendix). Both excitation and emission spectra for C153 with 40 wt% glucose in cryoprotectant mixture are blue shifted than the other probes. However, no significant changes were observed for cryoprotectant mixtures containing 0 to 30 wt% glucose. This indicates that the interaction between C153 and cryoprotectant mixtures with 0 to 30 wt% glucose is different than 40 wt% glucose. Up to 30 wt% glucose, pre-existing interaction between C153 and solvent, as well as microscopic polarity surrounding the probe, remain relatively unchanged. However, in 40 wt% mixture, glucose induces substantial modification in the fluorescence

spectral characteristics of C153 indicating a distinct change has occurred in the environment and interaction. On the other hand, the fluorescence spectral shift of C343 is nonmonotonic. This suggest that the interaction between hydrophilic C343 and solution species is influenced not only by dipolar interaction but also by the involvement of complex H-bonding between carboxylic group of C343 and hydroxyl group of solution species. The nonmonotonic fluorescence spectral shift of C343 in strongly hydrogen bonding system has been previously reported[72].
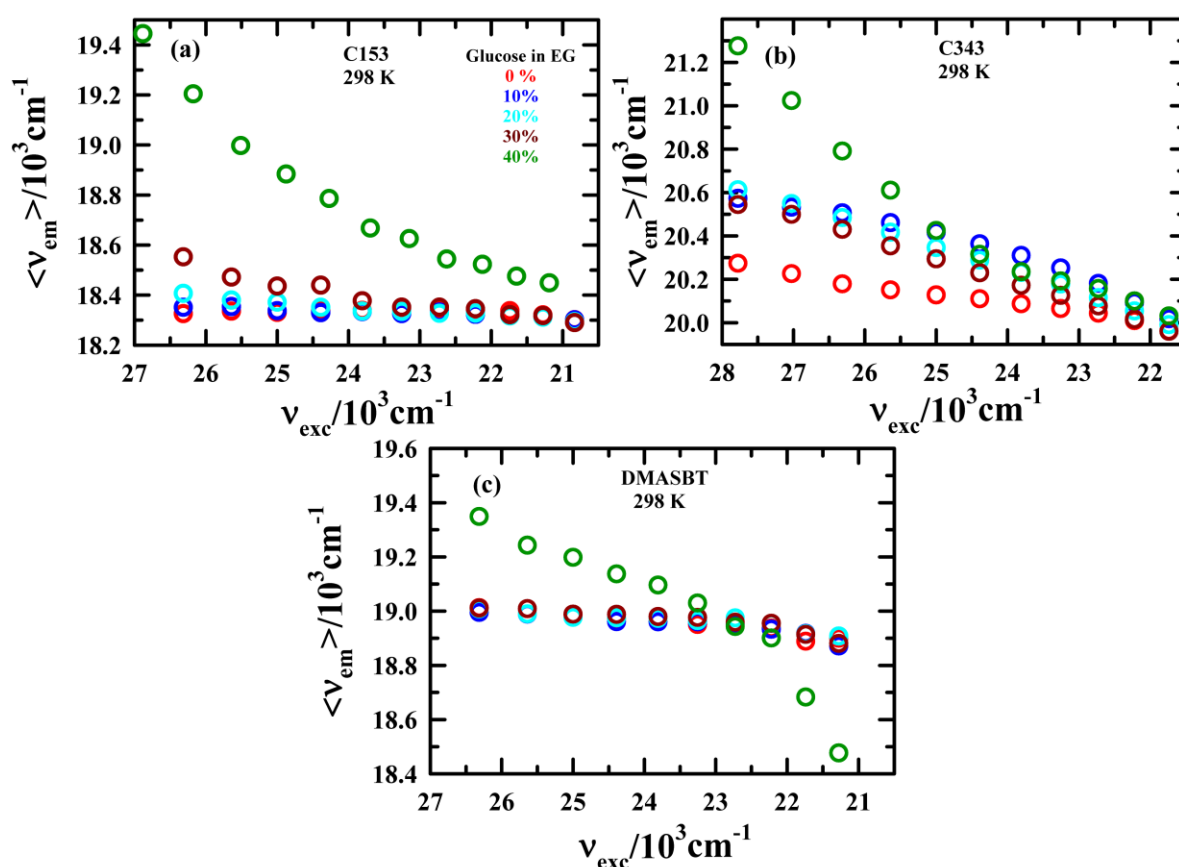
Figure 5.3: Excitation frequency dependence (ν_{exc}) average steady state fluorescence emission frequency ($<\nu_{em}>$) of (a) C153, (b) C343, and (c) DMASBT at various wt% of glucose in glucose/EG binary cryoprotectant mixtures and in pure EG at 298K. All representations are colour-coded.

Next, in order to search the spatial heterogeneity, we have performed excitation frequency (ν_{exc}) dependence fluorescence emission experiments[88,89] in these cryoprotectant mixtures. The ν_{exc} depended fluorescence spectra of all probes (C153, C343, and DMASBT) in 40% glucose/EG and C343 in 30% glucose/EG which are shown in Figure A5.6 (Appendix). The

ν_{exc} dependence average fluorescence emission frequency ($\langle\nu_{em}\rangle$) and full width half maxima (FWHM, Γ_{em})[90,91] in these cryo-mixtures are shown in Figure 5.3 and Figure A5.7 (Appendix) respectively. In cases where the medium density fluctuation time around the fluorescent probe is comparable to exited state lifetime of fluorescent probe, fluorescence emission of probe depends on excitation wavelength. The total shift of fluorescence emission ($\Delta\nu_{em} = \langle\nu_{em}\rangle_{blue\ end} - \langle\nu_{em}\rangle_{red\ end}$) with varying ν_{exc} in pure EG and glucose/EG mixtures at 298 K and 328 K are shown Figure 5.4. The $\Delta\nu_{em}$ of C153 and DMASBT reveals that 10 to 30 wt% glucose containing cryoprotectant mixture are homogeneous. Whereas C343 reported considerable heterogeneity[92–94] present in these media. The large shift in $\langle\nu_{em}\rangle$ (~600 cm^{-1}) observed in ν_{exc} dependent fluorescence emission for C343 from 10 to 30% glucose containing binary mixtures confirms that these are heterogeneous, with solvent relaxation time comparable to the C343 fluorescence lifetime and heterogeneity length scale comparable to C343 size.[93,95,96] In contrast, 40 wt% glucose/EG cryoprotectant mixture displays strong spatial heterogeneity[92–94] with respect to fluorescent probes C153, C343 and DMASBT. This suggests the presence of faster and slower structural relaxations within this mixture. Glucose concentration dependent strong heterogeneity persists in highest glucose containing (40%) cryoprotectant mixture. This indicates the existence of macro-cluster in this medium which is confirmed by DLS measurements. C153 and DMADBT molecules probe preferentially less polar region where glucose-glucose multimeric structure is formed. In contrast, C343 is a negatively charged molecule and prefers to reside in the interface of less and more polar region (EG dominated region). A schematic representation of microscopic structure of 40 wt% glucose system with two fluorescent probes, C153 and C343 shown in the Scheme 5.2. The heterogeneity of glucose/EG cryoprotectant mixture depends on wt% of glucose present in EG and decreases with increasing medium temperatures. The combined study of DSC and ν_{exc} dependence fluorescence emission measurements revealed that both T_g and system heterogeneity increases with increasing glucose concentration. This may suggest that T_g is directly proportional to the system heterogeneity.
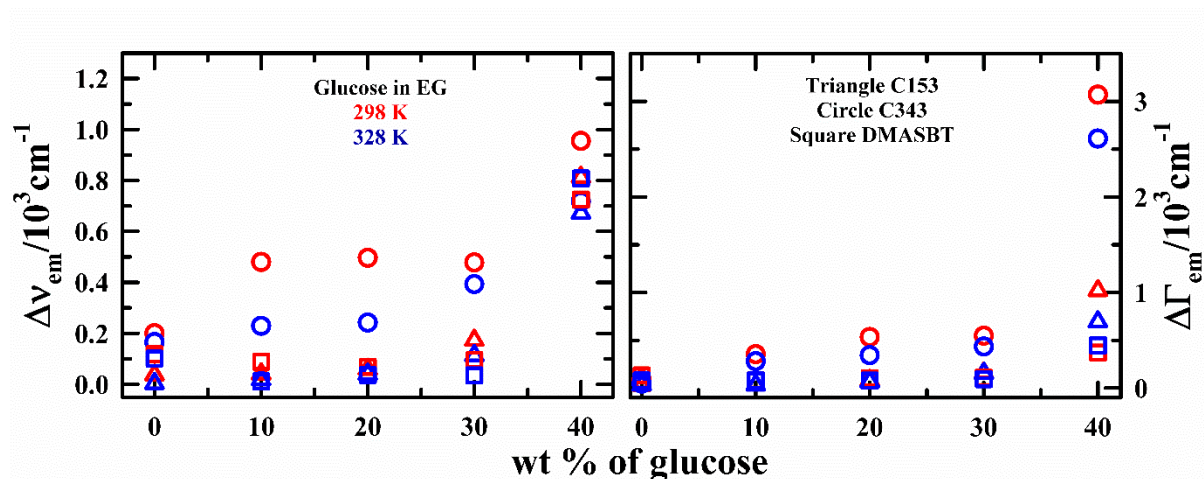
Figure 5.4: Excitation frequency dependent (ν_{exc}) induced total fluorescence emission shift ($\Delta\nu_{em}$) and corresponding total shift in width ($\Delta\Gamma_{em}$) of C153, C343, and DMASBT at various wt% of glucose in glucose/EG binary cryoprotectant mixtures and in pure EG at two temperatures. All representations are colour-coded.
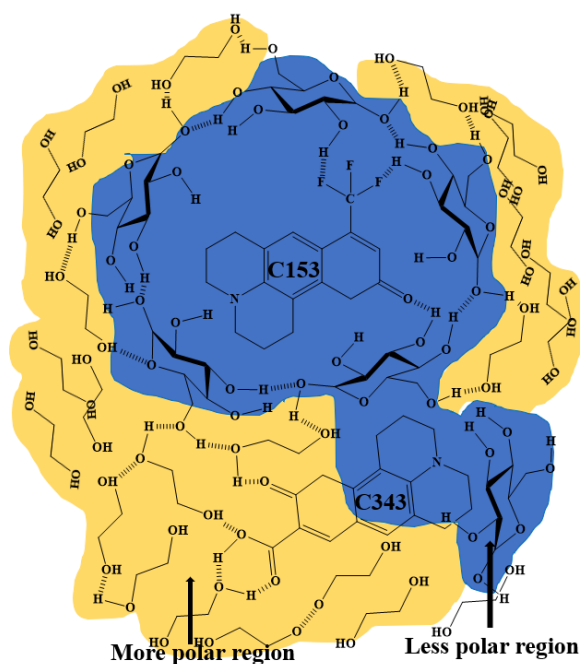
Scheme 5.2: A schematic representation of possible H-bond network formed by glucose-glucose, glucose-EG, and EG-EG interaction and formation of two different regions with varying polarity in 40 wt% glucose/EG mixture. The hydrophobic fluorescent probe C153 prefers to reside relatively less polar glucose rich region (blue shaded) whereas and hydrophilic C343 prefers more polar EG dominated region (yellow shaded). The other probe DMASBT resides in similar environment as C153 molecule.

5.3.4 Effects of Glucose on DRS measurements in Glucose/EG Mixtures

Figure 5.5 shows glucose wt % dependent real (ε') and imaginary (ε'') component of complex DR spectra in glucose/EG cryoprotectant mixtures at four temperatures. This depicts the peak in dielectric loss spectra appeared in our experimental frequency window. Corresponding DR fit residuals at 298 K and 328 K are shown in Figure A5.8 (Appendix). With successive addition of glucose in glucose/EG cryoprotectant mixtures, the DR loss peak shifted towards lower frequency region. Multi-Debye fittings model (solid line passes through experimental data ε' and ε'') were required for temperature and glucose concentration dependent complex DR spectra and the fit parameters and corresponding "goodness-of-fit" χ^2 are given in Table 5.2. As the glucose concentrations increases, new relaxation time emerges in the dielectric response. Additionally, all individual DR time components gradually slow down with increasing glucose concentration due to glucose induced increase of medium viscosity. Before we explore the glucose concentration dependent DR time in glucose/EG binary cryo-mixture, first we discuss about the static dielectric constant of these systems.
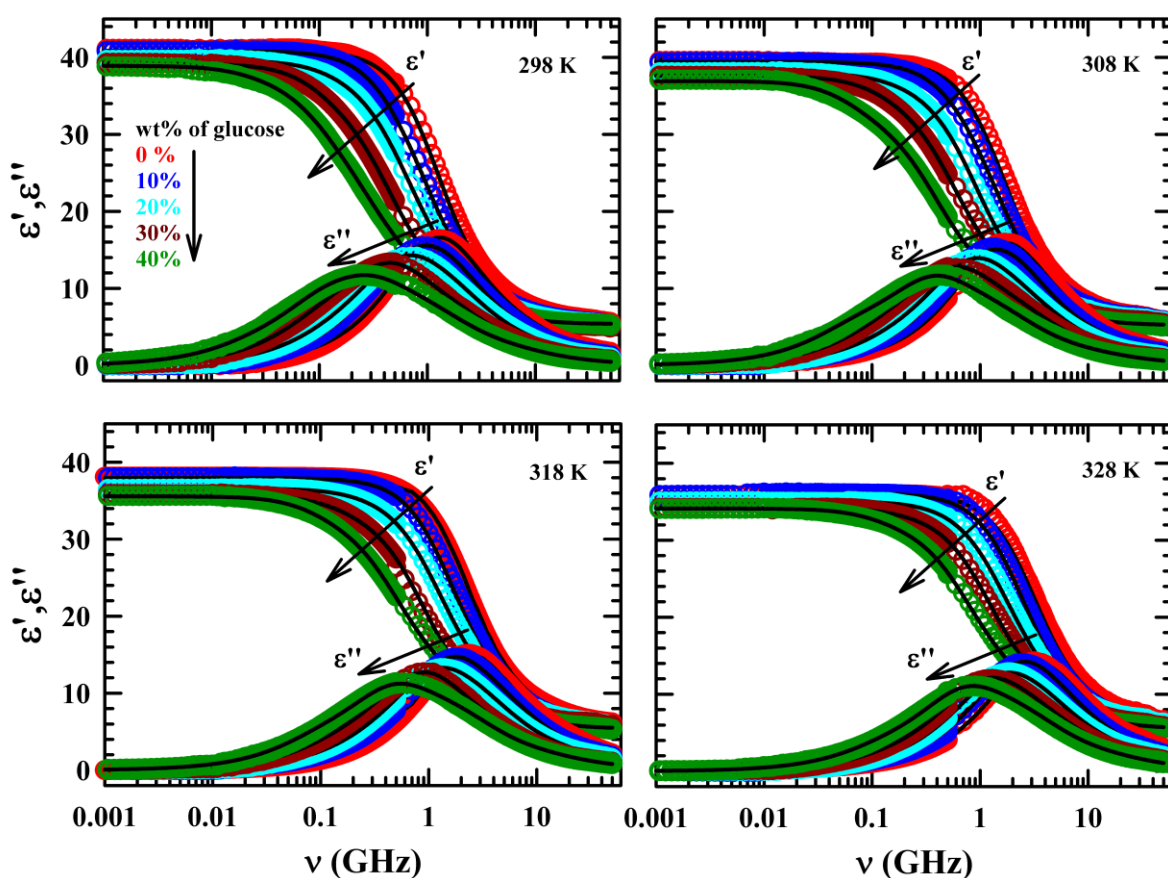
Figure 5.5: Glucose concentration dependent complex DR spectra with real (ε') and imaginary (ε'') component in glucose/EG binary mixtures at four temperatures. The line passing through experimental data points express multi-Debye fits. All representations are colour-coded.

5.3.4.1 Glucose Induced Static Dielectric Constant Reduction

The static dielectric (ε_s) constant was determined from plateau of the real part at low frequency region in complex DR spectra. Temperature and glucose wt% dependent estimated ε_s values for glucose/EG cytoprotectant mixtures are given in Table A5.9 (Appendix). As shown in Figure 5.6, the ε_s values of neat EG and glucose/EG mixtures decrease with increasing temperature and glucose concentrations. Our experimentally measured ε_s value (40.99) of pure EG at 298 K agrees well with literature values (40.5 to 42.23)[49–52,56]. With increasing glucose concentration as well as experimental temperature, ε_s of these systems gradually decreases. High H-bonding ability of glucose, effectively disrupts the liquid structure of pure EG and randomise the dipole orientation of the solvent molecules, leading to reduction in the effective dipole moment of these systems.[65] The effective collective dipole moment of both neat solvent and solution is also reduced with the temperature due to the higher kinetic energy of existing species in these systems that leads to dipole randomisation. Static dielectric constant (ε_s) of a system at given temperature T and volume V is expressed by the following equation[97,98] $\varepsilon_s = 1 + \langle M \rangle_{eff} / 3\varepsilon_0 V k_B T$. Where ε_0 and k_B are vacuum permittivity and the Boltzmann constant respectively. $\langle M \rangle_{eff}$ represents the total effective dipole moment. Above relation shows that the ε_s is directly proportional to the total effective dipole moment ($\langle M \rangle_{eff}$) and inversely proportional to T of the system. This explains temperature induced dipole randomisation reduces ε_s of both pure EG and glucose/EG mixtures. Decrement of ε_s with glucose concentration can be explained as follows: breaking of H-bonding cluster of pure EG due to interactions with glucose molecules in these mixtures.[65] Additionally, more EG molecules are involves in glucose solvation.
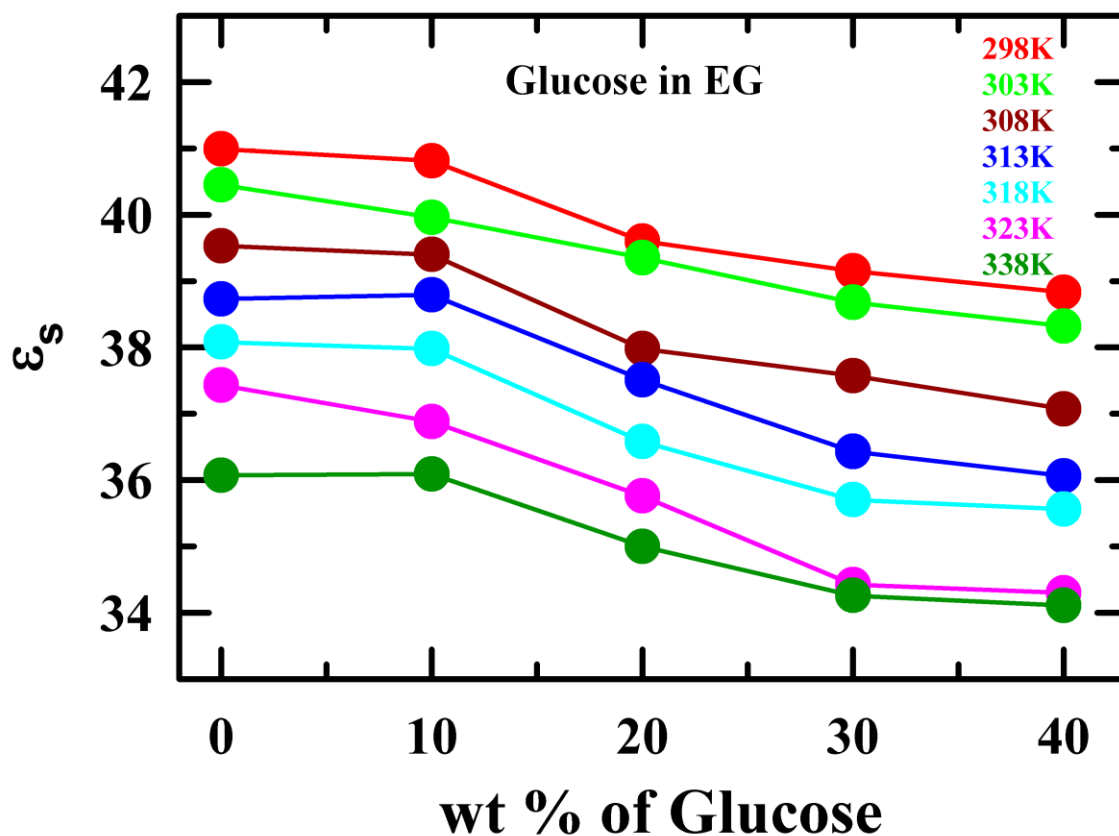
Figure 5.6: Temperature and glucose concentration dependent static dielectric constant (ε_s) of glucose/EG binary mixtures estimated from real (ε') component of complex dielectric spectra at low frequency regime where ε' attained plateau. Different temperatures are colour-coded

Table 5.2: Temperatures and glucose concentration dependent multi-Debye fit parameters of experimentally measured DR spectra (frequency regime: 4 KHz to 50 GHz) in neat EG and glucose/EG cryoprotectant mixtures.[a]

T/K	$\Delta\varepsilon_1$	τ_1/ps	$\Delta\varepsilon_2$	τ_2/ps	$\Delta\varepsilon_3$	τ_3/ps	$\Delta\varepsilon_4$	τ_4/ps	ε_∞	$\langle\tau_{DR}\rangle$ /ps	χ^2
Pure EG											
298			32.22 (91)	130			3.16 (9)	17	5.61	120	0.031
303			32.41 (93)	109			2.42 (7)	13	5.62	102	0.016
308			31.10 (92)	95			2.72 (8)	12	5.71	88	0.027
313			29.85 (91)	85			3.10 (9)	12	5.78	78	0.048

Chapter 5

318			29.31 (91)	71			2.92 (9)	10	5.85	65	0.037
323			28.65 (91)	62			2.94 (9)	9	5.93	57	0.039
328			27.71 (92)	49			2.39 (8)	7	5.97	46	0.033
10 wt% glucose in EG											
298			28,24 (80)	201	6.22 (18)	51	0.89 (2)	7	5.24	170	0.024
303			26.96 (79)	167	6.51 (19)	45	0.81 (2)	7	5.49	141	0.031
308			24.76 (73)	153	8.32 (25)	43	0.74 (2)	6	5.53	122	0.032
313			25.93 (78)	121	6.58 (20)	35	0.78 (2)	6	5.40	101	0.028
318			26.17 (80)	100	5.40 (17)	31	0.92 (3)	6	5.44	85	0.021
323			26.51 (85)	78	3.71 (12)	28	1.12 (3)	6	5.54	70	0.039
328			26.38 (87)	65	2.89 (9)	23	1.21 (4)	6	5.61	59	0.029
20 wt% glucose in EG											
298	2.62 (8)	1117	23.30 (65)	261	7.93 (23)	85	1.52 (4)	14	5.32	279	0.010
303	2.57 (7)	953	22.67 (67)	235	7.58 (23)	70	1.15 (3)	10	5.38	241	0.009
308	1.96 (6)	878	23.94 (74)	180	5.40 (17)	54	1.01 (3)	9	5.66	195	0.012
313	1.71 (5)	812	22.35 (70)	162	6.62 (21)	53	1.10 (4)	8	5.73	165	0.012
318	1.37 (4)	627	21.41 (70)	135	6.83 (22)	47	1.27 (4)	7	5.70	130	0.012
323	0.69 (2)	419	21.72 (72)	115	6.21 (21)	42	1.30 (5)	7	5.83	100	0.015
328	0.62 (2)	380	20.17 (69)	101	6.86 (24)	40	1.53 (5)	7	5.96	87	0.017
30 wt% glucose in EG											
298	6.17 (18)	1476	21.36 (63)	350	5.54 (16)	80	0.95 (3)	14	5.13	499	0.012
303	5.31 (16)	1307	21.07 (63)	312	6.15 (18)	75	0.99 (3)	12	5.16	419	0.011
308	3.93 (12)	1181	21.03 (66)	275	6.25 (19)	64	0.85 (3)	10	5.51	335	0.012
313	3.23 (10)	1018	21.02 (68)	232	5.77 (19)	57	0.83 (3)	9	5.58	271	0.010
318	3.08 (10)	942	22.93 (77)	177	3.25 (11)	39	0.66 (2)	8	5.78	234	0.017
323	2.13 (7)	889	24.03 (84)	142	2.01 (7)	23	0.52 (2)	7	5.73	183	0.019

328	1.17 (4)	829	20.42 (72)	138	5.76 (20)	41	1.17 (4)	7	5.74	141	0.013
40 wt% glucose in EG											
298	3.9 (11)	4828	14.52 (43)	868	14.0 (42)	253	1.24 (4)	15	5.06	1011	0.020
303	6.74 (20)	2839	18.13 (55)	510	7.19 (22)	114	0.95 (3)	13	5.19	874	0.019
308	5.74 (18)	2280	18.23 (58)	419	6.73 (21)	96	1.01 (3)	13	5.22	674	0.019
313	4.92 (16)	1745	18.42 (61)	339	6.12 (20)	76	0.99 (3)	12	5.32	502	0.014
318	4.03 (13)	1616	17.26 (57)	326	7.64 (26)	78	1.23 (4)	12	5.40	416	0.014
323	3.15 (11)	1408	16.05 (55)	273	8.77 (29)	72	1.33 (5)	10	5.46	326	0.013
328	2.74 (10)	1257	17.44 (61)	217	7.20 (25)	56	1.18 (4)	8	5.55	272	0.014

[a]DR time constants and corresponding to its amplitudes can be reproduced within ±5% of the reported values.

[b]Number in parenthesis denotes percentage of dispersion amplitude of a given dispersion step contributing to total dielectric dispersion.

5.3.4.2 Dielectric Relaxation of Pure EG: Origin of Timescale

Figures 5.7 represent the temperature dependent real (ε') and imaginary (ε'') component of complex dielectric spectra of pure EG. Note our experimental imaginary peak (~1.34 GHz) of DR spectra in pure EG is well corroborated with earlier dielectric study at ~1.34 GHz[52] and 1.32GHz[53] at 298K. Both 1Cole-Devidsion (1CD, β=0.82) and 2 Debye (2D) fit attempted for different pure EG are considered to better fit than Cole-Cole model. The fit performed and their respective residuals of four fitting model in pure EG are shown in Figure A5.10 and Figure A5.11 (Appendix). Previous dielectric relaxation studies[49–52,56] of pure EG are tabulated in Table A5.12 (Appendix) along with our present work. Our result agrees well with that of Schrödle et al[52]. An interesting observation is that the average DR time ($\langle\tau_{DR}\rangle$ = 120 ps) for pure EG closely matches with the characteristic time constant of DR peak ($\tau_{peak} = 1/2\pi\nu_{peak} \approx 119$ ps). The superposition of dielectric peak relaxation time from dielectric loss spectra and $\langle\tau_{DR}\rangle$ estimated from 2D fit of the of the same spectra further confirms that 2D fit is more appropriate than 1CD model fit. Additionally, residuals of both 1CD and 2D fit for complex DR spectra are suggested that 2D fit is best fit model in pure EG.
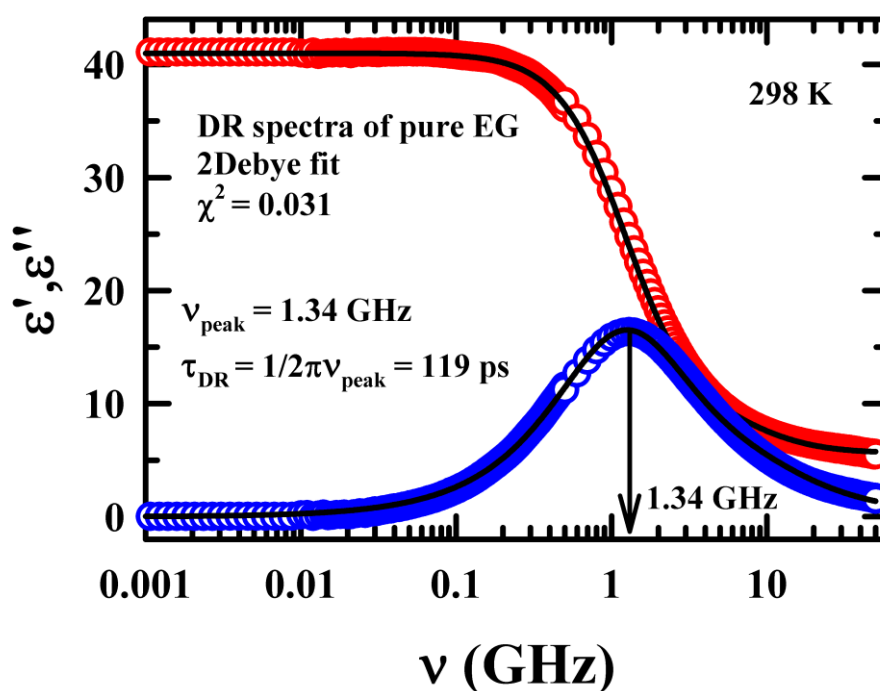
Figure 5.7: Complex DR spectra with real (ε') and imaginary (ε'') component in EG. The line passing through experimental data point express 2Debye model fits. All representations are colour-coded.

Next, we explore possible origin of DR time coming from pure EG. Slow DR time τ_2 ($\sim$ 130 ps) observed in pure EG, is found to be close to τ_{peak} of loss part with maxim amplitude ~91 %. Temperature dependence DR spectra and corresponding fit parameters of pure EG are shown in Figure 5.8 and Table 5.2. This is clearly observed that τ_2 decreases with increasing temperature while dispersion amplitude corresponding to this slow DR time τ_2 remains unchanged. τ_2 is very close to dipole reorientation of EG.[54,65] The theoretical single molecular rotational diffusion time for pure EG is calculated from Stoke-Einstein-Debye (SED) relation as $\tau_r = \frac{6Vfc\eta}{l(l+1)k_BT}$ where symbols l, V, f, c, Kk_B, and T represent the rank ($l = 1$ for DR measurements), van der Waal volume, molecular shape factor, coupling constant, Boltzmann constant and temperature (in Kelvin) respectively. Shape factor of EG molecule was taken 1.01 with prolate geometry [87] and van der Waal volume is determined 60.73 Å^3 [99] at 293K. τ_r values are Calculated from SED given in Table A5.13 (Appendix). This depicts that, τ_r of EG is six times larger than experimental slower DR time (τ_2) time at 298K. Thus, the single molecular rotation estimated from SED model under stick conditions does not provide a suitable

explanation for the origin τ_2. This may indicate that experimental slower DR time, τ_2 is coming from partial molecular dipole rotation of EG molecules.
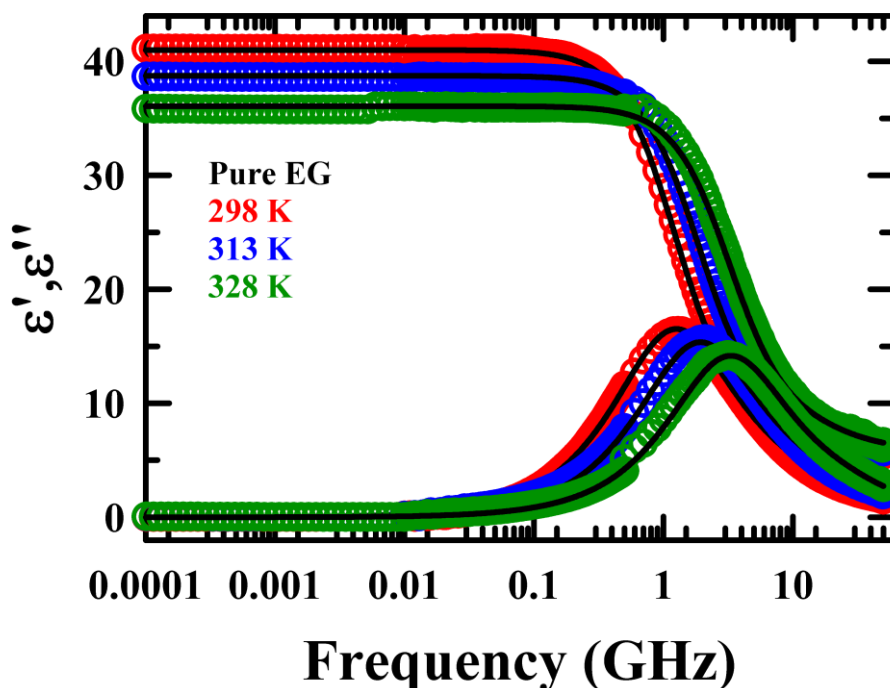
Figure 5.8: Temperature dependent complex DR spectra with real (ε') and imaginary (ε'') component in EG. The line passing through experimental data point express 2-Debye model fits. All representations are colour-coded.

The experiment and computer simulation of linear alkanols have indicated that they generally possess highly H-bonded cooperative clusters.[100–103] Similarly, DR experiment of simple diol have been given more logical explanation, suggesting that, the lower frequency dispersion time τ_2 is related to the cooperative dipole relaxation time of diol clusters.[52,104] In our previous work[65], we demonstrated that the reorientation relaxation (rank l=1) and structural hydrogen relaxations of EG are nearly same (~100 ps). Which is in good agreement with present slower DR time of EG (τ_2 = 120 ps). This confirms that EG possesses an extensive H-bonded clusters[54,104] and that slow DR time, τ_2 registered the dipole relaxation of EG molecules, which are cooperatively H-bonded in EG-EG clusters.[54,65,105,106]

Next, we focused on understanding the origin of relatively faster DR time (τ_4 ~ 17-7 ps) in pure EG, which contributes 6-8 % of the total DR process at temperature ranging 298 K to 328 K. This τ_4 DR time become faster with increasing temperatures. Earlier MD simulations[105,107] have shown that the characteristic H-bond relaxation lifetime in pure EG is approximately 18

ps at 298 K. Additionally, our previous work[65] demonstrated the presence of sub-picosecond features in structural H-bonding relaxation time, further suggesting the existence of faster H-bonding dynamics in pure EG. The faster picosecond H-bonding relaxation lifetime in pure EG closely matches our experimental faster DR time (τ_4). Hence this faster DR time, τ_4 is related to making and breaking of H-bonds through a partial rotation of pure EG.[65] Furthermore, the missing DR dispersion detection, $\varepsilon_\infty - n_D^2 = 5.54 - 2.04 = 3.5$, indicates a presence of ultrafast dynamics which are missing in our present DRS measurements. Note that the present DRS measurements have limitation in detecting ultrafast dynamics, such as the high frequency rotation and vibrational motion of OH group that has been detected in high frequency dielectric studies (in THz region) [52,65,104] in pure EG. Next, we will explore the possible origin of DR time components observed in glucose/EG solution.

5.3.4.3 Glucose wt% Dependence: Appearance of New DR Dispersion

First, we analyse a moderately slow DR time τ_2 in 0 to 40 wt% glucose in glucose/EG cryoprotectant mixtures. This relaxation time τ_2 varies from 130 ps to 868 ps with increasing glucose concentration. This sub-nanosecond DR time with large dispersion amplitude also present in pure EG and corroborates well with several DRS and MD simulation studies.[52,65,104–106] With increasing glucose concentration, τ_2 becomes slower with medum viscosity and it does not follow SED prediction (see Table A5.13 in Appendix). Furthermore, glucose concentration dependent experimental DR time, τ_2, are in well agreement with simulated[65] first rank dipole reorientation time and average structural H-bonding time of EG in these mixtures. This indicates moderately slow DR time, τ_2, originated from the co-operative dipole relaxation in H-bond cluster of EG molecules in these cryoprotectant mixtures.

Next, the fastest DR time ($\tau_4 \sim$ 15-14 ps) and its relaxation amplitude ($\Delta\varepsilon_4$) in these cryoprotectant mixtures are not significantly changing with increasing glucose or temperatures. This type of DR time is also present in DR of pure EG and it is insensitive to medium viscosity. This depicts that, DR time τ_4 arises from intermolecular H-bond lifetime of EG molecules.

A new slow DR time, τ_1 was observed in DRS measurement of 20 to 40 wt% of glucose containing mixtures. τ_1 increases abruptly with glucose concentrations because of the increasing medium viscosity. This indicate that slowest DR time, τ_1, is coming from DR involving glucose molecules. The full rotational diffusion times from SED with stick and slip conditions have been calculated for glucose molecule in these cryo-protectant mixtures and are shown in Table A5.13 (Appendix). These SED predicted times are much larger than DR time

τ_1. Again, our experimental DR time τ_1 correlates well with simulated[65] first rank dipole reorientation time of glucose molecules. The above discussion suggests that DR time, τ_1 is originated from partial rotation of glucose moiety.
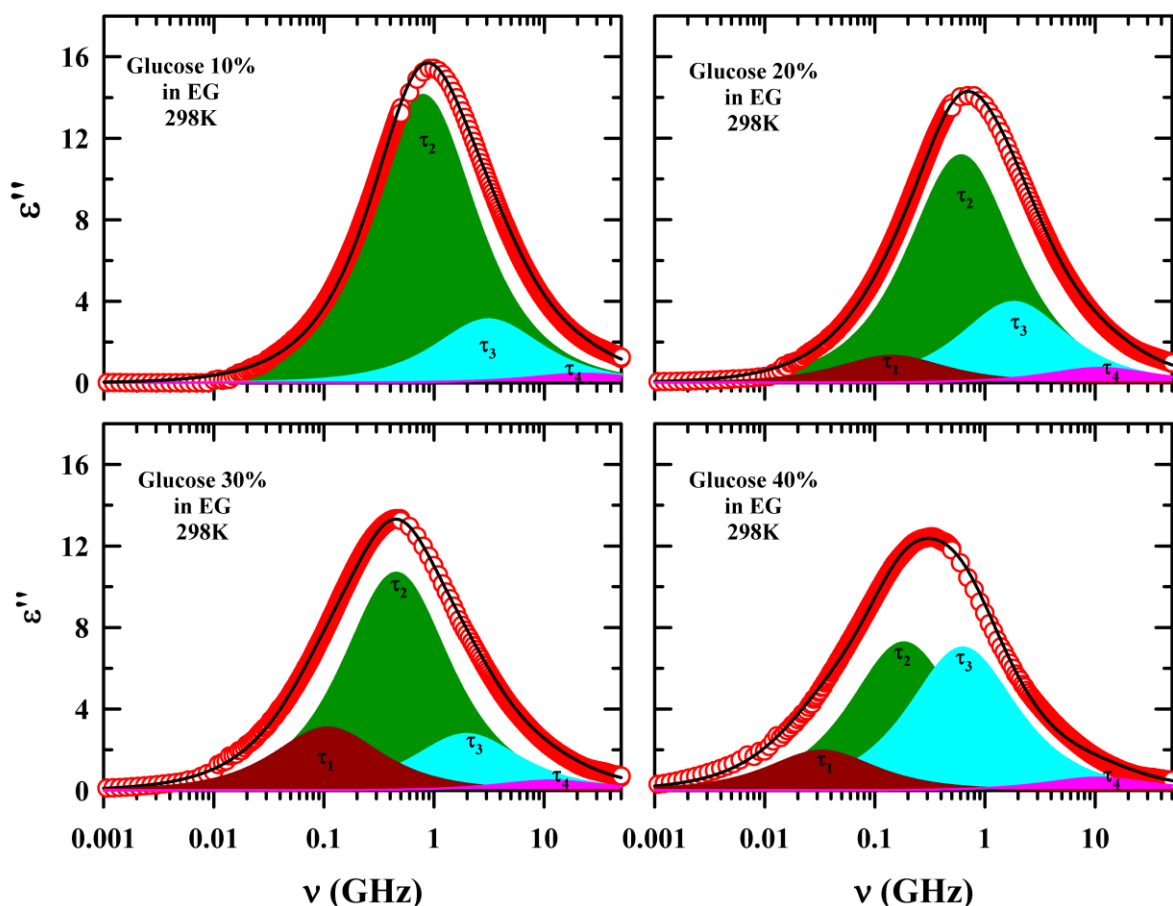
Figure 5.9: Deconvolution of the measured frequency-dependent dielectric loss (ε'') spectra into their individual time component contributions for 10, 20, 30, and 40 wt% glucose in EG at 298K. The red circles represent the experimental data and the solid lines going through them denote the multi-Debye fits (summarized in the Table 5.2). Different time component contributions are color-coded.

Another DR time (τ_3) emerges for DRS measurement of 10 to 40 wt % glucose in EG solutions. This comparatively faster relaxation time τ_3 assumed to be originated from structural H-bond relaxation involving interspecies glucose and EG in these viscous complex systems. Further MD simulation is required to comment on that DR time in this binary solution. The contributions of each of the DR step from the multi-Debye fits for the frequency-dependent DR loss spectra in four glucose/EG systems and in pure EG are shown in Figure 5.9 and Figure A5.14 respectively.
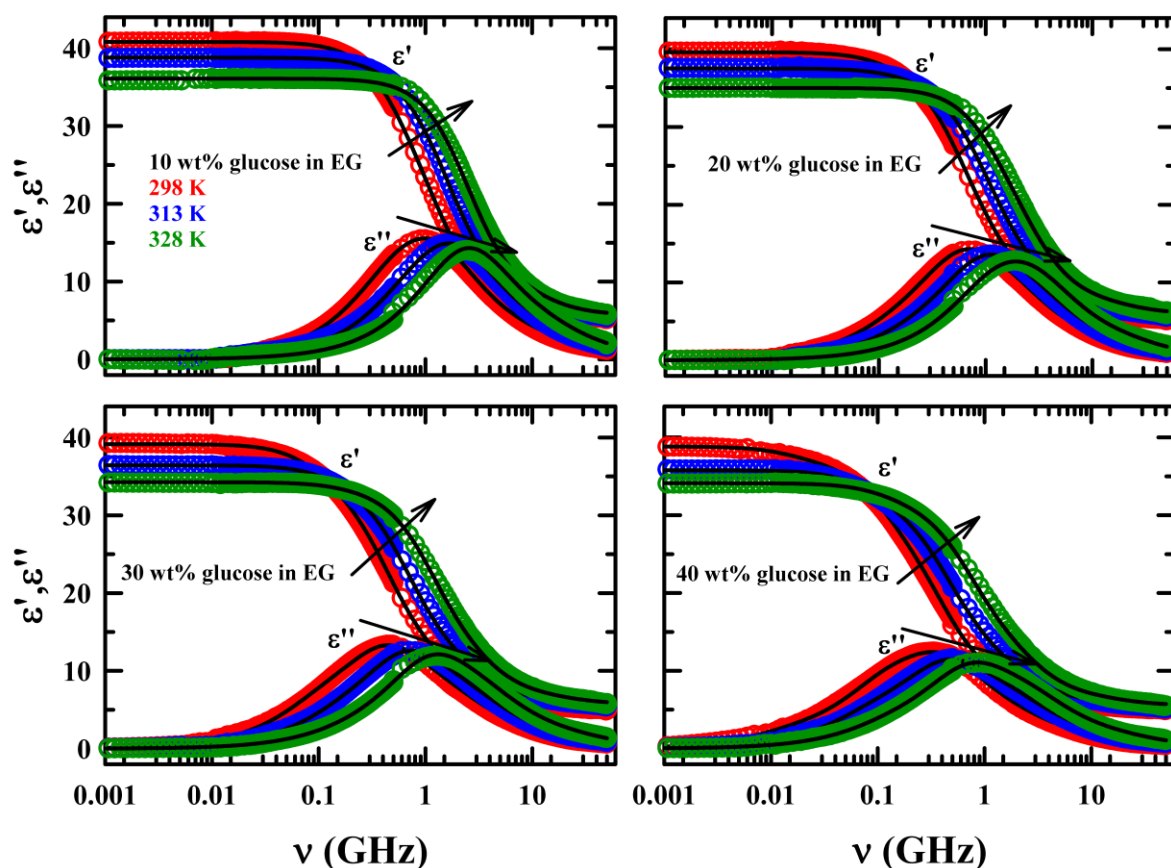
Figure 5.10: Temperature dependent complex DR spectra with real (ε') and imaginary (ε'') component in glucose/EG binary mixtures at various wt% of glucose. The line passing through experimental data point express multi-Debye model fits. All vignettes are colour-coded.

The Cole–Cole representations from fitted DR spectra are shown in Figure A5.15 (in Appendix). This depicts that impact of addition glucose on the frequency-dependent DR of glucose/EG cryoprotectant mixtures at two representative temperatures at 298 K and 328 K. Generally, a semicircle ("Debye semicircle") along with a radius[81], $(\varepsilon_s - \varepsilon_\infty)/2$ for a simple dipolar liquid system having single Debye relaxation time, have presented in Cole-Cole plot. A comparison between the experimental and the calculated Cole–Cole plots and normalised Cole–Cole plots, also presented in Figure A5.15 (in Appendix), reveals that the experimental DR spectra for all systems away from the calculated Debye semicircles. This confirmed the presence of inherent multi-Debye relaxation processes in these systems. The normalised Cole–Cole plot of these glucose/EG systems reveals that asymmetry of experimental DR spectra increases with increasing glucose concentrations. This reflects glucose induces inhomogeneity on dipole distribution with glucose concentrations in these glucose/EG systems. As we move temperature 298 K to 328 K, impact of glucose on inhomogeneous trend in DR distribution

seems to be the same but all experimental DR spectra are closer to calculated spectra. That suggest that heterogeneity each of the system laser than that from their lower temperature system.

5.3.4.4 Temperature Dependence DRS of Glucose/EG Mixtures

Temperature dependent complex dielectric spectra of various glucose containing glucose/EG mixtures are presented in Figure 5.10. This depicts that with increasing temperature, DR dynamics of all possible DR dispersion time components accelerate in all glucose/EG solutions. This can be attributed to temperature induced reduction in medium viscosity.

The average DR times ($\langle \tau_{DR} \rangle$) in glucose/EG mixtures are given in Table 5.2. This reveals that $\langle \tau_{DR} \rangle$ becomes faster with increasing temperature due to the decrease in medium viscosity. Again, viscosity of cryoprotectant mixtures gradually increases with increasing solute concentration. That is why $\langle \tau_{DR} \rangle$ was drastically slowed down with addition of glucose at fixed temperature. As a result, $\langle \tau_{DR} \rangle$ significantly slows down with increasing glucose concentration. However, when we are going to 30% to 40 wt% glucose containing mixture, DR time becomes abruptly slowed down, indicating that this mixture may undergo a transition into a macromolecular structure. Existence of such macromolecular structure in 40 wt% glucose containing mixture is also confirmed by the appearance of a large clusters (8-10 nm) in DLS measurement. With increasing temperature, micromolecular structure has been broken into small ones and $\langle \tau_{DR} \rangle$ rapidly decreases. The appearance of such large nanosecond time in DR process, attributed to the three-dimensional H-boding macromolecular structure of solute-solvent in cryoprotectant mixture, and its temperature dependency certified that the glucose/EG cryoprotectant mixtures is a promising candidate for cryopreservation of biomolecules. It allows for the modification of glass forming characteristics or fragility by varying the composition of the mixture components.

In the upper left panel of Figure 5.11, we compare the SED stick rotation time with experimental $\langle \tau_{DR} \rangle$ data. SED stick rotation time is calculated using the relation $\tau_{r(stick)} = \frac{3Vfc\eta}{K_BT}$ where V and f represent the van der Wall volume and shape factor of glucose and EG molecules respectively with $V = 60.73$ Å^3, $f = 1.01$(prolate geometry) for EG molecule and $V = 152$ Å^3, $f = 1.03$(oblate geometry) for glucose molecule and $c = 1$.[87,99] The experimental $\langle \tau_{DR} \rangle$ values in these systems are lower than the stick SED prediction at all experimental temperature. Furthermore, to investigate the coupling between the $\langle \tau_{DR} \rangle$ and temperature-reduced viscosity

variation, we used the relation $\tau \propto \left(\frac{\eta}{T}\right)^p$ where $p = 1$ indicates a viscosity coupled relaxation process (see upper left panel of Figure 5.11). p values in the present study varies from 0.84 to 0.69, from pure EG to the highest glucose containing binary cryoprotectant mixture. The deviation of p from unity implies that the relaxation process is not fully controlled by medium viscosity. This deviation is indicative of temporal heterogeneity in these systems. Increment of heterogeneity with glucose concentrations observed in DRS experiment of glucose/EG cryoprotectant mixtures also well corroborates with the excitation wavelength dependent fluorescence measurement of C343. DMSBT and C153 does not show any solution heterogeneity except 40 wt% glucose mixture. The above discussion suggests that size and relaxation time of probes involved in two different measurement processes may explain this type of observation.[93,95,96] The solution viscosity as well as cluster size increases (see viscosity data and DLS measurement) with glucose concentration this leads to the abruptly slowing down the DR relaxation in these systems. DR process collectively observed is an average over different dynamics. Finally, we are taking a global fit including all temperature and glucose concentration dependent data points and p value was estimated ~0.73. This fractional dependency of average DR time indicates the presence of temporal heterogeneity in these studied systems, as observed in DES[96,108], binary mixture[109], and other time resolved fluorescence study[110], micelle in water[111], cryoprotectant mixture[44]. Partial viscosity decoupling of molecular motion leading to temporal heterogeneity is a common phenomenon in supercooled liquids.[92–94,112,113]

Figure 5.11 (lower left panel) shows that temperature dependence $\langle \tau_{DR} \rangle$ in pure EG as well as glucose/EG mixtures follows an Arrhenius-type equation at temperature between 298 K to 328 K. Therefore, glucose concentration dependent activation energies, E_{DR} related to DR in pure EG and glucose/EG cryoprotectant mixtures were estimated from DRS measurements. The estimated activation energies (both for DR (E_{DR}) and viscous flow (E_η)) in these systems gradually increase with glucose concentration as shown in Figure 5.11 (lower right panel). Also, E_η is larger than E_{DR} at various glucose concentrations. The difference between E_η and E_{DR} increases from 20 wt% to 40 wt% glucose containing systems. This is also reflected in Figure 5.11 (inset of lower right panel), where glucose dependent coupling parameter (p) gradually decreases from 20 wt% to 40 wt% glucose systems. The above discussion suggests that temporal heterogeneity is inherent to these higher glucose containing systems. In the highest glucose concentration (40 wt%), the abrupt increase in E_{DR} indicates a different

solution structure compared to low glucose containing systems. The observation of macromolecular-type relaxation in the highest glucose concentration indicates the largest possibility of solute-solute interaction in addition to the previously observed solvent-solvent and solute-solvent interactions in lower concentration binary cryoprotectant mixtures.
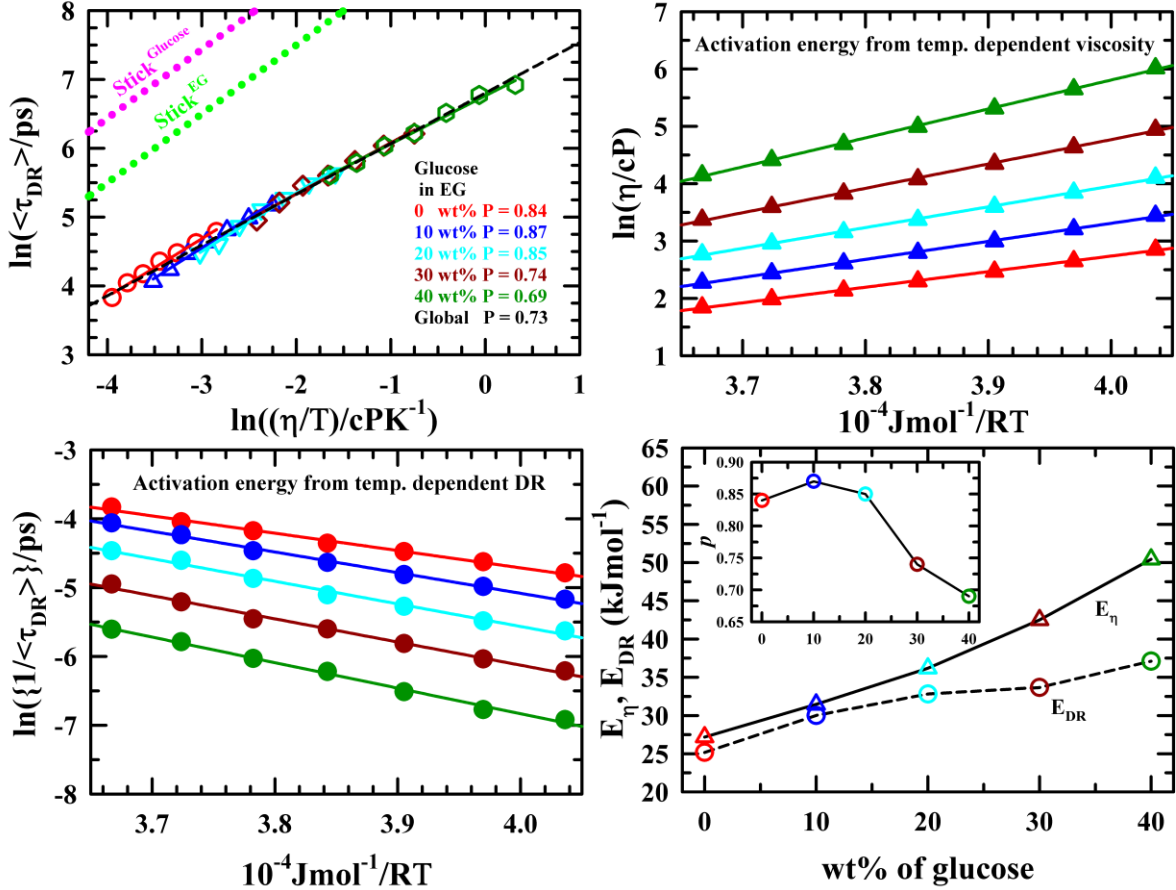
Figure 5.11: Representative temperature reduced viscosity ($\frac{\eta}{T}$) versus average DR relaxation times ($\langle\tau_{DR}\rangle$) in glucose/EG binary mixture (upper left panel). The SED predictions with stick boundary condition for EG and glucose molecules using the experimental temperature dependent solution viscosity coefficients (η) are also shown in these panels for comparison. Arrhenius temperature dependent plot of η (upper right panel), and $1/\langle\tau_{DR}\rangle$(lower left panel) for glucose/EG mixtures. Glucose concentrations dependent estimated activation energies from viscosity and DR rate in glucose/EG mixtures (lower right panel). The inset of lower right panel shows evolution of decoupling parameter (p) as a function of glucose concentration obtained from the fitting of $\frac{\eta}{T}$ versus $\langle\tau_{DR}\rangle$ data sets using the equation: $\ln\langle\tau_{DR}\rangle = A + p\ln\left(\frac{\eta}{T}\right)$. The lines joining the activation energy data and p value, are guides to the eyes. all vignettes are colour-coded.

5.4 Conclusion

In summary a series of experiments including DSC, DLS, steady-state fluorescence emission, and DRS experiments were conducted to investigate the phase transition phenomena, solution structure, interaction, dynamics and heterogeneity of Glucose/EG cryoprotectant mixture. The DSC measurements, varying glucose concentration in glucose/EG cryoprotectant mixture, exhibited suppression of solvent crystallization and elevation of glass transition temperature with higher glucose content. DLS analysis revealed the presence of micro-cluster in the 40 wt% glucose containing composite, with cluster size of approximately $D_h \sim$ 9-10 nm. The cluster size is also found to be dependent on temperature. Steady-state fluorescence emission experiments using different excitation wavelengths indicated strong spatial heterogeneity within the glucose/EG mixture. Additionally, analysis of fluorescence emission from probes C153, C343 and DMASBT suggested the presence of both slower and faster relaxation processes in 40 wt% glucose system. The DRS experiments, conducted in a wide frequency window 20 Hz - 50 GHz) and narrow temperature range (298 ≤ T/K ≤ 328) required a multi-Debye model to fit the measured DR spectra, indicating complex relaxation dynamics. The decrease in static dielectric constant with increasing glucose concentration was attributed to H-bond breaking among EG molecules. Neat EG exhibited two distinct DR times, attributed to cooperative dipole relaxations and H-bonding relaxations among -OH groups. With addition of glucose, intermediate DR time appeared. This DR time possibly originated from inter-molecular H-bonding interactions between glucose and EG molecules. A relatively slower DR time than other three DR times was observed from 20 to 40 wt% glucose containing systems. This slowest DR may have come from glucose molecules forming micromolecular structure which agrees well with DLS measurements. The Cole–Cole plots of DR data showed gradual deviation from the single Debye relaxation curve with increasing glucose concentrations, indicating enhanced dynamic heterogeneity. The decoupling of DR with solution viscosity with increasing glucose concentration suggested an increase in dynamic heterogeneity of glucose/EG cryoprotectant mixtures. Dynamic heterogeneity of these systems further confirmed by activation energy comparison between viscous flow and DR process. Overall, the combined analysis of steady state fluorescence and DRS measurements provided insight into the spatio-temporal heterogeneity of these systems. However, further studies are needed to gain a deeper molecular level understanding of cryopreservation technology using this cryoprotectant composite.

Appendix A5
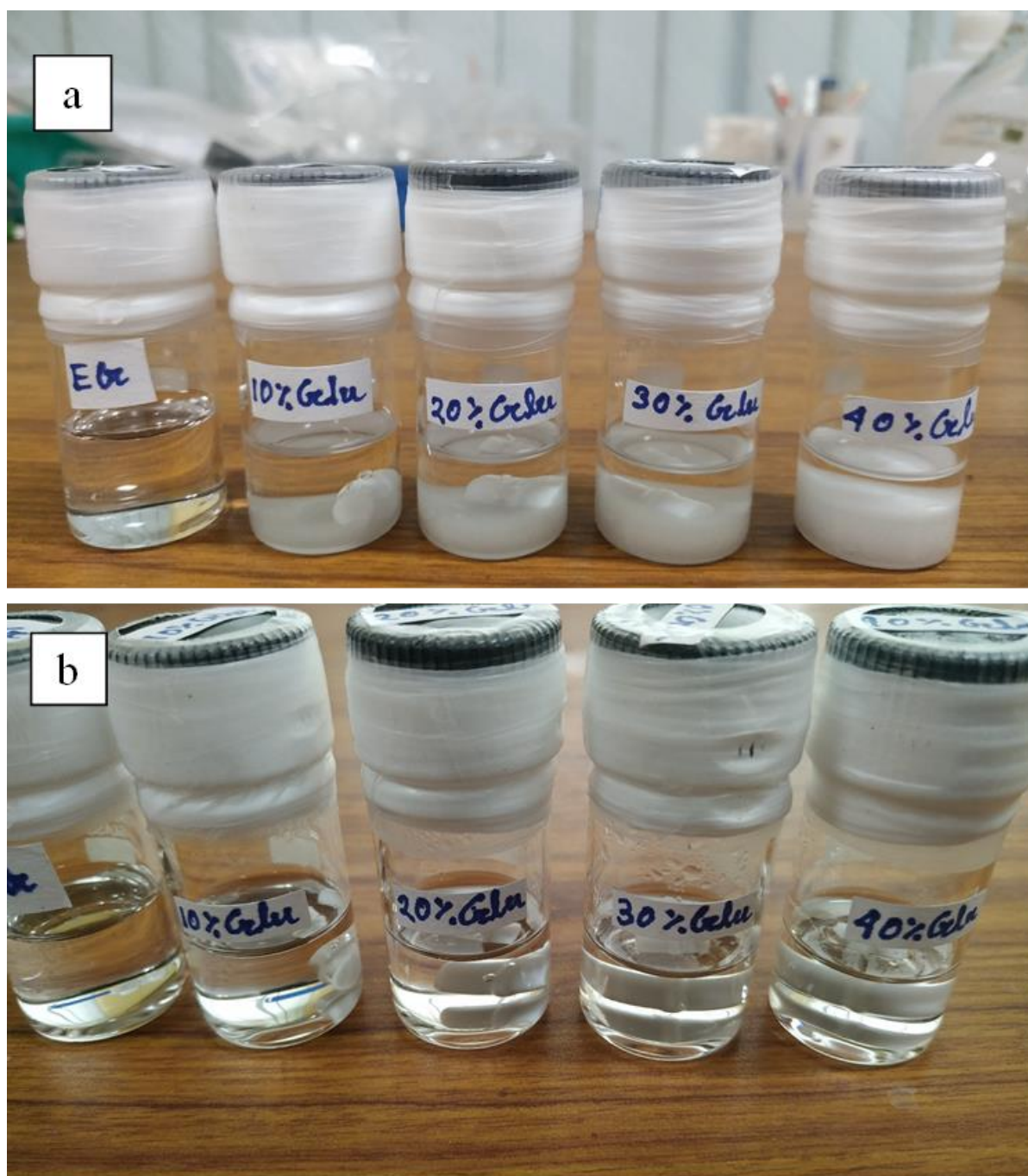
Scheme A5.1: Photo graphs of glucose/EG cryoprotectant composite (a) before and (b) after sample preparation.

Table A5.2: Temperature dependent refractive indices (n_D), densities (ρ), and viscosity coefficient (η) of pure EG and glucose/EG binary cryoprotectant mixtures.

Temperature (T/K)	Pure EG	10 wt% glucose	20 wt% glucose	30 wt % glucose	40 wt% glucose
Refractive index (n_D)[a]					
298	1.429	1.437	1.446	1.455	1.465
303	1.427	1.436	1.445	1.453	1.465
308	1.427	1.436	1.444	1.452	1.464
313	1.426	1.435	1.443	1.451	1.464
318	1.425	1.435	1.443	1.451	1.463
323	1.425	1.434	1.443	1.451	1.463
328	1.425	1.433	1.443	1.450	1.463
Density (ρ/gcm^{-3})[a]					
293	1.113	1.146	1.180	1.216	1.255
298	1.110	1.142	1.177	1.213	1.252
303	1.106	1.139	1.174	1.209	1.249
308	1.102	1.135	1.170	1.206	1.246
313	1.099	1.133	1.167	1.203	1.242
318	1.095	1.128	1.163	1.199	1.239
323	1.092	1.125	1.160	1.196	1.236
328	1.088	1.121	1.156	1.192	1.232
Viscosity (η/cP)[b]					
293	19.29	38.78	79.81	210.91	641.10
298	17.32	31.29	60.90	140.64	409.40
303	14.19	24.77	46.85	103.40	284.30
308	11.82	20.03	36.66	77.54	203.60
313	9.98	16.43	29.16	59.25	147.70
318	8.50	13.68	23.56	46.14	109.60
323	7.31	11.49	19.29	36.51	82.80
328	6.33	9.76	16.01	29.24	63.46

[a]Refractive index and density values can be reproduced within ± 5 % of the reported values.

[b]Viscosity coefficient values can be reproduced within range ± 5-12 % of the reported values.
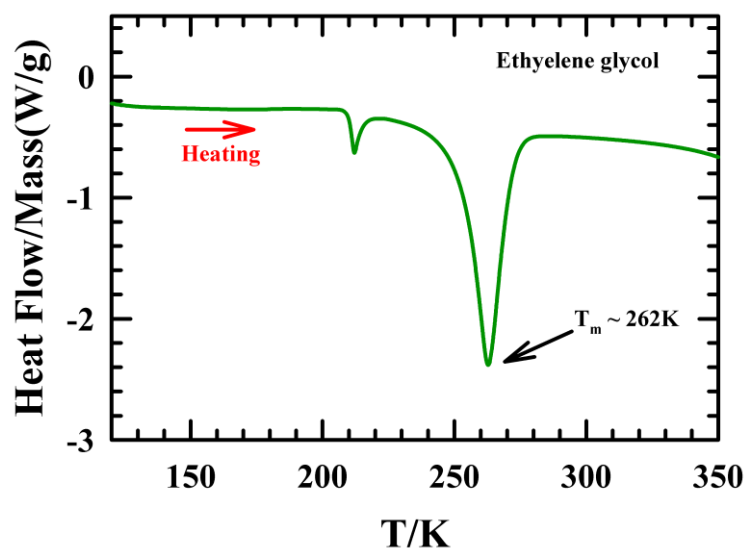
Figure A5.3: Representative DSC thermogram of pure EG.
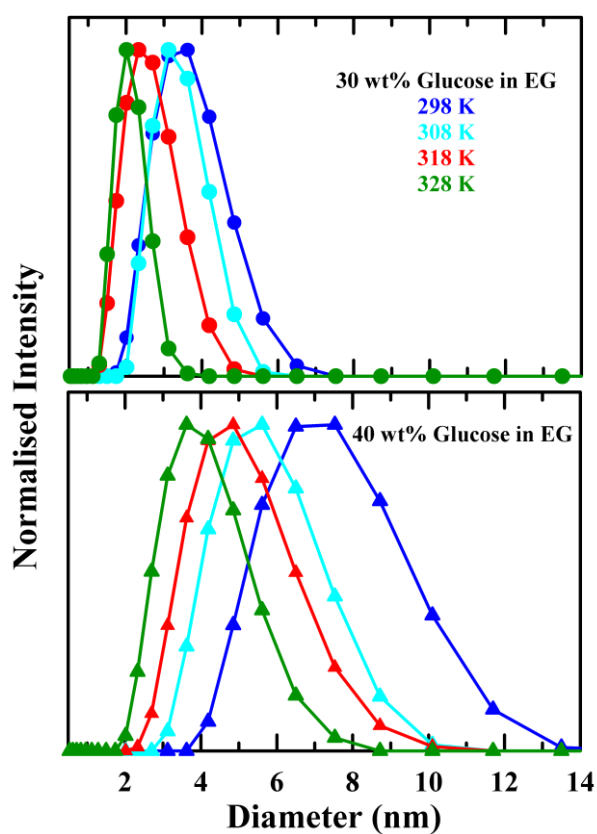
Figure A5.4: Temperature dependent normalised intensity and cluster diameter for 30 wt% (upper panel) and 40 wt% (lower panel) glucose in glucose/EG binary mixtures. All representations are colour-coded.
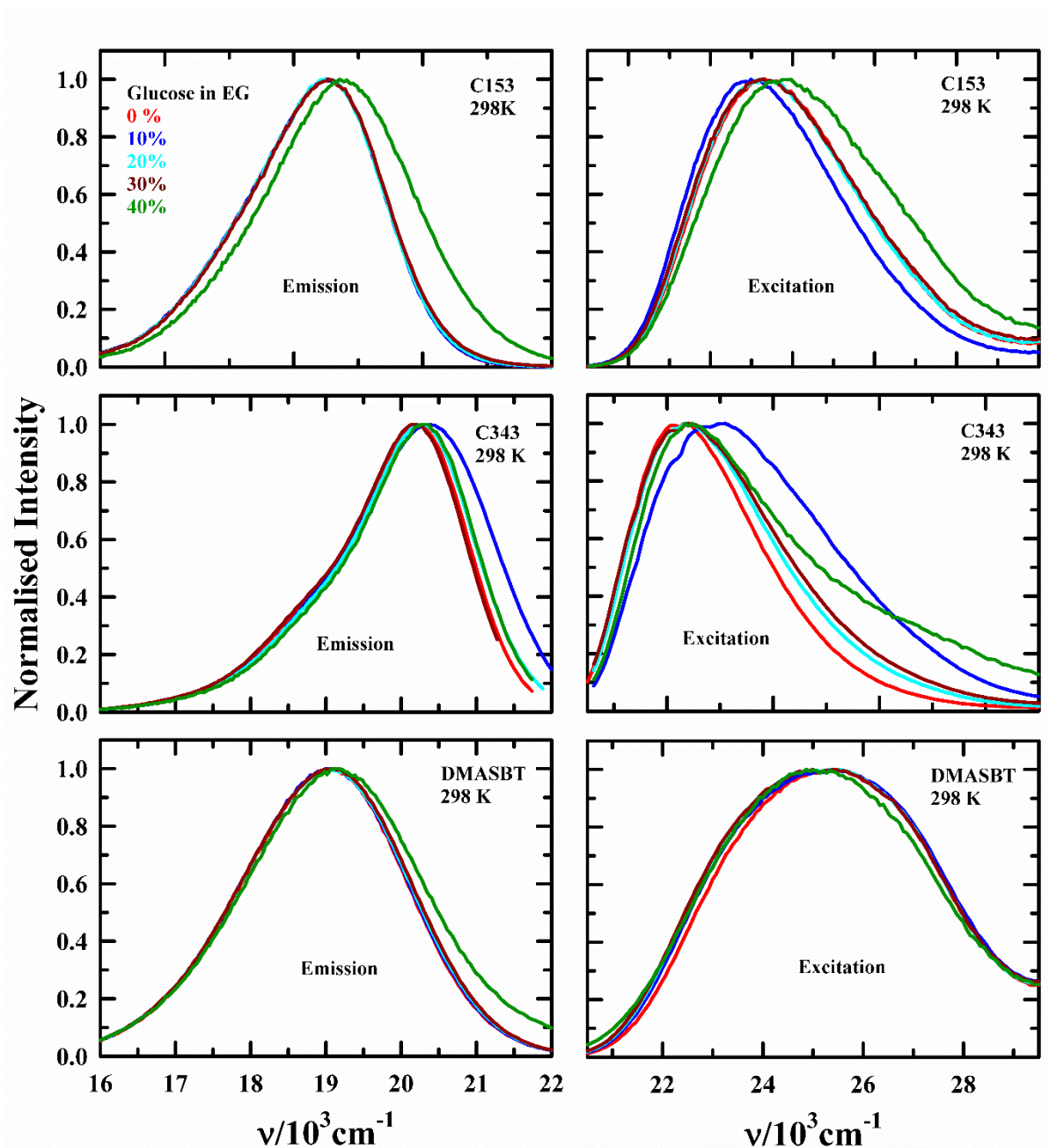
Figure A5.5: Steady-state excitation (right panel) and emission (left panel) spectra of C153 (upper panel), C343 (middle panel), DMASBT (lower panel) in various wt% of glucose in glucose/EG binary cryoprotectant mixtures and in pure EG at 298K. All representations are colour-coded.
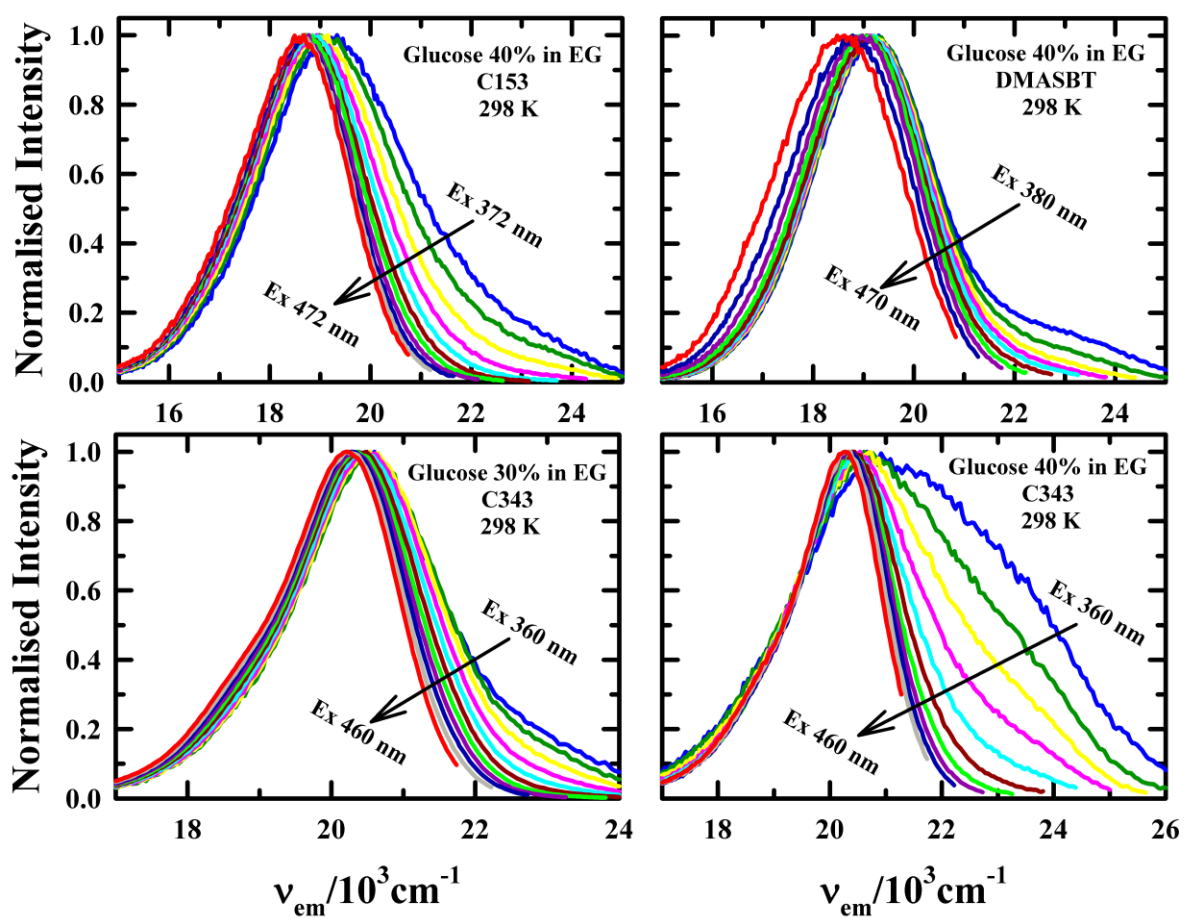
Figure A5.6: Excitation wavelength dependent (λ_{exc}) steady state fluorescence emission spectra of C153 (upper left panel), DMASBT (upper right panel), C343 (lower right panel) in 40 wt% glucose and C343 (lower left panel) in 30 wt% glucose in glucose/EG binary cryoprotectant mixture at 298K. All representations are colour-coded.
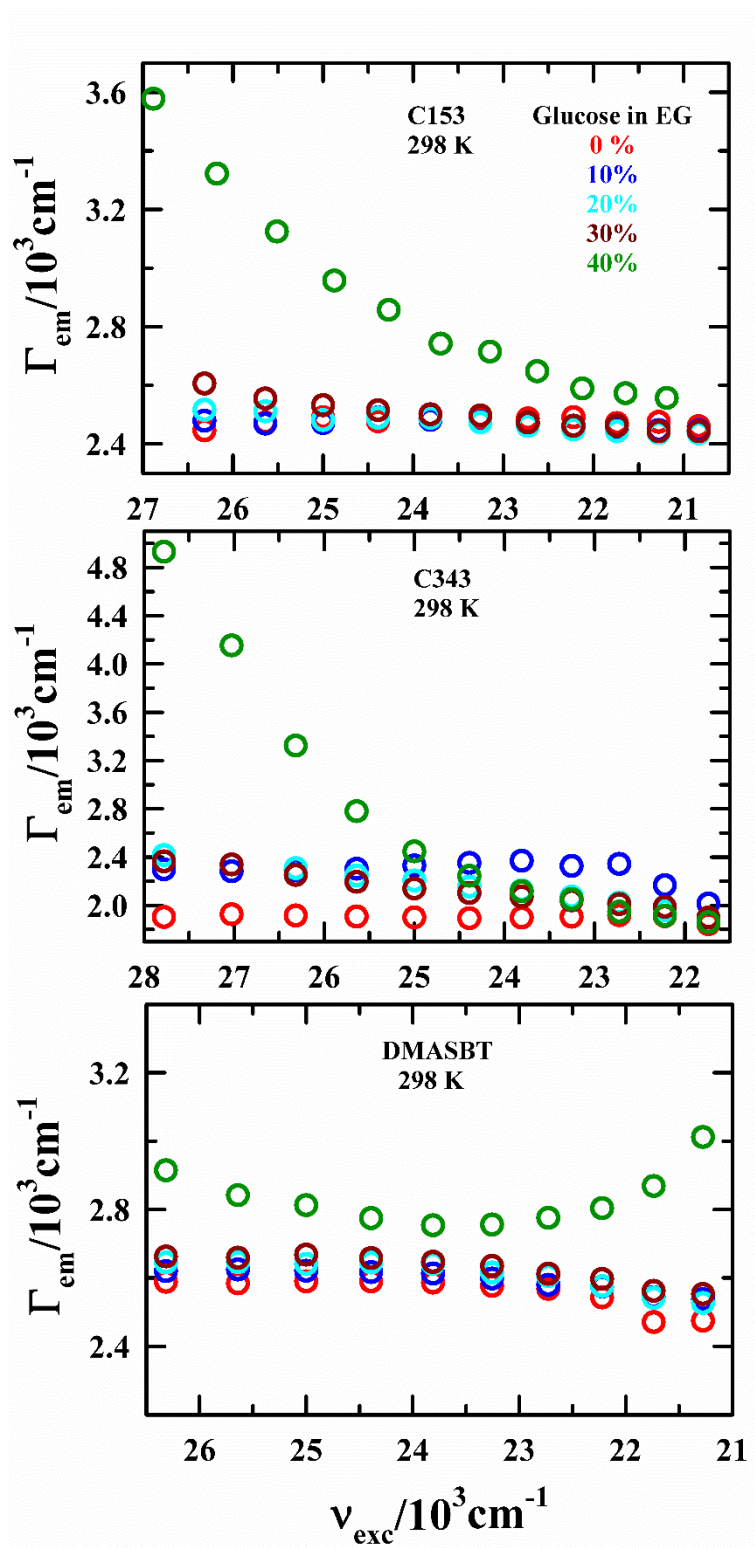
Figure A5.7: Excitation frequency dependent (ν_{exc}) steady state fluorescence emission spectral width (FWHM), Γ_{em} of C153 (upper panel), C343 (middle panel), and DMASBT (lower panel) at various wt% of glucose in glucose/EG binary cryoprotectant mixtures and in pure EG at 298K. All vignettes are colour-coded.
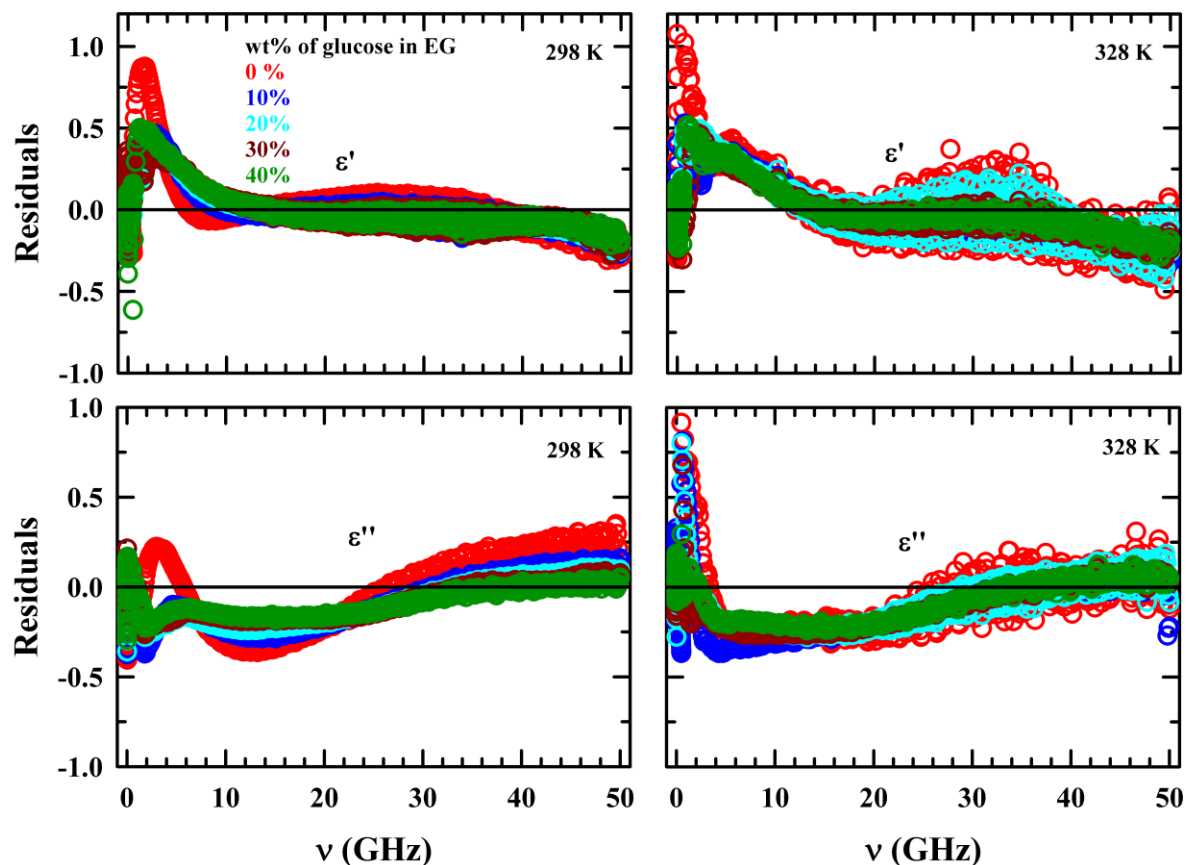
Figure A5.8: Residuals for real (ε') and imaginary (ε'') component fittings of complex DR spectra for various wt% of glucose in glucose/EG mixtures at 298 K and 328 K. The solid line represents zero base line. All presentations are colour-coded.

Table A5.9: Temperature dependent static dielectric constant (ε_s) for various wt% Glucose in EG.[c]

T/K	0 wt%	10 wt%	20 wt%	30 wt%	40 wt%
298	40.99	40.81	39.60	39.15	38.83
303	40.45	39.96	39.35	38.68	38.32
308	39.53	39.40	37.98	37.57	37.07
313	38.73	38.79	37.51	36.43	35.79
318	38.08	37.98	36.58	35.70	35.56
323	37.43	36.88	35.76	34.42	34.30
328	36.07	36.09	35.0	34.26	34.11

[c]Static dielectric constant values can be reproduced within ± 2 % of the reported values
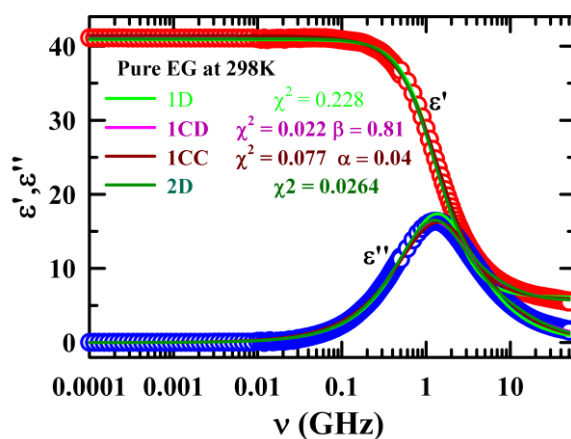
Figure A5.10: Real (ε') and imaginary (ε'') component of complex DR spectra for EG at 298K. The lines passing through experimental data points express different of fitting models, Debye (1D), Cole-Cole (1CC), Cole-Davidson (1CD) and Two Debye (2D). All vignettes are colour-coded.
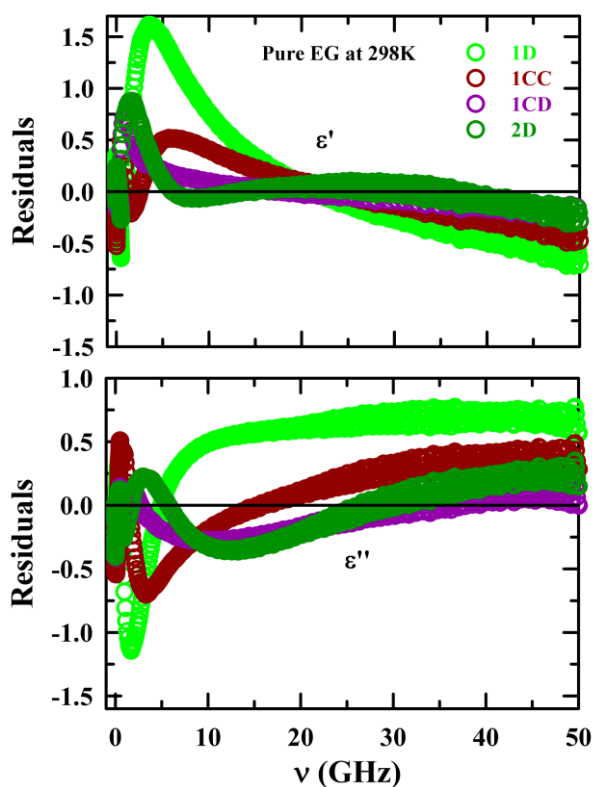
Figure A5.11: Residuals for real (ε') and imaginary (ε'') component fittings of complex DR spectra for EG at 298K. The data point represents here express different types of model fits like Debye (1D), Cole-Cole (1CC), Cole-Davidson (1CD) and two Debye (2D) which are colour-coded.

Table A5.12: Literature survey and present work: DRS studies of pure EG.

T/K	DRS frequency range	equation	ε_s	ε_2	τ_2/ps	ε_4	τ_4/ps	ε_5	τ_5/ps	ε_∞	Ref.
298	4KHz-50GHz	D+D	40.99	40.99	130	8.77	17	-	-	5.61	
300	4KHz-50GHz	D+D	40.45	40.45	109	7.69	13	-	-	5.62	
298	4KHz-50GHz	CD (0.81)	41.04	41.04	147	-	-	-	-	5.24	
298	150MHz-89GHz	D+D+D	40.58	40.23	118	6.94	14.3	4.74	1.82	3.54	ref[52]
303	300MH-34.8GHz	D+D	40.5	40.5	100	7.8	12	-	-	4.1	ref[50]
303	10MHz-20GHz	D	42.42	42.42	101	-	-	-	-		ref[56]
298	10MHz-10GHz	CC (0.14)	40.89	40.89	105	-	-	-	-	4.16	ref[51]
298	10MHz-20GHz	CC (0.09)	41.2	41.2	92.4	-	-	-	-	4.9	ref[49]
298	10MHz-25GHz		40.0	40.0	105.3					3.66	ref[55]

Table A5.13: Temperature dependent calculated translational diffusion time from Stokes-Einstein relation and rotational diffusion time from Stokes-Einstein-Debye relation[114] in glucose/EG cryoprotectant mixture.

Stokes-Einstein equation of translational diffusion for spherical particle: $D_{trans} = k_B T / C\pi\eta\sigma$ where k_B, T, C, η and σ are denoted Boltzmann constant, temperature, coupling constant for slip (2) and stick (3) condition, viscosity and diameter of species respectively. Relation between D_{trans} and translational diffusion time τ_{trans} is $\tau_{trans} = \sigma^2 / D_{trans} = \sigma^3 C\pi\eta / k_B T$, $\sigma_{EG} = 4.876$ Å, $\sigma_{Glucose} = 6.63$ Å,[87,114]

Stokes-Einstein-Debye equation for rotational diffusion time τ_{rot} with volume V, coupling constant C and molecular shape factor f is $\tau_{rot} = 3V\eta f C / k_B T$. At stick limiting condition $C = 1$, shape factor $f = 1.01$ for EG (prolate) and $f = 1.03$ for glucose (oblate), and $V =$ molecular volume= 60.73 Å³ (EG) and 152 Å³ (glucose).[87,99,114]

T/K	η/cP	Species	τ_{trans}/ns (stick)	τ_{trans}/ns (slip)	τ_{rot}/ns stick
			Pure EG		
298	17.32	EG	4.599	3.066	0.747
303	14.19	EG	3.706	2.471	0.581
308	11.82	EG	3.037	2.025	0.481
313	9.98	EG	2.523	1.682	0.390
318	8.49	EG	2.114	1.409	0.326
323	7.31	EG	1.790	1.193	0.267
328	6.32	EG	1.526	1.017	0.223
			10 wt% glucose in EG		
298	31.29	EG	8.309	5.539	1.400
		Glucose	20.888	13.925	3.574
303	24.77	EG	6.469	4.313	1.090
		Glucose	16.263	10.842	2.782
308	20.03	EG	5.146	3.431	0.867
		Glucose	12.937	8.625	2.213
313	16.43	EG	4.154	2.769	0.699
		Glucose	10.442	6.961	1.786
318	13.68	EG	3.404	2.269	0.574
		Glucose	8.558	5.705	1.464
323	11.49	EG	2.815	1.877	0.474
		Glucose	7.076	4.717	1.211
328	9.76	EG	2.355	1.569	0.397
		Glucose	5.919	3.946	1.013
			20 wt% glucose in EG		
298	60.9	EG	16.172008	10.781338	2.725008
		Glucose	40.654950	27.103300	6.955430
303	46.85	EG	12.235730	8.157153	2.061739

		Glucose	30.759507	20.506338	5.262474
308	36.66	EG	9.418997	6.279331	1.587116
		Glucose	23.678498	15.785665	4.051023
313	29.16	EG	7.372352	4.914902	1.242253
		Glucose	18.533421	12.355614	3.170780
318	23.56	EG	5.862881	3.908587	0.987905
		Glucose	14.738747	9.825831	2.521571
323	19.29	EG	4.725988	3.150659	0.796336
		Glucose	11.880702	7.920468	2.032604
328	16.01	EG	3.862606	2.575071	0.650855
		Glucose	9.710238	6.473492	1.661271
30 wt% glucose in EG					
298	140.6	EG	37.336359	24.890906	6.291235
		Glucose	93.860196	62.573464	16.058022
303	103.4	EG	27.004791	18.003194	4.550349
		Glucose	67.887578	45.258385	11.614510
308	77.54	EG	19.922232	13.281488	3.356927
		Glucose	50.082671	33.388447	8.568367
313	59.25	EG	14.979831	9.986554	2.524125
		Glucose	37.657928	25.105285	6.442686
318	46.14	EG	11.481890	7.654593	1.934716
		Glucose	28.864422	19.242948	4.938254
323	36.51	EG	8.944833	5.963222	1.507218
		Glucose	22.486492	14.990995	3.847090
328	29.24	EG	7.054503	4.703002	1.188695
		Glucose	17.734377	11.822918	3.034076
40 wt% glucose in EG					
298	409.4	EG	108.716254	72.477503	18.318858
		Glucose	273.302734	182.201823	46.757852
303	284.3	EG	74.250116	49.500078	12.511260
		Glucose	186.658011	124.438674	31.934286
308	203.6	EG	52.310632	34.873754	8.814423
		Glucose	131.504150	87.669433	22.498317
313	147.7	EG	37.342128	24.894752	6.292207
		Glucose	93.874699	62.583133	16.060503
318	109.6	EG	27.273843	18.182562	4.595685
		Glucose	68.563951	45.709301	11.730227
323	82.8	EG	20.285734	13.523823	3.418178
		Glucose	50.996482	33.997655	8.724706
328	63.46	EG	15.310491	10.206994	2.579842
		Glucose	38.489177	25.659451	6.584900
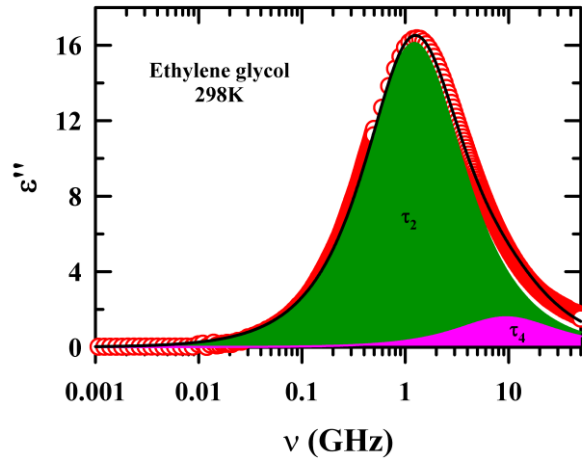
Figure A5.14: Deconvolution of the measured frequency-dependent dielectric loss (ε'') spectra into their individual time component contributions for 10, 20, 30, and 40 wt% glucose in EG at 298K. The red circles represent the experimental data and the solid lines going through them denote the multi-Debye fits (summarized in the Table 6.2). Different time component contributions are color-coded.
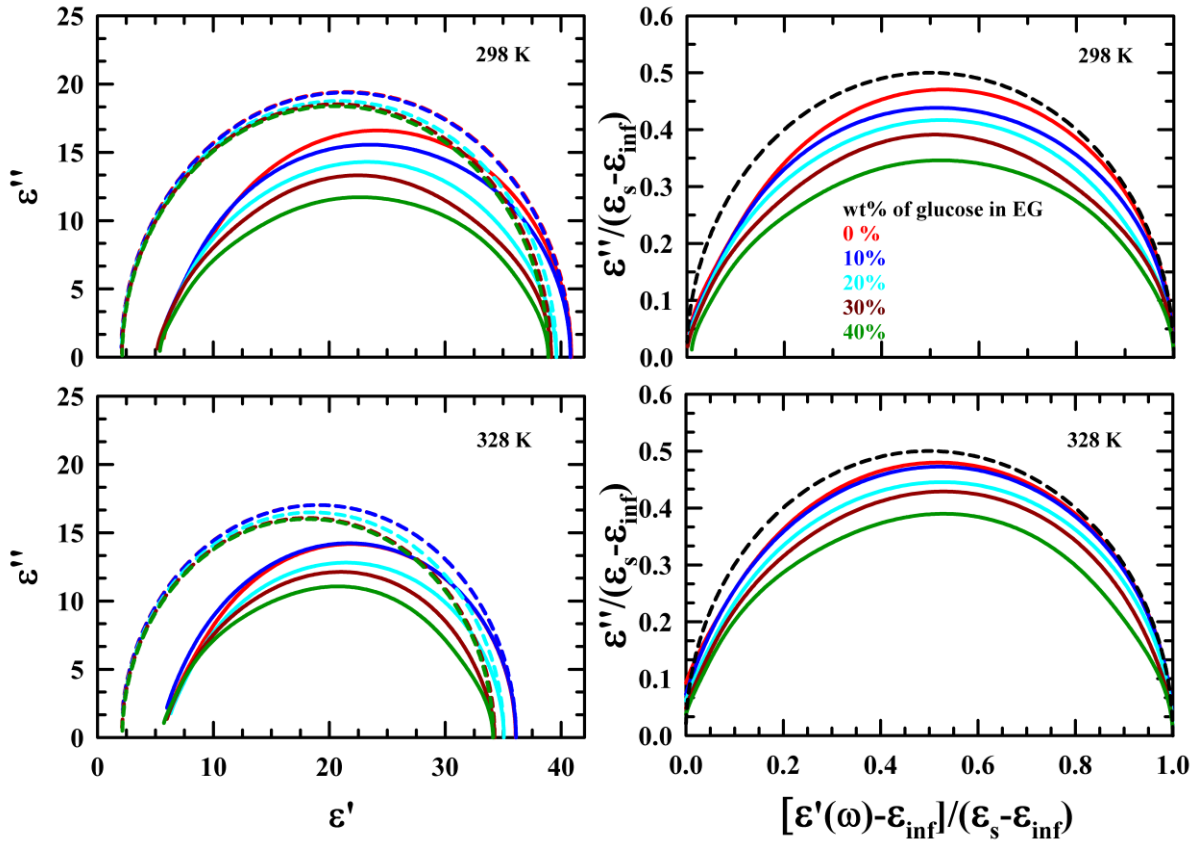
Figure A5.15: Cole-Cole plots (left panels) and normalised Cole-Cole plots (right panels) comparing form fitted DR of glucose concentration dependent (wt% = 0, 10, 20, 30, 40)

glucose/EG systems for two different temperatures, along with their Debye semicircles (left panels). Solid line represents the experimental data points. Dashed lines represent the Debye semicircles (formed via Cole-Cole plots) for hypothetical dipolar systems relaxing via a single Debye process with time constant equal to the measured average DR time, $\langle \tau_{DR} \rangle$, responsible for dispersion from the measured ε_s to the measured ε_∞. These Debye semicircles for hypothetical dipolar liquids were constructed by using the following relation: $\varepsilon'(\omega) = \varepsilon_\infty + \frac{\varepsilon_s - \varepsilon_\infty}{1 + \omega^2(\langle\tau_{DR}\rangle)^2}$ and $\varepsilon''(\omega) = \frac{(\varepsilon_s - \varepsilon_\infty)\omega\langle\tau_{DR}\rangle}{1 + \omega^2(\langle\tau_{DR}\rangle)^2}$. Normalization of X and Y axis in Cole-Cole plots left panels are performed as follows: $\frac{\varepsilon'(\omega) - \varepsilon_\infty}{\varepsilon_s - \varepsilon_\infty}$ and $\frac{\varepsilon''(\omega)}{\varepsilon_s - \varepsilon_\infty}$, respectively. All representations are color-coded.
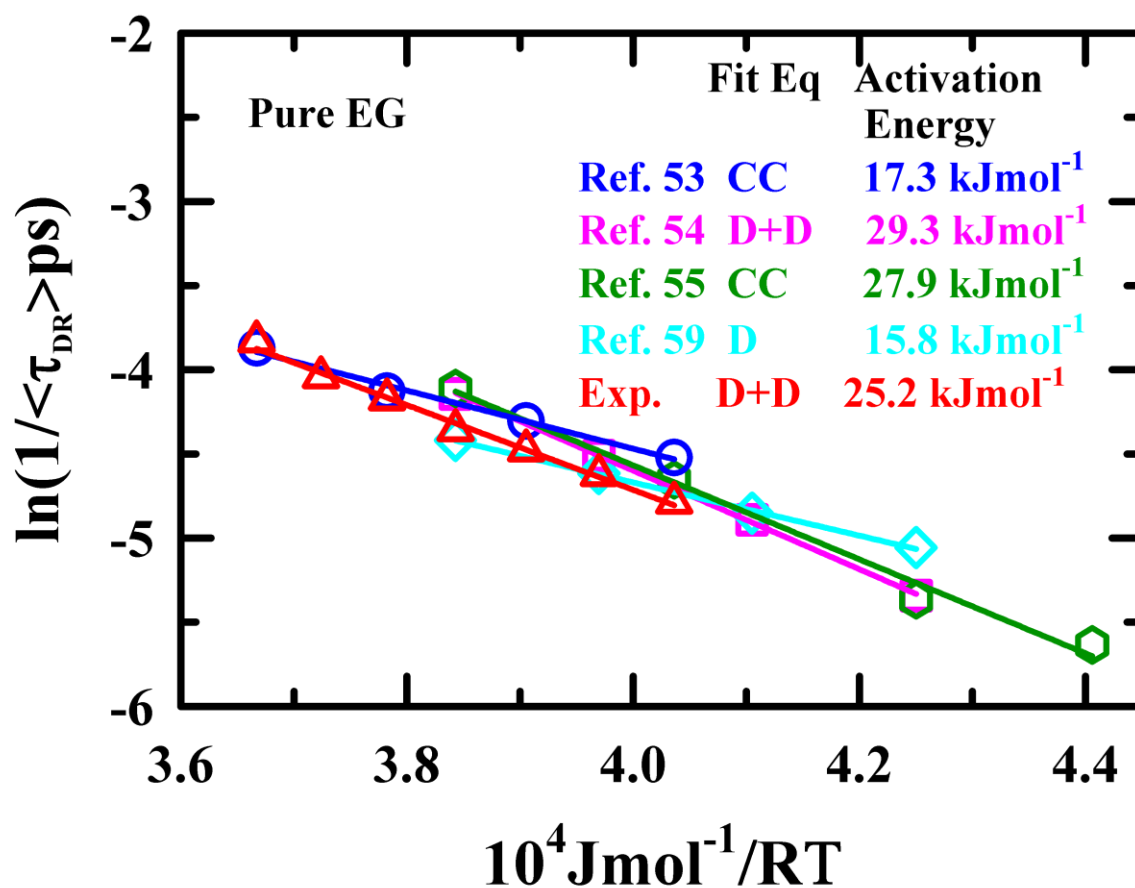
Figure A5.16: Temperature dependent Arrhenius plot of average dielectric relaxation time ($\langle \tau_{DR} \rangle$) from literature survey and our experimental measurements in pure EG. Fitting models and estimated activation energies in EG are shown in same figure. All vignettes are colour-coded.

References

1   C. Krembs, H. Eicken, K. Junge and J. W. Deming, *Deep-Sea Res. I: Oceanogr. Res. Pap.*, 2002, **49**, 2163-2181.

2   R. Gupta and R. Deswal, *J Biosci*, 2014, **39**, 931–944.

3   M. S. Clark and M. R. Worland, *J Comp Physiol B*, 2008, 178, 917–933.

4   G. N. Somero and A. L. DeVries, *Science (1979)*, 1967, **156**, 257–258.

5   K. B. Storey and J. M. Storey, *Physiol. Rev.*, 2017, **97**, 623–665.

6   J. P. Costanzo, R. E. Lee and P. H. Lortz, *J. exp. Biol*, 1993, **181**, 245–255.

7   O. Kandror, A. Deleon and A. L. Goldberg, *PNAS*, 2002, **99**, 9727–9732.

8   K. B. Storey, *Comp. Biochem. Physiol*, 1997, **117**, 319–326.

9   M. R. Michaud and D. L. Denlinger, *J. Comp. Physiol. B, Biochem. Syst. Environ.*, 2007, **177**, 753–763.

10   S. D. Rowley, W. I. Bensinger, T. A. Gooley and C. Dean Buckner, *Blood*, 1994, **83** 2731–2736.

11   J. K. Lewis, J. C. Bischof, I. Braslavsky, K. G. M. Brockbank, G. M. Fahy, B. J. Fuller, Y. Rabin, A. Tocchio, E. J. Woods, B. G. Wowk, J. P. Acker and S. Giwa, *Cryobiology*, 2016, **72**, 169–182.

12   J. Donnez, B. Martinez-Madrid, P. Jadoul, A. Van Langendonckt, D. Demylle and M. M. Dolmans, *Hum. Reprod. Update*, 2006, **12**, 519–535.

13   C. Olsson, H. Jansson and J. Swenson, *J. Phys. Chem. B*, 2016, **120**, 4723–4731.

14   Y. Xin, C. Kielar, S. Zhu, C. Sikeler, X. Xu, C. Möser, G. Grundmeier, T. Liedl, A. Heuer-Jungemann, D. M. Smith and A. Keller, *Small*, 2020, **16**, 1905959.

15   B. R. Chief, M. D. Carr, S. L. Guest Editors, M. D. Tan, G. Roger, P. D. Gosden and D. Sc, *Semin. Reprod. Med.*, 2002, **20**, 005–014.

16   P. A. King, M. N. Rosholt and K. B. Storey, *Can. J. Zool.*, 1995, **73**, 1-9.

17   G. M. Volk, J. L. Harris and K. E. Rotindo, *Cryobiology*, 2006, **52**, 305–308.

18   L. Zhang, L. Liu, Y. Qian and Y. Chen, *Eur. J. Pharm. Biopharm.*, 2008, **69**, 750–759.

19   A. P. R. Rodrigues, C. A. Amorim, S. H. F. Costa, M. H. T. Matos, R. R. Santos, C. M. Lucci, S. N. Báo, O. M. Ohashi and J. R. Figueiredo, *Theriogenology*, 2004, **61**, 1009–1024.

20   F. Chauvigné, E. Lubzens and J. Cerdà, *BMC Biotechnol*, BMC Biotechnol, 2011, **11**, 34.

21   Y. Q. A'Yun, N. Anita, A. Abinawanto, A. A. Jusuf, A. Awanis, I. Muhiardi and M. A. Rosvita, in *AIP Conference Proceedings*, American Institute of Physics Inc., 2019, vol. 2168.

22   É. C. G. Praxedes, G. L. Lima, A. M. da Silva, L. B. Camos, C. M. P. de Souza, S. Sandy. Moreira, M. F. de Oliveira and A. R. Silva, *Reprod. Dom. Anim.*, 2020, **55**, 154–161.

23   K. Tejaswi Naidu and N. Prakash Prabhu, *J. Biomol. Struct. Dyn.*, 2021, **40**, 11216-11228.

24   H. Yue, Y. Zhao, X. Ma and J. Gong, *Chem. Soc. Rev.*, 2012, **41**, 4218–4244.

25   M. De, L. Reyes, L. Saenz, L. Lapierre, J. Crosby, C. Barros and M. De Los Reyes, *Vet. Rec.*, 2002, **151**, 477–480.

26   L. L. Kuleshova, D. R. Macfarlane, A. O. Trounson and J. M. Shaw, *Cryobiology*, 1999, **38**, 119–130.

27   D. C. C. Brito, S. F. S. Domingues, A. P. R. Rodrigues, J. R. Figueiredo, R. R. Santos and J. C. Pieczarka, *Cryobiology*, 2018, **83**, 97–99.

28   R. R. Santos, T. Tharasanit, J. R. Figueiredo, T. Van Haeften and R. Van Den Hurk, *Cell Tissue Res.*, 2006, **325**, 523–531.

29   M. T. Cicerone and C. L. Soles, *Biophys. J.*, 2004, **86**, 3836–3845.

30   A. M. da Silva, L. G. P. Bezerra, E. C. G. Praxedes, S. S. J. Moreira, C. M. P. de Souza, M. F. de Oliveira, A. F. Pereira, P. Comizzoli and A. R. Silva, *Cryobiology*, 2019, **91**, 53–60.

31   W. X. Fan, X. H. Ma, D. Ge, T. Q. Liu and Z. F. Cui, *Cryobiology*, 2009, **58**, 28–36.

32   A. Sakai and F. Engelmann, *Cryo-Lett.*, 2007, **28**, 151–172.

33   Y. Tao, E. Sanger, A. Saewu and M. C. Leveille, *Reprod. Biol. Endocrinol.*, 2020, **18**, 17-undefined.

34   G. Vajta and Z. P. Nagy, *Reprod. Biomed. Online*, 2006, **12**, 779–796.

35   G. M. Fahy and B. Wowk, *Methods Mol. Biol.*, 2015, **1257**, 21–82.

36   G. D. Elliott, S. Wang and B. J. Fuller, *Cryobiology*, 2017, **76**, 74–91.

37   J. J. Towey, A. K. Soper and L. Dougan, *Faraday Discuss.*, 2013, **167**, 159–176.

38   S. D. Allison, B. Chang, T. W. Randolph and J. F. Carpenter, *Arch. Biochem. Biophys.*, 1999, **365**, 289–298.

39   G. Yu, R. Li and A. Hubel, *Langmuir*, 2019, **35**, 7388–7395.

40   J. J. Towey, A. K. Soper and L. Dougan, *J. Phys. Chem. B*, 2012, **116**, 13898–13904.

41   A. Lerbret, P. Bordat, F. Affouard, M. Descamps and F. Migliardo, *J. Phys. Chem. B*, 2005, **109**, 11046–11057.

42   L. Weng, S. L. Stott and M. Toner, *Annu. Rev. Biomed. Eng.*, 2019, **21**, 1–31.

43   L. Weng, C. Chen, J. Zuo and W. Li, *J. Phys. Chem. A*, 2011, **115**, 4729–4737.

44   S. Indra and R. Biswas, *J. Phys. Chem. B*, 2016, **120**, 11214–11228.

45   J. P. R. Motta, F. H. Paraguassú-Braga, L. F. Bouzas and L. C. Porto, *Cryobiology*, 2014, **68**, 343–348.

46   A. Simperler, A. Kornherr, R. Chopra, P. A. Bonnet, W. Jones, W. D. S. Motherwell and G. Zifferer, *J. Phys. Chem. B*, 2006, **110**, 19678–19684.

47   K. Takeda, K. Murata and S. Yamashita, *J. Non-Cryst. Solids*, 1998, **231**, 273–279.

48   C. A. Angell and D. L. Smlth, *J. Phys. Chem.*, 1982, **86**, 3845–3852.

49   R. J. Sengwa, *J. Mol. Liq.*, 2003, **108**, 47–60.

50   B. P. Jordan, R. J. Sheppard and S. Szwarnowski, *J. Phys. D: Appl. Phys.*, 1978, **11**, 695–701.

51   A. C. Kumbharkhane, S. M. Puranik and S. C. Mehrotra, *J. Solut. Chem.*, 1992 21, 201–212.

52   S. Schrödle, R. Buchner and W. Kunz, *J. Phys. Chem. B*, 2004, **108**, 6281–6287.

53   E. Hanke, K. von Roden and U. Kaatze, *J. Chem. Phys.*, 2006, **125**, 084507.

54   A. Kaiser, M. Ritter, R. Nazmutdinov and M. Probst, *J. Phys. Chem. B*, 2016, **120**, 10515–10523.

55   A. Mahendraprabu, A. C. Kumbharkhane, Y. S. Joshi, S. S. Shaikh, P. P. Kannan, N. K. Karthick and G. Arivazhagan, *J. Mol. Struct.*, 2017, **1136**, 303–308.

56   P. B. Undre, P. W. Khirade, V. S. Rajenimbalkar, S. N. Helambe and S. C. Mehrotra, *J. Korean Chem. Soc.*, 2012, **56**, 416–423.

57   R. J. Sengwa and K. Kaur, *J. Mol. Liq.*, 1999, **82**, 231–243.

58   S. Mashimo, N. Miura and T. Umehara, *J. Chem. Phys.*, 1992, **97**, 6759–6765.

59   J. Oh, J. A. Seo, H. K. Kim and Y. H. Hwang, *J Non Cryst Solids*, 2006, **352**, 4679–4684.

60   K. Kaminski, E. Kaminska, M. Paluch, J. Ziolo and K. L. Ngai, *J. Phys. Chem. B*, 2006, **110**, 25045–25049.

61   D. Fioretto, L. Comez, M. E. Gallina, A. Morresi, L. Palmieri, M. Paolantoni, P. Sassi and F. Scarponi, *Chem Phys Lett*, 2007, **441**, 232–236.

62   P. G. Hudge, M. P. Lokhande and A. C. Kumbharkhane, *Indian J. Phys.*, 2012, **86**, 813–818.

63   A. Dhali, R. S. Manik, S. K. Das, S. K. Singla and P. Palta, *Anim. Reprod. Sci.*, 2000, **63**, 159–165.

64   P. S. de Almeida-Monteiro, R. R. R. Pinheiro, M. S. Oliveira-Araújo, Y. S. Sales, R. V. do Nascimento, L. T. Nunes, V. A. Pereira, A. R. Montenegro, M. A. P. Melo-Maciel and C. S. B. Salmito-Vanderley, *Aquac. Res.*, 2020, **51**, 4565–4574.

65   D. Maji, N. C. Maity and R. Biswas, *Theor. Chem. Acc.*, 2023, **142**, 1–15.

66 M. Maroncelli and G. R. Fleming, *J. Chem. Phys.*, 1987, **86**, 6221–6239.

67 M. L. Horng, J. A. Gardecki, A. Papazyan and M. Maroncelli, *J. Phys. Chem.*, 1995, **99**, 17311–17337.

68 M. L. Horng, J. A. Gardecki and M. Maroncelli, *J. Phys. Chem. A*, 1997, **101**, 1030–1047.

69 H. Shirota and E. W. Castner, *J. Chem. Phys.*, 2000, **112**, 2367–2376.

70 R. Karmakar and A. Samanta, *J. Phys. Chem. A*, 2002, **106**, 4447–4452.

71 R. Baumann, C. Ferrante, E. Kneuper, F. W. Deeg and C. Bräuchle, *J. Phys. Chem. A*, 2003, **107**, 2422–2430.

72 S. Koley, H. Kaur and S. Ghosh, *Phys. Chem. Chem. Phys.*, 2014, **16**, 22352–22363.

73 B. Guchhait, S. Daschakraborty and R. Biswas, *J. Chem. Phys.*, 2012, **136**, 174503.

74 K. Kumbhakar, E. Tarif, K. Mukherjee and R. Biswas, *J. Mol. Liq.*, 2019, **290**, 111225.

75 M. Kondo, X. Li and M. Maroncelli, *J. Phys. Chem. B*, 2013, **117**, 12224–12233.

76 K. Mukherjee, A. Das, S. Choudhury, A. Barman and R. Biswas, *J. Phys. Chem. B*, 2015, **119**, 8063–8071.

77 A. Das and R. Biswas, *J. Phys. Chem. B*, 2015, **119**, 10102–10113.

78 N. C. Maity, A. Baksi, K. Kumbhakar and R. Biswas, *J. Photochem. Photobiol. A: Chem.*, 2023, **439**, 114600.

79 B. Guchhait and R. Biswas, *J. Chem. Phys.*, 2013, **138**, 114909.

80 T. Pradhan and R. Biswas, *J. Phys. Chem. A*, 2007, **111**, 11514–11523.

81 C. J. F. Böttcher and P. Bordewijk, *Theory of Electric Polarization: Dielectrics in Time-dependent*, Elsevier, Amsterdam, 1978.

82 A. Schönhals and F. Kremer, *Theory of Dielectric Relaxation*, Springer Berlin Heidelberg, 2003.

83 P. R. Bevington and D. K. Robinson, *Data reduction and error analysis for the physical sciences*, McGraw-Hill Education, New York, 3rdEdition, 2003.

84 K. Mukherjee, A. Barman and R. Biswas, *J. Mol. Liq.*, 2016, **222**, 495–502.

85 C. Gao, G. Y. Zhou, Y. Xu and T. C. Hua, *Thermochim. Acta*, 2005, **435**, 38–43.

86 D. L. Sidebottom, *Phys. Rev. E.*, 2007, 76, 011505.

87 J. T. Edward, *J. Chem. Educ.*, 1970, **47**, 261–270.

88 Z. Hu and C. J. Margulis, *Proc. Natl Acad. Sci. U. S. A.*, 2006, **103**, 831–836.

89 P. K. Mandal, M. Sarkar and A. Samanta, *J. Phys. Chem. A*, 2004, **108**, 9048–9053.

90 R. Biswas, J. E. Lewis and M. Maroncelli, *Chem. Phys. Lett.*, 1999, **310**, 485–494.

91   J. E. Lewis, R. Biswas, A. G. Robinson and M. Maroncelli, *J. Phys. Chem. B*, 2001, **105**, 3306–3318.

92   M. D. Ediger, C. A. Angell and S. R. Nagel, *J. Phys. Chem.*, 1996, **100**, 13200–13212.

93   M. D. Ediger, *Annu. Rev. Phys. Chem.*, 2000, **51**, 99–128.

94   H. Sillescu, *J. Non-Cryst. Solids*, 1999, **243**, 81–108.

95   W. Huang and R. Richert, *Phil. Mag.*, 2007, **87**, 371–382.

96   K. Mukherjee, S. Das, E. Tarif, A. Barman and R. Biswas, *J. Chem. Phys.*, 2018, **149**, 124501.

97   M. Neumann, *Mol. Phys.*, 1983, **50**, 841–858.

98   H. Froehlich, *In Theory of Dielectrics*, New York: Oxford University Press, 1958.

99   Y. H. Zhao, M. H. Abraham and A. M. Zissimos, *J. Orga. Chem.*, 2003, **68**, 7368–7373.

100   N. P. Franks, M. H. Abraham and W. R. Lieb, *J. Pharm. Sci.*, 1993, **82**, 466–470.

101   K. S. Vahvaselkä, R. Serimaa and M. Torkkeli, *J. Appl. Crystallogr.*, 1995, **28**, 189–195.

102   J. L. MacCallum and D. P. Tieleman, *J. Am. Chem. Soc.*, 2002, **124**, 15085–15093.

103   S. K. Garg and C. P. Smyth, *J. Phys. Chem.*, 1965, **69**, 1294–1301.

104   J. Barthel and R. Buchner, *Pure & Appl. Chem.*, 1991, **63**, 1473–1482.

105   N. Zhang, M. R. Li and F. S. Zhang, *Chem. Phys. Lett.*, 2019, **718**, 12–21.

106   A. Kaiser, O. Ismailova, A. Koskela, S. E. Huber, M. Ritter, B. Cosenza, W. Benger, R. Nazmutdinov and M. Probst, *J. Mol. Liq.*, 2014, **189**, 20–29.

107   S. Kaur, Shobhna and H. K. Kashyap, *J. Phys. Chem. B*, 2019, **123**, 6543–6553.

108   K. Mukherjee, E. Tarif, A. Barman and R. Biswas, *Fluid Phase Equilib*, 2017, **448**, 22–29.

109   E. Tarif, K. Mukherjee, A. Barman and R. Biswas, *J. Chem. Sci.*, 2019, **131**, 1–12.

110   E. Tarif, J. Mondal and R. Biswas, *J. Phys. Chem. B*, 2019, **123**, 9378–9387.

111   E. Tarif, K. Mukherjee, K. Kumbhakar, A. Barman and R. Biswas, *J. Chem. Phys.*, 2019, **151**, 154902.

112   C. A. Angell, *J. Chem. Phys.*, 1967, **46**, 4673–4679.

113   I. Chang, F. Fujara, B. Geil, G. Heuberger, T. Mangel and H. Sillescu, *J. Non-Cryst. Solids*, 1994, **172**, 248–255.

114   Biman Bagchi, *Molecular relaxation in liquids*, Oxford University Press, New York, 2012.

Chapter 6

Ultrafast Solvation Dynamics and Viscosity Decoupling in Glucose/Ethylene glycol Cryoprotectant Mixture: Time-Resolve Fluorescence Measurements Using Streak Camera and TCSPC Techniques

6.1 Introduction

At sub-zero conditions, bacteria, algae, fungi, protozoa, plants, fish, and vertebrates have evolved remarkable strategies for survival.[1–3] This strategy includes production of different anti-freezing chemicals for protection from cold-induced damage. Substances like sugars (glucose, trehalose, sucrose, etc.)[4–6] and polyols (ethylene glycol, glycerol, etc.)[7,8] are produced in significant concentration by diverse organisms to prevent the formation of ice in intra and inter-cellular fluids during freezing conditions. The insights gained from studying these mechanisms find practical applications in cryopreservation technologies for cells, organs, tissues, proteins, and DNA within the realms of biotechnology and food preservation technology.[9–11] Cryoprotective agents (CPAs)[12], or cryoprotectants, used in these processes must possess attributes such as environmental friendliness, biocompatibility, biodegradability, low toxicity, and easy availability. Glucose, being a prevalent bio-precursor in plant photosynthesis, stands out as an effective cryoprotective agent due to its biodegradability, biocompatibility, and ready availability.[13,14] Similarly, ethylene glycol, recognized for its low toxicity, cost-effectiveness, and ability to dissolve a wide range of organic solutes, is extensively utilized as a cryoprotectant.[15–18] To enhance cryopreservation efficiency, the use of two or three-component mixtures of cryoprotectants has proven more effective than single cryoprotectants. Note that, some binary cryoprotectant mixtures include glucose/glycerol[19], glucose/ethylene glycol[20], trehalose/ethylene glycol[21], sucrose/ethylene glycol[22], trehalose/glycerol[23], and ethylene glycol/dimethyl sulfoxide[24].

At sub-zero temperatures, the formation of ice crystals can lead to dehydration and demise of cells, organs, tissues, and other biomolecules. Cryoprotective agents play a key role in impeding ice crystal formation and minimizing cold-induced injury.[4,7] Vitrification[25] , a cooling process transforming liquid into a glassy state without crystallization, is facilitated by the

presence of cryoprotectants, resulting in a higher glass transition temperature $(\sim T_g)$[26,27]. The efficacy of vitrification is notably higher in concentration-dependent CPAs compared to traditional ones.[27] CPAs display a strong propensity towards hydrogen bonding (H-bonding) with both donor and acceptor capabilities.[28,29] Types and concentrations of inter-species and intra-species H-bonding influence the T_g of the cryopreservation system.

Solvation dynamics plays an important role in biological systems[30–34]. A thorough comprehension of solvation dynamics in cryoprotectant systems demands the ability to capture ultrafast events occurring on a sub-picosecond timescale. This type of ultrafast event can be achieved by employing some advanced spectroscopic techniques, such as fluorescence up-conversion[35] and Streak camera[36] based detection. Investigating solvation dynamics in cryoprotectant systems provides valuable insights into the solvation of biomolecules, offering crucial knowledge for applications in cryopreservation technology.

In this work, we have chosen two cryoprotectants: ethylene glycol (EG), functioning as intra-cellular CPA[22], and glucose, serving as extra-cellular CPA[4,5]. Our previous research findings, as detailed in Chapter 5, demonstrate that blending two cryoprotectants with significantly different glass transition temperatures(T_g (EG): 153 K[37,38], T_g(glucose): 295 K[39]) provides an opportunity to fine-tune the T_g, which may be useful in cryopreservation technology.

Although the structure and dynamics of glucose/EG cryoprotectant mixtures have been explored using molecular dynamics simulation[40] and dielectric relaxation spectroscopy (Chapter 5), fluorescence solute centric ultrafast solvation and solution heterogeneity of these cryoprotectant mixtures have remained unexplored. Both MD simulation and DRS indicate that glucose-glucose interactions predominate with glucose concentrations in these cryoprotectant mixtures. Based on this finding, our investigation focuses on ultrafast solvation dynamics through fluorescence Stokes shift measurements, where solution heterogeneity has been explored through viscosity decoupling of solute or solvent dynamics in glucose/EG mixtures at varying glucose concentrations (wt %). We employed steady-state absorption and fluorescence, time-resolved fluorescence with time-correlated single-photon counting (TCSPC), and two-dimensional streak camera (2DSC) measurements at 293 K. Glucose concentrations vary in the range of 0, 10, 20, 30, and 40 wt% in EG for all spectroscopic measurements.

The well-established non-reactive gold standard fluorescence probe, C153, has been used for solvation dynamics in wide range of systems like common dipolar solvents, binary mixtures,

deep eutectics, confined media, proteins, and other systems.[41–49] Earlier 2DSC-based solvation dynamics measurements of C153 in normal solvents captured considerable sub-picosecond solvent response.[50] Here, C153 is utilized to explore solvation dynamics and decoupling of solute or solvent dynamics from medium viscosity in glucose/EG cryoprotectant mixtures. The observed bimodal character of solvent response function in these systems lengthens with increasing glucose concentrations. The time-resolved fluorescence (TRF) anisotropy of C153 in these cryoprotectant systems indicates bimodal friction in solute-solvent interactions. Two rotation times of C153, characterized by a large difference in values (sub-picosecond to nanosecond), are well-described by solvent collision followed by probe rotation in these media. The correlation between solvent or solute dynamics and medium viscosity reveals an increase in the extent of viscosity decoupling with higher glucose concentrations.

6.2 Methods and Materials

6.2.1 Materials and Sample Preparation

D (+) Glucose (≥99.5), ethylene glycol (≥99%), and Coumarin 153 (C153) were purchased from Sigma Aldrich and used for the preparation of the sample without purification. For fluorescence spectroscopic measurements, 2–3 μL of freshly prepared solutions of C153 in hexane (carrier solvent) was taken in a glass container. Subsequently, the carrier solvent was evaporated by gently blowing hot air around the outer surface of the glass container. For the preparation of four experimental glucose/EG mixtures (10, 20, 30, and 40 wt% of glucose in EG), the requisite amount of glucose and ethylene glycol was weighed in fluorescence probes containing glass containers. A Detailed description of the sample preparation has already been provided in Chapter 5. Finally, 2-3 ml of the prepared sample with fluorescence probes was poured into a quartz cuvette with a 1 cm path length maintaining dye concentration of $\leq 10^{-5}$ M.

6.2.2 Refractive Index, Density and Viscosity Measurements

Detailed descriptions of refractive index (n_D), densities (ρ), and viscosities (η) measurements are provided in Chapter 5. Glucose wt% dependent n_D ρ, and η values in these glucose/EG binary cryoprotectant mixtures are summarised in Table 6.1.

6.2.3 Data Collection and Analysis for Steady-State UV-visible Absorption and Steady State Fluorescence Emission Measurement

Steady state UV-visible absorption and fluorescence emission spectra were recorded by a UV-visible spectrophotometer (UV-2600, Shimadzu) and a fluorimeter (Fluorolog, Jobin-Yvon, Horiba), respectively. Temperature was controlled by a Peltier temperature controller (accuracy ±0.5 K). The typical error bar for the determined spectral frequencies was ±200 cm^{-1}. The solvent-blank subtracted spectra were processed accordingly before further analyses and frequency determination.[51,52] Detailed descriptions of the steady state UV-Vis absorption and steady state fluorescence techniques are the same as those discussed in Chapter 2.

Table 6.1: Refractive index (n_D), density (ρ), and viscosity (η) of pure EG and glucose/EG binary cryoprotectant mixtures at 293 K.

Property	wt% of glucose				
	0	10	20	30	40
Refractive index (n_D)[a]	1.431	1.438	1.447	1.456	1.466
Density (ρ/gcm^{-3})[a]	1.113	1.146	1.180	1.216	1.255
Viscosity coefficient (η/cP)[b]	19.29	38.78	79.81	210.91	641.10

[a]Refractive index and density values can be reproduced within ±2 % of the reported values.

[b]Viscosity coefficient values can be reproduced within range ±5-10 % of the reported values.

6.2.4 Data Collection and Analysis for Time-Resolved Fluorescence Measurements from TCSPC

Time-resolved fluorescence measurements were performed with a time-correlated single-photon counting (TCSPC) system (LifeSpec-ps) from Edinburgh Instruments (Livingston, U.K.)[41,53]. We used a 409 nm diode laser and the full width at half-maximum (FWHM) of the instrument response function (IRF) was ~90 ps. Temperature dependent measurements were performed by using a Julabo temperature controller (accuracy ±1 K).

Lifetime measurements were conducted by recording magic angle decays at the steady-state emission spectrum of C153 and C343 dissolved in these systems. The data collection and fluorescence anisotropy followed the procedures outlined in Chapter 2 and references.[41,54–57]

6.2.5 Streak Camera Data Collection and Analysis for Dynamic Stokes Shift Measurements

In this experiment, the time-resolved fluorescence spectra were collected using a streak camera (Optoscope SC-10).[50] The laser pulse had a pulse duration of 150 fs and a repetition rate of 80 MHz, and the frequency-doubled light at 440 nm was generated by a BBO crystal from an 880 nm laser pulse. The sample of cryoprotectant mixtures with C153 was placed in a 1 cm path length quartz cuvette, and the excitation was focused onto the sample after passing through a 440 nm interference filter. The emitted fluorescence was collected at a right angle with respect to the excitation and was then focused by two lenses onto the entrance slit of the monochromator with a slit width of 10 μm and a height of 4 mm. The fluorescence was then passed through a bandpass filter of 475 nm to eliminate scattering, and the fluorescence data was collected at magic angle (54.7°) polarization. The instrument response function (IRF) of the streak camera using scattering particles was recorded to be ~2.5 ps FWHM. All images were collected in 1000 acquisitions, keeping the MCP gain at 800 V and delay at 32.5% with a sweep speed of 15 ps/mm. All streak camera TRF measurements were performed at 293K. Details of the measurement protocols and data analyses are the same as those discussed in Chapter 2.
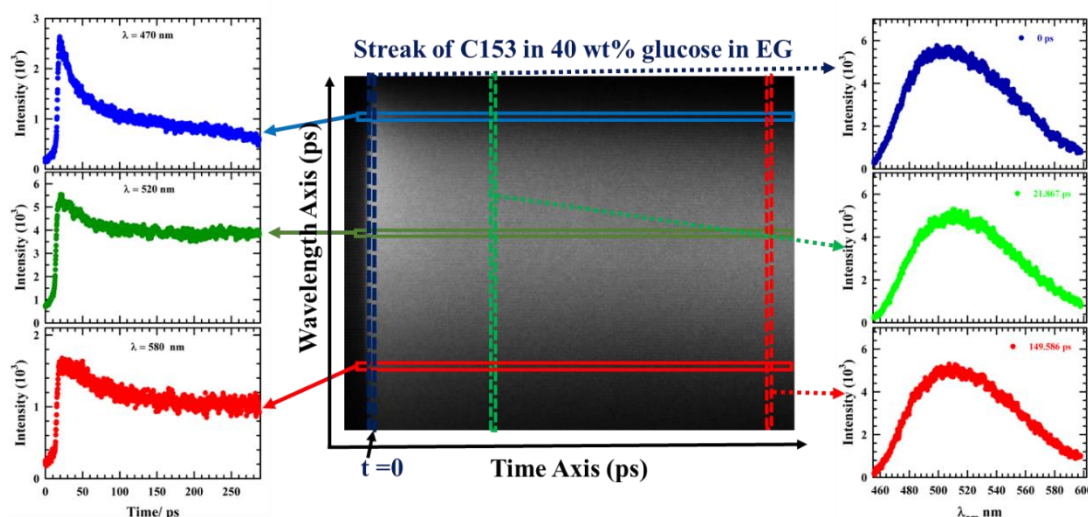
Figure 6.1: Two-dimension streak camera (2DSC) image of C153 in 40 wt% glucose in glucose/EG cryoprotectant mixture at 293 K. Horizontal axis line represents the time axis, and vertical axis line is wavelength axis. The various coloured rectangle dotted line box represents extraction of data from 2DSC image with intensity vs time (left side panel) at various wavelengths and the rectangle solid line box represents intensity vs wavelength at various times. Here t=0 denoted the initial time or zero time from where the TRF emission decay starts.

The extraction procedure for time-resolved emission spectra (TRES) is illustrated in Figure 6.1. In order to obtain TRES at specific delay times from the streak image, the wavelength-time 2D fluorescence profile was segmented into the required time intervals. The zero-time point was selected from the streak image, marking the beginning of fluorescence decay. TRES were acquired at intervals of 207 fs (1 pixel) from 0 to 2 ps, followed by 1034 fs (5 pixels) intervals up to 12 ps, then 2067 fs (10 pixels) intervals up to 40 ps, and finally, 4.961 ps (24 pixels) intervals up to 40–70 ps, with the remaining recorded in 10 ps intervals (48 pixels).

6.3 Results and Discussions

6.3.1 Steady-State UV-VIS Absorption and Fluorescence Emission Spectroscopic Measurements: Solvent Reorganizations Energy for C153 in Glucose/EG Cryoprotectant Mixtures

Figure 6.2 represents the steady-state UV-visible absorption and fluorescence emission of C153 in glucose/EG cryoprotectant mixtures at 293 K. The corresponding absorption and emission spectral average frequencies[58,59] and widths (FWHM) are summarized in Table A6.1 (Appendix). This depicts that there is no significant change with increasing glucose concentrations in these cryoprotectant mixtures, except for the system containing 40 wt% glucose. In this case absorption and emission spectra of C153 are broader and blue-shifted. Our earlier DRS measurements at 298 K (detailed in Chapter 5) revealed that, with an increase in glucose concentration, the dielectric constant decreases and spatial heterogeneity increases. The 40 wt% glucose containing medium exhibits strong heterogeneity compared to other systems. This indicates that interaction between C153 and cryoprotectant mixture is influenced by the solution structure of these cryoprotectant media. As the 40 % glucose containing system is more heterogeneous, prominently interacts with less polar glucose macromolecules observed in DLS measurements (see Chapter 5). Table A6.1 also indicates that the average frequency for steady state fluorescence emission gradually blue sifted with increasing glucose concentration in these cryoprotectant mixtures. This shift can be explained based on the reaction field (RF) and solvent reorganization energies (RE) in these cryoprotectant mixtures.[60] RF and RE are defined as follows: $RF = \left[\frac{(\varepsilon_s-1)}{(\varepsilon_s+2)}\right] - \left[\frac{(n_D^2-1)}{(n_D^2+2)}\right]$ with ε_s as the static dielectric constant and n_D as refractive index, and $RE = \frac{1}{2}\Delta\Delta\nu$ with $\Delta\Delta\nu = [\nu_{abs} - \nu_{em}]^{polar} - [\nu_{abs} - \nu_{em}]^{nonpolar}$. Here ν_{abs} and ν_{em} denote peak average steady state absorption and fluorescence emission frequencies. RF calculated at 298 K using data from Chapter 5 and RE calculated at 293 K, are

shown in Table A6.2 and Table A6.3 (Appendix). These results reveal that both these parameter decreases with increasing glucose concentrations in the cryoprotectant mixture. This suggests that solvent rearrangement around C153 changes with increasing glucose concentration, and C153 senses a less polar environment in these media. Note, the total difference of RE between pure EG and 40 wt% glucose containing system is ~370 cm^{-1} employing C153 at 293 K. These findings align with the earlier report of solvent polarity dependence reorganisation energy differences of C153.[48,50,60,61] Glucose concentration dependent difference in $\Delta\Delta\nu$ between these cryoprotectant mixtures suggests a simultaneous impact of refractive index and medium viscosity of cryoprotectant mixtures.
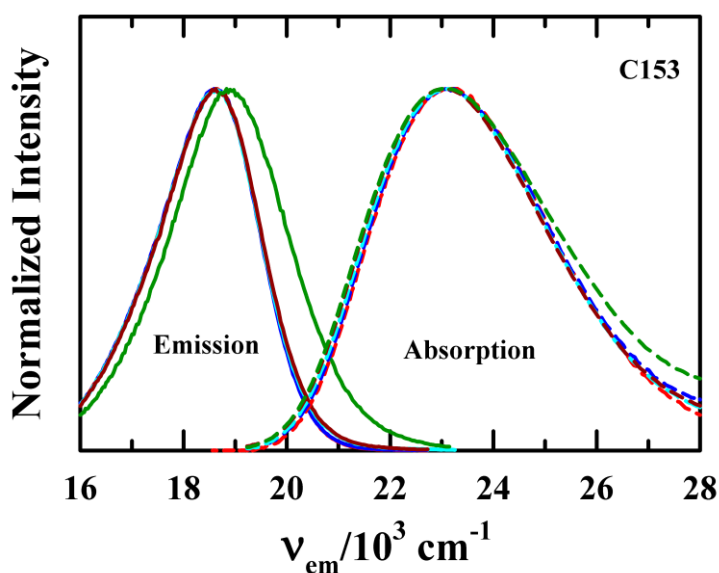
Figure 6.2: Steady state absorption and emission spectra of C153 in 0 (red), 10 (blue), 20 (cyan), 30 (dark red), and 40 (green) wt% glucose in glucose/EG binary cryoprotectant mixtures at 293 K. All representations are colour-coded.

6.3.2 Time-resolved Measurements of Cryoprotectant Mixture: Lifetime and Solvation Dynamics and TRF Anisotropy

6.3.2.1 Lifetime

The fluorescence lifetime decay of C153 in glucose/EG cryoprotectant mixtures and pure EG collected at 470 nm emission from TCSPC experiment (FWHM of IRF~90 ps) are shown in Figure 6.3 and Figure A6.4 (Appendix), respectively. Note, except 40 wt% glucose containing system, a significant portion of the lifetime decay of C153 in pure EG and glucose/EG mixtures is missed when collected at the steady state maxima at 440 nm (see Figure A6.5 in Appendix).

To address this issue, the lifetime data were collected slightly toward the red end at 470 nm from the steady state maxima. The average lifetime ($\langle \tau_{fl} \rangle$) data of C153 in these systems are summarized in Table 6.2. This depicts that, $\langle \tau_{fl} \rangle$ of C153 in pure EG is in good agreement with earlier results from combined 2DSC and TCSPC measurements.[50] The $\langle \tau_{fl} \rangle$ of C153 slightly increases as moving from pure EG to glucose/EG cryoprotectant mixtures.
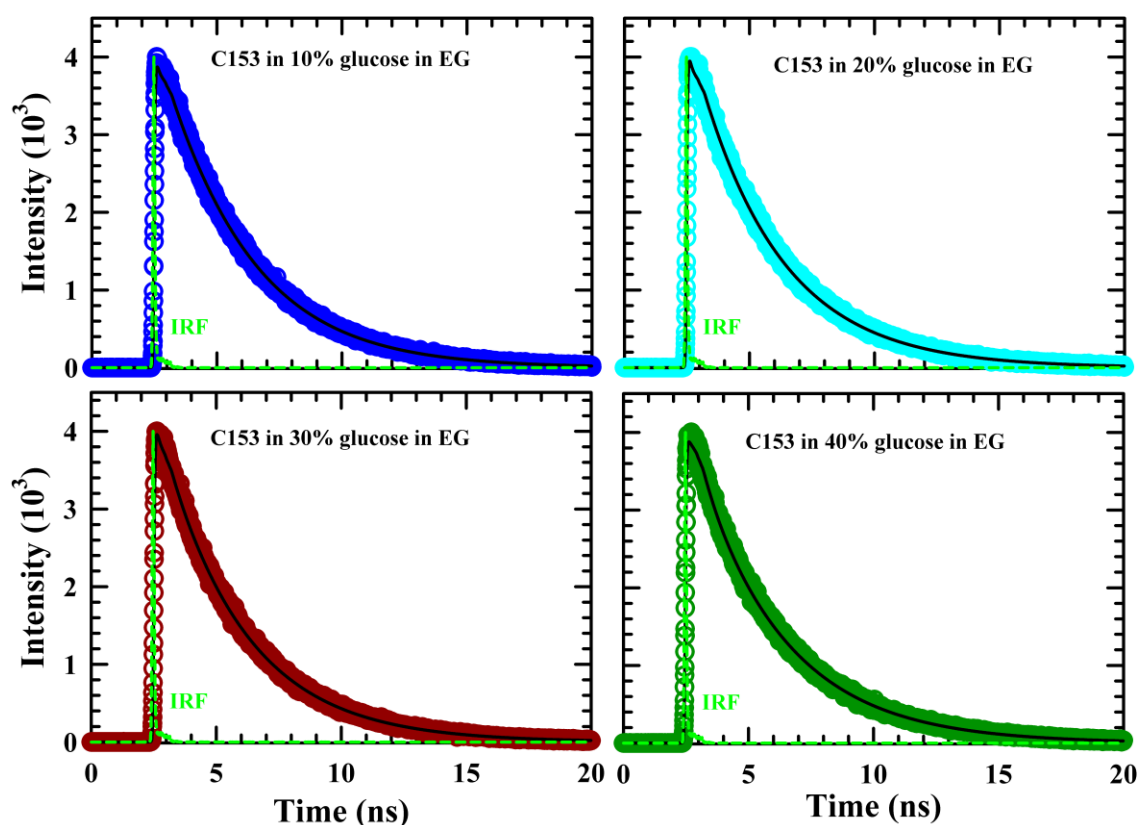
Figure 6.3: Fluorescence lifetime decays of C153 at 470 nm in glucose/EG cryoprotectant mixtures from TCSPC measurement at 293 K. The open symbols with different colour represent glucose concentrations dependent experimental lifetime data, and the black solid line corresponds to the multiexponential fitting of this data. The green short dashed line indicates the instrument response function (IRF) of the TCSPC setup. This result also reveals that after glucose addition, $\langle \tau_{fl} \rangle$ of C153 slightly increases and remains nearly same for all glucose/EG cryoprotectant mixtures. That suggests that C153 preferably interacts with the glucose molecules in these cryoprotectant mixtures. All representations are colour-coded.

Table 6.2: Average fluorescence lifetime ($\langle\tau_{fl}\rangle$) of C153 in pure EG and glucose/EG cryoprotectant mixture at 293 K. Value in parenthesis is taken from reference of C153 in pure EG.[50]

wt% of glucose	$\langle\tau_{fl}\rangle$ (ns)[c]
0	2.772 (2.694)
10	3.036
20	2.910
30	3.040
40	3.177

[c]Average lifetime ($\langle\tau_{fl}\rangle$) can be reproduced within $\pm$ 5%

6.3.2.2 Solvation Dynamics: Dynamic Stoke Shift and Ultra-fast Solvent Response Detection Using Streak Camera

In the exploration of dynamics in glucose/EG cryoprotectant mixtures via two-dimensional streak camera (2DSC) measurements, glucose concentration-dependent dynamic Stokes's shift dynamics were conducted. The left panel of Figure 6.1 represents the fluorescence emission decay of C153 in 40 wt% glucose containing cryoprotectant system at three different wavelengths (blue end, middle and red end) with respect to the steady state peak emission wavelength. The observed sharp decay and growth followed by decay when moving from the blue end to red end emission in Figure 6.1, signifies the characteristic signature of dynamic Stokes's shift[51,62]. The 2DSC images of C153 in four glucose/EG cryoprotectant mixtures are present in Figure 6.4.

The TRES of C153 in these systems were extracted, and log-normal line shape functions were fitted to these TRES. The time-dependent TRES at three different times for C153 in glucose/EG cryoprotectant mixtures and pure EG at 293K are shown in Figure 6.5 and Figure A6.6 (Appendix). These figures depict that both $t = 0$ and $t = \infty$ spectra are gradually blue shifted with increasing glucose concentrations. However, $t = 0$ spectra are significantly blue shifted due to the impact of glucose than $t = \infty$ spectra. This suggests that the hydrophobic probe C153 predominantly interacts with less polar glucose molecules as the glucose concentration increases in these cryoprotectant mixtures. After excitation, the polar solvation by hydroxyl group from both species is nearly similar for 0 to 30 wt% glucose mixtures due to enhanced dipole moment of C153.[63,64] On the other a significant change in $t = \infty$ observed for 40 wt% glucose containing mixture, which is in well agreement with our steady state fluorescence

emission experiments. Previous DLS measurements (see Chapter 5) have shown that particle size gradually increases with glucose wt%. It abruptly increases for 40 wt% glucose, indicating the formation of glucose-glucose macromolecular structures.
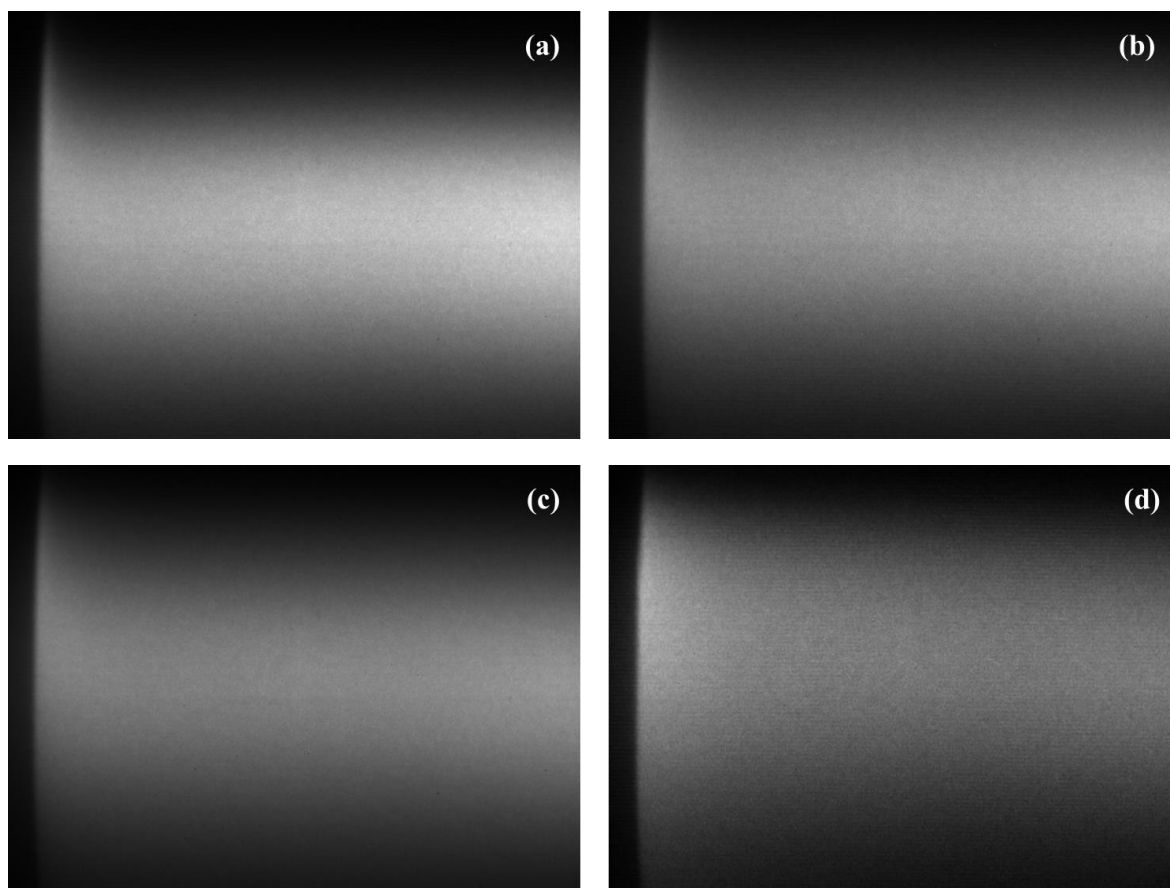
Figure 6.4: Two-dimensional streak camera image of C153 in glucose/EG cryoprotectant mixtures with glucose concentration (a) 10 wt%, (b) 20 wt%, (c) 30 wt%, and (d) 40 wt% at 293 K. The time evolution of fluorescence intensity is depicted on the horizontal axis, while the spatial variation (wavelength) of the fluorescence emission at a specific time is represented on the perpendicular axis.

This discussion suggests that C153 is encapsulated in a less polar macromolecular structure in 40 wt% glucose containing mixture, leading to a significant blue shift in both steady state fluorescence emission and TRES spectra in this system. All fitted spectra from TRES were appropriately converted from wavelength space to frequency space. Figure 6.6 and Figure A6.7 (Appendix) are representing TRES fits of C153 at various time points after excitation. For comparison, the steady state fluorescence emission spectrum of respective system is also included in the same figure. Note, the steady state fluorescence emission spectra of C153 are

gradually blue to red shifted with glucose concentration compared to the TRES at $t = \infty$. This suggests that the steady state fluorescence emission spectra of C153 in these cryoprotectant mixtures represent the emission coming from the incomplete to complete solvent relaxed excited state with increasing glucose concentrations.
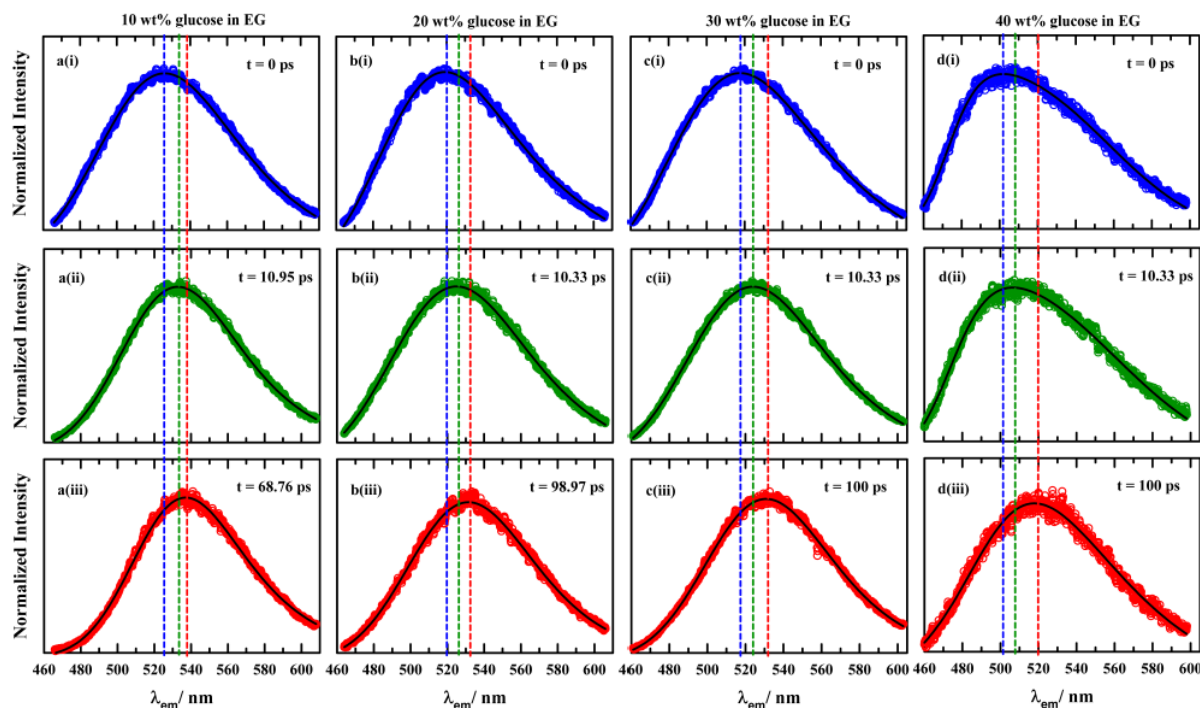
Figure 6.5: Representative TRES from the streak camera data of C153 in glucose/EG cryoprotectant mixtures with glucose concentration (a) 10 wt%, (b) 20 wt%, (c) 30 wt%, and (d) 40 wt% at 293 K. The solid black lines passing through the experimental data represent the log normal fit to the data. Vertical dashed lines are used to indicate the spectral shift over time. All representations are colour-coded.

The total observed dynamic Stokes shift ($\Delta v_{obs}^{t} = v^{t=0} - v^{t=\infty}$), estimated Stokes shift (Δv_{est}^{t})[65], and missing percentages of C153 in these cryoprotectant mixtures along with pure EG are illustrated in Table 6.3. This table depicts that present resolution of the 2DSC setup (IRF ~2 ps) has missed ~70-50% of the total Δv_{obs}^{t} for C153 in these systems. That indicates that, due to polar solvent solvation in these poly-hydroxy species, a significant portion of inherent ultrafast dynamics is present in these systems, which has been missed in our Stokes shift dynamics measurement. Additionally, the missing portion of Δv_{obs}^{t} decreases with increasing glucose concentration. That is attributed to the glucose dependent viscosity induced

gradual slowing down of the faster ultrafast component of Stokes shift dynamics to a comparatively slower one, falling within our present measurement window.
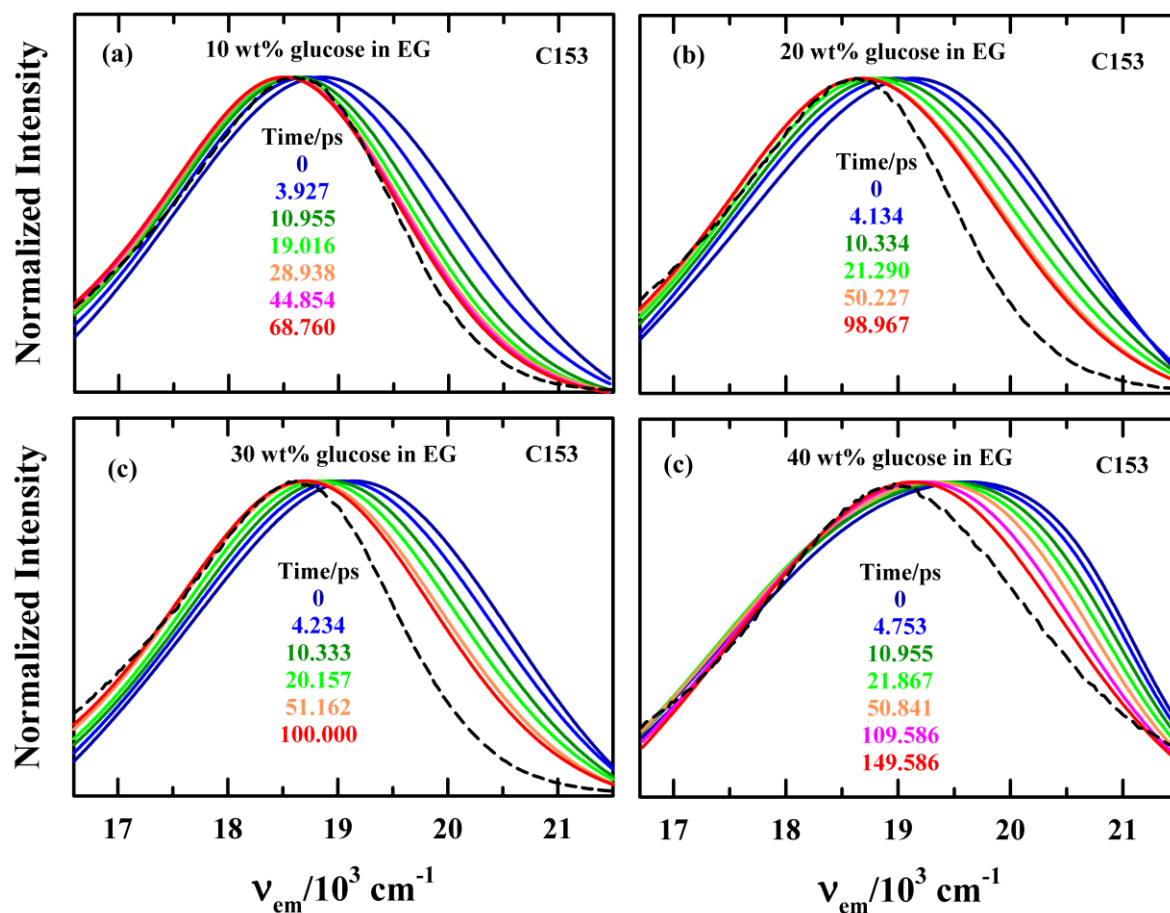
Figure 6.6: Representative time-resolved emission spectra (TRES) of C153 in glucose/EG cryoprotectant mixtures with glucose concentration (a) 10 wt%, (b) 20 wt%, (c) 30 wt%, and (d) 40 wt% at 293 K. The dashed lines in these panels represent the steady-state emission spectra of C153 in these glucose/EG cryoprotectant mixture. All representations are colour-coded.

Table 6.3: Magnitudes of estimated (Δv_{est}^{t}), observed (Δv_{obs}^{t}) and missing percentage of the total dynamic Stokes shift of C153 in pure EG and glucose/EG cryoprotectant mixture at 293 K.

Property	wt% of glucose				
	0	10	20	30	40
$\Delta v_{obs}^{t}/$ cm^{-1}	334	359	446	462	485
$\Delta v_{est}^{t}/$ cm^{-1}	1282	1287	1213	1156	972

% of missed	73	72	63	60	50
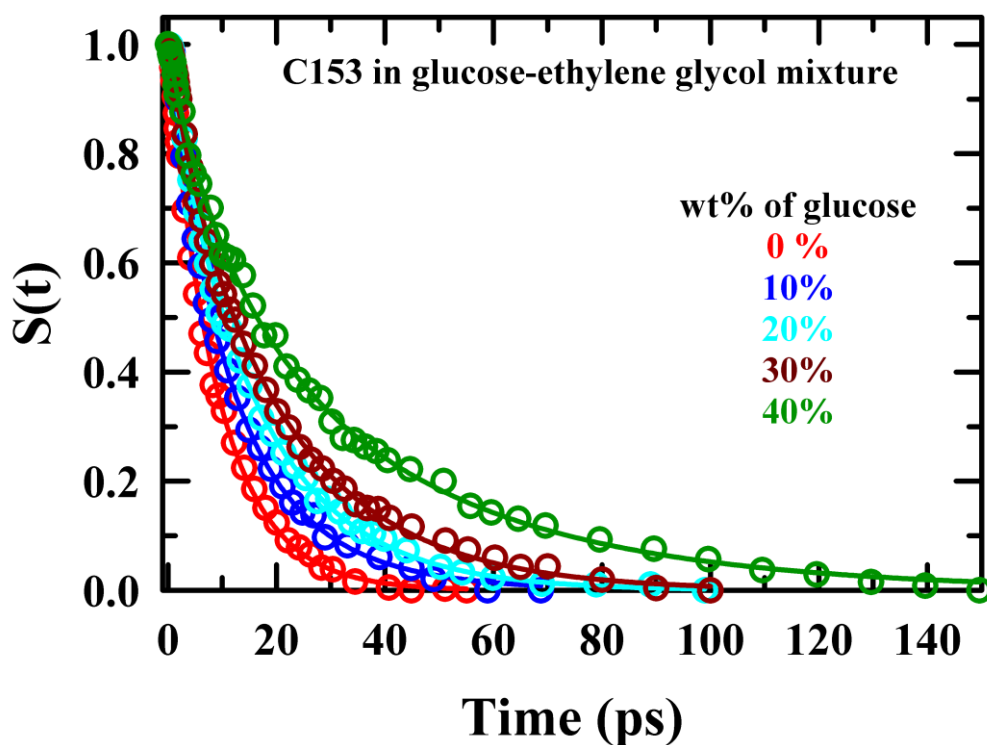
Figure 6.7: Solvation response functions (S(t)) of C153 in glucose/EG cryoprotectant mixtures with glucose concentration 0 (red), 10 wt% (blue), 20 wt% (cyan), 30 wt% (dark red), and 40 wt% (dark green) at 293 K. Solid lines passing through the data represent fits. All representations are colour-coded.

To obtain better statistics, we calculated peak average frequency (ν_{pk}^{av}) from the time evaluation fitted TRES. Glucose wt% dependent solvation response functions ($S(t)$) for C153 in these cryoprotectant systems are well described by multi-exponential function, as shown in Figure 6.7. Corresponding fitting parameters of $S(t)$ decays are provided in Table 6.4. The $S(t)$ decays of C153 are described by two sub-picosecond relaxations ($\tau_1 \sim 10 - 40$ ps, $\tau_2 \sim$ 5-13 ps) for EG and glucose/EG cryoprotectant mixtures, except 40 wt% glucose system where, in addition to the two solvent response time components, a new time component ($\tau_3 \sim 3.5$ ps) appears. The calculated translational diffusion time from the Stokes-Einstein relation and rotational diffusion time from the Stokes-Einstein-Debye relation[66] for both EG and glucose in pure EG and

glucose/ethylene glycol cryoprotectant mixtures are shown in Table A6.8 (Appendix). This indicates that the solvation responses are not contributed by molecular diffusion or rotation of both species present in these media. Solvation data suggest that -OH group attached to EG or glucose contributed to ultrafast polar solvation through restricted rotation (libration).[41,67] Individual solvent response times are slowing down with glucose concentration, indicating sluggish dynamics of these cryoprotectant mixtures due to enhanced medium viscosity. Interestingly, the amplitude of the relatively slower τ_1 decreases, while that for τ_2 increases with glucose concentration. Finally, the average solvation time ($\langle \tau_s \rangle$) slows down with increasing glucose concentration and this is attributed to the increase of medium viscosity of these systems.

Table 6.4: Temperature dependent $S(t)$ fit parameters for C153 in pure EG and glucose/EG cryoprotectant mixture at 293 K.[d]

wt% of glucose	a_1	τ_1/ps	a_2	τ_2/ps	a_3	τ_3/ps	$\langle \tau_s \rangle$/ps
0	0.95	10	0.05	5			9.75
10	0.89	13.42	0.11	4.95			12.57
20	0.63	19.56	0.37	9.19			15.84
30	0.51	28.17	0.49	11.21			19.85
40	0.60	40.82	0.33	13.39	0.07	3.56	29.14

[d]Individual amplitudes and time constants can be reproduced within ± 10 % of the reported values.

6.3.2.3 Time-resolved Fluorescence Anisotropy

TRF anisotropy measurements of C153 were conducted in glucose/EG binary mixtures and pure EG to provide insights into the influence of local medium friction on solute rotation[55]. Figure A6.9 in the Appendix presents representative parallel and perpendicular TRF emission decays of C153 in a 40 wt% glucose-containing cryoprotectant mixture at 293 K. Glucose concentration dependent $r(t)$ decays of C153 in these cryoprotectant mixtures and pure EG are depicted in Figure 6.8, and corresponding fit residuals are shown in Figure A6.10 (Appendix). Figure 6.9 illustrates the glucose concentration dependent $r(t)$ for few cryoprotectant mixtures at 293 K. This figure show that, with increasing glucose concentration, $r(t)$ exhibits a faster portion contributing more to the faster component, and slower portion extending more in the time axes. The bi-exponential $r(t)$ decay fit parameters are summarized

in Table 6.5. The bimodal TRF $r(t)$ decay for C153 in these binary cryoprotectant systems suggests that probe molecules experience time-dependent non-Markovian friction in these media. The bimodal $r(t)$ decays of C153 in binary cryoprotectant mixtures, with a large difference between that two-time component, are described by a faster time component (τ_1^r) of approximately 40 -50 ps and a longer nanosecond time (τ_2^r) of approximately 1-5 ns. The average rotation time, $\langle\tau_r\rangle$ as well as its individual time components of C153 in pure EG, are good agreement with the reported result[56] Next, we will discuss on origin of these two TRF anisotropy decay time constants.
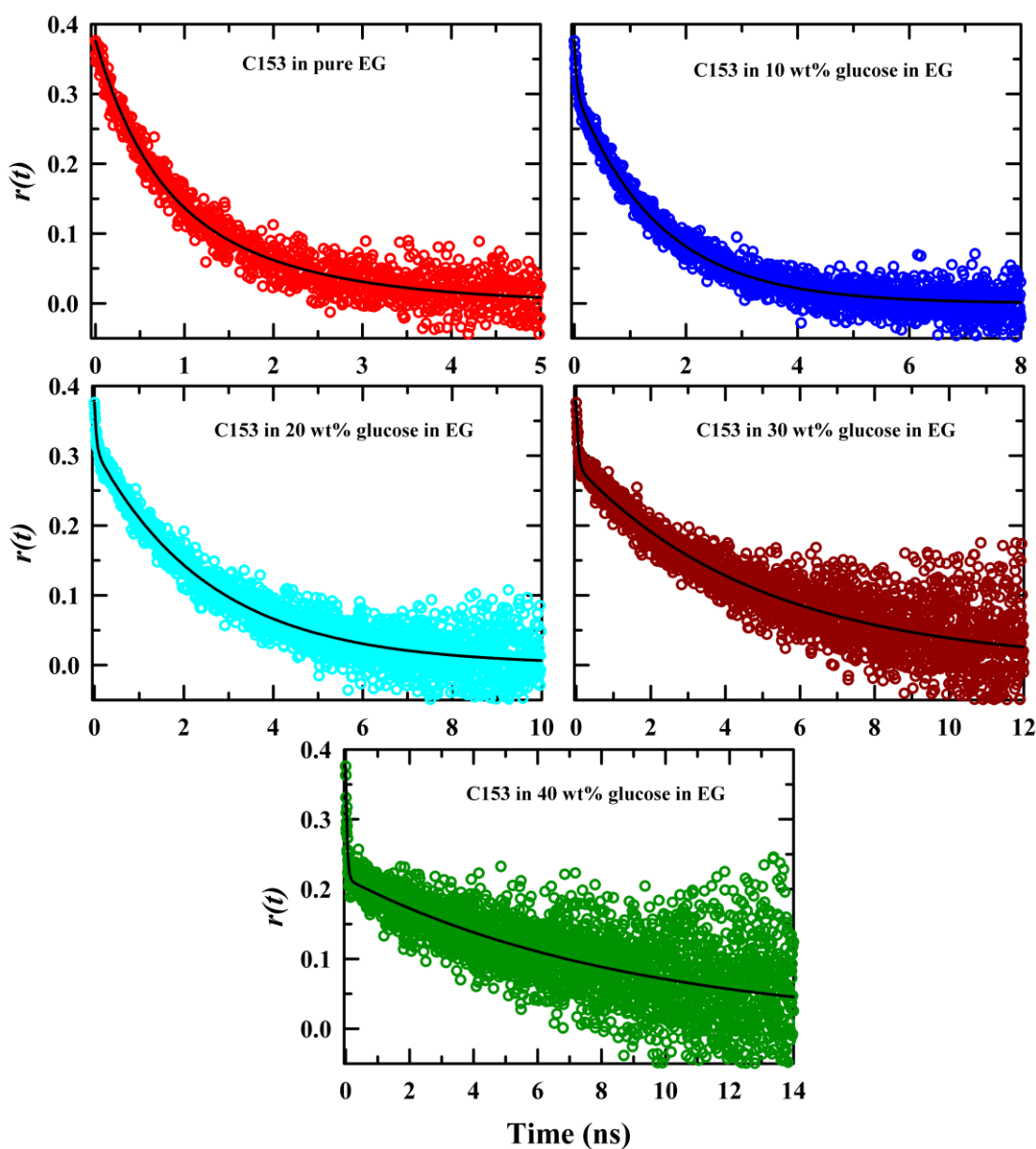
Figure 6.8: Representative fluorescence anisotropy $r(t)$ decay of C153 in glucose/EG cryoprotectant mixtures with glucose concentration 0 (red), 10 wt% (blue), 20 wt% (cyan), 30

wt% (dark red), and 40 wt% (green) at 293 K. Experimental data are shown by circles. The solid lines passing through the data points depict the bi-exponential fits. All representations are colour-coded.
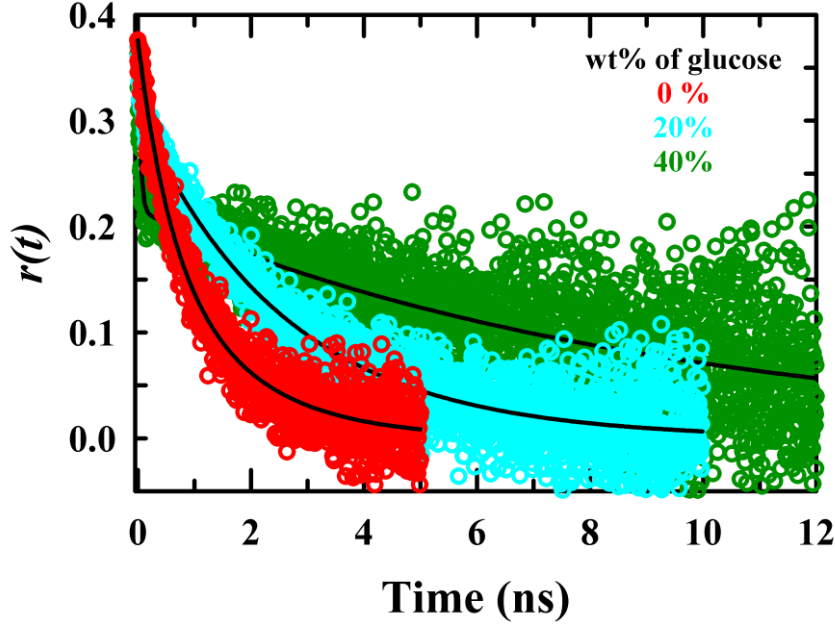
Figure 6.9: Comparison of fluorescence anisotropy $r(t)$ decay of C153 in pure EG and two glucose/EG cryoprotectant mixtures with glucose concentration 20 wt% (cyan), and 40 wt% (dark green) at 293 K. Experimental data are shown by circles. The solid lines passing through the data points depict the bi-exponential fits. All representations are colour-coded.

First, we examine the slower time constant, τ_1^r from TRF anisotropy of C153 in these binary cryoprotectant mixtures as well as in pure EG. Generally, this long nanosecond time constant, τ_1^r, originates from the rotational diffusion of C153 in these complex systems. That is further examined by the stick-slip limit of SED rotational diffusion. The theoretical rotational diffusion time for single molecular rotation is $\tau_r = 6\,V\eta C f_S/l(l+1)k_B T$ with l as the rank of the experimental method ($l = 2$ for fluorescence measurement), V and f_s are the volume and shape factor of solute respectively, C is the coupling parameter of the rotating solute with the surrounding environment. k_B and T are Boltzmann constant and temperature in Kelvin respectively. The modified SED equation for fluorescence measurement with $l = 2$, $\tau_r^{(2)} = V\eta C f_S/K_B T$. We used $V = 246$ Å^3, $f_s = 1.71$, $C = 0.24$ (slip) and 1 (stick) for C153[64]. The calculated $\tau_r^{(2)}$, with stick and slip prediction for C153 in these cryoprotectant systems at 293K,

are given in Table A6.11 (Appendix). In pure EG, long τ_1^r (1.170 ns) resides between stick (2.007 ns) and slip (0.481 ns) SED rotation time. However, it gets closer and closer to the slip limit condition with increasing glucose concentration. Finally, it enters the super slip region at the 40 wt% glucose system. These results suggest that probe rotation becomes more decoupled from medium viscosity with increasing glucose concentration.

Table 6.5: Glucose wt% dependent $r(t)$ decay fit parameters for C153 in pure EG and glucose/EG binary cryoprotectant mixtures.[e]

wt% of glucose	a_1	τ_1^r /ns	a_2	τ_2^r /ns	$\langle \tau_r \rangle$/ns
0	0.90	1.170	0.10	0.040	1.057
10	0.81	1.512	0.19	0.040	1.232
20	0.82	2.595	0.18	0.042	2.135
30	0.76	5.002	0.24	0.052	3.814
40	0.58	9	0.42	0.042	5.238

[e]Individual amplitudes and time constants can be reproduced within ± 10 % of the reported values.

Second, we explore the origin of the faster time τ_2^r in these binary cryoprotectant mixtures and pure EG. This τ_2^r remains constant in all investigated systems, while its contribution increases with increasing glucose concentrations. This sub-picosecond τ_2^r is comparable with the solvation response time of C153. It has been observed that the detection percentage of dynamic Stokes shift increases with increasing glucose concentration, along with a higher contribution from faster solvent response time. This type of faster solvent response arises from the OH group interactions from EG and the rigid pyranose glucose molecules. As glucose concentration increases from 0 to 40 wt%, more -OH groups of rigid glucose molecules interact with C153. The above discussion suggests that τ_2^r comes from the collisional motions of the probe molecule with the surrounding hydroxyl group of glucose and EG molecules.

The average rotation time ($\langle \tau_r \rangle$) slows down with increasing glucose concentration. This slowdown of $\langle \tau_r \rangle$ can be explained by the glucose dependent viscosity in these cryoprotectant mixtures. With increasing glucose concentration, cryoprotectant mixtures become more viscous, causing the solute to experience more hindrance in rotation in these systems.

6.3.2.4 Deviation from SED and Viscosity Decoupling: Signature of Dynamic Heterogeneity

Furthermore, the upper panel of Figure 6.10 compares between the experimental $\langle \tau_r \rangle$ and the calculated stick or slip rotation from the modified SED equation for C153 in binary cryoprotectant mixtures along with pure EG. The experimental $\langle \tau_r \rangle$ of C153 gradually transits from the sub-slip region to the super-slip region SED limit with glucose concentrations. This phenomenon can be explained by the fact that as glucose concentrations increase, glucose-glucose interaction intensifies. This solute-solute interaction led to formation of a more heterogeneous solution structure with glucose-glucose macromolecular structure in these systems. Consequently, C153 experiences a gradual reduction in friction due to the increasing heterogeneity of these systems with glucose concentrations. Furthermore, we evaluate the extent of viscosity coupling for the dynamics of both fluorescence solute and solution mixtures by using the flowing equations $\langle \tau_r \rangle \propto (\eta)^p$ and $\langle \tau_s \rangle \propto (\eta)^p$ respectively. Here $p = 1$ indicates a strong coupling of dynamics with medium viscosity, whereas p deviation from unity suggests that dynamic is decoupled from medium viscosity. In Figure 6.10, we also include data from dielectric relaxation (DR) measurements in these systems at 298 K as discussed in Chapter 5. The comparison reveals that, for all cases like probe rotation ($p = 0.49$), solvent dynamics from TRF measurement ($p = 0.30$), and solvent dynamics from DR measurement ($p = 0.68$) p value deviates from unity. It is important to note that the p values obtained from different measurement techniques are different, which can be explained by the size and relaxation time of probes involved in these different measurement processes.[68–70] But despite these variations, all measurements show a significant deviation from unity. Fractional p values, as observed in DR measurments[70,71], and TRF study[44,61,72–74], suggest cryoprotectant mixture are dynamically heterogeneous. Viscosity decouple dynamics leads to dynamical heterogeneity is a common phenomenon in supercooled liquid.[68,75–78] The above discussion revealed that viscosity decoupling for $\langle \tau_r \rangle$ increases with glucose concentration. This indicates dynamical heterogeneity of these binary cryoprotectant mixtures increases with glucose concentrations, which is consistent with our previous result (see Chapter 5).
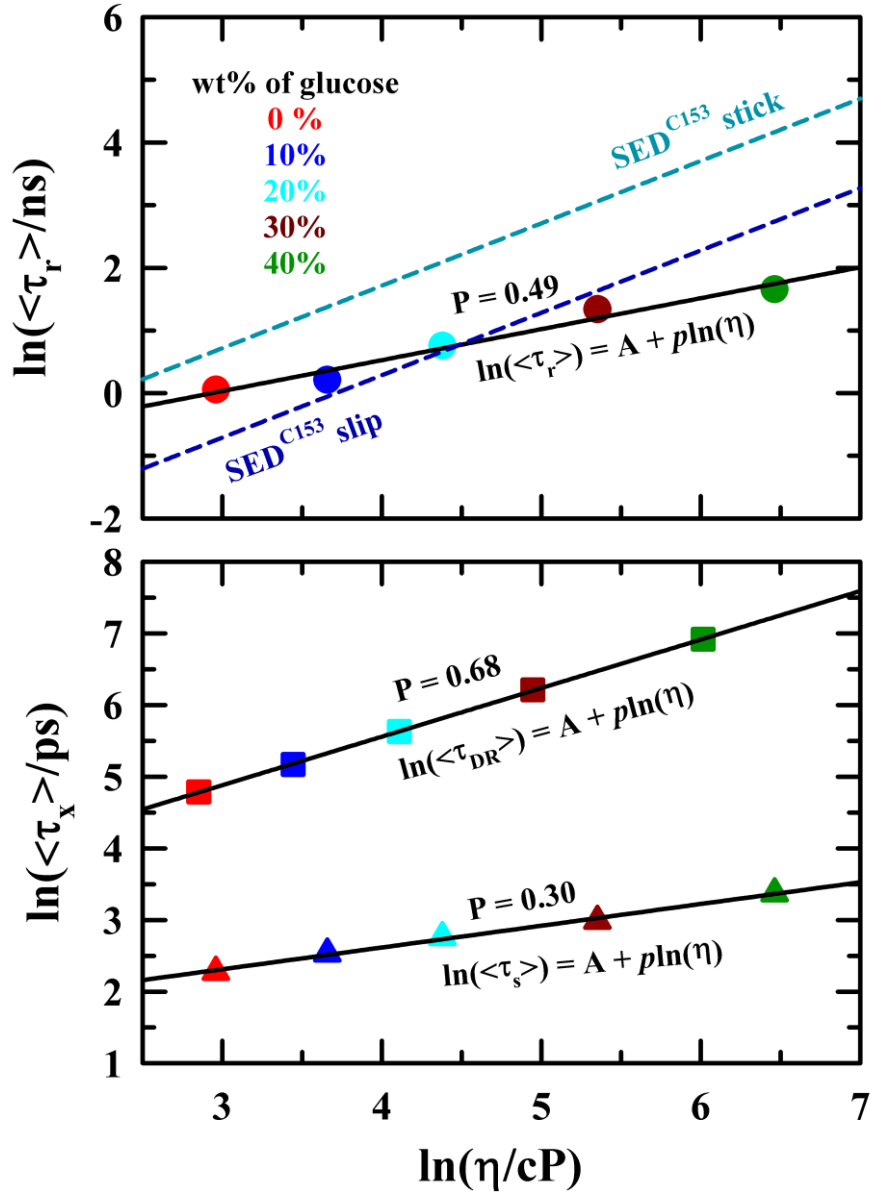
Figure 6.10: Representative double logarithmic plot of average rotational time, $\langle \tau_r \rangle$ vs. medium viscosity (η) (upper panel), and average solvation time, $\langle \tau_x \rangle$ vs η (lower panel) of C153 in glucose/EG cryoprotectant mixtures with glucose concentration 0 (red), 10 wt% (blue), 20 wt% (cyan), 30 wt% (dark red), and 40 wt% (dark green) at 293 K. Note, $\langle \tau_x \rangle$ in lower panel Y-axis reparents average dielectric relaxation time (x = DR) or solvation time (x = s). Average dielectric relaxation time, $\langle \tau_{DR} \rangle$ vs η data in these systems at 298 K form Chapter 6 are also presnt in lower panel. Calculated stick and slip lines from SED relation are presented by dashed lines (upper panel). Solid lines passing through the data points represent linear fits. All representations are colour-coded.

6.4 Conclusion

In summary, this work investigates the complex dynamics of glucose/EG cryoprotectant mixtures through extensive and thorough spectroscopic measurements. Using steady-state and time-resolved fluorescence techniques (2DSC and TCSPC), these measurements employing a fluorescence probe, C153, has provided deep insights into the solute and solvent interactions within these systems. The steady-state UV-visible absorption and fluorescence emission measurements revealed variations in solvent reorganization energy, with 40 wt% glucose-containing system displaying several distinctive features. Time-resolved fluorescence analyses, spanning lifetime, dynamic stoke shift, and anisotropy measurements, provide a detailed understanding of solvation dynamics and local medium friction, elucidating the impact of glucose concentration on these processes. The dynamic Stokes shift measurements using a 2DSC not only highlighted an increasing detection percentage with increasing glucose concentration but also revealed a bimodal ultrafast solvent response. The deviation from Stokes-Einstein-Debye (SED) behaviour in the external solute dynamics in these systems indicated the emergence of dynamic heterogeneity, increasing glucose concentration within the cryoprotectant mixtures, underscoring the complex nature of molecular interactions. Correlations between solute/solvent dynamics and medium viscosity, borne out by significantly lower p values (0.49 from TRF anisotropy, 0.30 from solvent repose, 0.68 from DRS measurement) validate the hypothesis of dynamic heterogeneity in these complex media. This comprehensive exploration not only enhances our understanding of solvation/solute dynamics but also sets the stage for further investigations into the complex world of molecular interactions within cryoprotectant mixtures.

Appendix A6

Table A6.1: Absorption and emission frequencies and spectral widths (FWHM) of C153 in glucose/ethylene glycol binary cryoprotectant mixtures and pure ethylene glycol at 293K.

wt % of glucose	FPK[a] 10^3 cm^{-1}	1st Mom. Freq 10^3 cm^{-1}	Avg. Freq[b]. 10^3 cm^{-1}	Peak avg[c] 10^3 cm^{-1}	FWHM 10^3 cm^{-1}
Absorption					
Pure EG	23.172	23.811	23.443	23.475	4.109
10	23.157	23.738	23.443	23.442	4.153
20	23.092	23.678	23.394	23.388	4.156
30	23.046	23.650	23.364	23.353	4.194
40	23.074	23.809	23.492	23.458	4.496
Emission					
Pure EG	18.535	18.161	18.312	18.336	2.487
10	18.515	18.157	18.307	18.326	2.475
20	18.524	18.169	18.313	18.335	2.473
30	18.535	18.199	18.324	18.352	2.497
40	18.747	18.619	18.699	18.688	2.857

[a]FPK is the peak frequency obtained from fit from the top 50% of the spectra taking two inverted parabolas.

[b]Avg. Freq. is the average of the frequencies at two half maxima points.

[c]Peak Avg. is the arithmetic mean of FPK, 1st Mom. Freq., and Avg. Freq.

Table A6.2: Reaction filed parameter calculation for glucose/EG cryoprotectant mixtures at 298 K.

wt % of glucose	Static dielectric constant (ε_s)[d]	Refractive index[d]	RF
0	40.99	1.429	0.672416
10	40.81	1.437	0.667936
20	39.60	1.446	0.661217
30	39.15	1.455	0.655778
40	38.83	1.465	0.650074

[d]Static dielectric constant (ε_s) and refractive index of these cryoprotectant mixtures at 298 K are taken from Chapter 5.

Table A6.3: Reorganization energy, $RE = \frac{1}{2}\Delta\Delta\nu = \frac{1}{2}[\nu^{abs.} - \nu^{em.}]^{polar} - [\nu^{abs.} - \nu^{em.}]^{hexane}$ for C153 in pure EG and EG/glucose mixtures.

wt % of glucose	Frequency	FPK[c]	1ˢᵗ Mom. Freq	Avg. Freq.[d]	Peak avg.[e]
Pure Hexene[e]	$\Delta\nu_{HEX}^{C153}$ (cm⁻¹)	3355	3963	3287	3535
Pure EG	$\Delta\nu_{EG}^{C153}$ (cm⁻¹)	4637	5650	5131	5139
10	$\Delta\nu_{GL10}^{C153}$ (cm⁻¹)	4642	5581	5126	5116
20	$\Delta\nu_{GL20}^{C153}$ (cm⁻¹)	4568	5509	5081	5053
30	$\Delta\nu_{GL30}^{C153}$ (cm⁻¹)	4511	5451	5040	5001
40	$\Delta\nu_{GL40}^{C153}$ (cm⁻¹)	4327	5190	4793	4770
Pure EG	$\Delta\Delta\nu(EG)$ (cm⁻¹)	1282	1687	1844	1604
10	$\Delta\Delta\nu(GL10)$ (cm⁻¹)	1287	1618	1839	1581
20	$\Delta\Delta\nu(GL20)$ (cm⁻¹)	1213	1546	1794	1518
30	$\Delta\Delta\nu(GL30)$ (cm⁻¹)	1156	1488	1753	1466
40	$\Delta\Delta\nu(GL40)$ (cm⁻¹)	972	1227	1506	1235

[e]From refrence[50]
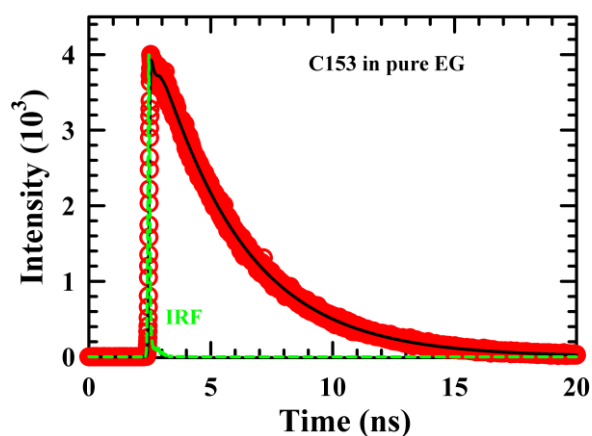
Figure A6.4: Fluorescence lifetime decays of C153 at 470 nm in EG from TCSPC measurement at 293 K. The red symbols represent the experimental lifetime data, and the black solid line corresponds to the multiexponential fitting of this data. The green short dashed line indicates the Instrument Response Function (IRF) of the TCSPC setup.
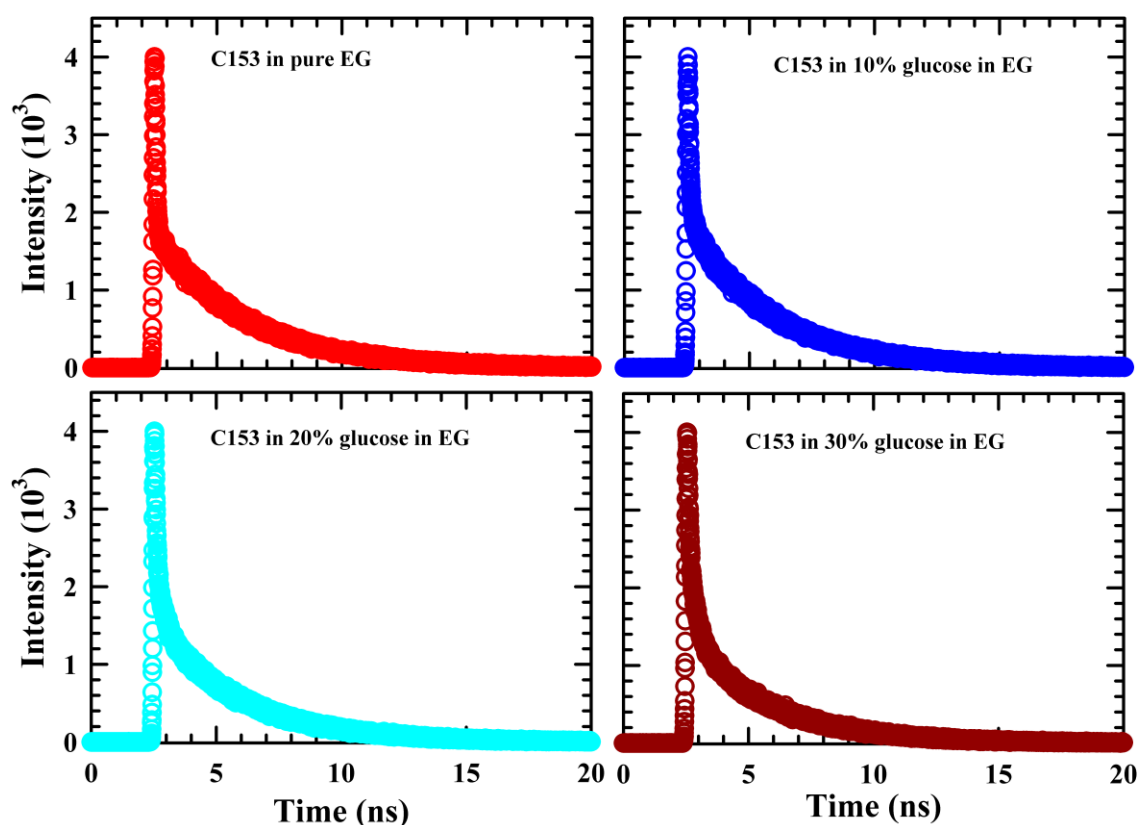
Figure A6.5: Fluorescence lifetime decays of C153 at 440 nm in glucose/EG cryoprotectant mixtures from TCSPC measurement at 293 K. The open symbols with different colour represent glucose concentrations dependent experimental lifetime data. All representations are colour coded.
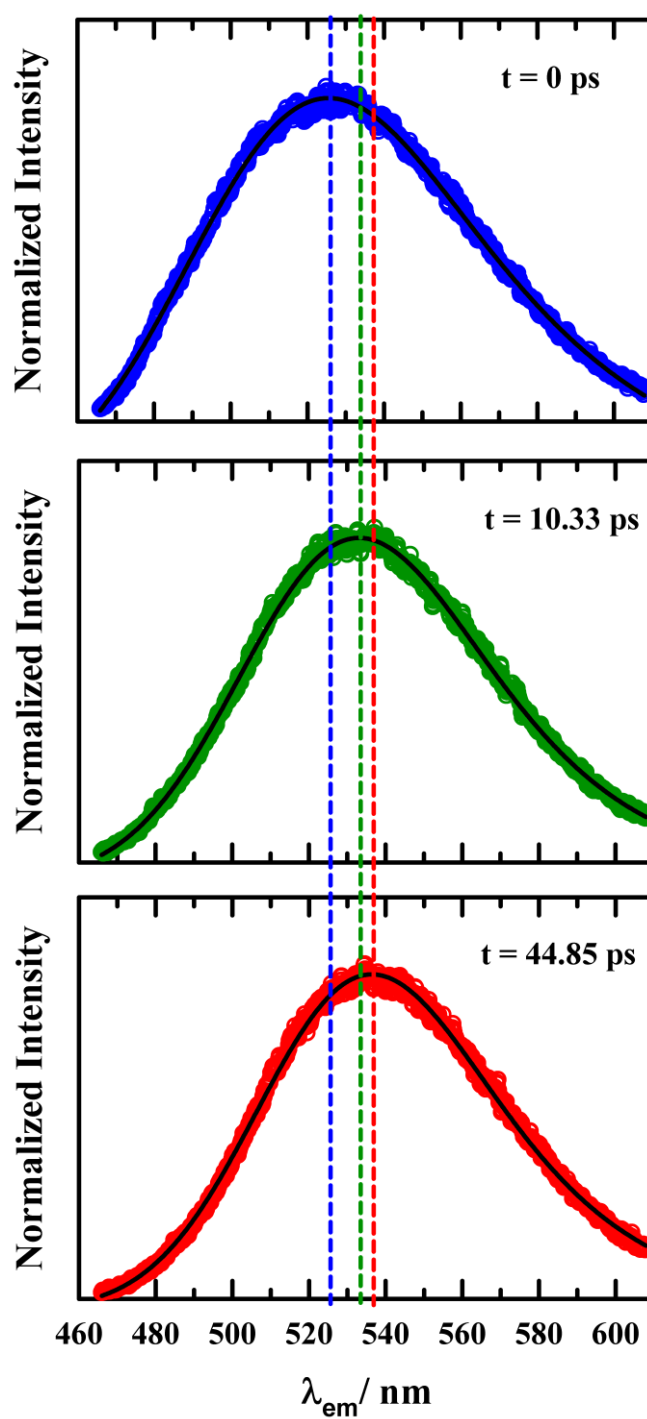
Figure A6.6: Representative TRES from the streak camera data of C153 in pure EG at 293 K. The solid black lines passing through the experimental data represent the log normal fit to the data. Vertical dashed lines are used to indicate the spectral shift over time. All representations are colour-coded.
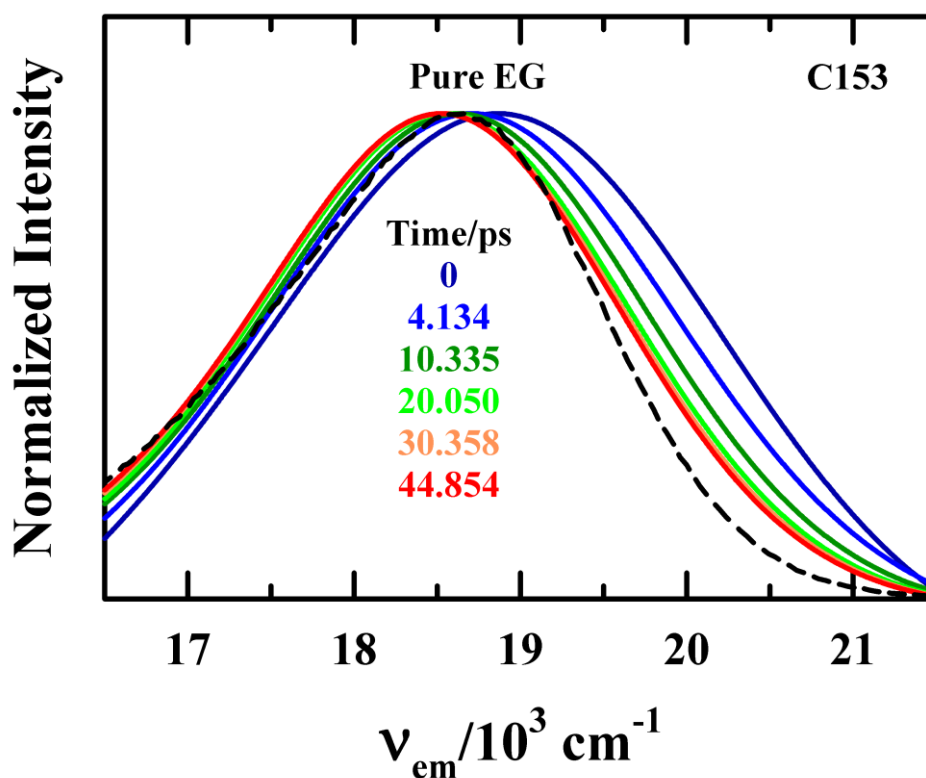
Figure A6.7: Representative time-resolved emission spectra (TRES) of C153 in pure EG at 293 K. The dashed lines in these panels represent the steady-state emission spectra of C153 in pure EG. All representations are colour-coded.

Table A6.8: Temperature dependent calculated translational diffusion time from Stokes-Einstein relation and rotational diffusion time from Stokes-Einstein-Debye relation[66] in glucose/ethylene glycol cryoprotectant mixture.

Stokes-Einstein equation of translational diffusion for spherical particle is as following $D_{trans} = K_B T / C\pi\eta\sigma$ where K_B, T, C, η and σ are denoted Boltzmann constant, temperature, coupling constant for slip (2) and stick (3) condition, viscosity and diameter of species respectively. Relation between D_{trans} and translational diffusion time τ_{trans} is $\tau_{trans} = \sigma^2/D_{trans} = \sigma^3 C\pi\eta/K_B T$ $\sigma_{EG} = 4.876$ Å, $\sigma_{Glucose} = 6.63$ Å, $\sigma_{OH} = 3.129$ Å.[66,79]

Stokes-Einstein-Debye equation for rotational diffusion time τ_{rot} with volume V, coupling constant C and molecular shape factor f is $\tau_{rot} = 3V\eta f C/K_B T$. At stick limiting condition $C = 1$, shape factor $f = 1.01$ for ethylene glycol (prolate) and $f = 1.03$ for glucose (oblate), and V = molecular volume= 60.73 Å³ (ethylene glycol), 152 Å³ (glucose) and 16.03 Å³.[66,79,80]

wt% of glucose	η/cP	Species	τ_{trans}/ps stick	τ_{trans}/ps slip	τ_{rot}/ps stick
Pure EG	19.29	EG	5210	3473	878
		OH	1376	917	23
10	38.78	EG	10473	6983	1765
		glucose	26330	17553	5505
		OH	2767	1845	46
20	79.81	EG	21555	14370	3632
		glucose	54187	36125	9271
		OH	5695	3796	95
30	210.91	EG	56963	37975	9598
		glucose	143199	95466	24499
		OH	15050	10033	254
40	641.10	EG	173149	115432	29175
		glucose	4532818	290187	74469
		OH	45749	30499	772
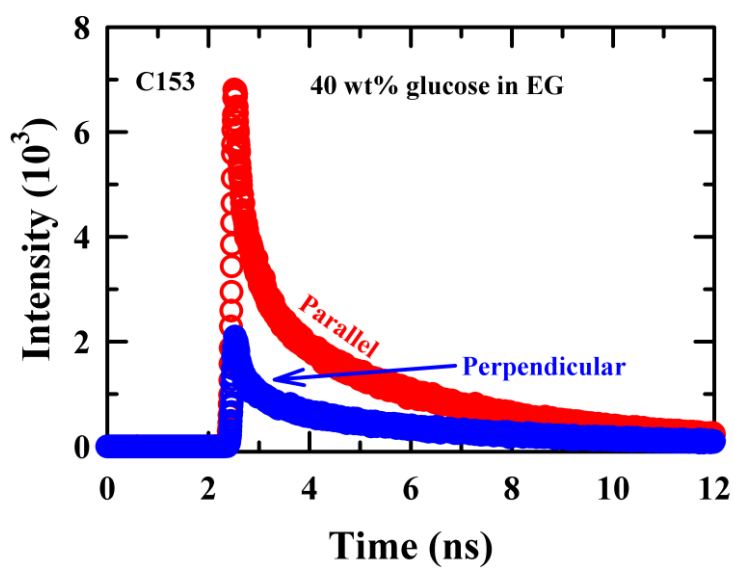
Figure A6.9: Representative Parallel and perpendicular fluorescence intensity decay of C153 in 40 wt% glucose/ethylene glycol cryoprotectant mixture at 293 K. All representations are color-coded.
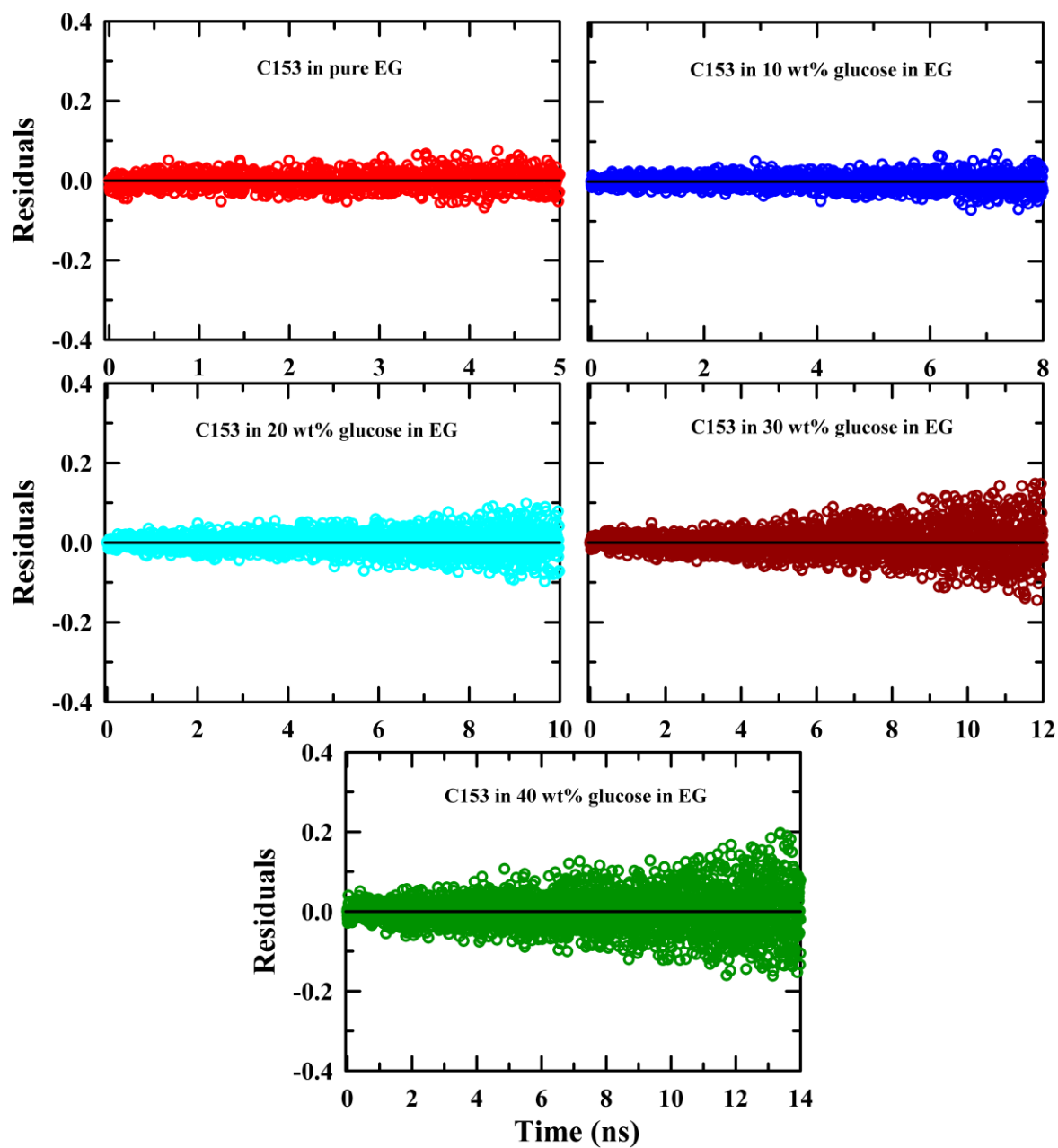
Figure A6.10: Residuals of TRF anisotropy $r(t)$ decays of C153 in glucose/EG cryoprotectant mixtures with glucose concentration 0 (red), 10 wt% (blue), 20 wt% (cyan), 30 wt% (dark red), and 40 wt% (dark green) at 293 K. Residuals from fit are shown by circle. All representations are colour-coded.

Table A6.11: Stokes-Einstein-Debye (SED) stick rotational diffusion time of single molecular rotation, is $\tau_r = 6V\eta C f_S/l(l+1)K_BT$ with l is rank of experimental method ($l = 2$ for fluorescence measurement), V and f_s are the volume and shape factor of solute respectively, C is the coupling parameter of the solute with the surrounding environment. k_B and T are Boltzmann constant and temperature in Kelvin respectively. Modified SED equation for fluorescence measurement with $l = 2$, $\tau_r^{(2)} = V\eta C f_S/K_BT$. We have used V = 246 Å³, f_s = 1.71, $C = 0.24$ (slip) and 1 (stick) for C153[64]. Estimated single molecular rotation time of C153 probe in pure EG and glucose/EG cryoprotectant mixtures are given below at 293K. Longer time scale τ_2^r (ps) estimated from fitting of $r(t)$ decays for both probes are given in same table.

wt% of glucose	η/cP	$\tau_r^{(2)}$/ns stick	$\tau_r^{(2)}$/ns slip	τ_2^r/ns in Exp
0	19.29	2.007	0.481	1.170
10	38.78	4.035	0.968	1.512
20	79.81	8.303	1.993	2.595
30	210.91	21.942	5.566	5.002
40	641.10	66.697	16.007	9

Reference

1   C. Krembs, H. Eicken, K. Junge and J. W. Deming, *Deep-Sea Res. I: Oceanogr. Res. Pap.*, 2002, 49, 2163-2181.

2   M. S. Clark and M. R. Worland, *J Comp Physiol B*, 2008, **178**, 917–933.

3   K. B. Storey and J. M. Storey, *Physiol. Rev.*, 2017, **97**, 623–665.

5   J. P. Costanzo, R. E. Lee and P. H. Lortz, *J. exp. Biol*, 1993, **181**, 245–255.

6   O. Kandror, A. Deleon and A. L. Goldberg, *PNAS*, 2002, **99**, 9727–9732.

7   K. B. Storey, *Comp. Biochem. Physiol*, 1997, **117**, 319–326.

8   M. R. Michaud and D. L. Denlinger, *J. Comp. Physiol. B, Biochem. Syst. Environ.*, 2007, **177**, 753–763.

9   S. D. Rowley, W. I. Bensinger, T. A. Gooley and C. Dean Buckner, *Blood*, 1994, **83** 2731–2736.

10   C. Olsson, H. Jansson and J. Swenson, *J. Phys. Chem. B*, 2016, **120**, 4723–4731.

11   Y. Xin, C. Kielar, S. Zhu, C. Sikeler, X. Xu, C. Möser, G. Grundmeier, T. Liedl, A. Heuer-Jungemann, D. M. Smith and A. Keller, *Small*, 2020, **16**, 1905959.

12   B. R. Chief, M. D. Carr, S. L. Guest Editors, M. D. Tan, G. Roger, P. D. Gosden and D. Sc, *Semin. Reprod. Med.*, 2002, **20**, 005–014.

13   P. A. King, M. N. Rosholt and K. B. Storey, *Seasonal changes in plasma membrane glucose transporters enhance cryoprotectant distribution in the f reeze-tolerant wood frog*, 1995, vol. 73.

14   L. Zhang, L. Liu, Y. Qian and Y. Chen, *European Journal of Pharmaceutics and Biopharmaceutics*, 2008, **69**, 750–759.

15   A. P. R. Rodrigues, C. A. Amorim, S. H. F. Costa, M. H. T. Matos, R. R. Santos, C. M. Lucci, S. N. Báo, O. M. Ohashi and J. R. Figueiredo, *Theriogenology*, 2004, **61**, 1009–1024.

16   F. Chauvigné, E. Lubzens and J. Cerdà, *BMC Biotechnol*, , DOI:10.1186/1472-6750-11-34.

17   Y. Q. A'Yun, N. Anita, A. Abinawanto, A. A. Jusuf, A. Awanis, I. Muhiardi and M. A. Rosvita, in *AIP Conference Proceedings*, American Institute of Physics Inc., 2019, vol. 2168.

18   É. C. G. Praxedes, G. L. Lima, A. M. da Silva, L. B. Camos, C. M. P. de Souza, S. Sandy. Moreira, M. F. de Oliveira and A. R. Silva, *Reprod. Dom. Anim.*, 2020, **55**, 154–161.

19   M. De, L. Reyes, L. Saenz, L. Lapierre, J. Crosby, C. Barros and M. De Los Reyes, *Vet. Rec.*, 2002, **151**, 477–480.

20   L. L. Kuleshova, D. R. Macfarlane, A. O. Trounson and J. M. Shaw, *Cryobiology*, 1999, **38**, 119–130.

21   D. C. C. Brito, S. F. S. Domingues, A. P. R. Rodrigues, J. R. Figueiredo, R. R. Santos and J. C. Pieczarka, *Cryobiology*, 2018, **83**, 97–99.

22   R. R. Santos, T. Tharasanit, J. R. Figueiredo, T. Van Haeften and R. Van Den Hurk, *Cell Tissue Res.*, 2006, **325**, 523–531.

23   M. T. Cicerone and C. L. Soles, *Biophys. J.*, 2004, **86**, 3836–3845.

24   A. M. da Silva, L. G. P. Bezerra, E. C. G. Praxedes, S. S. J. Moreira, C. M. P. de Souza, M. F. de Oliveira, A. F. Pereira, P. Comizzoli and A. R. Silva, *Cryobiology*, 2019, **91**, 53–60.

25   G. Vajta and Z. P. Nagy, *Reprod. Biomed. Online*, 2006, **12**, 779–796.

26   G. M. Fahy and B. Wowk, *Methods Mol. Biol.*, 2015, **1257**, 21–82.

27   G. D. Elliott, S. Wang and B. J. Fuller, *Cryobiology*, 2017, **76**, 74–91.

28   J. J. Towey, A. K. Soper and L. Dougan, *Faraday Discuss.*, 2013, **167**, 159–176.

29   S. D. Allison, B. Chang, T. W. Randolph and J. F. Carpenter, *Arch. Biochem. Biophys.*, 1999, **365**, 289–298.

30   N. Nandi, K. Bhattacharyya and B. Bagchi, *Chem. Rev.*, 2000, **100**, 2013–2045.

31   D. K. Sasmal, S. Ghosh, A. K. Das and K. Bhattacharyya, *Langmuir*, 2013, **29**, 2289–2298.

32   S. K. Pal and A. H. Zewail, *Chem. Rev.*, 2004, **104**, 2099–2123.

33   S. Bandyopadhyay, S. Chakraborty, S. Balasubramanian and B. Bagchi, *J. Am. Chem. Soc.*, 2005, **127**, 4071–4075.

34   S. Pal, P. K. Maiti, B. Bagchi and J. T. Hynes, *J. Phys. Chem. B*, 2006, **110**, 26396–26402.

35   H. Chosrowjan, S. Taniguchi and F. Tanaka, *FEBS J.*, 2015, **282**, 3003–3015.

36   I. H. M. van Stokkum, B. Gobets, T. Gensch, F. van Mourik, K. J. Hellingwerf, R. van Grondelle and J. T. M. Kennis, *Photochem. Photobiol.*, 2006, **82**, 380–388.

37   K. Takeda, K. Murata and S. Yamashita, *J. Non-Cryst. Solids*, 1998, **231**, 273–279.

38   C. A. Angell and D. L. Smlth, *J. Phys. Chem.*, 1982, **86**, 3845–3852.

39   A. Simperler, A. Kornherr, R. Chopra, P. A. Bonnet, W. Jones, W. D. S. Motherwell and G. Zifferer, *J. Phys. Chem. B*, 2006, **110**, 19678–19684.

40   D. Maji, N. C. Maity and R. Biswas, *Theor. Chem. Acc.*, 2023, **142**, 1–15.

41   M. L. Horng, J. A. Gardecki, A. Papazyan and M. Maroncelli, *J. Phys. Chem.*, 1995, **99**, 17311–17337.

42 X. X. Zhang, M. Liang, J. Hunger, R. Buchner and M. Maroncelli, *J. Phys. Chem. B*, 2013, **117**, 15356–15368.

43 B. Guchhait, S. Das, S. Daschakraborty and R. Biswas, *J. Chem. Phys.*, 2014, **140**, 104514.

44 E. Tarif, J. Mondal and R. Biswas, *J. Phys. Chem. B*, 2019, **123**, 9378–9387.

45 K. Sahu, S. K. Mondal, S. Ghosh and K. Bhattacharyya, *Bull. Chem. Soc. Jpn.*, 2007, **80**, 1033–1043.

46 B. Guchhait, R. Biswas and P. K. Ghorai, *J. Phys. Chem. B*, 2013, **117**, 3345–3361.

47 P. Dutta, P. Sen, A. Halder, S. Mukherjee, S. Sen and K. Bhattacharyya, *Chem. Phys. Lett.*, 2003, **377**, 229–235.

48 K. Kumbhakar, E. Tarif, K. Mukherjee and R. Biswas, *J. Mol. Liq.*, 2019, **290**, 111225.

49 R. Karmakar and A. Samanta, *J. Phys. Chem. A*, 2002, **106**, 4447–4452.

50 J. Mondal, N. C. Maity and R. Biswas, *J. Chem. Sci.*, 2023, **135**, 1–12.

51 B. Guchhait and R. Biswas, *J. Chem. Phys.*, 2013, **138**, 114909.

52 T. Pradhan and R. Biswas, *J. Phys. Chem. A*, 2007, **111**, 11514–11523.

53 T. Pradhan, H. Al, R. Gazi, B. Guchhait and R. Biswas, *J. Chem. Sci*, 2012, **124**, 355–373.

54 N. Sarma, J. M. Borah, S. Mahiuddin, H. A. R. Gazi, B. Guchhait and R. Biswas, *J. Phys. Chem. B*, 2011, **115**, 9040–9049.

55 J. R. Lakowicz, *Principles of Fluorescence Spectroscopy*, Springer, New York, 3rd edn., 2006.

56 M. L. Horng, J. A. Gardecki and M. Maroncelli, *J. Phys. Chem. A*, 1997, **101**, 1030–1047.

57 S. Koley, H. Kaur and S. Ghosh, *Phys. Chem. Chem. Phys.*, 2014, **16**, 22352–22363.

58 R. Biswas, J. E. Lewis and M. Maroncelli, *Chem. Phys. Lett.*, 1999, **310**, 485–494.

59 J. E. Lewis, R. Biswas, A. G. Robinson and M. Maroncelli, *J. Phys. Chem. B*, 2001, **105**, 3306–3318.

60 R. Biswas, J. E. Lewis and M. Maroncelli, *Chem. Phys. Lett.*, 1999, **310**, 485–494.

61 S. Dinda, A. Sil, A. Das, E. Tarif and R. Biswas, *J. Mol. Liq.*, 2022, **349**, 118126.

62 B. Guchhait, H. al Rasid Gazi, H. K. Kashyap and R. Biswas, *J. Phys. Chem. B*, 2010, **114**, 5066–5081.

63 R. Karmakar and A. Samanta, *J. Phys. Chem. A*, 2002, **106**, 4447–4452.

64 H. Jin, G. A. Baker, S. Arzhantsev, J. Dong and M. Maroncelli, *J. Phys. Chem. B*, 2007, **111**, 7291–7302.

65   R. S. Fee and M. Maroncelli, *Chem. Phys.*, 1994, **183**, 235–247.

66   Biman Bagchi, *Molecular relaxation in liquids*, Oxford University Press, New York, 2012.

67   B. Bagchi and R. Biswas, *Adv. Chem. Phys.*, 1999, **109**, 207–433.

68   M. D. Ediger, *Annu. Rev. Phys. Chem.*, 2000, **51**, 99–128.

69   W. Huang and R. Richert, *Phil. Mag.*, 2007, **87**, 371–382.

70   K. Mukherjee, S. Das, E. Tarif, A. Barman and R. Biswas, *J. Chem. Phys.*, 2018, 149,124501.

71   K. Mukherjee, E. Tarif, A. Barman and R. Biswas, *Fluid Phase Equilib*, 2017, **448**, 22–29.

72   S. Indra and R. Biswas, *J. Phys. Chem. B*, 2016, **120**, 11214–11228.

73   E. Tarif, K. Mukherjee, A. Barman and R. Biswas, *J. Chem. Sci.*, 2019, **131**, 1–12.

74   E. Tarif, K. Mukherjee, K. Kumbhakar, A. Barman and R. Biswas, *J. Chem. Phys.*, 2019, **151**, 154902.

75   M. D. Ediger, C. A. Angell and S. R. Nagel, *J. Phys. Chem.*, 1996, **100**, 13200–13212.

76   C. A. Angell, *J. Chem. Phys.*, 1967, **46**, 4673–4679.

77   H. Sillescu, *J. Non-Cryst. Solids*, 1999, **243**, 81–108.

78   I. Chang, F. Fujara, B. Geil, G. Heuberger, T. Mangel and H. Sillescu, *J. Non-Cryst. Solids*, 1994, **172**, 248–255.

79   J. T. Edward, *J. Chem. Educ.*, 1970, **47**, 261–270.

80   Y. H. Zhao, M. H. Abraham and A. M. Zissimos, *J. Orga. Chem.*, 2003, **68**, 7368–7373.

Chapter 7

Unraveling the Molecular-Level Insight into the Structure and Dynamics of Glycerol-Disaccharides Dihydrate Binary Mixtures: Integrating Experimental Observations with Molecular Dynamics Simulations

7.1. Introduction

Living organisms, such as bacteria, algae, fungi, protozoa, plants, fish, and vertebrates, have developed unique strategies to survive in extremely cold environments.[1–6] These organisms can synthesize various anti-freezing chemicals, such as sugars (glucose, trehalose, and sucrose)[7–9] and polyols (ethylene glycol and glycerol)[10,11], in high concentrations to prevent ice nucleation in their intra and inter-cellular fluids during freezing conditions. This metabolic synthesis of anti-freezing chemicals helps in the survival of various low temperature inhabitants, and the mechanism has been explored for cryopreservation in biotechnology and food preservation technology.[12–16] The chemicals used for cryopreservation, also known as cryoprotective agents (CPA) or cryoprotectants[17], have important characteristics such as being eco-friendly, biocompatible, biodegradable, low in toxicity, derived from biological sources, and easily available.[18,19] Trehalose (TRE) and sucrose (SUC), which are the most abundant bio-precursor from plant sources, are bio-degradable, biocompatible, and easily available, making them an effective CPA for cryopreservation technology.[16,20–27] Glycerol (GL), which is a trihydroxy alcohol with a 1,2,3-position of the propylene group, is a highly effective glass-former[28–31] material and CPA[22,32,33]. It has been observed that even biomolecules dissolved in glycerol retain their native structure.[22,32] Moreover, this triol molecule is commonly utilized as a solvent in green chemistry and is also known as green solvent due to its low toxicity, and excellent solubility for various organic solutes.[34–38] It has been discovered that utilizing a mixture of cryoprotectants can significantly enhance the efficiency of cryopreservation. The cryopreservation efficiency of a mixture containing two or three cryoprotectants surpasses that of a single cryoprotectant.[39,40] Effective cryoprotectant mixtures include trehalose/glycerol[22], glucose/glycerol[41], trehalose/ethylene glycol[42], glucose/ethylene glycol[43], sucrose/ethylene glycol[27], ethylene glycol/dimethyl sulfoxide[44], among others.

In sub-zero temperatures, the formation of ice crystals, both within and outside cells, tissues, organs, and other biological systems, can lead to dehydration and cold-related damage. The CPAs play a crucial role in mitigating ice crystal formation and reducing cold-induced damage.[8,11] Vitrification is a cooling process that transforms liquid to a glassy state without any crystallisation[45–47], resulting in higher glass transition temperature ($\sim T_g$) when CPAs are present[48,49]. The efficiency of the vitrification process is more pronounced in CPA concentrations compared to traditional cryoprotectants.[49] CPAs are known for their high propensity for hydrogen bonding (H-bonding) with the ability to both donate and accept H-bonds.[50,51] Cryoprotectant solutions in water enable various H-bonding interactions, including intra and inter-species interactions.[52–54] Additionally, cryoprotectant content larger number of H-bonds donor and acceptor site, exhibits intramolecular H-bonding within cryoprotectant.[53] The T_g of a cryopreservation system is influenced by the extent of inter and intramolecular H-bonding of CPAs, making the H-bonding properties of CPA mixtures crucial in cryogenic preservation.

CPA breaks the extensive intermolecular H-bonding among water molecules in extracellular fluid, and decreases tetrahedral H-bonding among water molecules in extra-cellular fluid at subzero temperatures, preventing water to ice transformation.[26] In contrast, intracellular CPAs, found within cells, facilitate the exclusion of bulk water from organless bio-entities, preventing hydrophobic hydration and reducing ice induced damage.[24,33,55]

In the present study, three cryoprotectants were chosen: trehalose and sucrose as the extra-cellular CPA[24,56,57] and glycerol as an intracellular CPA[27]. High T_g of natural CPAs like trehalose (368 K)[58] and sucrose (319 K)[58], are commonly employed in cryopreservation, which makes them highly effective for this purpose. Glycerol, widely used in biotechnology and pharmaceutical technology, has a lower T_g (190 K)[59] and is a suitable candidate for subzero stabilization. Combining these two types of CPAs (extracellular CPA and intracellular CPA) with varying concentrations allows for the attainment of desired T_g values and enables the development of cryopreservation techniques with varying levels of efficiency.

While the interaction and dynamics of neat glycerol[60], glycerol/water[61–64], disaccharide/water[26,53,65,66], and disaccharide/glycerol[25,53,67,68] systems have been studied via dielectric relaxation spectroscopy (DRS), there remains a need for a systematic investigation into the interaction, dynamics, and solution structure of disaccharides dihydrate/glycerol cryoprotectant mixtures. Earlier studies on disaccharides/glycerol cryoprotectant mixtures

have offered insight into the potential application of this binary mixture in cryopreservation technology.[22,67] Furthermore, there is interest in exploring the effect and structure of water in disaccharides dihydrate/glycerol systems, focusing on solution structure, dynamics, hydrogen bond network, and tetrahedral order parameter of water molecules. These explorations are carried out using differential scanning calorimetry (DSC), dynamic light scattering (DLS), DRS measurements, and molecular dynamics simulations (MD-simulations). In this study, we used disaccharides as trehalose and sucrose with two water molecules per disaccharide at a concentration of 20 wt% in glycerol, within the temperature range of 298K to 333K for all experimental measurements. Experimental studies involve estimation of glass transition temperatures (T_g), measurements of disaccharide-dependent cluster size, dielectric properties, and examination of coupling of the measured relaxation rates or timescales with medium viscosity. Simulations, on the other hand, provides information on radial distribution functions (RDFs), coordination number (CN), surface density functions (SDFs) around both disaccharides, solution H-bond structure, and water-water angle distributions ($P(\theta)$), tetrahedral order parameter distributions ($P(Q)$), and H-bonding relaxation timescales. Both experiments and simulations jointly uncover the impact of water on disaccharides in these multicomponent cryoprotectant systems.

7.2 Experimental Details

7.2.1 Materials and Sample Preparation

Glycerol (≥99%), D-(+)-trehalose dihydrate (≥99%), and sucrose (≥99.5%) were purchased from Sigma Aldrich and used without further purification. The structures of these molecules are shown in Scheme 7.1. Millipore water was used in the experiment. Three different solutions were prepared: trehalose dihydrate + glycerol (TRE_GL_W), sucrose dehydrate + glycerol (SUC_GL_W), and glycerol + water (GL_W). Each of these solutions contained 20 wt% of disaccharide dihydrate in glycerol. For water + glycerol solution, the amount of water mixed in glycerol was precisely equivalent to that present in disaccharides dihydrate (~ 1.9 wt% of water). All components were mixed in the glass container, and a Teflon-coated magnetic bar was introduced before sealing the container airtight with care using Teflon and parafilm wrap. The sealed glass container was then heated using a magnetic stirrer/hot plate at a specific temperature: 333 K for TRE_GL_W, 363 K for SUC_GL_W, and 323 K for GL_W. The heating process lasted for 2-3 hours at 600 rpm within an oil bath. This resulted in the formation of

colorless and transparent solutions without any visible solute crystals. Subsequently, the prepared solutions were then cooled to room temperature before performing DSC, DLS, and DRS experiments.
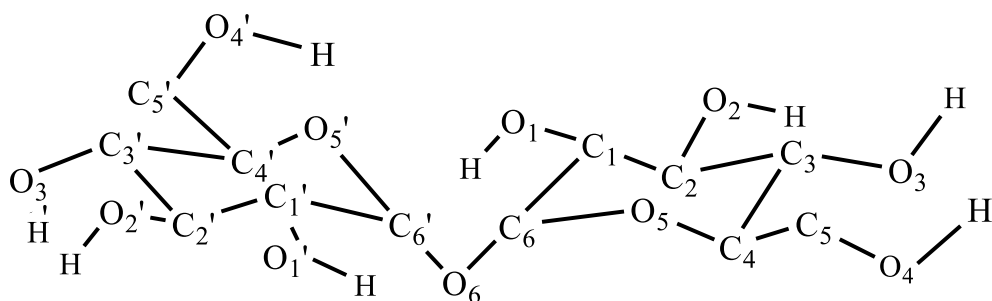
Trehalose
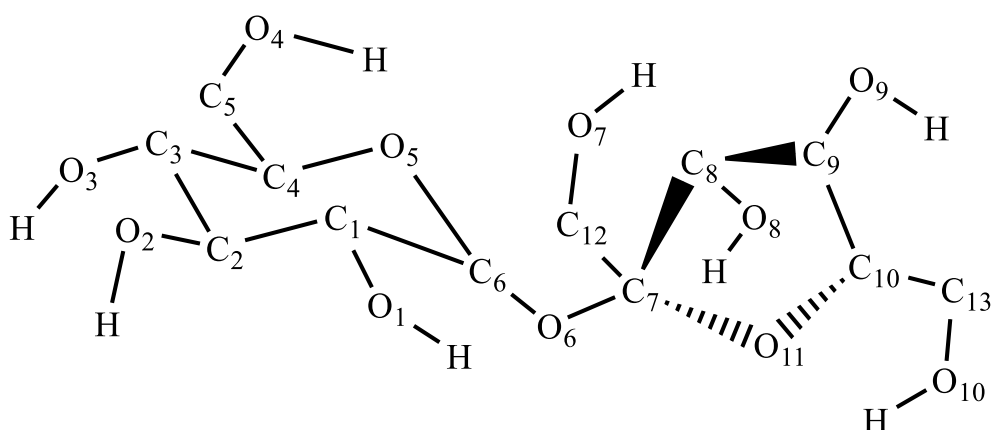
Sucrose
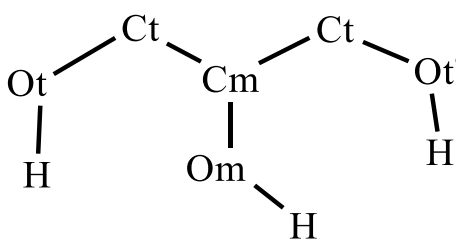
Glycerol

Scheme 7.1: Molecular structures of trehalose, sucrose and glycerol. In this representation, all carbon atoms are depicted as SP^3 hybridized, and hydrogen atoms attached to these carbon atoms have been omitted for clarity to enhance visualization.

7.2.2 Density, Refractive Index and Viscosity Measurements

Temperature dependent measurements of density (ρ), refractive index (n_D), and viscosity (η) in the experimental solutions were detailed in Chapter 3. Data from these measurements at various temperatures are summarized in Table A7.1 (Appendix).

7.2.3 Differential Scanning Calorimetry (DSC), and Dynamic Light Scattering (DLS) Measurements

Procedures regarding differential scanning calorimetry (DSC) and dynamic light scattering (DLS) measurements were described in detail already in Chapter 3 and Chapter 6, respectively. DSC measurements of cryoprotectant systems were conducted with a fixed heat flow rate 10 K/min.

7.2.4 Dielectric Relaxation Spectroscopy (DRS): Data Collection and Analysis

Three dielectric set-ups[69] were employed to measure the dielectric relaxation (DR) of the liquid samples. The first setup involved an E4990A impedance analyzer paired with a 16452A liquid test fixture, which covered low-frequency measurements spanning from 20 Hz to 10 MHz. For the intermediate frequency range, 10 MHz to 500 MHz, an E4991B impedance analyzer with open-ended high temperatures probe (N1501A) was used. Finally, for high-frequency measurements extending 200 MHz to 50 GHz, the N5235B PNA-L network analyzer was utilized in conjunction with an open-ended coaxial probe kit (performance probe N1501A). T the measurement protocols and data analysis procedures remained consistent with those discussed in Chapter 2. Additional details regarding the DRS measurements can be found in the references.[69–73] Temperature dependent DRS experiments were performed at the temperature range of 298K to 333K.

7.2.5 Simulation Details

We utilized the standard equilibrium molecular dynamics simulation technique to investigate various systems using GROMACS-2021.3[74], including five systems pure GL, GL-W, TRE_GL_W, SUC_GL_W, and pure water. For all simulations, we employed the non-polarizable three-point SPC/E model[75] to represent water, both in the solutions and in pure water. The OPLS-AA parameters for glycerol and disaccharides were generated using the LigParGen web server with CM1A (Atomic Charge Model-I) charge, which was scaled by a factor of 1.14 for neutral molecules.[76–79] Table A7.2 (in Appendix) summarizes the number of

species used in multicomponent mixtures and two neat systems considered in our simulation study.

Functional form of the model potential is as follows:

$$E_{ij} = \sum_{bonds} K_r(r - r_{eq})^2 + \sum_{angles} K_\theta(\theta - \theta_{eq})^2 + c_0 + c_1\{1 + \cos(\phi)\} + c_2\{1 - \cos(2\phi)\}$$

$$+c_3\{1 + \cos(3\phi)\} + \sum_{i=1}^{N-1}\sum_{j>i}^{N}\left\{4\epsilon_{ij}\left[\left(\frac{\sigma_{ij}}{r_{ij}}\right)^{12} - \left(\frac{\sigma_{ij}}{r_{ij}}\right)^{6}\right] + \frac{q_i q_j}{4\pi\epsilon_0 r_{ij}}\right\}. \tag{7.1}$$

In Eq. 8.1, K_r and K_θ are force constants for bond stretching and angle bending, respectively, r_{eq} and θ_{eq} denote the equilibrium bond length and angle value. ϕ is denoted torsional angle with the Fourier coefficients c_0, c_1, c_2, and c_4. Position and charge of an atom are described by r, and q, respectively. The van der Waals parameters are described by σ and ε. Note that the non-bonded and electrostatic interactions were represented by the Lennard-Jones (LJ) potential and the Coulomb equation, respectively.

To generate the initial configurations of molecules, we utilized the PACKMOL software[80] to place them within a cubic box. The configurations were then subjected to energy minimization using the steepest-descent algorithm. Next, we performed a NVT equilibration for 10 ns at 400 K. The annealing process was performed, starting at 400 K and decreasing at a rate of 0.04 K/ps until the temperature reached 333 K and every 20 K the system was equilibrated for 1 ns. For all simulated temperatures, we used the equilibration protocol mentioned above. Afterward, a final NPT equilibration was conducted for 10 ns. The density values obtained from this equilibration were in good agreement with experimental data. An MD production run of 200 ns long was conducted for each system within the NPT ensemble, and the trajectories were saved with a time gap of 1 ps. During the NPT equilibration and production run, we maintained the temperature using the V-rescale thermostat[81] with a time constant of 0.5 ps, and the pressure at 1 bar using the Parrinello-Rahman barostat[82] with a time constant of 2 ps. Bonded and non-bonded interactions were truncated at a cut-off distance of 1.2 nm. Electrostatic interactions were handled using the Particle Mesh Ewald (PME)[83,84] method. Simulation employed the Leapfrog algorithm with a time step of 1 fs to solve the equations of motion. Linear Constraint Solver (LINCS)[85] algorithm was used to constrain the bonds involving hydrogens.

7.2.5.1 Radial Distribution Function (RDF)

Spatial correlations were followed via calculating the radial distribution functions (RDFs), $g_{ij}(r)$:

$$g_{ij}(r) = \frac{\langle \rho_j(r) \rangle}{\rho_j^{ave}} = \frac{1}{N_i \rho_j^{ave}} \sum_i^{N_i} \sum_j^{N_j} \frac{\partial(r_{ij} - r)}{4\pi r^2} \tag{7.2}$$

where $\langle \rho_j(r) \rangle$ indicates density of j type particles around i type at a distance r and ρ_j^{ave} is the average number density of j type particles.

7.2.5.2 Hydrogen Bond Analysis

The H-bonds between water molecules are calculated following protocol[86,87]: a) the distance between the donor and the acceptor oxygen atom is less than 0.35 nm, b) $\angle DHA \geq 140°$, where D, H, A denote to donor, hydrogen, and acceptor, respectively.

Water-water continuous and structural H-bond autocorrelation function, ($S_{HB}(t)$ and $C_{HB}(t)$ respectively) were calculated by using the formula [88–91]

$$S_{HB}(t) = \langle h(0)H(t) \rangle / \langle h(0)^2 \rangle \tag{7.3}$$

$$C_{HB}(t) = \langle h(0)h(t) \rangle / \langle h(0)^2 \rangle , \tag{7.4}$$

where $H(t)$ is a variable which denotes presence or absence of H-bonds between pair of doner acceptor site. $H(t) = 1$ if a tagged donor-acceptor pair for which $h(0)$ is calculated, is hydrogen bonded for a time span t, otherwise zero. Again $h(t) = 1$ if a tagged donor-acceptor pair is hydrogen bonded at time t, otherwise zero. Average H-bond lifetime in each case was calculated via time integration of $S_{HB}(t)$ and $C_{HB}(t)$ as follows:

$$\langle \tau_{HB}^S \rangle = \int_0^\infty S_{HB}(t)dt \text{ and } \langle \tau_{HB}^C \rangle = \int_0^\infty C_{HB}(t)dt$$

7.2.5.3 Tetrahedral Order Parameter (Q) Analysis

The tetrahedral order parameter (Q) defined as follows[92]:

$$Q_i = 1 - \frac{3}{8} \sum_{j=1}^3 \sum_{k=j+1}^4 (cos\theta_{ijk} + 1/3)^2 \text{ and } \langle Q \rangle = \frac{1}{n_{water}} \sum_i Q_i, \tag{7.5}$$

where Q_i is the tetrahedral order parameter of the ith water, θ_{ijk}- the angle subtended by each pair (designated by j and k) of the nearest four water molecules on the central i[th] water molecule. For a random and uniform distribution of these angles, $Q = 0$; for a perfect tetrahedral structure, on the other hand, $Q = 1$.

7.3 Result and Discussion

7.3.1 DSC Measurement: Glass Transition Temperature Modification of Cryoprotectant Mixtures

DSC thermograms for pure GL and cryoprotectant mixtures are displayed in the left panel of Figure 7.1 , which includes GL-W, TRE_GL_W, SUC_GL_W systems within the temperature range $170 \leq T/\text{K} \leq 210$. Note, our DSC results of pure GL ($T_g = 193$) is well corroborated with the previously reported T_g (190 K)[59], providing strong support for the present findings. It was observed that the addition of 20 wt % trehalose dihydrate or an accurately measured amount of sucrose+water to glycerol resulted in an increase in T_g. However, this increase of T_g in disaccharide dihydrate/glycerol system was small. To further investigate this phenomenon, we conducted additional experiments involving GL-W system. Interestingly, introduction of water into pure GL caused a 4 K reduction of T_g in the GL_W system compared to pure GL. This suggests that the presence of an ultra-amount water decreases T_g and compensates for the T_g increment observed in the disaccharide dehydrate systems. High intermolecular H-bonding tendencies of disaccharide molecules, such as trehalose and sucrose, enhance the number of hydrogen bonds between disaccharide and GL, concurrently reducing the probability of GL-GL intermolecular H-bonding. However, the presence of ultra-small amount of water within disaccharides may interact with both disaccharides and GL, leading to reduced intermolecular interactions between disaccharides and GL molecules. This indicates that water reduces the fragility of the system.

Figure A7.3 (Appendix) represents a scaled Arrhenius plot depicting viscosity values for different types of liquids from Angell et al.[93,94], along with our recent pure GL value. This comparison reveals that the present experimental value for pure GL closely aligns with Angell et al.'s findings. This validation of experiential data provides an opportunity to interpret these values in the context of fragility for current cryoprotectant systems. The right panel of Figure 7.1 depicts that T_g scaled temperature dependent viscosities data for all four systems, exhibit linearity within our experimental temperature range. These data are well described by the following equation, $\eta_T = \eta_0 \exp{(DT_g/T)}$, where D is denoted fragility parameter. Systems

with small D values are generally referred to as 'fragile'.[93] The D values estimated from this fitting are also presented in Figure 7.1(left panel). The D value obtained for pure GL (15.15) is close to the result reported by Angell et al. ($D = 12$)[93]. This similarity allows us to discuss about fragility characteristics of the current cryoprotectant systems. When ultra-small amount of water was introduced into GL, the D value decreases, indicating an increase of fragility. However, the increase of D values in the presence of disaccharides suggests that the disaccharide systems (TRE_GL_W and SUC_GL_W) are less fragile, which is in good agreement with earlier studies of plasticizer-disaccharides mixtures[68,95,96]. Consequently, it becomes evident that the order of glass transition temperature (T_g), TRE_GL_W> SUC_GL_W>GL>GL_W, and this order parallels the fragility sequence. Previous literature supports the cryopreservation efficiency of sugar alcohol with low water content, in the same order as the glass transition temperature order (trehalose > maltose > sucrose > glycerol).[21,94,97] Furthermore, observation of the present work also indicates that multicomponent CPA mixtures elevated the glass transition temperature and reduced the system fragility. The discussion above implies that the extent of glass transition ability may play a pivotal role in determining the cryopreservation capabilities of cryoprotectant mixture in the field of cryopreservation technology. Hence, the variations in glass transition phenomena induced by disaccharides and water highlight the potential to fine-tune the glass transition and fragility characteristics, thereby enhancing the cryopreservation capabilities of cryoprotectant mixtures in the field of cryopreservation industry.
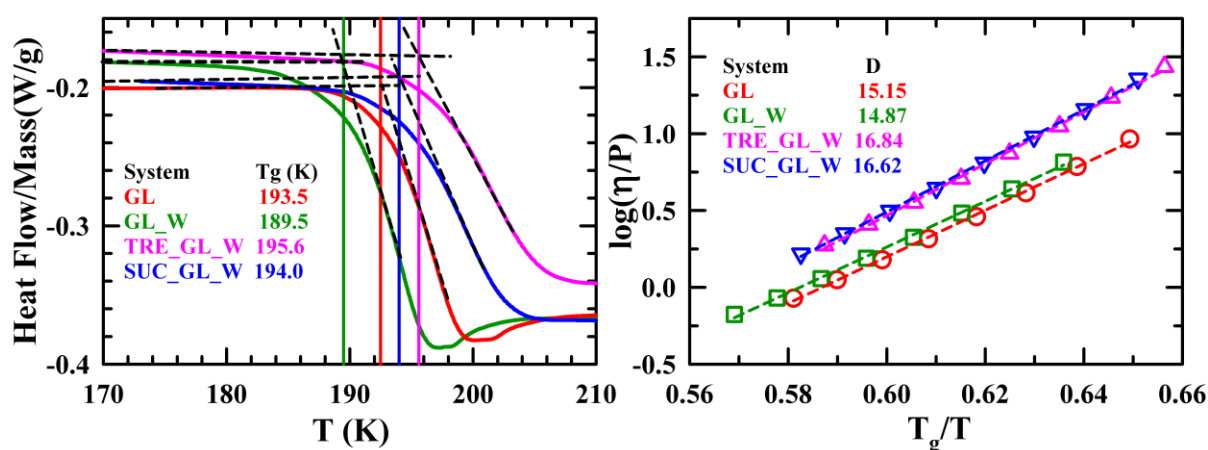
Figure 7.1: DSC thermogram (left panel) and scaled Arrhenius type viscosity values in GL, (red), GL-W (green), TRE_GL_W (pink) and SUC_GL_W (blue). During DSC experiment 10 K/min heating rate was maintained. All are colour coded.

7.3.2. Disaccharides Dependent Cluster Size: Signature of Micro-cluster

Dynamics light scattering (DLS) measurement serves a valuable tool for determining the hydrodynamic diameter (D_h) of macroscopic particles or clusters within the solution mixture. In this context, we conducted DLS experiments to explore how temperature and disaccharides influence the particles or cluster in both disaccharides dihydrate/glycerol systems, as depicted in Figure 7.2 and Table A7.4 (appendix). These experiments revealed that particle size in these two disaccharide systems (TRE_GL_W and SUC_GL_W) depends on the experimental temperature. In an aqueous solution, the diameter of trehalose (~ 1.3 nm) is greater than that of sucrose (~ 1 nm) at 298 K.[98,99] This trend is reflected in both TRE_GL_W and SUC_GL_W systems, whereas the particle size in these cryoprotectant mixtures at 298 K is larger than that of disaccharides in aqueous medium. However, similar-sized entities are observed in both systems at 333 K, as was found in aqueous solutions at 298 K[98,99]. These results indicate that intermolecular interactions between disaccharides molecules in both disaccharide systems are more prominent at lower temperatures and leads to the formation of a dimer complex. This intra-molecular interaction loosens with increasing temperature. A similar phenomenon of intermolecular sugar-sugar clustering (for both mono and di-saccharides) has been observed at higher concentrations (≥30 wt %) of aqueous sugar solutions.[100–103] This suggests that, as temperature decreases, disaccharide molecules exclude the solvent molecules and interact more extensively with each other. Extracellular disaccharide clustering has been observed in the cryopreservation process, highlighting the cryopreserving action of cryoprotectant at cryogenic temperature.[26] Above discussion indicates that TRE_GL_W and SUC_GL_W systems could find applications in cryopreservation. Again, at higher temperatures, the interaction propensity between trehalose molecules decreased, resulting in smaller sized entities. Both trehalose and sucrose display similar particle size distributions at higher temperatures, implying comparable types of intermolecular interactions under these conditions. However, at lower temperatures, the particle size in the TRE_GL_W system is larger and distribution comparatively broader than those for SUC_GL_W system, suggesting that trehalose molecules have a stronger tendency to interact with each other, thereby promoting the formation of larger clusters. This finding hints at the possibility that the cryopreservation efficiency of the TRE_GL_W system may be better than the SUC_GL_W system, which corroborated with earlier DSC measurements.
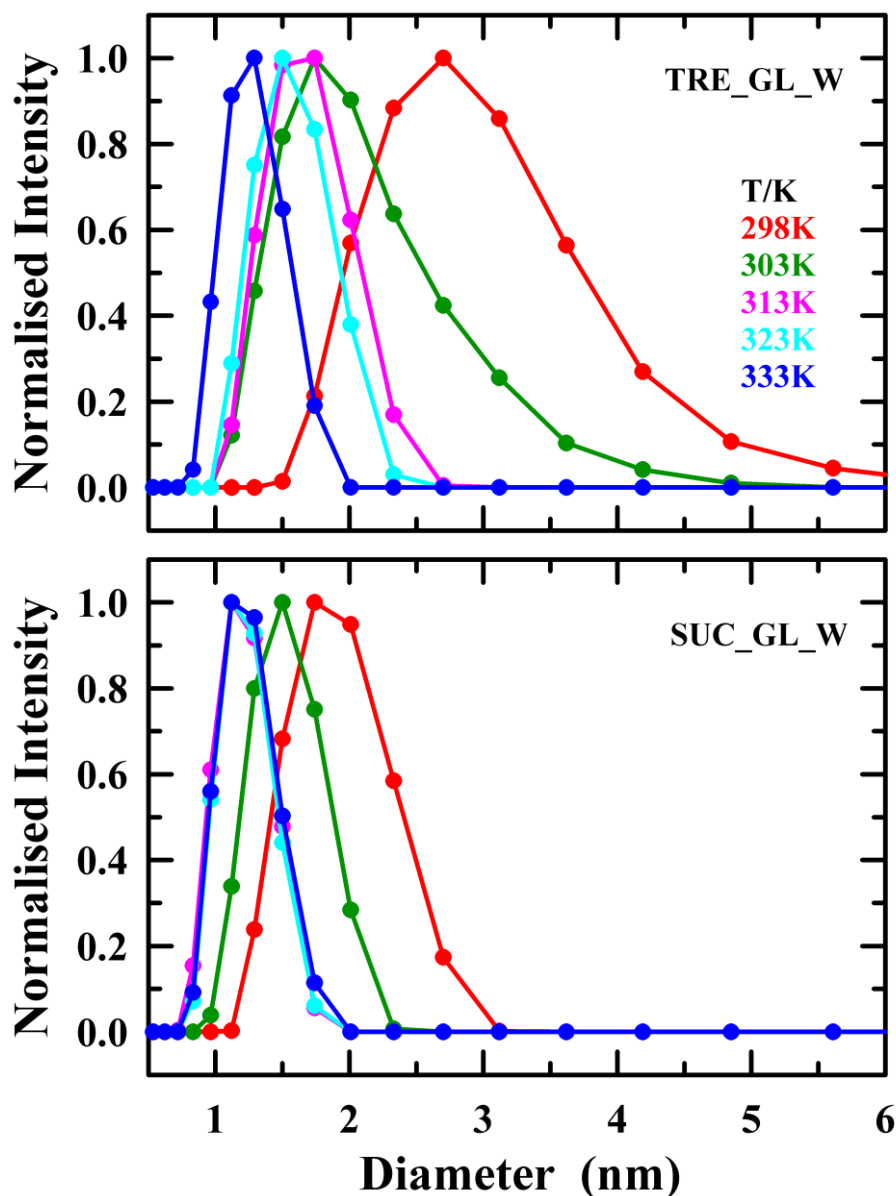
Figure 7.2: Temperature dependent particle size in TRE_GL_W and SUC_GL_W systems from dynamic light scattering (DLS) measurements. All representations are colour-coded.

7.3.3. Dielectric Relaxation Spectroscopy of Cryoprotectant Systems

Frequency dependent dielectric relaxation spectroscopy (DRS) experiments have been performed in pure GL, GL_W, TRE_GL_W, and SUC_GL_W systems. A representative plot of real (ε') and imaginary (ε'') components of complex DR spectra for TRE_GL_W mixture, collected from three different dielectric setups at 298K is shown in Figure A7.5 (Appendix). System dependence real (ε') and imaginary (ε'') components of complex dielectric spectra of four cryoprotectant systems are shown in Figure 7.3. Note that the peak at the dielectric loss

component of complex DR spectra arises within the experimental frequency range (20 Hz to 50 GHz). Residual of DR fitting for four systems, pure GL, GL_W, TRE_GL_W, and SUC_GL_W, are shown in Figure A7.6 and Figure A7.7 (in Appendix), indicating multi-Debye fits required for better fit than 1Cole-Devidsion-Debye and Cole-Cole -Debye models. Temperature dependent complex dielectric spectra of these four systems are shown in Figure 7.4. Dielectric fit parameters for all these systems are given in Table 8.1. With the addition of disaccharides dihydrate in GL, the DR loss peak shifted towards lower frequency region.
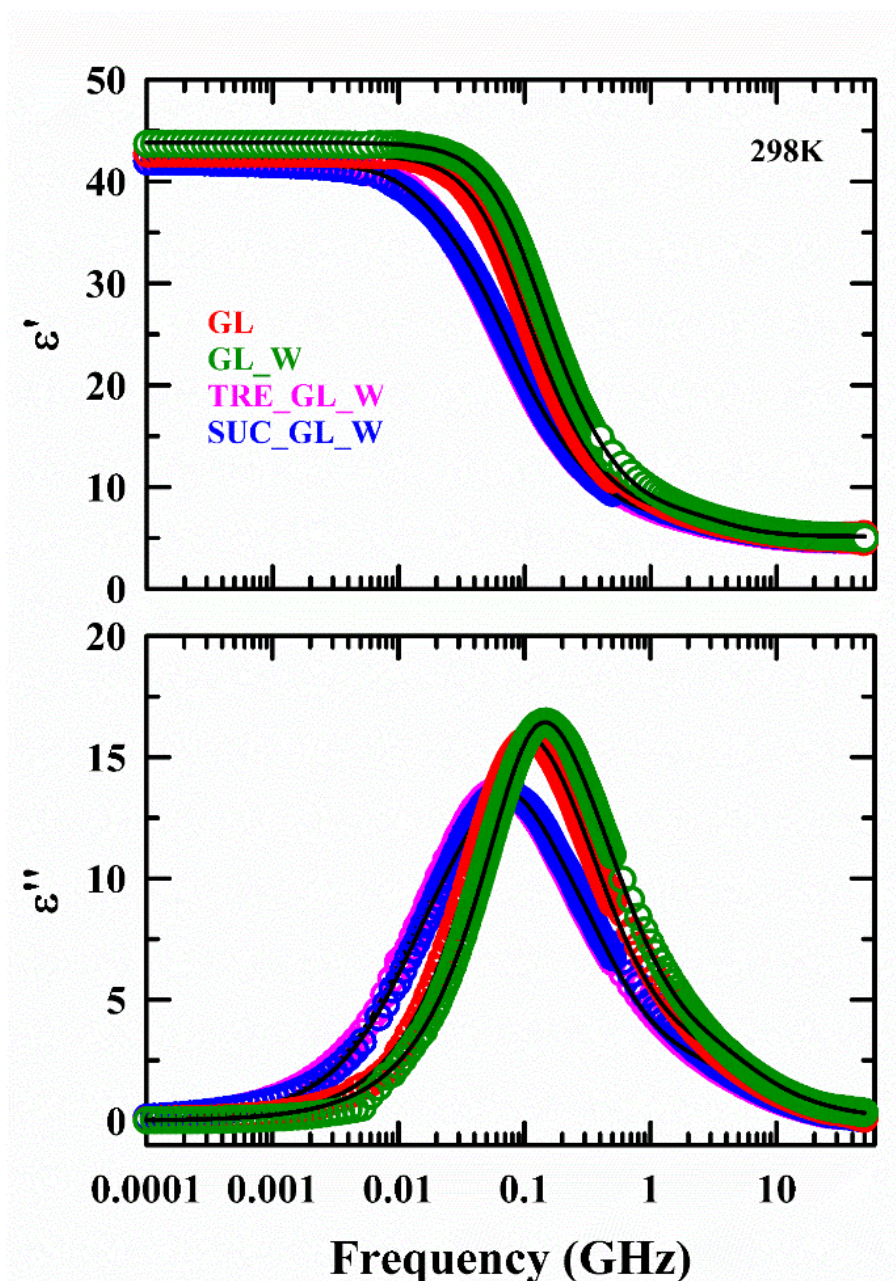
Figure 7.3: Complex DR spectra with real (ε') and imaginary (ε'') component in pure GL, GL_W, TRE_GL_W and SUC_GL_W systems at 298K. The line passing through experimental data points express multi-Debye model fit. All vignettes are colour-coded.
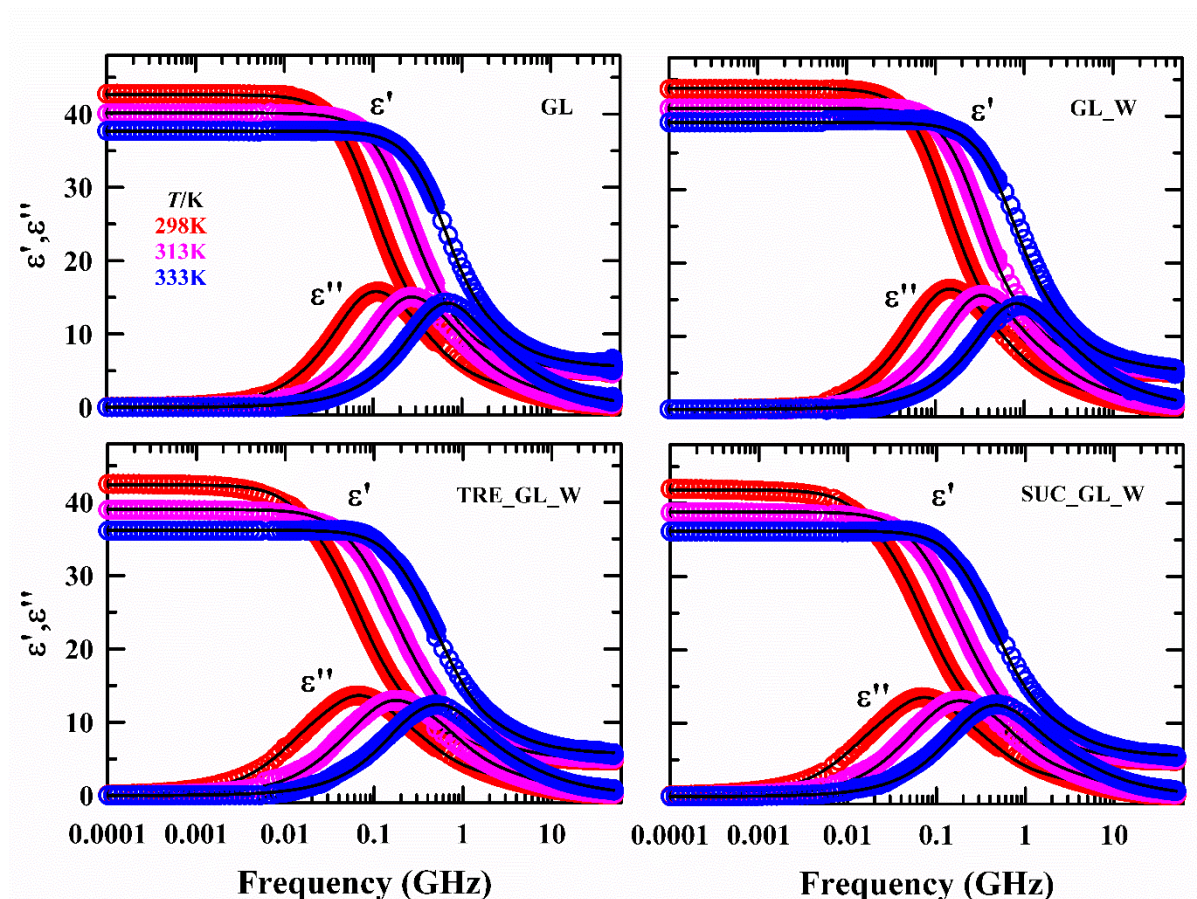
Figure 7.4: Complex DR spectra with real (ε') and imaginary (ε'') component in pure GL, GL_W, TRE_GL_W and SUC_GL_W systems at three representative temperatures. The line passing through experimental data points express multi-Debye model fit. All vignettes are colour-coded.

Table 7.1: 3-Debye/4-Debye fit parameters of measured DR spectra (frequency regime: 4KHz to 50GHz) in pure GL, GL_W, TRE_GL_W, and SUC_GL_W systems at different experimental temperatures.[a] Value present in the third barbet indicates relaxation time corresponding to peak frequency ($\tau_{peak} = 1/2\pi\nu_{peak}$). Number in parenthesis denoted the percentage of dispersion amplitude of a given dispersion step contributing to total dielectric dispersion.

Pure Glycerol (GL)												
T/K	ε_s	$\Delta\varepsilon_1$	τ_1/ps	$\Delta\varepsilon_2$	τ_2/ps	$\Delta\varepsilon_3$	τ_3/ps	$\Delta\varepsilon_4$	τ_4/ps	ε_∞	$\langle\tau\rangle$/ps	χ^2
298	42.63			25.93 (69)	1770	8.90 (24)	560	2.76 (07)	55	5.04	1360 [1449]	0.015
303	41.71			27.16 (74)	1206	7.48 (20)	319	2.31 (06)	41	4.76	959 [1056]	0.015

308	40.92			26.62 (74)	918	7.48 (21)	246	1.98 (05)	32	4.84	733 [785]	0.014
313	40.13			25.31 (72)	687	7.72 (22)	213	2.04 (06)	28	5.06	543 [581]	0.014
318	39.39			27.42 (80)	477	5.23 (15)	88	1.56 (05)	17	5.14	396 [446]	0.024
323	38.50			27.53 (82)	375	4.58 (14)	65	1.24 (04)	14	5.15	317 [354]	0.026
328	38.05			27.10 (83)	304	4.51 (14)	61	1.00 (03)	11	5.44	261 [285]	0.018
333	37.69			26.72 (83)	248	4.6 (14)	45	0.82 (03)	8	5.55	212 [229]	0.023
Glycerol +Water (GL_W)												
298	43.81			27.81 (72)	1277	8.23 (21)	387	2.63 (07)	44	5.14	1004 [1098]	0.010
303	43.11			27.02 (71)	964	8.37 (22)	301	2.51 (07)	37	5.18	753 [780]	0.009
308	42.22			26.56 (72)	742	8.14 (22)	231	2.37 (06)	29	5.15	587 [627]	0.013
313	41.08			29.2 (82)	507	5.05 (14)	94	1.44 (04)	17	5.42	430 [476]	0.038
318	40.32			28.98 (83)	401	5.1 (14)	62	1.04 (03)	11	5.20	341 [379]	0.056
323	39.85			28.15 (81)	322	5.46 (16)	51	0.91 (03)	7		269 [304]	0.044
328	39.45			27.06 (79)	273	6.17 (18)	50	1.12 (03)	7	5.10	225 [250]	0.044
333	39.13			25.88 (76)	216	6.7 (20)	47	1.25 (04)	7	5.30	173 [192]	0.056
Trehalose dihydrate (20%) +Glycerol (80%) (TRE_GL_W)												
298	42.37	8.19 (22)	8547	19.85 (53)	2264	6.91 (18)	563	2.52 (07)	63	4.90	3186 [2491]	0.008
303	40.76	6.23 (18)	6201	18.63 (55)	1651	7.46 (21)	434	2.20 (06)	53	5.24	2118 [1695]	0.017
308	39.93	5.35 (15)	4529	19.54 (56)	1296	7.79 (22)	337	2.34 (07)	40	4.91	1482 [1198]	0.019
313	39.01	3.86 (12)	3298	18.39 (54)	1066	9.49 (28)	300	2.08 (06)	39	5.19	1057 [900]	0.029
318	37.93	14.98 (46)	1145	14.09 (43)	363	2.67 (08)	65	0.83 (03)	19	5.36	688 [633]	0.024
323	37.19	13.96 (44)	855	14.67 (46)	282	2.50 (08)	41	0.51 (02)	10	5.55	509 [463]	0.029
328	36.58	13.16 (43)	684	14.65 (47)	243	2.74 (09)	37	0.4 (01)	8	5.63	412 [375]	0.041

333	36.2	11.23 (37)	589	15.7 (51)	221	3.0 (10)	37	0.52 (02)	8	5.75	334 [321]	0.038
			Sucrose dihydrate (20%) +Glycerol (80%) (SUC_GL_W)									
298	41.84	7.65 (20)	8341	19.75 (54)	2167	7.22 (20)	557	2.26 (06)	54	4.98	2953 [2186]	0.013
303	40.46	5.77 (16)	5981	20.07 (57)	1600	7.4 (21)	419	2.23 (06)	50	4.99	1960 [1522]	0.014
308	39.75	3.97 (12)	4891	19.4 (56)	1388	8.72 (25)	405	2.56 (07)	45	5.10	1468 [1206]	0.017
313	38.81	3.81 (11)	2884	17.65 (53)	1049	9.63 (29)	335	2.52 (07)	40	5.20	973 [871]	0.016
318	37.67	16.06 (50)	1072	13.09 (40)	358	2.67 (08)	51	0.6 (02)	16	5.27	683 [664]	0.025
323	37.25	15.32 (48)	856	13.15 (41)	304	2.96 (09)	45	0.48 (02)	11	5.34	539 [528]	0.033
328	36.75	14.32 (46)	695	13.32 (42)	263	3.24 (10)	43	0.58 (02)	9	5.28	435 [417]	0.037
333	36.17	13.0 (42)	542	13.25 (43)	234	3.81 (13)	43	0.64 (02)	8	5.54	334 [335]	0.042

[a]DR time constants and corresponding its amplitudes can be reproduced within ±5-10 % of the reported values.

Next, we explain about the possible origin of these observed DR time components in these systems. First, we explore the origin of dielectric relaxation time in pure glycerol. Table 7.1 indicates that the average DR time ($\langle \tau_{DR} \rangle$) for pure GL is in good agreement with the time constant calculated from the characteristic DR peak in the loss part ($\tau_{peak} = 1/2\pi\nu_{peak}$). Furthermore, rotation diffusional time of different species was calculated from the Stoke-Einstein-Debye (SED) relation shown in Table A7.8 (Appendix). This indicates that full rotation of GL in pure GL approximately 30 times lower than the lowest DR time τ_2 in pure GL. Interestingly, the slower DR time τ_2 (477 ps at 318 K) is closer to both longer time of structural H-bonding relaxation and translational diffusional time (489 ps and 359 ps respectively at 319.4 K)[104]. This type of cooperative relaxation time is typically associated with the β-relaxation process of viscous glass forming liquids like glycerol.[62,64,105,106] This indicated that translation diffusion through cooperative H-bonding relaxation coupled to the slower DR time τ_2 in pure GL.[104,107] Again the intermediate and faster DR time, τ_3 and τ_4 (88 ps and 17

ps at 318 K) in pure GL are well in agreement with conformation jump dynamics time (120 ps)[104] and neighbours exchange through cage breaking (11 ps) of glycerol in MD simulations. After the addition of small amount of water (1.9 wt%), which is an equivalent amount of water present in disaccharide dihydrate, dielectric time scales become faster. However, water doping in the pure GL does not produce any extra DR time in addition to the three DR times that have been observed in pure GL. Earlier studies[64,108,109] depicted that water in GL and water-glycerol mixture generally has three types of dielectric relaxation timescales: confined water (~90 ps), bound water (~40 ps), and bulk water (~8-10 ps) at 298 K. This indicates that water in these systems does not exist as bulk water; rather, it exists as a confined or bound water and populating the primary hydration shell of glycerol hydroxy groups.[69,73,110,111] The signature of 'freezable bound water'[112–115] has not been observed in DSC experiment of GL_W system. Furthermore, Figure 7.1 depicted the water-induced reduction of glass transition temperature in the GL_W system. Complete suppression of water crystallisation[109] in this GL_W system indicates that there is no dynamic water molecule present in the second solvation of glycerol hydroxy group other than firmly bound water as in the primary solvation shell. In the presence of disaccharides such as trehalose or sucrose, a slow nanosecond DR time τ_1 (~ 8.5 ns at 298) appears in dielectric measurements of TRE_GL_W and SUC_GL_W mixtures. Furthermore, amplitude $\Delta\varepsilon_1$ corresponds to τ_1, increases with temperatures. Earlier DLS measurements of these two mixtures showed large to small particle size distribution with increasing temperatures. The above discussion confirmed that τ_1 is coming from β-relaxation[68] of disaccharides-glycerol-water co-operative H-bonding complex in these two mixers. Other DR times, τ_2, τ_3, and τ_4 may originate from co-operative relaxation, jump dynamics and neighbour-exchange through cage breaking of bulk glycerol in TRE_GL_W and SUC_GL_W mixtures. Again, there is no signature of bulk water-like or freezable water in these two mixtures. The DR and DSC measurements raise the following questions: (i) how closely do these water molecules resemble to typical water in terms of structure, H-bonding, relaxation, and dielectric behaviour? (ii) How persistent is the heterogeneity within these cryoprotectant blends? We address the second concern first. Temperature dependent average DR time ($\langle\tau_{DR}\rangle$) in four systems are given in Table 7.1. This reveals that due to temperature induced reduction in medium viscosity, $\langle\tau_{DR}\rangle$ becomes faster for all of these systems. Again, addition of disaccharides, viscosity of the solution gradually increases. That is why $\langle\tau_{DR}\rangle$ was drastically slowed down in the presence of disaccharide. The coupling between $\langle\tau_{DR}\rangle$ and temperature-reduced viscosity in these systems was investigated via the relation, $\tau \propto \left(\frac{\eta}{T}\right)^p$, where $p = 1$

denotes viscosity-regulated hydrodynamic relaxation process. Deviation of p value from unity means DR is not fully governed by the hydrodynamic-predicted medium viscosity. Figure 7.5 shows a double logarithmic plot of $\langle \tau_{DR} \rangle$ and $\left(\frac{\eta}{T}\right)$ based on the above relation. The observed p values range between 0.75 to 0.80 across the four systems, indicating mild dynamic heterogeneity present in these systems.
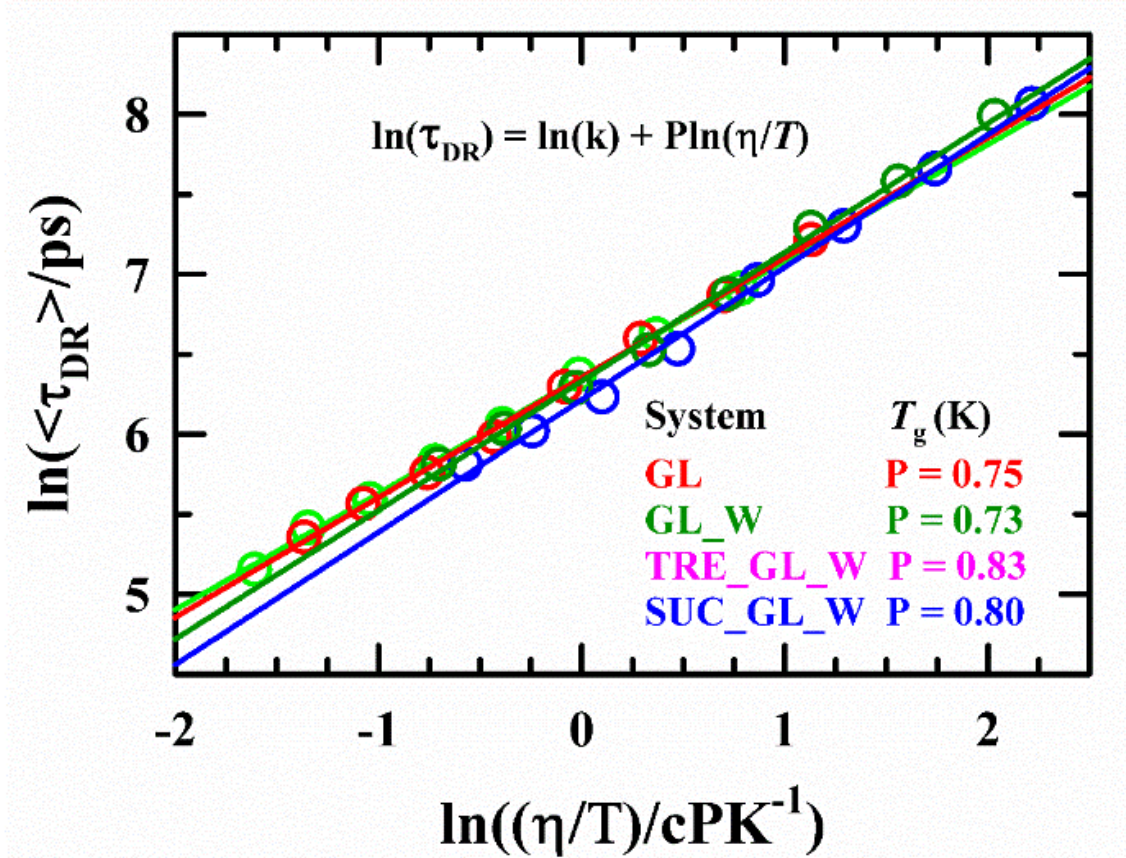
Figure 7.5: Representative temperature reduced viscosity ($\frac{\eta}{T}$) versus average DR relaxation times ($\langle \tau_{DR} \rangle$) in four systems.

Temperature dependence $\langle \tau_{DR} \rangle$ in pure GL as well as three mixtures obey the Arrhenius-type equation at 298K to 333K. Therefore, activation energies E_{DR} related to DR in these systems have been estimated from DRS measurement. Figure 7.6 shows that temperature dependence $\langle \tau_{DR} \rangle$ and viscosity in solution follow Arrhenius type with each system. The estimated activation energy both for DR (E_{DR}) and viscous flow (E_{η}) decreases in the presence of water while it increases with disaccharides shown in Figure 7.6. This indicates that E_{η} is larger than E_{DR} in pure GL and its three mixtures. This fractional viscosity dependence of DR activation

process confirms the conjecture that mild temporal heterogeneity is an inherent character of these systems. E_{DR} abruptly increases in the disaccharides systems.
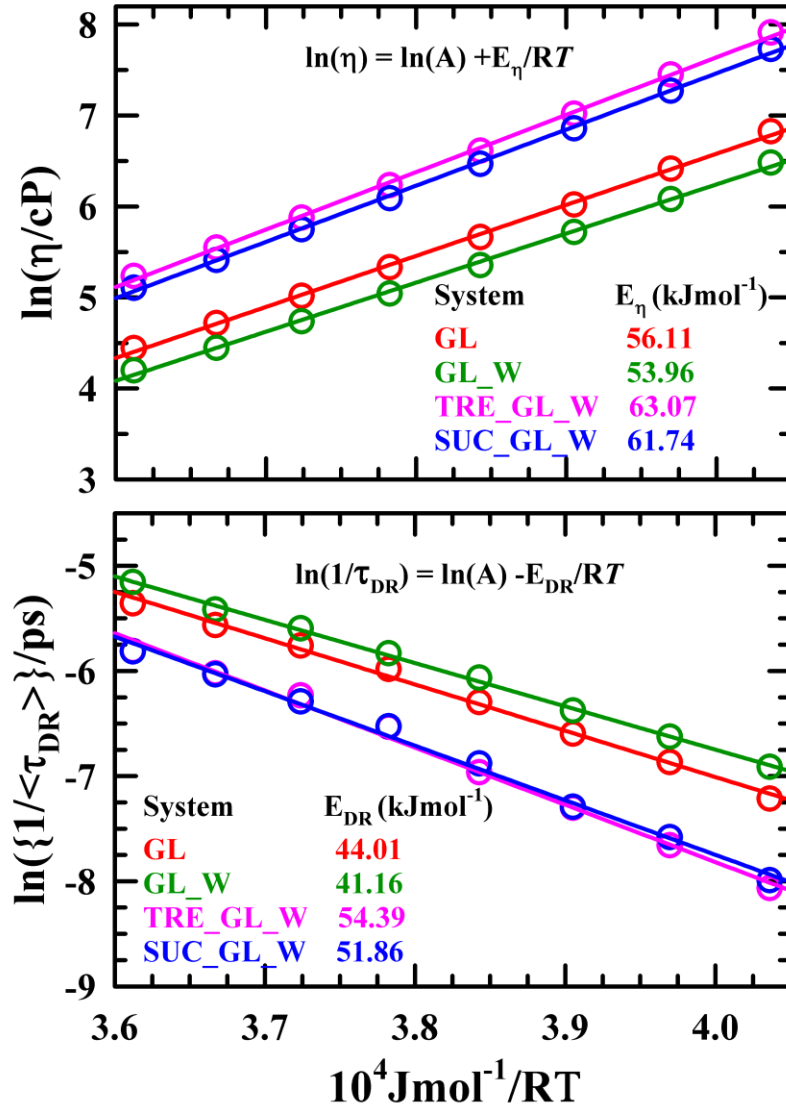
Figure 7.6: Temperature dependent Arrhenius plot of average dielectric relaxation time ($\langle \tau_{DR} \rangle$) for four systems. Estimated activation energies for these systems are shown in same figure. All vignettes are colour-coded.

7.3.4 Structure, H-bonding, and Water-Water Angle, Tetrahedral Order Parameter Distribution and H-bonding relaxation

7.3.4.1 Structure

Atom to atom and center of mass to center of mass (COM-COM) inter-species RDFs were calculated to reveal the microscopic structure of four systems named GL, GL-W, TRE_GL_W, and SUC_GL_W. All molecular species present in these investigated systems extensively participate in H-bonds. At first, we performed the RDFs involving inter and intra-species oxygen atoms. Intermolecular RDFs, between two oxygen atoms (O-O) of GL and O-O pairs from GL and water are shown in Figure A7.9 (Appendix). This indicates that the intermolecular terminal-to-terminal (Ot-Ot) interaction of GL in all investigating systems is more prominent than middle-to-middle (Om-Om). But in both cases, the first peaks of the RDFs arise at shorter distances indicating intermolecular H-bonding characteristics in between GL moity. The second peak appears at a larger distance due to long-range interactions of atoms that do not participate in H-boding. In the presence of water or disaccharide dihydrate in GL, the peak position and height of intermolecular O-O pairs RDFs for GL remain unaltered indicating that the inherent liquid structure of GL remains intact in GL_W, TRE_GL_W, and SUC_GL_W systems. Figure A7.9 (c) and (d) (Appendix) shows intermolecular RDFs for O-O atoms pairs between GL and water considering GL oxygen atom as reference. A sharp peak at a shorter distance in the RDFs indicates a stronger H-bonding interaction possible between both types of hydroxyl groups (terminal and middle) and water. Although peak positions and height remain same in these investigating systems. This suggests the distribution of water molecules around GL molecules remains same.

Next, we examine the RDFs for O-O pair interactions between disaccharides (trehalose and sucrose) and glycerol, focusing on the potential for intermolecular H-boding between these molecules. Figure 7.7 depicts interatomic O-O interactions, using the oxygen atom from the disaccharides as the reference atom. The RDFs reveal a principal peak in the distribution of hydroxyl oxygens interactions between disaccharides (trehalose and sucrose) and glycerol. Note, this peak is more pronounced compared to the peak observed in the distribution of interactions between ether oxygens and hydroxyl oxygens within the disaccharide and glycerol, respectively. This observation suggests a more favourable intermolecular H-bonding interaction involving the hydroxyl group of both species, as compared to interactions between ether oxygens and hydroxy groups of disaccharide and glycerol. Furthermore, the peak

intensities of RDFs for each pair of atoms are different from each other, indicating that the H-boding propensity varies between each pair of groups present between the disaccharides and glycerol.
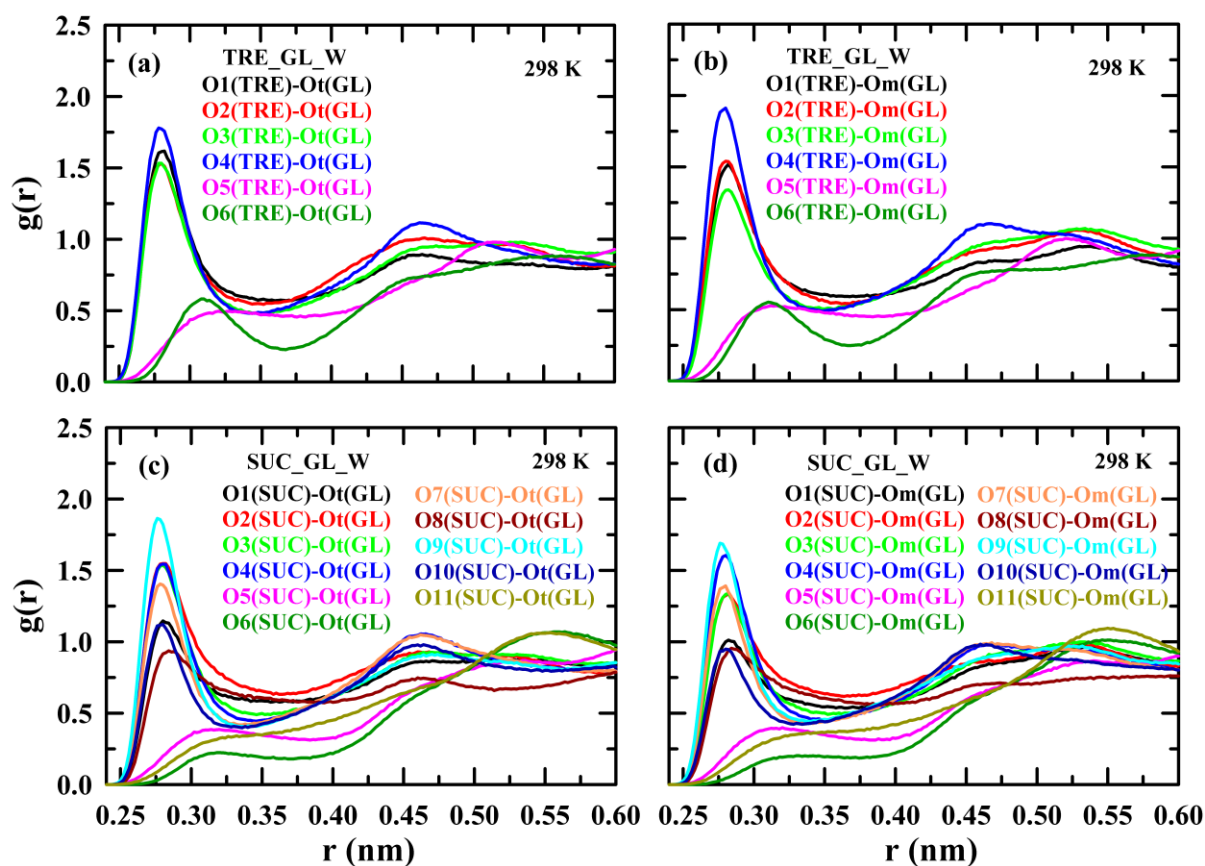
Figure 7.7: Intermolecular RDF for (a) O-O atom pairs for trehalose and terminal oxygen of glycerol in TRE_GL_W system, (b) O-O atom pairs for trehalose and middle oxygen of glycerol in TRE_GL_W system, (c) O-O atom pairs for sucrose and terminal oxygen of glycerol in SUC_GL_W system, (d) O-O atom pairs for sucrose and middle oxygen of glycerol in SUC_GL_W system at 298 K. All representations are color coded.
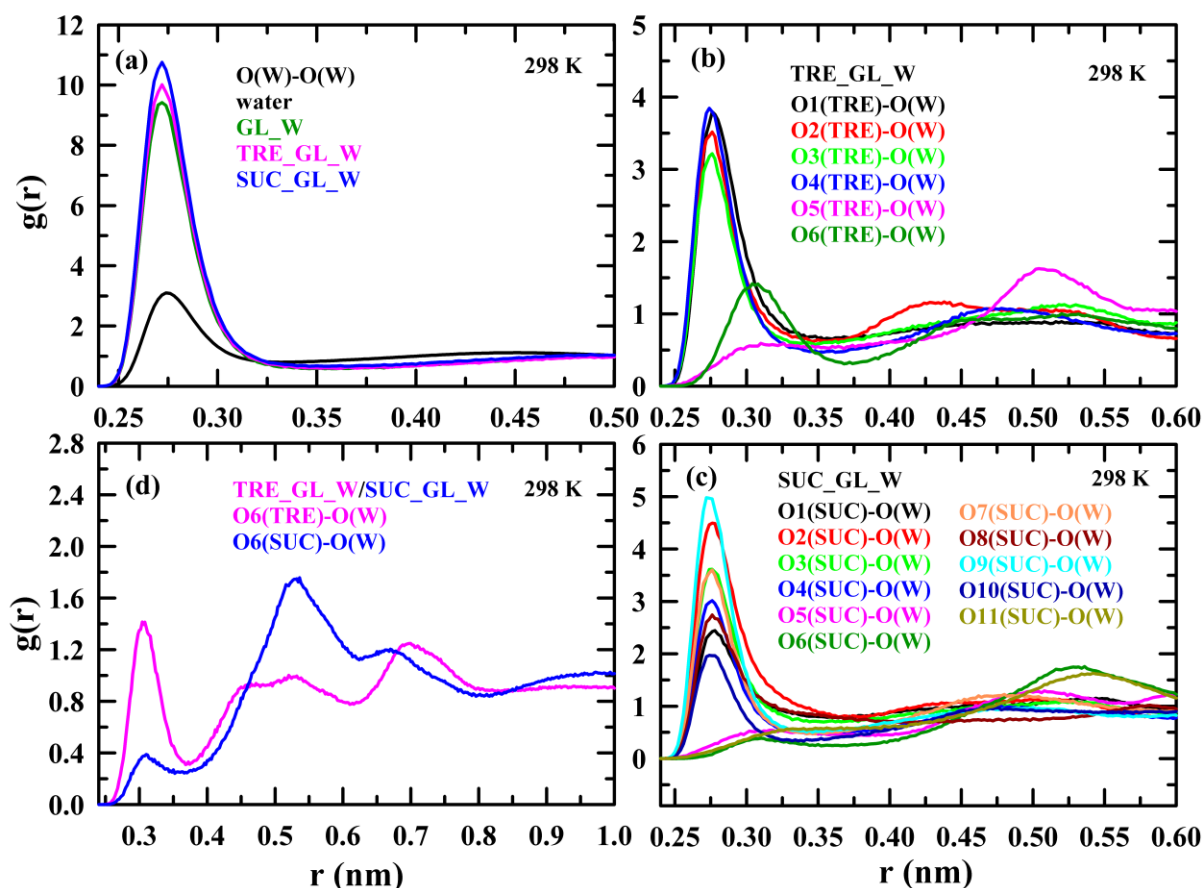
Figure 7.8: Intermolecular RDF for (a) O-O atom pairs for water and water in pure water, GL_W, TRE_GL_W, and SUC_GL_W systems, (b) O-O atom pairs for trehalose and water in TRE_GL_W system, (c) O-O atom pairs for sucrose and water in SUC_GL_W system, (d) O-O atom pairs for glycosidic oxygen of disaccharide and water in TRE_GL_W and SUC_GL_W systems at 298 K. All representations are color coded.

Next, we have investigated interactions among water molecules by examining the RDFs of O-O pair of two water molecules in both cryoprotectant mixtures and neat water. In Figure 7.8 (a), RDFs for these pairs are depicted in neat water and mixtures. The intensity of the first peaks in these cryoprotectant mixtures is greater than that of neat water. Note that the position of the first peak remains consistent across all systems. The outcome suggests the presence of stronger H-bonding interactions among water molecules in the mixtures, leading to the formation of water-water aggregates. Similar observations have been made in low water containing aqueous octanol mixture[69] and deep eutectic system[116]. The height of the first peak of O-O pairs between water molecules further increases from the trehalose system to the sucrose system. This indicates aggregation tendencies varies among water molecules in these systems, with SUC_GL_W > TRE_GL_W > GL_W. Figure 7.8 (b) and (c) illustrate the RDFs

for O-O pairs of disaccharide and water molecules, respectively. The prominent first peak in these RDFs occurs at a shorter distance for pairs involving the hydroxyl oxygen of disaccharide and water. This suggests that hydroxyl groups of both disaccharides (trehalose and sucrose) and water form stronger H-bonds than pairs involving the ether oxygen of disaccharide and water. Furthermore, these figures reveal that the distribution of water molecules around sucrose molecules is more heterogeneous than that around trehalose. Additionally, the RDF for O-O atom pairs of glycosidic oxygen of disaccharides and water in Figure 7.8 (d) indicates that the H-boding possibility between the glycosidic oxygen of trehalose and water is stronger than that for sucrose-water pairs. This property of trehalose highlights its inherent capability to trap water, as reflected in its crystal structure[117,118].
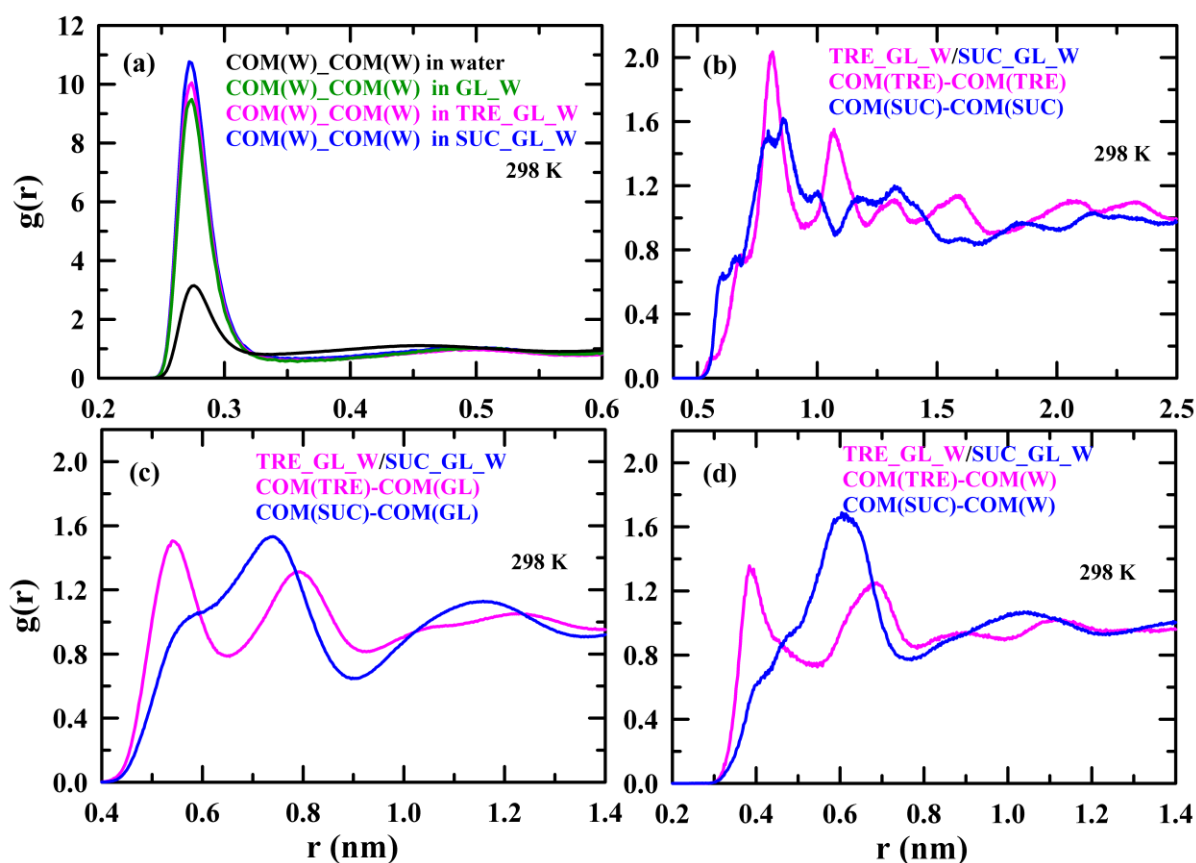
Figure 7.9: COM RDF for (a) water-water in pure water, GL_W, TRE_GL_W, and SUC_GL_W systems, (b) trehalose-trehalose and sucrose-sucrose, (c) disaccharide-glycerol, (d) disaccharide-water in TRE_GL_W and SUC_GL_W systems at 298 K. All representations are color coded.

Further, we investigate intra and inter-species alignment of molecules by calculating the center-of-mass (COM) RDFs in these simulated systems. The RDFs for both intra and inter-species COM-COM pairs are presented in Figure A7.10 (Appendix) and Figure 7.9, along with corresponding peak positions and coordination numbers outlined in Table A7.11. In the case of GL-GL, GL-water, and water-water RDFs, a distinct first peak is observed, which is qualitatively similar to the atom-atom RDFs. However, the peak positions of these RDFs occur at a greater distance for GL-GL and GL-water, mainly due to the larger size of the GL molecules. Note that the GL-GL and GL-water interactions remain consistent, while the water-water interaction displays the same characteristics as discussed earlier in O-O RDFs between water molecules.
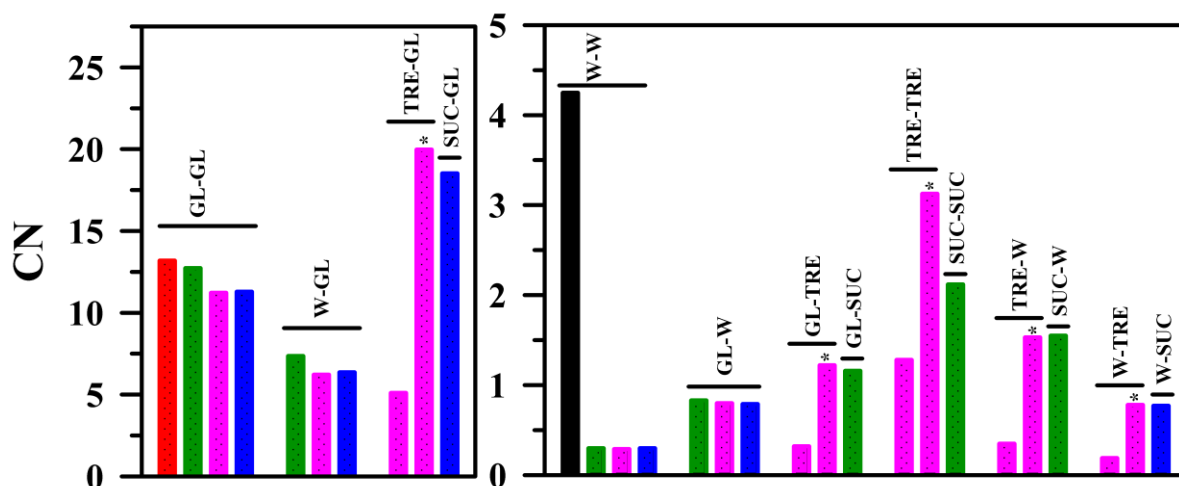
Figure 7.10: Coordination numbers obtained from COM-COM RDFs: GL around GL (GL-GL), GL around water (W-GL), GL around trehalose (TRE-GL), GL around sucrose (SUC-GL), water around water (W-W), water around GL (GL-W), trehalose around GL (GL-TRE), sucrose around GL (GL-SUC), trehalose around trehalose (TRE-TRE), sucrose around sucrose (SUC-SUC), water around trehalose (TRE-W), water around sucrose (SUC-W), trehalose around water (W-TRE), and sucrose around water (W-SUC) at 298 K. All representations are color coded as follows: pure GL: red, pure water: black, GL-W: green, TRE_GL_W: pink, SUC_GL_W: blue. A bar with a star marking indicates the CN values correspond to second minima. First peak and first peak minima of COM-COM RDFs in between sucrose and other species are not clear (see Figure 9.9 (b), (c), and (d)) and for this reason, CN values for trehalose and other species pairs at corresponding to second minima compare with CN values at COM-COM longer distance minima for sucrose and other species pairs.

On the other hand, Figure 7.9(b) illustrates that disaccharide interact with one or more disaccharide molecules in their solvation shell. Note that the interaction between trehalose molecules is more pronounced than that between sucrose molecules, which aligns well with DLS measurements. Figure 7.9 (c) and (d) depict the RDF of disaccharides and GL, and disaccharides and water, revealing that the interaction distance for trehalose-GL or trehalose-water is a shorter distance than sucrose-GL or sucrose-water. This behaviour can be attributed to the interactions between disaccharide molecules themselves. The RDFs for trehalose-trehalose and sucrose-sucrose indicate that the first and second solvation shells around trehalose molecules are clearly observed, whereas they merge for sucrose molecules. This suggests that trehalose molecule interact with another trehalose molecule. While sucrose molecule may stick with other sucrose molecule. These observations indicate that the SUC_GL_W system exhibits more heterogeneous character compared to the TRE_GL_W system.

A representative illustration of coordination number (CN) is presented in Figure 7.10, offering insight into the self and cross CN values for various intra and inter-species correlations within the simulated systems. The CN of GL around GL decreases with the introduction of a small amount of water (~1.9 wt%). This decrease becomes more pronounced with the presence of disaccharides. On the other hand, in the presence of disaccharides, CN of water around GL and GL around water slightly decreases compared to the GL_W system. Again, Figure 7.10 demonstrates that disaccharides interact with other species in their solvation shell, and vice versa. Note that greater number of trehalose molecules interact within the solvation shell of trehalose compared to sucrose around sucrose. DLS measurements of these two disaccharide systems support this observation, indicating that the particle size in the trehalose system is larger than that in the sucrose system. Finally, the CN of water-water interactions in mixtures significantly decreases compared to neat water. This observation suggests that the H-bonding network structure of neat water is significantly disrupted in these systems. The above discussion highlights that all species present in the multi-component cryoprotectant mixtures participate in intra and inter-species H-bonding with each other. That raises additional questions for our ongoing investigation into these systems, which will be addressed in the next H-boding network analysis section. Additionally, we have calculated the O-O-O angle distribution, tetrahedral order parameter, and continuous and structural H-bonding lifetime for water, providing insight into the local and global structure of water within all of these systems.
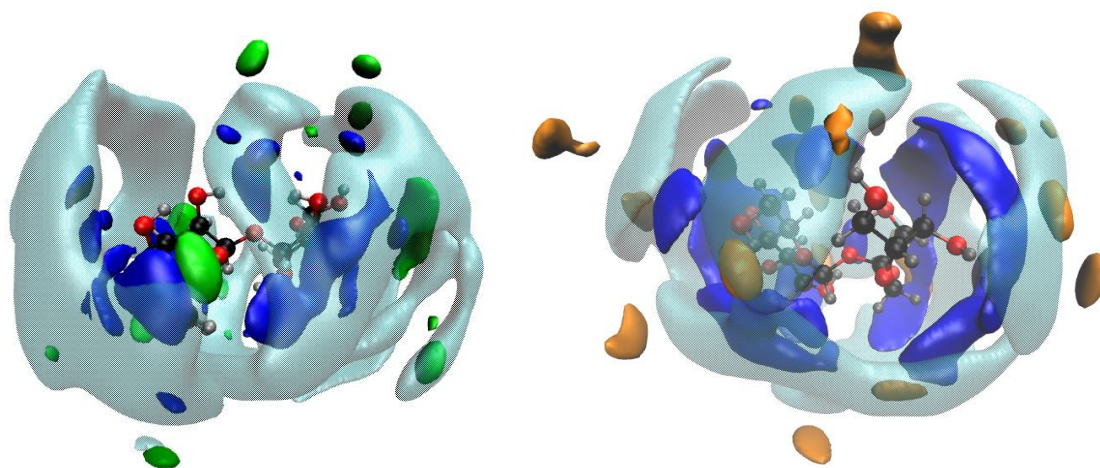
Figure 7.11: Spatial distribution functions of glycerol, water, disaccharide around trehalose (left side) or sucrose (right side). The blue, green, orange and transparent cyan, surfaces account for the water around disaccharides, trehalose around trehalose, sucrose around sucrose, respectively, and glycerol around disaccharides.

The analysis of RDFs and CN presented earlier provided a qualitative understanding of the two-dimensional special arrangement within TRE_GL_W and SUC_GL_W systems. However, these results do not offer a complete three-dimensional representation of the systems. To gain a more detailed insight into the solvation structure around the solute in the solution, we employed the concept of the spatial distribution function (SDF)[119,120] using TRAVIS[121] and VMD[122] software, as shown in Figure 7.11. Note that SDFs presented in this analysis consider only the COM of the entire species, which may result in less anisotropic representations compared to analyses involving interactions between individual atoms. The isodensity surface of GL, water, and disaccharides around the central disaccharide molecule reveals distinct differences in the solvation shells around trehalose and sucrose. However, water and disaccharides form more heterogeneous isodensity surfaces compared to glycerol. Note that the DLS peak of the TRE_GL_W system is broader than that in the SUC_GL_W system. The SDFs of both systems illustrate that the distribution of trehalose around trehalose is more heterogeneous with a wide range of isodensity surface sizes, ranging from small to large. This observation aligns with the DLS measurements of these two systems. Furthermore, a larger isodensity surface size of water around sucrose molecule is observed in comparison to trehalose. This finding is consistent with the earlier water-water RDFs in these two systems and confirms the conjecture that larger water clusters are formed in the sucrose system as compared to the trehalose system.
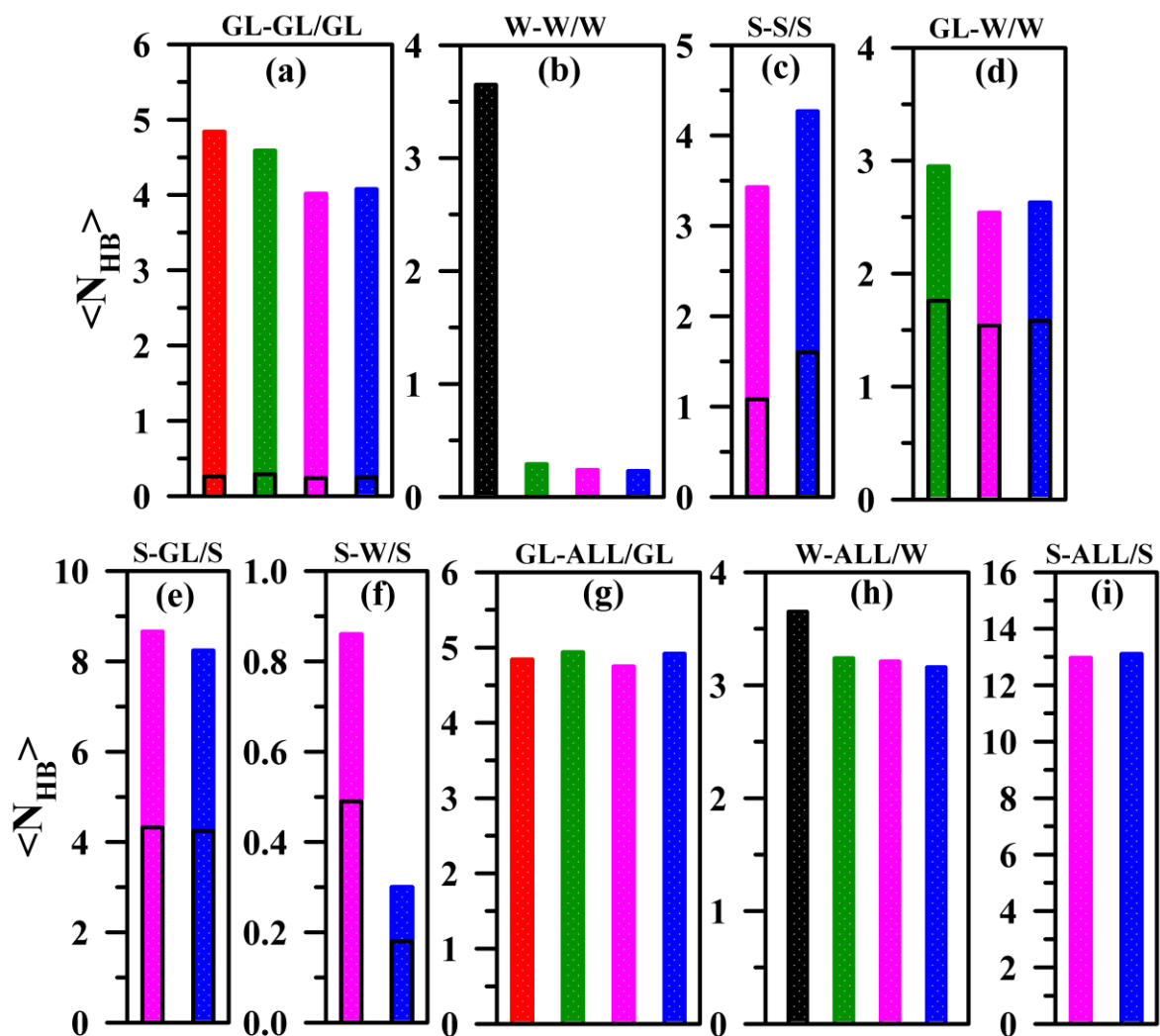
Figure 7.11: Representative plot of average number H-bond ($\langle N_{HB} \rangle$) for (a) GL-GL per GL (GL-GL/GL) and open black rectangle denoted average intramolecular H-bond in per GL molecule, (b) water-water per water (W-W/W), (c) disaccharides-disaccharides per disaccharide (S-S/S) and open black rectangle denoted average intramolecular H-bond in per disaccharide molecule (S) where S doted trehalose or sucrose, (d) GL-water per water (GL-W/W) and open black rectangle denoted $\langle N_{HB} \rangle$ where water act as a H-bond donor molecule, (e) disaccharide-GL per disaccharide (S-GL/S) and open black rectangle denoted $\langle N_{HB} \rangle$ where disaccharide act as a H-bond donor molecule, (f) disaccharide-water per disaccharide (S-W/S) and open black rectangle denoted $\langle N_{HB} \rangle$ where disaccharide act as a H-bond donor molecule, (g) total number of H-bond per GL considering all interactions (GL-ALL/GL), (h) total number of H-bond per water considering all interactions (W-ALL/W), and (i) total number of H-bond per disaccharide considering all interactions (S-ALL/S). All representations are color coded as follows: pure GL: red, pure water: black, GL-W: green, TRE_GL_W: pink, SUC_GL_W: blue.

7.3.4.2 Hydrogen Bond Network

The analysis of RDFs suggests the presence of a H-bond network within investigated systems. Each GL molecule provides three donor and three acceptor sites, whereas a disaccharide molecule (either trehalose or sucrose) offers eight donor and eleven acceptor sites. Water molecules, on the other hand, have highest likelihood of forming up to four H-bonds. This indicates that H-bonding affinity among these species plays a crucial role in shaping the structure and dynamics of these simulated systems. Here, we calculated the average number of intra and interspecies H-bonds ($\langle N_{HB} \rangle$) per molecule. The results are shown in Figure 7.11, and the corresponding values can be found in Table A7.12 (Appendix). The $\langle N_{HB} \rangle$ per GL molecule in neat GL, encompassing both intra and intermolecular interactions, was approximately 4.84 at 298 K, which is good corroborates with earlier study[123]. In the GL_W, $\langle N_{HB} \rangle$ per GL molecules for GL-GL interactions decrease compared to neat GL in the presence of a small amount of water, while the intra-molecular contribution remains very close. This indicates that GL molecules interact with water molecules, diluting the GL-GL H-bond interactions. Furthermore, the average number of GL-GL H-bonds per GL molecule decreases in the presence of disaccharides. However, the impact of both trehalose and sucrose on diminishing the GL-GL interaction is quite similar. Next, we explored the water-water H-bonds per water molecule in these systems. Figure 7.11(b) depicts a significant disruption in the water-water H-bonding in these cryoprotectant systems (~ 0.23-0.29) compared to the neat water (3.65). This result suggests that around 3/4 of the total water molecules do not participate in water-water H-bond in these mixtures. A similar severe disruption in water-water interaction has been observed in water mixtures[69,116] when water is the minor component. The H-bond analysis for both disaccharides is shown in Figure 7.11(c). It reveals that the propensity for both intra and inter-molecular H-bonding is larger among sucrose molecules than among trehalose molecules owing to their distinct molecular conformations. However, this result suggests that disaccharide molecules in both systems (TRE_GL_W and SUC_GL_W) preferentially interact with themselves at this disaccharide concentration. This finding is in good agreement with the previously discussed experimental and simulated results regarding the microscopic structure of solute-solute interactions.

In the exploration of inter-species H-bonding in these multicomponent systems, Figure 7.11(d) illustrates the $\langle N_{HB} \rangle$ between GL and water per water molecule. Note that the black rectangle bar represents cases where GL acts as an H-bond donor in different systems. This analysis reveals that the $\langle N_{HB} \rangle$ for GL-water interactions per water molecule significantly decreases in

the presence of disaccharides, suggesting that both GL and water molecules interact with the disaccharide molecules. Interestingly, the GL-water H-bonding propensity is slightly higher in the SUC_GL_W system compared to the TRE_GL_W system. This difference can be explained by the fact of intra and inter-molecular H-bond propensity among two disaccharides. As the propensity of intra and inter-molecular H-bonding among sucrose molecules is larger than among trehalose molecules, that facilitates more H-boding sites available in trehalose molecules to interact with GL and water (see Figure 7.11(e) and (f)). This aligns well with previous studies on aqueous solution of trehalose/sucrose.[53,100] Again, the interaction between trehalose and water forms three times more H-bonds than that between sucrose and water. This stronger H-boding effect of trehalose on water may be responsible for the greater disruption of the water structure in the trehalose system compared to sucrose, as reflected in the SDF of water around two disaccharides.

The total $\langle N_{HB} \rangle$ for GL/W/TRE/SUC, including all types of interactions, is shown in Figure 7.11(g)-(i). For GL molecules, the $\langle N_{HB} \rangle$ remains almost unchanged in the multicomponent mixture as in the neat system. However, the total $\langle N_{HB} \rangle$ for water in the mixtures decreases compared to neat water. This suggests that the arrangement of H-bonding partners around water molecules is responsible for the reduction in H-bond per water molecule in these crowded systems compared to neat water. This particular aspect will be explored further in the subsequent Section. On the other hand, total $\langle N_{HB} \rangle$ per disaccharide molecule, both for trehalose and sucrose, are very close to each other.

Figure 7.12 depicts the distribution of the number of H-bonds for water-water per water molecule, denoted as $P(N_{HB}/W)$, in both neat water and multi-component systems. $P(N_{HB}/W)$ in these mixtures significantly deviates from that in the neat system. In these investigated multicomponent cryoprotectant systems, the majority of water molecules have *zero* water-water H-bonds. Interestingly, the presence of water molecules with four water-water H-bonds is nearly non-existent in these systems. A very small population of water molecules exhibits three water-water H-bonds. This pattern of water-water H-bonding per water molecule aligns with observations made in an earlier study of water in octanol-rich system[69]. In terms of water-water H-bonds, the behaviour of water in these complex systems is markedly different from that of bulk water. Moreover, it is predicted that some 'free' water molecules exist in these cryoprotectant systems. The analysis of water-water H-bond highlights the disruption in the

local structure of water, this phenomenon will be further explored through the distribution of angle and tetrahedral order parameter of three adjacent oxygen atoms in water molecules in the upcoming section.
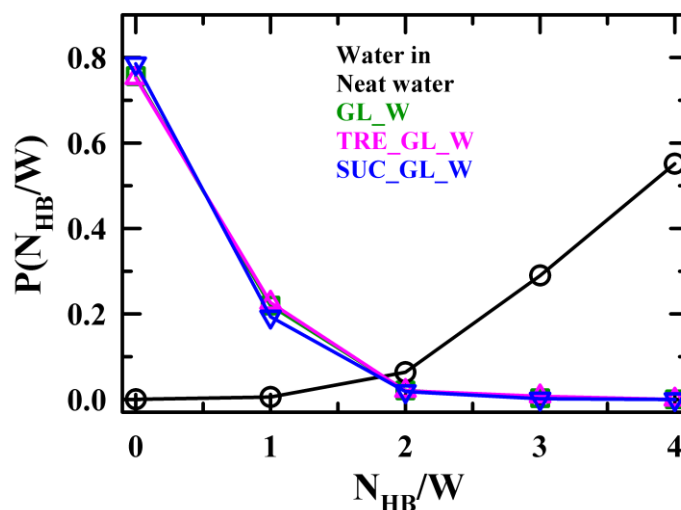
Figure 7.12: Representative plot of H-bond number distribution for water-water per water molecule P(N_{HB}/W) in different mixture and neat water at 298 K.

7.3.4.3 Angle and Tetrahedral Order Parameter Distributions of Water

Figure 7.13 depicts the distribution of angle ($P(\theta)$) and tetrahedral order parameter ($P(Q)$) between three oxygen atoms of the three nearest neighbour water molecules. For comparison, $P(\theta)$ and $P(Q)$ obtained for neat water are also presented in the same plot. The angle distributions for water in these systems are broader than those for ambient water. Additionally, the population of water molecules in bulk water with $\theta \sim 104^o$ is largely replaced in these systems by water populations that are constrained to assume angles within the range of $0^o \leq \theta \leq 60^o$. What's particularly intriguing is that in these multicomponent cryoprotectant mixtures, water can sustain considerable populations with angles $\theta < 50^o$ (peaks at $\theta \sim 20^o$ and $\theta \sim 40^o$), which is not observed in neat water. This arrangement with $\theta \sim 50 - 60^o$ corresponds to the triangular arrangement of water molecules, a feature also present in neat water. Water molecules with angles ranging from 0 to 50° are thus orientationally constrained, and as a result, a significant number of water molecules in these systems deviate from the typical behavior of water.

A similar deviation from the behavior of neat water is also evident in Figure 7.13 lower panel, where the system-dependent order parameter distribution, $P(Q)$, is shown as a function of the order parameter, Q. Note that in these multicomponent systems, $< Q >$ ranges from zero to large negative values, which has been reported for water in aqueous electrolyte and water in other mixtures.[69,124–127] This implies that the overall tetrahedrality of water in these systems has been significantly disrupted, although a certain population of water molecules retains a tetrahedral order parameter similar to that found in neat water.
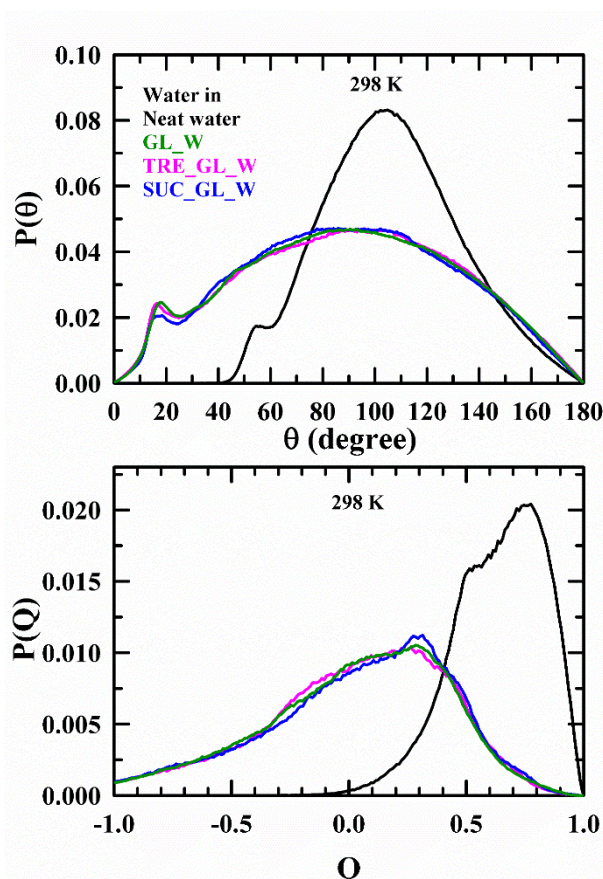
Figure 7.13: Distribution of tetrahedral angle $P(\theta)$ between three nearest neighbour hydrogen bonded water molecules for three systems (upper panel). Corresponding distribution for neat water system also given same panel. Distribution of tetrahedral order parameter $P(Q)$ for three systems (lower panel). Corresponding distribution for neat water system also given here.

7.3.4.4 H-Bond Dynamics of Water

Figure 7.14 represents the continuous and structural hydrogen bond relaxations for water-water interactions in these systems, with neat water included for comparison. The average continuous H-bonding lifetime $\langle \tau_{S_{HB}} \rangle$, and structural H-bonding lifetime $\langle \tau_{C_{HB}} \rangle$, in the multicomponent

cryoprotectant mixtures and neat water at 298 K are depicted in Figure 7.15. The continuous H-boding lifetimes among the water molecules in these mixtures are very similar, but longer than those in neat water. In contrast, the structural water–water H-bond relaxation times in these systems are significantly slower, approximately 10 times slower, than in neat water. whereas this factor is nearly 4 for $S_{HB}(t)$. This abrupt slowdown of H-bond relaxation of water arises from the sluggish dynamics of water molecules within these multicomponent cryoprotectant systems due to the high viscosity of these media.
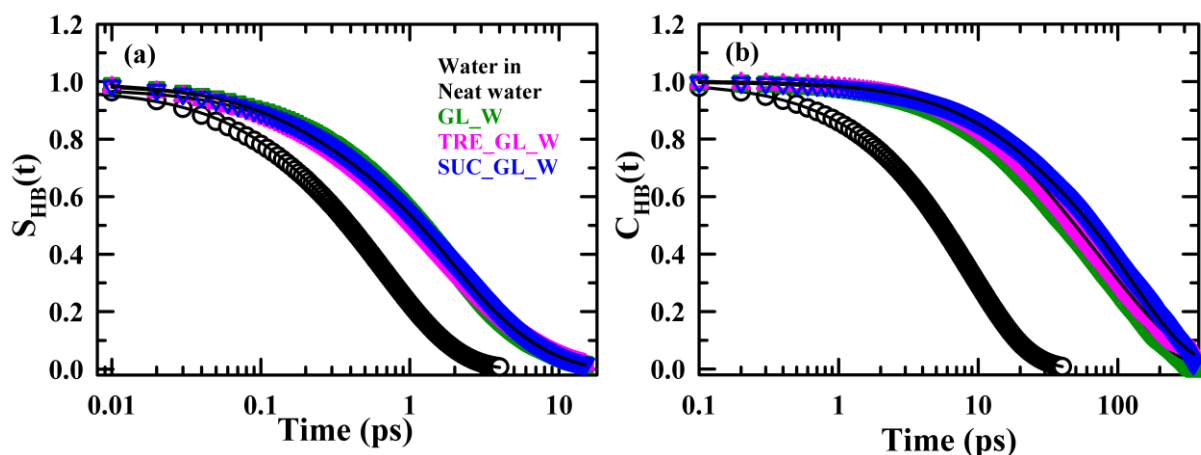
Figure 7.14: Representative plot of (a) water-water continuous H-boning lifetime decay, and (b) water-water structural H-bonding lifetime decay in multicomponent mixture and neat water at 298 K.
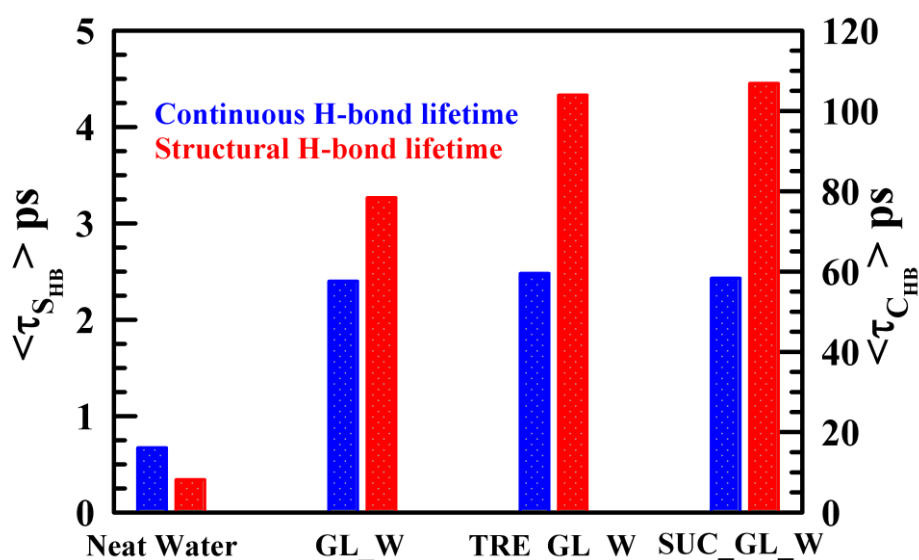
Figure 7.15: water-water average continuous H-bonding lifetime, $\langle\tau_{S_{HB}}\rangle$, and structural H-bonding lifetime $\langle\tau_{C_{HB}}\rangle$, in multicomponent mixtures and neat water at 298 K.

7.4 Conclusion

In summary, a comprehensive investigation combining DSC, DLS, DRS experiments and computer simulations was conducted to explore the solution structure, system heterogeneity, interaction, and dynamics of four cryoprotectant systems. DSC measurements revealed that the addition of disaccharides, namely trehalose and sucrose, increased the T_g, indicating enhances glass-forming characteristics. Interestingly, the presence of a minute amount of water in these mixtures counteracted this decrease in T_g, suggesting that water plays a role in increasing fragility and decreasing system stability. Further analysis using viscosity measurements and Arrhenius plots revealed that the fragility parameter (D) decreased with the introduction of water, indicating increased fragility. In contrast, the presence of disaccharides led to an increase in D, implying a less fragile or stronger glass-forming behavior. The order of T_g values (TRE_GL_W > SUC_GL_W > GL > GL_W) aligned with the extent of fragility, highlighting the intricate relationship between glass transition ability and cryoprotective capabilities. DLS experiments provided insights into micro-cluster dynamics, showing temperature-dependent variations in particle size in disaccharide dihydrate/GL systems. DRS analysis showcased changes in relaxation times and activation energies, emphasizing the influence of water and disaccharides on the dynamic behaviour of the cryoprotectant mixtures. Structural investigations, including RDFs and CN, demonstrated the intricate H-bonding networks within these systems. SDFs further depicted the heterogeneity in solvation shells around trehalose and sucrose. Analysis of intra and inter-species H-bond in these cryoprotectant systems revealed disruption of water's H-bonding structure and emphasized the preference for disaccharide self-interactions. Analysis of angle distributions, tetrahedral order parameters and H-bonding dynamics of water molecules unveiled deviations from bulk water behaviour in the cryoprotectant mixtures. The disruption in the tetrahedrality of water and the presence of constrained angle distributions suggested a unique structural arrangement induced by the complex mixtures. The findings from this work will be provide valuable insights for fine-tuning cryopreservation capabilities, showcasing the potential applications of these mixtures in the field of cryopreservation technology.

Appendix A7

Table A7.1: Temperature dependent density (ρ), refractive index (n_D) and viscosity coefficient (η) of pure GL, GL_W, TRE_GL_W, SUC_GL_W systems.

T/K	GL	GL_W	TRE_GL_W	SUC_GL_W
Refractive index (n_D)[a]				
298	1.4723	1.4716	1.4809	1.4805
303	1.4722	1.4715	1.4808	1.4802
308	1.4720	1.4713	1.4806	1.4799
313	1.4719	1.4710	1.4804	1.4798
318	1.4718	1.4705	1.4803	1.4796
323	1.4716	1.4704	1.4801	1.4794
328	1.4713	1.4704	1.4799	1.4792
333	1.4710	1.4704	1.4799	1.4792
Density (ρ/kgm^{-3})[a]				
298	1257	1253	1299	1296
303	1254	1249	1295	1293
308	1251	1246	1292	1290
313	1248	1243	1289	1286
318	1245	1240	1286	1284
323	1242	1237	1283	1281
328	1238	1234	1279	1277
333	1235	1230	1276	1274
Viscosity (η/cP)[b]				
298	922	653.3	2733	2276
303	611	437.4	1721	1440
308	412	304.3	1119	952
313	288	211.8	744	644
318	207	154.7	510	442
323	151	114.1	357	314
328	112	85.3	257	224
333	85	66.6	188	165

Table A7.2: Numbers of species is considered in our simulation study for pure and multicomponent cryoprotectant mixtures.

System	Trehalose/Sucrose	Glycerol	Water
W			608
GL		1216	
GL_W		1088	128
TRE_GL_W	64	1024	128
SUC_GL_W	64	1024	128
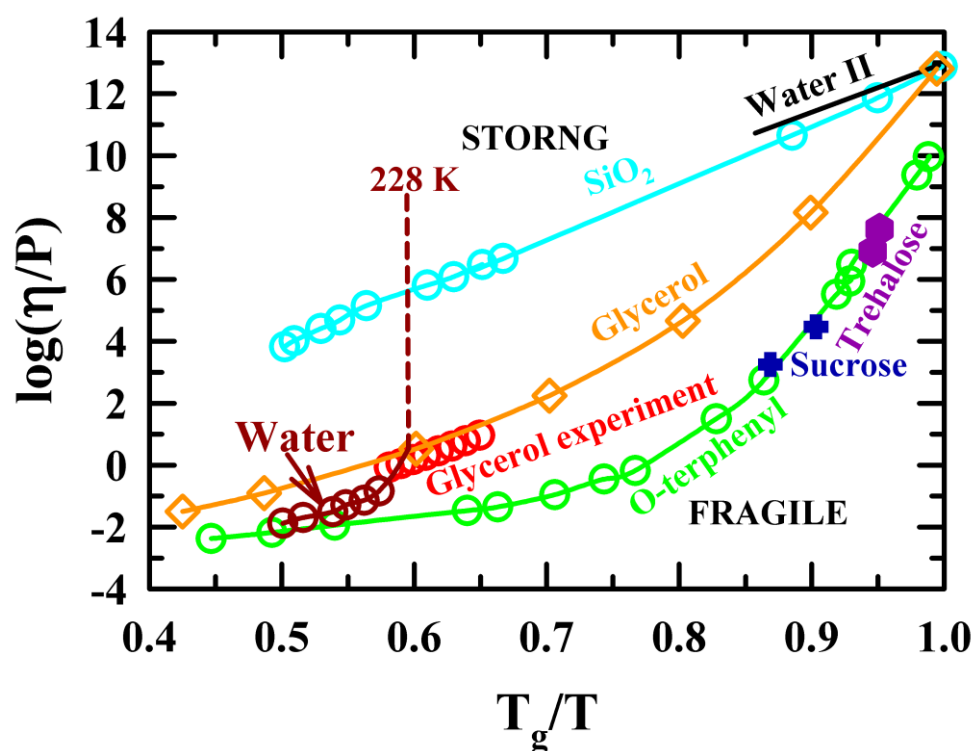
Figure A7.3: A representative scaled Arrhenius plot of viscosity data for various types of liquids from Angell et al. and our experiment data from pure GL (red open circle), reveals that the clear difference between strong and fragile behavior. The T_g value use for scaling factors, determined at a heating rate 10 K/min. All representations are color coded. Experimental values

from pure GL (shown in red color) are closely align to that of Angell et al., validate the accuracy of our DSC experiments. Note 'Water II' is denoted amorous water after annealing.

Table A7.4: Particle size in TRE_GL_W and SUC_GL_W cryoprotectant mixtures at five different temperatures from DLS measurements.

System	TRE_GL_W		SUC_GL_W	
T/K	Diameter at peak maxima (nm)	Average diameter (nm)	Diameter at peak maxima (nm)	Average diameter (nm)
333	1.29	1.24	1.12	1.24
323	1.50	1.67	1.12	1.24
313	1.74	1.81	1.12	1.24
303	1.74	2.36	1.50	1.44
298	2.7	3.47	1.74	1.93
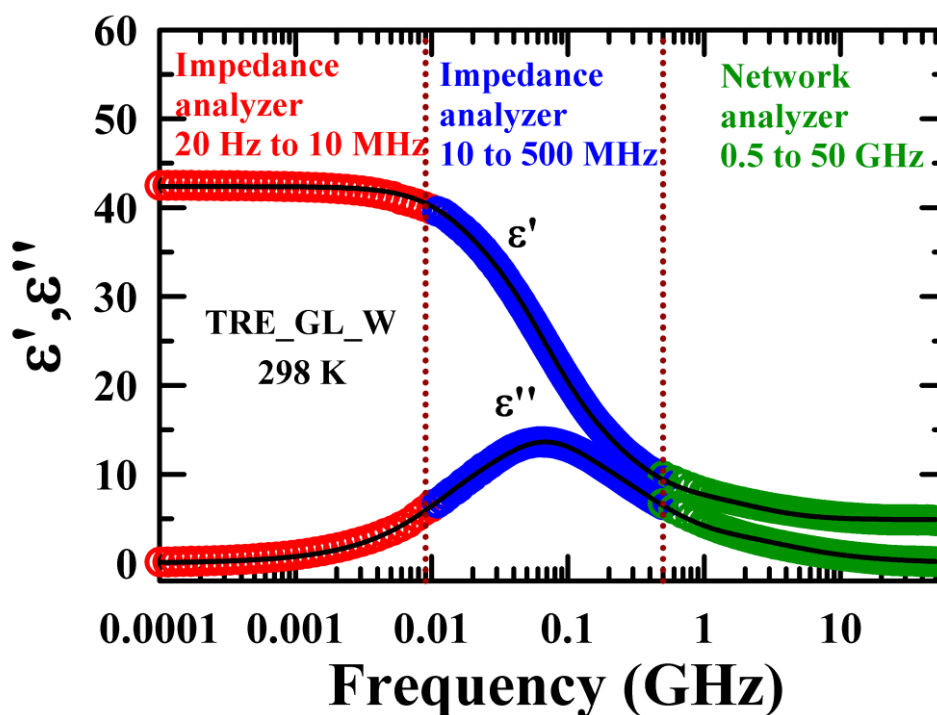
Figure A7.5: The real (ε') and imaginary (ε'') components of complex DR spectra for TRE_GL_W cryoprotectant mixtures collected from three different dielectric setup at 298K. All presentations are colour coded.
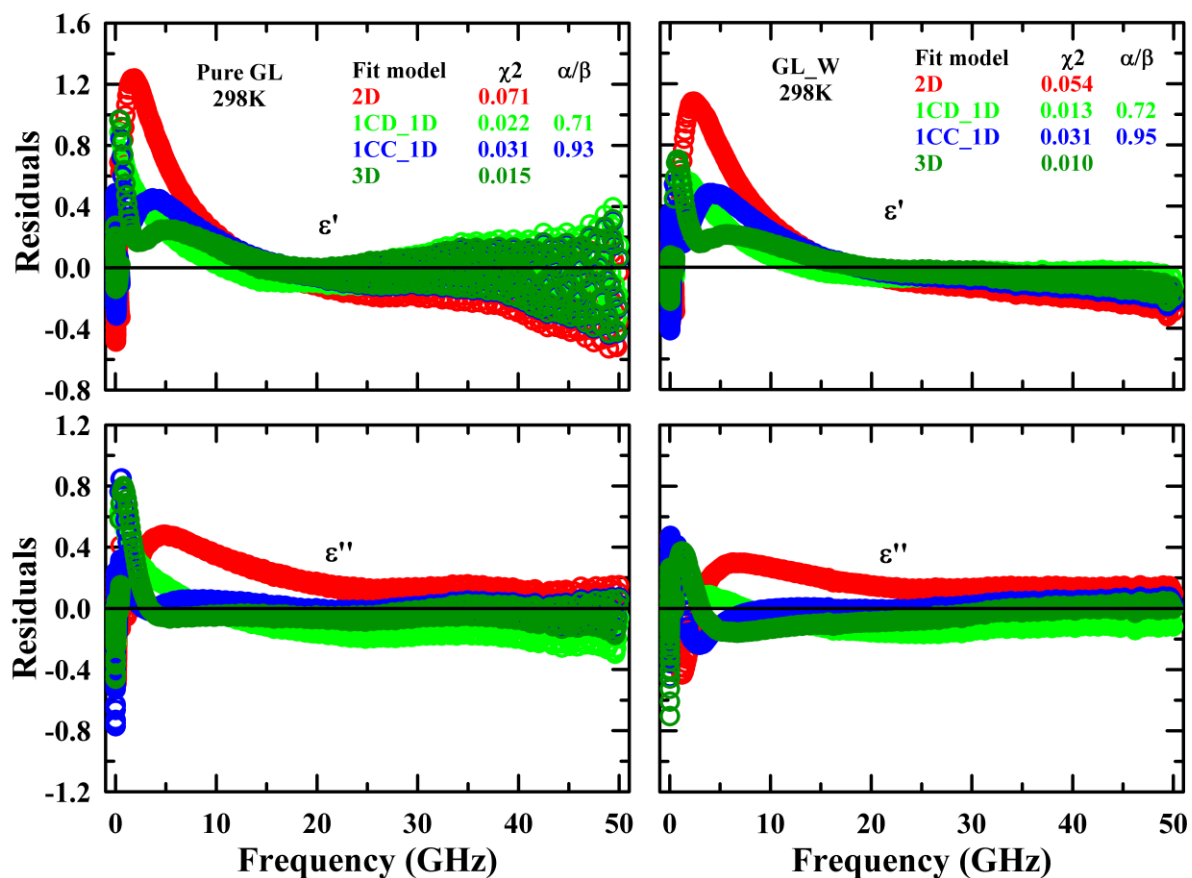
Figure A7.6: Residual of fittings for real (ε') and imaginary (ε'') components of complex DR spectra in pure GL (left panel) and GL_W (right panel) systems at 298K. The solid black line represents zero base line. All representations are colour-coded.
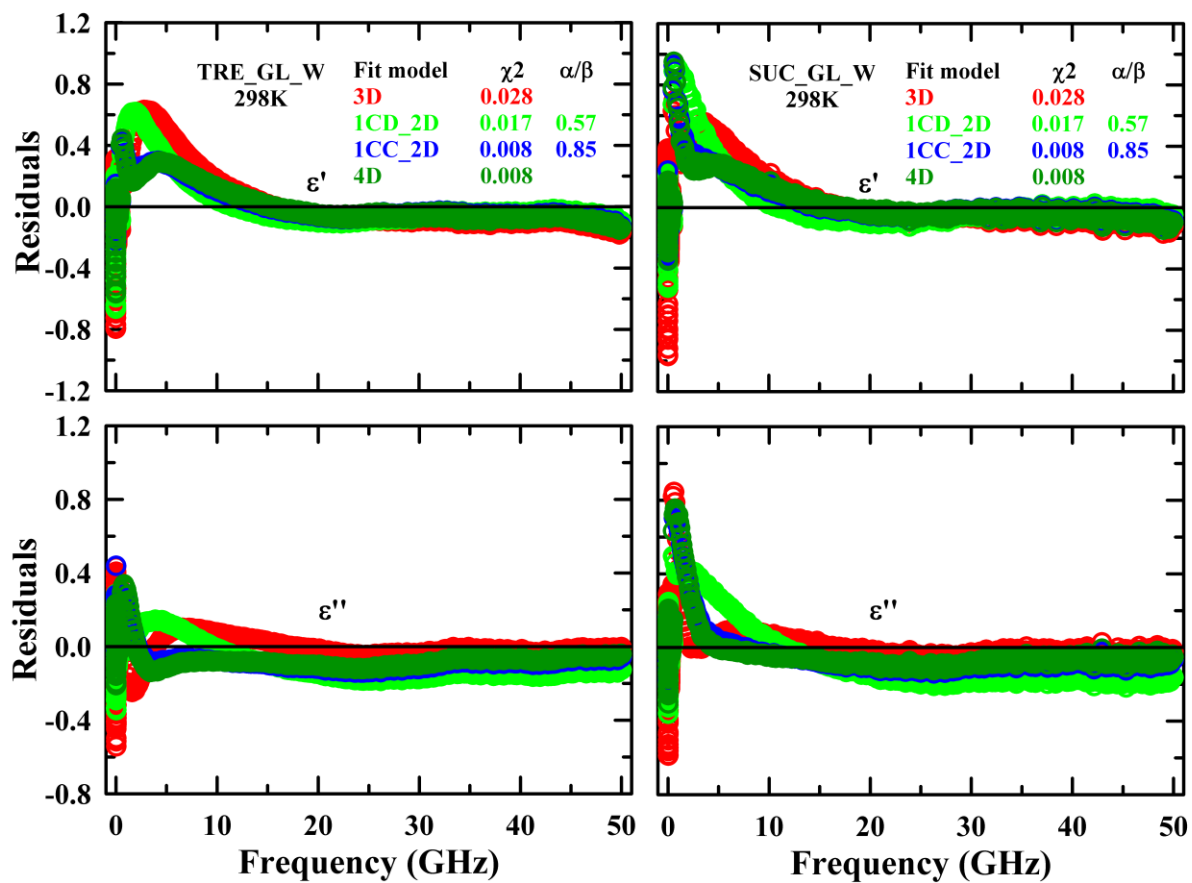
Figure A7.7: Residuals of fittings for real (ε') and imaginary (ε'') component of complex DR spectra in TRE_GL_W (left panel) and SUC_GL_W (right panel) systems at 298K. The solid black line represents zero base line. All representations are colour-coded.

Table A7.8: The calculated translational diffusion time from the Stokes-Einstein relation and rotational diffusion time from Stokes-Einstein-Debye relation[128] in pure GL, GL_W, TRE_GL_W, and SUC_GL_W at 298 K.

Stokes-Einstein equation of translational diffusion for a spherical particle is as follows $D_{trans} = K_B T / C\pi\eta\sigma$ where K_B, T, C, η and σ are denoted Boltzmann constant, temperature, coupling constant for slip (2) and stick (3) condition, viscosity, and diameter of species respectively. Relation between D_{trans} and translational diffusion time τ_{trans} is $\tau_{trans} = \sigma^2/D_{trans} = \sigma^3 C\pi\eta/K_B T$, $\sigma_W = 3.4\,\text{Å}$, $\sigma_{GL} = 5.53\,\text{Å}$, $\sigma_{TRE} = 8.876\,\text{Å}$, $\sigma_{SUC} = 8.195\,\text{Å}$.[99,128,129]

Stokes-Einstein-Debye equation for rotational diffusion time τ_{rot} with volume V, coupling constant C and molecular shape factor f is $\tau_{rot} = 3V\eta f C/K_B T$. At stick limiting condition $C = 1$, shape factor $f = 1$ for water (spherical), $f = 1.01$ for glycerol (prolate) and $f = 1.29$ for trehalose and sucrose (prolate), and V = molecular volume= 20.6 Å³ (water), 88.5 Å³ (glycerol), 330 Å³ (trehalose), and 288 Å³ (sucrose).[99,128,129]

T/K	η/cP	Species	τ_{trans}/ns stick	τ_{trans}/ns slip	τ_{rot}/ns stick
GL	922	GL	357.160	238.106	60.120
GL_W	653.3	GL	253.071	168.145	42.599
		W	58.817	39.211	9.817
TRE_GL_W	2733	GL	1058.694	705.796	178.209
		W	246.054	164.036	41.071
		TRE	4377.711	2918.473	848.729
SUC_GL_W	2276	SUC	2869.291	1912.861	616.511
		GL	881.664	587.776	148.410
		W	204.911	136.507	34.545
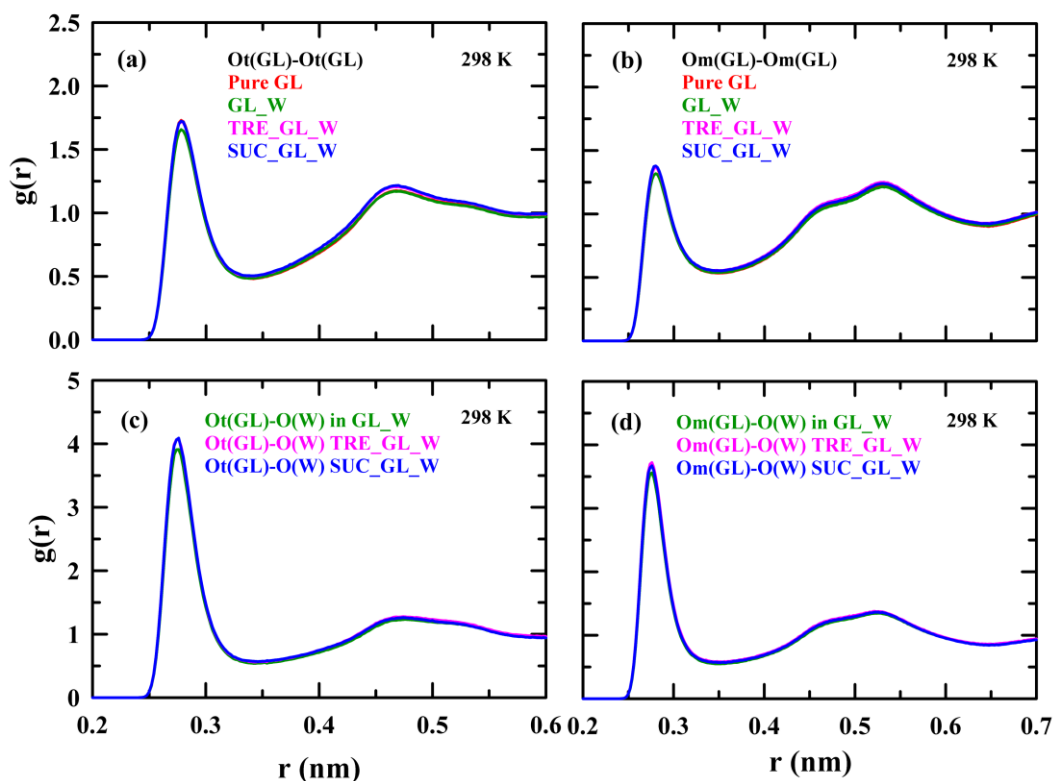
Figure A7.9: Intermolecular RDF for (a) O-O atom pairs between terminal oxygen of glycerol in pure GL, GL_W, TRE_GL_W, and SUC_GL_W systems, (b) O-O atom pairs between middle oxygen of glycerol in pure GL, GL_W, TRE_GL_W, and SUC_GL_W systems, (c) O-O atom pairs for terminal oxygen of GL and water in GL_W, TRE_GL_W, and SUC_GL_W systems. (d) O-O atom pairs for middle oxygen of GL and water in GL_W, TRE_GL_W, and SUC_GL_W systems at 298 K. All representations are colour-coded.
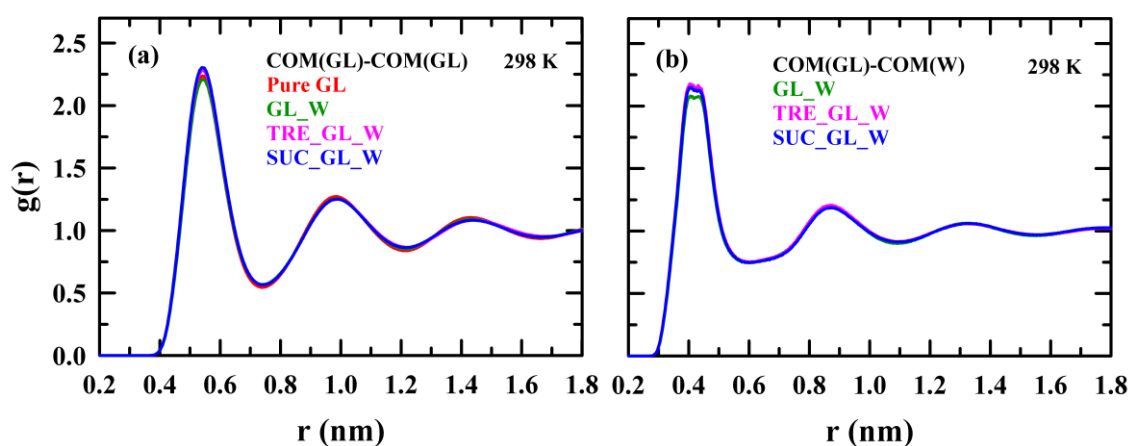
Figure A7.10: Center of mass (COM) RDFs for (a) GL-GL in pure GL, GL_W, TRE_GL_W, and SUC_GL_W systems, (b) GL-water in GL_W, TRE_GL_W, and SUC_GL_W systems at 298 K. All representations are colour-coded.

Table A7.11: Positions (in nm) of first maximum and first minimum, and coordination number of intermolecular centre-of-mass (COM)-centre-of-mass (COM) RDFs for pre glycerol (GL), pure water (w), glycerol-water (GL_W), trehalose dihydrate-glycerol (TRE_GL_W), and sucrose dihydrate-glycerol (SUC_GL_W) systems at 298 K.

RDF pairs between COM	System	r_{max}	r_{min}	Coordination number (CN)			
				GL	W	TRE	SUC
GL-GL	Pure GL	0.54	0.74	13.19			
	GL_W	0.542	0.736	12.74			
	TRE_GL_W	0.542	0.742	11.23			
	SUC_GL_W	0.542	0.742	11.29			
W-W	Pure W	0.276	0.332		4.45		
	GL_W	0.274	0.356		0.3		
	TRE_GL_W	0.274	0.360		0.29		
	SUC_GL_W	0.272	0.356		0.3		
TRE-TRE	TRE_GL_W	0.812	9.52			1.28	
		1.068*	1.210*			3.127*	
SUC-SUC	SUC_GL_W	0.868	1.082				2.119
GL-W	GL_W	0.432	0.598		0.83		
	TRE_GL_W	0.404	0.602		0.80		
	SUC_GL_W	0.408	0.604		0.79		
W-GL	GL_W	0.425	0.604	7.36			
	TRE_GL_W	0.409	0.594	6.22			
	SUC_GL_W	0.408	0.604	6.37			
GL-TRE	TRE_GL_W	0.540	0.648			0.32	
		0.749*	0.919*			1.22*	
TRE-GL	TRE_GL_W	0.540	0.648	5.11			
		0.797*	0.926*	19.98*			
GL-SUC	SUC_GL_W	0.745	0.904				1.16
SUC- GL	SUC_GL_W	0.745	0.904	18.52			
TRE-W	TRE_GL_W	0.384	0.534		0.35		
		0.676*	0.784*		1.53*		

W-TRE	TRE_GL_W	0.386	0.546			0.19	
		0.689*	0.788*			0.78*	
SUC-w	SUC_GL_W	0.610	0.764				1.55
W-SUC	SUC_GL_W	0.610	0.764				0.77

*Valu from second peak maxima, second peak minima and CN corresponding to second peak minima from simulated RDFs and CN calculations.

Table A7.12: Number of H-bond (N_{HB}) for GL-GL per GL (GL-GL/ GL), water-water per water (W-W/W), disaccharides-disaccharides per disaccharide (S-S/S), GL-water per water (GL-W/W) or per GL (GL-W/GL), disaccharide-GL per disaccharide (S-GL/S) or per GL (S-GL/GL), disaccharide-water per disaccharide (S-W/S) or per water(S-W/W), and total number of H-bond each molecule considering all interactions in different systems at 298 K. Arrow is denoted H-bond donor to acceptor pair.

H-bond pairs and with reference molecule		Pure GL or W	GL_W	TRE_GL_W	SUC_GL_W
GL-GL/GL	intra	0.26	0.29	0.24	0.25
	inter	4.58	4.30	3.78	3.83
	total	4.84	4.59	4.02	4.08
W-W/W		3.65	0.29	0.24	0.23
S-S/S	intra			1.08	1.61
	inter			2.35	2.66
	total			3.43	4.27
GL→W/W			1.19	1.00	1.04
W→GL/W			1.76	1.54	1.58
GL→W/GL			0.14	0.13	0.13
W→GL/GL			0.21	0.19	0.19
S→GL/S				4.34	4.00
GL→S/S				4.32	4.24
S→GL/GL				0.27	0.25
GL→S/GL				0.27	0.27
S→W/S				0.37	0.23

W→S/S			0.49	0.37
S→W/W			0.18	0.12
W→S/W			0.26	0.18
Total number of H-bond per molecule considering all interactions.				
GL	4.84	4.94	4.75	4.93
Water	3.65	3.24	3.20	3.16
Trehalose/Sucrose			12.96	13.11

References

1   K. B. Storey and J. M. Storey, *Physiol. Rev.*, 2017, **97**, 623–665.

2   U. Bechtold, *Front. Plant Sci.*, 2018, **9**, 1–8.

3   C. Krembs, H. Eicken, K. Junge and J. W. Deming, *Deep-Sea Res. I: Oceanogr. Res. Pap.*, 2002, **49**, 2163-2181.

4   G. N. Somero and A. L. DeVries, *Science (1979)*, 1967, **156**, 257–258.

5   R. Gupta and R. Deswal, *J Biosci*, 2014, **39**, 931–944.

6   M. S. Clark and M. R. Worland, *J Comp Physiol B*, 2008, 178, 917–933.

7   J. P. Costanzo, R. E. Lee and P. H. Lortz, *J. exp. Biol*, 1993, **181**, 245–255.

8   K. B. Storey and J. M. Storey, *Physiol. Rev.*, 2017, **97**, 623–665.

9   O. Kandror, A. Deleon and A. L. Goldberg, *PNAS*, 2002, **99**, 9727–9732.

10   M. R. Michaud and D. L. Denlinger, *J. Comp. Physiol. B, Biochem. Syst. Environ.*, 2007, **177**, 753–763.

11   K. B. Storey, *Comp. Biochem. Physiol*, 1997, **117**, 319–326.

12   S. D. Rowley, W. I. Bensinger, T. A. Gooley and C. Dean Buckner, *Blood*, 1994, **83** 2731–2736.

13   J. Donnez, B. Martinez-Madrid, P. Jadoul, A. Van Langendonckt, D. Demylle and M. M. Dolmans, *Hum. Reprod. Update*, 2006, **12**, 519–535.

14   J. K. Lewis, J. C. Bischof, I. Braslavsky, K. G. M. Brockbank, G. M. Fahy, B. J. Fuller, Y. Rabin, A. Tocchio, E. J. Woods, B. G. Wowk, J. P. Acker and S. Giwa, *Cryobiology*, 2016, **72**, 169–182.

15   Y. Xin, C. Kielar, S. Zhu, C. Sikeler, X. Xu, C. Möser, G. Grundmeier, T. Liedl, A. Heuer-Jungemann, D. M. Smith and A. Keller, *Small*, 2020, **16**, 1905959.

16   C. Olsson, H. Jansson and J. Swenson, *J. Phys. Chem. B*, 2016, **120**, 4723–4731.

17   B. R. Chief, M. D. Carr, S. L. Guest Editors, M. D. Tan, G. Roger, P. D. Gosden and D. Sc, *Semin. Reprod. Med.*, 2002, **20**, 005–014.

18   P. A. King, M. N. Rosholt and K. B. Storey, *Can. J. Zool.*, 1995, **73**, 1-9.

19   L. Zhang, L. Liu, Y. Qian and Y. Chen, *Eur. J. Pharm. Biopharm.*, 2008, **69**, 750–759.

20   L. M. Crowe, D. S. Reid and J. H. Crowe, *Biophys. J.*, 1996, **71**, 2087-2093.

21   L. M. Crowe, J. H. Crowe, A. Rudolph, C. Womersley and L. Appel, *Arch. Biochem. Biophys.*, 1985, **242**, 240–247.

22   M. T. Cicerone and C. L. Soles, *Biophys. J.*, 2004, **86**, 3836–3845.

23   A. S. Rudolph and J. H. Crowe, *Cryobiology*, 1985, **22**, 367–377.

24   J. P. R. Motta, F. H. Paraguassú-Braga, L. F. Bouzas and L. C. Porto, *Cryobiology*, 2014, **68**, 343–348.

25   T. Starciuc, B. Malfait, F. Danede, L. Paccou, Y. Guinet, N. T. Correia and A. Hedoux, *J. Pharm. Sci.*, 2020, **109**, 496–504.

26   G. Yu, R. Li and A. Hubel, *Langmuir*, 2019, **35**, 7388–7395.

27   R. R. Santos, T. Tharasanit, J. R. Figueiredo, T. Van Haeften and R. Van Den Hurk, *Cell Tissue Res.*, 2006, **325**, 523–531.

28   C. A. Angell, K. L. Ngai, G. B. McKenna, P. F. McMillan and S. W. Martin, *J. Appl. Phys.*, 2000, **88**, 3113.

29   L. M. Wang and R. Richert, *J. Chem. Phys.*, 2004, **121**, 11170–11176.

30   M. D. Ediger, C. A. Angell and S. R. Nagel, *J. Phys. Chem.*, 1996, **100**, 13200–13212.

31   C. A. Angell, *Science*, 1995, **267**, 1924–1935.

32   A. P. R. Rodrigues, C. A. Amorim, S. H. F. Costa, M. H. T. Matos, R. R. Santos, C. M. Lucci, S. N. Báo, O. M. Ohashi and J. R. Figueiredo, *Theriogenology*, 2004, **61**, 1009–1024.

33   L. Weng, C. Chen, J. Zuo and W. Li, *J. Phys. Chem. A*, 2011, **115**, 4729–4737.

34   Y. Gu and F. Jérôme, *Green Chemistry*, 2010, **12**, 1127–1138.

35   A. P. Abbott, R. C. Harris, K. S. Ryder, C. D'Agostino, L. F. Gladden and M. D. Mantle, *Green Chemistry*, 2011, **13**, 82–90.

36   D. M. Sanderson, *J. Pharm. Pharmacol.*, 2011, **11**, 150–156.

37   A. E. Díaz-Álvarez, J. Francos, B. Lastra-Barreira, P. Crochet and V. Cadierno, *Chem. Commun.*, 2011, **47**, 6208–6227.

38   Y. Gu, J. Barrault and F. Jérôme, *Adv. Synth. Catal.*, 2008, **350**, 2007–2012.

39   S. Clark, N. M. Jomha and J. A. W. Elliott, *J. Phys. Chem. B*, 2022, **126**, 9566–9579.

40   N. Shardt, Z. Chen, S. C. Yuan, K. Wu, L. Laouar, N. M. Jomha and J. A. W. Elliott, *Cryobiology*, 2020, **92**, 180–188.

41   M. De, L. Reyes, L. Saenz, L. Lapierre, J. Crosby, C. Barros and M. De Los Reyes, *Vet. Rec.*, 2002, **151**, 477–480.

42   D. C. C. Brito, S. F. S. Domingues, A. P. R. Rodrigues, J. R. Figueiredo, R. R. Santos and J. C. Pieczarka, *Cryobiology*, 2018, **83**, 97–99.

43   L. L. Kuleshova, D. R. Macfarlane, A. O. Trounson and J. M. Shaw, *Cryobiology*, 1999, **38**, 119–130.

44   A. M. da Silva, L. G. P. Bezerra, E. C. G. Praxedes, S. S. J. Moreira, C. M. P. de Souza, M. F. de Oliveira, A. F. Pereira, P. Comizzoli and A. R. Silva, *Cryobiology*, 2019, **91**, 53–60.

45   A. Sakai and F. Engelmann, *Cryo-Lett.*, 2007, **28**, 151–172.

46   Y. Tao, E. Sanger, A. Saewu and M. C. Leveille, *Reprod. Biol. Endocrinol.*, 2020, **18**, 17-undefined.

47   G. Vajta and Z. P. Nagy, *Reprod. Biomed. Online*, 2006, **12**, 779–796.

48   G. M. Fahy and B. Wowk, *Methods Mol. Biol.*, 2015, **1257**, 21–82.

49   G. D. Elliott, S. Wang and B. J. Fuller, *Cryobiology*, 2017, **76**, 74–91.

50   J. J. Towey, A. K. Soper and L. Dougan, *Faraday Discuss.*, 2013, **167**, 159–176.

51   S. D. Allison, B. Chang, T. W. Randolph and J. F. Carpenter, *Arch. Biochem. Biophys.*, 1999, **365**, 289–298.

52   J. J. Towey, A. K. Soper and L. Dougan, *J. Phys. Chem. B*, 2012, **116**, 13898–13904.

53   A. Lerbret, P. Bordat, F. Affouard, M. Descamps and F. Migliardo, *J. Phys. Chem. B*, 2005, **109**, 11046–11057.

54   L. Weng, S. L. Stott and M. Toner, *Annu. Rev. Biomed. Eng.*, 2019, **21**, 1–31.

55   S. Indra and R. Biswas, *J. Phys. Chem. B*, 2016, **120**, 11214–11228.

56   F. L. Janz, A. A. Debes, R. C. Cavaglieri, S. A. Duarte, C. M. Romão, A. F. Morón, M. Zugaib and S. P. Bydlowski, *J. Biomed. Biotechnol.*, 2012, 1-10.

57   C. Hunt and C. J. Hunt, *Transfus. Med. Hemotherapy*, 2011, **38**, 107–123.

58   A. Simperler, A. Kornherr, R. Chopra, P. A. Bonnet, W. Jones, W. D. S. Motherwell and G. Zifferer, *J. Phys. Chem. B*, 2006, **110**, 19678–19684.

59   W. Zheng and S. L. Simon, *J. Chem. Phys.*, 2007, **127**, 194501.

60   D. W. Davidson and R. H. Cole, *J. Chem. Phys.*, 1951, **19**, 1484–1490.

61   G. E. McDuffie, R. G. Quinn, T. A. Litovitz, A. Phys Lett, J. Chem Phys and G. E. McDuFFIE, *J. Chem. Phys.*, 1962, **37**, 239–242.

62   A. Puzenko, Y. Hayashi, Y. E. Ryabov, I. Balin, Y. Feldman, U. Kaatze and R. Behrends, *J. Phys. Chem. B*, 2005, **109**, 6031–6035.

63   Y. Hayashi, A. Puzenko, I. Balin, Y. E. Ryabov and Y. Feldman, *J. Phys. Chem. B*, 2005, **109**, 9174–9177.

64   A. Charkhesht, D. Lou, B. Sindle, C. Wen, S. Cheng and N. Q. Vinh, *J. Phys. Chem. B*, 2019, **123**, 8791–8799.

65   E. Heid, P. Honegger, D. Braun, A. Szabadi, T. Stankovic, O. Steinhauser and C. Schröder, *J. Chem. Phys.*, 2019, **150**, 175102.

66   G. I. Olgenblum, L. Sapir and D. Harries, *J. Chem. Theory Comput.*, 2020, **16**, 1249–1262.

67   D. Averett, M. T. Cicerone, J. F. Douglas and J. J. De Pablo, *Soft Matter*, 2012, **8**, 4936–4945.

68   A. Anopchenko, T. Psurek, D. Vanderhart, J. F. Douglas and J. Obrzut, *Phys. Rev. E Stat. Nonlin. Soft Matter Phys.*, 2006, **74**, 031501.

69   N. C. Maity, A. Baksi, K. Kumbhakar and R. Biswas, *J. Photochem. Photobiol. A: Chem.*, 2023, **439**, 114600.

70   C. J. F. Böttcher and P. Bordewijk, *Theory of Electric Polarization: Dielectrics in Time-dependent*, Elsevier, Amsterdam, 1978

71   A. Schönhals and F. Kremer, *Theory of Dielectric Relaxation*, Springer Berlin Heidelberg, 2003.

72   P. R. Bevington and D. K. Robinson, *Data reduction and error analysis for the physical sciences*, McGraw-Hill Education, New York, 3rdEdition, 2003.

73   K. Mukherjee, A. Barman and R. Biswas, *J. Mol. Liq.*, 2016, **222**, 495–502.

74   E. Lindhal, M. Abraham, B. Hess and D. van der Spoel, GROMACS 2021.4 Manual, https://doi. org/10.5281/ZENODO.5053220, https://zenodo.org/record/5053220.

75   M. Iannuzzi, A. Laio and M. Parrinello, *Phys. Rev. Lett.*, 2003, **90**, 4.

76   L. S. Dodda, I. C. De Vaca, J. Tirado-Rives and W. L. Jorgensen, *Nucleic Acids Res.*, 2017, **45**, W331–W336.

77   W. L. Jorgensen and J. Tirado-Rives, *PNAS*, 2005, **102**, 6665-6670.

78   L. S. Dodda, J. Z. Vilseck, J. Tirado-Rives and W. L. Jorgensen, *J. Phys. Chem. B*, 2017, **121**, 3864–3870.

79   http://zarbi.chem.yale.edu/ligpargen/.

80   L. Martinez, R. Andrade, E. G. Birgin and J. M. Martínez, *J. Comput. Chem.*, 2009, **30**, 2157–2164.

81   G. Bussi, D. Donadio and M. Parrinello, *J. Chem. Phys.*, 2007, **126**, 14101.

82   M. Parrinello and A. Rahman, *J. Appl. Phys.*, 1998, **52**, 7182.

83   T. Darden, D. York and L. Pedersen, *J. Chem. Phys.*, 1998, **98**, 10089.

84   A. Aguado and P. A. Madden, *J. Chem. Phys.*, 2003, **119**, 7471.

85   B. Hess, H. Bekker, H. J. C. Berendsen and J. G. E. M. Fraaije, *J. Comput. Chem.*, 1997, **18**, 14631472.

86   A. Luzar, *Faraday Discuss*, 1996, **103**, 29–40.

87   A. Luzar and D. Chandler, *J. Chem. Phys.*, 1993, **98**, 8160–8173.

88   A. Luzar and D. Chandler, *Nature*, 1996, **379**, 55–57.

89   D. C. Rapaport, *Mol Phys*, 1983, **50**, 1151–1162.

90   A. Chandra, *Phys. Rev. Lett.*, 2000, **85**, 768.

91   S. Balasubramanian, S. Pal and B. Bagchi, *Phys. Rev. Lett.*, 2002, 89, 115505.

92   J. R. Errington and P. G. Debenedetti, *Nature,* 2001, **409**, 318–321.

93   C. A. Angell, *Chem. Rev.*, 2002, **102**, 2627–2650.

94   J. L. Green and C. A. Angell, *J. Phys. Chem.*, 1989, **93**, 2880–2882.

95   R. A. Riggleman, K. Yoshimoto, J. F. Douglas and J. J. De Pablo, *Phys. Rev. Lett.*, 2006, **97**, 045502.

96   D. Lourdin, S. G. Ring and P. Colonna, *Carbohydr Res*, 1998, **306**, 551–558.

97   J. H. Crowe, L. M. Crowe and R. Mouradian, *Cryobiology*, 1983, **20**, 346–356.

98   M. Kaszuba, D. McKnight, M. T. Connah, F. K. McNeil-Watson and U. Nobbmann, *J Nanopart Res.,* 2008, **10**, 823–829.

99   M. E. Gallina, L. Comez, A. Morresi, M. Paolantoni, S. Perticaroli, P. Sassi and D. Fioretto, *J. Chem. Phys.*, 2010, **132**, 214508.

100   C. Olsson and J. Swenson, *J. Phys. Chem. B*, 2020, **124**, 3074–3082.

101   M. T. Sonoda and M. S. Skaf, *J. Phys. Chem. B*, 2007, **111**, 11948–11956.

102   D. Maji, N. C. Maity and R. Biswas, *Theor. Chem. Acc.*, 2023, **142**, 1–15.

103   D. L. Sidebottom, *Phys. Rev. E.,*2019, **100**, 029901.

104   R. Chelli, P. Procacci, G. Cardini and S. Califano, *Phys. Chem. Chem. Phys.*, 1999, **1**, 879–885.

105   U. Schneider, P. Lunkenheimer, R. Brand and A. Loidl, *J. Non-Cryst. Solids*, 1998, **235–237**, 173–179.

106   D. Beece, L. Eisenstein, H. Frauenfelder, D. Good, M. C. Marden, L. Reinisch, K. T. Yue, A. H. Reynolds and L. B. Sorensen, *Biochemistry*, 1980, **19**, 5147–5157.

107   K. Mukherjee, S. Das, E. Tarif, A. Barman and R. Biswas, *J. Chem. Phys.*, 2018, **149**, 124501.

108   T. Sato and R. Buchner, *J. Phys. Chem. A*, 2004, **108**, 5007–5015.

109   K. Mukherjee, A. Barman and R. Biswas, *J. Chem.Phys.*, 2019, **151**, 184901.

110   Y. Sakai, S. Kuroki and M. Satoh, *Langmuir*, 2008, **24**, 6981–6987.

111   M. A. Bag and L. M. Valenzuela, *Int. J. Mol. Sci.,* 2017, **18**, 1422.

112   B. Gestblom, *J. Phys. Chem.*, 1991, **95**, 6064–6066.

113   S. Mashimo, S. Kuwabara, S. Yagihara and K. Higasi, *J. Phys. Chem.*, 1987, **91**, 6337–6338.

114   N. Nandi and B. Bagchi, *J. Phys. Chem. B*, 1997, **101**, 10954–10961.

115   N. Nandi, K. Bhattacharyya and B. Bagchi, *Chem. Rev.*, 2000, **100**, 2013–2045.

116   A. Baksi, J. Rajbangshi and R. Biswas, *Phys. Chem. Chem. Phys.*, 2021, **23**, 12191–12203.

117 G. M. Brown, D. C. Rohrer, B. Berking, C. A. Beevers, R. O. Gould and R. Simpson, *Acta Cryst.*, 1972, **B28**, 3145–3158.

118 G. M. Brown and H. A. Levy, *Acta Crystallogr. B*, 1973, **29**, 790–797.

119 S. Kaur, A. Gupta, H. K. Kashyap and H. K. Kashyap, *J. Phys. Chem. B*, 2020, **124**, 2230–2237.

120 A. Baksi and R. Biswas, *ACS Omega*, 2022, **7**, 10970–10984.

121 M. Brehm and B. Kirchner, *J. Cheminformatics*, 2012, **4**, 1–2.

122 W. Humphrey, A. Dalke and K. Schulten, *J. Mol. Graphics*, 1996, **14**, 33–38.

123 D. A. Jahn, F. O. Akinkunmi and N. Giovambattista, *J. Phys. Chem. B*, 2014, **118**, 11284–11294.

124 S. Yadav and A. Chandra, *Jo. Chem. Phys.*, 2017, **147**, 244503.

125 B. Das, B. Sharma and A. Chandra, *J. Phys. Chem. C*, 2018, **122**, 9374–9388.

126 A. Baksi and R. Biswas, *J. Phys. Chem. B*, 2020, **124**, 11718–11729.

127 A. A. Sandilya, U. Natarajan and M. H. Priya, *ACS Omega*, 2020, **5**, 25655–25667.

128 Biman Bagchi, *Molecular relaxation in liquids*, Oxford University Press, New York, 2012.

129 J. T. Edward, *J. Chem. Educ.*, 1970, **47**, 261–270.

Chapter 8

Co-solvent Dependent Modulation of Solution Structure and Dynamics of Li-based Battery Electrolytes for Enhanced Performance

8.1 Introduction

Nowadays, the focus of research and development efforts have increasingly shifted towards energy materials in order to address the demands of future energy needs. One area of current attention is lithium-ion batteries (LIBs), which have captured the market as a preferred energy storage solution due to high energy density and long lifecycle.[1,2] Scientific and technological investigation on LIBs constitute a growing area of research and designated for solving the crisis of electronic and electric vehicle purposes. An integral component of LIBs, as well as capacitors and fuel cells, is proper choice of electrolyte systems, electrodes and the solvent matrix.[3–6] The electrolyte is entrusted with the role of facilitating the movement of charges. Consequently, electrolytes used in LIBs must exhibit specific characteristics such as excellent thermal stability, low toxicity, high conductivity, immunity to electrode corrosion, and an extended operational lifespan. In parallel, the solvent used for preparing of electrolyte solution holds crucial properties like high static dielectric constant (ε_s) and low viscosity to facilitate the dissociation of the lithium salt and enable the unimpeded motion of ions towards electrodes. The electrolytes for LIBs incorporated lithium salt as bis-(trifluoromethane)sulfonimide lithium salt (LiTFSI), lithium perchlorate (LiClO$_4$), lithium hexafluorophosphate (LiPF$_6$), lithium fluoroborate (LiBF4), lithium trifluoromethanesulfonate (LiCF$_3$SO$_3$), lithium bis(fluorosulfonyl)imide (LiFSI).[3] These lithium salts are dissolved in individual or mixture of organic cyclic and acyclic carbonates such as ethylene carbonate (EC), propylene carbonate (PC), and dimethyl carbonate (DMC) or nitriles like acetonitrile (AN), glutaronitrile (GLN), adiponitrile (ADN), succinonitrile (SN).[3] This wide range of components finds extensive application in industrial settings for rechargeable LIBs.

Our primary objective revolves around comprehending the intricate architecture, dynamics behaviour, conductivity, and various intrinsic characteristics such as melting point, glass transition temperature, and viscosity of electrolyte systems used in LIBs. This comprehensive

understanding stands as a pivotal foundation for the future integration of these electrolytes into electronic and transportation devices. In our study, we have chosen lithium salt as LiTFSI because of its exceptional attributes, including excellent thermal stability, chemical inertness towards electrode reactions and easily soluble in a wide variety of organic solvents.[7] Two types of solvents and their mixtures are used for the preparation of LiTFSI-based electrolyte solutions. One of those solvents is ADN characterized by a notably elevated electrochemical oxidation potential (~ 5V), a moderate static dielectric constant (ε_s), low viscosity, and wide operating temperature range.[8,9] An alternative solvent, EC has emerged as a promising solvent for LIBs electrolytes due to its high static dielectric constant, rendering it proficiency in dissolving most of lithium-ion salt.[10] LiTFSI in EC shows high conductivity but has a voltage capacity (~ 3.5 V) lower than the LiTFSI/ADN electrolyte (~ 6 V) system.[8,11] By incorporating a solvent like EC, we can modify solid electrolyte interface (SEI).[8,12]

Researchers have explored the use of LiTFSI in ADN without any additional co-solvent suitable for LIB applications.[13] The ion transportation in these systems, containing various concentrations of Li-salt in and, has been studied through NMR, X-ray diffraction, electrochemical methods, Raman scattering and MD simulations.[14–18] The conductivity of LiTFSI/ADN electrolyte system tends to improve with the addition of co-solvents like EC.[8] However the combination of LiTFSI with solvent mixtures such as ADN+EC is gaining interest, though there are limited experimental and computational studies on this.[8,12] There is a need to investigate the LiTFSI/(ADN +EC) systems comprehensively, focusing on its structural, dynamical, thermo-physical and transport properties. ADN and EC are both polar liquids, with a significant difference in ε_s, yet they exhibit a small difference in medium viscosity. This contrast in solvent polarity offers a unique opportunity to explore its impact on ion transport.

In the present work, we have investigated the structural, dynamical, and thermophysical aspects of 1M LiTFSI in [xEC + (1−x)ADN] via differential scanning calorimetry (DSC), conductivity (σ) measurements, dielectric relaxation spectroscopy (DRS) and molecular dynamic (MD) simulations, where x denotes mole fraction of EC. Here, LiTFSI concentration was fixed at 1M LiTFSI in ADN which gives maximum conductivity as shown in Figure 8.1 and also corroborates well with earlier reported studies[13]. EC was added to 1M LiTFSI electrolyte solutions replacing ADN by their mole fraction and it acted as a co-solvent. DSC measurements revealed that electrolyte with moderate EC content (X_{EC} = 0.4 or 0.6) exhibit a wider temperature window of accessibility compared to electrolytes containing a single solvent. Conductivity (σ) of electrolyte solution increases with increasing EC concentration and this

can be explained by two factors: (1) reduction of viscosity, and (2) better dissolution due to high dielectric solvent EC shielding electrostatic interaction in between cation and anion. Multi-Debye dielectric relaxation has been observed in these electrolyte solutions and that may originate from solvent in bulk (slow τ_1^s ~120-60 ps), solvent in solvation shell around ion (moderately slow τ_2^s ~45-35 ps), and zig-zag motion of anion side chain (fast τ_3^s ~7-5 ps). The static dielectric constant (ε_s) of electrolyte solutions increases with addition of high dielectric co-solvent EC. But dielectric decrement from solvent to respective electrolyte solution also increases with EC concentrations. Later, Kirkwood G factor (G_K) calculation in the MD simulation section in these systems decoded this phenomenon. Coupling between medium viscosity and DR/conductivity evaluated via the relation $\tau \propto \left(\frac{\eta}{T}\right)^p$ and $\sigma \propto \left(\frac{T}{\eta}\right)^p$ which suggests that with increasing EC concentration, electrolyte systems are dynamically more homogeneous. Activation energy of both DR and conductivity is decoupled from viscosity activation. That indicates DR dynamics and ion transport are governed by local friction, not bulk viscosity. Both p value and activation energy data suggested that coupling between rotation and translational dynamics may occur at higher EC concentrations ($X_{EC} \geq 0.6$). The solution structure has been investigated by analyzing radial distribution function (RDF), coordination number (CN) and spatial distribution function (SDF). Self-diffusion coefficient of all the species in these electrolyte solutions indicates that ions travel with their solvation shell. The total conductivity (σ_{total}) of electrolyte solutions has been explored in terms of Nernst-Einstein conductivity (σ_{NE}, from the self-diffusion part) and intra and inter-species distinct ionic conductivity (correlated motion of ions). This analysis revealed that the reduction of total conductivity from Nernst-Einstein conductivity mainly happens due to the negative contribution of anion-anion distinct correlation to the net conductivity.

8.2 Experimental Details

8.2.1 Materials and Sample Preparation

LiTFSI (Sigma Aldrich, ≥99%), and ADN (Sigma Aldrich, ≥99%) and EC (Alfa Aesar, ≥99%) were purchased and used without further purification. The structures of these chemical species are shown in Scheme 8.1. The samples were prepared in two steps as follows: first, the ADN-EC binary solvent mixture prepared by taking required amount of ADN and EC in a glass container, and a Teflon-coated magnetic bar was added before sealing and making it airtight by proper care with Teflon and parafilm tapes. The sample was mixed well on a magnetic stirrer until it formed a clear liquid at 298 K. Second, a required amount of LiTFSI was added to the

neat (EC or ADN) and binary solvent mixture to make 1M electrolyte solution. The solutions were mixed again on a magnetic stirrer until it appeared clear solution. Note, for the preparation of 1M LiTFSI in EC, the solution mixture was prepared at 313 K and then it cooled to 298 K. The prepared clear solutions were used to perform density, refractive index, viscosity, conductivity, DSC, and DRS measurements.
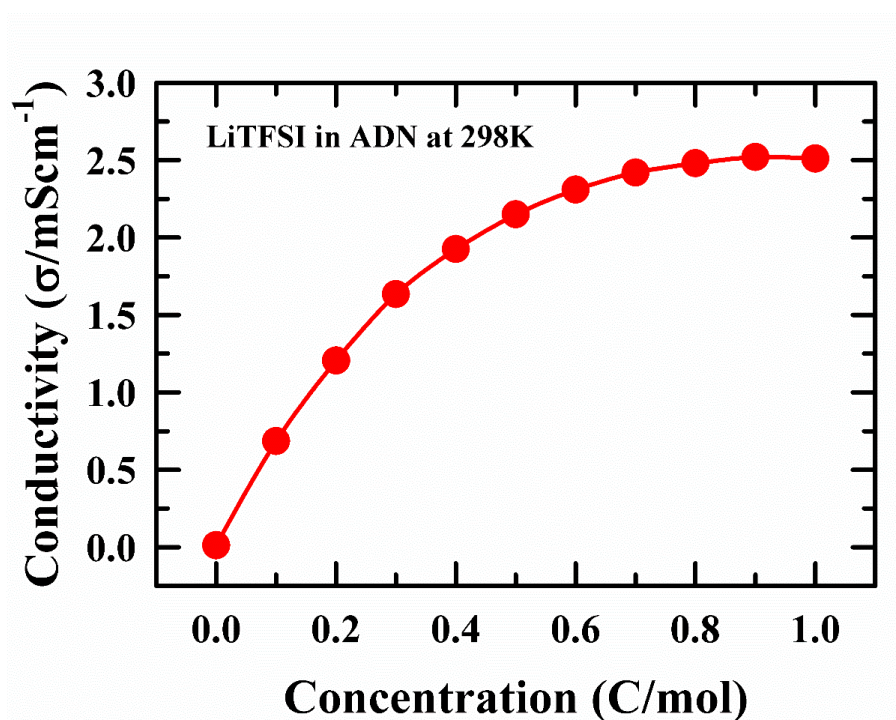
Figure 8.1: Salt concentration dependent conductivity in LiTFSI/ADN electrolyte systems.
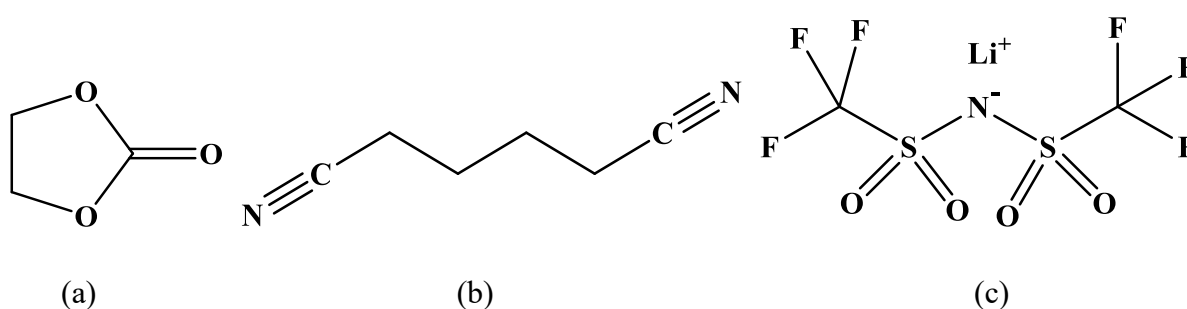
Scheme 8.1: Chemical structures of (a) EC, (b) ADN, (c) LiTFSI.

8.2.2 Density, Refractive Index, Viscosity and Conductivity Measurements

An automated temperature-controlled density cum sound analyzer (Anton Parr, model DSA 5000) was used to measure the density (ρ) and sound velocity (v) of the experimental

solution.[19] The refractive index (n_D) was determined using an automated temperature-controlled refractometer (RUDOLPH, J357).[20] The solution viscosity coefficient (η), which is dependent on both temperature and EC concentration, was measured for all systems using a Lovis 2000 M viscometer (Anton Parr, 0.5% accuracy and 0.1% repeatability), conductivity (σ) of 1M LiTFSI in binary as well as their neat electrolyte solvent was measured by a benchtop multi-parameter electrochemical meter (SESHIN BIOTECH, Model:ECM-610). Temperature-dependent experiments were conducted within the range of 298K to 323K. The measured values of ρ, v, and n_D at different temperatures for 1M LiTFSI in xEC+(1-x)ADN are provided in Table A8.1 (Appendix). The η and σ values of all these systems are given in Table 8.1. Also, the values of ρ, v, and n_D, at different temperatures for xEC+(1-x)ADN solvent systems are presented in Table A8.2 (Appendix).

Table 8.1: Temperature and EC concentration dependent viscosity coefficient (η) and conductivity (σ) of 1M LiTFSI in xEC+(1-x)ADN electrolyte solutions.

X_{EC}	0	0.2	0.4	0.6	0.8	1
T/K	η/cP[a]					
298	17.74	15.56	13.11	10.65	7.86	6.23
303	15.02	13.20	11.24	9.21	6.82	5.68
308	12.83	11.34	9.71	7.97	5.96	5.08
313	11.10	9.86	8.48	6.96	5.32	4.60
318	9.67	8.62	7.47	6.13	4.76	4.20
323	8.49	7.60	6.63	5.50	4.39	3.85
σ/ mScm^{-1}[b]						
298	2.653	3.069	3.422	4.275	5.189	6.329
303	2.871	3.415	3.856	4.604	5.646	7.032
308	3.312	3.794	4.321	5.222	6.366	7.753
313	3.780	4.309	4.832	5.821	7.038	8.441
318	4.285	4.899	5.404	6.464	7.653	9.182
323	4.773	5.386	6.289	7.100	8.413	10.026

[a]Viscosity coefficient (η) values can be reproduced within ± 5% of the reported values.

[b] Conductivity (σ) values can be reproduced within ± 5-7% of the reported values.

8.2.3 Differential Scanning Calorimetry (DSC) Measurements

To investigate the glass transition temperature (T_g) and melting point temperature (T_m) of the electrolyte solutions, we employed differential scanning calorimetry (DSC) (TA Instruments Q200).[21] The heat flow and temperature were calibrated for each measurement using a standard indium sample. DSC measurements of all experimental samples were conducted with a fixed heat flow rate 5 K/min. The samples were contained in an airtight aluminum pan with an aluminum cap (40 μl, Tzero, TA Instruments).

8.2.4 DRS Data Collection and Analysis

The N5235B PNA-L network analyser (200 MHz to 50 GHz) with open ended coaxial probe kit (performance probe for N5235B) was used for DR measurement of liquid.[21] Details of the measurement protocols and data analyses are the same as those discussed in Chapter 2. More details about DRS measurements are available in ref [21–25]. Temperature-dependent DRS experiments were conducted within the range of 298K to 323K.

8.2.5 Simulation Details

We utilized the standard equilibrium molecular dynamics simulation technique to investigate six electrolyte mixtures with 1M LiTFSI in various mole fractions of ADN and EC ($X_{EC} = 0$, 0.2, 0.4, 0.6, 0.8, 1) at temperatures 298 K, 303 K, 313 K, 323 K, and also two neat systems consisting of ADN and EC using GROMACS-2021.3[26] at 323 K. For all simulations, we used the non-polarizable OPLS-AA ionic liquid model for TFSI$^-$ anion.[27,28] For Li$^+$, ADN and EC, we were employed OPLS-AA[29–32] parameters with RESP charge using Gaussian16 package via the B3LYP basis set 6-311++G (d,p). Partial Charges and Lennard-Jones parameters for species EC, ADN, Li$^+$, and TFSI$^-$ are given in Table A8.3 to Table A8.5 (Appendix). Table A8.6 (Appendix) presents the number of species used in multicomponent mixtures and two neat systems considered in our simulation study.

Functional form of the model potential is as follows:

$$E_{ij} = \sum_{bonds} K_r (r - r_{eq})^2 + \sum_{angles} K_\theta \left(\theta - \theta_{eq} \right)^2 + c_0 + c_1 \{ 1 + \cos(\phi) \} + c_2 \{ 1 - \cos(2\phi) \}$$

$$+ c_3 \{ 1 + \cos(3\phi) \} + \sum_{i=1}^{N-1} \sum_{j>i}^{N} \left\{ 4\epsilon_{ij} \left[\left(\frac{\sigma_{ij}}{r_{ij}} \right)^{12} - \left(\frac{\sigma_{ij}}{r_{ij}} \right)^6 \right] + \frac{q_i q_j}{4\pi\epsilon_0 r_{ij}} \right\}. \tag{8.1}$$

In eq. 3.1, K_r and K_θ are force constants of bond stretching and angle bending, respectively, r_{eq} and θ_{eq} denote the equilibrium bond length and angle value. ϕ denotes torsional angle with the Fourier coefficients c_0, c_1, c_2, and c_3 in the torsional, Position and charge of an atom are described by r and q, respectively. The Van der Waals parameters are described by σ and ε. Note that the non-bonded and electrostatic interactions were represented by the Lennard-Jones (LJ) potential and the Coulomb equation, respectively.

To generate the initial molecular configurations, we utilized the PACKMOL software[33] to place them within a cubic box (8 nm edge). The configurations were then subjected to energy minimization using the steepest-descent algorithm. Next, we performed an NVT equilibration for 10 ns at 323 K. For all simulated temperatures we used the equilibration protocol mentioned above. Afterward, temperature annealing was performed, starting at 400 K and decreasing at a rate of 0.04 K/ps until the temperature reached 323 K, and every 20 K the system was equilibrated for 1 ns in NPT ensemble and additional NPT equilibration was conducted for 10 ns. The density values obtained from this equilibration were in good agreement with experimental data, as shown in Figure 8.2 (left panel) and Table 8.2. During the NPT equilibration, we maintained the desired temperature values using the V-rescale thermostat[34] with a time constant of 0.5 ps, and the pressure at 1 bar using the Parrinello-Rahman barostat[35] with a time constant of 2 ps. Bonded and non-bonded interactions were truncated at a cut-off distance of 1.2 nm. Electrostatic interactions were handled using the Particle Mesh Ewald (PME)[36,37] method. Simulation employed Leapfrog algorithm with a time step of 1 fs to solve the equations of motion. Linear Constraint Solver (LINCS)[38] algorithm was used to constrain the bonds involving hydrogens.

An MD production run of 100 ns long was conducted for each electrolyte system within NPT ensemble for radial distribution functions (RDFs), static dielectric constant (ε_s), Kirkwood G factor (G_K), and diffusion coefficient (D) values and the trajectories were saved with a time-gap of 0.2 ps. Throughout the MD production run, temperature and pressure were maintained by using V-rescale thermostat[34] with a time constant of 0.5 ps and the Parrinello-Rahman barostat[35] at 1 bar with a time constant of 2 ps respectively. Note here that a 100 ns production run was necessary to achieve convergence in collective dipole moment fluctuations and minimize errors associated with the computed ε_s and G_K. Simulations employed periodic boundary conditions in all three directions and adhered to minimum image conventions

throughout the entire simulation. Note that the Kirkwood G factor and structural properties were calculated from the data obtained from the NPT production run.

Table 8.2: Experimental and simulated density (ρ, Kg/m^3) of 1M LiTFSI in xEC+(1-x)ADN electrolyte solutions at four temperatures.

System	298K		303K		313K		323K	
X_{EC}	Exp	Simu	Exp	Simu	Exp	Simu	Exp	Simu
0	1087.2	1095.8	1083.3	1090.9	1075.3	1081.1	1067.3	1071.9
0.20	1127.8	1148.7	1123.6	1143.9	1115.2	1133.5	1106.8	1123.9
0.40	1172.8	1197.9	1168.4	1192.8	1159.6	1182.6	1150.7	1172.3
0.60	1240.1	1251.4	1235.3	1245.8	1225.8	1235.5	1216.3	1225.5
0.80	1318.2	1321.6	1313.1	1315.8	1302.7	1304.4	1292.3	1293.1
1	1418.8	1406.2	1413.1	1399.9	1401.6	1388.5	1390.2	1376.8
Neat ADN							939.8	911.5
Neat EC							1309.5	1262.7

8.2.5.1 Viscosity

From the equilibrium simulation trajectory, shear viscosity (η) was calculated by using the Green-Kubo relation[39,40] employing pressure autocorrelation function

$$\eta = \frac{\langle V \rangle}{k_B T} \int_0^\infty dt \langle P_{\alpha\beta}(0) P_{\alpha\beta}(t) \rangle \tag{8.2}$$

In the above equation, V, k_B, and T are the ensemble volume of the simulation box, Boltzmann constant, and temperature, respectively. $P_{\alpha\beta}$ denotes cross-diagonal elements of pressure tensor.

To calculate viscosity, we performed 10 independent NVT production runs, trajectories were saved each 5-fs intervals up to 5ns. Before performing NVT production runs, the pre-equilibrated NPT ensemble further equilibrated in the NVT ensemble for a period 2 ns. During the NVT production runs, temperature control was maintained using V-rescale thermostat[34] with a time constant of 0.5 ps.

To reduce the fluctuation in running integral of the autocorrelation function from the Green-Kubo relation, we averaged 7-10 independent data sets. Finally, shear viscosity was obtained from the average running integral by fitting double-exponential function

$$\eta(t) = A_1\tau_1\left(1 - e^{-t/\tau_1}\right) + A_2\tau_2\left(1 - e^{-t/\tau_2}\right) \tag{8.3}$$

EC mole fraction-dependent time evaluation shear viscosity with time at two temperatures and its fits are shown in Figure A8.7 (Appendix). Time average integrated shear viscosity at various temperatures and EC concentration are shown in Figure 8.2 (right panel) and corresponding values are given in Table 8.3.

Table 8.3: Experimental and simulated viscosity (η, cP) of 1M LiTFSI in xEC+(1-x)ADN electrolyte solutions at four temperatures.

System	298K		303K		313K		323K	
X_{EC}	Exp	Simu	Exp	Simu	Exp	Simu	Exp	Simu
0	17.74	18.53	15.02	15.88	11.10	11.08	8.49	8.91
0.20	15.56	17.09	13.20	14.36	9.86	10.85	7.60	8.59
0.40	13.11	15.05	11.24	12.60	8.48	8.81	6.63	7.29
0.60	10.65	11.46	9.21	9.74	6.96	7.293	5.50	6.17
0.80	7.86	9.92	6.82	7.79	5.32	6.40	4.39	5.53
1	6.23	6.81	5.68	6.05	4.60	5.08	3.85	4.63

8.2.5.2 Radial Distribution Functions (RDFs)

Spatial correlations were tracked computing the radial distribution functions (RDFs), denoted as $g_{ij}(r)$:

$$g_{ij}(r) = \frac{\langle\rho_j(r)\rangle}{\rho_j^{ave}} = \frac{1}{N_i\rho_j^{ave}}\sum_i^{N_i}\sum_j^{N_j}\frac{\delta(r_{ij}-r)}{4\pi r^2} \tag{8.4}$$

here $\langle\rho_j(r)\rangle$ represents the density of particle j around those of type i at a distance r and ρ_j^{ave} is the average number density of particles of type j. N_i and N_j denote the total number of

particles of type i and j respectively. $\delta(r_{ij} - r)$ serves as a representation of a delta function, indicating the presence of another particle of type j at a distance r_{ij} from the central particle of i.

8.2.5.3 Static Dielectric Constant (ε_s) and Kirkwood G Factor (G_K)

Static dielectric constants (ε_s) and Kirkwood G factor (G_K) for the systems studied were calculated by ensemble-averaged over the extended time segment, typically the last 20 ns, out of the 100 ns NPT production run, during which dipole fluctuations had sufficiently dampened. The ε_s was calculated from the following formula[25,41],

$$\varepsilon_s = 1 + \frac{<M^2> - <M>^2}{3\varepsilon_0 k_B T <V>} \tag{8.5}$$

where M is the total dipole moment of the simulation box. T being the temperature and $<V>$ the ensemble averaged volume of the simulation box over the time considered for the calculation. ε_0 denotes the free space permittivity.

G_K was calculated from the equation[42,43],

$$G_K = [\langle M^2 \rangle - \langle M \rangle^2]/N\mu^2 \tag{8.6}$$

where μ and N are the average dipole moment of individual molecule and number of molecular dipoles. The total dipole moment calculated as the vector summation of individual dipole moment $M = \sum_{i=1}^{N} \mu_i$, where μ_i is defined $\mu_i = \sum q_i r_i$ is a vector quantity. Consequently, the value of G_K varies depending on the orientation of diploes among the molecules. Specifically, $G_K = 1$ signifies random or uncorrelated orientations among molecular dipoles, $G_K > 1$ suggests parallel alignment of dipoles and $G_K < 1$ indicates an antiparallel arrangement of dipoles.

8.2.5.4 Centre of Mass Diffusion Coefficient (D)

The translational dynamics of different species were characterized by computing the mean square displacements (MSDs) based on the simulated trajectories. The self-diffusion coefficients were determined from the Einstein relation[44]

$$D = \frac{1}{6} \lim_{t \to \infty} \frac{d}{dt} \langle |\boldsymbol{r}_i(t) - \boldsymbol{r}_i(0)|^2 \rangle \tag{8.7}$$

Here D, and r_i denotes self-diffusion coefficient, and position of center-of-mass of the ith molecule, respectively. The angular bracket denotes an ensemble average over all molecules. The self-diffusion coefficients were calculated from the diffusive regime of the respective MSDs, defined by MSD $= t^{\beta(t)}$ and $\beta(t) = 1$ for diffusive regime, where

$$\beta(t) = \frac{dlog\langle |r_i(t) - r_i(0)|^2 \rangle}{dlog(t)} \tag{8.8}$$

8.2.5.5 Ionic Conductivity: Uncorrelated Ion Motion and Correlated Ions Motion

To understand correlation in ion movement, we use Onsager transport coefficient framework[45,46] to break-up conductivity into different components arising from the directional correlation between the movements of ions of same or opposite type due to electrostatic interactions. Since in our case, we have cation, anion and charge neutral solvent molecules, we need to calculate three independent transport coefficients L^{++}, L^{--} and L^{+-}. L^{+-} can capture correlated motion between cations and anions, while L^{++}/L^{--} can capture correlated motion between like charged particles[47]. For a binary electrolyte, net ionic conductivity (σ_{Total}) can be calculated from these transport coefficients and can be partitioned into three components as follows

$$\sigma_{Total} = F^2 \sum_i \sum_j L^{ij} z_i z_j = F^2 (z_+^2 L^{++} + z_-^2 L^{--} + 2z_+ z_- L^{+-}) = \sigma^{++} + \sigma^{--} - 2\sigma^{+-} \tag{8.9}$$

Where F is Faraday's constant, z is the charge of species. These coefficients can be calculated using molecular dynamics simulation from mean squared displacement of particle positions analogous to computing self-diffusion coefficient. Here, we compute L^{ij} using particle positions as follows[48]:

$$L^{ij} = \frac{1}{6k_B TV} \lim_{t\to\infty} \frac{d}{dt} \left\langle \sum_\alpha [\vec{r}_i^\alpha(t) - \vec{r}_i^\alpha(0)] \bullet \sum_\beta \left[\vec{r}_j^\beta(t) - \vec{r}_j^\beta(0) \right] \right\rangle \tag{8.10}$$

$$L^{ii} = \frac{1}{6k_B TV} \lim_{t\to\infty} \frac{d}{dt} \sum_\alpha \sum_\beta \left\langle [\vec{r}_i^\alpha(t) - \vec{r}_i^\alpha(0)] \bullet \left[\vec{r}_i^\beta(t) - \vec{r}_i^\beta(0) \right] \right\rangle \tag{8.11}$$

Where $\vec{r}_i^\alpha$ is the position of the αth particle of species i (cation or anion) relative to the center-of-mass position of the entire system (barycentric reference frame), V is the volume of the simulation box, T is the temperature and k_B is the Boltzmann constant.

L^{++} and L^{--} can be further divided into a self-part and distinct part. In equation 8.11, summation for $\alpha = \beta$ is the self-part and $\alpha \neq \beta$ is the distinct part. Therefore, self-part of L^{ii} is calculated using

$$L_{self}^{ii} = \frac{1}{6k_B TV} \lim_{t \to \infty} \frac{d}{dt} \sum_{\alpha} \langle [\vec{r}_i^{\alpha}(t) - \vec{r}_i^{\alpha}(0)]^2 \rangle \tag{8.12}$$

and the distinct part can be obtained from

$$L_{distinct}^{ii} = L^{ii} - L_{self}^{ii} \tag{8.13}$$

While the self-parts are related to the self-diffusion coefficients of cations and anions, distinct parts account for directional correlation between the movements of distinct ions of same type. Using equation 8.13, total conductivity in equation 8.9 can be portioned into five components

$$\sigma_{Total} = \sigma_{self}^{+} + \sigma_{self}^{-} + \sigma_{distinct}^{++} + \sigma_{distinct}^{--} + (-2\sigma^{+-}) \tag{8.13}$$

If ions of same type move preferentially into the same direction (positive correlation), distinct parts ($\sigma_{distinct}^{++}$ and $\sigma_{distinct}^{--}$) are positive. If ions of same type move into the opposite directions (anticorrelated), distinct parts are negative. If cations and anions move preferentially in same direction, then $\sigma^{+-} > 0$ and this cation-anion positive correlation decreases conductivity. Conversely, when cations and anions move in opposite directions, then $\sigma^{+-} < 0$ and this cation-anion anti-correlation increases conductivity[46].

We calculated conductivity covering various mole fractions of EC (e.g., $X_{EC} = 0.0, 0.2, 0.4, 0.6, 0.8 \& 1.0$) for 1M LiTFSI in xEC + (1-x)ADN mixtures at a 323K temperature. 400 ns long simulation trajectories were created in NVT ensemble for all six different EC mole fractions at 323 K temperature. Before performing NVT production run, equilibrated NPT ensemble further equilibrated at NVT ensembles up to 2 ns. During NVT production run, temperature was maintained by using V-rescale thermostat[34] with a time constant of 0.5 ps.

8.2.5.6 Force Field Validation

In this work, we employed classical non-polarisable model interaction potential for all species within Li-based electrolyte systems. To extract valuable structural and dynamical insight from simulated electrolyte solutions, we compared the simulated density and viscosity with experimental data at four distinct temperatures (298 K, 303 K, 313 K, 323 K). These compressions are shown in Figure 8.2, and the corresponding numerical values are provided in

Table 8.2 & Table 8.3. The excellent agreement observed between experimental and simulated density and viscosity data indicates that the model potential used in this study is highly effective in predicting the structural and dynamical properties of these electrolyte solutions. This suggests that our model offers a high degree of accuracy across different temperature for these systems.
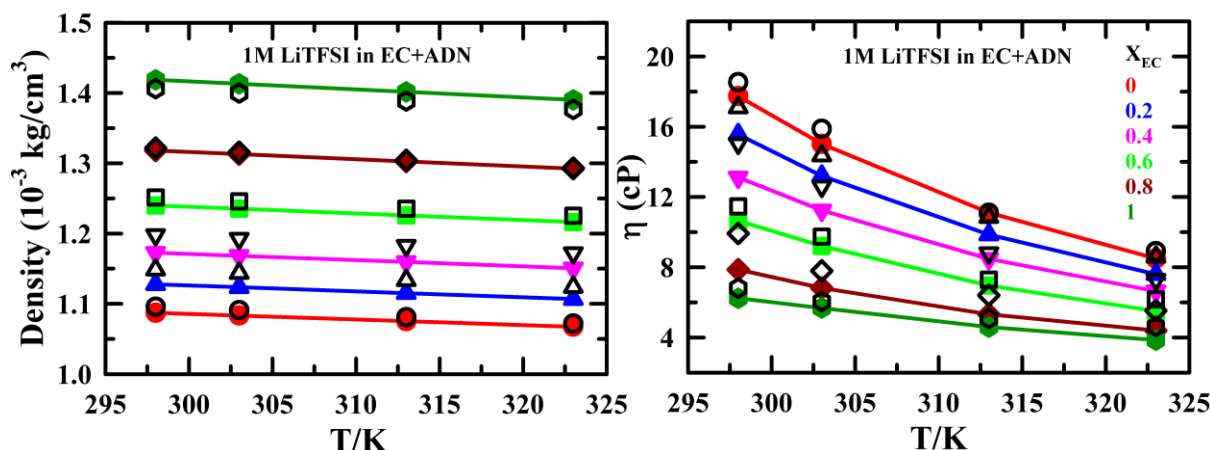
Figure 8.2: Concentration and temperature dependent density (left panel) and viscosity (right panel) obtained from MD simulations and experimental measurements for 1M LiTFSI in xEC+(1-x)ADN electrolyte solutions. In this plot, experimental data points are represented by filled symbols with colour coding, while simulated densities are indicated by the open black symbol. The straight solid line that passes through the data points are simply visual aids for interpreting the data.

8.3 Result and Discussion

In this section, we will begin by presenting experimental results that are dependent on the EC mole fraction in 1M LiTFSI in xEC+(1-x)ADN within a temperature range of 298 K to 323 K. These results encompass first and second-order phase transition phenomena from DSC, conductivity measurements and DRS measurements for 1M LiTFSI in xEC+(1-x)ADN electrolyte solutions. Dielectric property of electrolyte solutions explained in the light of experimental and possible MD simulation findings. Next, we will present the result obtained from the MD simulation, which provided a detailed the molecular-level understanding of the structure, dynamics, and transport properties within these simulated electrolyte systems. Additionally, we will explore the contribution arising from the self and cross-correlation of ions present in these systems to the total conductivity.

8.3.1 DSC Measurement: Cosolvent Modified Electrolyte Glass Transition, Pre-crystallization and Melting

The glass transition temperature (T_g) and melting temperature (T_m) are the important parameters for determination of system fragility and working window of the battery electrolyte. These aspects of query are explored in this section with various co-solvent (EC) concentrations at a fixed salt concentration (1M). Understanding these phenomena will help establish a lower-limit temperature window for the practical application of these electrolyte mixtures in LIBs. DSC thermograms of pure ADN and pure EC are also shown in Figure A8.8 (Appendix). Additionally, Table A9.9 (Appendix) provides details such as melting temperature (T_m), boiling temperature (T_b), and flash point temperature for both pure solvents ADN and EC, and along with the T_m of LiTFSI, as sourced from references.[49,50] Solvent concentration dependent DSC thermogram of 1M LiTFSI in xEC+(1-x)ADN within the temperature window 133 K to 363K is depicted in Figure 8.3. These thermograms reveal the presence of three distinct types of thermodynamics phase transitions, including glass transition, pre-crystallization (exothermic peak), and melting (endothermic peak), within these electrolyte solutions. Similar pre-crystallization phenomena have been observed in Li-electrolyte systems[8,51] and other systems[52]. EC concentration dependent T_g and T_m are shown in Figure 8.3 (lower panel). Notably, the T_g of electrolytes with binary solvents is lower than that of their corresponding electrolyte salt in solvent alone. This observation suggests that cooperative interaction in the one-solvent electrolyte systems is stronger compared to binary solvent electrolyte systems. This stronger cooperativity makes it more fragile in one-solvent electrolyte solutions than of binary solvent electrolytes. The T_m in these systems exhibits a non-monotonic nature with increasing EC concentration. It shows minimum at $X_{EC} = 0.6$. The presence of a double-hump endothermic nature in the $X_{EC} = 0.6$ electrolyte solution indicates the existence different type of Li$^+$-solvent crystals within this system. The above discussion reveals that the operating temperature window of Li-electrolytes in LIBs is also influenced by the concentration of co-solvent added to the electrolyte systems. The pre-crystallisation temperatures (T_{pc}) are provided in Table 8.4. This demonstrates that, as temperature increases, the pre-crystallisation phenomena (as indicated by the exothermic nature of the DSC curve) commences immediately after glass-to-supercool liquid transition in all systems. The presence of broadened pre-crystallisation (multi or one-step) peaks suggests the existence of different types of ion-solvent complex crystals (Li$[\text{ADN}]_n^+$, Li$[\text{EC}]_m^+$ and Li$[(\text{ADN})_n(\text{EC})_m]^+$) within these systems[8,51] and which will be shown in the structure section (from MD simulation). Here we observed that co-

solvent (EC) concentration significantly influenced the system fragility and working window of the battery electrolyte. This raises another inquiry: how does the concentration of the co-solvent affect electrolyte conductivity? This aspect will be addressed in the following section.
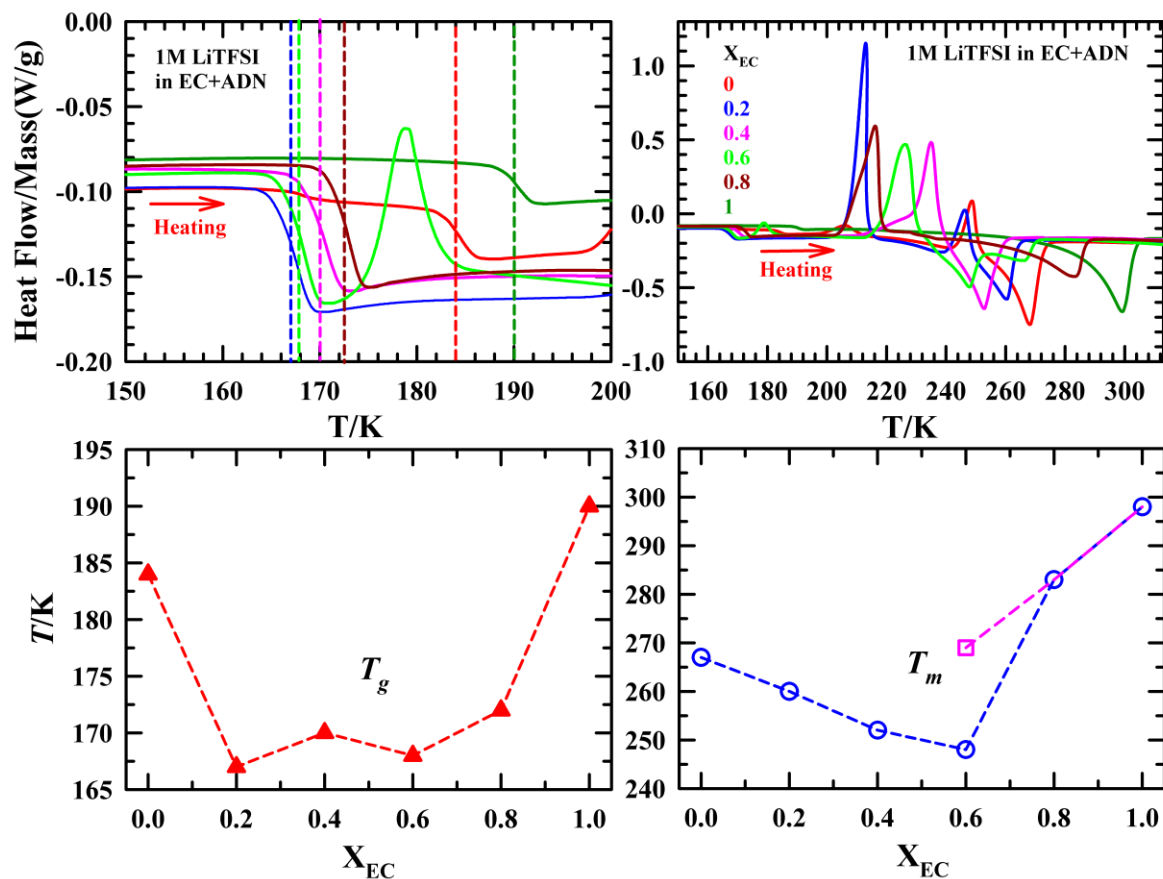
Figure 8.3: EC concentration dependent DSC thermogram (upper panels) and T_g or T_m (lower panels) of 1M LiTFSI in xEC+(1-x)ADN electrolyte. During DSC experiment 5 K/min heating rate was maintained. Note two distinct T_m observed (blue and pink symbols) for $X_{EC} = 0.6$ mole fraction EC electrolyte system. All presentations are colour coded.

Table 8.4: EC concentration dependent glass transition temperature (T_g), melting temperature (T_m), and pre-crystallisation (T_{pc}) estimated from DSC thermogram of 1M LiTFSI in xEC+(1-x)ADN electrolytes in the temperature window 133K to 363K.

X_{EC}	T_g (K)[a]	T_m (K)[b]	T_{pc} (K)
0	184	267	248, 205
0.2	167	260	246, 206
0.4	170	252	234
0.6	168	248,269	226, 178
0.8	172	283	216
1	190	298	

8.3.2 Temperature and EC Concentration Dependent Conductivity

The conductivity (σ) of LiTFSI in ADN, varying with salt concentration, is depicted in Figure 8.1. These results revealed that the maximum σ is achieved with 1M LiTFSI in ADN at 298 K, consistent with previous study.[13] Temperature and co-solvent (EC) concentration dependent σ of Li-electrolytes (1M LiTFSI in xEC+(1-x)ADN) are shown in Figure 8.4. σ increases as EC concentration increases under isothermal conditions (see left panel of Figure 8.4). This increase in σ with EC concentrations at a fixed temperature can be explained by two factors. Firstly, the diffusivity of conducting ions increases due to reduction in viscosity of electrolyte solutions with EC concentration (as observed in Table 8.1). Secondly, the static dielectric constant (ε_s) of EC ($\varepsilon_s\sim91.7$ at 313 K) is greater than ADN ($\varepsilon_s\sim32.7$ at 313 K). Consequently, ε_s rises with increasing EC concentration, leading to a higher number of conducting ions owing to enhanced salt dissolution capability. This aspect is further substantiated by DRS measurements and MD simulation, elaborated upon in their respective sections. Moreover, as temperature increases, the mediums viscosity decreases and the mobility of conducting ions in these electrolyte solutions increases. Therefore, σ of electrolyte at a particular EC concentration increases with temperature. The discussion underscores how the addition of co-solvent such as EC can significantly modify the conductivity of these electrolyte solutions. A more microscopic explanation of this co-solvent dependent conductivity provided in simulation Section. Next, we will discuss the dielectric properties and dynamics observed both without and with salt in solvent in these EC concentration dependent solvent mixtures and neat solvent.
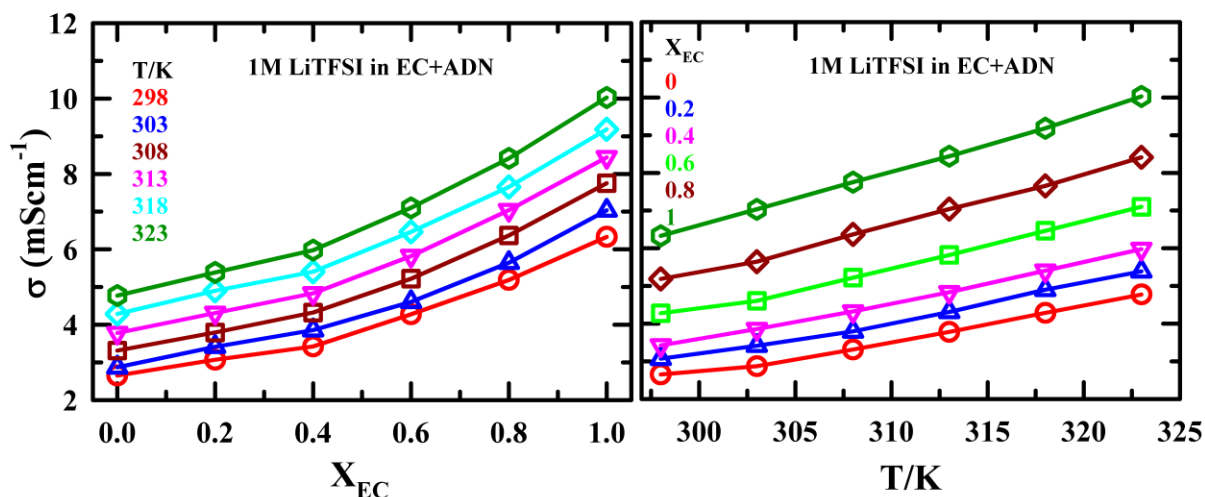
Figure 8.4: EC mole fraction and temperatures dependent conductivities of 1M LiTFSI in xEC+(1-x)ADN electrolyte systems. All representations are colour coded.

8.3.3 Composition and Temperature Dependent Dielectric Measurement: Impact of EC

Figure 8.5 illustrates the co-solvent (EC) concentration dependent behavior of the real (ε') and imaginary (ε'') component of complex dielectric spectra for 1M LiTFSI in xEC+(1-x)ADN electrolyte solutions at four different temperatures. Additionally, temperature dependent complex DR spectra with ε' and ε'' component for 1M LiTFSI in xEC+(1-x)ADN electrolyte solutions at six electrolyte systems are shown in Figure A8.10 (Appendix). Note that, the peak in the imaginary dielectric component (ε'') of complex DR spectra arises in the frequency range 200 MHz to 50 GHz. To accurately describe the complex dielectric behavior observed in the Li-electrolytes, multi-Debye fitting models were employed (as indicated by black solid lines fitted to the experimental dielectric data of ε' and ε''). The dielectric fit parameters, along with the corresponding "goodness-of-fit", χ^2 values, are provided in Table 8.5. Note, to decode the dielectric behaviour of electrolyte systems, we also conducted DRS measurement of binary solvent mixtures along with neat solvents, EC and ADN, in the absence of Li-salt. Representative plots of EC mole fractions dependent DRS spectra in binary solvent mixtures are shown in Figure A8.11 (Appendix). Additionally, temperature and EC mole fraction dependent DR fit parameters of these solvent systems are detailed in Table A8.12 (Appendix).
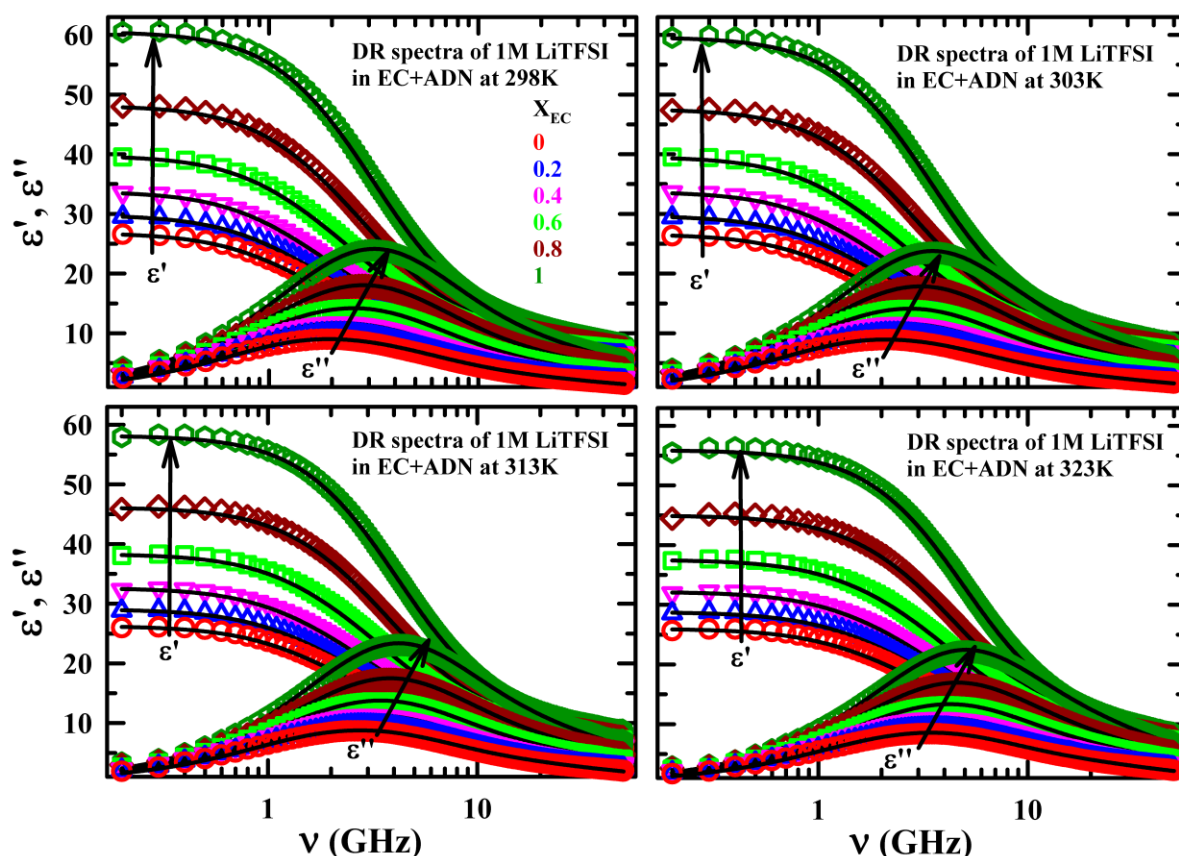
Figure 8.5: EC mole fraction dependent complex DR spectra with real (ε') and imaginary (ε'') component in 1M LiTFSI in xEC+(1-x)ADN electrolyte solutions at four temperatures. The lines passing through experimental data points express multi-Debye model fits. All presentations are colour-coded.

8.3.3.1 Origin of DR Times in EC Concentration Dependent Electrolyte Solutions

Let's discuss the origin of the DR times observed in neat and binary solvent mixtures. Two types of DR times [a slow τ_1 (~ 47-30 ps) and τ_2 (~ 14-9 ps)] are present in pure ADN in the temperature window 298 K to 323 K. To qualitatively understand the rotation diffusion of ADN molecule and -CN group in ADN, we calculate it using Stokes-Einstein-Debye (SED) equation, $\tau_{rot}^{SED} = 3V\eta/k_BT$. Where V, η, k_B, and T denote volume of species, medium viscosity, Boltzmann constant and medium temperature, respectively. The calculated rotation diffusion times are listed in the Table A8.13 (Appendix). Note that, slow DR time ($\tau_1 \sim 36$ ps) in neat ADN at 313 K is closer to the rotational diffusion time of the -CN group ($\tau_{rot}^{CN} \sim 86$ ps) than the hole molecule rotation of ADN ($\tau_{rot}^{ADN} \sim 353$ ps). This indicates -CN group attached to ADN cannot perform a full rotation. Hence, the slow DR time, τ_1, in neat ADN likely originates from

the reorientation of the -CN group around the attached CH2 group present in ADN. Faster DR time τ_2 probably arises from the dipole orientation change of -CN group due to the zig-zag motion of linear ADN molecules. In contrast, a single DR time is observed in neat EC, which is shorter (29 ps at 313 K) than the rotational diffusion time of EC ($\tau_{rot}^{EC} \sim 96$ ps at 313 K) predicted from the SED equation. This suggests that due to the steric hindrance, cyclic EC molecules cannot perform full rotation in neat EC. Hence, the DR time in neat EC arises from the fractional reorientation of EC molecules. However, after the addition of EC to ADN, no additional DR time is observed. This indicates that the dipolar relaxation time of ADN and EC are so close to each other that their individual contributions to DR relaxations overlap in these binary solvent mixtures. Furthermore, the slow DR time τ_1 gradually becomes faster with increasing EC mole fraction. The addition of EC ($\eta = 1.925$ cP at 313K)[53] to the ADN ($\eta = 4.11$ cP at 313K)[54] results in a reduction in medium viscosity, and therefore DR time becomes faster with increasing EC concentration. With higher temperature ($T \geq 313$K) or higher EC mole fraction (greater than $X_{EC} = 0.4$), τ_2 completely vanishes, indicating that the dynamics of faster DR process may be out of the present high frequency limitations of DR measurement.

Now, let's explain the origin of DR times observed in EC concentration dependent electrolyte solutions at six different temperatures. In these systems, three DR timescales are observed in the presence of LiTFSI in xEC+(1-x)ADN. Calculations of rotation diffusion times of Li$^+$, TFSI$^-$, ADN, EC, and -CN using the SED equation group are also provided in Table A8.13 (Appendix). Although this SED calculation does not offer insights into the DR times in electrolyte solutions. The fastest DR time ($\tau_3^s \sim 6$-5 ps) in the electrolyte solutions is insensitive to both temperature and EC mole fraction, and its contribution remains nearly constant. τ_3^s is also present in 1M LiTFSI +EC electrolyte system. Which confirmed that τ_3^s is not coming from the -CN group zig-zag motion. This fastest DR time, τ_3^s may arise from the side group motion of TFSI$^-$ anion. The intermediate DR time ($\tau_2^s \sim 46 - 31$ ps) becomes faster with temperatures but remains constant with increasing EC mole fraction at a fixed temperature in these electrolyte solutions. This indicates that τ_2^s is associated with the tumbling of solvent molecules present in the first solvation shell of ions. Thus, τ_2^s is strongly sensitive to the local friction but not to bulk viscosity. With increasing temperature, solvent molecules become more kinetically activated, and more molecules from bulk solvent participate in ions solvation, resulting in τ_2^s becoming faster while its contribution increases with temperatures. Next, we explore the origin of the slowest DR time τ_1^s ($120 - 64$ ps) in these electrolytes. The ratio of DR times from solution(s) to solvent (τ_1^s/τ_1) is 2.69 for ADN and 1.28 for EC in single solvent

systems. These ratios are well corroborated with the viscosity ratio ($\eta_{ADN}^s/\eta_{ADN} = 2.70$ and $\eta_{EC}^s/\eta_{EC} = 2.39$) in ADN and EC systems at 313 K. τ_1^s is sensitive to medium viscosity and temperatures. This confirms the conjecture that the slowest DR time τ_1^s arises from the dipole relaxation of bulk solvent molecules. The contribution of τ_1^s in these systems decreases with increasing EC concentration. This can be explained by the fact that linear ADN molecules, with two dipole relaxation sites (two CN groups), are replaced by cyclic EC molecules with EC mole fractions increases. That results in a decrease in the number of rotating dipoles.

Table 8.5: Temperatures and EC mole fraction dependent multi-Debye fit parameters of experimentally measured DR spectra (frequency regime: 200 MHz to 50 GHz) in 1M LiTFSI in xEC+(1-x)ADN electrolyte.[c]

T/K	ε_s	$\Delta\varepsilon_1$	τ_1^s/ps	$\Delta\varepsilon_2$	τ_2^s/ps	$\Delta\varepsilon_3$	τ_3^s/ps	$\langle\tau_{DR}^s\rangle$/ps	ε_∞	χ^2
				1M LiTFSI in ADN						
298	26.82	11.87 (56)	119	8.01 (37)	45	1.45 (7)	6	84	5.49	0.0228
303	26.62	11.07 (52)	115	8.63 (40)	44	1.61 (08)	6	78	5.31	0.0234
308	26.41	9.70 (46)	107	9.6 (46)	42	1.77 (8)	6	69	5.34	0.0253
313	26.26	9.00 (43)	97	9.96 (48)	39	1.88 (9)	6	61	5.42	0.0250
318	26.08	7.99 (39)	91	10.57 (51)	37	2.04 (10)	6	55	5.48	0.0266
323	25.99	7.10 (34)	88	11.21 (55)	36	2.18 (11)	6	50	5.53	0.0283
				1M LiTFSI in $X_{EC} = 0.2$						
298	29.83	12.02 (50)	120	10.29 (43)	46	1.79 (7)	6	80	5.73	0.0244
303	29.69	11.14 (46)	112	10.96 (46)	44	2.01 (8)	6	72	5.58	0.0252
308	29.19	10.09 (43)	104	11.48 (48)	42	2.16 (9)	6	65	5.46	0.0310
313	29.07	8.82 (37)	98	12.87 (53)	40	2.29 (10)	6	58	5.58	0.0286
318	28.84	7.87 (34)	91	12.86 (56)	37	2.45 (10)	6	52	5.66	0.0297
323	28.79	7.27 (32)	87	13.17 (57)	35	2.56 (11)	5	48	5.79	0.0315
				1M LiTFSI in $X_{EC} = 0.4$						
298	33.75	13.11 (47)	117	12.64 (45)	46	2.19 (8)	5	76	5.92	0.0286
303	33.71	11.68 (42)	110	13.61 (49)	44	2.44 (9)	5	68	5.98	0.0280

308	33.28	11.31 (41)	98	13.59 (50)	40	2.52 (9)	5	61	5.86	0.0256
313	32.63	9.09 (34)	96	15.11 (56)	39	2.75 (10)	5	55	5.68	0.0351
318	32.49	8.23 (31)	90	15.52 (58)	36	2.88 (11)	5	50	5.86	0.0318
323	32.18	7.15 (27)	87	16.09 (61)	35	3.05 (12)	5	45	5.89	0.0341
1M LiTFSI in $X_{EC} = 0.6$										
298	39.76	12.54 (37)	113	18.11 (54)	46	2.89 (9)	5	67	6.22	0.0334
303	39.57	12.13 (36)	105	18.12 (55)	44	3.12 (09)	5	62	6.20	0.0309
308	39.07	11.68 (35)	93	18.07 (55)	39	3.2 (10)	5	55	6.07	0.0318
313	38.32	9.49 (30)	90	19.46 (60)	38	3.42 (10)	5	50	5.95	0.0306
318	37.95	7.96 (25)	88	20.32 (64)	35	3.58 (11)	5	45	6.09	0.0378
323	37.54	6.79 (22)	86	20.87 (66)	33	3.76 (12)	5	41	6.12	0.0361
1M LiTFSI in $X_{EC} = 0.8$										
298	48.14	14.02 (34)	96	23.79 (57)	45	3.93 (9)	5	59	6.40	0.0340
303	47.56	11.94 (29)	92	25.11 (61)	43	4.07 (10)	5	53	6.44	0.0406
308	47.09	11.08 (27)	84	25.76 (63)	39	3.89 (10)	5	48	6.36	0.0351
313	46.14	9.15 (23)	79	26.66 (67)	37	4.07 (10)	5	43	6.26	0.0480
318	45.66	8.17 (20)	76	27.08 (69)	34	4.18 (11)	5	39	6.23	0.0443
323	44.97	6.63 (17)	74	27.65 (72)	32	4.37 (11)	5	36	6.32	0.0460
1M LiTFSI in $X_{EC} = 1$										
298	60.54	13.58 (25)	81	35.48 (66)	44	4.85 (9)	5	50	6.63	0.0359
303	59.61	11.56 (22)	74	36.32 (69)	41	5.00 (9)	5	45	6.74	0.0452
308	59.00	10.24 (19)	70	37.53 (72)	38	4.69 (9)	5	41	6.54	0.0361
313	58.15	8.32 (16)	65	38.36 (74)	35	4.97 (10)	5	37	6.50	0.0537
318	56.83	6.23 (12)	64	39.16 (78)	33	4.93 (10)	5	34	6.51	0.0590
323	55.92	4.63 (09)	64	39.69 (80)	31	5.1 (11)	5	31	6.50	0.0529

[c]DR time constants and respective amplitudes can be reproduced within ±5% of the reported values.

[d]Number in parenthesis denotes percentage of dispersion amplitude of a given dispersion step contributing to total dielectric dispersion.

8.3.3.2 Static and Dynamic Decrement in ε_s: Experimental Evidence

Next, we look into the static dielectric constant (ε_s) of solvent mixtures and electrolyte solutions, exploring its dependence on temperature and EC mole fraction. ε_s is a crucial parameter for electrolyte solutions, as it strongly influences dielectric screening. The dielectric screening plays a vital role in determining the strength of the Coulombic interactions between oppositely charged ions. It is created by the solvent layer in the solvation shell of ions. The solubility of salt in an electrolyte solution, which forms solvent-separated ions pair, depends significantly on the ε_s of the solvent. It's important to note that the ε_s of EC (91.9 at 313 K) is larger than ADN (32.6 at 313 K). That is why ε_s of binary solvent mixtures [xEC + (1-x)ADN] and their electrolyte solutions [LiTFSI in xEC + (1-x)ADN] increase with increasing EC concentrations, as shown in Figure 8.6(a) and Figure 8.6(b) respectively. Note that, the ε_s values of these electrolyte systems are lower than the respective solvent mixture or net solvents. EC mole fraction dependent dielectric decrement ($\Delta\varepsilon_{DD} = \varepsilon_s(\text{solution}) - \varepsilon_s(\text{solvent})$) in these electrolyte solutions at various temperatures are shown in Figure 8.6(c) and Table A8.14 (appendix). This kind of ion-induced dielectric decrement ($\Delta\varepsilon_{DD}$) has also been observed in conventional electrolyte solutions[55–63], battery electrolytes[64–66], and ionic deep eutectic systems[67–70]. This phenomena in electrolyte solutions can be explained as follows: Firstly, polar solvent molecules in the first solvation shell are tightly bound to ions through electrostatic interactions. Consequently, these solvent molecules do not respond to DR measurement promptly or they show a delay in restoring polarization corresponding to local electric field. Solvent molecules that are strongly bound to ions resemble rotationally frozen entities and are insensitive to frequency-dependent DR measurements. This phenomenon is referred to as kinetic dielectric decrement ($\Delta\varepsilon_{DD}^k$) in ε_s.[69]
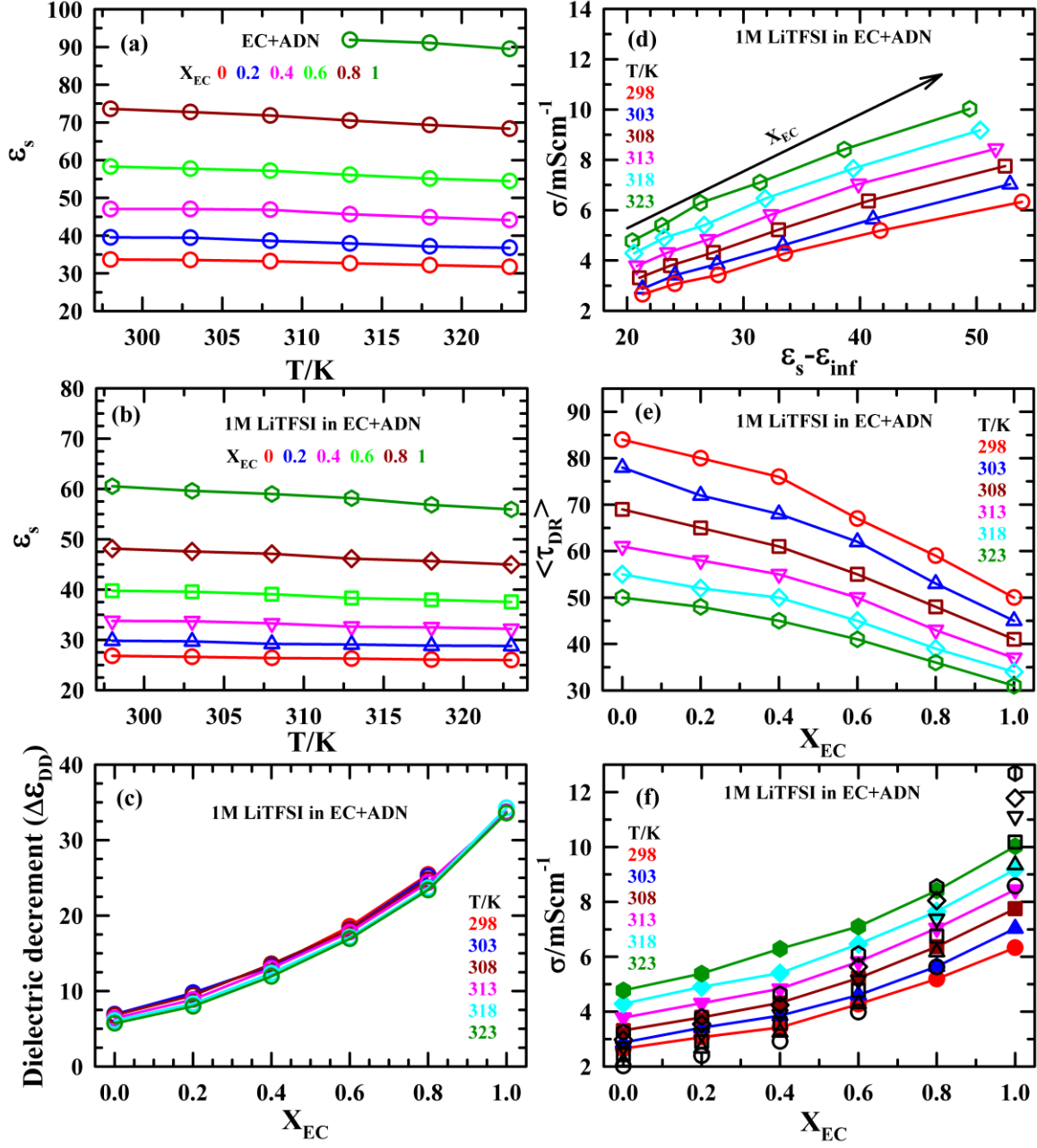
Figure 8.6: Temperature and EC mole fraction dependent (a) static dielectric constant (ε_s) of (xEC+(1-x)ADN binary solvent mixtures, (b) ε_s of 1M LiTFSI in xEC+(1-x)ADN electrolyte solutions, (c) dielectric decrement ($\Delta\varepsilon_{DD}$) in 1M LiTFSI in xEC+(1-x)ADN electrolyte solutions from respective solvent, (d) conductivities variation with total dielectric dispersion ($\varepsilon_s - \varepsilon_\infty$, left panel) for 1M LiTFSI in xEC+(1-x)ADN electrolyte solutions, (e) DR time ($\langle\tau_{DR}\rangle$) for 1M LiTFSI in xEC+(1-x)ADN electrolyte solutions, and (f) comparison between experimental conductivities (filed colour symbols) and calculated conductivities (black open symbols) for 1M LiTFSI in xEC+(1-x)ADN. Note ε_{inf} presented in figure 6(d) represent ε_∞. All representations are colour-coded.

The second origin of the dielectric decrement ($\Delta\varepsilon_{DD}$) arises from the randomization of static dipole orientation among solvent molecules when ions are introduced. This results in a low value of G_K for electrolytes compared to the absence of electrolyte salt.[69] This phenomenon is known as static dielectric decrement ($\Delta\varepsilon_{DD}^s$). The dielectric decrement ($\Delta\varepsilon_{DD}$) aspect is further discussed in the MD simulation section.

EC concentration dependent σ as a function of total dielectric dispersion ($\varepsilon_s - \varepsilon_\infty$) in these electrolytes at various temperatures is shown in Figure 8.6(d). This depicts that at a specific temperature, the σ of the solution linearly increases with $\varepsilon_s - \varepsilon_\infty$. Again, Figure 8.6(e) reveals that the $\langle\tau_{DR}\rangle$ of electrolyte solutions becomes faster with EC concentrations. This discussion reveals that the σ of the electrolyte solution depends on the both total dielectric dispersion and the dielectric relaxation of the system at a given temperature.[62] These two factors influence the electrical conductivity as follows: Dielectric constant: The increased dielectric constant of electrolyte solutions enhances ionic conductivity by promoting the formation of solvent separated conducting ions. This effect arises because the electrostatic interaction between oppositely charged ions is reduced by dielectric screening provided by the solvent layer around the ions. As the dielectric constant increases, the dielectric screening effect becomes more prominent. That is why ionic mobility as well as electrical conductivity increases. Solvent dynamics: Faster solvent dynamics also lead to increased ionic mobility, thus higher conductivity of electrolyte solutions. Comparison between experimental and theoretical[62] conductivities in EC mole fraction dependent electrolyte solutions at various temperatures are presented in Figure 8.6(f). Theoretical conductivities were calculated using the continuum model of Onsager relation[62], given by $\sigma_{cal} = (\varepsilon_s - \varepsilon_\infty)/4\pi\tau_D$ where τ_D represents the Debye relaxation[71] time of solvent. It is important to note that this theoretical model makes several simplifications, such as assuming ions are point charges, solvent molecules are point dipoles with Debye relaxation, and all solutes are completely dissociated (i.e., low salt concentration). While this assumption may not fully represent practical conditions, this theoretical model provides a qualitative understanding of the experimental results. Figure 8.6(f) shows that EC mole fraction dependent conductivities, both calculated and experimental, exhibit similar trends. Note that, $\varepsilon_s - \varepsilon_\infty$ (which increases ~2.5 times from ADN to EC for all temperatures) appears to be the dominant factor influencing the calculated conductivity values than solvent dynamics (~1.3 times faster from ADN to EC at various temperatures). This discussion highlights the significance of solvent dielectric properties on battery electrolyte solutions, with the total dielectric increment playing a crucial role in conductivity enhancement.

8.3.3.3 Coupling Between Dynamics and Medium Viscosity, and Activation Energy

To investigate the coupling between dynamical properties (such as dipole reorientation $\langle \tau_{DR} \rangle$ or ion transitional σ) and medium viscosity, the relation between $\langle \tau_{DR} \rangle$ or σ with temperature dependent viscosity was examined. This relationship is expressed through the power low $\tau \propto \left(\frac{\eta}{T} \right)^p$ and $\sigma \propto \left(\frac{T}{\eta} \right)^p$, where $p = 1$ indicates solution dynamics fully coupling with medium viscosity. Deviation from 1 suggests a partial coupling between dynamics and medium viscosity. Figure 8.7(a) and Figure 8.7(b) present a double logarithmic plot of $\langle \tau_{DR} \rangle$ vs $\frac{\eta}{T}$ and σ vs $\frac{\eta}{T}$. In this case of the DR process, the p values range from 0.65 to 0.84, and while for conductivity, that ranges from 0.74 to 0.80, depending on the EC mole fraction in 1M LiTFSI in xEC+(1-x)ADN electrolyte systems. Deviation of p from unity indicates electrolyte systems are prone to dynamic heterogeneity. Fractional viscosity dependence or $p < 1$ has been observed in various systems, including battery electrolytes[66,72], deep eutectic solvents (DES)[73,74], cryoprotectant mixtures[75], binary mixtures[76], time-resolved fluorescence study[77], and micelle in water[78]. This behavior is typically attributed to the presence of temporal heterogeneity, especially at near-room temperature conditions. Temporal heterogeneity is commonly observed in supercooled liquid.[79–83] However, the detection of temporal heterogeneity also depends on the size and relaxation time of dipole molecules being probed in the electrolyte solutions.[73,79,84] In this study, lower p values remain consistent up to $X_{EC} \leq 0.6$, after which p values increase with higher EC concentrations in these electrolytes. This suggests that temporal heterogeneity is more pronounced in electrolytes with higher ADN mole fractions. A global fit, including all temperature and EC mole fraction dependent data points for the DR process, yields an estimated p value of ~0.60. This value suggests the presence of temporal heterogeneity, as indicated by DRS measurements. Additionally, the p value for conductivity ($p \sim 0.81$) is larger than that for the DR process, indicating that conductivity (diffusion of ion) is more coupled to medium viscosity up to an EC mole fraction of 0.6. However, at higher EC mole fractions, both DR and conductivity exhibit close to each other. Figure 8.7(c) illustrates the difference of p value from DR and conductivity decreases with increasing EC concentrations. Beyond an EC mole- fraction of 0.6, p values of the DR process become larger than those for conductivity, indicating that rotation and diffusion coupling occur under these conditions.
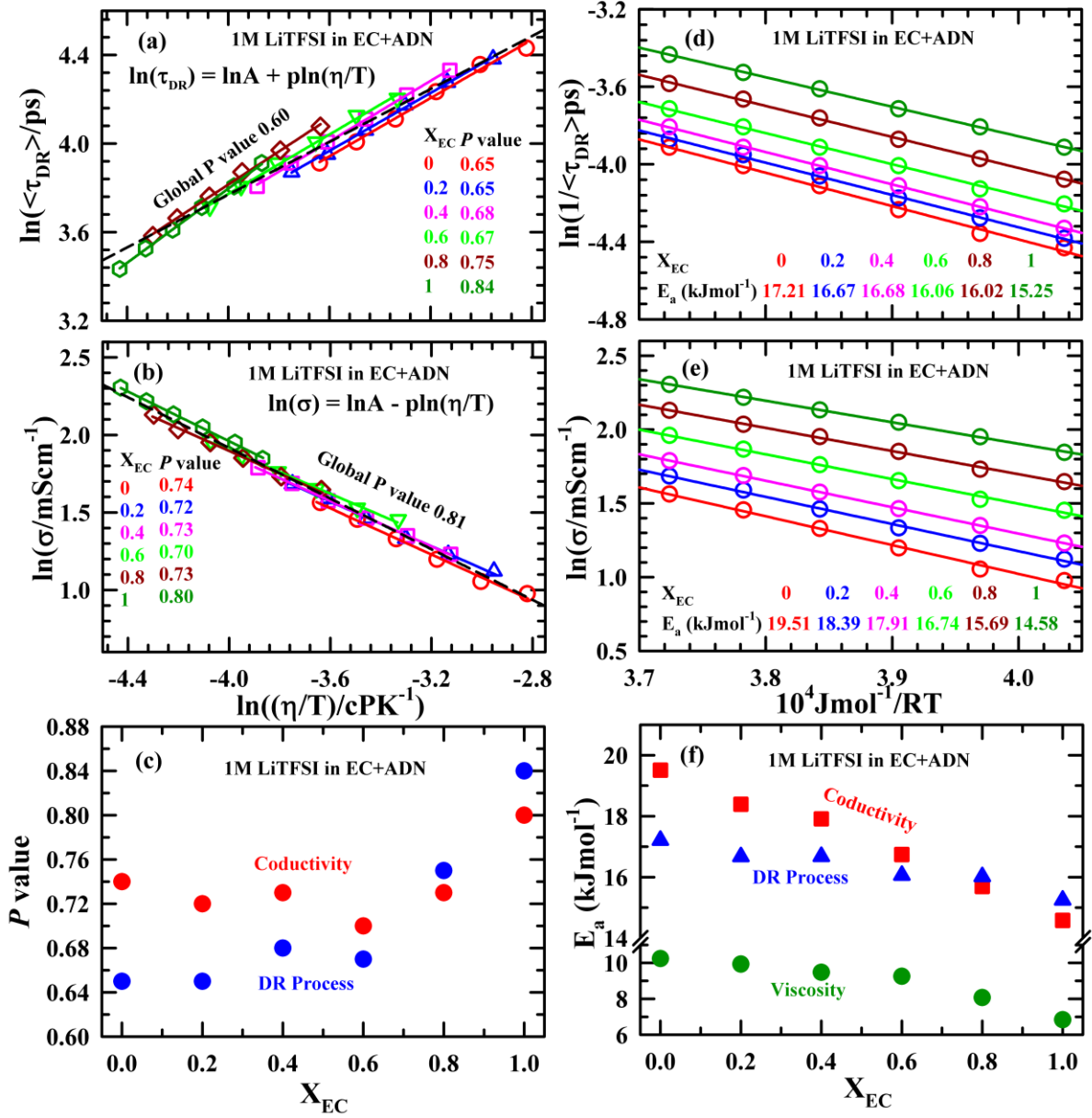
Figure 8.7: Representative plot of (a) temperature reduced viscosity $(\frac{\eta}{T})$ vs $\langle\tau_{DR}\rangle$, (b) $\frac{\eta}{T}$ vs σ for 1M LiTFSI in xEC+(1-x)ADN electrolyte solutions. p values estimated from DR and conductivity process are also presented in their respective panel. (c) p value compare between DR and conductivity process. Temperature dependent Arrhenius-type dependence of (d) $\langle\tau_{DR}\rangle$, (e) σ for all electrolyte solutions. Estimated activation energy at various EC mole fraction for all electrolyte solutions are shown. Solid lines passing though symbols represent linear fits. (f) activation energies comparison from viscosity, DR and conductivity process. All representations are colour-coded.

Temperature dependence viscosity, $\langle \tau_{DR} \rangle$, and conductivities in these electrolyte solutions follow an Arrhenius-type relation over the temperature of 298 K to 323 K. Therefore, activation energies E_η, E_{DR}, and E_σ associated with viscosity, DR, and conductivity in the electrolyte solutions were estimated from Figure 8.7(d), Figure 8.7(e) and Figure A8.15 (Appendix). The estimated activation energies decrease with EC mole fraction as shown in Figure 8.7(f). Note, E_η is smaller than both E_{DR} and E_σ in all of these electrolyte solutions. The difference between activation energies E_η and E_σ slightly decreases with increasing EC mole fraction, while it remains same between E_η and E_{DR} in these electrolyte solutions. From these findings, it is evident that the DR and conductivity (ion transport) process are decoupled from the viscous flow of these electrolyte solutions. This result suggests that both DR and ion transport are sensitive to local friction, not bulk viscosity in these electrolyte solutions. This observation confirms the presence of temporal heterogeneity in these systems, as previously conjectured.

8.3.4 MD Simulation of Li-electrolytes: Structure, Static Dielectric Constant and Kirkwood G factor (G_K), Dynamics and Ionic Conductivity

8.3.4.1 Structure

Figure 8.8 shows the radial distribution function (RDF) between inter and intra-species Centre of Mass (COM) for 1M LiTFSI in ADN or EC electrolyte solutions. Weak interactions are observed between opposite ion pairs, ion-ADN pairs, and anion-EC pairs except for Li^+-EC pairs. This can be explained as follows: (i) the electrolyte salt dissolves well in solvent, leading to the formation of a greater number of solvents separated individual ions. (ii) The Charge density of the larger anion is smaller than that of the cation, resulting in weaker interaction with solvent molecules. (iii) Linear chain dinitrile molecules like ADN have lower dipole density (see dipole distribution in Figure A8.16) leading to weaker interaction with cation and broadening of RDF for Li^+-ADN is observed because linear ADN has a possibility of flickering around cation. (iv) Cyclic EC always have higher dipole densities, and they interact with Li^+ ion in a fixed dipole orientation. Therefore, the probability of finding COM of EC at a particular distance is sharp and higher than for other pairs. Figure 8.9 (a-e) represents inter-species COM-COM RDF and coordination numbers (CN) with varying EC concentrations. This depicts that better interactions occur between cation and solvent with decreasing each of the solvent mole fraction. While the RDF between anions and solvents follows the solvent mole fraction dependency. This difference between the RDF of cation or anion with solvent can be explained

by the size of the ions. Very small cation Li^+ tends to form clusters with solvent molecules at lower mole fractions in the binary solvent in electrolytes. In contrast, the larger anion, $TFSI^-$ undergoes solvent replacement effect with changes in solvent mole fraction, although this effect is very small observed in both cases. However, the CN of anion around the cation decreases with EC mole fractions. This reflects that salt solubility increases with EC mole fraction in these electrolyte solutions. DR studies show that ε_s of the electrolyte solution increases with EC concentration. This growing dielectric constant with EC promotes the phenomena of dielectric screening between two opposite charge ions, resulting weakening of the short electrostatic interaction between cation and anion.
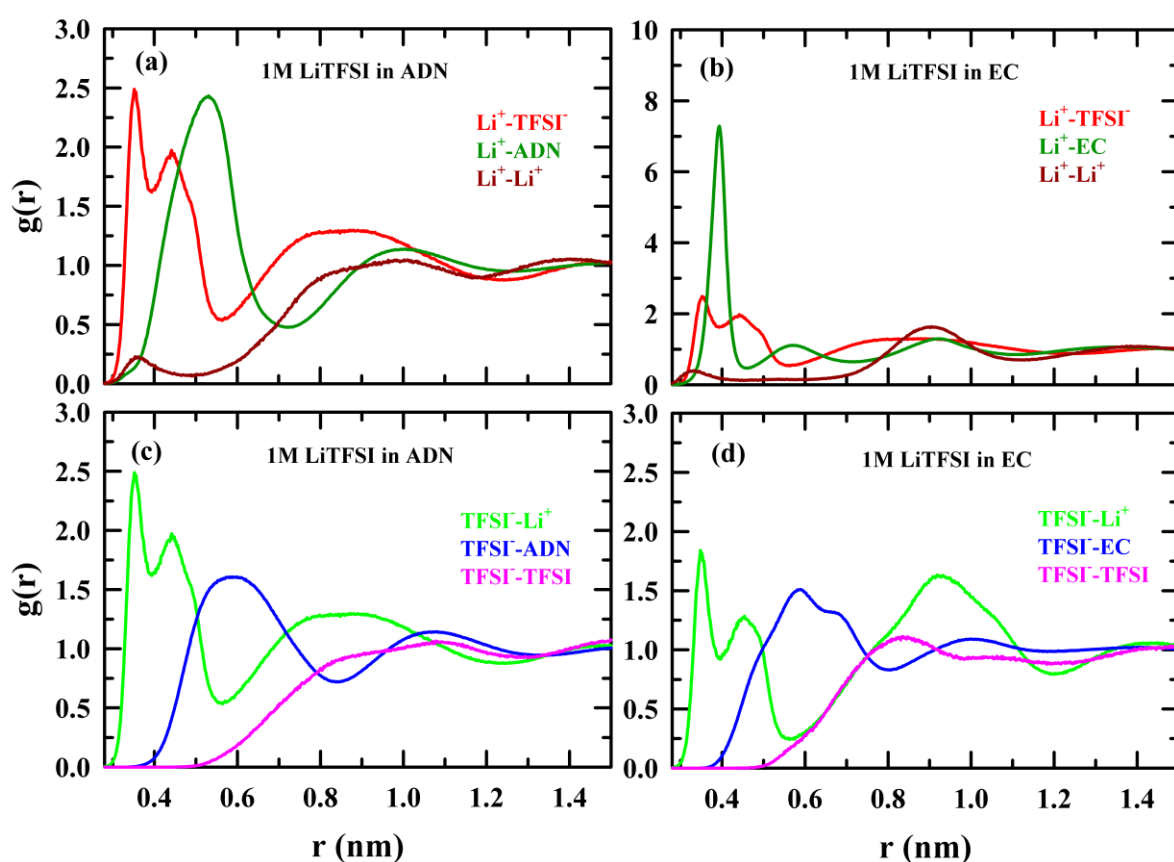
Figure 8.8: COM-COM radial distribution function (RDF) of two inter-species for (a) Li^+ and $TFSI^-$ (red), Li^+ and ADN (dark green), Li^+-Li^+ (dark red) in 1M LiTFSI in ADN, (b) Li^+ and $TFSI^-$ (red), Li^+ and EC, Li^+ and ADN (dark green), Li^+- Li^+ (dark red) in 1M LiTFSI in EC, (c) $TFSI^-$ and Li^+ (green), $TFSI^-$ and ADN (blue), $TFSI^-$-$TFSI^-$, (pink) in of 1M LiTFSI in ADN, (d) $TFSI^-$ and Li^+ (green), $TFSI^-$ and EC (blue), $TFSI^-$-$TFSI^-$ (pink) in of 1M LiTFSI in EC. All representations are colour-coded.
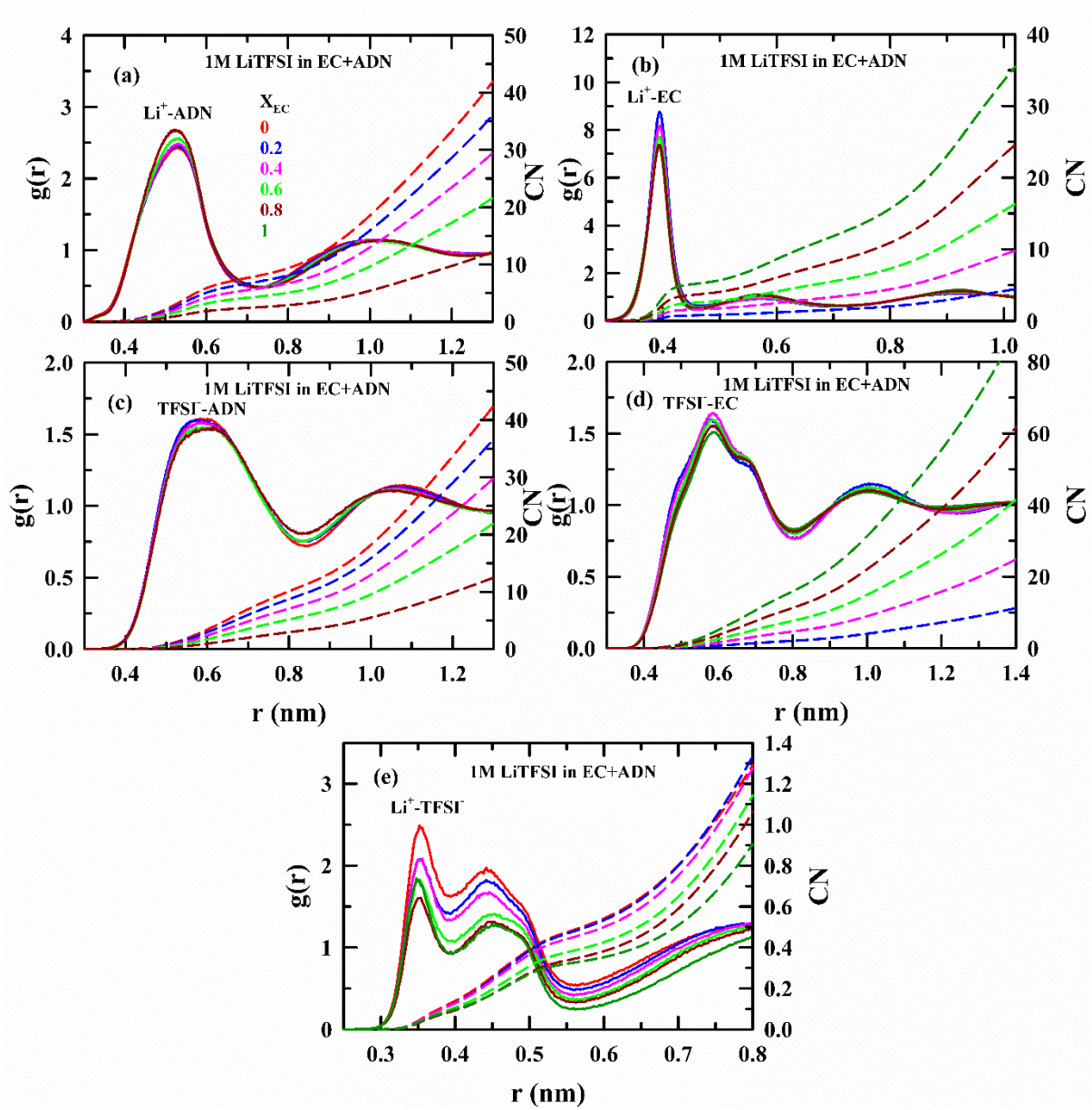
Figure 8.9: COM-COM radial distribution function (RDF) and coordination number (CN) of two inter-species for (a) Li$^+$ and ADN, (b) Li$^+$ and EC, (c) TFSI$^-$ and ADN, (d) TFSI$^-$ and EC, and (e) Li$^+$ and TFSI$^-$ in 1M LiTFSI in xEC+(1-x)ADN electrolyte solutions. All representations are colour-coded.

To investigate interaction at the atomistic level, the orientations of ADN, EC, and TFSI$^-$ around Li$^+$ ion from the simulation box of 1M LiTFSI in ADN or EC are shown in Figure 8.10. This presentation reveals that, Li$^+$ ion resides near the nitrogen of ADN, while Li$^+$ interacts with the carbonyl oxygen of EC. That confirms that first solvation shell of Li$^+$ ions is formed by nitrogen

and carbonyl oxygen atoms of ADN and EC, respectively. Figure 8.10 and Figure A8.17 (Appendix) depict that Li^+ strongly interacts with sulfonyl oxygen of $TFSI^-$ in these systems. For better clarity, RDF and CN of each corresponding RDF are presented with a double Y-axis plot in Figure 8.11(a-c). The CN of ion-solvent reveals that the number of solvent molecules of each solvent around Li^+ ion increases with their mole fraction. This static structure provides a clear picture of solvent replacement in an ion solvation shell by added co-solvent. Figure 8.11(c) shows that the relative finding oxygen atom of $TFSI^-$ around Li^+ is maximum at a distance of 0.22 nm in all electrolyte systems, indicating the RDF peak. The RDF peak height gradually decreases with increasing EC mole fraction, and CN decreases in the same direction. This suggests that with increasing high dielectric EC concentrations, dielectric screening weakens the interactions between opposite charged ions.
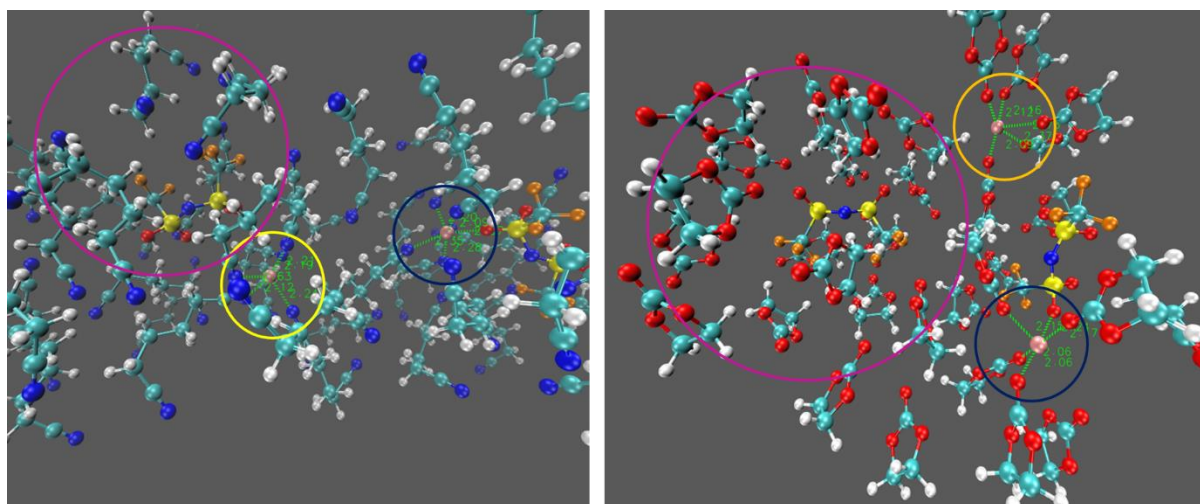
Figure 8.10: Snap shot of a simulation frame in 1M LiTFSI/ADN (left panel) and 1M LiTFSI/EC (right panel). Yellow and blue circle indicate Li^+ ion surrounded by solvent and solvent with anion respectively. Pink circle denotes anion surrounded by solvent.

Next, we explore the CN of solvent molecules in the first solvation shell around the two opposite charged ions, as well as the cation-anion CN from COM-COM RDF as shown in Figure 8.11(d) & Figure 8.11(e). In the first solvation shell, the CN of Li^+ in 1M LiTFSI/ADN is greater than Li^+ in 1M LiTFSI/EC. However, when we examine the atomistic details, CN of Li^+ with the atom nitrogen of ADN or oxygen of EC shows nearly equal in both cases. This apparent consistency between the atomistic analysis and the COM analysis was resolved by

visualizing the static structure of two systems, particularly 1M LiTFSI/ADN and 1M LiTFSI/EC, from a simulation frame, as shown in Figure 8.10. This visualization reveals that the arrangement of EC around Li$^+$ is more orderly due to its cyclic conformation and higher unidirectional dipole moment compared to ADN. The COM distribution of flexible linear dinitrile (ADN) around Li$^+$ is larger in distance than EC. This allows the COM of two or more ADN molecules enter to the first solvation shell without interacting with the Li$^+$ ion. The total CN formed by both solvents (ADN+EC) around Li$^+$ does not significantly change up to $X_{EC} = 0.6$, but it decreases $X_{EC} \geq 0.8$. On the other hand, the CN of TFSI$^-$ surrounded by EC is greater in 1M LiTFSI/EC than that of ADN around TFSI$^-$ in 1M LiTFSI/ADN system. Figure 8.10 shows that the orientation of solvent molecules like ADN or EC around anion is random. This indicates that the interaction between TFSI$^-$ and ADN/EC is very weak due to the low charge density (large anion). Again, the total CN coming from ADN and EC around TFSI$^-$ increases with increasing EC mole fraction. Note that the Van der Walls volume of ADN (approximately 123.78 Å^3) is larger than that of EC (71.82 Å^3). This reveals that, fewer ADN molecules required to wetting the anion compared to EC molecules. CN of cation surrounded by anion, as shown in Figure 8.11(e), decreases with increasing EC concentrations. This can be explained using Debye-Hückel screening length or simply Debye screening length (λ_D), as follows $\lambda_D = \left(\varepsilon_s K_B T / \sum_{i=1}^{N} n_j q_j \right)^{1/2}$ where $\varepsilon_s, K_B, T, N, n_j$ and q_j are static dielectric constant of Boltzmann constant, temperature, total number of ionic species, mean concentration of charge species j and electronic charge of species j respectively., λ_D is proportional to the square root of ε_s, i.e., $\lambda_D \propto \sqrt{\varepsilon_s}$. As observed in Figure 8.6 (b), ε_s increases with EC mole fraction in these electrolyte solutions, leading to an increase in λ_D, leading to a decrease in the electrostatic interaction between Li$^+$ and TFSI$^-$.

Figure A8.18 (Appendix) shows the spatial distribution (SDF) of ADN, EC, Li$^+$ and TFSI$^-$ around TFSI$^-$ as a reference. This clearly illustrates that COM of EC molecules in this electrolyte mixtures penetrates further in the inner portion of SDF compared to ADN. EC mole fraction dependent SDF of Li$^+$ around TFSI$^-$ confirms that the probability of a finding cation-anion pair decreases with increasing EC concentration which is also already observed in Figure 8.11(e).
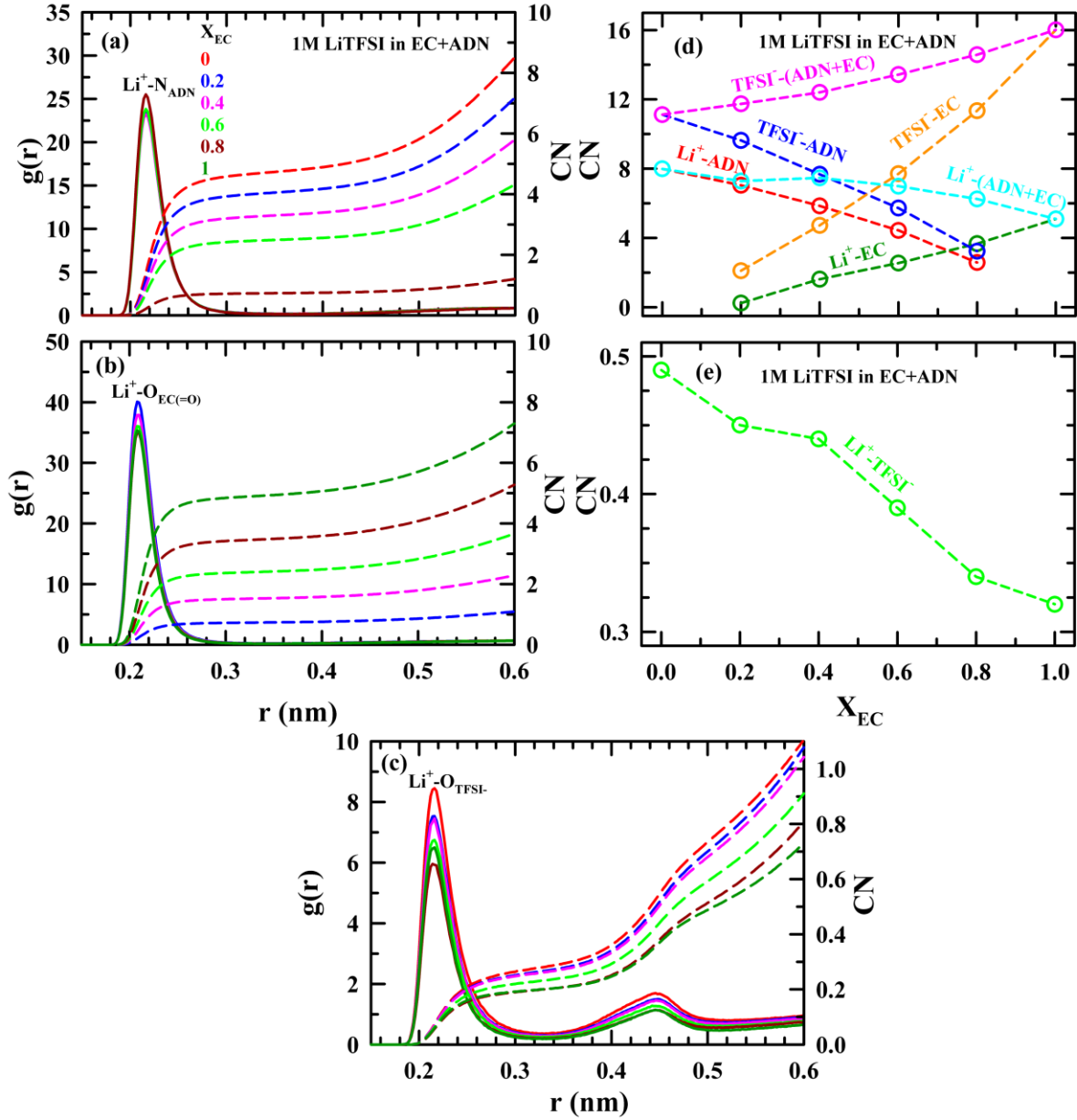
Figure 8.11: Inter atomic radial distribution function (RDF) of two inter-species for (a) Li^+ and nitrogen of adiponitrile, (b) Li^+ and double bond carbonyls oxygen of ethylene carbonate, and (c) Li^+ and sulfonyl oxygen of $TFSI^-$ anion of 1M LiTFSI in xEC+(1-x)ADN electrolyte solutions. All representations are colour-coded.

8.3.4.2 Static Dielectric Constant and Kirkwood G Factor (G_K): Dipole Randomisation and Dielectric Decrement

Figure 8.12(a,b) illustrate the time evolution ε_s in solvents and their electrolyte solutions with EC mole fractions. It is observed that ε_s values are getting plateau within the time of the production runs in these simulated systems. Compression between experimental and simulated ε_s for all solvents and their electrolyte solutions are presented in the upper panel of Figure A8.19 (Appendix). This comparison indicates that although non-polarisable model potentials yield slightly lower ε_s values compared to their respective experimental systems, the qualitative agreement between experiment and simulations is satisfactory. Moreover, the static dielectric decrement ($\Delta\varepsilon_{DD}$) and normalised $\Delta\varepsilon_{DD}$ with respect to higher values (inset) for both cases (experiments and simulations) are illustrated in Figure 8.12(c). This depicts qualitatively similar trends, offering an opportunity to explore the dielectric phenomena through Kirkwood G factor (G_K) calculation. Which provides a molecular level picture of dipole distributions in these systems. The simulated G_K from MD simulation for both solvents and their electrolyte solutions are depicted in Figure 8.12(d-f). The time evaluation of G_K and its fluctuations over time indicate G_K reaches an equilibrium value, where its fluctuation is minimal, within the simulated time duration. G_K values of both electrolytes, LiTFSI/ADN and LiTFSI/EC, are significantly lower than those of their respective neat solvents. This suggests that the orientation of solvent dipoles in electrolyte solutions is more randomized than in their neat solvents. The extent of decrease in G_K values depend on the identity of the solvent at a particular salt concentration in the electrolyte solutions. It is important to note that the average dipole moment of neat ADN and EC are 0.81(trans)/5.65(cis) D and 5.45 D, respectively (as shown in Figure A8.16(a,b) in the Appendix). However, the dipole moment population of EC is more than 10 times larger than that of ADN, even though both systems contain the same number of molecules. ε_s depends on orientation of molecular dipole vectors, and larger dipole population of EC results in a greater static dielectric permittivity than ADN. Figure A8.16(c,d) (Appendix) depict that dipole moment populations depend on the number molecules present in each system, and this is an additive property. In order to explore the effect electrolyte on self-dipole, dipole moment distribution is normalized by number of respective species present in each system, as shown in Figure A8.16(e,f) (Appendix). These figures indicate that dipole moment distribution of ADN molecules slightly shifted towards cis species, whereas it remains unchanged all in these electrolytes. The decrement of G_K depends on the dipole arrangement of the solvent in the system. The cyclic structure of EC is responsible for greater dipole moment
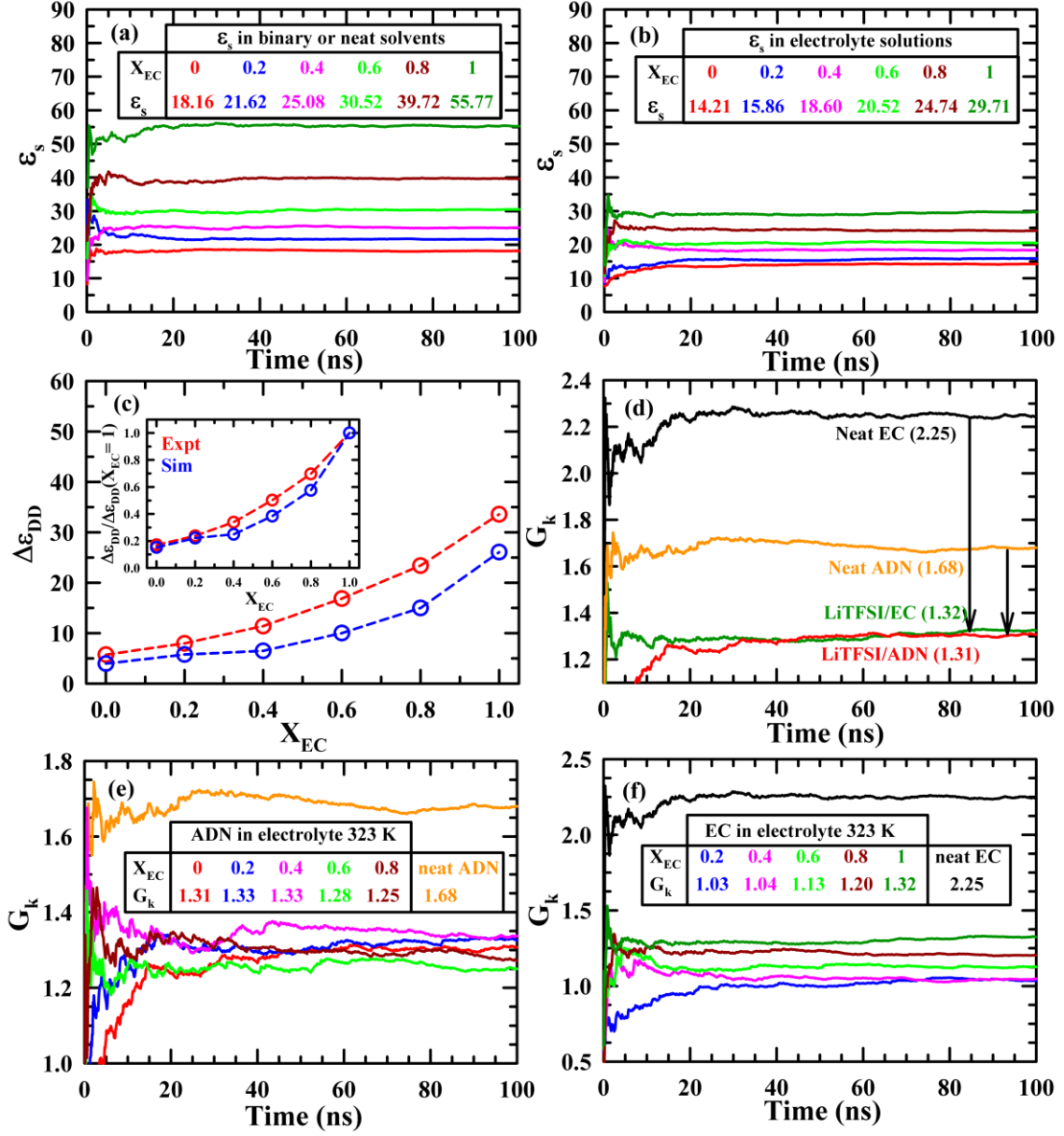
Figure 8.12: EC mole fraction dependent time evolution of static dielectric constant (ε_s) of (a) xEC+(1-x)ADN binary solvent mixtures, and (b) 1M LiTFSI in xEC+(1-x)ADN electrolyte solutions at 323 K. (c) Comparison between experimental and simulated static dielectric decrement ($\Delta\varepsilon_{DD}$) of electrolyte solutions from their respective binary or neat solvent with EC mole fraction at 323 K. Kirkwood G factor (G_K) evaluation with time for (d) 1M LiTFSI in ADN or EC and also their neat solvent, (e) ADN in electrolyte and neat solvent, and (f) EC in electrolyte and neat solvent. All representations are colour-coded.

population than ADN, resulting in a greater dipole moment cancelation due to ions induced dipole randomization. This leads to garter decrease of G_K in LiTFSI/EC from neat EC. Hence $\Delta\varepsilon_{DD}$ is larger in the EC-electrolyte system than in ADN-electrolyte system. Figure 8.12(e) & Figure 8.12(f) show that G_K values of ADN in all simulated electrolyte solutions are not significantly changed, whereas it increases for EC with EC mole fractions. This indicates the bulk dipole density of EC increases with EC mole fractions, leading to an increase in the ε_s of electrolyte solutions, as observed in DRS measurements. The lower panel of Figure A8.19 (Appendix) depicts that total G_K of electrolyte solutions reduces from their solvent systems. This illustrates that due to dipole ion induced solvent dipole randomization, a significant portion of the dielectric decrement observed in DRS experiments for an electrolyte solution from its solvent system. The difference in G_K value between electrolyte solutions and their solvents increases with increasing EC concentration. This suggests that ion induced dipole randomization dominates with the replacement of lower dipole density molecules ADN by higher dipole density molecules EC.

8.3.4.3 Dynamic: Self-diffusion, Transport Number and Conductivity

8.3.4.3.1 Self-diffusion and Transport Numbers

Figure 8.13 represents means squared displacement (MSD) for all species present in 1M LiTFSI in xEC+(1-x)ADN at 323 K. Self-diffusion coefficients were calculated from MSD as described in Section 8.2.5.4 in the diffusion limit for all species (β(t) ~ 1). EC mole fraction β(t) for ADN, EC, Li^+ and $TFSI^-$ at temperature 323 K, are shown in Figure A8.20 (Appendix). Self-diffusion coefficients (D) at various EC mole fractions are displayed in Figure 8.14. This depicts that the self-diffusion coefficients of ADN (D_{ADN}) and Li^+ (D_{Li+}) are very close to each other. While the self-diffusion coefficient of $TFSI^-$ (D_{TFSI-}) is slower than both of them (ADN and Li^+). This suggests that the cation is moving with solvent molecules within the solvation shell and anion may not. After the addition of 0.2 mole fraction EC, D_{ADN}, D_{Li+} and D_{TFSI-} are not significantly changed. On the other hand, the self-diffusion coefficient of EC (D_{EC}) shows maximum value than other species present in this system. With increasing EC concentrations, the diffusion coefficient increases for all species present in these electrolyte systems. This can be explained by the fact of reduction of solution viscosity with EC mole fractions. In these electrolyte systems, D_{EC} faster than D_{ADN}. Note that, molecular mass and Van der Wall volume of ADN (M_{ADN} = 108.14 g/mol and V_{ADN} = 123.78 $Å^3$) are larger than EC (M_{EC} = 88.06 g/mol

and V_{EC} = 71.82 Å^3)[85], leading to slower motion of ADN compared to EC. Additionally, we have calculated Stoke-Einstein (SE) diffusion with stick and slip prediction for all species that helps to understand molecular level interaction for diffusion in these systems. SE diffusions for all species with their stick-slip limits in these systems are shown in Table A8.21 and Figure A8.22(Appendix). The sub-slip diffusion of ADN is observed in all electrolyte systems.
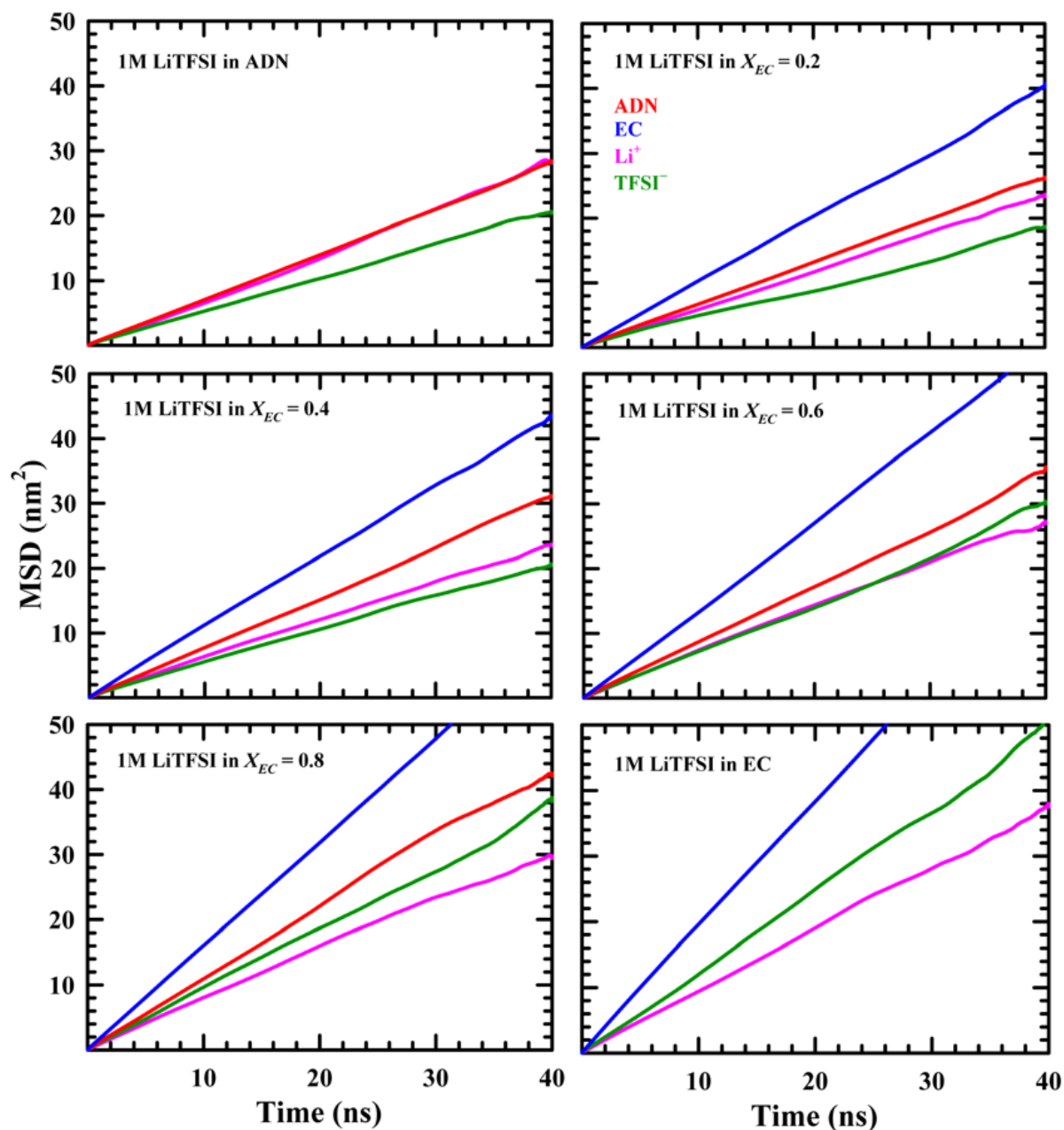
Figure 8.13: EC concentration dependent MSD for ADN (red), EC (blue), Li+ (pink) and TFSI (green) in 1M LiTFSI in xEC+(1-x)ADN at temperature 323 K. All presentations are colour-coded.
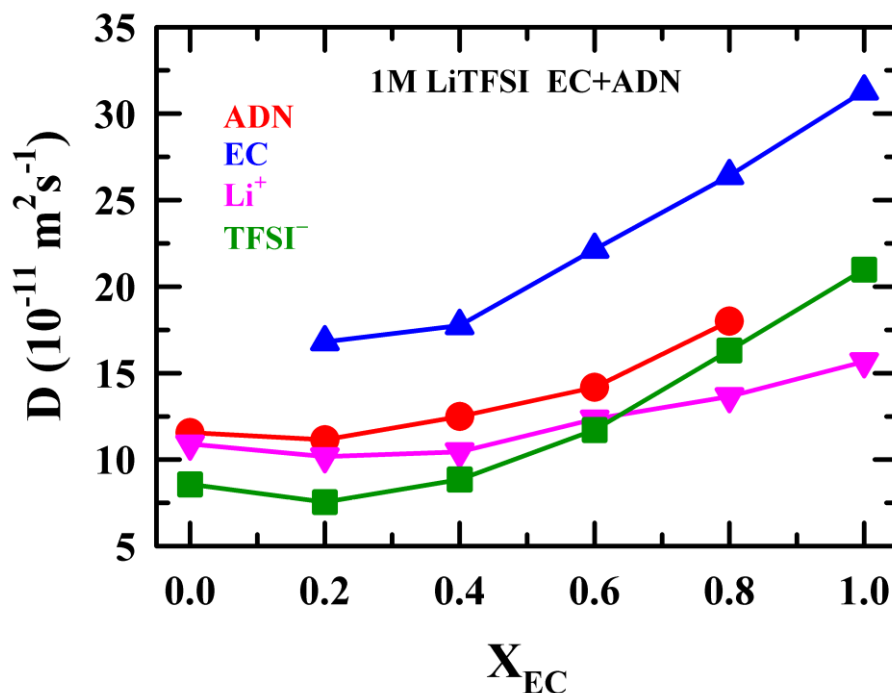
Figure 8.14: EC mole fraction dependent self-diffusion coefficient of ADN (red), EC (blue), Li^+ (pink) and $TFSI^-$ (green) in 1M LiTFSI in xEC+(1-x)ADN electrolyte solutions at 323 K. All presentations are colour-coded.

Whereas EC shows slip-diffusion pattern in all cases. But SE diffusion of Li^+ is 3 to 8 times faster (depending upon stick and slip conditions) than self-diffusion values. Interestingly, when we considering Li^+ ion with solvation shell (cutoff from RDF), SE diffusion values are very close to the self-diffusion values. This indicates that solvated Li^+ diffuses with solvent molecules present in the first solvation shell in these electrolytes. On the other hand, the self-diffusion of $TFSI^-$ follows the SE stick prediction. Which suggests that larger anion, $TFSI^-$ may diffuse alone. With EC concentration, the increment rate of D_{TFSI^-} is greater than that of D_{Li^+}. Note, SE diffusion prediction shows that Li^+ ion moves with solvation and $TFSI^-$ may not. So, diffusion of $TFSI^-$ is more bulk viscosity sensitive than Li^+-solvent clusters (sensitive to local friction). That is why, dissimilar increments of self-diffusion of cation and anion may appear with increasing EC concentration. Even after $X_{EC} = 0.6$, D_{TFSI^-} values cross over D_{Li^+}. This situation raises a new question, how do transport number changes with EC concentrations? This perspective gives an insight into battery efficiency which is explored in the next section.

Next, let's briefly discuss transport number, which provides insights into charge carrier efficiency in lithium-ion electrolytes. The transport number of cation (t_+) is calculated using the formula, $t_+ = \frac{D_+}{D_+ + D_-}$, where D_+ and D_- are denotes diffusion coefficients of cation and anion respectively. During charging and discharging, a high t_+ (≥ 0.5) is an essential condition for a good battery electrolyte, as it indicates a lower bulk resistance for major positive ions carriers. EC concentration dependent t_+ in 1M LiTFSI in xEC + (1-x)ADN electrolyte solutions at 323 K are shown in Figure 8.15. This depicts that t_+ in these electrolytes exhibits nonmonotonic changes with EC concentrations. With the addition of $X_{EC} \geq 0.2$, t_+ slightly increases compared to the ADN-electrolyte system. However, after this, t_+ steadily decreases with increasing EC concentrations. Variations of dielectric properties and viscosity with EC concentration may promote better electrolyte dissolution and enhance the diffusivity of both ions, leading to increase conductivity of these electrolyte solutions. However, the diffusivity increase rate of the anion is greater than the cation (Figure 8.14). These findings indicate that LiTFSI in ADN +EC performs as a good battery electrolyte, especially in low mole fraction ($X_{EC} \leq 0.6$) additives like high dielectric solvent EC.
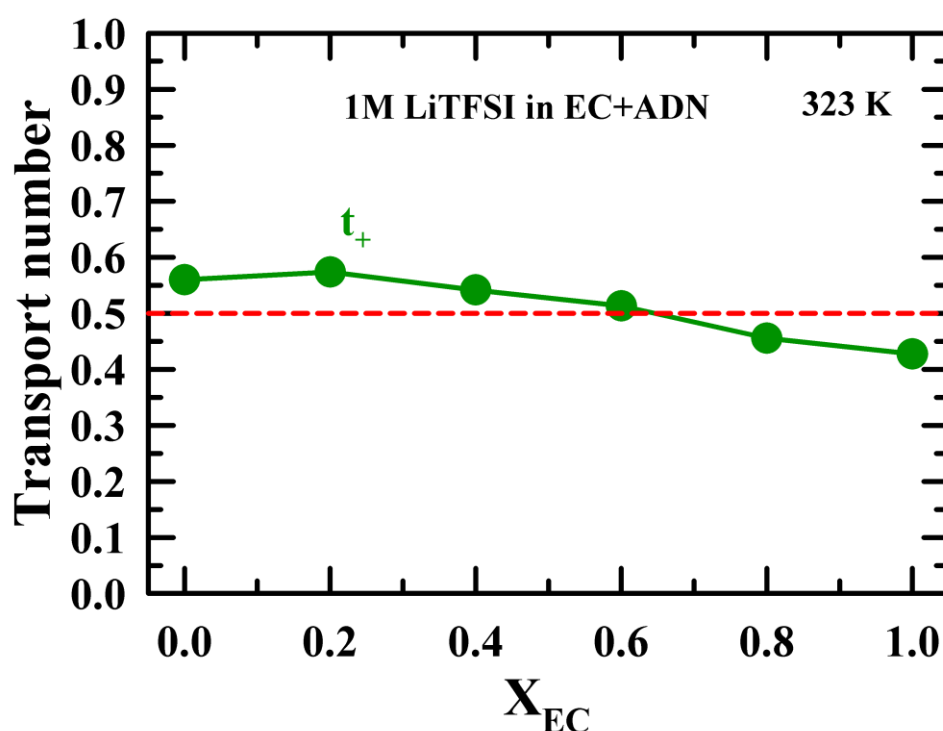
Figure 8.15: EC mole fraction dependent transport number of cation (t_+) in 1M LiTFSI in xEC + (1-x)ADN electrolyte solutions at 323K.

8.3.4.3.2 Conductivity

Generally, conductivity is calculated using the Nernst-Einstein (NE) equation relies on the self-diffusion coefficients of cations and anions which can be obtained either from experiment[86] or molecular dynamics simulation[87]. However, NE equation[88] is applicable primarily at low salt concentrations, as it does not account for directional correlations in ion movements, which become significant at higher salt concentrations (e.g. ≥1M) commonly used in lithium-ion batteries (LIB)[89]. In such scenarios, total conductivity is always smaller than the NE value. In this section, the effect of co-solvent on ionic conductivity is investigated by correlated ion motion (intra or inter) to decode component-wise conductivity contribution of ions to the total coactivity (σ_{total}) and Nernst-Einstein conductivities (σ_{NE}) in 1M LiTFSI in xEC + (1-x)ADN electrolyte solutions. To gain insights, we calculated total coactivity (σ_{total}), Nernst-Einstein conductivities ($\sigma_{NE} = \sigma_{self}^+ + \sigma_{self}^-$, conductivity from self-part), contribution to the total conductivity stemming from the distinct cation-cation correlation ($\sigma_{distinct}^{++}$), anion-anion correlation ($\sigma_{distinct}^{--}$) and cation-anion correlation (σ^{+-}). To improve statistical accuracy in conductivity calculations, we divided each 400 ns long trajectory into 40 parts of 10 ns each and determined the displacements of ionic species for each of the sub-trajectories, and then the average was taken over these 40 individual segments[90]. A representative plot is shown in Figure A8.23 (Appendix). The slopes of the line after averaging were used to calculate L^{++}, L^{--}, L^{+-}, L_{self}^{++} and L_{self}^{--} as outlined in equations 8.10, 8.11 & 8.12. To ensure accurate determination of diffusion transport, slopes were calculated when terms in the angular bracket in equations 8.10, 8.11 & 8.12 exhibited linear behavior over time (e.g. $\sum_\alpha \langle [\vec{r}_i^\alpha(t) - \vec{r}_i^\alpha(0)]^2 \rangle \propto t^\beta$ with $\beta = 1$). For most simulations in this work, β ranged between 0.96 to 1.03. After calculating the coefficients, we determined total conductivity (net value) along with its various components. The comparison between simulated and experimental conductivity, as well as the contribution coming from different correlated motions between ions in these electrolyte solutions at 323 K, is depicted in Figure 8.16, with corresponding values provided in Table A8.24 (appendix). Figure 8.16(a) depicts that the simulated conductivities are well corroborated with experimental conductivity values at different mole fractions of EC in 1M LiTFSI in xEC + (1-x)ADN electrolyte solutions at 323K. Inspite of using a non-polarizable force field, the simulated and experimental values are close enough to allow further conclusions about ion correlations to be drawn from these data. Figure 8.16(b) shows the different components of σ_{total}. This depicts σ_{total} values are smaller than σ_{NE}.
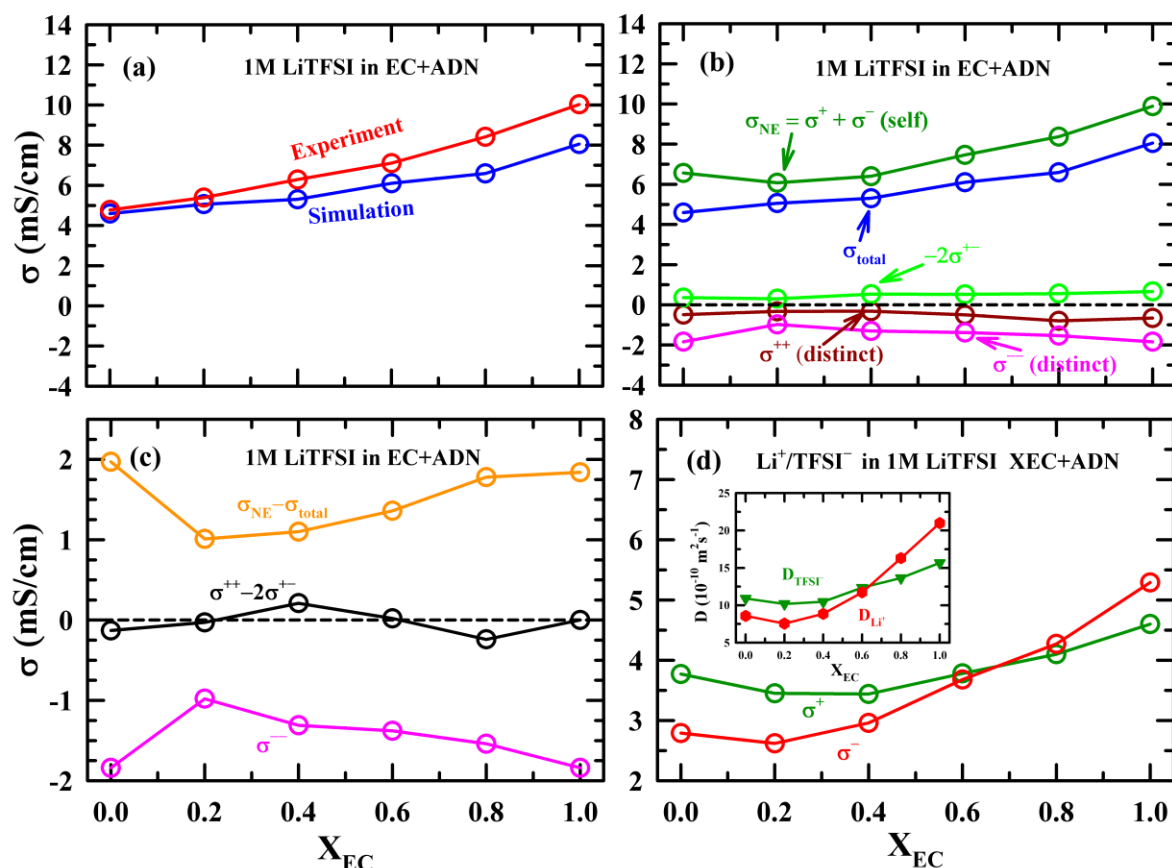
Figure 8.16: EC mole fraction dependent (a)simulated conductivity values are compared with experimental values and (b) total conductivity and different components of ionic conductivity, (c) conductivity difference between Nerst-Einstein and total part, and components, (d) self-conductivity of cation and anion from simulation are shown in 1M LiTFSI in xEC + (1-x)ADN electrolyte solutions at 323 K. Inset of Figure 3.16(d) represent EC mole fraction dependent diffusion coefficient Li^+ (green) and $TFSI^-$ (red) in 1M LiTFSI in xEC+(1-x)ADN electrolyte solutions at 323 K. All representations are color coded.

Contributions coming from intra-species distinct ions conductivities ($\sigma^{++}_{distinct}$ and $\sigma^{--}_{distinct}$) both make negative contributions for all EC mole fractions, indicating that motion between distinct ions of same species is anti-correlated. The contribution from the cation-anion cross term ($-2\sigma^{+-}$) is very small but positive, suggesting that cation-anion motion is also anti-correlated. The high dielectric constant (≥ 30) of the solutions at all EC mole fractions results in significant salt dissolution (less CIP), leading to the absence of a positive correlation between cation-anion movements. Scrutiny of conductivity contributions from distinct parts and self-part is provided in Figure 8.16(c). This depicts that contributions from cation-anion anti-correlation and distinct cation-cation anticorrelation almost cancel each other. Therefore, anti-

correlation between distinct anion motions is primarily responsible for the decrease in conductivity from the ideal NE value. This result provides a microscopic view of the different ion motion couplings in our systems. Figure 8.16(c) reveals that the deviation of total conductivity from the Nernst-Einstein part ($\sigma_{NE} - \sigma_{total}$) is minimized when the impact from distinct anion correlation has less negative value. Irrespective of the more negative contribution from the distinct anion-anion correlation, the σ_{total} increases with increasing EC concentration. This increase in total conductivity can be explained as decrease of medium viscosity and the increase of solvent dielectric (increase of dielectric screening) promoting faster ion movement with EC concentration and leading to a prominent increase in the self-conductivity of both types of ions (see Figure 8.16(d)). With EC concentration, more Li$^+$ is strongly coordinated with EC molecules and forms stable Li$^+$-EC complex. Consequently, the self-conductivity increment rate is larger for anion, specifically TFSI$^-$, than that for Li$^+$-EC complex with EC concentrations, which follow the self-diffusion patterns (see inset of Figure 8.16(d)).

8.4 Conclusion

In summary, the present study of 1M LiTFSI in xEC + (1-x)ADN electrolyte solutions reveals that conductivity, working temperature window, and electrolyte efficiency can be improved by changing co-solvent concentration in binary solvent electrolyte systems. DSC measurement reveals that $X_{EC} = 0.6$ electrolyte has the lowest melting temperature indicating a wider working temperature window of this battery electrolyte. Conductivity increases with increasing high dielectric solvent in these electrolytes due to better salt dissolution and reduced medium viscosity. Though the dielectric constant of electrolyte solutions increases with EC concentrations, but dielectric decrement from solvent to their respective electrolyte solution increases. This later observation is explained by the Kirkwood G factor of electrolyte solutions and their solvent. This reflects that ion-induced dipole randomization of solvent molecules is responsible for dielectric decrement with EC concentrations in these electrolyte solutions. Three types of DR were observed in these systems, where $\tau_1^S \sim 80\text{-}120$ ps DR time corresponds to bulk solvent reorientation, $\tau_2^S \sim 30\text{-}46$ ps resembles to partial rotation of solvent in solvation shell of ions, $\tau_3^S \sim 5\text{-}6$ ps assumed to originating from side group motion of TFSI$^-$ anion. Both p value and activation energy profile of the dielectric and conductivity process show solution heterogeneity decreases with EC concentrations and rotation-diffusion coupling prominent in high EC concentration ($X_{EC} \geq 0.6$) electrolyte systems. Solvent repayment by another solvent

and better salt dissolution with EC have been observed from RDF and CN in these systems. Deviation of total conductivity from Nernst-Einstein conductivity has been observed at all electrolyte solutions mainly due to anion-anion anti-correlated motion (results in negative distinct conductivity). Both conductivity difference ($\sigma_{NE} - \sigma_{total}$) and transport number ($t_+$) values indicate that low to moderate EC containing electrolyte systems are efficient in implementing LIBs.

Appendix A8

Table A8.1: Temperature dependent refractive indices (n_D), densities (ρ), and sound velocities (v) of 1M LiTFSI in xEC+(1-x)ADN electrolyte solutions.

T/K	n_D[a]	ρ kg/m³)[b]	v (m/s)[c]
1M LiTFSI in ADN			
298	1.4298	1087.2	1479
303	1.4292	1083.3	1465
308	1.4292	1079.3	1452
313	1.4286	1075.3	1438
318	1.4275	1071.3	1424
323	1.4266	1067.3	1411
1M LiTFSI in $X_{EC} = 0.2$			
298	1.4288	1127.8	1481
303	1.4285	1123.6	1466
308	1.4281	1119.4	1452
313	1.4268	1115.2	1438
318	1.4256	1111.1	1424
323	1.4254	1106.8	1411
1M LiTFSI in $X_{EC} = 0.4$			
298	1.4287	1172.8	1481
303	1.4277	1168.4	1466
308	1.4261	1163.9	1452
313	1.4237	1159.6	1438
318	1.4222	1155.1	1424
323	1.4211	1150.7	1411
1M LiTFSI in $X_{EC} = 0.6$			
298	1.4268	1240.1	1485
303	1.4245	1235.3	1470
308	1.4225	1230.6	1455
313	1.4213	1225.8	1440

T/K	n_D	ρ (kg/m³)	v (m/s)
318	1.4199	1221.1	1425
323	1.4175	1216.3	1411
1M LiTFSI in $X_{EC} = 0.8$			
298	1.4236	1318.2	1491
303	1.4217	1313.1	1475
308	1.4203	1307.8	1460
313	1.4177	1302.7	1444
318	1.4157	1297.4	1429
323	1.4142	1292.3	1414
1M LiTFSI in EC			
298	1.4218	1418.8	1504
303	1.4205	1413.1	1488
308	1.4182	1407.3	1471
313	1.4161	1401.6	1455
318	1.4144	1395.9	1439
323	1.4128	1390.2	1423

[a]Standard uncertainty in densities is 0.0005.

[b]Standard uncertainty in refractive indices is 0.00003.

[c] sound velocity values can be reproduced within ± 3% of the reported values.

Table A8.2: Temperature dependent n_D, ρ, and v in xEC+(1-x)ADN solvent systems.

T/K	n_D	ρ (kg/m³)	v (m/s)
ADN			
298	1.4369	958.7	1570
303	1.4354	954.9	1555
308	1.4337	951.1	1539
313	1.4307	947.3	1524
318	1.4292	943.5	1508
323	1.4281	939.8	1493
$X_{EC} = 0.2$			
298	1.4354	1006.8	1564
303	1.4338	1002.7	1548

308	1.4308	998.7	1532
313	1.4292	994.7	1517
318	1.4282	990.7	1501
323	1.4268	986.7	1485
$X_{EC} = 0.4$			
298	1.4334	1059.9	1560
303	1.4304	1055.6	1544
308	1.4290	1051.3	1528
313	1.4279	1047.0	1512
318	1.4264	1042.7	1496
323	1.4242	1038.4	1480
$X_{EC} = 0.6$			
298	1.4298	1133.5	1559
303	1.4285	1128.8	1542
308	1.4272	1124.1	1526
313	1.4253	1119.4	1509
318	1.4232	1114.7	1493
323	1.4220	1110.1	1417
$X_{EC} = 0.8$			
298	1.4283	1221.5	1563
303	1.4268	1216.4	1545
308	1.4244	1211.2	1528
313	1.4224	1206.1	1512
318	1.4212	1201.0	1494
323	1.4198	1195.8	1477
EC			
313	1.4204	1320.9	1521
318	1.4183	1315.2	1503
323	1.4166	1309.5	1486

[c]Standard uncertainty in ρ is 0.0005.

[d]Standard uncertainty in n_D is 0.00003.

[e] v values can be reproduced within ± 3% of the reported values.

Table A8.3: Partial Charges and Lennard-Jones parameters for ethylene carbonate (EC).
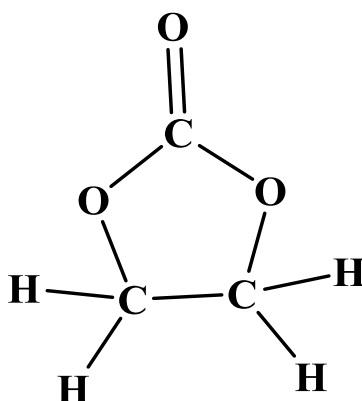
Atoms	Charge (e)	ε (kcal/mol)	Sigma (Å)
O (carbonyl)	-0.516776	0.21	2.96
C (carbonyl)	0.811230	0.07	3.55
O (ring)	-0.365210	0.14	2.90
C (CH$_2$, ring)	0.086891	0.066	3.50
H (CH2)	0.065546	0.03	2.50

Table A8.4: Partial Charges and Lennard-Jones parameters for adiponitrile (ADN).
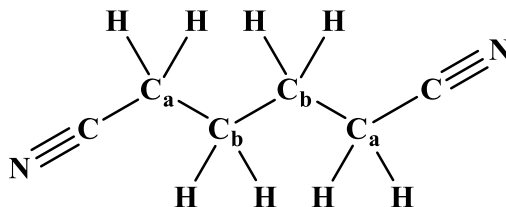
Atoms	Charge (e)	ε (kcal/mol)	Sigma (Å)
N (CN)	-0.484949	0.17	3.20
C (CN)	0.356621	0.066	3.30
C$_a$	-0.140182	0.066	3.50
C$_b$	0.035247	0.066	3.50
H (C$_a$)	0.090271	0.03	2.50
H (C$_b$)	0.026359	0.03	2.50

Table A8.5: Partial Charges and Lennard-Jones parameters for Li$^+$ and bis-(trifluoromethane)sulfonimide anion (TFSI$^-$).[27,28]
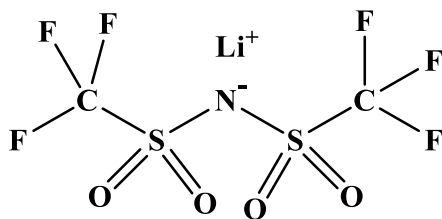
Atoms	Charge (e)	ε (kcal/mol)	Sigma (Å)
Li$^+$	0.8	0.01828	2.12645
N(TFSI$^-$)	-0.528	0.17	3.25
S(-SO$_2$-)	0.816	0.25	3.55
O(-SO$_2$-)	-0.424	0.21	2.96
C(-CF$_3$)	0.28	0.066	3.50
F	-0.128	0.053	2.95

Table A8.6: Number of molecules for each simulated system.

X_{EC}	ADN	EC	LiTFSI	Total molecules
Neat ADN	500			500
Neat EC		500		500
0	889		111	1000
0.2	711	177	112	1000
0.4	535	361	104	1000
0.6	362	545	93	1000
0.8	183	734	83	1000
1		929	71	1000
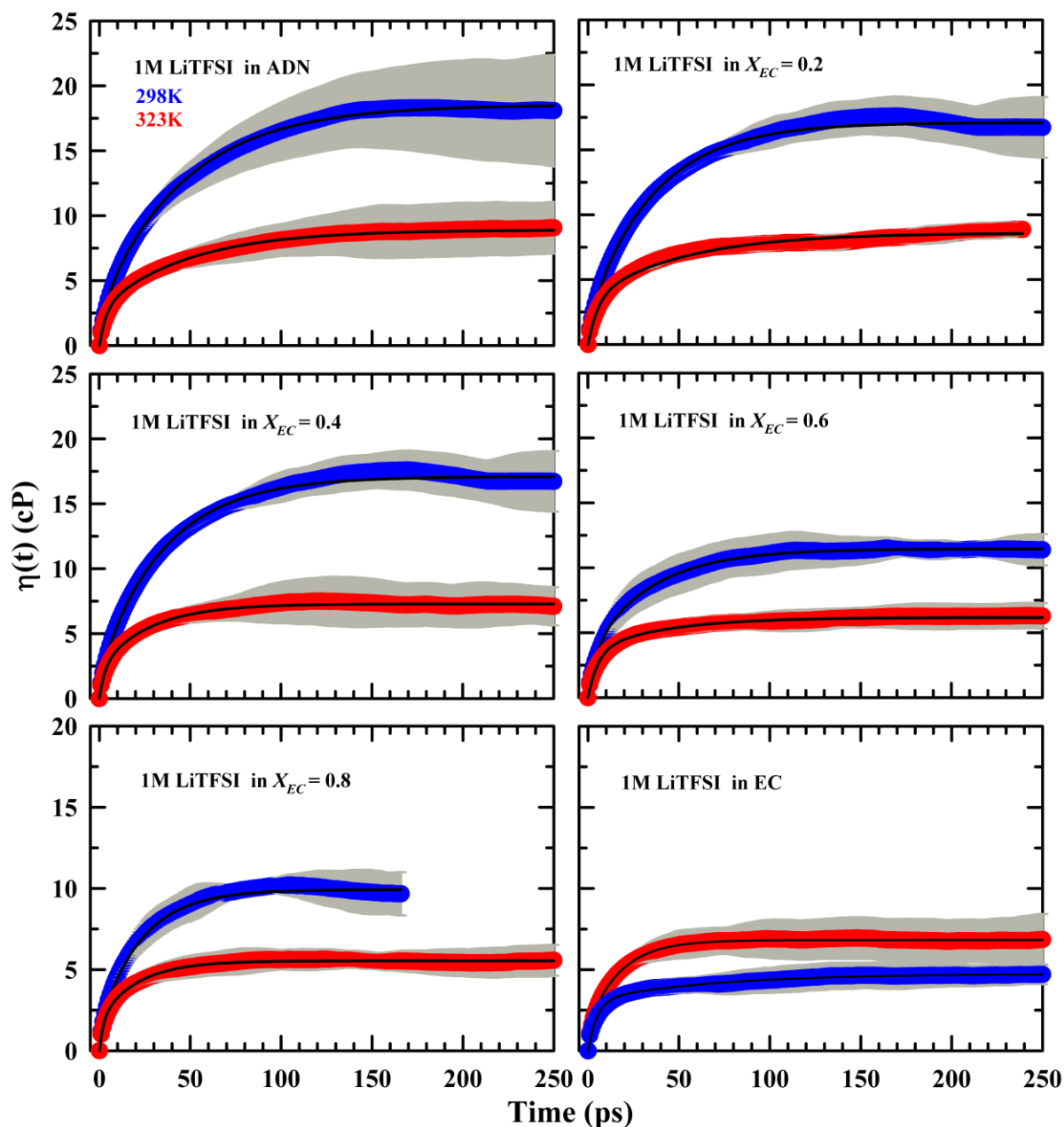
Figure A8.7: Time evaluation average shear viscosity ($\eta(t)$) from running integral of pressure-pressure auto-correlation function for six electrolyte solutions at two temperatures 298K and 323 K. Shaded portions indicate error bars calculated from standard deviation of 7-10 independent simulations runs. Solid black lines passing through the symbol are represent double exponential fits to average $\eta(t)$. All representations are colour coded.
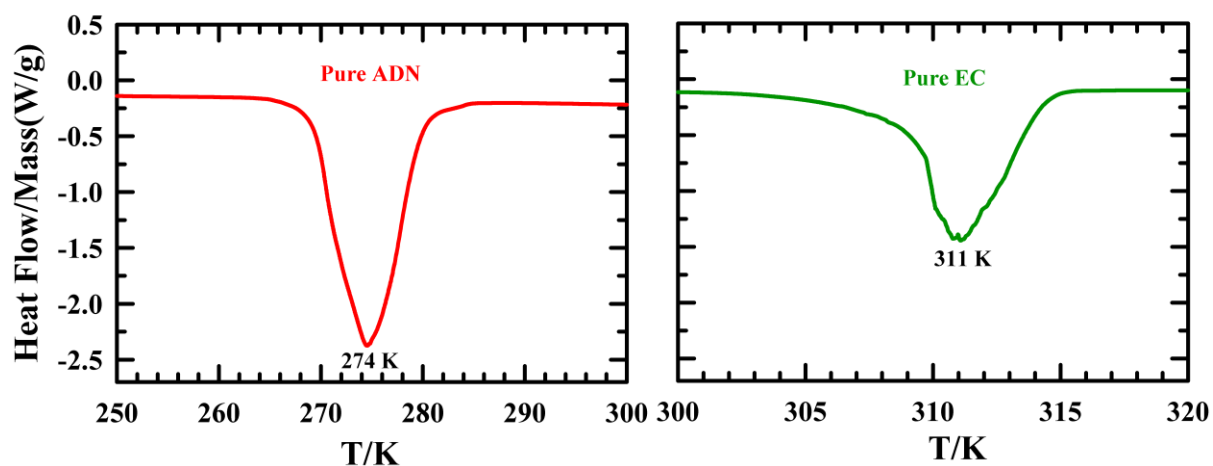
Figure A8.8: DSC thermogram of pure ADN (left panel) and EC (right panel). During DSC experiment 5 K/min heating rate was maintained. All representations are colour coded.

Table A8.9: Melting temperature (T_m), boiling point (T_b) and flash point of ADN and EC

Compound	T_m/K	T_b/K	T_{fs}/K
Pure ADN[1]	275 (274)	568	432
Pure EC[2]	309.4 (311)	521	433
LiTFSI[2]	507		

Data given in parenthesis was collected from our present DSC measurement of pure ADN and pure EC.
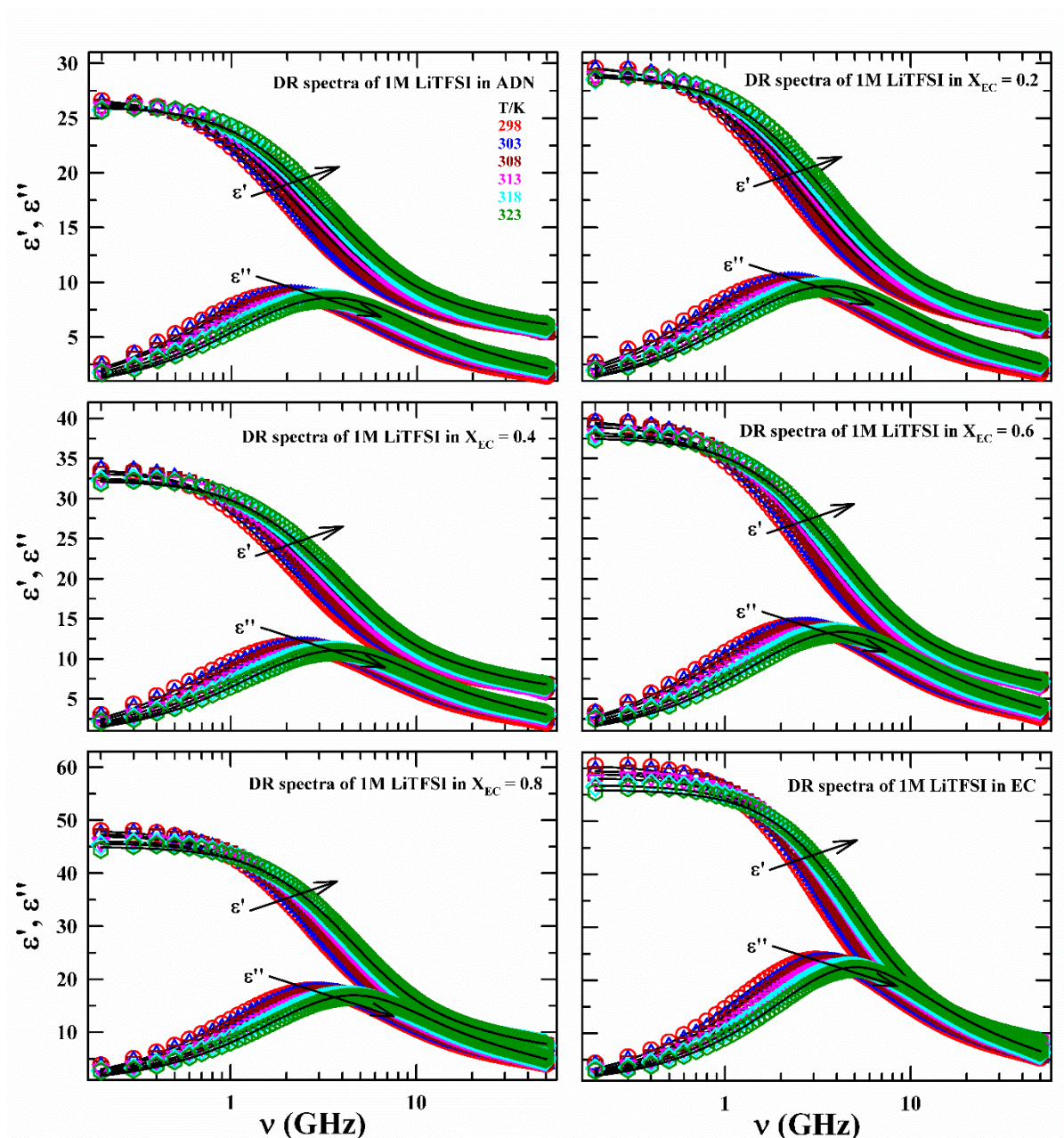
Figure A8.10: Temperature dependent complex DR spectra with real (ε') and imaginary (ε'') component in 1M LiTFSI in xEC+(1-x)ADN electrolyte solutions at six electrolyte systems. The lines passing through experimental data points express multi-Debye model fits. All presentations are colour-coded.
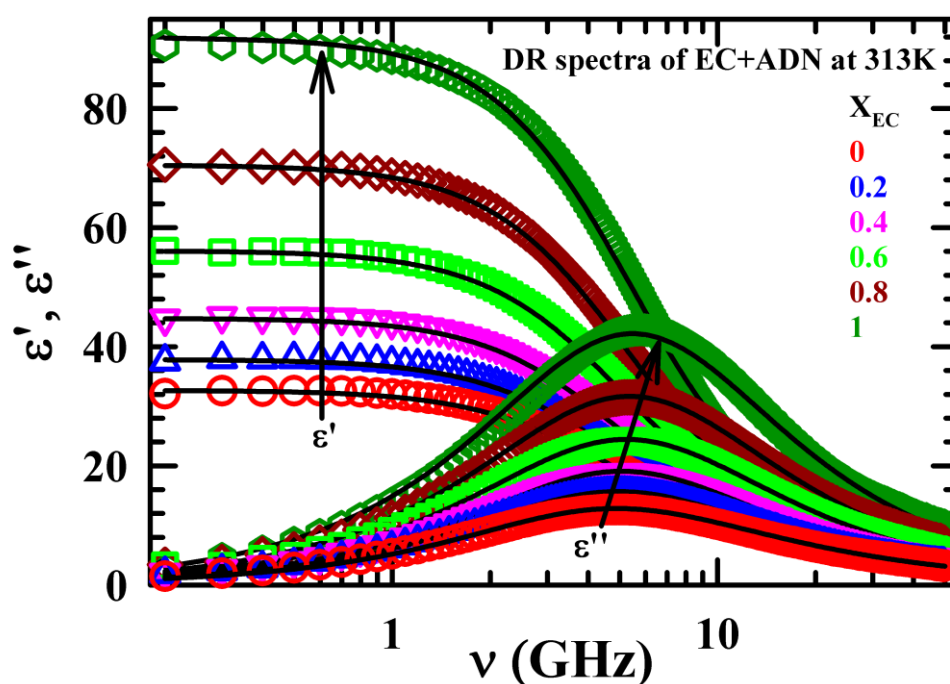
Figure A8.11: EC mole fraction dependent complex DR spectra with real (ε') and imaginary (ε'') component of xEC+(1-x)ADN binary solvent and their neat solvent at 313 K. The lines passing through experimental data points express double Debye or single Debye model fits. All representations are colour-coded.

Table A8.12: Temperatures and EC mole fraction dependent double-Debye or single-Debye fit parameters of experimentally measured DR spectra of solvent systems (absence of electrolyte salt) in xEC+(1-x)ADN electrolyte.

T/K	ε_s	$\Delta\varepsilon_1$	τ_1/ps	$\Delta\varepsilon_2$	τ_2/ps	$\langle\tau_{DR}\rangle$/ps	ε_∞	χ^2
ADN								
298	33.66	24.22 (86)	47	3.87 (14)	14	42	5.57	0.0400
303	33.55	24.17 (87)	43	3.67 (13)	13	39	5.71	0.0376
308	33.11	23.3 (85)	40	4.08 (15)	13	36	5.73	0.0407
313	32.60	22.93 (85)	36	3.94 (15)	11	32	5.73	0.0392
318	32.39	22.96 (86)	33	3.71 (14)	10	28	5.72	0.0366
323	31.71	23.04 (88)	30	3.16 (12)	9	27	5.67	0.0348

				$X_{EC} = 0.2$				
298	39.52	32.24 (97)	41	0.99 (03)	13	40	6.29	0.0313
303	39.47	32.14 (98)	38	0.72 (02)	13	40	6.49	0.0358
308	38.63	31.74 (99)	36	0.44 (01)	12	36	6.34	0.0544
313	37.77	31.43	32			32	6.34	0.0542
318	37.16	30.79	29			29	6.37	0.0639
323	36.76	30.32	27			27	6.44	0.0575
				$X_{EC} = 0.4$				
298	47.06	39.46 (0.98)	39	0.79 (02)	13	38	6.81	0.0348
303	46.81	39.61 (99)	37	0.35 (01)	5	37	6.85	0.0447
308	45.61	38.87	33			33	6.74	0.0602
313	44.86	38.14	31			31	6.72	0.0625
318	44.12	37.36	29			29	6.76	0.0678
323	43.57	36.79	27			27	6.78	0.0723
				$X_{EC} = 0.6$				
298	58.04	51.24	37			37	6.80	0.0685
303	57.53	50.73	35			35	6.80	0.06635
308	56.99	50.03	32			32	6.96	0.0557
313	55.96	49.02	30			30	6.94	0.0516
318	55.00	48.11	28			28	6.89	0.0498
323	54.38	47.43	26			26	6.95	0.0499
				$X_{EC} = 0.8$				
298	73.59	66.39	36			36	7.20	0.0477
303	72.77	65.62	34			34	7.15	0.0580
308	71.86	64.61	32			32	7.25	0.0485
313	70.51	63.34	30			30	7.17	0.0487
318	69.34	62.18	28			28	7.16	0.0502
323	68.36	61.20	26			26	7.16	0.0545
				EC				
313	91.9	84.40	29			29	7.5	0.4930
318	91.1	83.60	28			28	7.5	0.4545
323	89.5	82.00	26			26	7.5	0.4503

Table A8.13: Temperature and EC mole fractions dependent calculated rotational diffusion time from Stokes-Einstein-Debye relation **[1]** for ADN, TFSI⁻, EC and CN in 1M LiTFSI/xEC+(1-x)ADN electrolyte solutions. Also, rotational diffusion of ADN, CN and EC calculated in neat system given below.

Stokes-Einstein-Debye equation for rotational diffusion time considering stick limiting condition, τ_{rot}^{SED} with volume V, $\tau_{rot}^{SED} = 3V\eta/k_BT$.[91] Volume of ADN, TFSI⁻, EC and CN calculated from ref[85] and given as $V_{TFSI^-} = 132.09$ Å³, $V_{ADN} = 123.78$ Å³, $V_{EC} = 71.82$ Å³, and $V_{CN} = 30.26$ Å³. τ_{rot}^{SED} for ADN molecule and CN group calculated in neat ADN ($\eta = 4.11$ cP) are 353 ps and 86 ps respectively whereas for EC molecule in neat EC ($\eta = 1.925$ cP) 96 ps at 313 K.

T/K	η (cP)	$\tau_{rot}^{TFSI^-}$/ps	τ_{rot}^{ADN}/ps	τ_{rot}^{EC}/ps	τ_{rot}^{CN}/ps
1M LiTFSI in ADN					
298	17.74	1709	1602	929	392
303	15.02	1423	1334	774	326
308	12.83	1196	1121	650	274
313	11.10	1018	954	554	233
318	9.67	873	818	475	200
323	8.49	755	707	410	173
1M LiTFSI in $X_{EC} = 0.2$					
298	15.56	1499	1405	815	343
303	13.20	1251	1172	680	287
308	11.34	1057	991	575	242
313	9.86	905	848	492	207
318	8.62	778	729	423	178
323	7.60	676	633	367	155
1M LiTFSI in $X_{EC} = 0.4$					
298	13.11	1263	1184	687	289
303	11.24	1065	998	579	244
308	9.71	905	848	492	207
313	8.48	778	729	423	178
318	7.47	675	632	367	155
323	6.63	589	552	320	135
1M LiTFSI in $X_{EC} = 0.6$					
298	10.65	1026	962	558	235
303	9.21	873	818	475	200
308	7.97	743	696	404	170
313	6.96	639	598	347	146
318	6.13	554	519	301	127
323	5.50	489	458	266	112
1M LiTFSI in $X_{EC} = 0.8$					
298	7.86	757	710	412	173
303	6.82	646	606	351	148

| 308	5.96	556	521	302	127
313	5.32	488	457	265	112
318	4.76	430	403	234	98
323	4.39	390	366	212	89
1M LiTFSI in EC					
298	6.23	600	563	326	138
303	5.68	538	504	293	123
308	5.08	474	444	258	108
313	4.60	422	395	229	97
318	4.20	379	355	206	87
323	3.85	342	321	186	78

Table A8.14: Temperature and EC mole fraction dependent dielectric decrement ($\Delta\varepsilon_{DD}$) in 1M LiTFSI in [xEC+(1-x)ADN]. Where $\Delta\varepsilon_{DD} = \varepsilon_s(\text{solution}) - \varepsilon_s(\text{solvent})$.

| X_{EC}	$\Delta\varepsilon_{DD}$					
	298 K	303 K	308 K	313 K	318 K	323 K
0	6.84	6.93	6.82	6.42	6.09	5.72
0.2	9.71	9.78	9.44	8.87	8.32	7.97
0.4	13.29	13.34	13.58	13.02	12.37	11.94
0.6	18.55	18.18	18.12	17.80	17.16	16.92
0.8	25.45	25.21	24.77	24.37	23.68	23.39
1				33.75	34.27	33.58
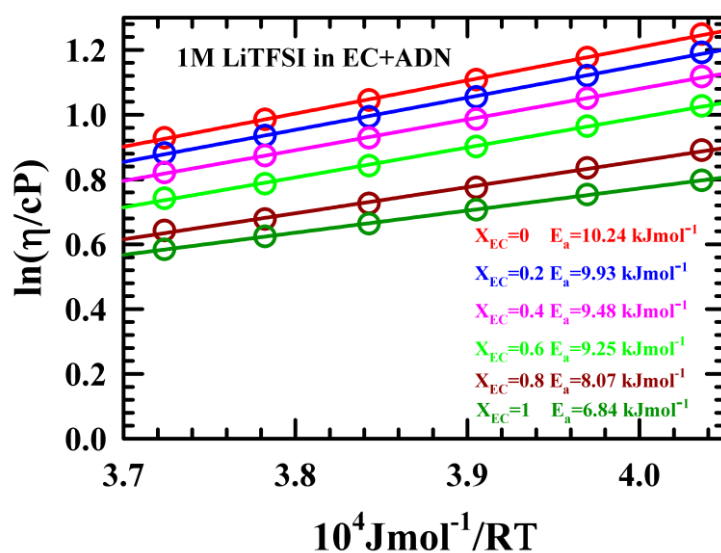
Figure A8.15: Temperature dependent Arrhenius-type dependence of viscosity (η) for 1M LiTFSI in xEC+(1-x)ADN. Estimated activation energy at various EC mole fraction for all

electrolyte solutions are shown. Solid lines passing through symbols represent linear fits. All presentations are colour-coded.
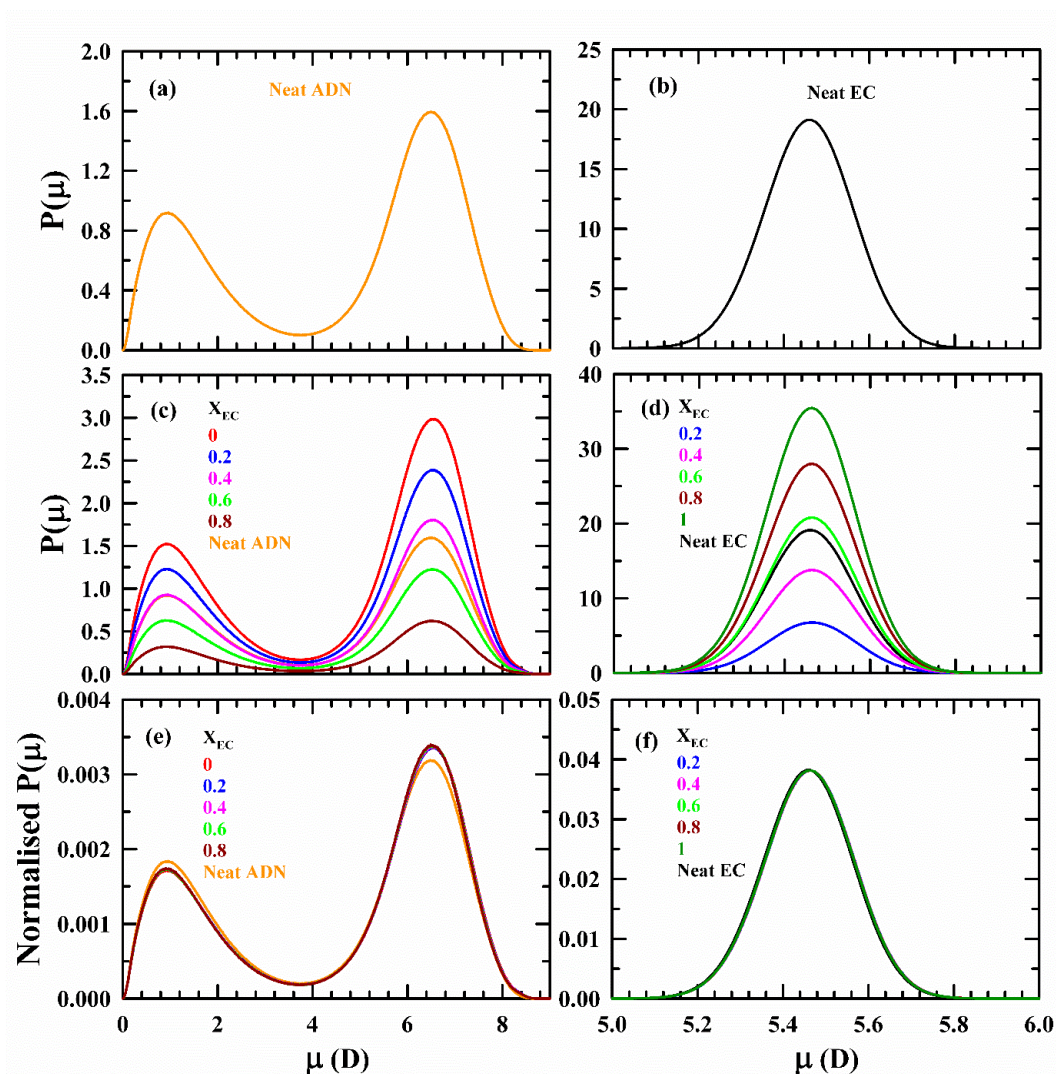
Figure A8.16: Dipole moment distribution of (a) neat ADN molecules, (b) neat EC molecules, (c) ADN in 1M LiTFSI in xEC+(1-x)ADN electrolyte solutions and compare with neat ADN, (d) EC in 1M LiTFSI in xEC+(1-x)ADN electrolyte solutions and compare with neat EC. Normalised dipole moment distribution of (e) ADN in 1M LiTFSI in xEC+(1-x)ADN electrolyte solutions and compare with neat ADN, (f) EC in 1M LiTFSI in xEC+(1-x)ADN electrolyte solutions and compare with neat EC. For normalised dipole distribution, dipole population is normalised by number of corresponding molecules present in electrolyte system. All presentations are colour-coded.
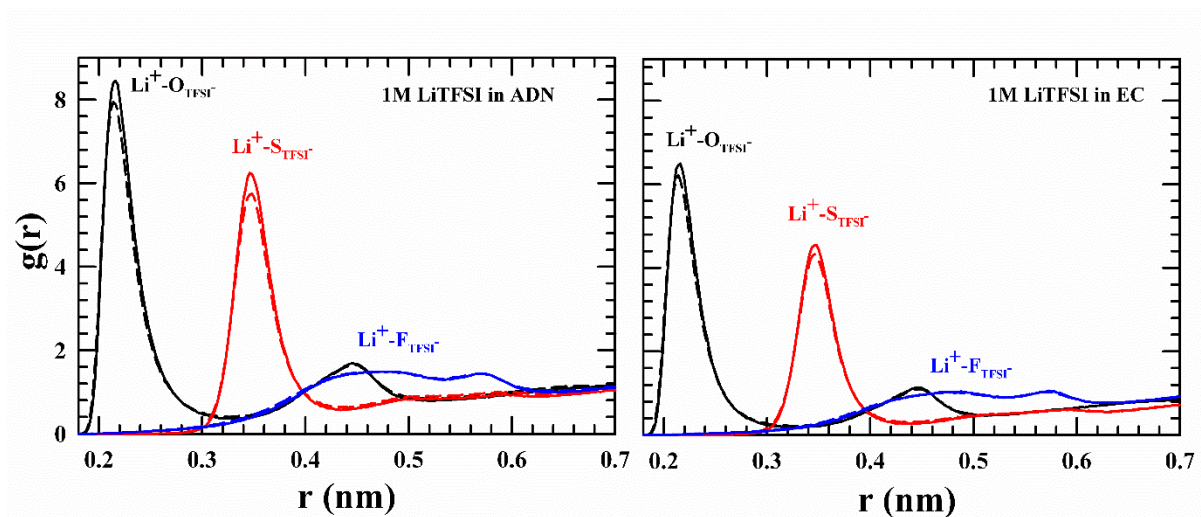
Figure A8.17: Inter atomic radial distribution function (RDF) of two inter-species for Li$^+$ and sulfonyls oxygen of TFSI$^-$, Li$^+$ and sulfur of TFSI$^-$, and Li$^+$ and fluorine of TFSI$^-$ in both system 1M LiTFSI/ADN (left panel) and 1M LiTFSI/EC (right panel). All representations are colour-coded.
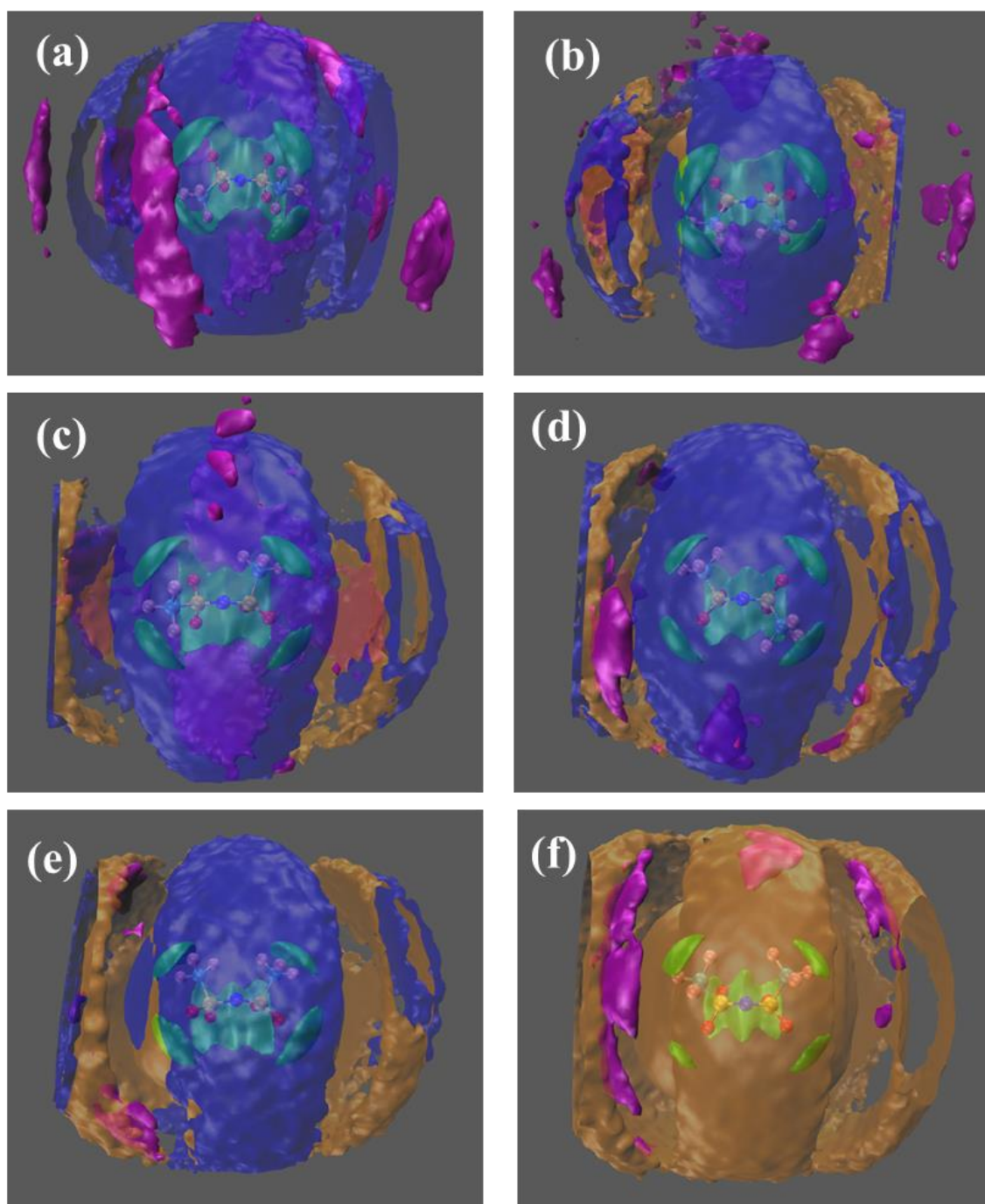
Figure A8.18: EC concentration dependent Spatial distribution function (SDF) of Li+ (green), ADN (blue) EC (orange) and TFSI- (violet) around reference molecule TFSI-.
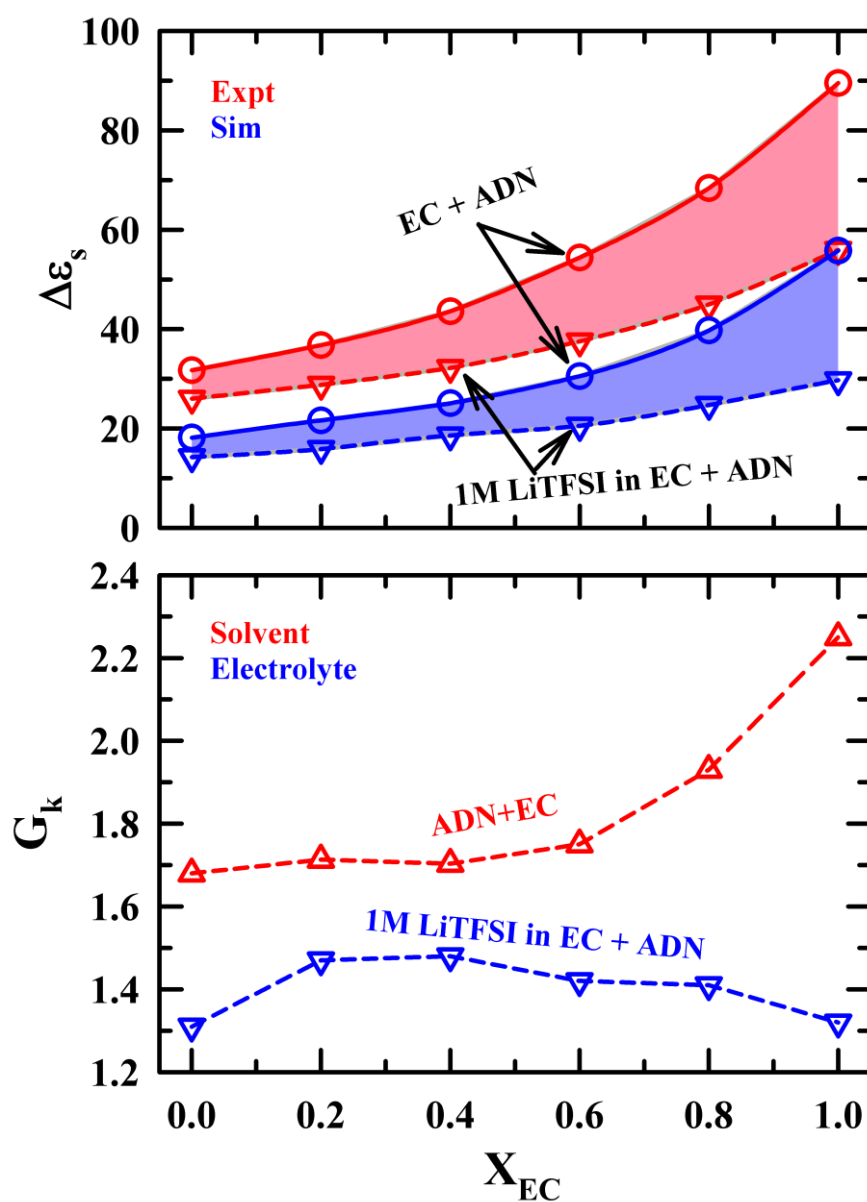
Figure A8.19: Upper panel shows comparison between experiment and simulated static dielectric constant (ε_s) of xEC+(1-x)ADN binary solvents and neat solvents, and 1M LiTFSI in xEC+(1-x)ADN electrolyte solutions at 323 K. Shaded portion represents static dielectric decrement ($\Delta\varepsilon_{DD}$) of electrolyte solutions from their respective binary or neat solvent with EC mole fraction at 323 K. Simulated total Kirkwood G factor (G_k) of solvents and electrolyte solutions at 323 K (lower panel). All presentations are colour-coded.
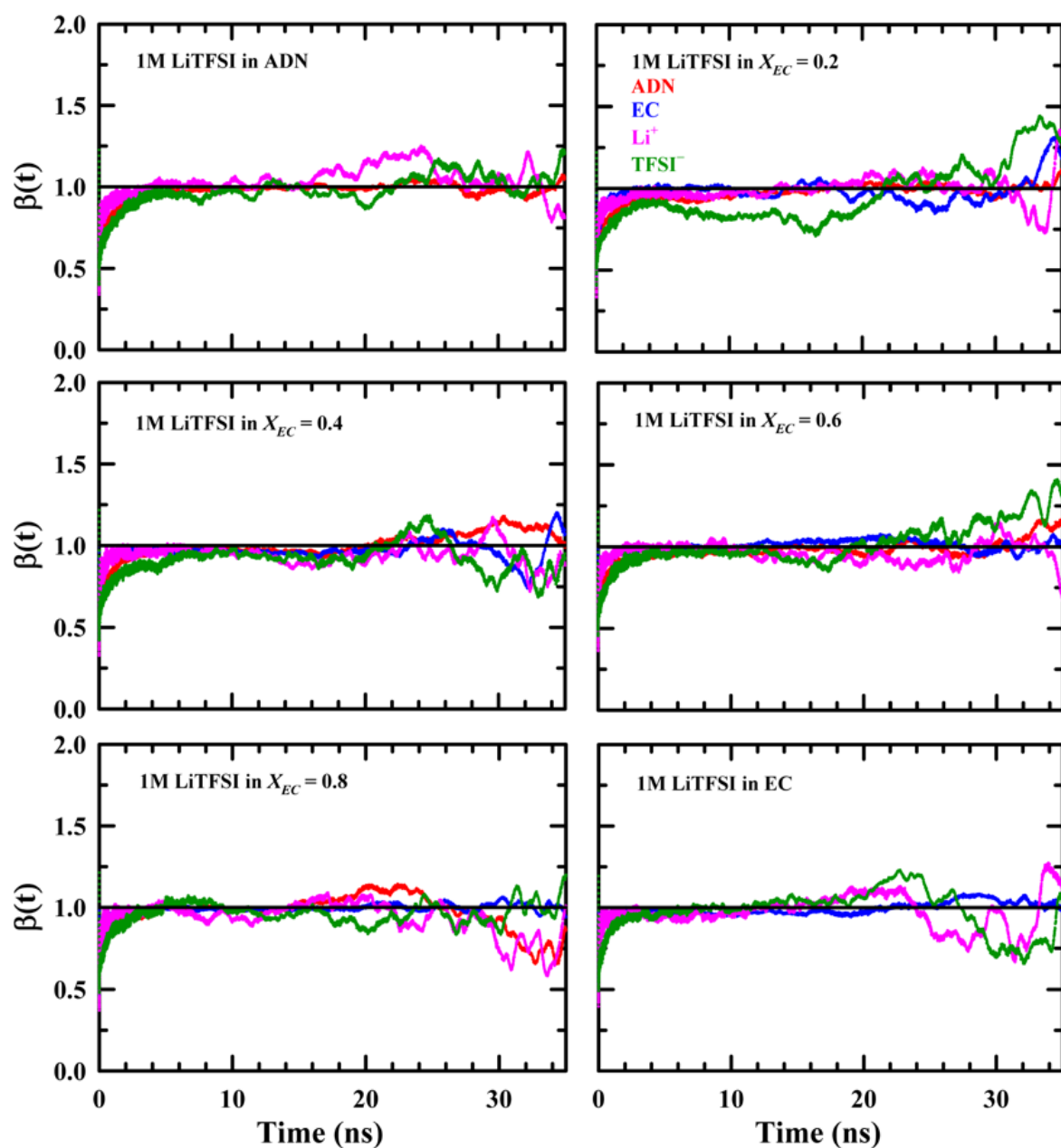
Figure A8.20: EC concentration dependent β(t) for ADN (red), EC (blue), Li+ (pink) and TFSI (green) in 1M LiTFSI in xEC+(1-x)ADN at two ambient temperature 298 K and 323 K. All presentations are colour-coded

Table A8.21: EC concentration dependent calculated translational diffusion time from Stokes-Einstein relation (SE) and rotational diffusion from[91] for ADN, TFSI-, EC and CN in 1M LiTFSI/xEC+(1-x)ADN electrolyte solutions. Stokes-Einstein equation of translational diffusion for spherical particle is as following $D_{trans} = k_B T/2C\pi\eta r$ where k_B, T, C, η and σ are denoted Boltzmann constant, temperature, coupling constant for slip (2) and stick (3) condition, viscosity and diameter of species respectively.

Volume of ADN, TFSI-, EC and CN calculated from ref[85] and given as $V_{Li+} = 1.839$ Å^3 ($r_{Li+} = 0.76$ Å), $V_{TFSI-} = 132.09$ Å^3 ($r_{TFSI-} = 3.16$ Å), $V_{ADN} = 123.78$ Å^3 ($r_{ADN} = 3.09$ Å), and $V_{EC} = 71.82$ Å^3 ($r_{EC} = 2.58$ Å). Note simulated viscosity is used for diffusion coefficient calculation.

X_{EC}	η (cP)	D_{ADN}		D_{EC}		D_{Li+}		D_{TFSI-}	
		Stick	Slip	Stick	Slip	Stick	Slip	Stick	Slip
0	8.91	8.59	12.89	10.29	15.44	34.94	52.41	8.40	12.60
0.2	8.59	8.91	13.37	10.68	16.01	36.24	54.36	8.72	13.07
0.4	7.29	10.50	15.75	12.58	18.87	42.70	64.05	10.27	15.41
0.6	6.17	12.41	18.61	14.86	22.29	50.45	75.68	12.13	18.20
0.8	5.53	13.85	20.77	16.58	24.87	56.29	84.44	13.53	20.31
1	4.63	16.54	24.81	19.81	29.71	67.24	100.85	16.17	24.26

	Cation-solvent complex				
X_{EC}	η (cP)	$D_{Li+-ADN}$		D_{Li+-EC}	
		Stick	Slip	Stick	Slip
0	8.91	3.59	5.38	5.78	8.66
0.2	8.59	3.72	5.58	5.99	8.98
0.4	7.29	4.39	6.58	7.06	10.58
0.6	6.17	5.18	7.78	8.34	12.50
0.8	5.53	5.78	8.68	9.30	13.95
1	4.63	6.91	10.36	11.11	16.66
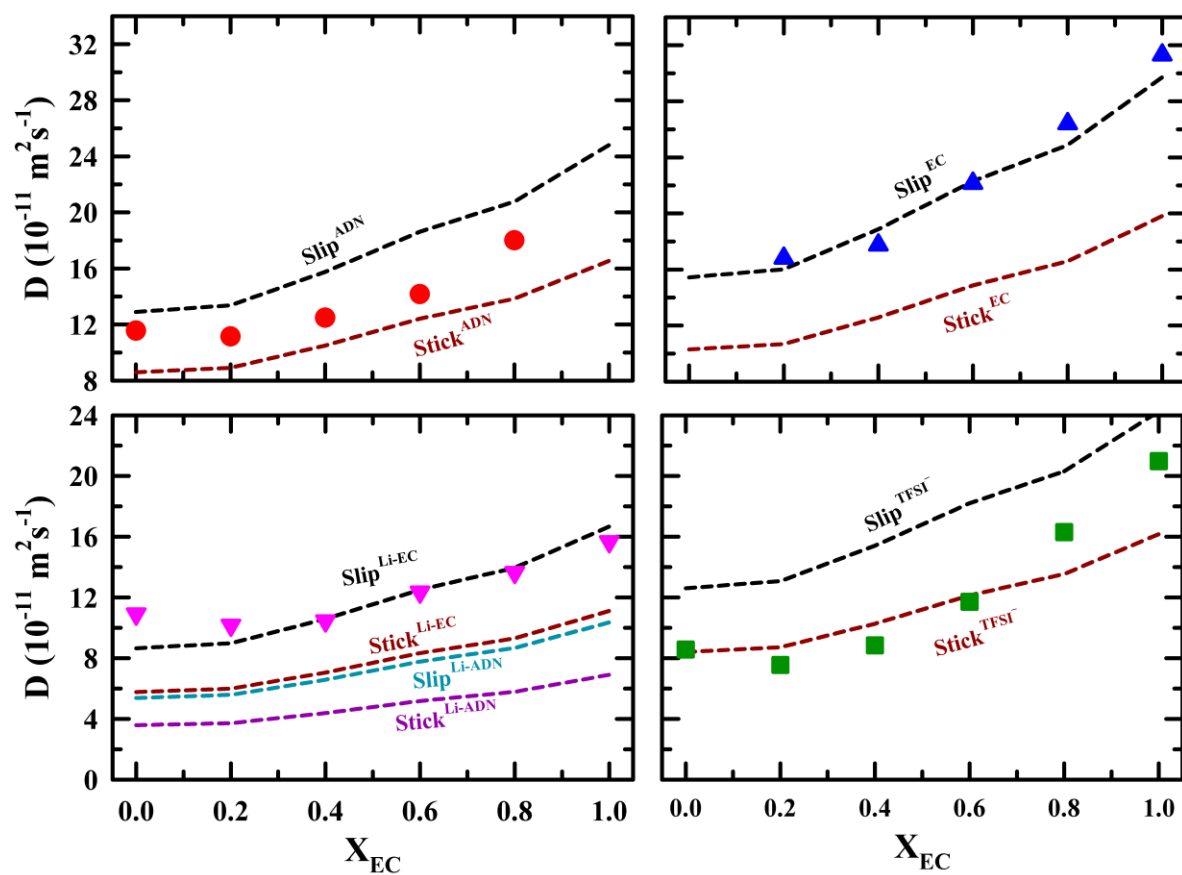
Figure A8.22: EC mole fraction dependent self-diffusion coefficient of ADN (red), EC (blue), Li$^+$ (pink) and TFSI$^-$ (green) in 1M LiTFSI in xEC+(1-x)ADN electrolyte solutions at 323 K. Calculated stick and slip lines from SE relation are presented by dashed lines. All representations are colour-coded.
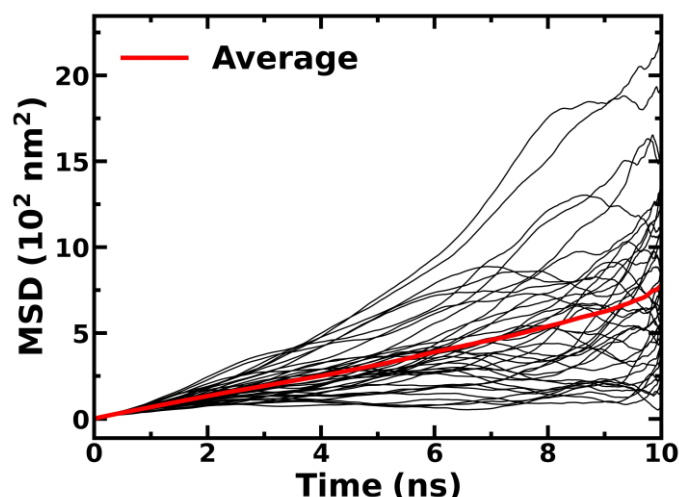
Figure A8.23: Collective mean squared displacements (MSD in general term) of all 40 trajectories are shown along with the average line (red line). Slope of the red line was used to calculate L++ for x=0.2 EC mole fraction at 323K temperature. Same procedure was applied to calculate all other Onsager transport coefficients for all mole fractions of EC.

Table A8.24: Temperature and EC concentration dependent viscosity coefficient (η) and conductivity (σ) of 1M LiTFSI in xEC+(1-x)ADN electrolyte solutions.

x	σ_{self}^{+} (mS/cm)	σ_{self}^{-} (mS/cm)	$\sigma_{distinct}^{++}$ (mS/cm)	$\sigma_{distinct}^{--}$ (mS/cm)	$-2\sigma^{+-}$ (mS/cm)	σ_{Total} (mS/cm)	σ_{NE} (mS/cm)	σ_{EXPT} (mS/cm)
0.0	3.77 (0.96)	2.79 (0.96)	-0.49 (0.96)	-1.84 (1.03)	0.36 (0.95)	4.59	6.56	4.77
0.2	3.45 (0.96)	2.62 (0.97)	-0.33 (0.96)	-0.98 (0.98)	0.30 (0.98)	5.06	6.07	5.39
0.4	3.44 (0.96)	2.96 (0.97)	-0.32 (0.97)	-1.31 (0.99)	0.53 (0.99)	5.30	6.40	6.29
0.6	3.78 (0.97)	3.68 (0.97)	-0.50 (0.97)	-1.38 (0.96)	0.52 (0.99)	6.10	7.46	7.10
0.8	4.10 (0.97)	4.27 (0.96)	-0.80 (0.97)	-1.54 (0.97)	0.56 (1.01)	6.59	8.37	8.41
1.0	4.60 (0.98)	5.29 (0.96)	-0.66 (0.97)	-1.84 (0.97)	0.66 (0.99)	8.05	9.89	10.03

The value written in the parenthesis is represent β value for respective conductivities calculation.

Reference

1   D. Deng, *Energy Sci. Eng.*, 2015, **3**, 385–418.

2   F. Arshad, J. Lin, N. Manurkar, E. Fan, A. Ahmad, M. N. Tariq, F. Wu, R. Chen and L. Li, *Resour. Conserv. Recycl.*, 2022, **180**, 106164.

3   K. Xu, *Chem. Rev.*, 2014, **114**, 11503–11618.

4   P. Simon and Y. Gogotsi, *Nat. Materials*, 2008, **7**, 845–854.

5   J. M. Tarascon and M. Armand, *Nature* , 2001, **414**, 359–367.

6   M. Armand and J.-M. Tarascon, *Nature*, 2008, **451**, 652–657.

7   N. von Aspern, G. V. Röschenthaler, M. Winter and I. Cekic-Laskovic, *Angew. Chem., Int. Ed.*, 2019, **58**, 15978–16000.

8   Y. Abu-Lebdeh and I. Davidson, *J. Electrochem. Soc.*, 2009, **156**, A60.

9   PubChem. Adiponitrile. https://pubchem.ncbi.nlm.nih.gov/ compound/8128 (accessed Apr 1, 2021)., (accessed 31 May 2023).

10   S. Tobishima, M. Arakawa, T. Hirai and J. Yamaki, *J. Power Sources*, 1989, **26**, 449–454.

11   J. Neuhaus, E. Forte, E. von Harbou and H. Hasse, *J. Power Sources*, 2018, **398**, 215–223.

12   K. M. Kim and S. Kim, *Bull. Korean. Chem. Soc.*, 2015, **36**, 99–103.

13   D. Farhat, F. Ghamouss, J. Maibach, K. Edström and D. Lemordant, *ChemPhysChem*, 2017, **18**, 1333–1344.

14   C. J. Franko, C.-H. Yim, F. Årén, G. Åvall, P. S. Whitfield, P. Johansson, Y. A. Abu-Lebdeh and G. R. Goward, *J. Electrochem. Soc.*, 2020, **167**, 160532.

15   S. Li, D. Zhao, P. Wang, X. Cui and F. Tang, *Electrochim. Acta*, 2016, **222**, 668–677.

16   T. R. Kartha and B. S. Mallik, *J. Physi. Chem. B*, 2021, **125**, 7231–7240.

17   Y. Ugata, M. L. Thomas, T. Mandai, K. Ueno, K. Dokko and M. Watanabe, *Phys. Chem. Chem. Phys.*, 2019, **21**, 9759–9768.

18   A. Narayanan Kirshnamoorthy, K. Oldiges, M. Winter, A. Heuer, I. Cekic-Laskovic, C. Holm and J. Smiatek, *Phys. Chem. Chem. Phys.*, 2018, **20**, 25701–25715.

19   H. A. L. Rasidgazi, H. K. Kashyap and R. Biswas, *J. Chem. Sci.*, 2015, **127**, 61–70.

20   A. Das and R. Biswas, *J. Phys. Chem. B*, 2015, **119**, 10102–10113.

21   N. C. Maity, A. Baksi, K. Kumbhakar and R. Biswas, *J. Photochem. Photobiol. A: Chem.*, 2023, **439**, 114600.

22   A. Schönhals and F. Kremer, *Theory of Dielectric Relaxation*, Springer Berlin Heidelberg, 2003.

23   P. R. Bevington and. D. K. Robinson, *Data reduction and error analysis for the physical sciences*, McGraw-Hill Education, New York, 3rdEdition, 2003.

24   K. Mukherjee, A. Barman and R. Biswas, *J. Mol. Liq.*, 2016, **222**, 495–502.

25   C. J. F. Böttcher and P. Bordewijk, *Theory of Electric Polarization: Dielectrics in Time-dependent*, Elsevier, Amsterdam, 1978.

26   E. Lindhal, M. Abraham, B. Hess and D. van der Spoel, GROMACS 2021.4 Manual, https://doi. org/10.5281/ZENODO.5053220, https://zenodo.org/record/5053220.

27   S. V. Sambasivarao and O. Acevedo, *J. Chem. Theory Comput.*, 2009, **5**, 1038–1050.

28   B. Doherty, X. Zhong, S. Gathiaka, B. Li and O. Acevedo, *J. Chem. Theory Comput.*, 2017, **13**, 6131–6135.

29   L. S. Dodda, I. C. De Vaca, J. Tirado-Rives and W. L. Jorgensen, *Nucleic Acids Res.*, 2017, **45**, W331–W336.

30   W. L. Jorgensen and J. Tirado-Rives, *PNAS*, 2005, **102**, 6665-6670.

31   L. S. Dodda, J. Z. Vilseck, J. Tirado-Rives and W. L. Jorgensen, *J. Phys. Chem. B*, 2017, **121**, 3864–3870.

32   http://zarbi.chem.yale.edu/ligpargen/.

33   L. Martinez, R. Andrade, E. G. Birgin and J. M. Martínez, *J. Comput. Chem.*, 2009, **30**, 2157–2164.

34   G. Bussi, D. Donadio and M. Parrinello, *J. Chem. Phys.*, 2007, **126**, 14101.

35   M. Parrinello and A. Rahman, *J. Appl. Phys.*, 1998, **52**, 7182.

36   T. Darden, D. York and L. Pedersen, *J. Chem. Phys.*, 1998, **98**, 10089.

37   A. Aguado and P. A. Madden, *J. Chem. Phys.*, 2003, **119**, 7471.

38   B. Hess, H. Bekker, H. J. C. Berendsen and J. G. E. M. Fraaije, *J. Comput. Chem.*, 1997, **18**, 14631472.

39   M. P. Allen and D. J. Tildesley, *Computer Simulation of Liquids*, Clarendon, Oxford, 1987.

40   J.-P. Hansen and I. R. McDonald, *Theory of Simple Liquids*, Academic Press, 2006.

41   J.-P. Hansen and I. R. McDonald, *Theory of Simple Liquids With Applications to Soft Matter*, Elsevier, Fourth Edition., 2013.

42   J. G. Kirkwood, *J. Chem. Phys.*, 1939, **7**, 911–919.

43   M. Neumann, *J. Chem. Phys.*, 1986, **85**, 1567–1580.

44   A. Einstein, *Ann. Phys.*, 1905, **322**, 549–560.

45   K. D. Fong, H. K. Bergstrom, B. D. McCloskey and K. K. Mandadapu, *AIChE Journal*, 2020, **66**, e17091.

46   N. M. Vargas-Barbosa and B. Roling, *ChemElectroChem*, 2020, **7**, 367–385.

47   K. D. Fong, J. Self, B. D. McCloskey and K. A. Persson, *Macromolecules*, 2021, **54**, 2575–2591.

48   K. D. Fong, J. Self, B. D. McCloskey and K. A. Persson, *Macromolecules*, 2020, **53**, 9503–9512.

49   K. Xu, *Chem. Rev.*, 2004, **104**, 4303–4417.

50   ICSC   0211   -   Adiponitrile, http://www.ilo.org/dyn/icsc/showcard.display?p_card_id=0211&p_version=2&p_lang=en, (accessed 5 June 2023).

51   A. Abouimrane, P. S. Whitfield, S. Niketic and I. J. Davidson, *J. Power Sources*, 2007, **174**, 883–888.

52   F. N. Luiz, F. R. Scremin, E. Werncke, R. L. de O. Basso, E. Possan and P. R. S. Bittencourt, *Waste Biomass Valorization*, 2020, **11**, 367–373.

53   G. Petrella and A. Sacco, *J. Chem. Soc., Faraday Trans.*, 1978, **74**, 2070–2076.

54   F. Ghamouss, A. Brugere and J. Jacquemin, *J. Phys. Chem. C*, 2014, **118**, 14107–14123.

55   S. Seal, K. Doblhoff-Dier and J. Meyer, *J. Phys. Chem. B*, 2019, **123**, 9912–9921.

56   J. Sala, E. Gùrdia and J. Martí, *J. Chem. Phys.*, 2010, **132**, 214505-1.

57   A. Y. Zasetsky and I. M. Svishchev, *J. Chem. Phys.*, 2001, **115**, 1448–1454.

58   K. F. Rinne, S. Gekle and R. R. Netz, *J. Chem. Phys.*, 2014, **118**, 11667–11677.

59   A. Chandra and G. N. Patey, *J. Chem. Phys.*, 1994, **100**, 8385–8391.

60   A. Chandra, D. Wei and G. N. Patey, *J. Chem. Phys.*, 1993, **98**, 4959–4966.

61   S. Chowdhuri and A. Chandra, *J. Chem. Phys.*, 2001, **115**, 3732–3741.

62   J. Hubbard and L. Onsager, *J. Chem. Phys.*, 1977, **67**, 4850–4857.

63   P. G. Kusalik and G. N. Patey, *J. Chem. Phys.*, 1983, **79**, 4468–4474.

64   J. Barthel and R. Buchner, *Pure Appl. Chem.*, 1986, **58**, 1077–1090.

65   R. Buchner and G. Hefter, *Phys. Chem. Chem. Phys.*, 2009, **11**, 8984–8999.

66   K. Mukherjee, K. Kumbhakar and R. Biswas, *J. Mol. Liq.*, 2022, **360**, 119491.

67   A. Amico, G. Berchiesi, C. Cametti and A. Di Biasio, *J. Chem. Soc., Faraday Trans.2*, 1987, **83**, 619–626.

68   G. Berchiesi, *J. Mol. Liq.*, 1999, **83**, 271–282.

69   D. Maji and R. Biswas, *J. Chem. Phys.*, 2023, **158**, 174503.

70   S. Das, R. Biswas and B. Mukherjee, *J. Chem. Phys.*, 2016, **145**, 084504.

71   P. J. W. Debye, *Polar Molecules*, Chemical Catalog Company, Incorporated, 1929.

72   K. Kumbhakar, E. Tarif, K. Mukherjee and R. Biswas, *J. Mol. Liq.*, 2019, **290**, 111225.

73   K. Mukherjee, S. Das, E. Tarif, A. Barman and R. Biswas, *J. Chem. Phys.*, 2018, **149**, 124501.

74   K. Mukherjee, E. Tarif, A. Barman and R. Biswas, *Fluid Phase Equilib*, 2017, **448**, 22–29.

75   S. Indra and R. Biswas, *J. Phys. Chem. B*, 2016, **120**, 11214–11228.

76   E. Tarif, K. Mukherjee, A. Barman and R. Biswas, *J. Chem. Sci.*, 2019, **131**, 1–12.

77   E. Tarif, J. Mondal and R. Biswas, *J. Phys. Chem. B*, 2019, **123**, 9378–9387.

78   E. Tarif, K. Mukherjee, K. Kumbhakar, A. Barman and R. Biswas, *J. Chem. Phys.*, 2019, **151**, 154902.

79   M. D. Ediger, *Annu. Rev. Phys. Chem.*, 2000, **51**, 99–128.

80   M. D. Ediger, C. A. Angell and S. R. Nagel, *J. Phys. Chem.*, 1996, **100**, 13200–13212.

81   C. A. Angell, in *J. Chem. Phys.*, 1967, **46**, 4673–4679.

82   H. Sillescu, *J. Non-Cryst. Solids*, 1999, **243**, 81–108.

83   I. Chang, F. Fujara, B. Geil, G. Heuberger, T. Mangel and H. Sillescu, *J. Non-Cryst. Solids*, 1994, **172**, 248–255.

84   W. Huang and R. Richert, *Phil. Mag.*, 2007, **87**, 371–382.

85   Y. H. Zhao, M. H. Abraham and A. M. Zissimos, *J. Orga. Chem.*, 2003, **68**, 7368–7373.

86   K. Hayamizu, *J Chem Eng Data*, 2012, **57**, 2012–2017.

87   A. Sirjoosingh, S. Alavi and T. K. Woo, *J Phys Chem B*, 2009, **113**, 8103–8113.

88   M. H. Kowsari, S. Alavi, M. Ashrafizaadeh and B. Najafi, *J Chem Phys*, 2009, **130**, 14703.

89   G. Gachot, S. Grugeon, M. Armand, S. Pilard, P. Guenot, J.-M. Tarascon and S. Laruelle, *J Power Sources*, 2008, **178**, 409–421.

90   P. Kubisiak and A. Eilmes, *J Phys Chem B*, 2020, **124**, 9680–9689.

91   Biman Bagchi, *Molecular relaxation in liquids*, Oxford University Press, New York, 2012.

Chapter 9

Sol-Gel Transition of Hyaluronic Acid Leading to Organ Dysfunction: Exploring the Critical Concentration for Sol-Gel Transition, Structure and Dynamics of Organic Solutes in Aqueous Solutions of Hyaluronic Acid

9.1 Introduction

Hyaluronic acid (HA) aggregation and subsequent formation of high viscous stiffy material in various organs like lung, kidney, brain, muscle and liver is associated with the pathology of organ dysfunction or fibrosis.[1,2] HA is produced from fibroblasts, stellate cells, cancer associated fibroblasts, and fasciacytes.[3–5] HA level in organ or cell indicates the stage of organ dysfunction as well as detection of different stage of pathological conditions.[6–10] HA is present in extracellular matrix (ECM) of organs and involved in controlling cell growth, migration and differentiation.[11] However, HA aggregates, depending on molecular weights (MW) of the aggregated structures, can execute different and even opposite biological roles.[12] For example, high MW HA polymer ($\geq 10^6$ Da) can participate in gel formation, increasing the risk of tissue-stiffness mediated fibrosis.[1,13,14] This consideration itself highlights how critically important it is to determine the critical threshold concentration that promotes sol→gel transition of high MW HA polymer in aqueous solution.

HA, being biocompatible, non-toxic and non-immunogenic in nature,[11,15–18] has found extensive use in hydrogel preparation for medical applications.[4,5,11,18] Hydrogel is a three dimensional framework formed via cross-linking of polymer chains through covalent and non-covalent interaction and possesses high water retention property.[19] HA hydrogel-based bio-scaffold have found wide applications in a variety of medical treatment processes and in tissue engineering.[4,5,11,15,16,18,20] Two types of crosslinks are used for HA-hydrogel preparation. Physical crosslinking can be set in through agitation, change in pressure or temperature, whereas chemical crosslinking can be initiated via adding a foreign crosslinker to hydrogel scaffold. These chemical crosslinkers enhance the physical strength and biodegradability time,[21] although the added chemical crosslinker may increase the toxicity level of the

hydrogel.[22] Fortunately, HA possesses the ability to form hydrogel via both physical and chemical crosslinkings.[22–25]

Although structure, physical properties and dynamics of HA-based hydrogel were studied with or without chemical crosslinkers at higher HA concentration (≥1 wt%) systems[17,23,24,26–34], a systematic concentration dependent study of HA-water mixture are required to detect actual sol→gel transition point. We report such a study in this paper where the sol→gel transition was found to occur in aqueous solutions at ~ 0.5-0.65 wt% HA. Steady state and time-resolved fluorescence (TRF) lifetime measurements of Thioflavin-T (ThT) were used to track sol→gel transition via probing HA concentration dependent fluorescence intensity and excited state lifetime. HA concentration dependence TRF anisotropy of both solutes (C343 and C153) shows opposite trends in post-gel concentration indicates microenvironment around these two solutes is not same. Seeking completely different environment these hydrophilic C343 and hydrophobic C153 can be understood their functional group present on their ring framework. Morphological characteristics of HA sol or gel systems were conducted employing Cryo-SEM techniques. This revealed that sol→gel transition occurred in between 0.5 to 0.65 with appearing 3D polymer structures. With increasing HA, solvent volume in the polymer pocket decreases.

9.2. Experimental Details

9.2.1 Materials and Sample Preparation

Hyaluronic acid sodium salt (HA) from Streptococcaus equi (bacterial glycosaminoglycan polysaccharide), laser grade Thioflavin-T (ThT), Coumarin-343(C343), Coumarin 153 (C153), and water were purchased from Sigma-Aldrich. The chemical structure of HA, ThT, C343, and C153, are shown in Scheme A9.1.

Required amount of HA and water was weighing in glass container for sample preparation. The aqueous solution of HA (wt% of HA= 0, 0.15, 0.3, 0.5, 0.65, 0.75, 1, 1.5, 2) were prepared well mixing via shaking with shaker incubator at 250 rpm for 1hr. After shaking, samples were sonicated by ultra-sonic sonication for about 5 minutes for expelling air bubbles from the sample. All these experimental samples were prepared at room temperature and these were left one night for complete dissolution. A representative picture of before and after sample preparation are shown in Scheme 9.1. For UV-visible and fluorescence measurements of HA-

water mixtures were performed as follows: 2–3 μL of freshly prepared solutions of C153 in hexane (carrier solvent) was taken in a glass container. The carrier solvent was then evaporated off by gently blowing hot air around the outer surface of the container. Then sample preparation was carried out same as discussed before. In different measurements, water solution of ThT or C343 were directly added to sample mixtures. Proper care was taken to ensure the complete dissolution of all probe molecules. Approximately 2 mL of sample was then poured into the cuvette quartz with a 1 cm optical path length for optical measurement. Concentrations of ThT/C343/C153 in each of these samples were maintained at $\leq 10^{-5}$ M.
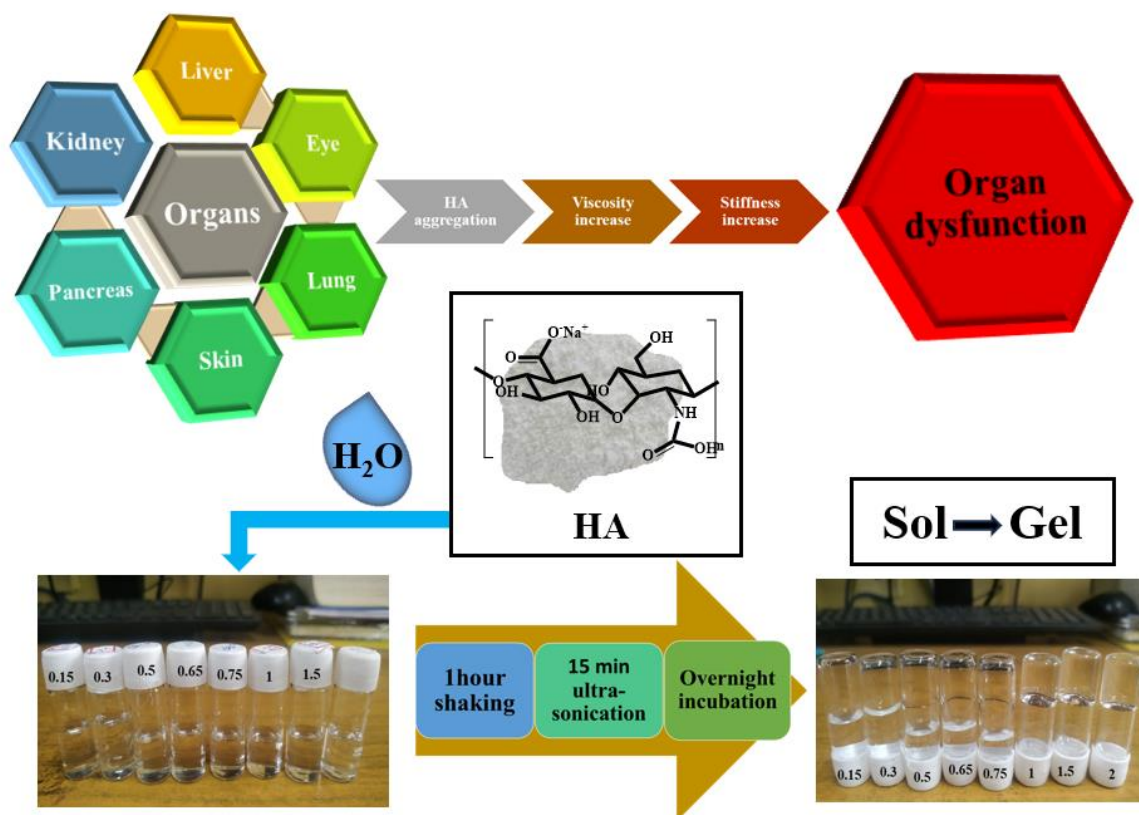
Scheme 9.1: Schematic diagram of HA aggregation related organ dysfunction and HA concentration dependent sol-gel preparation procedure for HA in water systems.

9.2.2 Refractive Index Measurements

Refractive index (n_D) was recorded using an automated temperature-controlled refractometer (RUDOLPH, J357).[35] Measured n_D values are summarized in Table A9.2 (Appendix).

9.2.3. Data Collection and Analysis for Absorption and Steady-State Fluorescence Emission Measurement

Steady-state UV-Visible absorption and fluorescence emission spectra of aqueous HA mixtures were recorded by using a UV-Visible spectrophotometer (UV-2600, Shimadzu) and a fluorimeter (Fluorolog, Jobin-Yvon, Horiba), respectively. Temperature was controlled by a Peltier temperature controller (accuracy ±0.5K). The solvent-blank subtracted spectra were processed accordingly before further analyses.[36,37] Detailed descriptions of the steady state UV-Vis absorption and steady state fluorescence techniques are the same as those discussed in Chapter 2.

9.2.4 Data Collection and Analysis for Time-Resolved Fluorescence Measurements

9.2.4.1 Streak Camera Measurements

In these measurements, the time-resolved fluorescence spectra were collected using a streak camera (Optoscope SC-10).[38] The laser pulse had a pulse duration of 150 fs and a repetition rate of 80 MHz, and the frequency-doubled light at 440 nm was generated by a BBO crystal from an 880 nm laser pulse. The sample of aqueous HA mixtures with C153 was placed in a 1 cm path length quartz cuvette, and the excitation was focused onto the sample after passing through a 440 nm interference filter. The emitted fluorescence was collected at a right angle with respect to the excitation and was then focused by two lenses onto the entrance slit of the monochromator with a slit width of 10 μm and a height of 4 mm. The fluorescence was then passed through a bandpass filter of 475 nm to eliminate scattering, and the fluorescence data was collected at magic angle (54.7°) polarization. The instrument response function (IRF) of the streak camera using scattering particles was recorded to be ~2.5 ps FWHM. All images were collected in 2000 acquisitions, keeping the MCP gain at 800 V and delay at 33.5% with a sweep speed of 15 ps/mm. All streak camera TRF measurements were performed at 293K. Details of the measurement protocol and data analysis are the same as those discussed in Chapter 2.

9.2.4.2 Rotational Anisotropy Measurements from TCSPC Measurements

Time-resolved fluorescence measurements were performed with a time-correlated single-photon counting (TCSPC) system (LifeSpec-ps) from Edinburgh Instruments (Livingston, U.K.).[39,40] We used a 409 nm diode laser and the full width at half-maximum (FWHM) of the

instrument response function (IRF) was ~87 ps. Temperature dependent measurements were performed by using a Julabo temperature controller (accuracy ±1 K). The TRF emission of all probes (C343, C153) in these experiments were collected at their steady state fluorescence emission maxima. The data collection and fluorescence anisotropy followed the procedures outlined in Chapter 2 and references.[40–44]

9.2.5 Cryogenic Scanning Electron Microscope Experiment

The samples are first mounted on a Cryo-SEM sample holder (stub) and then plunged into liquid N_2 bath. Once the sample stub was cooled down specimen was transferred to a slush chamber by a shuttle at low temperature and vacuum conditions. Immediately stub and shuttle were transferred to the prep chamber for cutting the surface of the samples. Then the sublimation was done on the sample's surface at -105°C for 30 min. After sublimation, sputtering was done on the sample to improve its conductivity. After the Sputtering, the imaging was performed by Zeiss Gemini 2 Scanning Electron microscope. During specimen observation, the cryo-stage in the SEM was cooled to −185 °C, and the anti-contamination aperture was cooled to −190 ° C. Secondary electron (SE) micrographs were recorded at an electron high tension (EHT) of 10 kV and a working distance of approximately 8 mm.

9.3 Results and Discussion

9.3.1 Concentration Dependent sol→gel Transition in Aqueous HA

HA concentrations dependent refractive index (RI) of HA-water mixtures are shown in Figure 9.1(a). The RI of HA-water mixture increases from pure water with HA concentration. This depicts that RI increases with increasing HA concentrations. But in between 0.65 to 1 wt% HA concentration, the RI of HA-water mixtures suddenly changes slop and increases linearly after this up to highest HA concentration. This indicates that sol→gel transition may occurred in between 0.65 to 0.75 wt% HA. The RI increment during sol→gel transition (by heat or UV light treatment) has been also observed in in various systems.[45,46] This point may correspond to HA concentration dependence 'sol→gel' transition in HA-water mixtures. In order to confirm this the above observation, next we will present Thioflavin-T (ThT) fluorescence emission measurements in these systems.
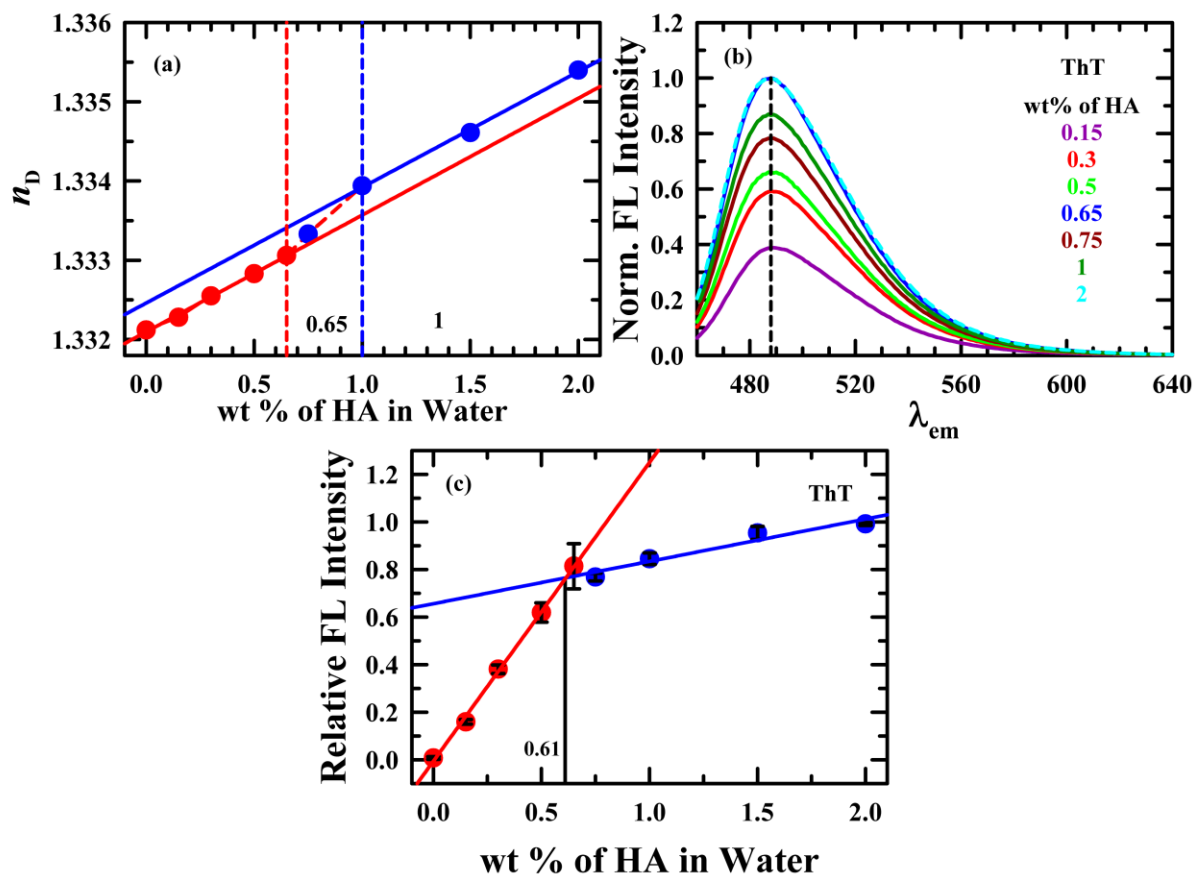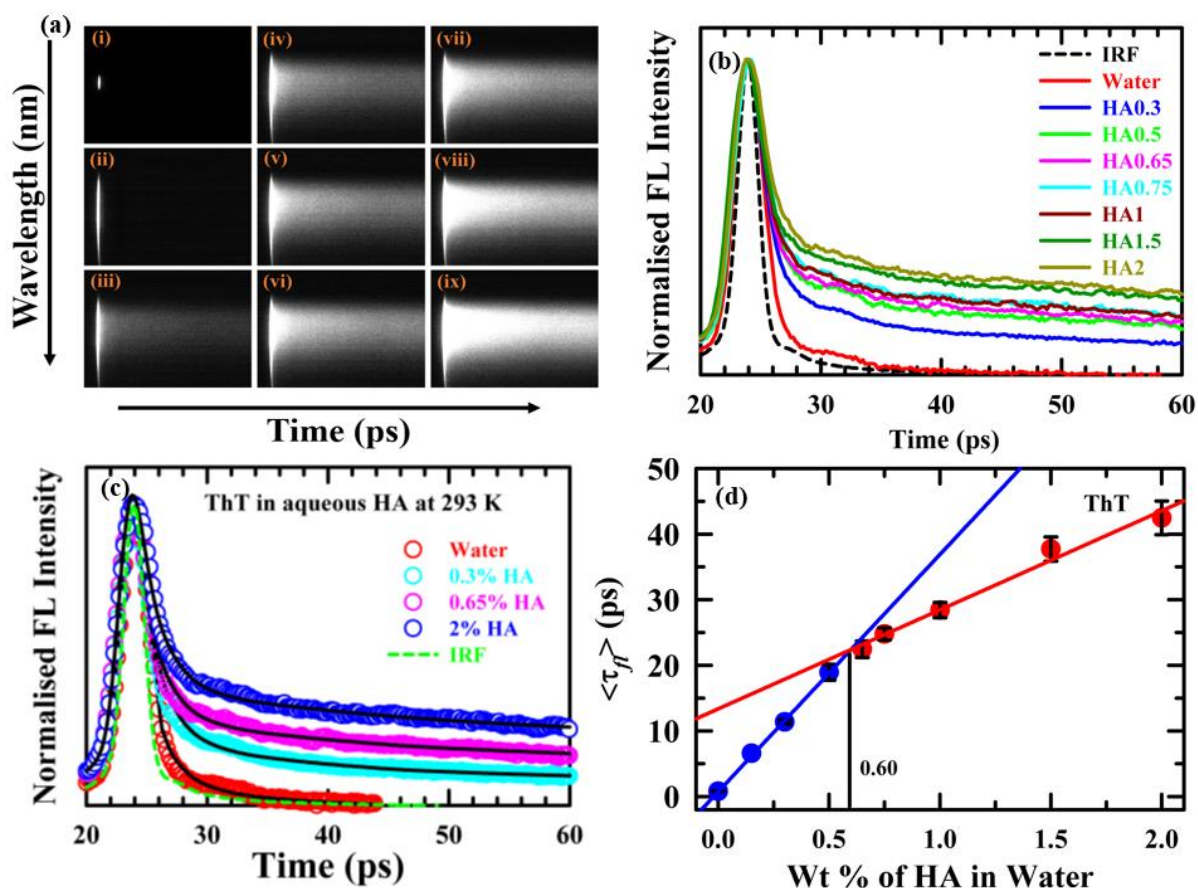
Figure 9.1: HA concentration dependent (a) refractive index (RI, n_D), (b) normalised steady-state fluorescence emission spectra of ThT with respect to highest HA coating system (2 wt%) and (c)corresponding relative emission intensity of ThT at 488 nm Note in water at 293 K is shown in Figure A9.3 (Appendix). Solid lines passing through experimental data are represent respective linear fit. All representations are colour-coded.

Normalised steady-state fluorescence spectra of ThT in with respect to steady state emission peak maxima at 2 wt% HA, in different HA wt% are presented in Figure 9.1(b). Figure 9.1(c) depicts HA concentrations dependent relative steady-state fluorescence intensity (I_{re}^{f}) of ThT with respect to 2 wt% HA system at 488 nm in aqueous HA mixtures. This illustrates that steady-state fluorescence intensity increases with increasing HA concentrations. This can be explained by the fact that restriction feels in torsional motion around the central c-c single bond of ThT. The steady state fluorescence intensity (I_{s}^{f}) depends non-linearly on radiative (K_r) and non-radiative (K_{nr}) rates through the relation[42], $I_{s}^{f} = \varphi_f I_0 (1 - 10^{-A})$, where φ_f denotes quantum yield with $\varphi_f = K_r/(K_r + K_{nr})$, I_0 and A are incident light intensity and absorbance

respectively. With increasing HA concentration, ThT molecule felt higher restriction in torsional rotation process in photo excited state. For this reason, K_{nr} decreases and φ_f increases with HA concentration. Since, I_s^f directly proportional to the φ_f of ThT molecule, I_s^f also increases with HA concentration. HA concentration dependent I_{re}^f increment was fitted with two distinct straight lines with different slopes. Interestingly, HA concentration dependent slope change in I_{re}^f increment around 0.61 wt% indicates HA aggregation assisted sol→gel transition in aqueous HA at 293 K. This reflects the threshold concentration for sol→gel aggregation in aqueous HA mixtures. Moreover, I_s^f is directly related to number of fluorophore molecules and average fluorescence lifetime of fluorophore ($\langle\tau_{fl}\rangle = 1/(K_r + K_{nr})$, $\varphi_f = \langle\tau_{fl}\rangle K_r$). Note, the number of fluorescent molecules were kept constant throughout the experiments. Following this next we will explore how sol→gel transition affects the exited state lifetime of this restriction sensitive fluorescent molecules.

Figure 9.2(a) represents streak images of instrument response function (IRF ~ 2 ps) and TRF emission of ThT in HA sol-gel systems along with neat water. This depicts that TRF emission intensity of ThT increases as well as lengthen with HA concentrations. TRF lifetime decays and IRF extracted from Figure 9.2(a) streak image are shown in Figure 9.2(b). Note that the lifetime decays of ThT are, irrespective of composition, well described by tri-exponential fit function and corresponding fitted spectra with few aqueous HA systems and neat water presented in inset of Figure 9.2(c). The average lifetime $\langle\tau_{fl}\rangle$ with standard deviation around data of ThT in these systems are shown in Figure 9.2(d). Inflection point estimated through two straight lines fitting along with different slop of $\langle\tau_{fl}\rangle$ enhancement suggests sol→gel occurred around 0.60 wt% HA concentration. Pattern observe in the slope change of $\langle\tau_{fl}\rangle$ increment in these HA-water mixtures is similar to that observed for I_{re}^f. Two steps $\langle\tau_{fl}\rangle$ enhancement of ThT observed with HA concentration. First step of $\langle\tau_{fl}\rangle$ enhancement of ThT is believed to be associated with restriction experiencing by gradual increase of molecular crowding. Second step of $\langle\tau_{fl}\rangle$ increment is assuming that ThT incorporated in gel near interface of polymer matrix and water. Because ThT molecule is positively charged and it preferentially interact with $-COO^-$ group of HA polymer backbone. Thus, ThT experience increasing friction due to self-aggregation of HA molecules, resulting enhancement in $\langle\tau_{fl}\rangle$.

Figure 9.2: HA concentration dependent (a) Two-dimensional streak camera image of (i) IRF and ThT TRF emission in (ii) water, (iii) 0.30 wt%, (iv) 0.50 wt%, (v) 0.65 wt%, (vi) 0.75 wt%, (vii) 1 wt%, (viii) 1.5 wt%, (ix) 2 wt% HA systems at 293 K. Horizontal axis represents time evolution (0 → 287 ps) of the fluorescence intensity, while the perpendicular axis denotes wavelength variation (455 → 600 nm) of the fluorescence emission at a given time. (b) TRF fluorescence lifetime spectra of ThT in aqueous HA systems along with neat water from two-dimensional streak camera experiments. (c) Representative TRF fluorescence lifetime spectra fitting of ThT in few aqueous HA systems along with neat water. (d) The average fluorescence lifetime ($\langle \tau_{fl} \rangle$) of ThT in aqueous HA at 293 K. Error bars in the different panel represent standard deviation obtained from 4-5 independent measurements. All representations are colour-coded.
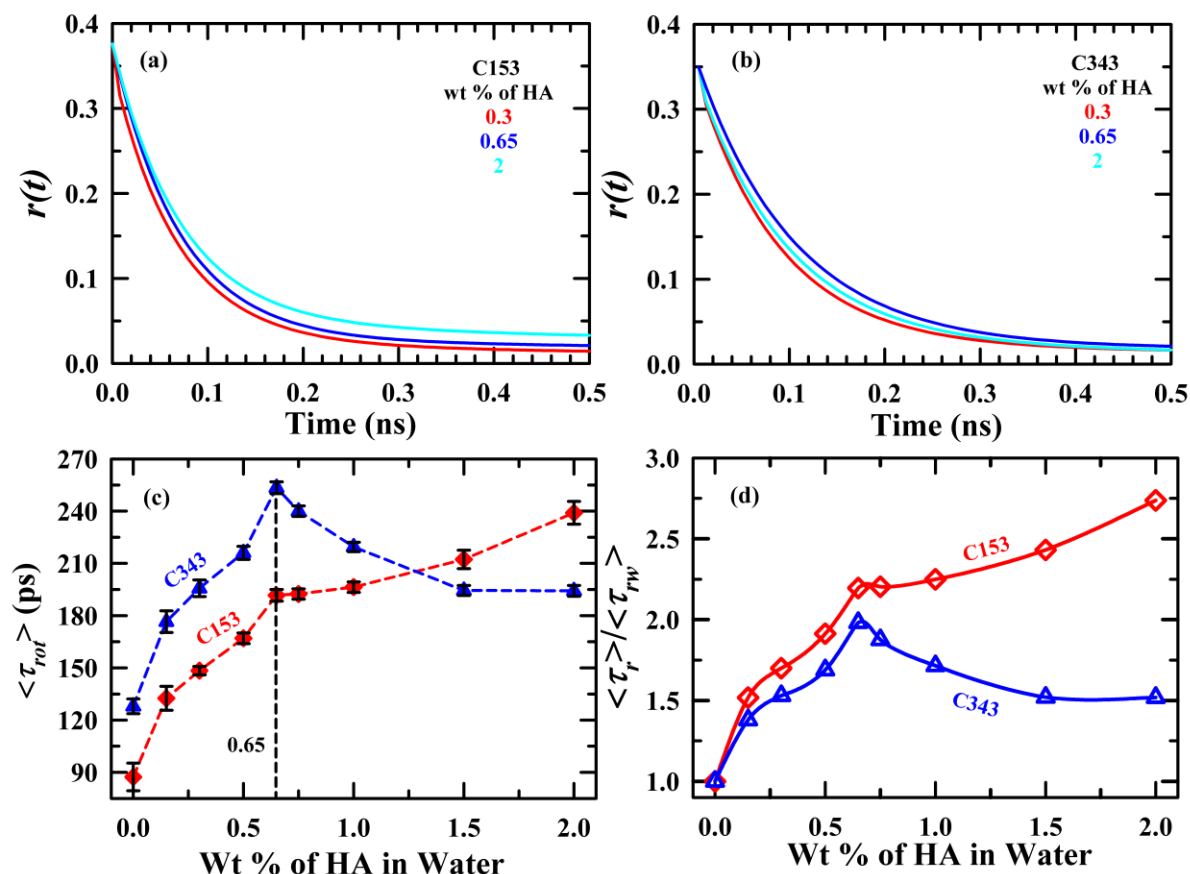
Figure 9.3: *r(t)* decay fit for (a) 153 and (b) C343 in 0, 0.65 and 2 wt% HA systems at 293 K. (c) The average rotation time ($\langle\tau_{rot}\rangle$) of C153 and C343 in in HA sol-gel systems along with neat water at 293 K. Error bars in the different panel represent standard deviation obtained from 4-5 independent measurements. (d) Ratio of *r(t)* between sample and water for both probe C153 and C343 in aqueous HA mixtures and neat water at 293 K. All representations are colour-coded.

Environment change due to sol→gel transition was further probed by two non-reactive fluorescent molecules with different chemical natures via time-resolved fluorescence anisotropy measurements. C153 being hydrophobic and C343 negatively charged, they locate in different local environments. This study reveals that, how rotational dynamics of external fluorescent molecules is influenced by the local environments in these sol-gel systems.[42] A representative parallel and perpendicular TRF intensity decays of C343 and C153 in 2 wt% aqueous HA gel at 293K are shown in Figure A9.4 (Appendix). TRF anisotropy (*r(t)*) decays for C343 and C153 in water and 2 wt% HA gel are shown in Figure A9.5 (Appendix). *r(t)* decay fits with few HA concentrations are represented for both probe C153 and C343 in Figure 9.3(a & b). HA concentrations dependent fit parameters of *r(t)* are summarised in Table A9.6

(Appendix). Mean average rotation time $\langle \tau_{rot} \rangle$ of C343 and C153 along with standard deviation are shown in Figure 9.3(c). This clearly depicts that $\langle \tau_{rot} \rangle$ follows same trend for both probes before gel formation. But beyond post gel transition two probes show different rotational dynamics. C343 shows strong non-monotonic dependence and reflects strict location dependence because of the charge. Note although both probes have nearly same size (V_{C343} = 243 Å^3 and V_{C153} = 246 Å^3)[47,48] but their chemical nature is responsible for different rotational diffusion characteristics beyond post gel transition. Hydrophobic C153 locates itself in hydrophobic region of gel (near the interface of polymer aggregate and water), whereas charged C343 preferentially reside in water like region. That can only happen when the C343 is relocating itself in encapsulated water within the size of the confinement. Order of magnitude change in the $\langle \tau_{rot} \rangle$ for both probe in these sol-gel systems with respect to water are shown inset of the Figure 9.3(d). That reveals that $\langle \tau_{rot} \rangle$ enhancement of C153 in sol or gel state from water system always larger than that of C343. This suggest that C153 strongly interact with HA molecule than C343. Before gel formation polymer chains (here HA polymer) are randomly spreads in solvent. At this phase probe molecules feel inhomogeneous friction with increasing polymer concentration. Beginning of sol→gel transition means cross linkage occurred due to esterification of carboxylate and hydroxyl groups of different chains or same chain. That leads to flexible disorder (sol) to rigid order (gel) structural transition in these media. In this state water is encapsulated in gel matrices and it behave like bulk water. Hydrophobic C153 prefers to reside in hydrophobic region in gel network. With increasing HA concentration, gel network is more rigid. For this reason, C153 experiences increasing friction with HA concentration in gel region. On the other hand, negative charge probe C343 loves more water like region. With increasing HA concentration, gel structure becomes more ordered and water encapsulated in hydrophobic core behaves like bulk water. After gel formation, C343 can explore more bulk like water, resulting the fastening of rotational dynamics.

9.3.2 Temperature Dependent ThT Fluorescence in 2% HA: Hydrogel Thermo-Reversibility

We have checked thermo-reversibility of HA gel at the highest HA containing (2 %) by employing temperature dependent fluorescence emission of restriction sensitivity probe ThT. Any restriction sensing in the cis to trans isomerization of ThT in the medium will increase the fluorescence intensity. Figure 9.4 left panel shows florescence emission spectra of ThT during heating (spectra with solid lie) and cooling (spectra with short dashed line) at few

representative temperatures in 2 wt% HA hydrogel. This indicates that fluorescence decreases with increasing temperature. As discussed earlier, fluorescence intensity or quantum yield depends on the radiative and non-radiative decay rate of the fluorophore and cis-trans isomerisation is a main factor for enhanced non-radiative rate. Medium viscosity as well as hydrogel rigidity decreases with temperatures and this will predominately enhance non radiative rate through reducing the restriction barrier between two rings of ThT molecules. During cooling, the phenomena reflect in the steady state fluorescence emission spectra of ThT in 2 wt% HA hydrogel is exactly opposite from heating phenomena. Earlier work has shown pH[49] or thermal[50] reversibility of hydrogel via fluorescence spectroscopy of fluorophores in gel. Temperature dependent normalised fluorescence intensities with the lowest temperature (283 K) value of ThT during heating and cooling are shown in Figure 9.4 (right panel). This depicts that fluorescence intensity in 2 wt% HA hydrogel during heating and cooling at a particular temperature remain same. This confirm that of HA hydrogel is a thermoreversible hydrogel.
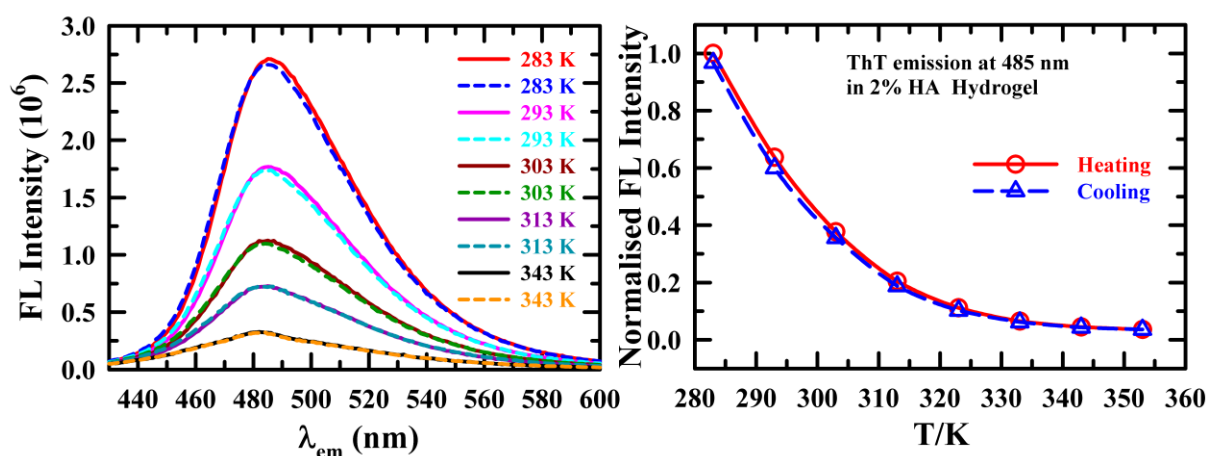
Figure 9.4: Temperature fluorescence emission spectra (left panel) and normalised fluorescence intensity with lowest temperature (283 K) value of ThT in 2% HA hydrogel. Heating (red) and colling (blue) cycle shown in same figure. All representations are color-coded.
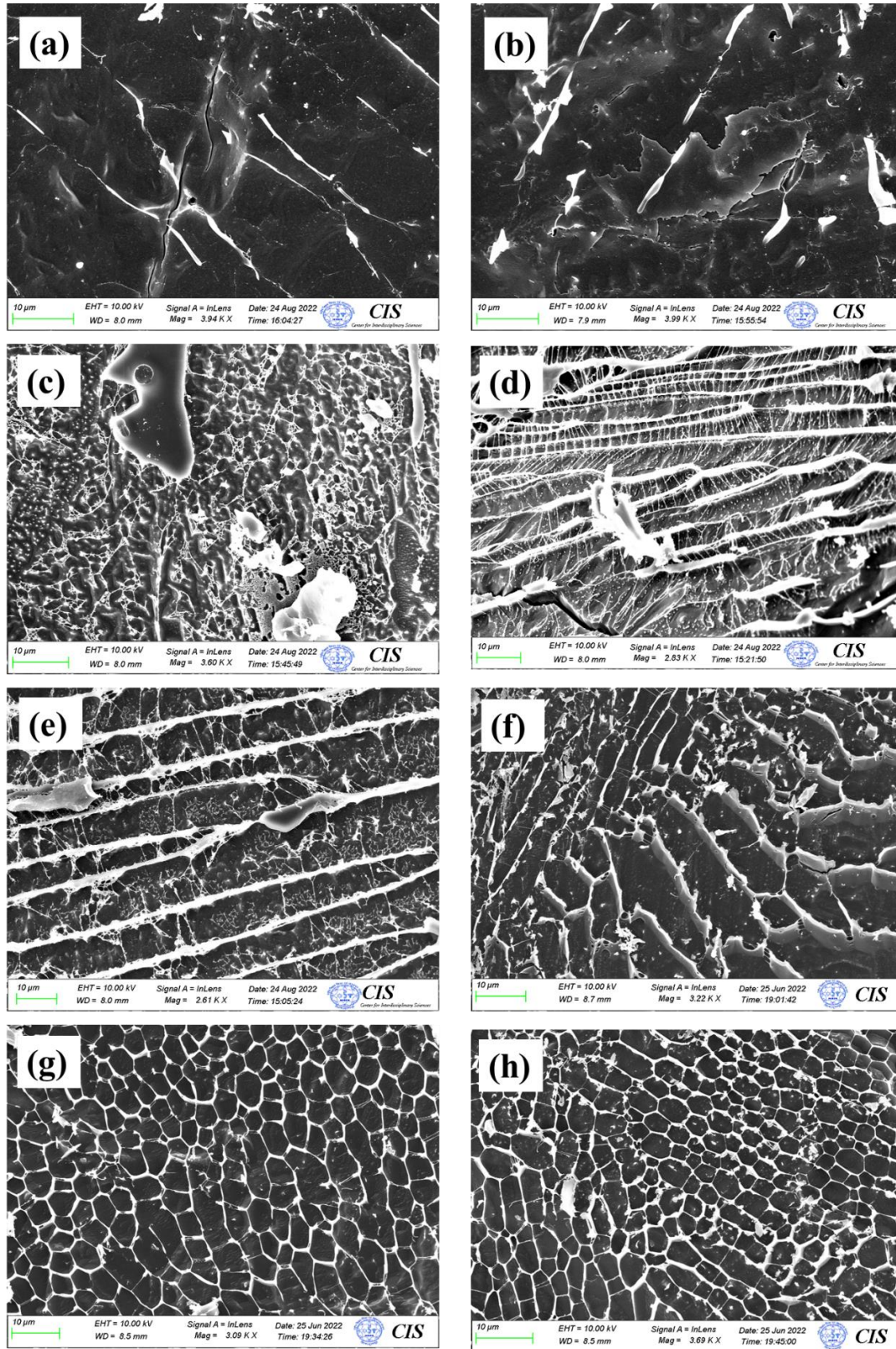
Figure 9.5: HA concentration dependent Cryo-SEM images of (a) 0.15 wt%, (b) 0.30 wt%, (c) 0.50 wt%, (d) 0.65 wt%, (e) 0.75 wt%, (f) 1 wt%, (g) 1.5 wt%, (h) 2 wt% HA in water.

9.3.3 Structural Morphology of HA Sol and Gel

The sol or gel structure in solution state of aqueous HA at various concentrations were examined via cryo-SEM technique. Figure 9.5(a-h) represents the HA concentration dependent cryo-SEM images of aqueous HA mixtures in sol or gel state. This depicts that ≤0.3 wt% HA systems show laminated[51] 2D structure. Interestingly, cryo-SEM image of 0.5 wt% HA shows initiation of 3D spider wave like small structure.[52,53] That confirms that 0.5 wt% HA in water is a threshold concentration for gel formation initiation. Again, 3D pattern gel structure was observed from 0.65 to 2 wt% HA containing systems. But HA concentrations dependent gel structure showed various type of aggregated patterns. 0.65 and 0.75 wt% HA polymer containing systems display fibrils like structure with huge solvent pocket and these fibrils are parallelly interconnected with each other by innumerable small fibres. Width of both fibrils and solvent pockets ranges ~0.4-2.8 μm and ~2-13 μm, respectively. Finally, 1 to 2 wt% HA gels appear wall like structure with finite void length and width. Polymer wall width in these 1 to 2 wt% HA gels ranges ~0.2-0.8 μm. Length and width of solvent pockets in 1 wt% HA gel spans in the range ~10-40 μm and ~2.5-13 μm, respectively. In contrast, 1.5 and 2 wt% HA gel produce honeycomb[25,51,54] like structure with pocket length and width ~9-18 μm and ~2.5-7 μm, respectively.

9.4 Conclusion

In summary, sol→gel critical point was observed in between 0.5 to 0.65 wt% of HA in water, as determined by refractive index, and Thioflavin-T fluorescence measurements. Temperature dependent ThT fluorescence emission studies in 2 wt% HA hydrogel indicated that HA hydrogels possess thermoreversible characteristics. TRF characteristics of organic solute with chemically attached different functional group (C343 and C153) in HA-water mixture exhibited opposite behaviour after sol→gel transition. This suggest that C343 and C153 probes located in completely different microenvironment within these hydrogels due to their difference in chemical nature. Morphological features of the aqueous HA mixture from Cryo-SEM images confirm that the sol→gel critical point lies between 0.5 and 0.65 wt% HA-water mixture. Aqueous HA gel shows different structural morphologies at various HA concentrations. These findings will be helpful in the remediation of organ dysfunction resulting from hyaluronic acid (HA) aggregation and application of drug molecules with different chemical properties.

Appendix A9

(a)

(b)

(c)

(d)

(e)
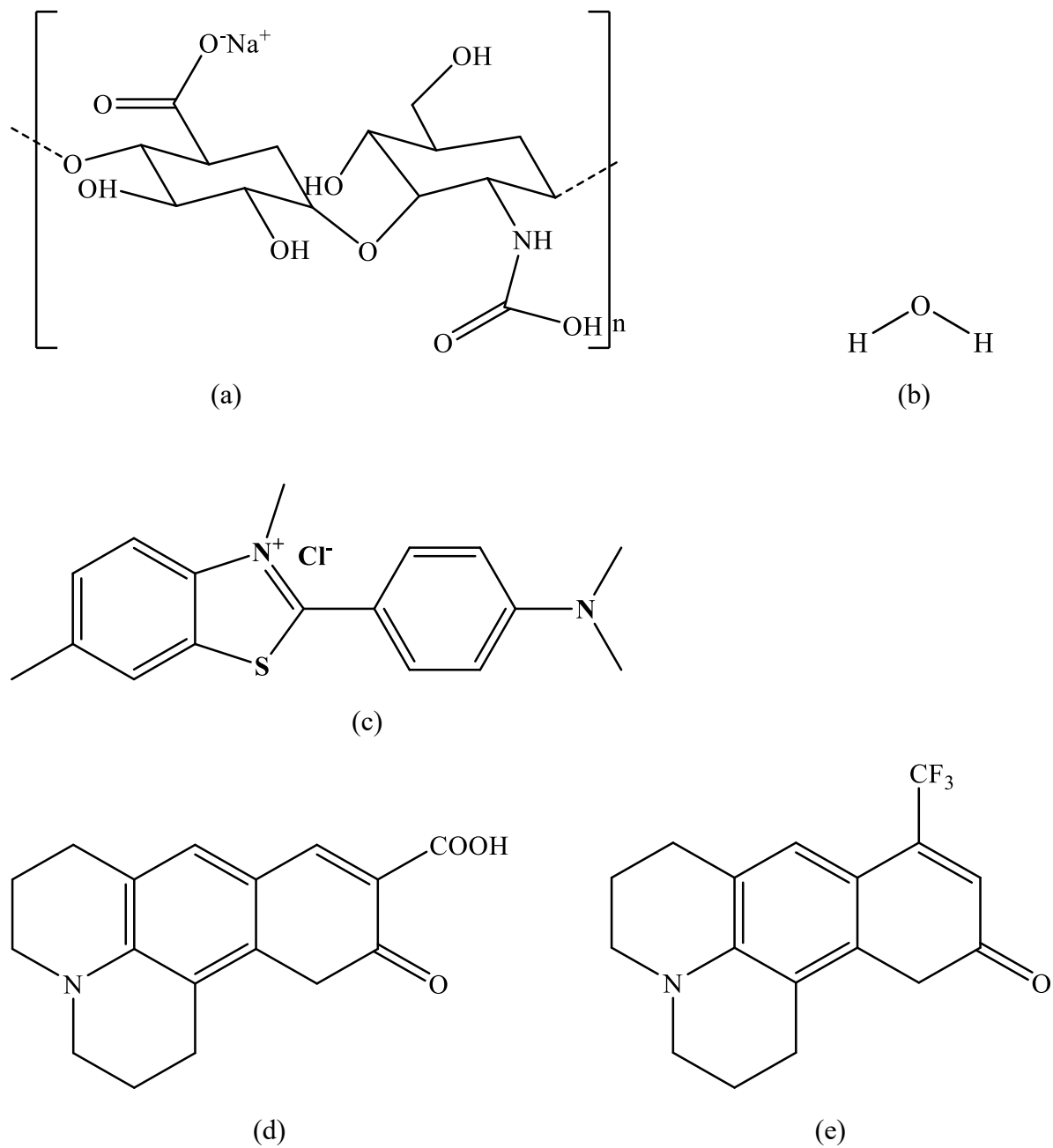
Scheme A9.1: Chemical structures of (a) Hyaluronic acid sodium salt (HA), (b) Water, (c) Thioflavin-T, (d) Coumarin 343, (e) Coumarin 153.

Table A9.2: HA concentration dependent refractive indices (RI, n_D)[a] of in aqueous HA mixtures at 293 K.

Cons. Of HA (wt%)	refractive indices (RI, n_D)
0.00	1.33212
0.15	1.33228
0.30	1.33255
0.50	1.33283
0.65	1.33306
0.75	1.33333
1.00	1.33394
1.50	1.33461
2.00	1.33540

[a]Standard uncertainty in RI (n_D) is 0.00002.
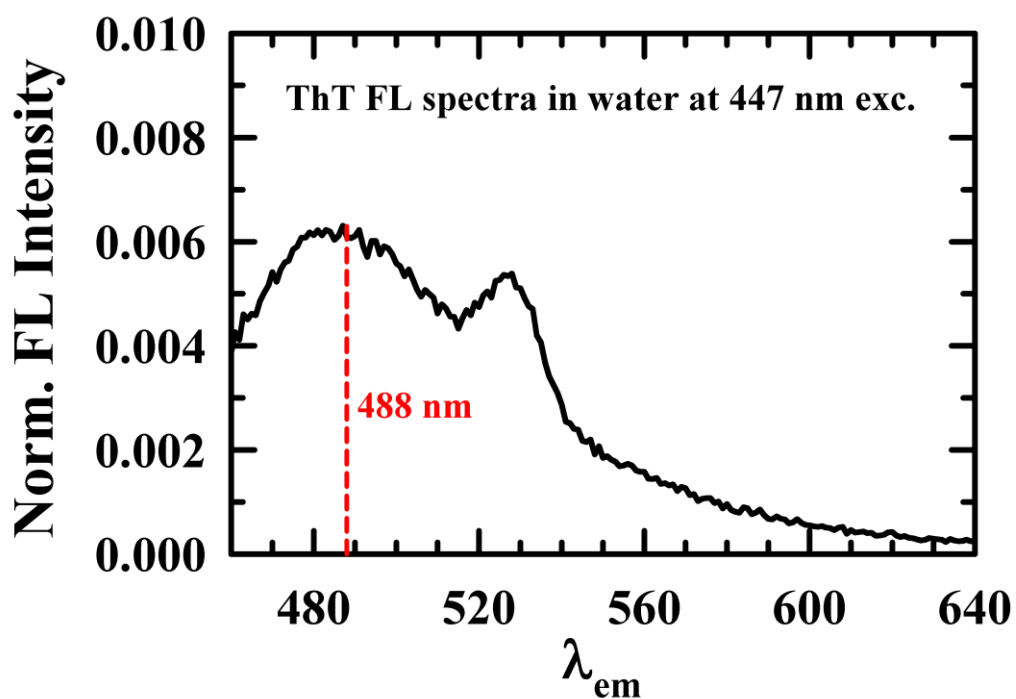
Figure A9.3: Normalised steady-state fluorescence emission spectra of ThT with respect to highest HA (2 wt%) gel system in water at 293K.
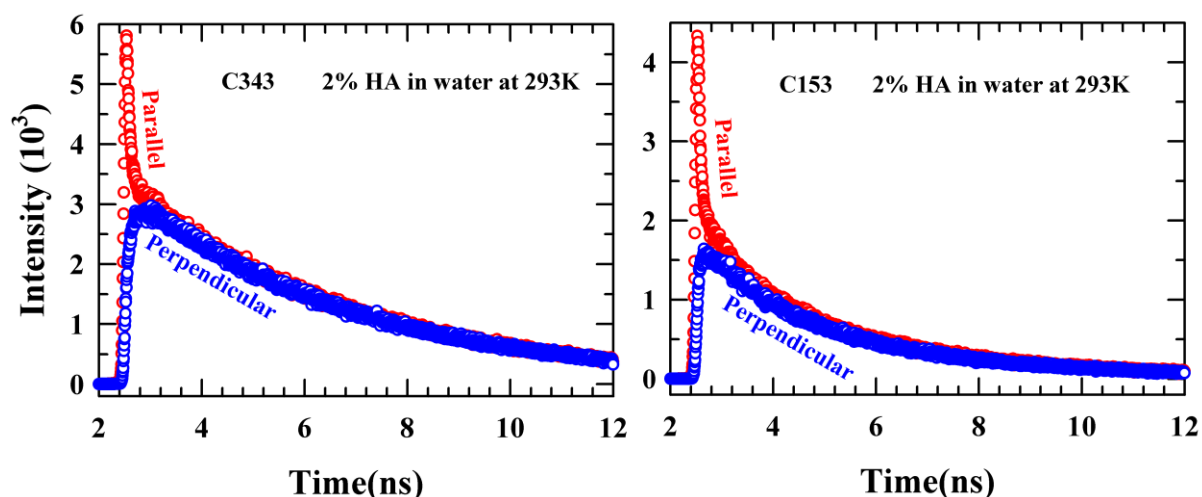
Figure A9.4: Representative parallel and perpendicular fluorescence intensity decay of C343 (left panel) and C153 (right panel) with two polarizations (parallel, 0^0, and perpendicular, 90^0) in 2 % HA-water mixture at 293K. All representations are color-coded.
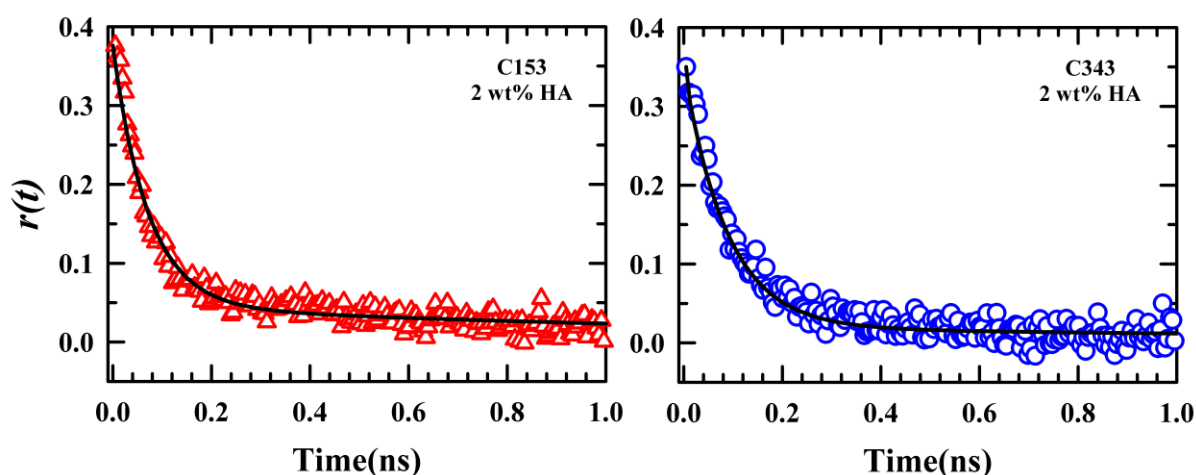
Figure A9.5: TRF anisotropy ($r(t)$) decay for C153 (left panel) and C343 (right panel) in 2 % HA-water mixture at 293 K. Experimental data are shown by circle. The solid lines passing through the data points depict the single/bi-exponential fits. All representations are colour-coded.

Table A9.6: HA concentration dependent fluorescence anisotropy decay ($r(t)$) fit parameters for both fluorophores (C153 and C343) in aqueous HA sol-gel systems at 293K.[b]

% of HA	$a_1(\%)$	τ_1/ps	$a_2(\%)$	τ_2/ps	$\langle \tau_{rot} \rangle$/ps
C343					
2	94	88	6	1923	192

1.5	94	85	6	1887	196
1	92	84	8	1852	220
0.75	92	97	8	1818	241
0.65	92	99	8	1961	249
0.5	92	85	8	1786	215
0.3	94	96	6	1754	200
0.15	94	88	6	1724	184
0	100	130	-	-	130
C153					
2	88	71	12	1494	244
1.5	91	64	9	1786	213
1	93	68	7	1887	197
0.75	93	64	7	1961	190
0.65	93	70	7	1754	193
0.5	78	55	22	578	169
0.3	87	80	13	604	149
0.15	88	72	12	685	143
0	100	80	-	-	80

[b]Individual amplitudes and time constants can be reproduced within ± 10-15% of the reported values.

Reference

1   A. Stecco, M. Cowman, N. Pirri, P. Raghavan and C. Pirri, *Bioengineering*, 2022, **9**, 159.

2   P. G. Pavan, A. Stecco, R. Stern and C. Stecco, *Curr. Pain Headache Rep.*, 2014, **18**, 1–8.

3   J. R. E. Fraser, T. C. Laurent and U. B. G. Laurent, *J. Intern. Med.*, 1997, **242**, 27–33.

4   M. N. Collins and C. Birkinshaw, *Carbohydr. Polym.*, 2013, **92**, 1262–1279.

5   A. Mero and M. Campisi, *Polymers*, 2014, **6**, 346–369.

6   M. G. Neuman, L. B. Cohen and R. M. Nanau, *Clin. Biochem.*, 2016, **49**, 302–315.

7   A. Suzuki, P. Angulo, J. Lymp, D. Li, S. Satomura and K. Lindor, *Liver Int.*, 2005, **25**, 779–786.

8   M. Majeed, F. McQueen, S. Yeoman and L. McLean, *Ann. Rheum. Dis.*, 2004, **63**, 1166–1168.

9   V. B. Lokeshwar, C. Öbek, H. T. Pham, D. Wei, M. J. Young, R. C. Duncan, M. S. Soloway and N. L. Block, *J. Urol.*, 2000, **163**, 348–356.

10   C. Peng, M. Wallwiener, A. Rudolph, K. Cük, U. Eilber, M. Celik, C. Modugno, A. Trumpp, J. Heil, F. Marmé, D. Madhavan, J. Nees, S. Riethdorf, S. Schott, C. Sohn, K. Pantel, A. Schneeweiss, J. Chang-Claude, R. Yang and B. Burwinkel, *Int. J. Cancer.*, 2016, **138**, 2499–2509.

11   M. Hemshekhar, R. M. Thushara, S. Chandranayaka, L. S. Sherman, K. Kemparaju and K. S. Girish, *Int. J. Biol. Macromol.*, 2016, **86**, 917–928.

12   A. G. Tavianatou, I. Caon, M. Franchi, Z. Piperigkou, D. Galesso and N. K. Karamanos, *FEBS J.*, 2019, **286**, 2883–2908.

13   A. M. Handorf, Y. Zhou, M. A. Halanski and W. J. Li, *Organogenesis*, 2015, **11**, 1–15.

14   N. L. Spartano, J. A. Augustine, W. K. Lefferts, W. E. Hughes, J. Garay Redmond, E. D. Martin, J. T. Kuvin, B. B. Gump and K. S. Heffernan, *Curr. Biomark. Find.*, 2014, **4**, 23-34.

15   R. James, G. Kesturu, G. Balian and A. B. Chhabra, *J. Hand Surg.*, 2008, **33**, 102–112.

16   K. S. Girish and K. Kemparaju, *Life Sci.*, 2007, **80**, 1921–1943.

17   B. P. Toole, *Nat. Rev. Cancer*, 2004, **4**, 528–539.

18   C. B. Highley, G. D. Prestwich and J. A. Burdick, *Curr. Opin. Biotechnol.*, 2016, **40**, 35–40.

19   E. Caló and V. V. Khutoryanskiy, *Eur. Polym. J.*, 2015, **65**, 252–267.

20   A. J. Day and C. A. de La Motte, *Trends Immunol.*, 2005, **26**, 637–643.

21   H. J. Chung and T. G. Park, *Nano Today*, 2009, **4**, 429–437.

22   X. Xu, A. K. Jha, D. A. Harrington, M. C. Farach-Carson and X. Jia, *Soft Matter*, 2012, **8**, 3280–3294.

23   J. Fujiwara, M. Takahashi, T. Hatakeyama and H. Hatakeyama, *Polym. Int.*, 2000, **49**, 1604–1608.

24   A. Panagopoulou, J. V. Molina, A. Kyritsis, M. M. Pradas, A. V. Lluch, G. G. Ferrer and P. Pissis, *Food Biophys.*, 2013, **8**, 192–202.

25   J. M. Silva Garcia, A. Panitch and S. Calve, *Acta Biomater.*, 2019, **84**, 169–179.

26   A. Jacobson, M. Rahmanian, K. Rubin and P. Heldin, *Int. J. Cancer*, 2002, **102**, 212–219.

27   T. C. Flynn, D. H. Thompson, S. H. Hyun and D. J. Howell, *Dermatol. Surg.*, 2015, **41**, S143–S152.

28   T. Vuletić, S. Dolanski Babić, T. Ivek, D. Grgičin, S. Tomić and R. Podgornik, *Phys. Rev. E*, 2010, **82**, 011922.

29   S. Kripotou, K. Zafeiris, M. Culebras-Martínez, G. Gallego Ferrer and A. Kyritsis, *Eur. Phys. J. E*, 2019, **42**, 1–18.

30   B. J. Kong, A. Kim and S. N. Park, *Carbohydr. Polym.*, 2016, **147**, 473–481.

31   R. Barbucci, R. Rappuoli, A. Borzacchiello and L. Ambrosio, *J. Biomater. Sci. Polym. Ed.*, 2012, **11**, 383–399.

32   I. Jacoboni, U. Valdrè, G. Mori, D. Quaglino and I. Pasquali-Ronchetti, *J. Struct. Biol.*, 1999, **126**, 52–58.

33   Y. Luo, K. R. Kirker and G. D. Prestwich, *J. Control. Release*, 2000, **69**, 169–184.

34   B. Tavsanli and O. Okay, *Carbohydr. Polym.*, 2020, **229**, 115458.

35   K. Mukherjee, A. Das, S. Choudhury, A. Barman and R. Biswas, *Journal of Physical Chemistry B*, 2015, **119**, 8063–8071.

36   T. Pradhan and R. Biswas, *J. Phys. Chem. A*, 2007, **111**, 11514–11523.

37   B. Guchhait and R. Biswas, *J. Chem. Phys.*, 2013, **138**, 114909.

38   J. Mondal, N. C. Maity and R. Biswas, *J. Chem. Sci.*, 2023, **135**, 1–12.

39   T. Pradhan, H. Al, R. Gazi, B. Guchhait and R. Biswas, *J. Chem. Sci*, 2012, **124**, 355–373.

40   M. L. Horng, J. A. Gardecki, A. Papazyan and M. Maroncelli, *J. Phys. Chem.*, 1995, **99**, 17311–17337.

41   N. Sarma, J. M. Borah, S. Mahiuddin, H. A. R. Gazi, B. Guchhait and R. Biswas, *J. Phys. Chem. B*, 2011, **115**, 9040–9049.

42   J. R. Lakowicz, *Principles of Fluorescence Spectroscopy*, Springer, New York, 3rd edn., 2006.

43 M. L. Horng, J. A. Gardecki and M. Maroncelli, *J. Phys. Chem. A*, 1997, **101**, 1030–1047.

44 S. Koley, H. Kaur and S. Ghosh, *Phys. Chem. Chem. Phys.*, 2014, **16**, 22352–22363.

45 A. Moujoud, Z. Saddiki, T. Touam and S. I. Najafi, *Thin Solid Films*, 2002, **422**, 161–165.

46 M. Langlet, M. Burgos, C. Coutier, C. Jimenez, C. Morant and M. Manso, *J. Sol-Gel Sci. Technol.*, 2001, **22**, 139–150.

47 G. B. Dutt and T. K. Ghanty, *J. Phys. Chem. B*, 2003, **107**, 3257–3264.

48 H. Jin, G. A. Baker, S. Arzhantsev, J. Dong and M. Maroncelli, *J. Phys. Chem. B*, 2007, **111**, 7291–7302.

49 S. Lu, S. Wang, J. Zhao, J. Sun and X. Yang, *Chem. Commun.*, 2018, **54**, 4621–4624.

50 H. Wang, W. Zhang, X. Dong and Y. Yang, *Talanta*, 2009, **77**, 1864–1868.

51 M. Yoshinobu, M. Morita, M. Higuchi and I. Sakata, *J. Appl. Polym. Sci.*, 1994, **53**, 1203–1209.

52 J. Li, S. Li, J. Huang, A. Q. Khan, B. An, X. Zhou, Z. Liu, M. Zhu, J. Li, S. Li, J. Huang, A. Q. Khan, Z. Liu, B. An, X. Zhou and M. Zhu, *Adv. Sci.*, 2022, **9**, 2103965.

53 Q. Wang, X. Pan, X. Wang, H. Gao, Y. Chen, L. Chen, Y. Ni, S. Cao and X. Ma, *Compos. B. Eng.*, 2020, **197**, 108187.

54 T. Walimbe, S. Calve, A. Panitch and M. P. Sivasankar, *Acta Biomater.*, 2019, **87**, 97–107.

Chapter 10

Concluding Remarks and Future Problems

10.1 Concluding Remarks

This thesis investigates structure and dynamics of both neat and multi-component media. This investigation is carried out by employing various experimental methods and techniques, such as, dielectric relaxation spectroscopy (DRS), steady-state UV-visible absorption and emission, as well as time-resolved fluorescence (TRF) with two-dimensional streak camera (2DSC) and time-correlated single-photon counting (TCSPC) based measurements. Additionally, the molecular-level structure and thermophysical or thermodynamic properties of these media have been comprehensively examined in this thesis. This thorough analysis has utilized computer-based molecular dynamics simulations, along with several other experimental measurements, for example, differential scanning calorimetry (DSC), dynamic light scattering (DLS), viscosity, refractive index and density measurements, and cryogenic transmission electron microscopy (cryo-TEM). This thesis focuses on various multi-component systems, including octanol-water mixtures within the octanol-rich region, cryoprotectant mixtures, lithium-ion battery (LIB) electrolyte solutions, and aqueous solutions of hyaluronic acid (HA). Each chapter of this Thesis contains separate and individual conclusion.

Rather than providing a single summarized conclusion, we briefly discuss here several interesting and relevant problems that could serve as avenues for future exploration.

10.2 Future Research Problems

10.2.1 Investigating the Impact of Co-Solvents on Ion Solvation and Dynamics in High-Performance Dinitrile-Based Li-Ion Battery Electrolyte Solutions: Experiments and Computer Simulations

High-performance Li-ion batteries (LBs) have become indispensable.[1] Enhancing the operational efficiency of Li-batteries involves strategies such as increasing energy storage

capacity and expanding the operating voltage window. However, challenges arise with the use of highly volatile organic alkyl carbonate solvents like ethylene carbonate (EC) and dimethyl carbonate (DMC). These solvents tend to decompose at electrode voltages, affecting the passive solid electrolyte surface (SEI), and exhibit higher melting points.[2,3] To eliminate solvent-related issues, alkyl carbonates are being used as co-solvent with alkyl dinitriles, such as acetonitrile (AN), succinonitrile (SN), glutaronitrile (GLN) and adiponitrile (ADN).[4,5] The incorporation of dinitriles addresses concerns related to electrical conductivity and viscosity in electrolyte solutions when combined with EC or DMC or polypropylene carbonate (PC). Lithium bis-(trifluoromethane sulfonyl) imide (LiTFSI) stands out as a widely utilized lithium salt in LBs, known for its efficacy in electrochemical lithiation, compatibility with graphite anodes, excellent thermal stability, and easily soluble in a wide variety of organic solvents.[6]

Recent investigations on ADN/EC/LiTFSI electrolyte, discussed in Chapter 8 of the current Thesis, have unveiled co-solvent-dependent solution structure and dynamics in these electrolyte solutions. Consequently, exploring the effects of co-solvents in various combinations of Li-based electrolyte solutions, while keeping the salt concentration constant, becomes a compelling avenue. Examples such as SN/EC/LiTFSI, GLN/EC/LiTFSI, GLN/PC/LiTFSI, ADN/PC/LiTFSI, ADN/DMC/LiTFSI, and others present opportunities for in-depth study using a combination of experimental and computer simulation techniques.

10.2.2 Exploring the Structure, Dynamics and Heterogeneity of Multi-Component Cryoprotectant Mixtures for Enhanced Bio-Cryopreservation Efficiency

Various sugars, sugar alcohols, and antifreeze proteins serve as crucial cryoprotectant agents (CPA) in cryogenic preservation.[7] The essential characteristics of CPAs include environmental friendliness, biocompatibility, biodegradability, low toxicity, natural occurrence, and ready availability. It is evident that the cryopreservation efficiency of mixtures of cryoprotectants surpasses that of individual cryoprotectant.[8,9] Some of the most effective cryoprotectant mixtures include glucose/glycerol[10] and trehalose/glycerol[11]. trehalose/ethylene glycol[12], glucose/ethylene glycol[13], sucrose/ethylene glycol[14], ethylene glycol/dimethyl sulfoxide[15]. Earlier investigations into trehalose/glycerol[16] and glucose/ethylene glycol binary mixtures, discussed in Chapter 5, Chapter 6, and Chapter 7 in the current Thesis, have delved into the structure, dynamics, and heterogeneity at various concentrations of multi-component cryoprotectant mixtures. Thus, exploring the structure, dynamics, and heterogeneity of these

systems, along with their relevance to bio-cryopreservation, presents an intriguing avenue. Examples such as xylitol/glycerol, trehalose/proline, proline/glycerol, and sucrose/proline, proline/glycerol/heparin are among the cryoprotectant mixtures that could be studied using various experimental and MD-simulation techniques.

10.2.3 Optimizing Rechargeable Lithium-Ion Battery Performance: Insights into the Structure and Dynamics of Advanced Gel-Polymer Electrolytes

Rechargeable lithium-ion batteries play a crucial role in powering electronic devices and electric vehicles today.[17,18] Gel-polymer electrolytes represent a blend of polymers and liquid electrolytes, forming a mixture where ion transfer occurs through an organic solution confined within the polymer network.[19] Polymeric substances such as polyethylene oxide (PEO), poly(vinylidene difluoride) (PVdF), polyvinyl chloride (PVC), polypropylene oxide (PPO), and polymethyl methacrylate (PMMA) are commonly employed in polymer gel electrolytes. These polymers are combined with organic solvents like ethylene carbonate (EC), dimethyl carbonate (DMC), propylene carbonate (PC), adiponitrile (ADN), glutaronitrile (GLN), and others. Investigating the influence of altering polymer concentrations, employing binary organic solvents while maintaining a constant polymer concentration, or modifying the polymer chain length through a combination of experimental and computer simulation approaches would be fascinating to observe, especially regarding their impact on solvent structure and mobility within polymer gel electrolyte systems.

10.2.4 Molecular-Level Investigation of Azeotropes: Exploring Intra and Interspecies Interactions, Structure, Dynamics, and Thermodynamic Properties for a Novel Azeotrope Definition

Azeotropes[20], multi-component mixtures that exhibit pseudo-compound behavior by boiling at a fixed temperature under specific pressure without changing compositions, find diverse applications in areas such as organic acid extraction, art restoration[21], and cleaning fluids[22]. Previous reports have identified approximately 450 binary and 150 ternary azeotropes in the presence of water.[23] However, the separation of individual components from azeotropes and their purification often necessitates expensive processes like pressure swing adsorption or distillation, or the addition of a chemically inert component known as an entrainer.[24–26]

Given these challenges, there is a critical need to investigate groups of azeotropes at azeotropic conditions to gain a molecular-level understanding of their intra and interspecies interactions. Such an exploration may reveal correlations in their structure, dynamics, and thermodynamic properties, paving the way for a new definition of azeotropes.

References

1   L. Lu, X. Han, J. Li, J. Hua and M. Ouyang, *J. Power Sources*, 2013, **226**, 272–288.

2   P. Isken, C. Dippel, R. Schmitz, R. W. Schmitz, M. Kunze, S. Passerini, M. Winter and A. Lex-Balducci, *Electrochim. Acta*, 2011, **56**, 7530–7535.

3   S. J. An, J. Li, C. Daniel, D. Mohanty, S. Nagpure and D. L. Wood, *Carbon N Y*, 2016, **105**, 52–76.

4   K. M. Kim and S. Kim, *Bull. Korean. Chem. Soc.*, 2015, **36**, 99–103.

5   M. Dahbi, F. Ghamouss, M. Anouti, D. Lemordant and F. Tran-Van, *J. Appl. Electrochem.*, 2013, **43**, 375–385.

6   N. von Aspern, G. V. Röschenthaler, M. Winter and I. Cekic-Laskovic, *Angew. Chem., Int. Ed.*, 2019, **58**, 15978–16000.

7   J. Donnez, B. Martinez-Madrid, P. Jadoul, A. Van Langendonckt, D. Demylle and M. M. Dolmans, *Hum. Reprod. Update*, 2006, **12**, 519–535.

8   S. Clark, N. M. Jomha and J. A. W. Elliott, *J. Phys. Chem. B*, 2022, **126**, 9566–9579.

9   N. Shardt, Z. Chen, S. C. Yuan, K. Wu, L. Laouar, N. M. Jomha and J. A. W. Elliott, *Cryobiology*, 2020, **92**, 180–188.

10   M. De, L. Reyes, L. Saenz, L. Lapierre, J. Crosby, C. Barros and M. De Los Reyes, *Vet. Rec.*, 2002, **151**, 477–480.

11   M. T. Cicerone and C. L. Soles, *Biophys. J.*, 2004, **86**, 3836–3845.

12   D. C. C. Brito, S. F. S. Domingues, A. P. R. Rodrigues, J. R. Figueiredo, R. R. Santos and J. C. Pieczarka, *Cryobiology*, 2018, **83**, 97–99.

13   L. L. Kuleshova, D. R. Macfarlane, A. O. Trounson and J. M. Shaw, *Cryobiology*, 1999, **38**, 119–130.

14   R. R. Santos, T. Tharasanit, J. R. Figueiredo, T. Van Haeften and R. Van Den Hurk, *Cell Tissue Res.*, 2006, **325**, 523–531.

15   A. M. da Silva, L. G. P. Bezerra, E. C. G. Praxedes, S. S. J. Moreira, C. M. P. de Souza, M. F. de Oliveira, A. F. Pereira, P. Comizzoli and A. R. Silva, *Cryobiology*, 2019, **91**, 53–60.

16   S. Indra and R. Biswas, *J. Phys. Chem. B*, 2016, **120**, 11214–11228.

17   M. Armand and J.-M. Tarascon, *Nature*, 2008, **451**, 652–657.

18   Y. C. Lu, Z. Xu, H. A. Gasteiger, S. Chen, K. Hamad-Schifferli and Y. Shao-Horn, *J. Am. Chem. Soc.*, 2010, **132**, 12170–12171.

19   W. K. Shin, J. Cho, A. G. Kannan, Y. S. Lee and D. W. Kim, *Sci. Rep.*, 2016, **6**, 1–10.

20   P. W. Atkins and J. de Paula, *Physical Chemistry*, Oxford University Press, 1994.

21   M. S. Carrison, The Room Temperature Evaporation Behavior of Purported Azeotropes Used as Cleaning Solutions in Art Conservation; Purdue University, 2014., (accessed 11 April 2023).

22   Kenyon W. G., *Trans. IMF*, 1996, **74**, 142–147.

23   L. H. Horsley, (Compiler). Azeotropic data II, Advances in Chemistry Series (35), 1962 ,The Dow Chemical Company, American Chemical Society, (accessed 11 April 2023).

24   J. P. Knapp and M. F. Doherty, *Ind. Eng. Chem. Res.*, 1992, **31**, 346–357.

25   Z. A. Abdel-Rahman, A. M. Mahmood and A. J. Ali, *Iraqi J. Chem. Pet. Eng.*, 2014, **15**, 1–7.

26   I. Rodríguez-Donis, V. Gerbaud and X. Joulia, *Ind. Eng. Chem. Res.*, 2001, **40**, 2729–2741.